REPORT DOCUMENTATION PAGE

Form Approved OMB NO. 0704-0188

1. REPORT DATE (DD-MM-YYYY)	2. REPORT TYPE	3. DATES COVERED (From - To)
27-06-2022	Final Report	21-May-2021 - 31-May-2022

4. TITLE AND SUBTITLE
Final Report: 21st Polymer Electrolyte Fuel Cells & Electrolyzers Symposium (PEFC&E21)

5a. CONTRACT NUMBER
W911NF-21-1-0261

5b. GRANT NUMBER

5c. PROGRAM ELEMENT NUMBER
611102

6. AUTHORS

5d. PROJECT NUMBER

5e. TASK NUMBER

5f. WORK UNIT NUMBER

7. PERFORMING ORGANIZATION NAMES AND ADDRESSES
The Electrochemical Society
65 South Main Street
Building D
Pennington, NJ 08534 -2839

8. PERFORMING ORGANIZATION REPORT NUMBER

9. SPONSORING/MONITORING AGENCY NAME(S) AND ADDRESS (ES)
U.S. Army Research Office
P.O. Box 12211
Research Triangle Park, NC 27709-2211

10. SPONSOR/MONITOR'S ACRONYM(S)
ARO

11. SPONSOR/MONITOR'S REPORT NUMBER(S)
78780-CH-CF.1

12. DISTRIBUTION AVAILIBILITY STATEMENT
Approved for public release; distribution is unlimited.

13. SUPPLEMENTARY NOTES
The views, opinions and/or findings contained in this report are those of the author(s) and should not contrued as an official Department of the Army position, policy or decision, unless so designated by other documentation.

14. ABSTRACT

15. SUBJECT TERMS

16. SECURITY CLASSIFICATION OF:			17. LIMITATION OF ABSTRACT	15. NUMBER OF PAGES	19a. NAME OF RESPONSIBLE PERSON
a. REPORT	b. ABSTRACT	c. THIS PAGE			Karen Swider-Lyons
UU	UU	UU	UU		19b. TELEPHONE NUMBER 703-403-5987

RPPR Final Report
as of 27-Jun-2022

Agency Code: 21XD

Proposal Number: 78780CHCF **Agreement Number: W911NF-21-1-0261**
INVESTIGATOR(S):

Name: Karen Swider-Lyons
Email: kswiderlyons@plugpower.com
Phone Number: 7034035987
Principal: Y

Organization: **The Electrochemical Society**
Address: 65 South Main Street, Pennington, NJ 085342839
Country: USA
DUNS Number: 067386755 EIN: 131771269

Report Date: 31-Aug-2022 Date Received: 27-Jun-2022
Final Report for Period Beginning 21-May-2021 and Ending 31-May-2022
Title: 21st Polymer Electrolyte Fuel Cells & Electrolyzers Symposium (PEFC&E21)
Begin Performance Period: 21-May-2021 **End Performance Period:** 31-May-2022
Report Term: 0-Other

Submitted By: Kellie Gilbert Email: development@electrochem.org
Phone: (609) 737-1902101

Distribution Statement: 1-Approved for public release; distribution is unlimited.

STEM Degrees: **STEM Participants:**

Major Goals: The 21st Polymer Electrolyte Fuel Cells & Electrolyzers (PEFC&E-21) symposium at the 240th Meeting of The Electrochemical Society (ECS) was held digitally from October 10-14, 2021.

PEFC&E-21 was devoted to all aspects of research, development, and engineering of polymer electrolyte fuel cells (PEFCs) and electrolysis systems. The symposium brought together the international community working on the subject to enable effective interactions between research and engineering communities.

The symposium had 6 sections covering: (a) Diagnostics/Characterization Methods, Membrane Electrode Design, (b) Cells, Stacks and Systems, (c) Cation-Exchange Membrane Performance & Durability, (d) Catalysts for Acidic Fuel Cells, (e) Materials for Alkaline Fuel Cells, and (f) Polymer-Electrolyte Electrolysis.

Accomplishments: Three hundred and fourteen talks were submitted to the PEFC&E-21 symposium. Of the submitted talks, 164 digital files were uploaded for viewing as part of the digital event. PEFC&E-21 also conducted a total of 19 live sessions over 5 days. A total of 38 papers were published in ECS Transactions (ECST) - Volume 104, Issue 8 (https://iopscience.iop.org/issue/1938-5862/104/8).

With the $5,000 in financial support from the Army Research Office, and $10,00 from the Office of Naval Research (ONR), the Electrochemical Society (ECS) provided 101 students with registration awards, giving them opportunity to present their work to the international community.

Training Opportunities: Nothing to Report

Results Dissemination: The proceedings from PEFC&E-21 were published in ECS Transactions (ECST) Volume 104, Issue 8 (https://iopscience.iop.org/issue/1938-5862/104/8). A total of 38 papers were published.

RPPR Final Report
as of 27-Jun-2022

Honors and Awards: The PEFC&E-21 Symposium presented 3 student poster awards to honor the work of promising young students.

First Place: “Oxygen Reduction Reaction Properties and Microstructure of Pt/Nb:SnO2 Model Catalysts Fabricated on Pt Single Crystal Surfaces”
Yoshihiro Chida, Graduate School on Environmental Studies, Tohoku University, Japan

Second Place: “Hydrogen Peroxide Generation and Hydrogen Oxidation Reaction Properties of Pt/Ir(111) and Ir/Pt (111) Bimetallic Surfaces”
Kenta Hayashi, Graduate School of Environmental Studies, Tohoku University, Japan

Third Place: “Molecular Dynamics Study of Proton Conductivity at an Interface between Nafion and Graphene Sheet”
Rikki Tanaka, Tohoku University Graduate School of Engineering, Japan

(https://www.electrochem.org/ecsnews/240th-ecs-meeting-pefce-best-poster-and-presentation-winners/)

Protocol Activity Status:

Technology Transfer: Nothing to Report

PARTICIPANTS:

Participant Type: PD/PI
Participant: Karen Swider-Lyons
Person Months Worked: 12.00 **Funding Support:**
Project Contribution:
National Academy Member: N

Partners

,

I certify that the information in the report is complete and accurate:
Signature: Kellie Gilbert
Signature Date: 6/27/22 1:23PM

Polymer Electrolyte Fuel Cells & Electrolyzers 21 (PEFC&E 21)

Editors:

F. N. Buechi
A. Kusoglu
B. S. Pivovar
C. A. Rice
H. Uchida
K. E. Ayers
D. R. Dekel
J. M. Fenton
H. Jia
D. J. Jones
Y. T. Kim
E. Kjeang
U. I. Kramm
B. Lakshmanan
R. A. Mantz
S. Mitsushima
W. Mustain
P. N. Pintauro
P. Strasser
K. Swider-Lyons
A. Z. Weber
H. Xu
I. V. Zenyuk

Sponsoring Divisions:

Energy Technology

Battery

Corrosion

Industrial Electrochemistry and Electrochemical Engineering

Physical and Analytical Electrochemistry

Published by
The Electrochemical Society
65 South Main Street, Building D
Pennington, NJ 08534-2839, USA
tel 609 737 1902
fax 609 737 2743
www.electrochem.org

ecstransactions™
Vol. 104, No. 8

Published by:

The Electrochemical Society
65 South Main Street
Pennington, New Jersey 08534-2839, USA

Telephone 609.737.1902
Fax 609.737.2743
e-mail: ecs@electrochem.org
Web: www.electrochem.org

ISSN 1938-6737 (online)
ISSN 1938-5862 (print)

ISBN 978-1-60768-930-0 (PDF)

Printed in the United States of America.

Preface

The papers included in this issue of *ECS Transactions* were originally presented in the symposium “Polymer Electrolyte Fuel Cells & Electrolyzers 21 (PEFC&E 21)”, held during the 240th meeting of The Electrochemical, from October 10-14, 2021.

***ECS Transactions*, Volume 104, Issue 8**
Polymer Electrolyte Fuel Cells & Electrolyzers 21 (PEFC&E 21)

Table of Contents

Chapter 3
Gas Diffusion Layer

Chapter 4
12 MPL & Imaging Methods

Chapter 5
Poster Session

Chapter 6
Catalyst Layer 1

Chapter 7
22 Catalyst Layer 2

Chapter 8
32 Cell Level Characterization

Chapter 11
Poster Session

Part C – Cation-Exchange Membrane Development, Performance, and Durability

Chapter 12
Poster Session

Chapter 13
Membrane Durability

Part D – Catalyst Activity/Durability for Hydrogen(-Reformate) Acidic Fuel Cells

Chapter 14
Non-PGM Catalysts 2

Chapter 15
Non-PGM Catalysts - Digital Session

Chapter 16
Poster Session

Chapter 17
Non-PGM Catalysts & Pt-Based Catalysts

Chapter 18
Pt-Based Catalysts and New Supports -Digital Session

Chapter 19
Pt-Based Catalyst Layers 2

Part E – Polymer-Electrolyte Electrolysis

Chapter 20
12 Electrolysis Modeling and Transport

Chapter 21
32 Electrolysis Electrocatalysis

Facts about ECS

The Electrochemical Society (ECS) is an international, nonprofit, scientific, educational organization advancing the theory and practice of electrochemistry and solid state science and technology, and allied subjects. The Society was founded in Philadelphia in 1902 and incorporated in 1930. There are currently over 8,000 members from around the globe representing 13 technical division and 23 geographical sections and a growing student membership program with over 100 student chapters. The Society is also supported by more than 2,000 corporations, government agencies, and academic institutions through institutional membership, corporate programs, and subscriptions.

The technical activities of the Society are carried on by divisions. Sections of the Society host symposia, programs, and events focused on their respective geographic regions. Major international meetings of the Society are held in the spring and fall of each year. At these meetings, the divisions and partnered organizations hold general sessions and sponsor symposia on specialized subjects.

The Society has an active publications program that includes the following:

Journal of The Electrochemical Society — (JES) is the flagship journal of The Electrochemical Society and the oldest peer-reviewed journal in its field. Since its founding in 1902, JES has evolved into one of the most highly cited and prestigious journals in electrochemistry and materials science with a cited half-life of greater than 10 years.

ECS Journal of Solid State Science and Technology — (JSS) is a peer-reviewed journal covering fundamental and applied areas of solid state science and technology, including experimental and theoretical aspects of the chemistry, and physics of materials and devices.

ECS Transactions (ECST) — is the official conference proceedings publication of The Electrochemistry Society — a high-quality venue for authors and an excellent resource for researchers. ECST offers the full-text content of proceedings from ECS meetings and ECS sponsored conferences.

The Electrochemical Society Interface — Interface is an authoritative yet accessible publication for those in the field of solid state and electrochemical science and technology. Published quarterly, this full-color magazine contains technical articles about the latest developments in the field, and presents news and information about the Society.

ECS Books Series — ECS books and monographs provide authoritative, detailed accounts of specific topics in electrochemistry and solid state science and technology. These titles are sponsored by ECS and published in cooperation with noted publishers such as John A. Wiley & Sons.

For more information on these publications and other Society activities, visit the ECS website:

www.electrochem.org

Chapter 1

Modeling

ECS Transactions, 104 (8) 3-26 (2021)
10.1149/10408.0003ecst ©The Electrochemical Society

Modeling of Fuel Cell Stack for High-Speed Computation and Implementation to Integrated System Model

S. Hasegawa [a, b], M Kimata [c], Y. Ikogi [b],
Miho Kageyama [a], Sanghong Kim [d] and M. Kawase [a]

[a] Department of Chemical Engineering, Kyoto University,
Kyotodaigaku-Katsura, Nishikyo-Ku, Kyoto 615-8510, Japan
[b] Commercial ZEV product development division, TOYOTA MOTOR CORPORATION,
1, Toyota-cho, Toyota, Aichi, 471-8571 Japan
[c] Measurement Instrumentation & Digital Development Innovation Div.,
TOYOTA MOTOR CORPORATION, 1, Toyota-cho, Toyota, Aichi, 471-8571 Japan
[d] Department of Applied Physics and Chemical Engineering, Tokyo University of
Agriculture and Technology, Tokyo 184-8588, JAPAN

Modeling methods for high-speed computation of fuel cell mass transport and polarization are investigated. To ensure dynamic numerical simulation of life-long system operation in permissible calculation time and accuracy. Physical and empirical models of mass transfer, heat transfer, and electrochemistry in fuel cell stack with proper resolution are developed and integrated. This model is validated and verified by comparison with the experimental data collected with commercial fuel cell system of a 2nd-generation MIRAI, a fuel cell electric vehicle (FCEV), in a variety of operating conditions, such as low to high loads, operating temperatures, and total pressures.

Introduction

Hydrogen energy is one of the most promising alternative energies to fossil fuels not only for transportation but also for stationary applications to increase energy efficiency and reduce emissions. To enhance utilization and distribution of hydrogen energy, fuel cell system manufactures are being required to apply their products to commercial applications such as trucks, buses, rail, marine, and stationary power generators, etc.

On the other hand, due to the complexity of the hardware and software configuration of fuel cell systems, significant effort and cost from fuel cell system manufacturers is required for the development of each commercial application. These costs stands as one of the largest barrier to entry to the fuel cell industry, as is shown in Fig. 1(a). The purpose of this research is to propose a state-of-art model-based development (MBD) process, where fuel cell system manufactures can work on virtual design and evaluation platforms and reduce such difficulties described above and as shown in Fig. 1(b).

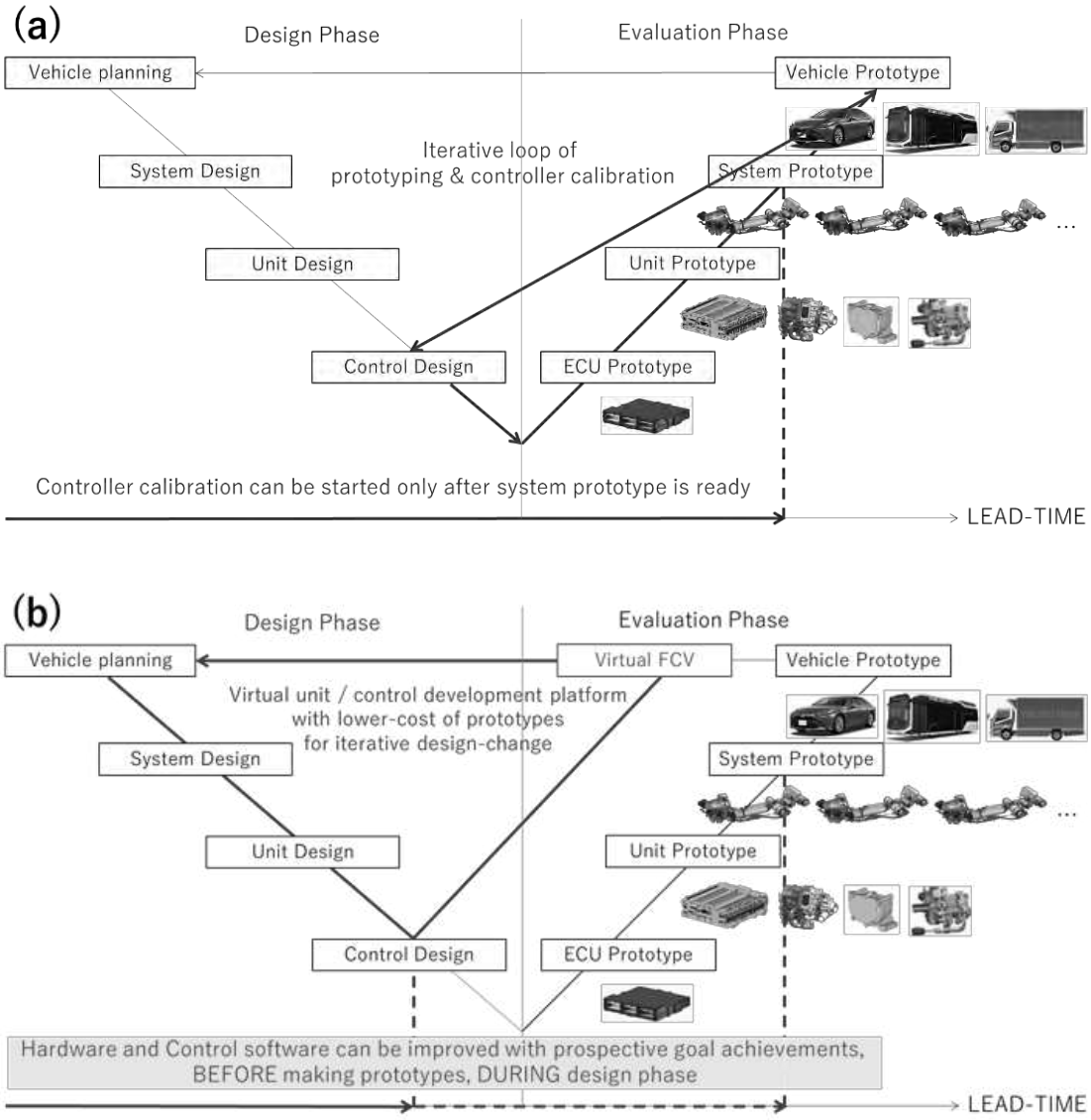

Fig. 1. Process chart of the FCEV-development,
(a) Before, and (b) after introduction of the physical model-based development

Modeling and implementation strategy

The physics and modeling methods implemented in the fuel cell stack model are listed in Table 1. The feature of the proposed models in this study is commented as 'This study' in the column of reference in this table.

Table 1. List of considered physics and modeling methods in the model

Category	Component	Physics	Modeling method	Eq.	Ref.
Mass-transport	Cell	In-plane distribution	Empirical weighting model of in-plane distribution	1–2, Fig. 2	This study
	GDL, MPL	Mass transport in through-plane directio	Maxwell–Stefan equation	3–5	1,2
		Gas diffusivity	Chapman–Enskog equation	6	1
			Knudsen diffusion equation	7–8	1,2
	CL	Mass transport from pore to catalyst surface	Mass transfer resistance model	9	8
		Humidity effect on mass transport	Empirical mass transport resistance function	10, Fig. 7	This study
			Limiting current density model	11	7
	PEM	Mass transport at polymer-gas boundary	Empirical discrete-first-order-lag model	12–15	This study
		Water diffusion	Fick's law	18–19	2
		Water uptake	Empirical water uptake function	Fig. 9(a)	2
		Water diffusivity	Empirical water diffusivity function	Fig. 9(b)	2
		Electro-osmotic drag	Water flux by electro-osmotic drag	20	2
			Empirical drag coefficient function	21	6
		Gas diffusion	Fick's law	25	7,8
		Gas diffusivity	Empirical gas diffusivity function	24	7,8
Polari-zation	Cell	Short-circuit current	Short circuit current model	32–33	This study
	CL	Open circuit voltage	Empirical function of standard Gibbs free energy	34	2
			Standard electrode potential	35	3
			Nernst equation	36–37	3
		Activation overpotential	Butler-Volmer equation	41,47	3
		Concentration overpotential	Butler-Volmer equation	42,48	3
		Catalyst utilization by H^+ limitation	Empirical catalyst utilization function	Fig. 12(b)	7
		Direct combustion reaction	Empirical direct-combustion reaction model	24–29	This study
	PEM	Proton conductivity	Empirical proton conductivity function	50, Fig. 13	2
	GDL, MPL	Ohmic overpotential	Ohmic law	51	2
		Electric resistance	Empirical electric resistance	51	This study

The role of the empirical weighting model in table 1 is to level the inlet and outlet state variables with a proper weighting ratio as is shown in Figs. 2 and 4. It is implemented for the reduction of the model dimension from 1+1D (in-plane + through-plane direction distribution), to 1D (in-plane direction distribution), for the reduction of computational load by iterative convergence calculation. The mass transfer resistance and limiting current density model describe the complicated catalyst layer structures in a simple expression defining the relationship between overall mass transfer resistances in catalyst layer and limiting current. The empirical mass transport resistance function of the catalyst layer is implemented to describe the impact of humidity on the mass transport resistance by gas permeability deterioration of the electrode ionomer in low humidity condition and the pore flooding in high humidity conditions in a simple empirical model without solving phase change and mass balance of water in the catalyst layer. The empirical discrete first order lag model of water transport in PEM is implemented to describe the water adsorption and desorption onto PEM by the simple empirical parameters of time-constants, which can be easily calibrated with the transient impedance data in dynamic operating conditions. The

short circuit current model and the direct-combustion model are implemented to describe the dynamic cell voltage response under zero to low current conditions accurately.

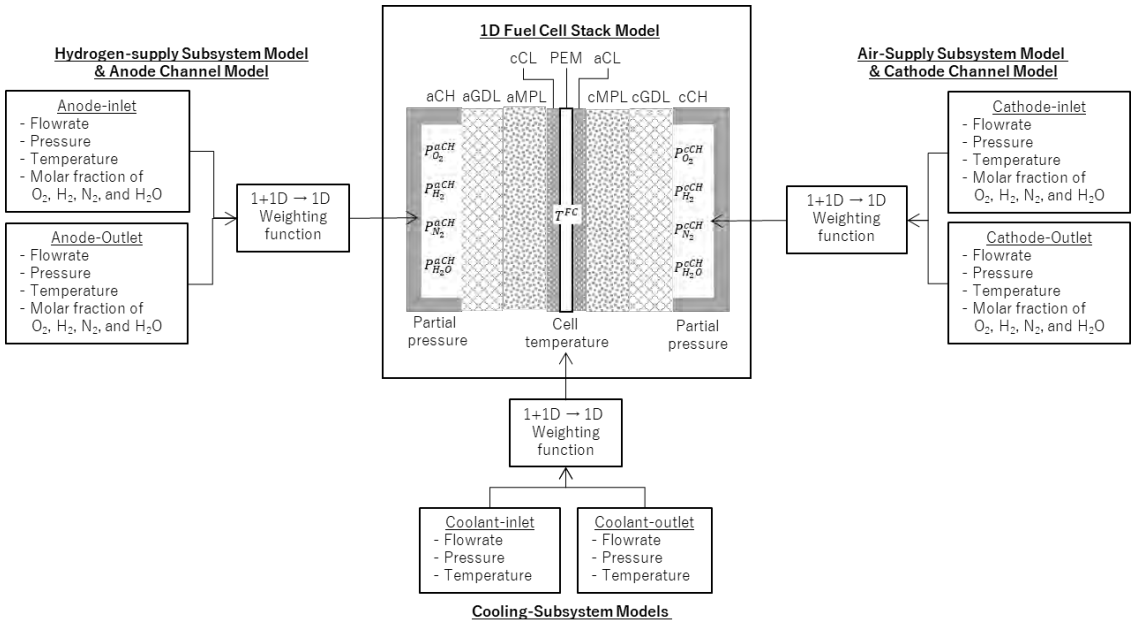

Fig. 2. Schematic drawing of model configuration

The other models were employed from the literature (1, 2, 3). The model parameters were collected from literature (4, 5, 6) and calibrated by the microscopic measurement results of geometrical structures as well as electrochemical test results measured in a variety of current, gas composition, humidity, and temperature conditions using small cells (7), as is shown in Fig. 3.

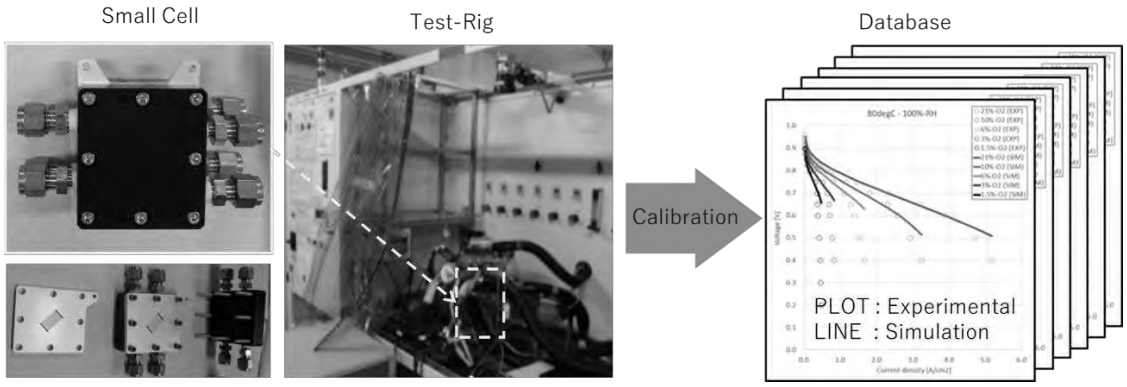

Fig. 3. The process of data collection with a small cell and parameter calibration

All the models are implemented on MATLAB® and SIMULINK® platform, where the dynamic simulation algorithms and the existing controller library can be implemented and integrated easily. The interface of the fuel cell stack model was designed so that it could be easily integrated with the balance-of-plants models such as air-supply, hydrogen-supply, and cooling sub-systems.

Model reduction of in-plane distribution

For a high-speed computation, the in-plane distribution in the channels were reduced. For total pressure, temperature, O_2, H_2, and N_2 partial pressure in the channels, inlet and outlet variables were represented as follows:

$$P_{\mathrm{tot}}^{\mathrm{CH}} = \frac{P_{\mathrm{tot}}^{\mathrm{CHin}} + P_{\mathrm{tot}}^{\mathrm{CHout}}}{2} \quad [1a]$$

$$T = \frac{T^{\mathrm{CHin}} + T^{\mathrm{CHout}}}{2} \quad [1b]$$

$$P_i^{\mathrm{CH}} = \frac{P_i^{\mathrm{CHin}} + P_i^{\mathrm{CHout}}}{2} \quad (i = \mathrm{O_2}, \mathrm{H_2}, \mathrm{N_2}, \text{and } \mathrm{H_2O}) \quad [1c]$$

where $P_{\mathrm{tot}}^{\mathrm{CH}}$, $P_{\mathrm{tot}}^{\mathrm{CHin}}$, and $P_{\mathrm{tot}}^{\mathrm{CHout}}$ are weighted, inlet, and outlet total pressure at the anode and cathode channels [Pa], T, T^{CHin}, and T^{CHout} are weighted, inlet, and outlet cell temperature, P_i^{CH}, P_i^{CHin}, and P_i^{CHout} are weighted, inlet, and outlet partial pressure [Pa] of gas component $\boldsymbol{i}$ ($i = \mathrm{O_2}, \mathrm{H_2}, \mathrm{N_2}, \text{and } \mathrm{H_2O}$) at anode and cathode channels.

To describe the internal moisture circulation effects inside the cell of the counter-flow geometry, as shown in Fig. 4(a), an additional weighting function is implemented. This weighting function corrects the relative humidity at the pore of anode catalyst layer using the anode inlet relative humidity as follows:

$$a_{\mathrm{H_2O}}^{\mathrm{aCLpore,corr}} = \eta a_{\mathrm{H_2O}}^{\mathrm{aCLpore}} + (1-\eta) a_{\mathrm{H_2O}}^{\mathrm{aCHin}} \quad [2]$$

where $a_{\mathrm{H_2O}}^{\mathrm{aCLpore,corr}}$ and $a_{\mathrm{H_2O}}^{\mathrm{aCLpore}}$ are the corrected and calculated relative humidity at the pore of anode catalyst layer, and $a_{\mathrm{H_2O}}^{\mathrm{aCHin}}$ is the relative humidity at the inlet of anode channel, and η is the weighting function [–]. Weighting function η in equation [2] is depicted in Fig. 4(b). This function enhances the through-plane water transport by increasing the difference in the relative humidity between the wet region around the cathode outlet and the dry region around the anode inlet. With such modeling methods, complex in-plane distribution can be described with simple empirical models and the computational load of the iterative calculations for the convergence of in-plane distribution can be eliminated.

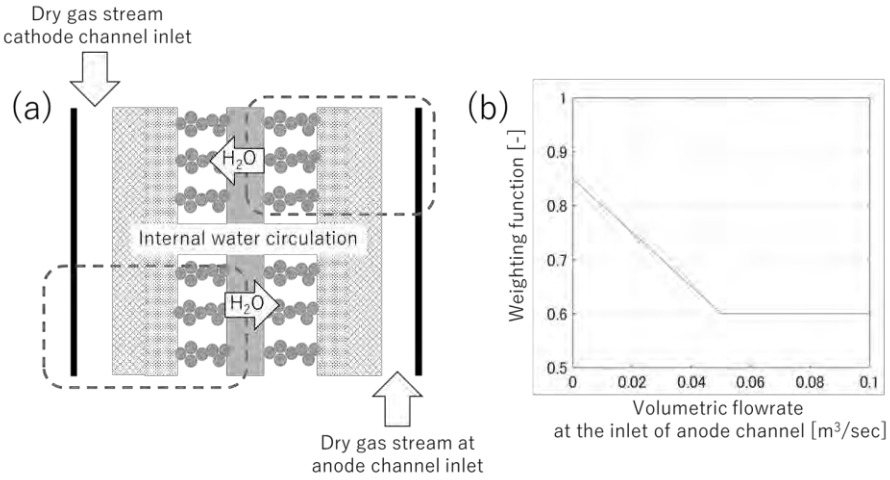

Fig. 4. (a) The internal moisture circulation effects inside the cell of the counter-flow geometry, (b) Weighting function of the relative humidity at the pore of anode catalyst layer.

Mass-transport models in through-plane direction of MEA

Fig. 5 shows the sandwich structure of a fuel cell in through-plane direction and the positions where state variables are defined. For anode and cathode GDLs, aGDL and cGDL, and MPLs, aMPL and cMPL, state variables are defined at the outer and inner surface. For anode and cathode catalyst layers, aCL and cCL, mass transport from the outer surface of CLs, aCLpore and cCLpore, to the surface of catalyst particles inside electrode ionomer, aCLion and cCLion, are modeled.

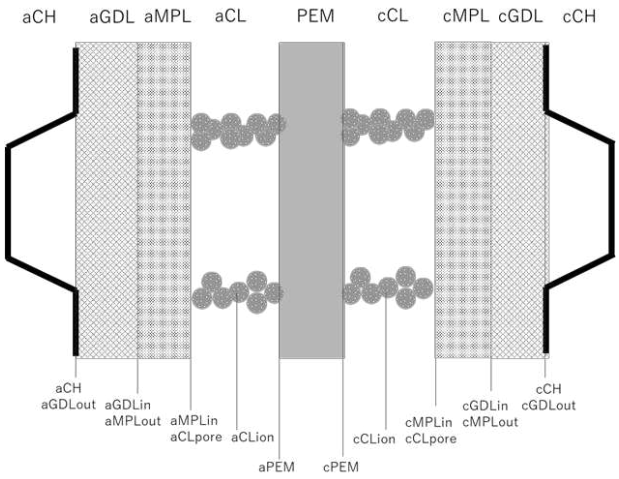

Fig. 5. Schematic drawing of the sandwich structure of a fuel cell and the positions where state variables are defined

***Gas diffusion layer* (*GDL*) *and micro porous layer* (*MPL*)**

Mass transport in porous media (GDLs and MPLs) considering Knudsen diffusion was modeled by Maxwell–Stefan equation as follows.

$$\nabla x_i = \sum_{j=1}^{N}\left[\frac{1}{C_{\mathrm{tot}}^{\mathrm{out}} D_{i-j}^{\mathrm{eff}}}\left(x_j^{\mathrm{out}} N_i - x_i^{\mathrm{out}} N_j\right)\right] - \frac{N_i}{D_{i,\mathrm{Knud}}^{\mathrm{eff}}} \quad (i,j = \mathrm{O_2}, \mathrm{H_2}, \mathrm{N_2}, \text{and } \mathrm{H_2O}) \qquad [3]$$

This equation is implemented by the following equations:

$$C_{\mathrm{O_2}}^{\mathrm{in}} = C_{\mathrm{O_2}}^{\mathrm{out}} + \delta\left(\frac{x_{\mathrm{O_2}}^{\mathrm{out}} N_{\mathrm{H_2}} - x_{\mathrm{H_2}}^{\mathrm{out}} N_{\mathrm{O_2}}}{D_{\mathrm{O_2-H_2}}^{\mathrm{eff}}} + \frac{x_{\mathrm{O_2}}^{\mathrm{out}} N_{\mathrm{N_2}} - x_{\mathrm{N_2}}^{\mathrm{out}} N_{\mathrm{O_2}}}{D_{\mathrm{O_2-N_2}}^{\mathrm{eff}}} + \frac{x_{\mathrm{O_2}}^{\mathrm{out}} N_{\mathrm{H_2O}} - x_{\mathrm{H_2O}}^{\mathrm{out}} N_{\mathrm{O_2}}}{D_{\mathrm{O_2-H_2O}}^{\mathrm{eff}}} - \frac{N_{\mathrm{O_2}}}{D_{\mathrm{O_2,Knud}}^{\mathrm{eff}}}\right) \qquad [4a]$$

$$C_{\mathrm{H_2}}^{\mathrm{in}} = C_{\mathrm{H_2}}^{\mathrm{out}} + \delta\left(\frac{x_{\mathrm{H_2}}^{\mathrm{out}} N_{\mathrm{O_2}} - x_{\mathrm{O_2}}^{\mathrm{out}} N_{\mathrm{H_2}}}{D_{\mathrm{O_2-H_2}}^{\mathrm{eff}}} + \frac{x_{\mathrm{H_2}}^{\mathrm{out}} N_{\mathrm{N_2}} - x_{\mathrm{N_2}}^{\mathrm{out}} N_{\mathrm{H_2}}}{D_{\mathrm{H_2-N_2}}^{\mathrm{eff}}} + \frac{x_{\mathrm{H_2}}^{\mathrm{out}} N_{\mathrm{H_2O}} - x_{\mathrm{H_2O}}^{\mathrm{out}} N_{\mathrm{H_2}}}{D_{\mathrm{H_2-H_2O}}^{\mathrm{eff}}} - \frac{N_{\mathrm{O_2}}}{D_{\mathrm{H_2,Knud}}^{\mathrm{eff}}}\right) \qquad [4a]$$

$$C_{\mathrm{N_2}}^{\mathrm{in}} = C_{\mathrm{N_2}}^{\mathrm{out}} + \delta\left(\frac{x_{\mathrm{N_2}}^{\mathrm{out}} N_{\mathrm{O_2}} - x_{\mathrm{O_2}}^{\mathrm{out}} N_{\mathrm{N_2}}}{D_{\mathrm{O_2-N_2}}^{\mathrm{eff}}} + \frac{x_{\mathrm{N_2}}^{\mathrm{out}} N_{\mathrm{H_2}} - x_{\mathrm{H_2}}^{\mathrm{out}} N_{\mathrm{N_2}}}{D_{\mathrm{H_2-N_2}}^{\mathrm{eff}}} + \frac{x_{\mathrm{N_2}}^{\mathrm{out}} N_{\mathrm{H_2O}} - x_{\mathrm{H_2O}}^{\mathrm{out}} N_{\mathrm{N_2}}}{D_{\mathrm{N_2-H_2O}}^{\mathrm{eff}}} - \frac{N_{\mathrm{N_2}}}{D_{\mathrm{N_2,Knud}}^{\mathrm{eff}}}\right) \qquad [4c]$$

$$C_{\mathrm{H_2O}}^{\mathrm{in}} = C_{\mathrm{H_2O}}^{\mathrm{out}} + \delta\left(\frac{x_{\mathrm{H_2O}}^{\mathrm{out}} N_{\mathrm{O_2}} - x_{\mathrm{O_2}}^{\mathrm{out}} N_{\mathrm{H_2O}}}{D_{\mathrm{O_2-H_2O}}^{\mathrm{eff}}} + \frac{x_{\mathrm{H_2O}}^{\mathrm{out}} N_{\mathrm{H_2}} - x_{\mathrm{H_2}}^{\mathrm{out}} N_{\mathrm{H_2O}}}{D_{\mathrm{H_2-H_2O}}^{\mathrm{eff}}} + \frac{x_{\mathrm{H_2O}}^{\mathrm{out}} N_{\mathrm{N_2}} - x_{\mathrm{N_2}}^{\mathrm{out}} N_{\mathrm{H_2O}}}{D_{\mathrm{N_2-H_2O}}^{\mathrm{eff}}} - \frac{N_{\mathrm{N_2}}}{D_{\mathrm{N_2,Knud}}^{\mathrm{eff}}}\right) \qquad [4d]$$

where C_i^{in} and C_i^{out} are molar concentration [mol/m^3] of the gas component ***i*** at the inner and outer surface of a porous media, x_i^{out} is mole fraction [–] of the gas component ***i*** at the outer surface of a porous media, N_i is molar flux [mol/(m^2 s)] of the gas component ***i*** through a porous media. D_{i-j}^{eff} in equation [4] is the effective binary diffusion coefficient [m^2/s] of gas components ***i*** and ***j***, and expressed as follows:

$$D_{i-j}^{\mathrm{eff}} = \frac{1}{\left(\frac{C_{\mathrm{tot}}^{\mathrm{out}}}{C_{\mathrm{ref}}}\right)}\left(\frac{\varepsilon^{\mathrm{pore}}}{\tau^{\mathrm{pore}}}\right) D_{i-j} \qquad [5]$$

where $C_{\mathrm{tot}}^{\mathrm{out}}$ is total molar concentration [mol/m^3] at the outer surface of porous media, C_{ref} is reference molar concentration (101325 Pa / ***RT*** [mol/m^3]), $\varepsilon^{\mathrm{pore}}$ and τ^{pore} are porosity [–] and tortuosity [–] of the pore, and D_{i-j}^{ref} is the reference binary diffusion coefficient [m^2/s]. D_{i-j}^{ref} is derived from the following Chapman–Enskog equation:

$$D_{i-j} = \frac{2.2646 \times 10^{-3}}{{\sigma_{i-j}}^2 \Omega_{i-j}} \frac{\sqrt{T\left(\frac{1}{M_i} + \frac{1}{M_j}\right)}}{P} \qquad [6]$$

where ***P*** is total pressure, ***T*** is temperature [K], $\boldsymbol{M_i}$ is molar weight [kg/mol] of gas component ***i***, σ_{i-j} and Ω_{i-j} are the parameters determined by the molecular dynamics theory.

$D_{i,\mathrm{Knud}}^{\mathrm{eff}}$ in equation [4] is the effective Knudsen gas diffusion coefficient of the gas component ***i*** and expressed as follows:

$$D_{i,\mathrm{Knud}}^{\mathrm{eff}} = \left(\frac{\varepsilon^{\mathrm{pore}}}{\tau^{\mathrm{pore}}}\right) D_{i,\mathrm{Knud}}^{\mathrm{ref}} \qquad [7]$$

$$D_{i,\mathrm{Knud}}^{\mathrm{eff}} = \frac{2}{3} r_{\mathrm{pore}} \sqrt{\frac{8RT}{\pi M_i}} \qquad [8]$$

where $D_{i,\mathrm{Knud}}^{\mathrm{ref}}$ is the reference Knudsen diffusion coefficient, r_{pore} is pore radius [m] of GDL/MPL, $\boldsymbol{R}$ is the gas constant [J/(mol K)], and π is circular constant [–].

***Catalyst layer* (*CL*)**

Modeling method of mass transport in the catalyst layer is shown in Fig. 6. Complex mass transport phenomena through pore, electrolyte film, and agglomerate, as shown in Fig. 6(a), was described as the following simple mass-transport resistance model shown in Fig. 6(b).

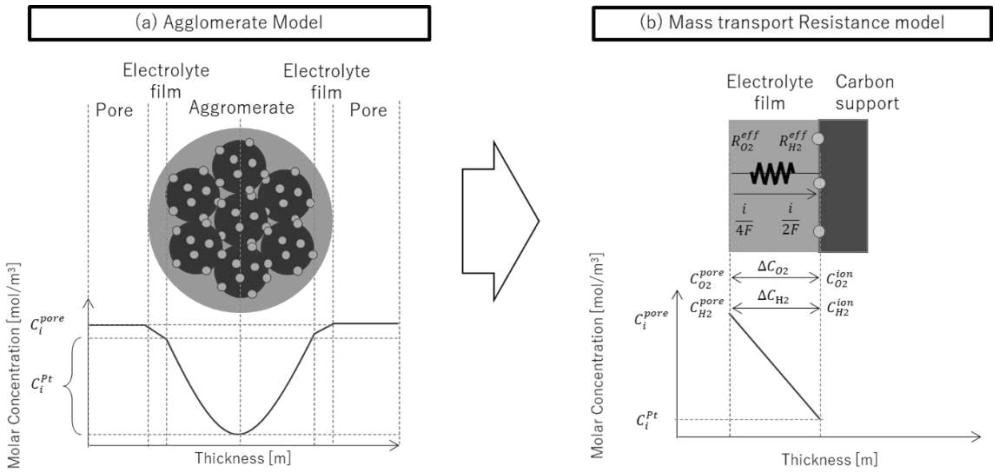

Fig. 6. Schematic drawing of (a) Agglomerate model and (b) Mass-transport resistance model

Mass-transport resistance in the catalyst layer is expressed by the following solution when the molar concentration of the reactant gas becomes zero in the limiting current density:

$$\begin{aligned} &\text{(Anode)} \quad \frac{i_{\mathrm{lim}}^{\mathrm{H_2}}}{2F} \times R_{\mathrm{H_2}}^{\mathrm{eff}} = C_{\mathrm{H_2}}^{\mathrm{aCLpore}} - 0 \quad \leftrightarrow \quad i_{\mathrm{lim}}^{\mathrm{H_2}} = \frac{2F C_{\mathrm{H_2}}^{\mathrm{aCLpore}}}{R_{\mathrm{H_2}}^{\mathrm{eff}}} \\ &\text{(Cathode)} \quad \frac{i_{lim}^{\mathrm{O_2}}}{4F} \times R_{\mathrm{O_2}}^{\mathrm{eff}} = C_{\mathrm{O_2}}^{\mathrm{cCLpore}} - 0 \quad \leftrightarrow \quad i_{\mathrm{lim}}^{\mathrm{O_2}} = \frac{4F C_{\mathrm{O_2}}^{\mathrm{cCLpore}}}{R_{\mathrm{O_2}}^{\mathrm{eff}}} \end{aligned} \qquad [9]$$

where i_{lim}^{i} is the limiting current density [A/m^2] of the gas component $\boldsymbol{i}$ ($\boldsymbol{i}$ = H_2 or O_2), R_i^{eff} is the effective mass transport resistance [s/m], and $\boldsymbol{F}$ is the Faraday constant [C/mol]. R_i^{eff} is a function of the relative humidity in the catalyst layer as expressed by equation [10].

$$R_i^{\mathrm{eff}} = \eta_{R_i} R_i^{\mathrm{ref}} \qquad [10]$$

where R_i^{ref} is the reference mass transport resistance [s/m], and η_{R_i} is the correction coefficient [–] of mass transport resistance of gas component ***i*** shown in Fig. 7.

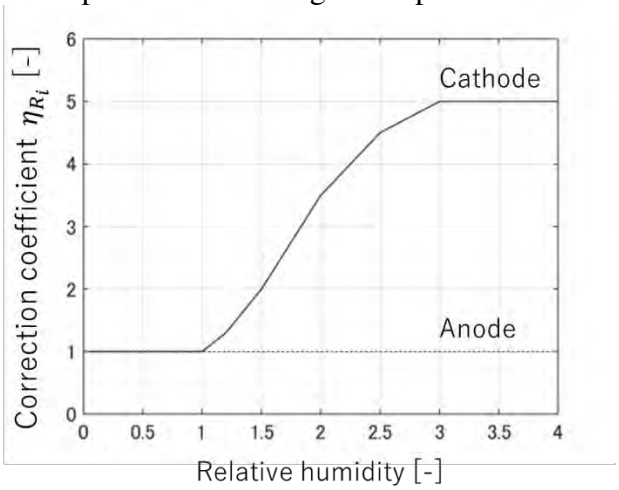

Fig. 7. Correction coefficients of mass transfer resistance in anode and cathode catalyst layers

Molar concentration of the reactant inside the electrode ionomer, that is the surface of the catalyst particles, is derived from the reactant concentration in the pore using the limiting current density as follows,

$$\begin{aligned}
&\text{(Anode)} \quad C_{\mathrm{H_2}}^{\mathrm{aCLion}} = C_{\mathrm{H_2}}^{\mathrm{aCLpore}} \left(1 - \frac{i}{i_{\mathrm{lim}}^{\mathrm{H_2}}}\right)^{\tau_{\mathrm{agg}}^{\mathrm{aCL}}} \\
&\text{(Cathode)} \quad C_{\mathrm{O_2}}^{\mathrm{cCLion}} = C_{\mathrm{O_2}}^{\mathrm{cCLpore}} \left(1 - \frac{i}{i_{lim}^{\mathrm{O_2}}}\right)^{\tau_{\mathrm{agg}}^{\mathrm{cCL}}}
\end{aligned} \qquad [11]$$

where $\tau_{\mathrm{agg}}^{\mathrm{aCL}}$ and $\tau_{\mathrm{agg}}^{\mathrm{cCL}}$ are the coefficients to express the mass transport characteristics caused by the agglomerate structure and the impact of these coefficients are shown in Fig. 8

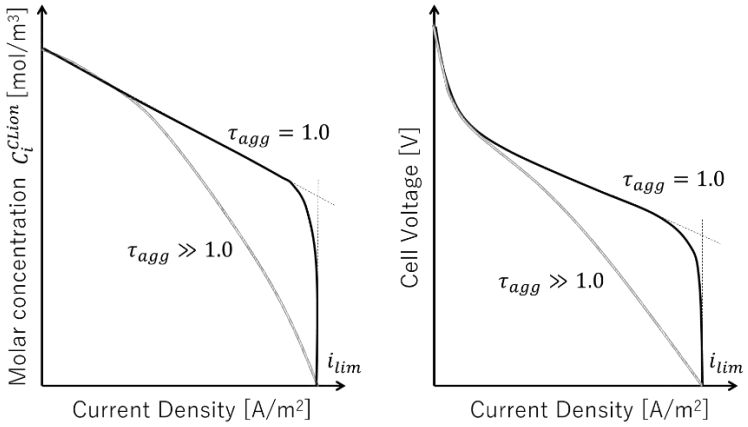

Fig. 8. Schematic drawing about the impact of agglomerate coefficient on (a) molar concentration of reactant at the surface of the catalyst and (b) I–V performance

Water-Transport in Polymer Electrolyte Membrane (PEM)

The relationships between equilibrium water uptake in PEM and relative humidity, and water diffusion coefficient in PEM and equilibrium water uptake are shown in Fig. 9, which are prepared by the equations (2).

.

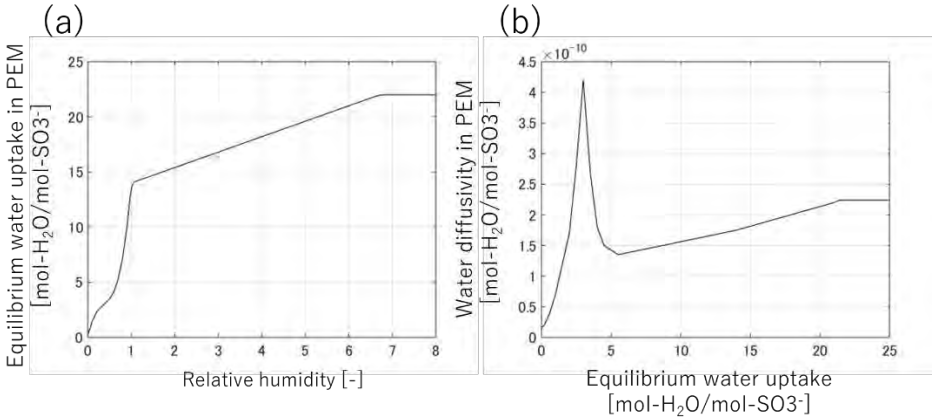

Fig. 9. The relationship between (a) Equilibrium water uptake in PEM and relative humidity, and (b) Water diffusion coefficient in PEM and equilibrium water uptake in PEM

To ensure a high-speed computation, PEM is treated as single layer, in the same manner as GDL, MPL and CL. In addition, dynamic interfacial water transport between the catalyst layer pore and PEM surface is expressed by a discrete first order lag model represented by Equations [12]–[14],

$$\lambda_{H_2O}^{aPEM} = \text{interpolation}\left(\text{Fig. } 9(a),\ a_{H_2O}^{aCLpore}\right)$$
$$\lambda_{H_2O}^{cPEM} = \text{interpolation}\left(\text{Fig. } 9(a),\ a_{H_2O}^{cCLpore}\right) \quad [12]$$

$$\lambda_{H_2O}^{PEM} = \frac{\lambda_{H_2O}^{aPEM} + \lambda_{H_2O}^{cPEM}}{2} \quad [13]$$

$$\lambda_{H_2O}^{PEM} = \alpha_{H_2O}^{PEM}\lambda_{H_2O}^{PEM} + (1 - \alpha_{H_2O}^{PEM})\lambda_{H_2O}^{PEM,old} \quad [14]$$

where $\lambda_{H_2O}^{aPEM}$ and $\lambda_{H_2O}^{cPEM}$ are the equilibrium water uptake [mol-H_2O / mol-SO_3^-] in PEM at the anode and cathode boundary, $a_{H_2O}^{aCLpore}$ and $a_{H_2O}^{cCLpore}$ are the relative humidity [–] at the anode and cathode catalyst layer pore, $\lambda_{H_2O}^{PEM}$ and $\lambda_{H_2O}^{PEM,old}$ are the equilibrium water uptake [mol-H_2O/mol-SO_3^-] in PEM at the latest and previous time step, and $\alpha_{H_2O}^{PEM}$ is the relaxation factor [–] of the dynamic water adsorption or desorption response. $\alpha_{H_2O}^{PEM}$ is defined as follows,

$$\text{when } \lambda_{H_2O}^{PEM} \geq \lambda_{H_2O}^{PEM,old} \text{ (Adsorption)}, \quad \alpha_{H_2O}^{PEM} = \frac{\Delta t}{\tau_{PEM}^{ads}}$$
$$\text{when } \lambda_{H_2O}^{PEM} < \lambda_{H_2O}^{PEM,old} \text{ (Desorption)}, \quad \alpha_{H_2O}^{PEM} = \frac{\Delta t}{\tau_{PEM}^{des}} \quad [15]$$

where Δt is the time step of the simulation [s], and τ_{PEM}^{ads} and τ_{PEM}^{des} are the time-constants of adsorption and desorption of water at the surface of PEM [s]. τ_{PEM}^{ads} and τ_{PEM}^{des} are calibrated with the transient response data of cell resistance as shown in Fig. 17. The calibrated values in Equation [15] are listed in Table 2.

Table 2. Calibrated results of the parameters in equation [15]

Variable	Symbol	Unit	Value
Simulation time step	Δt	s	0.016384
Time-constant of water adsorption onto PEM	τ_{PEM}^{ads}	s	0.016384
Time-constant of water desorption onto PEM	τ_{PEM}^{des}	s	16.384
Relaxation factor of water adsorption onto PEM	$\alpha_{H_2O}^{PEM}$	-	1.000
Relaxation factor of water adsorption onto PEM	$\alpha_{H_2O}^{PEM}$	-	0.001

With such methods, dynamic mass transport model can be replaced with pseudo-dynamic model, where the transient responses of water transport through PEM can be modeled as a series of the snapshots of steady-state mass transport equations and each snapshot is connected with each other by the discrete first order lag functions, as shown in Fig. 10. By implementing such a framework, iterative calculations to converge the through-plane water distribution in each time step can be canceled and a remarkable reduction of the computational load can be achieved.

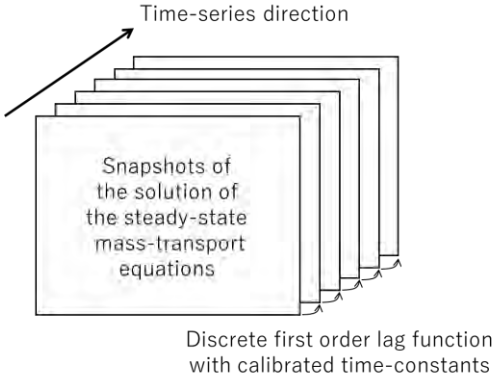

Fig. 10. A conceptual drawing of pseudo-dynamic model

Water diffusivity [m^2/s] in PEM is determined by the following equation:

$$D_{H_2O}^{PEM} = D_{H_2O}^{PEM,ref} \times \exp\left[-\frac{\Delta G_{diff}^{PEM}}{R}\left(\frac{1}{T} - \frac{1}{T_{diff}^{PEM,ref}}\right)\right] \quad [16]$$

$$D_{H_2O}^{PEM,ref} = \text{interpolation}\left(\text{Fig. 9(b)}, \lambda_{H_2O}^{PEM}\right) \quad [17]$$

where $D_{\mathrm{H_2O}}^{\mathrm{PEM}}$ and $D_{\mathrm{H_2O}}^{\mathrm{PEM,ref}}$ are the water diffusivity and reference water diffusivity in PEM, $\Delta G_{\mathrm{diff}}^{\mathrm{PEM}}$ is the activation energy [J/mol], and T and $T_{\mathrm{diff}}^{\mathrm{PEM,ref}}$ are the PEM temperature and reference PEM temperature [K]. Molar concentration at the anode and cathode boundary are as follows:

$$C_{\mathrm{H_2O}}^{\mathrm{aPEM}} = \lambda_{\mathrm{H_2O}}^{\mathrm{aPEM}} \left(\frac{\rho_{\mathrm{dry}}^{PEM}}{EW^{\mathrm{PEM}}} \right)$$
$$C_{\mathrm{H_2O}}^{\mathrm{cPEM}} = \lambda_{\mathrm{H_2O}}^{\mathrm{cPEM}} \left(\frac{\rho_{\mathrm{dry}}^{\mathrm{PEM}}}{EW^{\mathrm{PEM}}} \right) \quad [18]$$

where $\rho_{\mathrm{dry}}^{\mathrm{PEM}}$ is the dry density [kg/m^3] of PEM and EW^{PEM} is the equivalent weight [kg/mol-SO_3^-] of PEM. Through-plane Fickian water flux (cathode to anode direction is positive) from cathode to anode is calculated as follows:

$$N_{\mathrm{H_2O}}^{\mathrm{PEM,diff}} = -D_{\mathrm{H_2O}}^{\mathrm{PEM}} \frac{C_{\mathrm{H_2O}}^{\mathrm{cCL}} - C_{\mathrm{H_2O}}^{\mathrm{aCL}}}{\delta^{\mathrm{PEM}}} \quad [19]$$

where $N_{\mathrm{H_2O}}^{\mathrm{PEM,diff}}$ is the through-plane water flux [mol/(m^2 s)] and δ^{PEM} is the PEM thickness [m]. Through-plane water flux by electro-osmotic drag is expressed as follows:

$$N_{\mathrm{H_2O}}^{\mathrm{PEM,drag}} = n_{\mathrm{drag}}^{\mathrm{PEM}} \frac{i}{F} \quad [20]$$

$$n_{\mathrm{H_2O}}^{\mathrm{PEM,drag}} = \left(n_{\mathrm{drag}}^{\mathrm{PEM,ref}} + \eta_{\mathrm{drag}}^{\mathrm{PEM}} \lambda_{\mathrm{H_2O}}^{\mathrm{PEM}} \right) exp\left[-\frac{\Delta G_{\mathrm{drag}}^{\mathrm{PEM}}}{R} \left(\frac{1}{T} - \frac{1}{T_{\mathrm{drag}}^{\mathrm{PEM,ref}}} \right) \right] \quad [21]$$

where $N_{\mathrm{H_2O}}^{\mathrm{PEM,drag}}$ is the through-plane water flux [mol/(m^2 s)] by electro-osmotic drag (anode to cathode direction is positive), $n_{\mathrm{drag}}^{\mathrm{PEM}}$ and $n_{\mathrm{drag}}^{\mathrm{PEM,ref}}$ are drag coefficient and reference drag coefficient [–], $\eta_{\mathrm{drag}}^{\mathrm{PEM}}$ is the correction factor [–] of $n_{\mathrm{drag}}^{\mathrm{PEM,ref}}$ for the water uptake dependency, $\Delta G_{\mathrm{drag}}^{\mathrm{PEM}}$ is the activation energy [J/mol], and $T_{\mathrm{drag}}^{\mathrm{PEM,ref}}$ is the reference PEM temperature [K]. Water generation flux [mol/(m^2 s)] in the cathodic electrochemical reaction of $\mathrm{O_2 + 4H^+ + 4e^- \rightarrow 2H_2O}$ is

$$N_{\mathrm{H_2O}}^{\mathrm{ECR,cCL}} = \frac{i}{2F} \quad [22]$$

From Equations [19], [20], and [22], water flux [mol/(m^2 s)] to aCH and cCH are expressed as follows:

$$N_{\mathrm{H_2O}}^{\mathrm{aCH}} = +N_{\mathrm{H_2O}}^{\mathrm{PEM,diff}} - N_{\mathrm{H_2O}}^{\mathrm{PEM,drag}}$$
$$N_{\mathrm{H_2O}}^{\mathrm{cCH}} = -N_{\mathrm{H_2O}}^{\mathrm{PEM,diff}} + N_{\mathrm{H_2O}}^{\mathrm{PEM,drag}} + N_{\mathrm{H_2O}}^{\mathrm{ECR,cCL}} \quad [23]$$

Gas-Transport in Polymer Electrolyte Membrane (PEM)

Diffusivity of gas component ***i*** (***i*** = O_2, H_2, N_2) in PEM is expressed by the following Fickian equation:

$$D_{\mathrm{i}}^{\mathrm{PEM}} = \left(D_i^{\mathrm{PEM,ref}} + \eta_{\mathrm{diff},i}^{\mathrm{PEM}}\lambda_{\mathrm{H_2O}}^{\mathrm{PEM}}\right)\exp\left[-\frac{\Delta G_{\mathrm{diff},i}^{\mathrm{PEM}}}{R}\left(\frac{1}{T}-\frac{1}{T_{\mathrm{diff},i}^{\mathrm{PEM,ref}}}\right)\right] \quad [24]$$

where D_i^{PEM} and $D_i^{\mathrm{PEM,ref}}$ is diffusivity and reference diffusivity [m^2/s] of gas component ***i*** in PEM, $\eta_{\mathrm{diff},i}^{\mathrm{PEM}}$ is the correction factor [–] for the water uptake dependency, $\Delta G_{\mathrm{diff},i}^{\mathrm{PEM}}$ is the activation energy [J/mol], and T and $T_{\mathrm{diff},i}^{\mathrm{PEM,ref}}$ are the PEM temperature and reference PEM temperature [K]. Through-plane Fickian gas flux (CL to CH direction is positive) is as follows:

$$N_i^{\mathrm{CHdiff}} = -D_{\mathrm{i}}^{\mathrm{PEM}}\frac{C_i^{\mathrm{CH}} - C_{\mathrm{i}}^{\mathrm{CL}}}{\delta^{\mathrm{PEM}}} \quad [25]$$

Direct-combustion reaction (***DCR***)

In case of no load condition, an electrochemical reaction does not occur in the fuel cell and O_2 and H_2 transported between anode and cathode react directly as $O_2 + 2H_2 \rightarrow 2H_2O$ on the catalyst particles in anode and cathode catalyst layers. O_2 and H_2 direct combustion reaction rate and H_2O generation rate by DCR in the anode catalyst layer is as follows:

$$N_{\mathrm{O_2}}^{\mathrm{DCR,aCL}} = -K_{O_2\mathrm{dcr}}\left(C_{\mathrm{O_2}}^{\mathrm{aCL}}\right)^{\gamma_{\mathrm{O_2dcr}}}\left(C_{\mathrm{H2}}^{\mathrm{cCL}}\right)^{\gamma_{\mathrm{H_2dcr}}} \quad [26a]$$

$$N_{\mathrm{H_2}}^{\mathrm{DCR,aCL}} = +2N_{\mathrm{O_2}}^{\mathrm{DCR,aCL}} \quad [26b]$$

$$N_{\mathrm{H_2O}}^{\mathrm{DCR,aCL}} = -2N_{\mathrm{O_2}}^{\mathrm{DCR,aCL}} \quad [26c]$$

where $N_{\mathrm{O_2}}^{\mathrm{DCR,aCL}}$, $N_{\mathrm{H_2}}^{\mathrm{DCR,aCL}}$, and $N_{\mathrm{H_2}}^{\mathrm{DCR,aCL}}$ are the O_2 and H_2 direct combustion reaction rate and H_2O generation rate by DCR in the anode catalyst layer (+: generation, –: consumption) [mol/(m^2 s)], $K_{\mathrm{O_2dcr}}$ is the reaction rate constant of O_2 combustion reaction, $\gamma_{\mathrm{O_2dcr}}$ and $\gamma_{\mathrm{H_2dcr}}$ are the reaction orders [–] for O_2 and H_2 concentrations. The limitation of reaction rate by the molar amount of H_2 and O_2 in the cell volume is expressed as follows:

$$N_{\mathrm{O_2}}^{\mathrm{DCR,aCL}} = \min\left(N_{\mathrm{O_2}}^{\mathrm{DCR,aCL}}, \quad -\left(\frac{V_{\mathrm{gas}}^{\mathrm{aCH}} + V_{\mathrm{gas}}^{\mathrm{aGDL}}}{C_{\mathrm{O_2}}^{\mathrm{aCL}}}\right)\frac{1}{\Delta t}, \quad -\frac{1}{2}\left(\frac{V_{\mathrm{gas}}^{\mathrm{aCH}} + V_{\mathrm{gas}}^{\mathrm{aGDL}}}{C_{\mathrm{H_2}}^{\mathrm{aCL}}}\right)\frac{1}{\Delta t}\right) \quad [27]$$

where $V_{\mathrm{gas}}^{\mathrm{aCH}}$ and $V_{\mathrm{gas}}^{\mathrm{aGDL}}$ are the channel and GDL volume at anode side [m^3].

In the same way for cathode catalyst layer,

$$N_{\mathrm{O_2}}^{\mathrm{DCR,cCL}} = -K_{\mathrm{dcr}}\left(C_{\mathrm{O_2}}^{\mathrm{cCL}}\right)^{\gamma_{\mathrm{O_2dcr}}}\left(C_{\mathrm{H_2}}^{\mathrm{cCL}}\right)^{\gamma_{\mathrm{H_2dcr}}} \quad [28a]$$

$$N_{\mathrm{H_2}}^{\mathrm{DCR,cCL}} = +2N_{\mathrm{O_2}}^{\mathrm{DCR,cCL}} \quad [28b]$$

$$N_{\mathrm{H_2O}}^{\mathrm{DCR,cCL}} = -2N_{\mathrm{O_2}}^{\mathrm{DCR,cCL}} \quad [28c]$$

$$N_{\mathrm{O_2}}^{\mathrm{DCR,cCL}} = \min\left(N_{\mathrm{O_2}}^{\mathrm{DCR,cCL}}, \quad -\left(\frac{V_{\mathrm{gas}}^{\mathrm{cCH}} + V_{\mathrm{gas}}^{\mathrm{cGDL}}}{C_{\mathrm{O_2}}^{\mathrm{cCL}}}\right)\frac{1}{\Delta t}, \quad -\frac{1}{2}\left(\frac{V_{\mathrm{gas}}^{\mathrm{cCH}} + V_{\mathrm{gas}}^{\mathrm{cGDL}}}{C_{\mathrm{H_2}}^{\mathrm{cCL}}}\right)\frac{1}{\Delta t}\right) \quad [29]$$

These reaction rates of O_2, H_2, and H_2O in the anode and cathode catalyst layer are used for the correction of the through-plane flux of water and gas as follows:

$$N_{\mathrm{H_2O}}^{\mathrm{aCH,tot}} = N_{\mathrm{H_2O}}^{\mathrm{aCH}} + N_{\mathrm{H_2O}}^{\mathrm{DCR,aCL}} \quad [30a]$$

$$N_{O_2}^{\mathrm{aCHdiff,tot}} = N_{\mathrm{O_2}}^{\mathrm{aCHdiff}} + N_{\mathrm{O_2}}^{\mathrm{DCR,aCL}} \quad [30b]$$

$$N_{\mathrm{H_2}}^{\mathrm{aCHdiff,tot}} = N_{\mathrm{H_2}}^{\mathrm{aCHdiff}} + N_{\mathrm{H_2}}^{\mathrm{DCR,aCL}} \quad [30c]$$

$$N_{\mathrm{H_2O}}^{\mathrm{cCH,tot}} = N_{\mathrm{H_2O}}^{\mathrm{cCH}} + N_{\mathrm{H_2O}}^{\mathrm{DCR,caCL}} \quad [31a]$$

$$N_{\mathrm{O_2}}^{\mathrm{cCHdiff,tot}} = N_{\mathrm{O_2}}^{\mathrm{cCHdiff}} + N_{\mathrm{O_2}}^{\mathrm{DCR,cCL}} \quad [31b$$

$$N_{\mathrm{H_2}}^{\mathrm{cCHdiff,tot}} = N_{\mathrm{H_2}}^{\mathrm{cCHdiff}} + N_{\mathrm{H_2}}^{\mathrm{DCR,cCL}} \quad [31c]$$

where $N_{\mathrm{H_2O}}^{\mathrm{aCH,tot}}$ and $N_{\mathrm{H_2O}}^{\mathrm{cCH,tot}}$, $N_{\mathrm{O_2}}^{\mathrm{aCHdiff,tot}}$ and $N_{\mathrm{O_2}}^{\mathrm{cCHdiff,tot}}$, $N_{\mathrm{H_2}}^{\mathrm{aCHdiff,tot}}$ and $N_{\mathrm{H_2}}^{\mathrm{cCHdiff,tot}}$ are the total flux [mol/(m^2 s)] of H_2O, O_2, and H_2 in the through-plane direction (CL to CH direction is positive).

Polarization models

Short-circuit (SC) current model

Penetration of PEM by GDL fibers causes the short circuit current, which is expressed by Ohmic law as follows:

$$i_{\mathrm{SC}} = \frac{V_{\mathrm{cell}}}{R_{\mathrm{SC}}} \quad [32]$$

where V_{cell} is the cell voltage [V], i_{SC} is the short-circuit current density [A/m^2], and R_{SC} is the short-circuit resistance [Ω m^2]. Effective fuel cell current is expressed using the short-circuit current as follows:

$$i = i_{\mathrm{EC}} + i_{\mathrm{SC}} \quad [33]$$

where i and i_{EC} are the effective fuel cell current density and fuel cell current density caused by the external circuits. Short-circuit current causes a shift of the polarization curve to the negative current direction, resulting in voltage drops especially under the low current conditions as shown in Fig. 12.

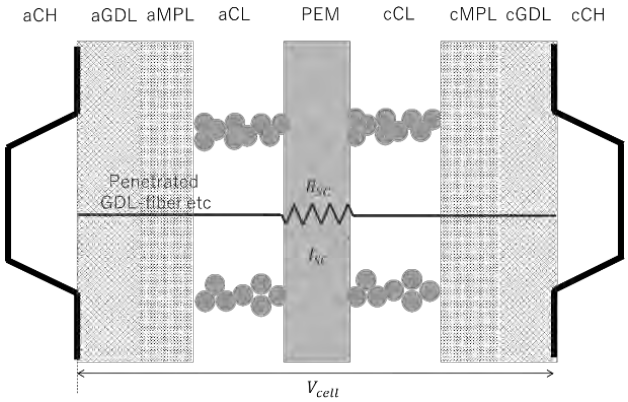

Fig. 11. Schematic drawing of short-circuit (SC) current

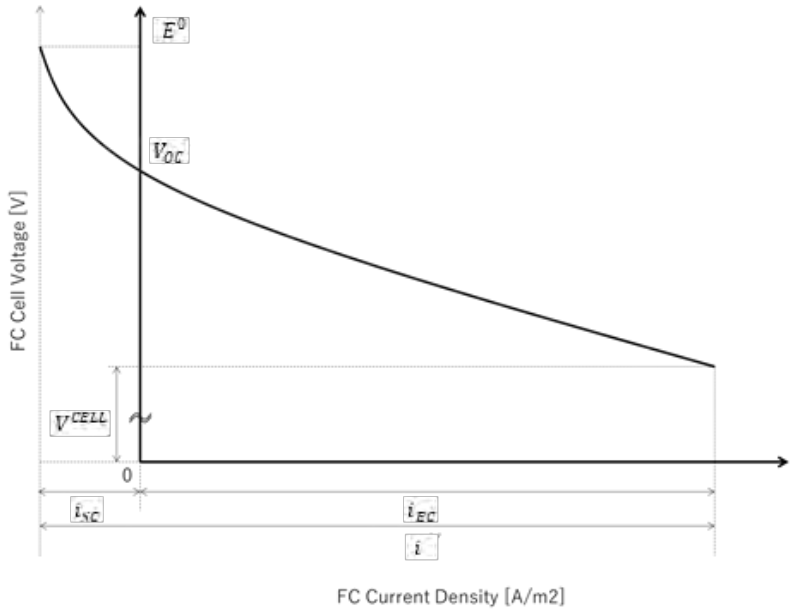

Fig. 12. Impact of short-circuit current on polarization curve

Open-circuit (OC) voltage model

Standard Gibbs energy [J/mol] of fuel cell reaction $\mathrm{H_2} + \frac{1}{2}\mathrm{O_2} \rightarrow \mathrm{H_2O}$ can be expressed as a function of temperature as follows:

$$\Delta G^0_{\mathrm{ref}} = \left\{-241.15 + 51.109\left(\frac{T}{1000\ \mathrm{K}}\right) - 85.16\left(\frac{T}{1000\ \mathrm{K}}\right)^2 + 296.21\left(\frac{T}{1000\ \mathrm{K}}\right)^3 - 408.33\left(\frac{T}{1000\ \mathrm{K}}\right)^4 + 209.37\left(\frac{T}{1000\ \mathrm{K}}\right)^5\right\} \times 1000\ \mathrm{J/mol} \quad [34]$$

Standard equilibrium potential E^0_{ref} [V] is derived from standard Gibbs energy as follows:

$$E^0_{\mathrm{ref}} = \frac{\Delta G^0_{\mathrm{ref}}}{2F} \quad [35]$$

Equilibrium potential E^0 [V], which is used as open-circuit voltage ($\boldsymbol{V}_{\mathrm{OC}}$) in this study, is derived by the following the Nernst equation:

$$E^0 = E^0_{\mathrm{ref}} + \frac{RT}{2F}\ln\left(\frac{a^{\mathrm{cCH}}_{\mathrm{O_2}}{}^{\frac{1}{2}} a^{\mathrm{cCH}}_{\mathrm{H_2O}}}{a^{\mathrm{aCH}}_{\mathrm{H_2}}}\right) \equiv V_{\mathrm{OC}} \quad [36]$$

$a^{\mathrm{cCH}}_{\mathrm{O_2}}$, $a^{\mathrm{cCH}}_{\mathrm{H_2O}}$, and $a^{\mathrm{aCH}}_{\mathrm{H_2}}$are activities [–] of O_2 and H_2O at the cathode channel, and H_2 at anode channel and derived by the following equations:

$$a^{\mathrm{cCH}}_{\mathrm{O_2}} = \frac{P^{\mathrm{cCH}}_{\mathrm{O_2}}}{P^{\mathrm{ref}}} = \frac{P^{\mathrm{cCH}}_{\mathrm{O_2}}}{101325\ \mathrm{Pa}} \quad [37a]$$

$$a^{\mathrm{aCH}}_{\mathrm{H_2}} = \frac{P^{\mathrm{aCH}}_{\mathrm{H_2}}}{P^{\mathrm{ref}}} = \frac{P^{\mathrm{aCH}}_{\mathrm{H_2}}}{101325\ \mathrm{Pa}} \quad [37b]$$

$$a^{\mathrm{cCH}}_{\mathrm{H_2O}} = \frac{P^{\mathrm{cCH}}_{\mathrm{H_2}O}}{P^{\mathrm{sat}}_{\mathrm{H_2}O}} \quad [37c]$$

where $P^{\mathrm{sat}}_{\mathrm{H_2O}}$ is saturated water vapor pressure [Pa].

Cathode overpotential

Cathode overpotential was modeled by the following Butler–Volmer equation:

$$\begin{aligned} i &= i_0^{\mathrm{cCL,eff}}\left(\frac{\mathrm{C}^{\mathrm{cCLion}}_{\mathrm{O_2}}}{C^{\mathrm{ref}}}\right)^{\gamma_{\mathrm{O_2}}}\left\{\exp\left(+\frac{\alpha_{\mathrm{c1}}F}{RT}\Delta V^{\mathrm{cCL}}\right) - \exp\left(-\frac{\alpha_{\mathrm{c2}}F}{RT}\Delta V^{\mathrm{cCL}}\right)\right\} \\ &\approx i_0^{\mathrm{cCL,eff}}\left(\frac{C^{\mathrm{cCLion}}_{\mathrm{O_2}}}{C^{\mathrm{ref}}}\right)^{\gamma_{\mathrm{O_2}}}\exp\left(+\frac{\alpha_{\mathrm{c1}}F}{RT}\Delta V^{\mathrm{cCL}}\right) \end{aligned} \quad [38]$$

where $i_0^{\mathrm{cCL,ref}}$ is the reference exchange current density [A/m^2-Pt. Equation [38] can be rearranged to yield the following equation:

$$\Delta V^{\mathrm{cCL}} = \frac{RT}{\alpha_{\mathrm{c1}}F}\ln\left(\frac{i}{i_0^{\mathrm{cCL,eff}}}\right) - \gamma_{\mathrm{O_2}}\frac{RT}{\alpha_{\mathrm{c2}}F}\ln\left(\frac{\mathrm{C}^{\mathrm{cCLion}}_{\mathrm{O_2}}}{C^{\mathrm{ref}}}\right) \quad [39]$$

where α_{c1}, α_{c2} are the electron transfer coefficients [–], $\gamma_{\mathrm{O_2}}$ is the reaction order [–]. $i_0^{\mathrm{cCL,eff}}$ is the effective exchange current density [A/m^2] and expressed by the following equation:

$$i_0^{\mathrm{cCL,eff}} = \eta_{i_0}^{\mathrm{cCL}} i_0^{\mathrm{cCL,ref}} A_{\mathrm{Pt}}^{\mathrm{cCL}} \exp\left[-\frac{\Delta G_{i_0}^{\mathrm{cCL}}}{R}\left(\frac{1}{T} - \frac{1}{T_{i_0}^{\mathrm{cCL,ref}}}\right)\right] \quad [40]$$

where $i_0^{\mathrm{cCL,ref}}$ is the reference exchange current density [A/m^2-Pt], $A_{\mathrm{Pt}}^{\mathrm{cCL}}$ is the effective electrochemical surface area [m^2-Pt], $\Delta G_{i_0}^{\mathrm{cCL}}$ is the activation energy [J/mol], and $T_{i_0}^{\mathrm{cCL,ref}}$ is the reference temperature [K]. $\eta_{i_0}^{\mathrm{cCL}}$ is the correction coefficient [–] of the exchange current density, considering the proton conduction limitation in the through-plane direction of the catalyst layer by moisture distribution as shown in Fig. 13.

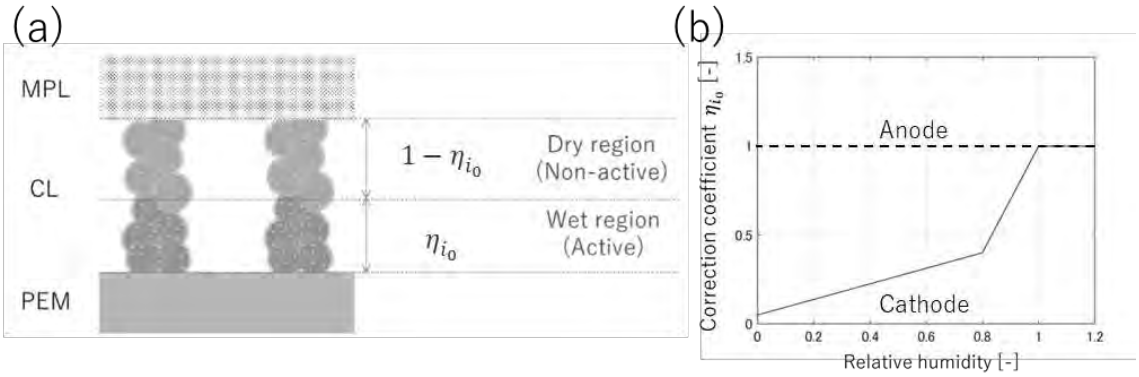

Fig. 13. (a) Schematic drawing of physical image and (b) Correction coefficients of exchange current density

Equation [39] can be broken down into the terms of activation and concentration overpotential as follows:

$$\Delta V_{\mathrm{act}}^{\mathrm{cCL}} = \frac{RT}{\alpha_{\mathrm{c1}} F} \ln\left(\frac{i}{i_0^{\mathrm{cCL,eff}}}\right) \quad [41]$$

$$\Delta V_{\mathrm{cnc}}^{\mathrm{cCL}} = -\gamma_{\mathrm{O_2}} \frac{RT}{\alpha_{\mathrm{c1}} F} \ln\left(\frac{C_{\mathrm{O_2}}^{\mathrm{cCLion}}}{C^{\mathrm{ref}}}\right) \quad [42]$$

Anode overpotential

Anode overpotential was modeled by the following Butler-Volmer equation,

$$i = i_0^{\mathrm{aCL,eff}} \left(\frac{C_{\mathrm{H_2}}^{\mathrm{Pt}}}{C^{\mathrm{ref}}}\right)^{\gamma_{\mathrm{H_2}}} \left\{\exp\left(+\frac{\alpha_{\mathrm{a1}} F}{RT} \Delta V^{\mathrm{aCL}}\right) - \exp\left(-\frac{\alpha_{\mathrm{a2}} F}{RT} \Delta V^{\mathrm{aCL}}\right)\right\} \quad [43]$$

where $i_0^{\mathrm{aCL,eff}}$ is the effective exchange current density [A/m^2], α_{c1} and α_{c2} are the electron-transfer coefficient [–] ($\alpha_{\mathrm{a1}} = \alpha_{\mathrm{a2}} = 0.5 \equiv \alpha_{\mathrm{c}}$), and ΔV^{aCL} is the overall anode overpotential. $i_0^{\mathrm{aCL,eff}}$ is expressed in the same way as Equation [40].

$$i_0^{\mathrm{aCL,eff}} = \eta_{i_0}^{\mathrm{aCL}} i_0^{\mathrm{aCL,ref}} A_{\mathrm{Pt}}^{\mathrm{aCL}} \exp\left[-\frac{\Delta G_{i_0}^{\mathrm{aCL}}}{R}\left(\frac{1}{T} - \frac{1}{T_{i_0}^{\mathrm{aCL,ref}}}\right)\right] \quad [44]$$

Equation [43] can be rearranged to yield equation [45] using hyperbolic function in equation.

$$\Delta V^{\mathrm{aCL}} = \frac{RT}{\alpha_a F}\operatorname{arcsinh}\left(\frac{i}{2i_0^{\mathrm{aCL,eff}}\left(\frac{C_{\mathrm{H_2}}^{\mathrm{aCLion}}}{C^{\mathrm{ref}}}\right)^{\gamma_{\mathrm{H_2}}}}\right) \quad [45]$$

As activation overpotential is defined as the overall overpotential when $C_{\mathrm{H_2}}^{\mathrm{aCLion}} = C^{\mathrm{ref}}$, Equation [45] can be broken down into the terms of activation and concentration overpotential as following,

$$\Delta V_{\mathrm{act}}^{\mathrm{aCL}} = \frac{RT}{\alpha_a F}\operatorname{arcsinh}\left(\frac{i}{2i_0^{\mathrm{aCL,eff}}}\right) \quad [46]$$

$$\Delta V_{\mathrm{cnc}}^{\mathrm{aCL}} = \Delta V^{\mathrm{aCL}} - \Delta V_{\mathrm{act}}^{\mathrm{aCL}} \quad [47]$$

Ohmic overpotential

PEM resistance of proton conduction is described as follows:

$$R_{\mathrm{PEM}} = \frac{\delta_{\mathrm{PEM}}}{\sigma_{\mathrm{PEM}}^{\mathrm{eff}}} \quad [48]$$

where R_{PEM} is PEM resistance [Ω], δ_{PEM} is PEM thickness [m] and $\sigma_{\mathrm{PEM}}^{\mathrm{eff}}$ is the effective proton conductivity [S/m]. $\sigma_{\mathrm{PEM}}^{\mathrm{eff}}$ is again broken down by the following equation:

$$\sigma_{\mathrm{PEM}}^{\mathrm{eff}} = \sigma_{\mathrm{PEM}}^{\mathrm{ref}} \exp\left\{-\frac{\Delta G_{\mathrm{H^+}}^{\mathrm{PEM}}}{R}\left(\frac{1}{T} - \frac{1}{T_{\mathrm{H^+}}^{\mathrm{PEM,ref}}}\right)\right\} \quad [49]$$

where $\sigma_{\mathrm{PEM}}^{\mathrm{ref}}$ is reference proton conductivity [S/m], $\Delta G_{\mathrm{H^+}}^{\mathrm{PEM}}$ is the activation energy [J/mol]. $T_{\mathrm{H^+}}^{\mathrm{PEM,ref}}$ is the reference temperature [K]. The relationship between the equilibrium water uptake and the reference proton conductivity is expressed as an empirical function shown in Fig. 14, which is expressed by the equations (2).

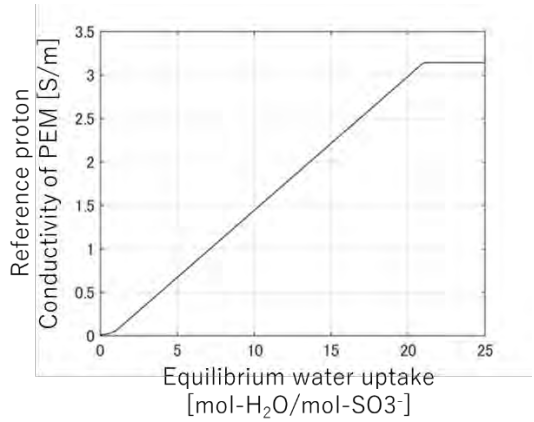

Fig. 14 The empirical function of reference proton conductivity.

Ohmic overpotential of cell is expressed as follows:

$$\Delta V_{\mathrm{ohm}}^{\mathrm{CELL}} = i(R_{\mathrm{PEM}} + R_{\mathrm{aGDL}} + R_{\mathrm{aMPL}} + R_{\mathrm{cGDL}} + R_{\mathrm{cMPL}}) \quad [50]$$

where i is current density [A/m^2], R_{aGDL} and R_{aMPL} are electric resistance of anode GDL and MPL, and R_{cGDL}, R_{cMPL}, are electric resistance of cathode GDL and MPL determined empirically [Ω].

Cell voltage

Cell voltage V_{cell} [V] is derived from Equations [36] [41] [42] [46] [47] [50] as follows:

$$V_{\mathrm{cell}} = V_{\mathrm{OC}} - \Delta V_{\mathrm{act}}^{\mathrm{aCL}} - \Delta V_{\mathrm{cnc}}^{\mathrm{aCL}} - \Delta V_{\mathrm{act}}^{\mathrm{cCL}} - \Delta V_{\mathrm{cnc}}^{\mathrm{cCL}} - \Delta V_{\mathrm{ohm}}^{\mathrm{CELL}} \quad [51]$$

Implementation and integration of the models

The model described in previous sections are integrated as the flow diagram shown in Fig. 15. A suite of physics listed in Table 1 are implemented in MATLAB® language in a proper resolution of functions so that the physical equations can be directly described as codes, and each MATLAB® function is integrated on SIMULINK® block diagrams as the stack and sub-system models of air, H_2 and cooling as shown in Fig. 16. With such implementation methods, the role and relationship of each function are clear and it is remarkably easy to modify, replace, add, and remove component specifications in the proposed model. This remarkably reduces the effort and troubles to develop various application-specific integrated system models.

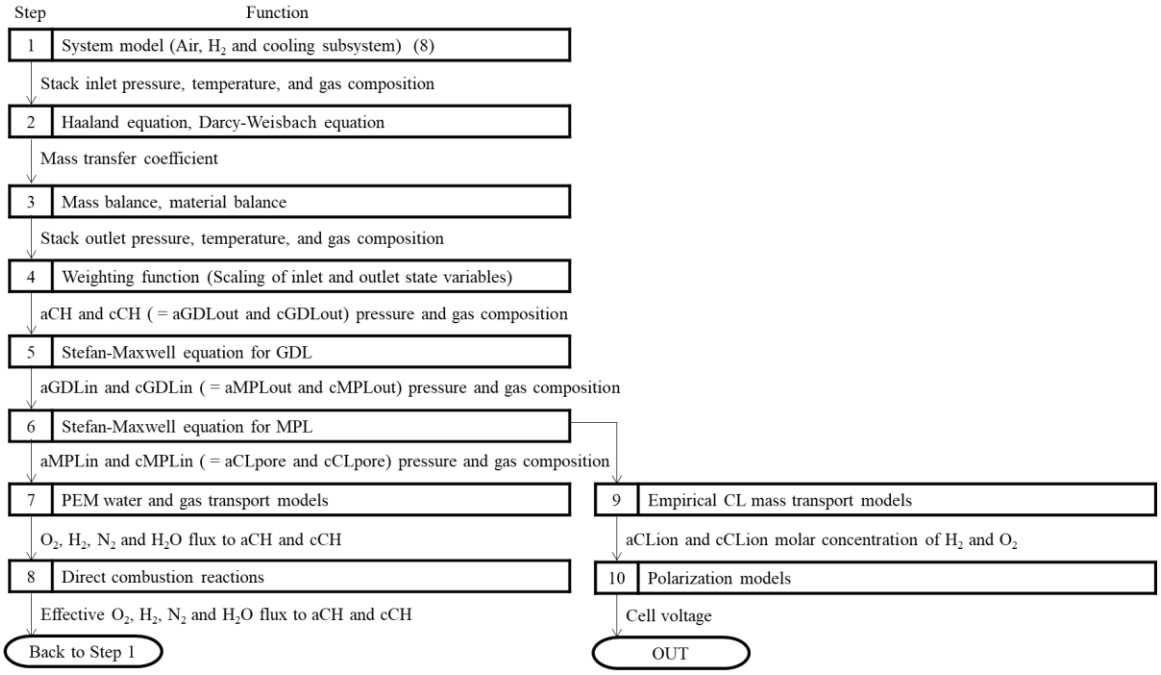

Fig. 15. Flow diagram of the integrated fuel cell model.

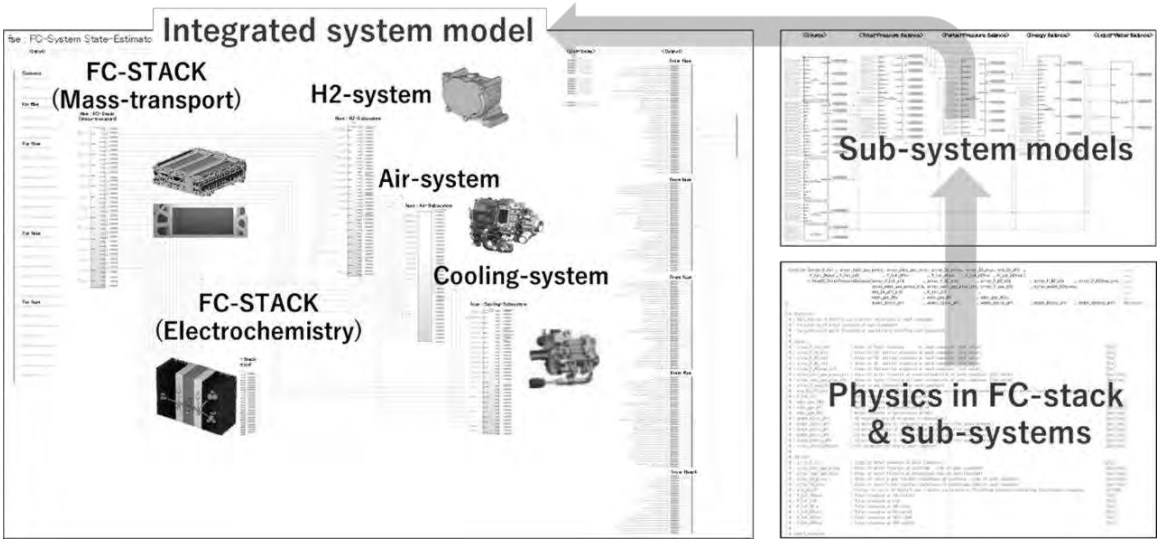

Fig. 16. Conceptual drawings of the model implementation methods

Results and discussion

Extensive testings were conducted with the actual fuel cell system of the 2nd-generation MIRAI, a fuel cell electric vehicle (FCEV), and a lot of validation data were collected in the variety of operating conditions such as low to high loads, operating temperatures, and total pressures. The validation data were utilized for the validation of the fuel cell stack model accuracy and modeling strategies.

An example of the validation results is shown in Fig. 17. Time-series data of the interfacial conditions of the fuel cell stack (current, temperature, flowrate, pressure, and gas composition) were input to the fuel cell stack model, and voltage and resistance were

calculated by the model. Then, calculated results and measured data were compared. Newly developed models listed in Table 1 were found to be working correctly and beneficial to reproduce acceleration and deceleration transients in experimental data. Strong agreements were confirmed between the experimental data and the simulation results throughout the collected database.

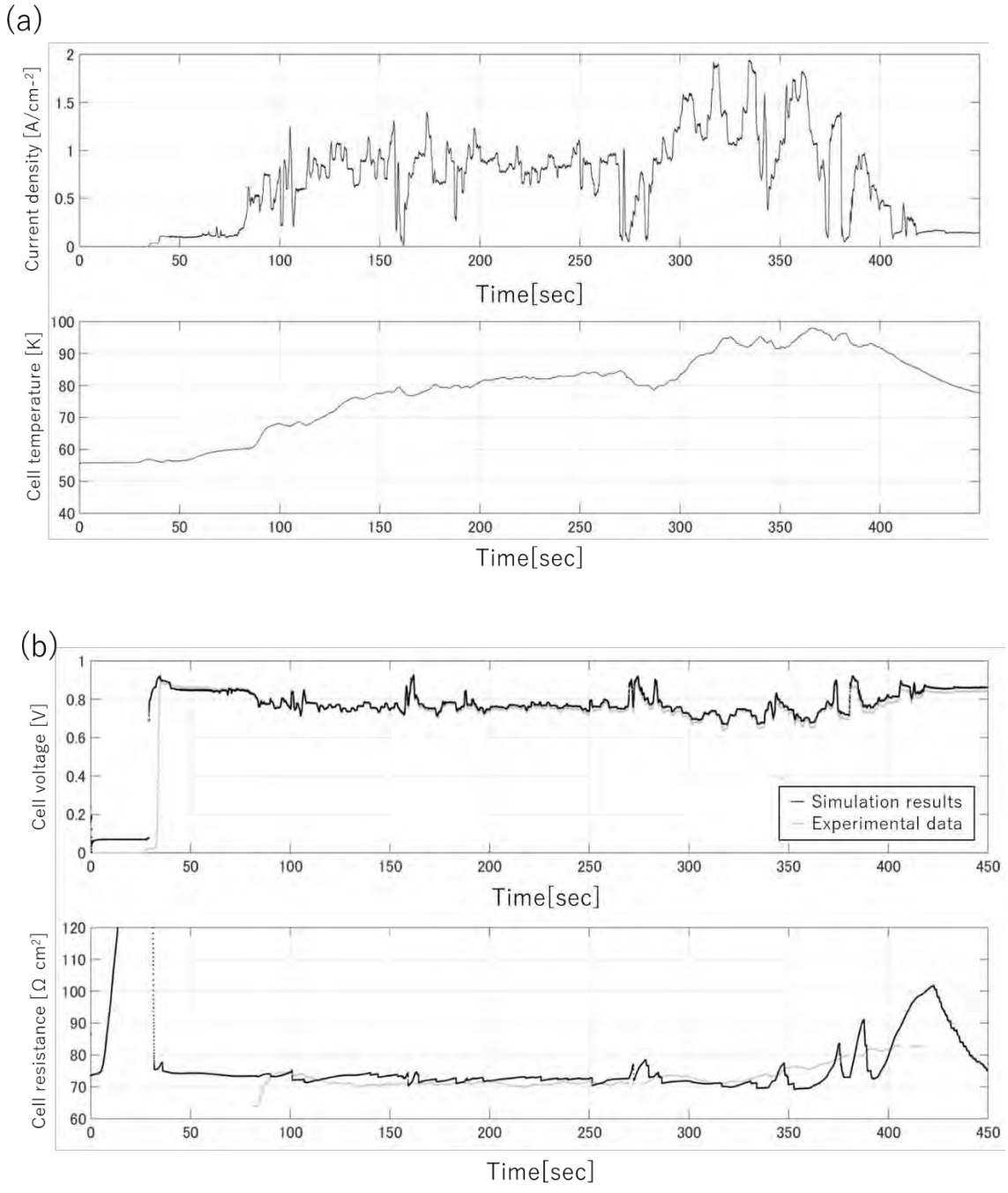

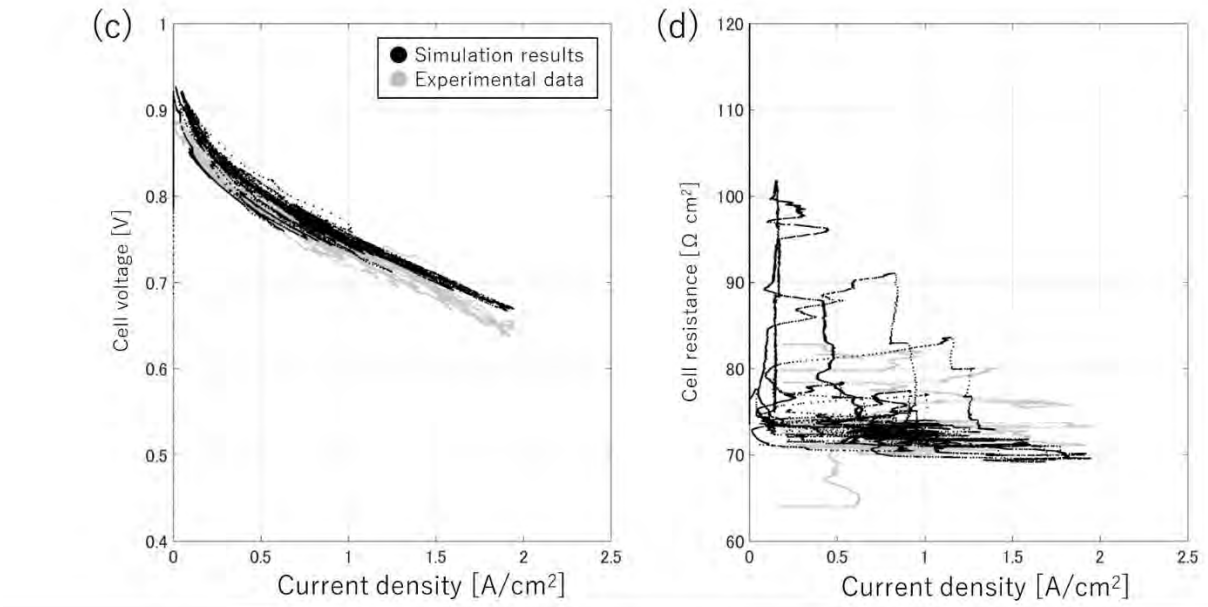

Fig. 17. Validation results of developed model, (a) Time-series current density and temperature, (b) Time-series cell voltage and resistance, Comparison of experimental data, (c) Scattered plot of cell voltage, (d) Resistance to current density

The computational time of the numerical simulation is listed in Tables 2 and 3. A considerable reduction in computation time, more than 50-times faster than real time, was confirmed even under the standard-performance computational resources.

Table 2. Computational resources

Hardware	CPU	Intel® Xeon® CPU E3-1230 v5 @ 3.40GHz, 3.41GHz
	RAM	8.00 GB
Software	OS	Windows 10® Enterprise
	MATLAB®	R2015a (8.5.0.197613)
	SIMULINK®	Version 8.5 (R2015a)

Table 3. Computational time of numerical simulation

Experimental data	Total time	700 sec
	Number of data	42724 time-steps (0.016384 sec/step)
Computational time		13.2 sec (×53.0 acceleration than real time)

Conclusions

1D fuel cell stack modeling method was investigated to ensure dynamic numerical simulation of life-long system operation in permissible calculation time and accuracy. The reported models in the literatures and newly developed mass transport, reaction, and polarization models are integrated and implemented on MATLAB® and SIMULINK® platform with a streamlined manner for the future modification and expansion of the

integrated models. This integrated model was validated and verified with the experimental data collected from the commercial fuel cell system of the 2nd-generation MIRAI, a fuel cell electric vehicle (FCEV) and strong agreement with experimental data was confirmed. Remarkably high computational speed was confirmed even under the standard-performance computational resources.

Current issues of this model and future development targets are summarized in Table 4. The simulation described in the previous sections are designed to be highly scalable and a wider range of state-of-the-arts achievements are to be incorporated following the academic and industrial demands.

Table 4. List of future model development targets

	Issues	Current status	Focus technical topics
(1)	Calibration effort of empirical functions	Weighting functions for in-plane Distribution	Expansion to 1+1D model with high-speed convergence algorithm
		Time-constant of interfacial water transport of PEM	Conversion from pseudo dynamic model to physical dynamic model considering CL and PEM geometry
		Correction coefficient of mass transport resistance at catalyst layer and exchange current density	Introduction of effective reaction rate constant considering rate-determining process of mass transport, proton conduction, and electrochemical reaction
(2)	Life-time estimation	Durability models not included	Implementation of - Platinum coarsening model - Carbon corrosion model - PEM chemical degradation model - PEM mechanical degradation model
(3)	Isothermal assumption in 1D direction	1D temperature distribution model	- Modeling of effective heat generation rate model - Modeling of effective latent heat - Determination methods of thermal parameters
(4)	Application to product system developments	System interfacial conditions from air, H_2, and cooling sub-systems are inputted	- Integration with sub-system models as a working fuel cell system model - Integration with controllers to serve closed-loop simulation platform for system planning and design.

Acknowledgement

This work was supported by the FC-Platform Program: Development of design-for-purpose numerical simulators for attaining long life and high performance project (FY 2020–2022) conducted by the New Energy and Industrial Technology Development Organization (NEDO), Japan.

References

(1) R.B. Bird, W.E. Stewart, and E.N. Lightfoot, ***Transport Phenomena***, ***Revised Second Edition***, (John Wiley & Sons, New York, 2006).

(2) T.E. Springer, T.A. Zawodzinski, and S. Gottesfeld, "Polymer electrolyte fuel cell model," ***J. Electrochem. Soc.***, **138**(8), 2334–2342 (1991).

(3) A.Z. Weber and J. Newman, "Modeling transport in polymer-electrolyte fuel cells," ***Chem. Rev.***, **104**, 4679−4726 (2004).

(4) H. Yamada and Y. Morimoto, "Electro-osmotic drag and diffusion coefficient of water in polymer electrolyte membrane," ***Abstracts of the Electrochemical Society of Japan,*** p. 316 (2003).

(5) K. Broka and P. Ekdunge, "Oxygen and hydrogen permeation properties and water uptake of Nafion 11 membrane and recast film for PEM fuel cell," ***J. Appl. Electrochem.,*** **27**, 117-123 (1997)**.**

(6) M. Mukaddam, E. Litwiller, and I. Pinnau, "Gas sorption, diffusion, and permeation in Nafion," Macromolecules, **49**, 280-286 (2016).

(7) T. Tsukamoto ***et al.***, "Three-dimensional numerical simulation of full-scale proton exchange membrane fuel cells at high current densities," ***J. Pow. Sour.***, **588**, 229412 (2021).

(8) S. Hasegawa ***et al.,*** "Application of model-based development to product fuel cell systems and controller design, physical modeling of the entire fuel cell system and implementation to controller," ***EVTeC2021***, ***in press*** (2021).

Chapter 2

Catalyst Characterization

ECS Transactions, 104 (8) 29-43 (2021)
10.1149/10408.0029ecst ©The Electrochemical Society

Synthesis And Characterization of Platinum on Carbon Nanoparticles Selectively Coated with Titanium Nitride (TiN)

Andres O. Godoy[a,b]*, Saidjafarzoda Ilhom[c], Mor Kattan[d], Pablo Zarama[a,b], Yair Ein-Eli[d], Necmi Biyikli[c], and Jasna Jankovic [a,b]**

[a]Institute of Materials Science, University of Connecticut, Storrs, USA.
[b]Center for Clean Energy Engineering, University of Connecticut, Storrs, USA
[c]Electrical and Computer Engineering, University of Connecticut, Storrs, USA.
[d]Material Science and Engineering, Technion - Israel Institute of Technology, Haifa, Israel
* richard.ortiz_godoy@uconn.edu; ** jasna.jankovic@uconn.edu

Here we propose a novel way to prevent the insidious effect of carbon corrosion in a Proton Exchange Membrane Fuel Cell (PEMFC) by depositing a corrosion-resistant layer (~1.5 nm thick) of Titanium Nitride (TiN) on the carbon substrate of a platinum on carbon (Pt/C) catalyst (in powder state), leaving the Pt catalyst centers uncoated and accessible for reagents reactions (oxygen O_2 and H^+ protons). The deposition was carried out at 150°C with a Hollow-Cathode Plasma-Assisted Atomic Layer Deposition (HCPA-ALD) using Tetrakis(dimethylamino)titanium (IV) (TDMAT) as the metal precursor in Ar/N_2 plasma, from which nitrogen was used as co-reactant. Additionally, Transmission Electron Microscopy (TEM) characterization allowed us to prove the successful formation of a homogenous coating on these nanoparticles and electrochemical characterization performed with a Rotating Disc Electrode (RDE) further confirmed the activity and effectiveness of our designed catalyst. Preliminary results have shown that highly conformal TiN can be successfully grown onto Pt/C nanoparticles by using HCPA-ALD with a custom-made agitator mechanism.

INTRODUCTION

The growing demand for clean and efficient energy sources has been a direct result of the serious effect on the climate and the environment associated to high emissions of pollutants that are mainly produced from fossil fuel-based energy generator[1–4]. Currently, a green technology like Proton Exchange Membrane Fuel Cell (PEMFC) can produce zero-emissions energy power by primarily using the electrochemical reactions of hydrogen and oxygen to generate electrical energy[5–7]. However, the development of highly efficient and reliable PEMFCs, mature enough to result in an increase application in the transportation and energy generation sectors, have been subjected to considerable scientific and industrial scrutiny[8]. In general, PEMFCs produce electricity through the electrochemical reaction of hydrogen and oxygen (or air) taking place in the Membrane Electrode Assembly (MEA) by converting chemical energy through the hydrogen oxidation reaction (HOR) and oxygen reduction reaction (ORR) into electrical energy with water as a byproduct[9]. Due to their

high activity, Platinum (Pt)/Pt-alloy nanoparticles distributed on a carbon catalyst support are considered the most efficient catalyst materials used in this technology. These materials are used to catalyze chemical reactions in PEMFCs for promoting electrochemical energy conversion[10].

However, the main drawbacks from this technology are (i) the scarcity of Pt, making it very expensive for widespread fuel cell application and commercialization[11], as well as the fact that (ii) catalyst can be prone to corrosion and degradation when operating even at the most typical PEMFC conditions. Usually, over the lifetime of the PEMFC, the catalysts must endure thousands of load cycles and operate under harsh conditions such as high temperature and potential, low pH, and oxygen atmosphere. Beside Pt degradation through Ostwald ripening, agglomeration and migration, carbon support corrosion is one of the culprits of catalyst degradation. The effect of carbon corrosion can induce the loss of Pt nanoparticles (NPs) active surface area when Pt detaches from the carbon support or agglomerates into larger Pt NPs, which can lead to premature performance losses in a PEMFC[12,13]. In addition, carbon corrosion can cause loss of catalyst layer porosity and conductivity, sometimes fully collapsing the electrode and resulting in the cell failure[14,15]. Consequently, improving the durability of the catalysts has been one of the most important issues tackled by scientists and the industry. To accomplish this, numerous research efforts have been made, like (i) changing the Pt NPs morphologies[16], (ii) incorporating Pt with other transition metals (core shell, alloys, etc.)[17] and (iii) creating more durable and corrosion resistant catalyst support materials with strong catalyst metal interactions[15]. Some promising results have been found when the Pt catalysts are immobilized by anchoring them to the carbon supports using polymers, ultra-thin carbon layers or inorganic materials. Transition metal oxides, nitrides and carbides/borides, such as titanium nitride, titanium carbide, boron carbide, silicon carbide, and titanium boride, have gathered significant interest as a result of their noble-metal-like catalytic properties, good electrical conductivity, and high resistance to corrosion and acid attack[18]. As electrocatalysts they also exhibit good catalytic activity and long-term durability. Transition metal nitrides, especially, can offer high electric conductive, thermal stability with high melting points, electrochemical stability at the operation conditions of PEMFC, they display excellent hardness and corrosion resistance, good catalyst–support interactions, high ORR activity and good electrochemical stability[18]. Avasarala et al[19]. reported that Pt/TiN catalyst presented different degradation mechanism compared to Pt/C, having Pt/TiN catalyst predominantly degraded through Pt agglomeration mechanism and not TiN corrosion, while Pt/C degradation mechanisms is more complex involving Pt agglomeration and carbon support corrosion mechanisms. They attributed such behavior to the higher resistance to corrosion that TiN has over that of carbon under electrochemical conditions reducing the role of the catalyst support corrosion mechanism in the degradation of Pt/TiN.

A TiN fabrication method that stand out is Atomic Layer Deposition (ALD) because it is a technique that allows the manufacturing of ultrathin films and uniformly distributed nanoparticles based on noble metals or metal oxides/nitrides with atomic scale layer by layer precision, tunable properties and it can be performed at relatively low temperatures in a very controlled way[20]. When working with powders a fluid bed reactor is needed to perform the uniform coating of the unsupported particle surface by converting the nanoparticles into a fluid-like state through rigorous mixing of the nanoparticles by suspension and vibration. This mechanism confers a good mixing, large gas solid contact area, high efficiency for mass and heat transfer, large-batch processing capability,

improves the vapor solid contact efficiency, better heat transfer coefficients, reduces particle aggregation and 3D structures can be covered with a conformal coating for high-aspect-ratio structures[21,22].

EXPERIMENTAL APPROACH

In this work, we propose a novel approach to prevent carbon corrosion by selectively depositing a corrosion-resistant layer (approximately 1.5 nm thickness) of titanium nitride (TiN) only on the surface of the carbon support while the Pt NPs catalyst centers were left uncoated and accessible for reagents reactions (oxygen O_2 and H^+ protons), see *fig. 1*. TiN was used as the coating material because of its attractive properties, such its electronic conductivity, which is enough to enable the free movement of electrons from the current collector toward the catalytic centers. TiN would also act as an anchoring mechanism of the Pt NPs, preventing their mobility on the carbon support and subsequent agglomeration.

The deposition of TiN layers was carried out at 150°C with a Hollow-Cathode Plasma-Assisted Atomic Layer Deposition (HCPA-ALD) while using Tetrakis(dimethylamino)titanium (IV) (TDMAT) as the metal precursor in Ar/N_2 plasma, from which nitrogen was used as co-reactant. Before HCPA-ALD, to prevent TiN from depositing on top of the Pt NPs, the surface of Pt NPs was selectively coated with a thin film of oleylamine (OAm)[23], a polymer that would only absorbs onto Pt NPs, which was later removed from the catalyst and TiN system (after the HCPA-ALD process is finished), by heat treatment at 185°C. Here we will mainly focus on the TiN deposition process and the subsequent Transmission Electron Microscopy (TEM) characterization performed on these nanoparticles, which allowed us to prove the successful formation of homogenous coating and architecture characteristics of these nanoparticles after oleylamine application and TiN deposition. Electrochemical characterization, including Cyclic Voltammetry (CV) and linear sweep voltammetry (LSV) to assess ORR activity, were performed in a Rotating Disc Electrode (RDE) to further confirm the activity and effectiveness of our designed catalyst. Our preliminary results have shown that highly conformal TiN can be successfully grown onto Pt/C nanoparticles (as powders) by using HCPA-ALD with a custom-made agitator mechanism. The second phase of this research will be focused on inspecting the degradation mechanisms this novel catalyst system experiences after potential cycling in a Membrane Electrode Assembly (MEA).

METHODS

Applying OAm on Pt/C nanoparticles: The Oleylamine OAm was purchased from J&K with a purity of 95% . 50% platinum on Vulcan XC-72 (from Fuel Cell Store) was mixed with a solution of 5 mM OAm diluted in ethanol, then sonicated in an ultrasonic bath for 60 min. To collect the catalyst powder coated with OAm, the mix was then filtered overnight using a hydrophobic Polyvinylidene Difluoride PVDF membrane filter with 0.22 μm pore size (Durapore® Membrane Filter from Millipore Sigma).

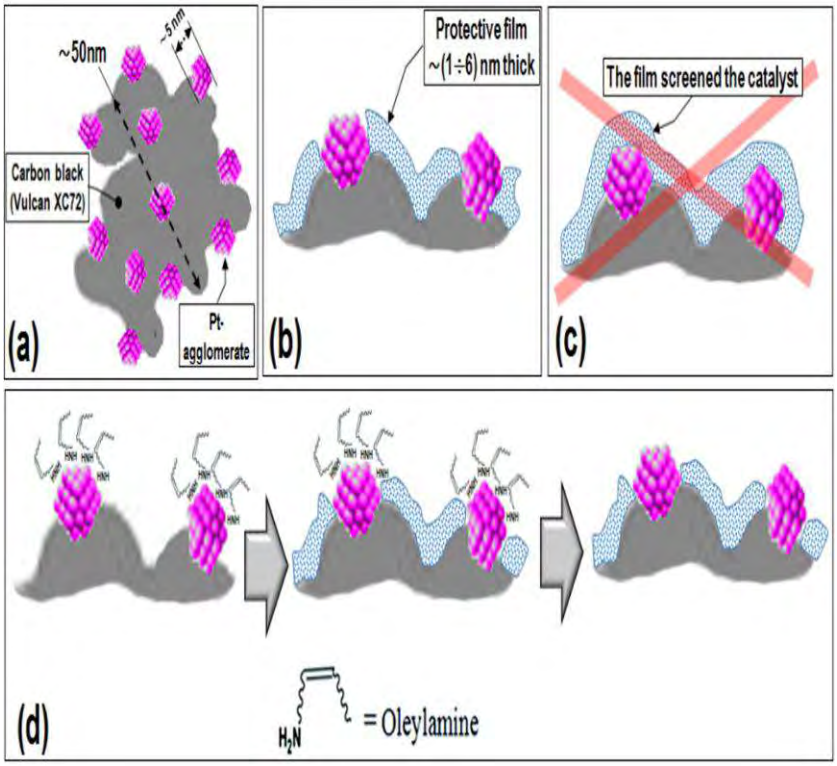

Figure 1. Schematics of the protection film design (a, b, c) and the coating procedure (d)

Hollow-Cathode Plasma-Assisted Atomic Layer Deposition (HCPA-ALD) was used to grow highly conformal Titanium Nitride (TiN) films on Pt/C nano-powders (bare and OAm coated). Tetrakis(dimethylamino)titanium (IV) (TDMAT) and Ar/N_2 plasma were used as the metal precursor and nitrogen as co-reactant, respectively, at 150°C. The catalyst in powder state were placed inside a custom-made agitator mechanism to ensure conformal film growth around the particles and to simulate the effect of a fluidized bed reactor. 240 ALD-cycles were performed at 100 msec per TDMAT pulse, 10/10 sec purge, and 10 sec plasma exposure at 50 W using Ar/N_2 (50/50 sccm) plasma chemistry. Ex-situ multi-wavelength ellipsometry measurements revealed the TiN film growth-per-cycle (GPC) on Si(100) sample at ~0.94 Å/cycle.

Thermogravimetric Analysis (TGA) was used to examine the thermal stability limits of the catalysts (with and without OAm) by determining mass loss due to sample decomposition or oxidation when the temperature is increased as a function of time. This process was carried out using a Netzsch STA 449 F1 Jupiter Simultaneous TGA/DSC Thermal Analyzer system. The samples were then heated up to 1573.15K (1300°C) at a rate of 10°C/min, in an air flow of 10ml/min rate.

N_2 adsorption-desorption isotherms of these catalysts were performed at 77 K using a Micromeritics ASAP2000 Accelerated Surface Area and Porosimetry Analyzer instrument. The samples were first degassed at 573 K (299.85 °C) for 6 hr. The specific surface areas were acquired using the Brunauer-Emmett-Teller (BET) method, based on a model of monolayer–multilayer adsorption, with a relative pressure range of ~0.1-0.15. The mesoporosity was calculated by Barrett-Joyner-Halenda (BJH) method using the adsorption branches and the maximum positions of the BJH curves were used to estimated

pore-size distributions while the volume of nitrogen adsorbed at a $P/P_o \sim 0.99$ was used to calculate the total pore volumes.

A Tube Furnace, Lindberg/Blue from Thermo Fisher Scientific, was used to heat the samples at a 5 °C/min up to 185 °C in air and maintained at this temperature for 1 hr, following Dr. Zhao et al.[24] oleylamine combustion removal method without including post heat treatment washing protocols.

Electron Microscopy: The morphology of the powders and the thickness of the electrodes (for RDE) were investigated using a high-resolution Field Emission Scanning Electron Microscope SEM system (FEI Quanta FEG 250) with Secondary Electrons (SE) in high vacuum mode at 20 kv. High resolution visualization and characterization of the nanoparticles was performed using a Thermo Scientific™ TalosF200 × 200 kV D6329 XTwin Transmission Electron Microscope (TEM), using both Bright Field and High Angle Annular Dark Field (HAADF) Scanning Transmission Electron Microscopy (STEM) modes. To prepare for this characterization and to prevent the destruction of the thin layers of OAm and TiN, dispersion by sonication was avoided and the powder samples were sprinkled on a holey carbon-coated Cu grid for TEM characterization. Energy Dispersive Spectroscopy (EDS) with a ChemiSTEM^{TM} technology system contained within the TEM was used for elemental analysis of the catalyst samples, using hyper- mapping collected by an ESPRIT Microanalysis Software. The mapping was performed using a screen current of 2.5 nA, beam dwells time of 1000 µs per pixel for one mapping cycle. For high-resolution STEM imaging, the samples were studied by Titan Themis 60-300. The S/TEM images were performed at 300 keV and with its DCorr^{+} probe corrector that corrects condenser spherical aberration higher than 25 mrad, enabling a spatial resolution down to 0.08 nm with 25 mrad convergence angle for its atomic resolved HAADF-STEM imaging.

Electrochemical Characterization of the catalysts were performed in a conventional three electrode Rotating Disc Electrode (RDE) set-up using a Bio-Logic SAS (model VSP) potentiostat in an electrochemical cell from Gamry Instruments (a five-compartment glass EuroCell - Standard Glass Cell ECC). The measurements were performed at 298 K using a catalyst-coated glassy carbon disc as a working electrode, a standard 6 in graphite rod as a counter electrode from Gamry Instruments, and a Hydrogen Reference Electrode (RHE) from eDAQ. To prepare the working electrode, it is necessary to deposit a thin catalyst film on the surface of a mirror polished glassy carbon (GC, from Pine Instruments). The catalyst ink was prepared by mixing 15.625 mg of 50%Pt/C catalyst with 3 mL isopropanol (IPA-99.9%, Sigma-Aldrich), 7 mL deionized water and 40 µL of Nafion ionomer solution (D521 Nafion™ Dispersion - Alcohol based 1100 EW at 5 wt% from Fuel Cell Store). To make a uniform suspension and to prevent the degradation of the OAm and TiN the samples were mixed at room temperature by (i) ultrasonication for 15 min and (ii) mixed overnight using a magnetic stirrer at 125 rpm. Using a micropipette, 10 µL droplet of the suspension was pipetted onto the 5 mm diameter (0.196 cm^2) GC disk and the resulting film is then dried for at least 3 hr in an ambient atmosphere. To get a reproducible voltammograms, prior to CV and ORR SLV measurements (after N_2 saturation for 1 hr), the working electrode was first electrochemically cleaned via potential cycling, in 0.1M perchloric acid ($HClO_4$) solution at the sweep rate of 200 mV/s from 0.06 V to 1 V versus RHE for 40 cycles. Then 5 cycles of CV were recorded from 0.006 V to 1.2 V at the sweep rate of 20 mV/s. ORR measurements were recorded at 5 cycles in an O_2 saturated atmosphere at 1600 rpm at the sweep rate of 20 mV/s from 0.2 V to 1.175 V versus RHE.

RESULTS AND DISCUSSION

Electron Microscopy: *SEM* was used to gain insight into the morphology and structure of the agglomerated powders before and after OAm application, as displayed in fig. 2 a-b. The main take away from the SEM micrographs is that it can be seen that after OAm application, the powders tend to agglomerate creating considerably larger agglomerates. However, the resolution provided by SEM was not enough to discern any remarkable difference between each sample, so a more in-depth nanometric analysis was performed using nitrogen gas surface adsorption/desorption and TEM based techniques.

The *TEM* characterization (fig. 3 a-b) shows that before the addition of OAm, the Pt NPs are almost spherical and evenly distributed on the surface of the carbon support. However, after the addition of OAm Pt NPs tend to heavily agglomerate in irregular shapes and sizes. On the other hand, the TEM micrographs also confirmed that our method of OAm deposition results in the desired protective layer on the surface of the Pt NPs, as displayed in the fig. 3b, with a thickness <1 nm, while it was challenging to determine if carbon areas were covered by OAm. Absorbed OAm on the carbon support cannot be ruled out only by TEM inspection even though the carbon nanostructure remains almost unchanged. To confirm that the thin film on Pt NPs was not a TEM artifact or the formation of a hydrocarbon film, a targeted large Pt NPs was exposed to the high intensity TEM beam for about 15min (fig. 4 a-b). The degradation of the OAm film can be observed until the end result is an almost bare and smoothed surface for the Pt NPs agglomerate, without a film on the Pt surface.

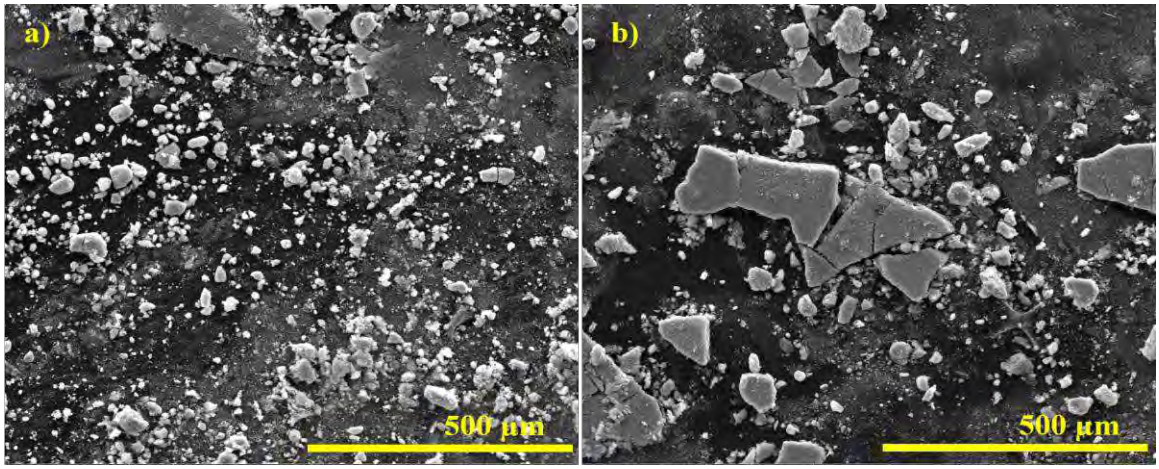

Figure 2. SEM micrographs of 50% platinum on Vulcan XC-72 a) without and b) with OAm.

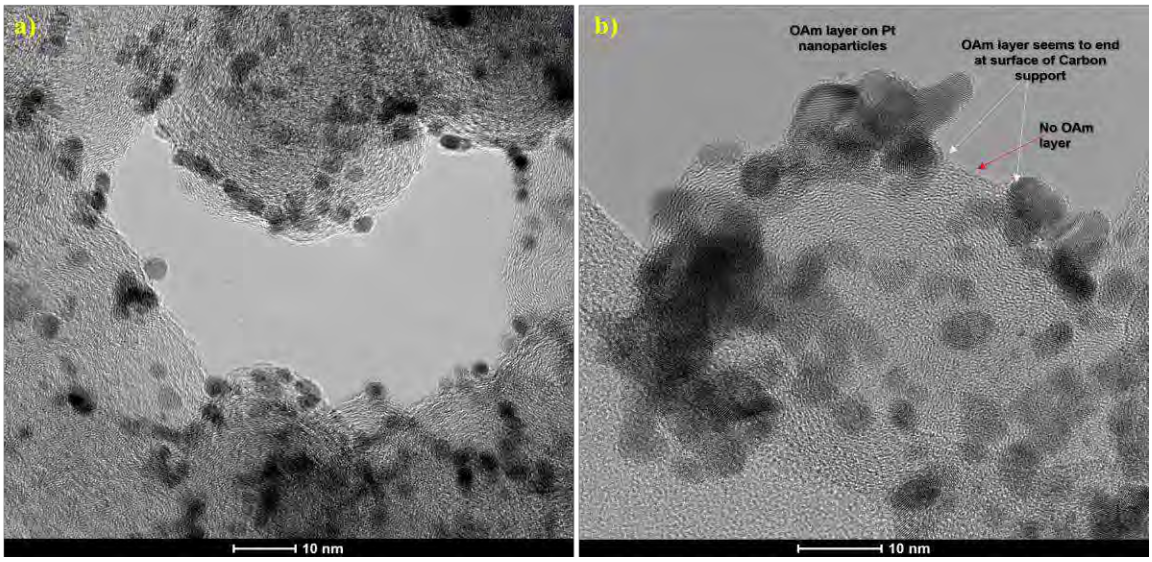

Figure 3. TEM micrographs of 50% platinum on Vulcan XC-72 a) without and b) with OAm.

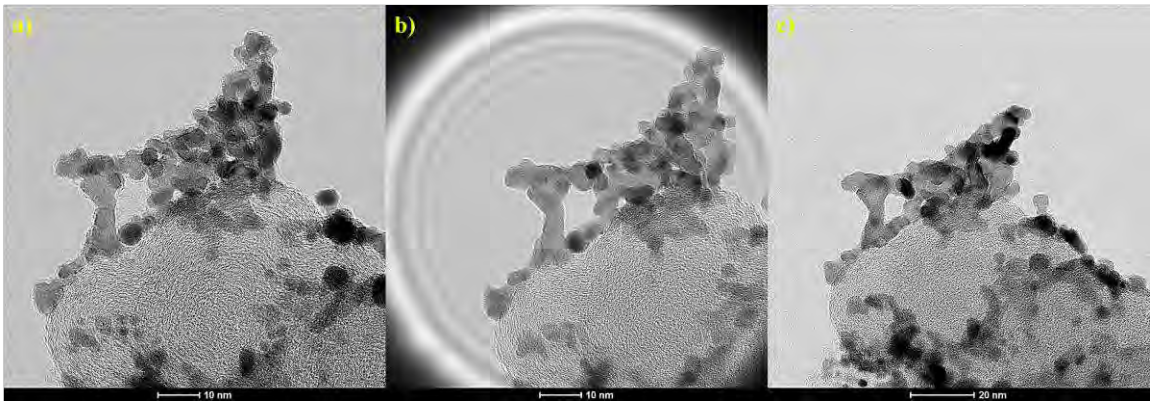

Figure 4. OAm film degradation around the Pt NPs under TEM beam at a) 0 min, b) 8 min and c) 15 min.

Fig. 5-6 show the HR-TEM micrographs of the nanoparticles after TiN deposition by HCPA-ALD. 50% Pt/C without OAm was used as a baseline. This allowed us to determine the feasibility of our deposition approach. The results confirmed the successful and uniform TiN coating of the bare NPs surface, with an average film thickness of 1.5 nm (with a 0.5–3.5 nm range). The presence of the Pt NPs and TiN thin film was furthere confirmed by the spotty rings in the Selected Area Diffraction (SAD) pattern in the insert of fig. 6, where the bright spots correspond to (400) and (222) Pt reflections, as well as (331) TiN reflections, while the additional diffused rings correspond to amorphous carbon. Fig. 6 also illustrates the HR-TEM micrographs and their corresponding STEM/EDS elemental maps, where the highly homogeneous and conformal TiN film is observed completely covering the surface of the entire agglomerate, having similar thickness on the surface of the Pt NPs and carbon support. This can imply that the growth rate of TiN on those two different surfaces (Pt and C) may also be similar.

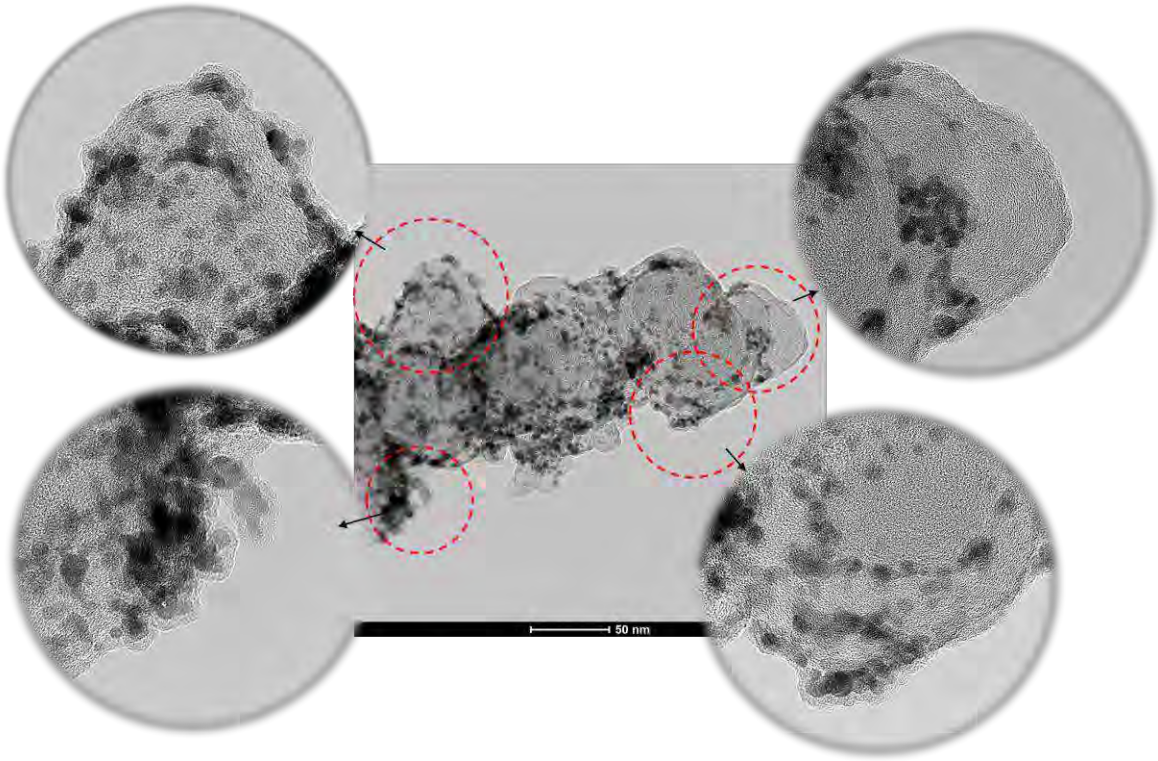

Figure 5. HR-TEM micrographs of 50% platinum on Vulcan XC-72 coated with TiN by HCPA-ALD.

Fig. 7-8, illustrate the effect of TiN deposition on 50% platinum on Vulcan XC-72 with OAm. The TiN film on these nanoparticles is not quite homogeneous or uniformly distributed, especially on the carbon support. This suggests that the presence of OAm, even though is not hindering the deposition process, is reducing the deposition rate in some areas of the agglomerates. The histogram in fig. 7 indicates that even though the average TiN film thickness of 1.84 nm is similar to TiN deposition on 50%Pt/C in the absence of OAm (1.5 nm), the thickness range is wider being 0.5 nm to 6 nm in the powders with OAm, and 0.5 to 3 nm without OAm. This heterogeneity of thickness for this sample can be also observed in the STEM/EDS elemental maps in fig. 8.

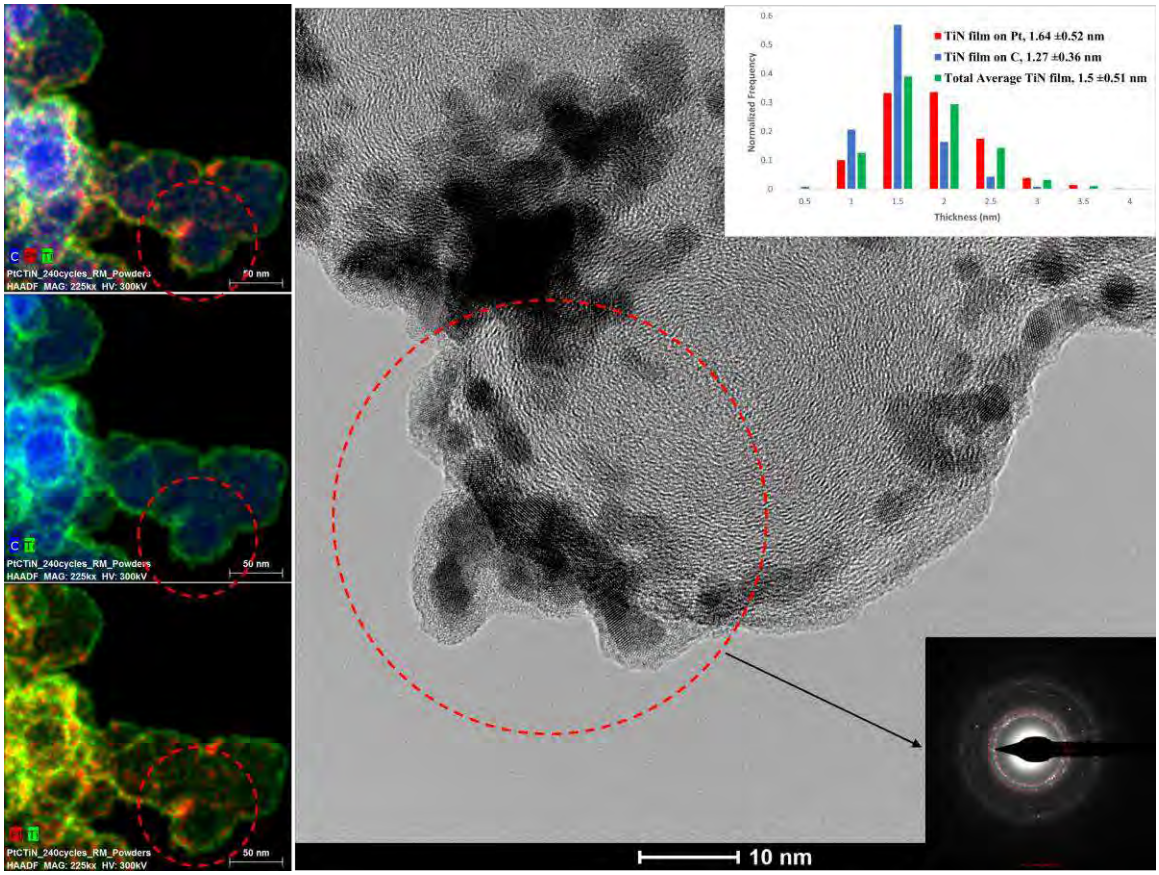

Figure 6. HR-TEM micrograph, STEM/EDS elemental maps, TiN thickness distribution and Selected Area Diffraction (SAD), of 50% platinum on Vulcan XC-72 coated with TiN by HCPA-ALD (no OAm).

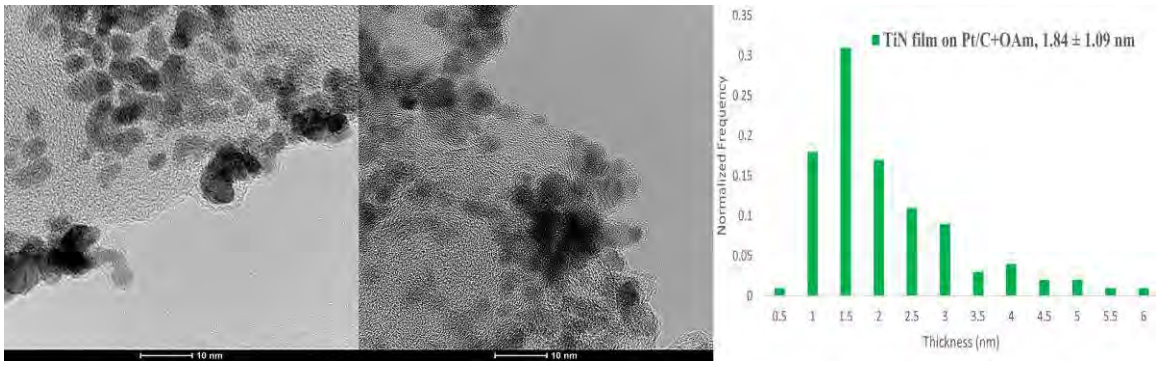

Figure 7. HR-TEM micrographs of 50% platinum on Vulcan XC-72 + OAm, coated with TiN by HCPA-ALD. TiN thickness distribution.

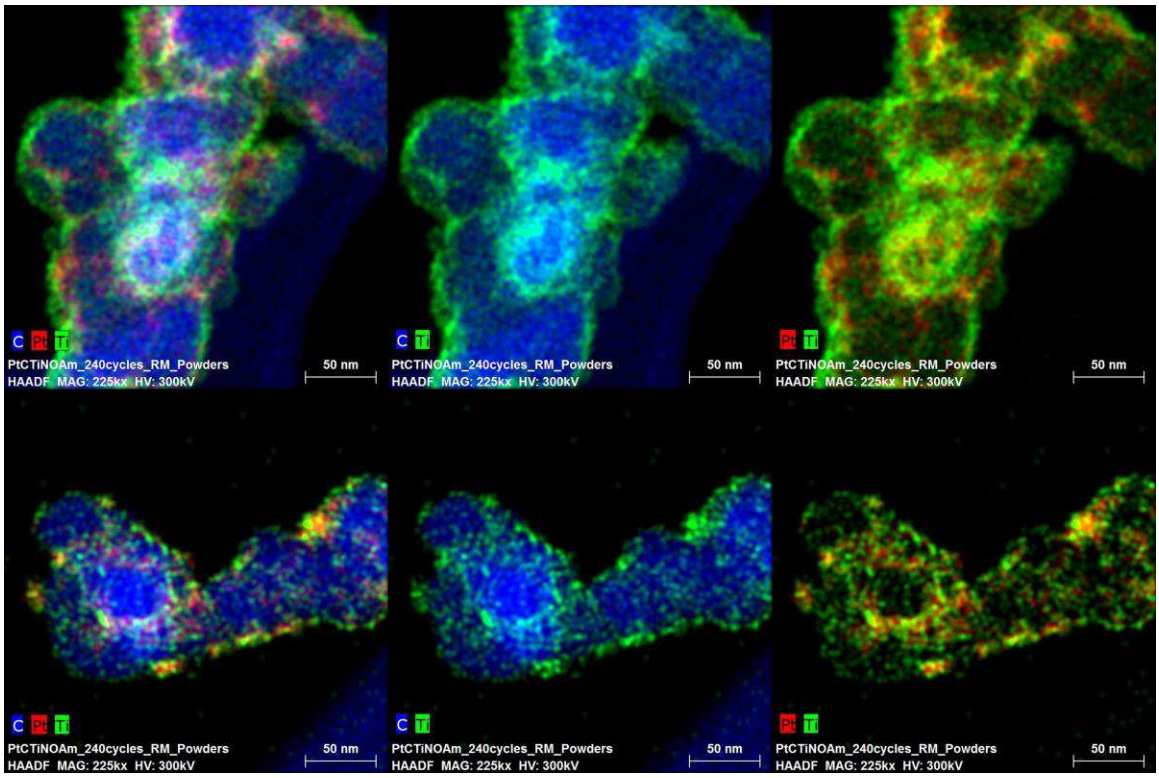

Figure 8. STEM/EDS elemental maps of 50% platinum on Vulcan XC-72 + OAm coated with TiN by HCPA-ALD.

N_2 Sorption: The hysteresis loop represents an important feature in the porous media, associated with the processes of capillary condensation and evaporation occurring in a mesopores structure[25]. For our samples, in fig. 9a, the onset of the loop was usually located at approximately P/P_o=0.9 followed almost immediately by a sharp rise in the adsorption/desorption curve up to about P/P_o=1.0 where saturation level was attained, indicating a complete pore filling and capillary condensation occurring in both meso- and macro- pores. This rise on the isotherm is caused by a sharp increase of adsorbed nitrogen[26]. Both isotherms, for bare Pt/C and Pt/C+OAm, are very similar, even though the curve seems to decrease with the addition of OAm. According to De Boer and Lippens[27] our samples fit the hysteresis loops pattern of a type V isotherm for mesoporous media with weak interaction, while the pore shapes for the hysteresis patterns fit a combination of H1 for cylinder-shaped pores and/or H3 for wedge-shaped pores created by the piling of flaky particles as stated by The International Union of Pure and Applied Chemistry (IUPAC)[28]. In addition, the BJH curve in figure 9.b are almost exactly the same, implying similar sizes in the diameter of the pore. Table 1 shows the quantitative data obtained from the BET and BJH methods. Even though there is a huge reduction on the BET surface area when OAm is added, this may be due to the increase on agglomeration of the powders, as seen on SEM, where OAm acts as a gluing media of the powders. However, the characteristics of the pores does not change that much, implying that OAm is in fact not covering much of the carbon surface or obstructing its porosity, which is what was expected.

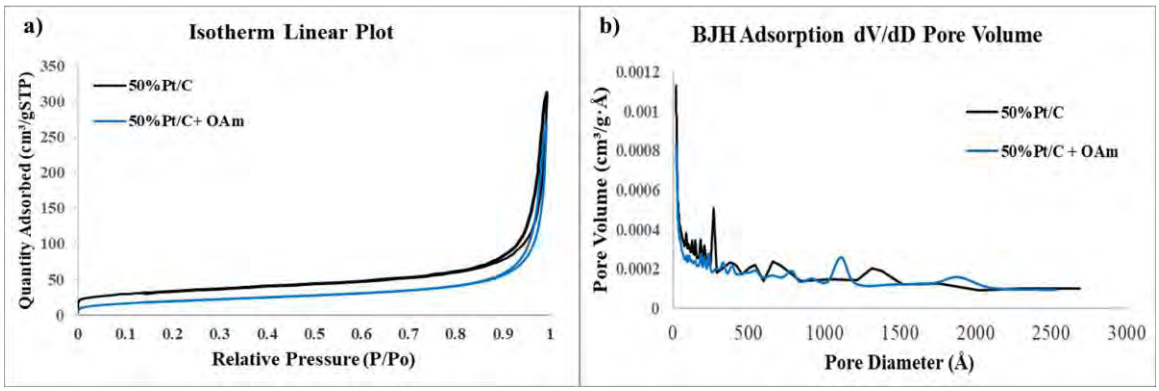

Figure 9. a) N_2 adsorption/desorption isotherm, b) Pore size distribution.

Table 1. Surface Area and Porosimetry

	50% Pt/C	**50% Pt/C + OAm**
BET Surface Area	115.45 m²/g	68.77 m²/g
BJH Adsorption cumulative volume of pores between 17.000 Å and 3000.000 Å diameter.	0.45 cm³/g	0.4 cm³/g
BJH Adsorption average pore diameter (4V/A)	267.95 Å	295.84 Å

Thermogravimetric Analyses: in an oxidizing atmosphere for 50% platinum on Vulcan XC-72 + OAm reveals two distinct weight loss steps, compared to the single carbon degradation step in the powders without OAm, fig. 10. The first step shows that the degradation of the OAm occurs between 90-220°C (which is in agreement with literature[29]) and loss of water molecules, yielding an anhydrous material. The second stages are related to the oxidation and decomposition of the carbon support occurring around 380°C in both samples, implying that the presence of OAm does not influence the thermal degradation of the carbon support[30]. Finally, the region of the graph that reaches a constant mass, around 50% for both samples, reflects the weight percent of the catalyst metal corresponding to its Pt content, plus impurities. This result indicates that low temperature heat treatment in the air can be effective removal method to attain OAm-free Pt catalyst surface, after TiN deposition.

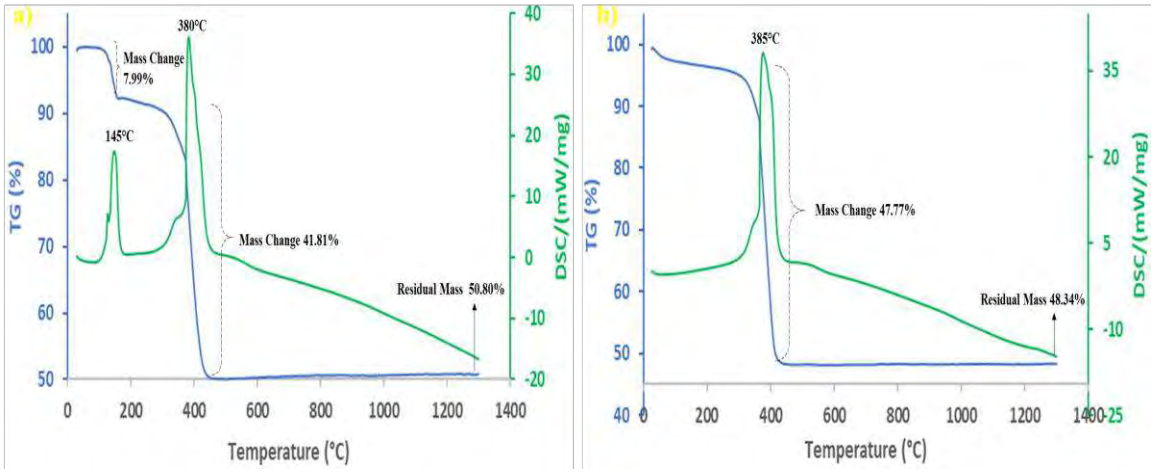

Figure 10. TG/DSC curves of 50% platinum on Vulcan XC-72 a) with and b) without OAm.

Electrochemical Characterization: SEM was used to study the catalyst film (coated on the GC) quality and its effective thickness for the RDE study, see Fig. 11. As can be observed in the image, the catalyst film has been mainly uniformly formed on the GC surface and its thickness is about 1μm, which according to the literature helps avoiding transport losses affecting ORR measurements. Thicker catalyst films have the detrimental effect of increasing the mass transport resistance and cause incomplete access to the electrochemical surface area of the catalyst[31].

Fig. 12 shows the CV profiles of 50% platinum on Vulcan XC-72 (*PtC*), PtC with OAm (*PtC/OAm*), PtC/OAm after heat treatment at 185°C (*PtC/185OAm*), PtC/TiN with OAm (*PtC/TiN/OAm*) and PtC/TiN/OAm after heat treatment at 185°C (*PtC/TiN/185OAm*). Typically, in a clean Pt surface, the CV profile reveals some characteristic voltametric features[32,33] describing the (i) hydrogen adsorption and desorption regime (underpotential deposition of hydrogen at 0.06–0.4V vs RHE), (ii) the double layer region (at intermediate potentials 0.4–0.6V vs RHE) and (iii) formation and reduction of Pt (hydro)oxide (above 0.6V vs RHE), respectively. The current density and the peaks depend on the catalytic activity of Pt. When the surface of the Pt NPs is not avaible to adsorb the reactants (O_2, H_2, H_2O or H^+) the reactions already mentioned would not occur. The CV regimes in the *no sonicated PtC samples,* though visible, were not as pronounced as in *the sonicated PtC samples* ones which usually have better dispersion and less Pt NPs agglomeration. However, for this study it was necessary not to use sonication when preparing the catalyst film in order to preserve the integrity of both coating mechanisms, OAm and TiN. Once OAm is added to PtC, the peaks representing those regimes are almost gone with a considerable reduction of the current density, indicating the presence of site-blockage species like OAm preventing the Pt NPs to be used as a catalyst. The removal of OAm on PtC by heat treatment seem to be successful, the CV shows a profile very similar to *PtC sonicated* from which the characteristic voltametric features described before are clearly pronounced. The addition of TiN to the PtC has a similar effect as the OAm addition. This is possibly due to not fully optimized deposition process, where TiN is still covering Pt active sites. *PtC/TiN/185OAm* profiles also matches that of *PtC sonicated*, proving that the active sites are exposed and available for reactions and the efficacy of our methods.

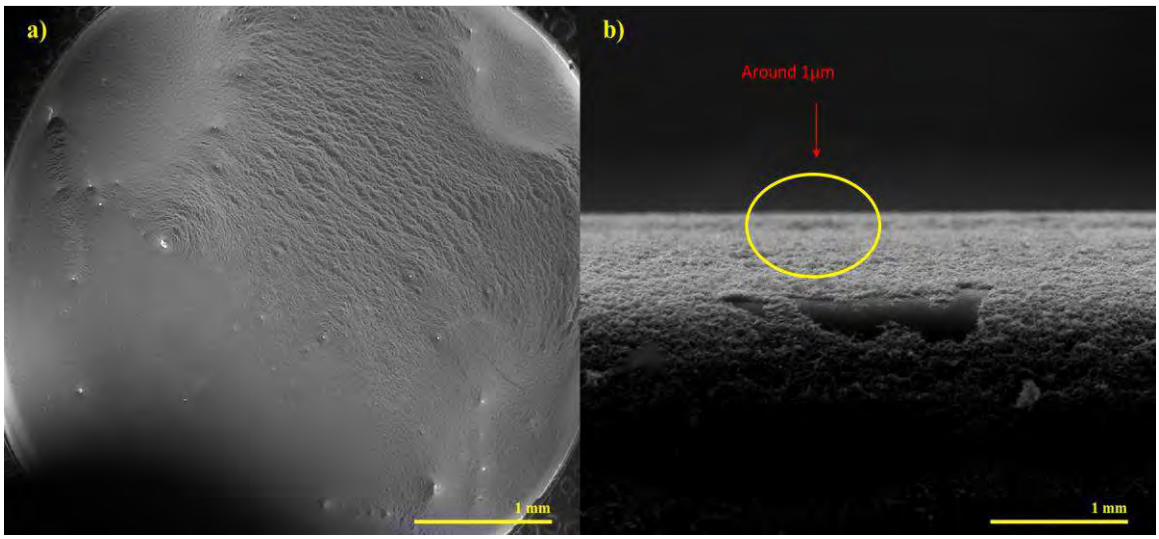

Figure 11.) SEM characterization of catalyst film.

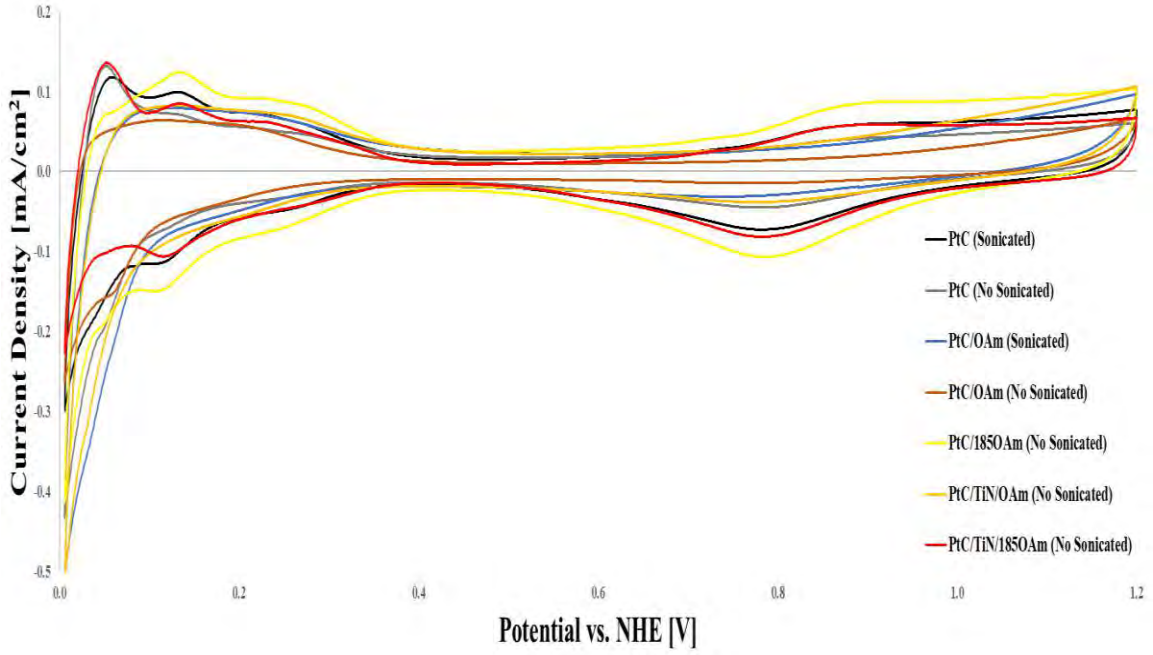

Figure 12.) Cyclic voltammetry curves at 20 mV/s

In general, the ORR in a good electrode film consists of a mixed kinetic-diffusion control in the potential region between 0.75–1.00 V vs RHE represented by a single steep reduction wave followed by a well-developed flat diffusion limited current density plateau between 0.20-0.70V vs RHE. In our samples, fig 13, the polarization curves for the samples with exposed catalyst metal (*PtC, PtC/185OAm and PtC/TiN/185OAm*) present a plateau-like behavior between 0.2–0.75V vs RHE, indicating the mass transport limiting current density for ORR in which the diffusion of reacting species towards the electrode surface dominates over the reaction kinetics[34]. However, these limiting current density plateaus are not as well developed or flat enough. Additionally, the onset potential transitioning from the mass-transport limiting region to the mixed kinetic-mass transport-controlled region takes place at ~0.7-0.8 V vs RHE, but we can also conclude that above 0.7 V vs RHE the current density starts to originate from the ORR kinetics of the Pt NPs, independent on the rotation speed of the electrode[32]. The coated samples (with OAm and TiN) have a different behavior, no steep reduction of plateaus is presented; these results reinforce the idea that OAm covers the platinum and thus prevents the catalytic activity from occurring. Moreover, samples *sonicated PtC/OAm*, and *no sonicated PtC/TiN/OAm* offers a vague representation of these features explained before but less pronounced, indicating a very small amount of catalyst exposure due to the degradation of the OAm film by (i) sonication and (ii) plasma power/temperature in the HCPA-ALD chamber. Furthermore, the activity towards the ORR can be related to the half-wave potential ($E_{1/2}$), defined as the half-way point between zero current and the diffusion limited current density plateau. $E_{1/2}$ is almost the same, 0.85V vs RHE, for samples *PtC (sonicated), PtC/185OAm* and *PtC/TiN/185OAm*, proving a succesful removal of the OAm screening materials. The significant activity of the electrocatalyst is indicated by its high $E_{1/2}$ and dependens on the quality of the catalyst cast film.

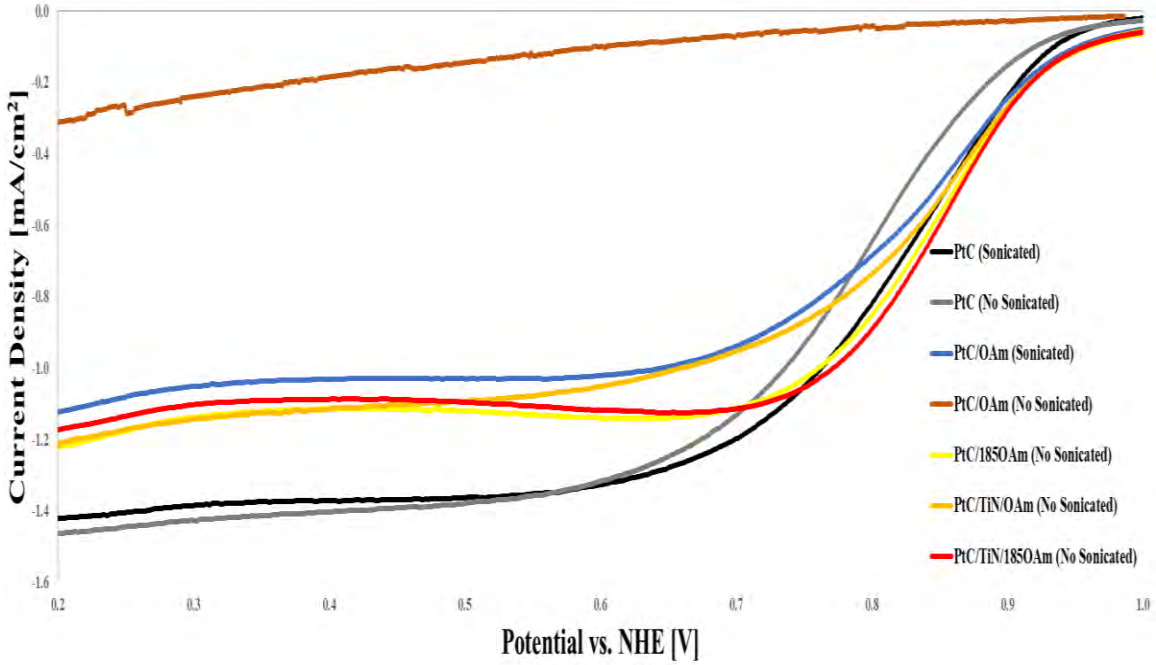

Figure 12. ORR polarization curves at 20 mV/s

CONCLUSION

In summary, we successfully carried out the deposition of a TiN film on the carbon substrate of a platinum on carbon (Pt/C) catalyst (in powder state), while keeping the Pt catalyst centers uncoated and available for reagents reactions using a HCPA-ALD accommodated to perform depositions on powder materials. However, the homogenity of the film can be compromised once OAm is added to the 50%Pt/C powders, and even though ALD processes are self-limiting surface reactions, an Area-Selective ALD process would be needed to deposit the desirable material in a more exact and control way. Additionally, the electrochemical response of our designed catalyst was similar to that of uncoated 50%Pt/C catalyst, showing promising capabilities as PEMFC catalyst, but leaving the possibility for some improvements.

REFERENCES

1. M. F. Mathias, R. Makharia, H. A. Gasteiger, J. J. Conley, T. J. Fuller, C. J. Gittleman, S. S. Kocha, D. P. Miller, C. K. Mittelsteadt, T. Xie, S. G. Yan, and P. T. Yu, Electrochem. Soc. Interface, (2005).
2. T. Covert, M. Greenstone, and C. R. Knittel, J. Econ. Perspect., **30**, 117–138 (2016).
3. S. Shafiei and R. A. Salim, Energy Policy, **66**, 547–556 (2014).
4. B. Machol and S. Rizk, Environ. Int., **52**, 75–80 (2013).
5. A. Kongkanand, W. Gu, and M. F. Mathias, Fuel Cells Hydrog. Prod. (2019).
6. J. Garche and L. Jörissen, Electrochem. Soc. Interface, **24**, 39–43 (2015).
7. P. Ruano, Intech, **13** (2016).
8. R. E. Yonoff, G. V. Ochoa, Y. Cardenas-Escorcia, J. I. Silva-Ortega, and L. Meriño-Stand, Heliyon, **5** (2019).
9. M. K. Debe, Nature, **486**, 43–51 (2012).

10. O. T. Holton and J. W. Stevenson, Platinum Met. Rev, **57**, 259–271 (2013).
11. R. Othman, A. L. Dicks, and Z. Zhu, Int. J. Hydrogen Energy, **37**, 357–372 (2012).
12. N. Yousfi-Steiner, P. Moçotéguy, D. Candusso, and D. Hissel, J. Power Sources, **194**, 130–145 (2009).
13. J. C. Meier, C. Galeano, I. Katsounaros, J. Witte, H. J. Bongard, A. A. Topalov, C. Baldizzone. S. Mezzavilla, F. Schüth and K. J. J. Mayrhofer, Beilstein J. Nanotechnol., **5**, 44–67 (2014).
14. J. Y. Kim, S. Lee, T. Y. Kim, C. Pak, and H. T. Kim, Carbon N. Y., **77**, 525–537 (2014)
15. S. Samad, K. S. Loh, W. Y. Wong, T. K. Lee, J. Sunarso, S. T. Chong and W. R. W. Daug, Int. J. Hydrogen Energy, **43**, 7823–7854 (2018)
16. J. Hou, M. Yang, C. Ke, C. Priest, Z. Qiao, G. Wu and J. Zhang, EnergyChem, **2**, 100023 (2020).
17. H. A. Gasteiger, S. S. Kocha, B. Sompalli, and F. T. Wagner, Appl. Catal. B Environ., **56**, 9–35 (2005).
18. S. Samad, K. S. Soh, W. Y. Wong, T. K. Lee, J. Sunarso, S. T. Chong and W. R. W. Daud, Int. J. Hydrogen Energy, **43**, 7823–7854 (2018).
19. L. Li, L. Hu, J. Li, and Z. Wei, Nano Res., **8**, 418–440 (2015).
20. B. Avasarala and P. Haldar, Energy, **57**, 545–553 (2013).
21. R. W. Johnson, A. Hultqvist, and S. F. Bent, Mater. Today, **17**, 236–246 (2014).
22. L. Hu, W. Qi, and Y. Li, Nanotechnol. Rev., **6**, 527–547 (2017).
23. A. W. Weimer, Particle atomic layer deposition, Journal of Nanoparticle Research, (2019).
24. S. Mourdikoudis and L. M. Liz-Marzán, Chem. Mater., **25**, 1465–1476 (2013).
25. Q. Zhao, H. Li, X. Zhang, S. Yu, S. Wang and G. Sun, J. Energy Chem., **41**, 120–125
26. C. Yang, J Zhang, S. Han, X. Wang, W. Yu and Z. Wang, J. Nat. Gas Sci. Eng., **34**, 1369–1381 (2016).
27. R. Wang, S. Sang, D. Zhu, S. Liu, and K. Yu, Energy Explor. Exploit., **36**, 43–65 (2018).
28. X. Tang, Z. Yiang, Z. Li, Z. Gao, Y. Bai, S. Zhao and J. Feng, J. Nat. Gas Sci. Eng., **23**, 464–473 (2015).
29. K. S. W. Sing, D. H. Everett, R. A. W. Haul, L. Moscou, R. A. Pierotti, J. Rouquerol and T. Siemieniewska , J. Med. Assoc. Thail., **81**, 420–430 (1998).
30. K. Rickard and D. Rende, Nanotechnol. Sci. Appl., 69–77 (2017).
31. O. A. Baturina, S. R. Aubuchon, and K. J. Wynne, Chem. Mater., **18**, 1498–1504 (2006).
32. Y. Garsany, O. A. Baturina, K. E. Swider-Lyons, and S. S. Kocha, Anal. Chem., **82**, 6321–6328 (2010).
33. I. A. Safo, C. Dosche, and M. Özaslan, ChemPhysChem, **20**, 3010–3023 (2019).
34. D. Y. Chung, K. J. Lee, and Y. E. Sung, J. Phys. Chem. C, **120**, 9028–9035 (2016).
35. N. Elgrishi et al., J. Chem. Educ., **95**, 197–206 (2018).

ECS Transactions, 104 (8) 45-58 (2021)
10.1149/10408.0045ecst ©The Electrochemical Society

Analysis Method of Oxygen Reduction Reaction Rate in PEFC Using Pt-Sputtered Catalyst

Hikaru Ogawa, Miho Kageyama, and Motoaki Kawase

Department of Chemical Engineering, Kyoto University, Kyotodaigaku-Katsura, Nishikyo-Ku, Kyoto 615-8510 Japan

For widespread use of polymer electrolyte fuel cell (PEFC), it is necessary to reduce the amount of platinum by optimizing the cathode catalyst layer (CCL) structure. Therefore, oxygen reduction reaction (ORR) rate which does not include the mass transfer resistance in CCL should be formulated. To measure the ORR rate which does not include the mass transfer resistance in the CCL, a thin layer electrode was prepared by directly sputtering platinum to microporous layer (MPL) on gas diffusion layer. Dependencies of ORR rate on temperature and relative humidity (RH), were measured and analyzed. From the measurement results, ORR parameters which do not include the effect of mass transfer resistance through the CCL were appropriately determined. The ORR rate and electrochemical surface area (ECSA) depend on RH and a half of RH dependency of ORR rate is ascribed to change in ECSA.

Introduction

Polymer electrolyte fuel cell (PEFC) converts the chemical energy of hydrogen to electricity. Recently, PEFC has been more and more utilized in residential co-generation systems and automobiles. (1, 2) Since PEFC can be operated at low temperature, it can be started up and shut down frequently. Therefore, PEFC is expected as one of the energy devices that can be applied to a wide range of applications.

Further technical breakthroughs are needed for PEFC to be more widely used and one of the challenging problems is to reduce platinum catalyst cost which accounts for 40 % of PEFC stack cost (2, 3). For widespread use of PEFC, optimization of the cathode catalyst layer is required in order to reduce platinum loading and improve efficiency. Proton transfer resistance and oxygen transfer resistance in the CCL, as shown in Figure 1, prevent the CCL from performing at the capable maximum reaction rate. Furthermore, oxygen permeation resistance through ionomer which coats the platinum nanoparticles also reduces ORR rate. Therefore, to establish the generic model of the cathode catalyst layer (CCL) (4), the oxygen reduction reaction (ORR) rate which does not include mass transfer resistance through the CCL should be formulated. Once it is formulated, mass transfer resistance can be separated and analyzed from experimental results using platinum-supported catalyst.

Theory

Neglecting the backward reaction, the current density is an integral of the local current density, which is proportional to ORR rate per geometric area, r_{gO}, over the whole

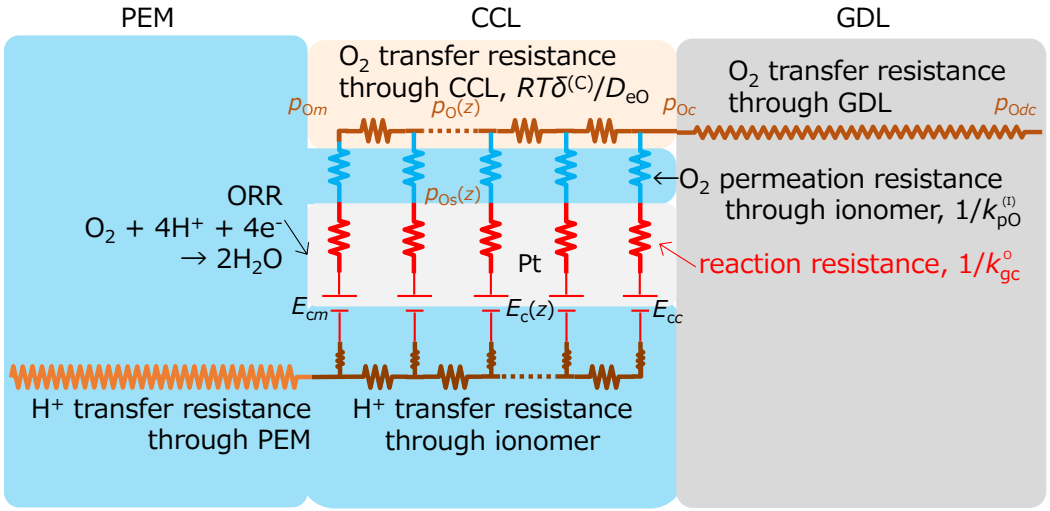

Figure 1. Mass transfer resistances in the CCL

thickness of the CL as follows:

$$i = -4F \int_0^{\delta^{(C)}} (-r_{gO}) dz \ [A/cm^2] \quad [1]$$

where F is the Faraday constant [C/mol] and $\delta^{(C)}$ is the CCL thickness.

r_{gO} [mol/(m^2·s)] is proportional to oxygen partial pressure (4, 5).

$$r_{gO} = k_{gc}\, p_O F_e \quad [2]$$

where F_e is the effectiveness factor of the CCL. $k_{gc}F_e$ [mol/(Pa·m^2·s)] is the observed reaction rate constant per geometric area. F_e is defined as the ratio of the observed reaction rate to the reaction rate which does not include the effect of mass transfer resistance in the through-plane direction. $k_{gc}F_e$ [mol/(Pa·m^2·s)] is the observed reaction rate constant which includes the effect of proton and oxygen transfer resistance in the through-plane direction of CCL.

Moreover, k_{gc} includes not only resistance to ORR but resistance to oxygen permeation through the ionomer layer coating platinum nanoparticles as follows:

$$1/k_{gc} = 1/k_{po} + 1/k^{\circ}_{gc} \quad [3]$$

where k_{pO} is the oxygen permeance of the ionomer layer [mol/(Pa·m^2·s)] and k°_{gc} is the intrinsic reaction rate constant [mol/(Pa·m^2·s)], which does not include the mass transfer resistance of the CCL thickness nor the resistance of the ionomer layer.

k°_{gc} is a function of temperature T [K] and cathode electromotive force E_c [V] as follows:

$$k^{\circ}_{gc} = k^{\circ}_{gc0} \exp(-E/RT - E_c/b_c) = k^{\circ}_{gc0} \exp\{-(E+4aFE_c)/RT\} \quad [4]$$

where E is the activation energy [J/mol], b_c is the Tafel slope [V] which is a function of temperature, and $4a$ is the transfer coefficient.

Objective

The value of the activation energy, E, has been reported to be 20 to 60 kJ/mol (6, 7, 8, 9). An Apparent ORR rate constant was obtained instead of the ORR intrinsic rate when mass transfer resistance of the CCL was not eliminated or Tafel slope dependency on temperature was not considered. In addition, it has been reported that the ORR rate depends on relative humidity (RH) (10).

The objective of this study is, therefore, to develop a measurement method of temperature, RH and E_c dependencies of the ORR rate constant which does not include the influence of mass transfer resistances. There are two methods to determine the intrinsic ORR rate. The first one is to analyze mass transfer resistance of the CCL with the commercial supported catalyst to determine the intrinsic ORR rate parameters. The second one is that to directly measure the ORR rate under ideal conditions which do not have the influence of mass transfer resistance in the CCL. As the former method, ORR rate dependency on CCL thickness and platinum loading have been investigated (11, 12). In this study, the latter method was examined and the ORR rate which does not have any effect of mass transfer resistance of the CCL was measured under ideal conditions. An ideal catalyst layer whose thickness can be regarded as 0 was prepared by directly sputtering platinum on a microporous layer (MPL) on a carbon paper.

Experimental

Preparation of Pt Thin-Layer Cathode

Pt thin-layer cathode (0.054 mg/cm^2) was prepared by sputtering (AOV, SPAD-4240UM). First of all, an MPL on a carbon paper (SIGRACET-GDL 29 BC) substrate whose thickness was 235–238 μm was weighed and cleaned by ion cleaning at 5 Pa at room temperature (*ca*. 25 ºC). Argon was supplied at 20 cm^3/min (0 ºC, 1 atm). The input power, substrate rotation speed of rotation, deposition angle was 20 W, 10 rpm and 30º, respectively. After ion cleaning, the substrate was weighed again and Pt was sputtered from a Pt target (99.99 wt%) to the MPL on the carbon paper at 100 ºC. Except temperature, the identical conditions to those of ion cleaning were applied to sputtering.

Assembling the Cell

A Japan Automobile Research Institute (JARI) standard cell whose active area was 50 mm × 50 mm or modified to 20 mm × 20 mm were used in the experiments. A membrane-anode assembly (MAA, Eiwa Corp.) was composed of a proton exchange membrane (PEM, Nafion® NR-212) and an 8.3–9.8 μm thick (0.19–0.24 mg/cm^2) anode which was made of Pt/Vulcan® XC-72 catalyst (Pt/C weight ratio: 1) with a Nafion® ionomer (ionomer/carbon weight ratio: 0.74). This MAA and a Pt-thin-layer cathode prepared by sputtering were stacked in a PEFC as shown in Figure 2. While Pt-sputtered carbon paper is used as the cathode GDL, a carbon paper (Toray TGP-H-060, hydrophobically treated with 10 wt% PTFE) is used as the anode GDL. A carbon current collector had a single serpentine flow channel, the width and depth of which were 1.0 mm and the pitch of the ribs was 2.0 mm. H_2 and O_2 were humidified at 60–80 ºC through bubblers and their flow rates were 600 and 300 cm^3/min (20 ºC, 1 atm), respectively. The cell inlet RH was calculated from the saturated water vapor pressure at the bubbler temperature and the cell temperature. The cell was operated at 65–80 ºC.

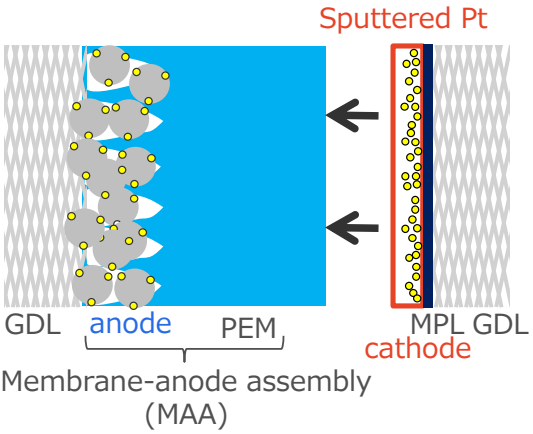

Figure 2. Structure of Pt-sputtered catalyst

The pressure at the cell outlet was ambient pressure (*ca*. 1 atm). Polarization curves were measured using an electrochemical measurement system (Hokuto Denko, HZ-7000). The resistance of PEM was measured from high frequency resistance and the electrochemical surface area (ECSA) was also measured from cyclic voltammetry. Its sweep range and sweep rate was 0.05–0.9 V and 3 V/s, respectively. Electrochemical hydrogen adsorption and desorption amount was assumed as 2.1 C/m^2. XRD (Rigaku, Ultima IV) was used in order to characterize the platinum-sputtered catalyst.

Results and discussion

Characterization of Pt-Sputtered Catalyst

1. Argon Ion Cleaning Time. It is important to clean the substrate surface prior to platinum sputtering in order not to deteriorate the catalyst performance. Figure 3 shows the temporal change in the substrate weight during the argon ion cleaning. The slope from 25 to 135 minutes is less than a half of the slope from 0 to 25 minutes. It indicates that fine dusts and hydrophobized coatings on the MPL surface are removed in the first 25 minutes, and after that, polytetrafluoroethylene (PTFE), the main additive of MPL, was abrased. That is to say, 30 minutes is enough to remove almost all the hydrophobized coatings on the MPL surface. In this study 40-minute ion cleaning was applied.

2. Sputtering Time. Figure 4 shows the Pt loading is proportional to the sputtering time. 50-minute sputtering were employed in all experiments. Pt loading is 0.054 mg/cm^2 on average when Pt was sputtered for 50 minutes.

3. XRD pattern of platinum sputtered catalyst. Figure 5 shows the XRD patterns of platinum-sputtered catalyst on the MPL surface, Pt powders and pristine MPL surface (13). There are some peaks in the case of the platinum-sputtered MPL surface besides carbon peaks ascribed to MPL substrate. In addition, the XRD pattern of Pt-sputtered catalyst has (111), (200) and (220) orientations and it is identical to the Pt powder patterns. Since platinum particle is supported on carbon black in case of platinum supported catalyst, platinum is randomly oriented and the XRD patterns of the platinum-supported catalyst is identical to that of platinum powder patterns. From these results, the difference in catalytic activity between the sputtered catalyst and the supported catalyst due to crystal orientation does not need to be considered.

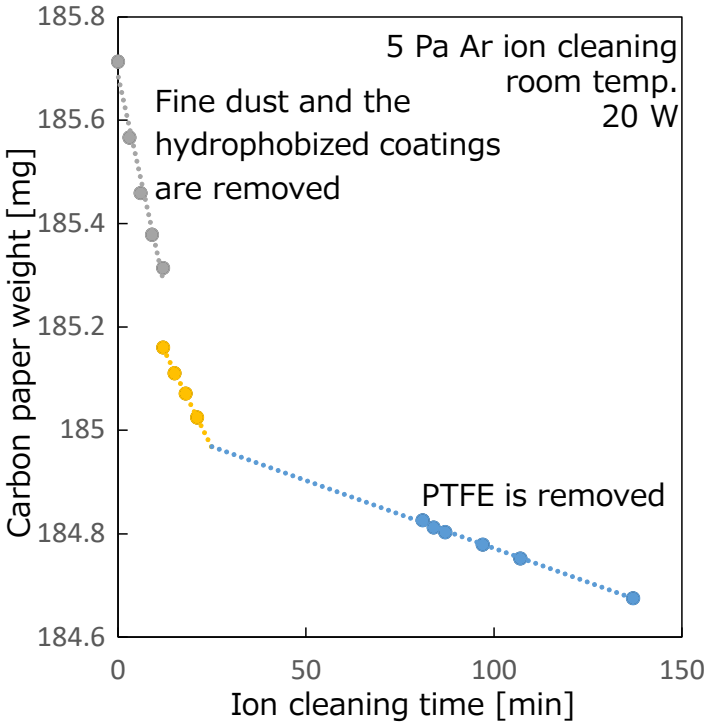

Figure 3. Carbon paper weight vs. ion cleaning time

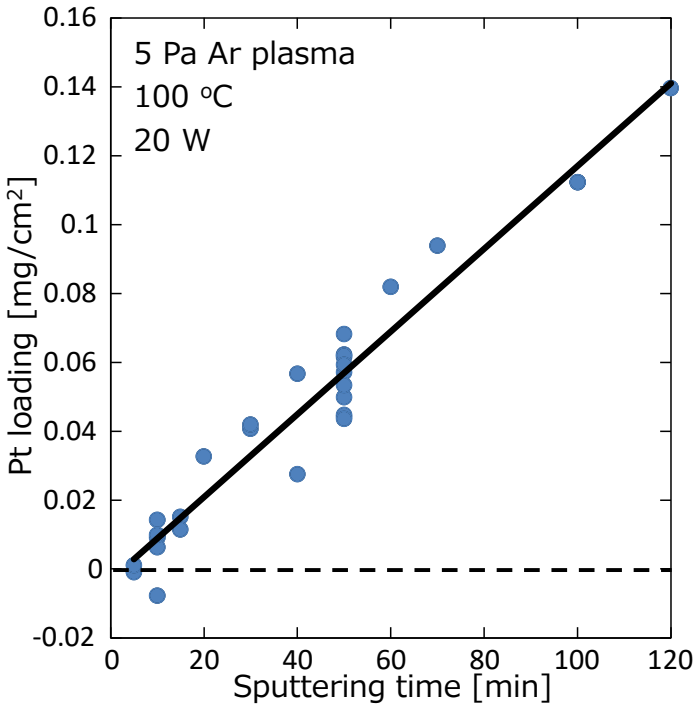

Figure 4. Pt loading vs. sputtering time

4. Particle Diameter. The surface of the Pt-sputtered catalyst was observed with a field emission scanning electron microscope SEM-EDS (Hitachi High Technologies, SU8220), and the element fractions on the surface was measured. Figures 6-1, 6-2 and 6-3 show the surface after 40-minute ion cleaning, 20-minute Pt sputtering and 50-minute Pt sputtering, respectively. Carbon black particles consisting of the MPL have a diameter of approximately 40 μm as shown in Figure 6-1. In addition, platinum particle growth was observed with increase in the sputtering time in Figure 6-3 compared with

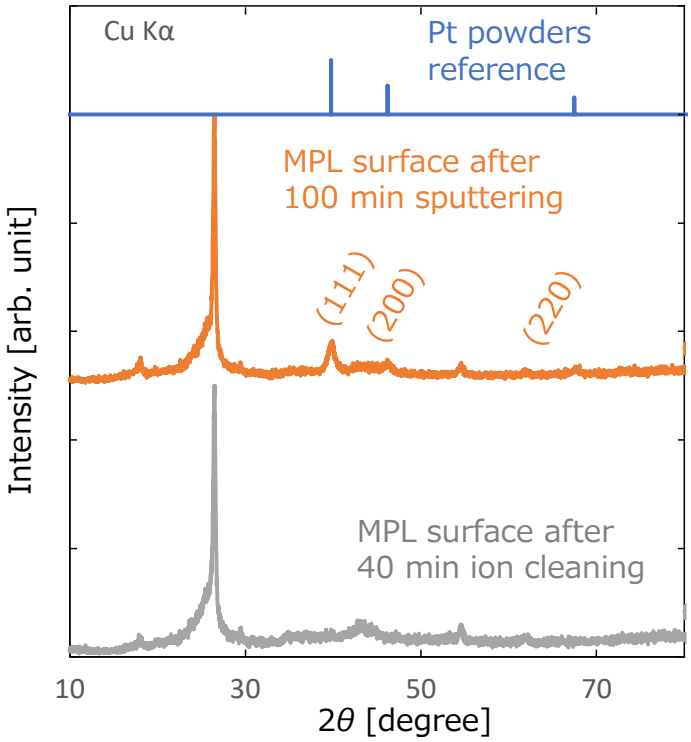

Figure 5. XRD patterns of sputtered Pt and MPL(13)

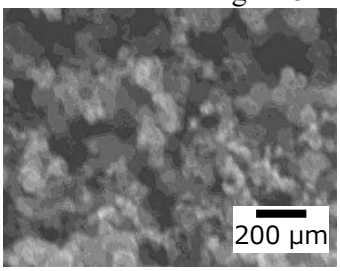

Figure 6-1. MPL surface after 40-minute ion cleaning

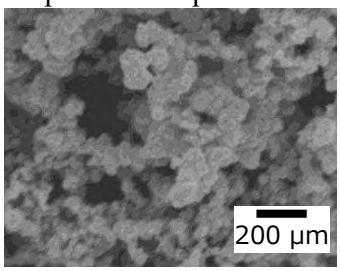

Figure 6-2. MPL surface after 20-minute sputtering

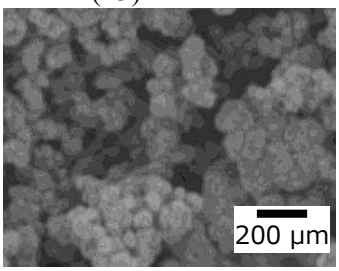

Figure 6-3. MPL surface after 50-minute sputtering

Figure 6-2. Figure 7 shows the MPL surface after 50-minute Pt sputtering. Approximately ten nanometer Pt particles and hundreds nanometer Pt clusters were observed. Carbon black on the MPL surface is covered with platinum grains whose diameter is from 10 to 20 nm.

Figure 8 shows element fractions of the MPL surface after 40-minute ion cleaning, 20-minute Pt sputtering and 50-minute Pt sputtering. In any case fluorine derived from polytetrafluoroethylene on the MPL was detected. In addition, the platinum fraction increased with increase in the sputtering time.

5. Mass Transport Structure of Platinum Sputtered Catalyst Although the platinum-sputtered catalyst does not have ionomer layer, which is a path for proton conduction, the cell using the platinum sputtered catalyst can generate electricity. It can be inferred that protons move through water adsorbed on platinum particles and finally reach the platinum surface as shown in Figure 9. Electrons move through the carbon black and reach the platinum coating on the carbon black.

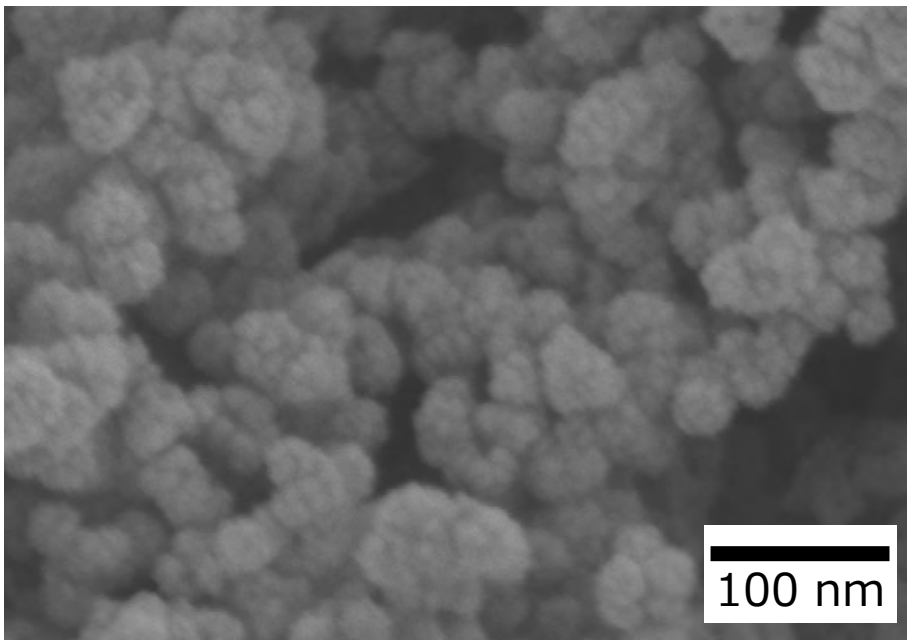

Figure 7. MPL surface after 50-minute sputtering

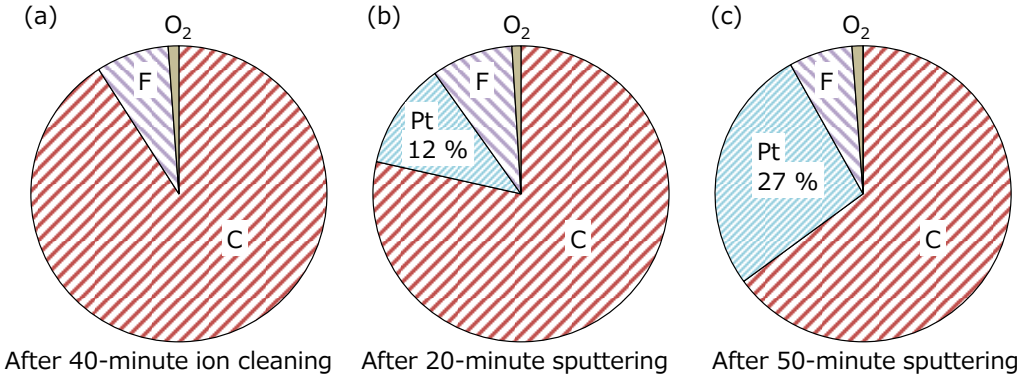

Figure 8 Elemental mass fractions of the MPL surface (a) after 40-minute ion cleaning, (b) 20-minute Pt sputtering and (c) 50-minute Pt sputtering

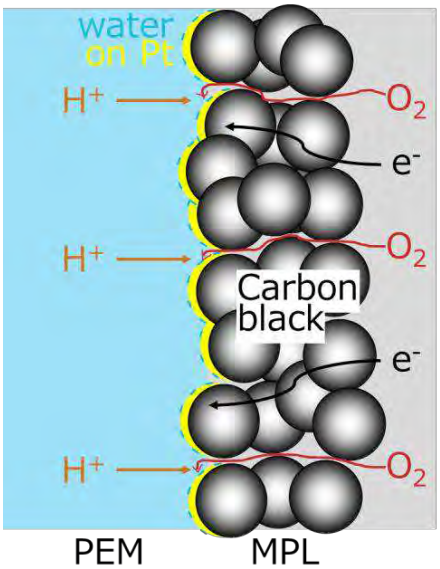

Figure 9. Mass transport sturucture of platinum-sputtered catalyst

RH Dependency of ORR Rate

Figure 10 shows the polarization curves measured at the cell temperature of 80 °C. Current density at a fixed E_c increased with raising RH. By the way, effectiveness factor, F_e in Equation [2] is defined as the ratio of the observed reaction rate to the reaction rate which does not include the effect of mass transfer resistance in the through-plane direction and current density is proportional to F_e. If RH changes, F_e changes according to changes in proton transfer resistance and oxygen permeation resistance through ionomer. That means F_e should be 1 in case of platinum sputtered catalyst since this catalyst does not have CCL thickness and it should not have the effect of mass transfer resistance of CCL. Hence, polarization curves should be identical regardless of RH. Despite this background, polarization curves, that is, ORR rate was actually dependent on RH as shown in Figure 10. This result suggests that there are other RH dependent factors except mass transfer resistance in CCL and the oxygen permeation resistance through ionomer. In fact, it was found that electrochemical surface area, ECSA has RH dependency as shown in Figure 11. Leiming and coauthors also reported this dependency (14).

Considering the current per ECSA instead of current density, RH dependency of ORR rate is narrowed to approximately 50 % as shown in Figure 12. That means ECSA contributes 50 % RH dependency of ORR rate. At the same time, the factors which describe the remaining dependency of ORR rate on RH should be clarified. At least five causative reasons exist as follows:

1. Adsorption of Water and Sulfonic Group on Platinum. Adsorption of the anionic moieties of ionomer on ORR active sites suppress the ORR activities of Pt catalysts (15, 16, 17). That means the ratio of water to sulfonic groups adsorbed on the platinum surface may also contribute to the ORR dependency on RH. It is important to clarify the surface state of platinum while operating the PEFC cell.

2. Platinum Oxidation at High Voltage. The platinum surface is partially oxidized

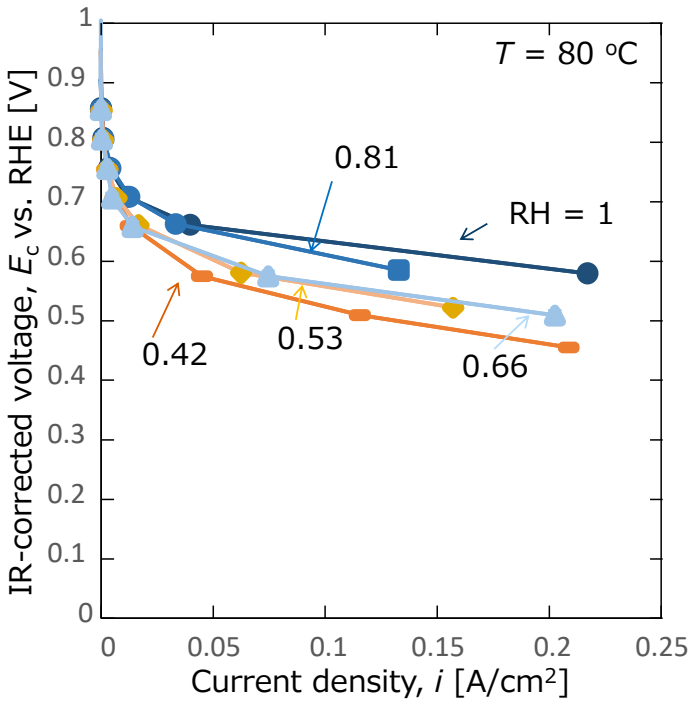

Figure 10. ORR rate dependency on RH

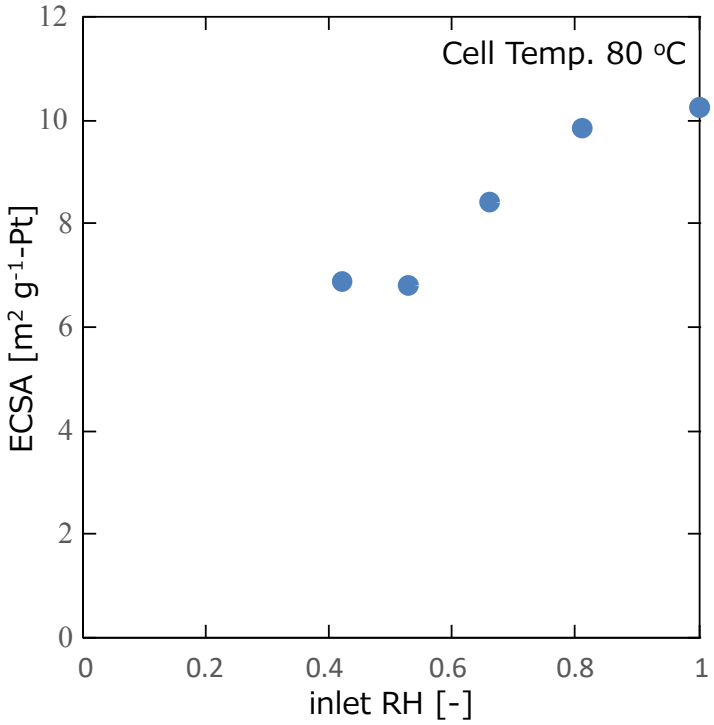

Figure 11. Electrochemical surface area (ECSA) vs. RH

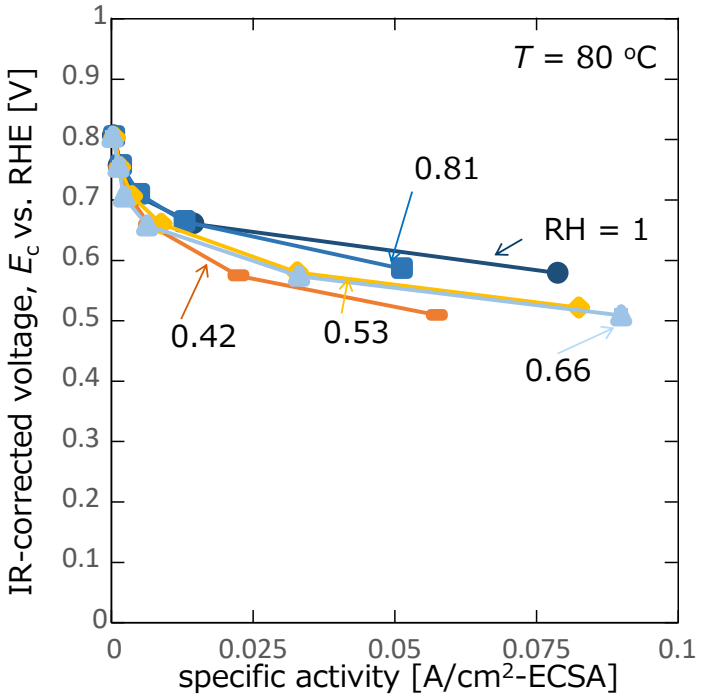

Figure 12. RH dependency of specific activity

especially at high voltage. Thus, it is possible that the ORR dependency on RH on the platinum oxide catalyst has been measured. Of course, platinum and platinum oxide have different hydrophilicity, so the degree of RH dependence of ORR rate may differ.

3. Water Uptake in Ionomer. Although some researchers reported that under high RH conditions, the ionomer swelled, which increased the oxygen permeation, the effect of RH on the accessibility of oxygen at the catalyst/ionomer interface is still unclear, especially under over-saturated conditions (18, 19). Therefore, it is important to

elucidate the mechanism of ionomer swelling and how ionomer swelling affect oxygen permeation through ionomer under high RH conditions. Since the cathode catalyst in this study is a sputtering catalyst, it does not contain ionomers. It is possible, however, that oxygen permeates through the surface layer of the PEM in contact with the thin cathode and consequently the RH dependency of the oxygen permeation resistance resulted in the measured RH dependency of the ORR rate.

4. The Influence of the Reverse Reaction. When the IR corrected voltage, E_c is 0.75 V or higher, the effect of the reverse reaction is large. Since water is the reaction product, raising RH can increases the effect of the reverse reaction under high voltage and reduces the ORR rate, that is, the current.

5. Local Flooding. When RH increases, local flooding is likely to occur during generation. It makes oxygen transport resistance in CCL higher. As a result, ORR rate will decrease under high RH conditions.

The influence of the reverse reaction and local flooding suppress the ORR rate with increase in RH. All of these causative RH dependency factors should be elucidated.

Measurement of Temperature Dependency of ORR Rate

Polarization curves were measured at the estimated inlet RH of 0.81. As shown in Figure 13, current density at a fixed E_c increased with a rise in temperature as expected from Equation [4]. Based on these polarization curves, ORR rate at the fixed E_c was analyzed in order to determine the ORR rate parameters which do not have the influence of mass transfer resistance in the through-plane direction in CCL.

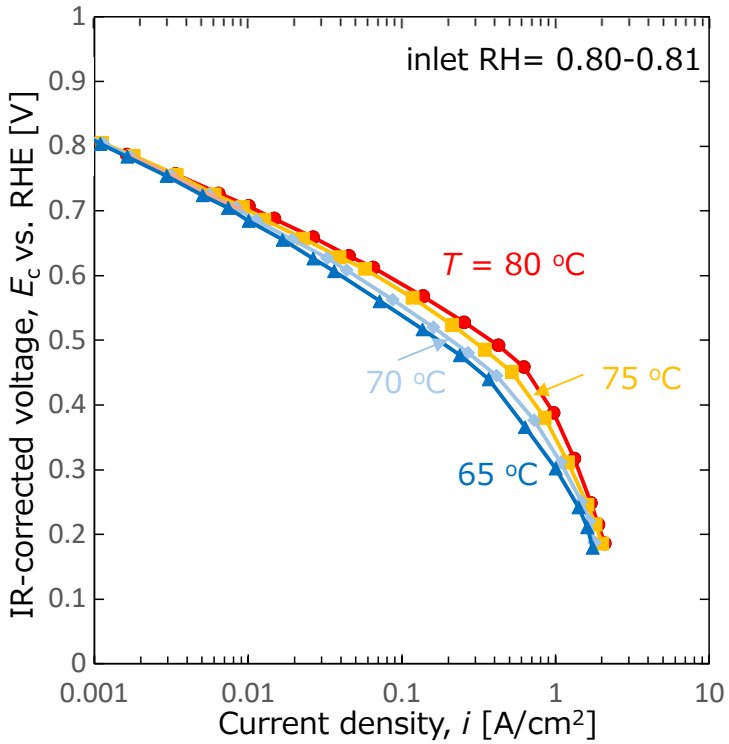

Figure 13. Temperature dependency of polarization curve

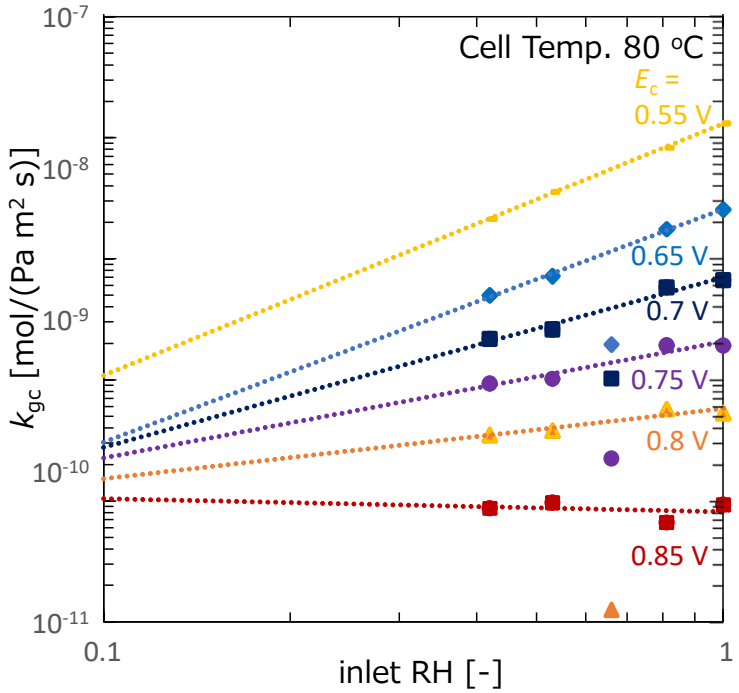

Figure 14. k_{gc} vs. inlet RH

Analysis of Temperature Dependency of ORR Rate

Data in the E_c range of 0.55 to 0.75 V, which is in the reaction control region and does not include the influence of the reverse reaction, were analyzed. ORR rate parameters were determined by using non-linear least square method and calculated results are listed in TABLE I and TABLE II. $k_{gc}^{\circ\prime}$ means the intrinsic ORR rate constant per geometric area at the 100 % of RH. Figure 14 shows that log-log plot of k_{gc} vs. RH. k_{gc} depends on RH in reaction control region and the slope of this log-log plot shows k_{gc} is proportional to RH–RH^2. This result also indicates that ORR rate dependency on RH cannot be explained only by RH dependency of ECSA. ORR rate parameters were calculated under two extreme assumptions: the first one is that ORR rate constant is proportional to RH in kinetic region. The second one is that ORR rate is proportional to a square of RH. Eventually, the reaction rate constant is expressed by Eqs. [5] and [6] as follows:

$$k_{gc}^{\circ} = 9.4 \text{ mol/(Pa m}^2 \text{ s)} \exp\left(-\frac{26 \text{ kJ/mol} + 0.52FE_c}{RT}\right)\text{RH} \quad [5]$$

$$k_{gc}^{\circ} = 46 \text{ mol/(Pa m}^2 \text{ s)} \exp\left(-\frac{30 \text{ kJ/mol} + 0.55FE_c}{RT}\right)\text{RH}^2 \quad [6]$$

Figure 15 and Figure 16 show the Arrhenius plot of recalculated reaction rate constant and observed values under different assumptions. The ORR rate dependencies on temperature, RH and E_c were properly reproduced, respectively. Thus, the ORR rate parameters were appropriately determined.

TABLE I. Determined ORR Rate Parameters under the assumption that k_{gc} is proportional to RH

rate equation	k_{gc0} [mol/(Pa m^2 s)]	E [kJ/mol]	4α [-]
$-r_{gc} = k_{gc}^{\circ\prime}$ RH	9.4	26	0.52
$-r_{gc} = k_{gc}^{\circ\prime}$ RH^2	46	30	0.55

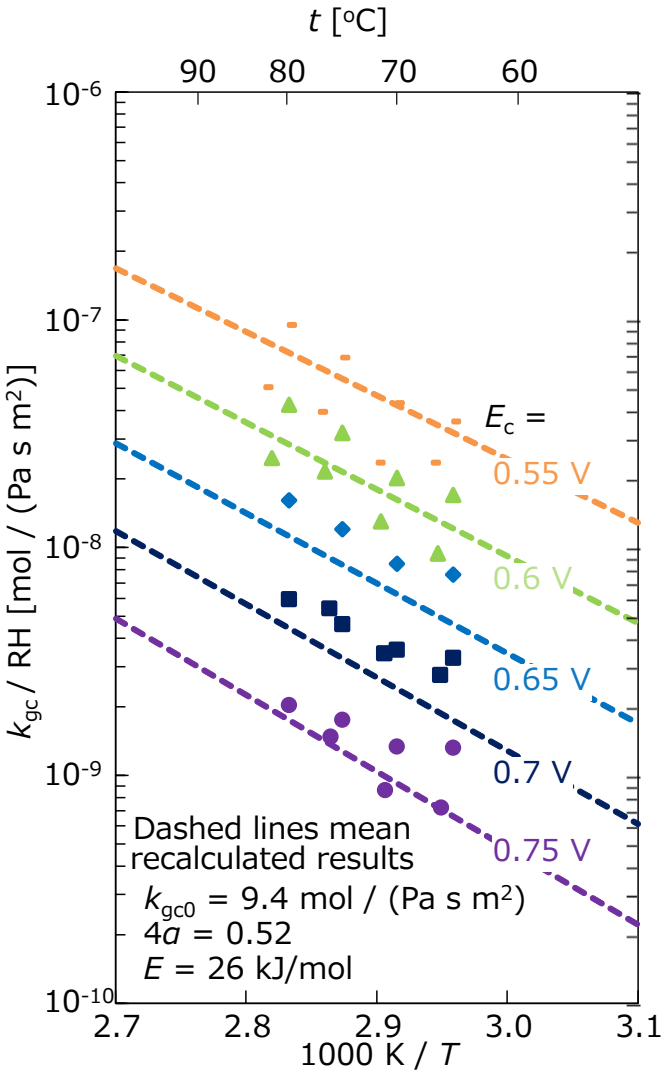

Figure 15. Determined ORR rate dependency on T, RH and E_c under the assumption that k_{gc} is proportional to RH

Conclusions

Temperature, relative humidity (RH) and E_c dependencies of the ORR rate constant which does not include the influence of mass transfer resistance in the through-plane direction in the CCL were measured using platinum-sputtered catalyst in order to determine ORR rate parameters, E, $4a$ and k_{gc0}.

ORR rate dependency on RH was observed although its effectiveness factor should be 1 since Pt-sputtered catalyst does not have cathode catalyst thickness. In addition, it was found that ECSA depends on RH and it contributes to a half of the RH dependency of ORR rate. It was confirmed that there are other factors which depend on RH except mass transfer resistance and ECSA. Adsorption of water and sulfonic group on platinum, platinum oxidation at high voltage range and water uptake in ionomer are possible causes of the remaining half of the RH dependency and these factors cause the ORR rate to be a function of the first order or higher of RH. These RH dependent factors

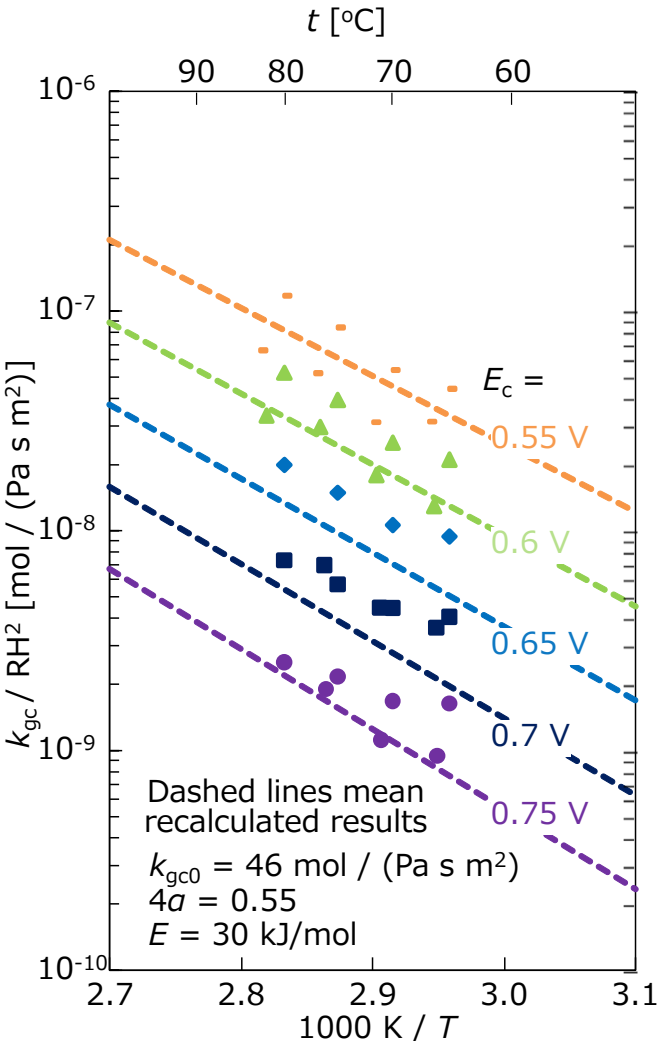

Figure 16. Determined ORR rate dependency on T, RH and E_c under the assumption that k_{gc} is proportional to square of RH

should be quantified and analyzed in the future.

ORR dependency on temperature was analyzed and ORR rate parameters were appropriately determined by using nonlinear least square method under the assumption that ORR rate is proportional to RH or square of RH. As a result, E = 26 kJ/mol, $4a$ = 0.52 and k_{gc0} = 9.4 mol/(Pa m^2 s) are appropriately determined under the first assumption. Under the second assumption, E = 30 kJ/mol, $4a$ = 0.55 and k_{gc0} = 46 mol/(Pa m^2 s) are appropriately determined. Thus, ORR rate equation can be expressed as Eq. [5] or Eq. [6]. This result means that the activation energy of ORR rate is in the range of 26 to 30 kJ/mol.

Acknowledgement

This work was supported by the FC-Platform Program: Development of design-for-purpose numerical simulators for attaining long life and high performance project (FY 2020–2022) conducted by the New Energy and Industrial Technology Development Organization (NEDO), Japan.

References

1. T. Yoshida and K. Kojima, *Electrochem*. *Soc*. *Interf*ace **24**, 45–49 (2015).
2. T. Nagai, A. Kuwaki, R. Jinnouchi, and Yu Morimoto, *Nat*. *Nanotechnol*. **16** 140–147 (2021).
3. DOE Hydrogen and Fuel Cells Program Record, Record #17007, Nov. 30, 2017.
4. M. Kawase, K. Sato, R. Mitsui, H. Asonuma, M. Kageyama, K. Yamaguchi, and G. Inoue, *AIChE J*., **63**(1), 249–256 (2017).
5. M. Nagayoshi, Y. Nobuta, M. Kageyama, G. Inoue and M. Kawase, Proceedings 9th WCCE & 15th APCChE Congress (Seoul, Aug. 2013), Mop–T1–170.
6. A. Velázquez-Palenzuela, F. Centellas, E. Brillas, C. Arias, R. M. Rodríguez, J. A. Garrido, and P. L. Cabot, *Int. J. Hydrogen Ene.*, **37**(23), 17828–17836 (2012).
7. V. Stamenković, T.J. Schmidt, P.N. Ross, and N.M. Marković, *J. Electroanal*. *Chem*., **554**–**555**(1), 191–199 (2003).
8. J. M. Ziegelbauer, V. S.Murthi, C. O'Laoire, A. F. Gullá, and S. Mukerjee, *Electrochim. Acta*, **53**(17), 5587–5596 (2008).
9. N. Wakabayashi, M. Takeichi, H. Uchida, and M. Watanabe, *J. Electroanal. Chem.*, **574**(2), 339–346 (2005).
10. M. Kawase, H. Asonuma, Y. Nobuta, M. Kageyama, and G. Inoue, International Conference on Sustainable Energy and Environment (Bangkok, Nov. 19-21, 2014) E-016.
11. M. Kageyama, K. Yamaguchi, H. Dalia, Y. Ma, H. Ogawa, and M. Kawase, *ECS Trans*., **98**(9), 163–175 (2020).
12. Y. Ma, M. Kageyama, K. Yamaguchi, H. Ogawa, and M. Kawase, The 62nd Battery Symposium, Japan, 2G03 (2020). [in Japanese]
13. H. E. Swanson and E. Tatge, *Natl*. *Bur*. *Stand*. (*U*. *S*.), *Circ*. *539*, **1**, 31 (1953).
14. Leiming Hu, Muxing Zhang, Siddharth Komini Babu, Anusorn Kongkanand, and Shawn Litster, *ChemElectroChem*, **6**(10), 2659–2666 (2019).
15. R. Subbaraman, D. Strmcnik, V. Stamenkovic, and N. M. Markovic, *J. Phys. Chem.* C **114**, 8414–8422 (2010).
16. K. Shinozaki, Y. Morimoto, B. S. Pivovar, and S. S. Kocha, *J. Pow*. *Sour*., **325**, 745–751 (2016).
17. K. Kodama, K. Motobayashi, A. Shinohara, N. Hasegawa, K. Kudo, R. Jinnouchi, M. Osawa, and Y. Morimoto, *ACS Catal.* **8**, 694–700 (2018).
18. H. Oh, Y. I. Lee, G. Lee, K. Min, and J. S. Yi, *J. Pow*. *Sour*., **345**, 67–77 (2017).
19. D. Novitski and S. Holdcroft, *ACS Appl*. *Mater*. *Interfaces*, **7**(49), 27314–27323 (2015).

ECS Transactions, 104 (8) 59-71 (2021)
10.1149/10408.0059ecst ©The Electrochemical Society

Synthesis and Characterization of Nitrogen Doped Reduced Graphene Oxide Based Cobalt-ZIF-8 Catalysts for Oxygen Reduction Reaction

H. Shirzadi Jahromi[a], S.Saxena[b], S. Sridhar[a], M. K. Ghantasala[a], R.Guda[b], E. Rozhkova [c], and K. Suthar[d]

[a] Department of Mechanical and Aerospace Engineering, Western Michigan University, Kalamazoo, Michigan 49008, USA
[b] Department of Chemistry, Western Michigan University, Kalamazoo, Michigan 49008, USA
[c] Center for Nanoscale Materials, Argonne National Laboratory, Lemont, Illinois 60439, USA
[d] Advanced Photon Source, Argonne National Laboratory, Lemont, Illinois 60439, USA

In this paper, we report the synthesis and characterization of Nitrogen-doped Graphene oxide with Metal-Organic Framework (MOF) material as a catalyst for Polymer Electrolyte Membrane Fuel Cell (PEMFC). Transition metal, Cobalt is doped into Zeolitic Imidazolate Frameworks (ZIF-8) in varying amounts (different molar ratios of metal precursor to ZIF-8, 0.6, 0.9 and 1.2) to understand its effect on the catalytic performance. Various characterization techniques, viz., FTIR, Raman spectroscopy, XRD, SEM and EDS were performed to analyze various physical and chemical properties. XRD results showed the formation of the (100) Cobalt-doped ZIF-8 phase with grain size around 20 nm. Cyclic Voltammetry studies showed that the addition of the transition metal plays a major role in the enhancement of electrochemical performance compared to that of non-transition metal carbon-based catalysts. The electrochemical performance is correlated with the physical properties for different metal precursor loadings (0.6, 0.9 and1.2 molar ratios).

Introduction

Hybrid technologies involving fuel cells are increasingly considered as viable alternatives for the realization of reduction in pollutant gas emissions and in the development of eco-friendly automotive and transportation vehicles (1-3). Rapid progress in fuel cells electric vehicle technologies with improved battery performance characteristics is the key in achieving the 2025 US Department of Energy (DOE) durability target for automotive vehicles requiring 8000 hours or 150,000 miles drive with less than 10% performance loss (4-9). However, the current durability status due to catalyst deactivation is significantly below the target (10). Thus, there is a need to develop catalytic material with high efficiency for fuel cell reactions. Though, Platinum is well acknowledged as the best performing catalyst so far for fuel cell applications, it is quite expensive which has been identified as one of the major obstacles in the rapid commercialization of fuel cell technology (11-12). Transition metals (e.g., Iron, cobalt and nickel) could be a less

expensive substitute but the sluggish oxygen reduction reaction (ORR) kinetics with these materials affect the overall performance of fuel cells (13,14).

In general, ORR occurs at cathode in the presence of a catalyst providing an adsorption site for intermediate species such as [O] or [OH], which is the rate determining step of the reaction (15-17). Ge et.al (18) recently explored Fe-N-Carbon aerogel as a catalyst for ORR, which shows a path for the use of similar materials. In addition, using atomically dispersed transition Metal-Nitrogen-Carbon (M-N-C) catalysts has been explored to reduce the cost of PEMFCs for quite some time now (19). However, low performance is observed in terms of their durability, stability, and membrane electrode assembly (MEA) (20). In recent years, the M-N-C catalysts have demonstrated catalytic activity comparable to that of Pt/C catalysts in acidic media (21). For such catalysts, carbon-based materials are widely used as support due to their high conductivity, low cost, and increasing catalytic efficiency (22). Graphene and their derivatives, due to their interesting mechanical, electrical and chemical properties, were found to be attractive for various applications including fuel cells (23-27). With nitrogen doping of graphene, the improved electronic properties can help improve the ORR characteristics (28-31). As a result of corrosion, Metal free carbon-based catalysts exposed to high potentials degrade the catalyst performance via migration and agglomeration (32). Therefore, combining carbon with transition metals will eliminate such obstacles.

In this work, Nitrogen-doped/ Reduced Graphene oxide along with Metal-Organic Framework (MOF) samples were synthesized using wet chemical and pyrolysis techniques for the development of an efficient catalytic material. Transition metal, Cobalt, is doped into Zeolitic Imidazolate Framework (ZIF-8) using Cobalt Nitrate as precursor. The synthesized MOF precursor (Co-ZIFx) were produced with varying amounts of metals (different molar ratios of cobalt to Zinc, x= 0.6, 0.9 and 1.2) to analyze the effect of elemental proportion on the electrochemical performance. The materials were further modified using nitrogen-doped reduced graphene oxide (N-Gr) and reduced graphene oxide (Gr) through wet chemical process and are named as N-Gr-Co-ZIFx and Gr-Co-ZIFx. Samples were carbonized by one-step pyrolysis in an argon atmosphere at 600^{o}C and named as N-Gr-CoZIFx-600. Characterization techniques, viz., Fourier-transform infrared spectroscopy (FTIR), Raman spectroscopy, X-ray diffraction (XRD), scanning electron microscope (SEM), energy dispersive spectroscopy (EDS), Cyclic voltammetry (CV) were performed to analyze various physical, chemical and the electrochemical performances of the synthesized materials.

Experimental Section

Synthesis

Synthesis of Cobalt doped ZIF-8. Cobalt doped ZIF-8 is synthesized using 2-methylimidazole, $Co(NO_3)_2.6H_2O$ dispersed into methanol solution by stirring for two hours at room temperature. zinc nitrate hexahydrate salt is added to this solution, while continued stirring until a light violet Cobalt doped ZIF-8 MOF is formed. The resulting solution is centrifuged to obtain the precipitate which is washed several times using DI water and ethanol solution to clean the impurities.

The above procedure is repeated by taking different ratios of Cobalt and zinc salts for making the samples with three different compositions, having Co/Zn ratios of 0.6, 0.9 and 1.2. The obtained salts were dried in a vacuum oven at 80 °C overnight to obtain Co-ZIF-8 material. The as prepared MOFs were modified to synthesize Nitrogen doped- reduced graphene oxide- cobalt- ZIF-8 (N-Gr-Co-ZIFx) samples.

Synthesis of N-Gr-O and Gr-O. For graphene oxide synthesis, graphite flakes are taken with $NaNO_3$ and cooled in an ice bath. Conc. H_2SO_4 is added to the mixture, which is followed by adding $KMnO_4$ (3:1 with graphite flakes), in small portions while stirring at 35ºC for 7 hours. In the next step, same amount of $KMnO_4$ is added all at once and is stirred for 12 more hours. At this stage, Melamine is added into the suspension and continued stirring for another 12 hours. This mixture is diluted with hot DI water to quench the reaction, while the temperature is maintained at 90ºC for 1 hour. A 30% H_2O_2 solution is added to reduce the $KMnO_4$ to $MnSO_4$, and ultrasonicated for 30 min. Afterwards, it is centrifuged and washed with deionized water and ethanol several times to derive a solution with neutral pH and is dried in an oven at 40º C for several days. The dried N-Gr is reduced by adding 1µL hydrazine monohydrate per 3 mg of Nitrogen doped graphene oxide to get N-doped reduced graphene oxide.

Synthesis of N-Gr-Co-ZIFx and Gr-Co-ZIFx. The catalyst material is prepared by adding N doped carbon materials (N-Gr and Gr) to Co-ZIF-8. N doped carbon support material (N-Gr/Gr) and Co-ZIF-8 salt are dispersed in methanol separately and sonicated for 3 and 5 hours, respectively. The solution is centrifuged separating precipitate salts from the supernatant solution. The solid particles were washed with DI water and ethanol several times and dried in a vacuum oven overnight at 80°C to obtain N-Gr- Co-ZIF/ Gr-Co-ZIF material. The samples were pyrolyzed at 600ºC in argon atmosphere for 2 hours for carburizing the material. For carburizing, the system chamber is evacuated to 1 mbar and back filled with ultrahigh purity argon (99.999%) to 70 mbar. Substrate holder is heated to 600ºC in one hour and maintained at that temperature for two hours. Figure 1 shows the schematic representation of Cobalt embedded in ZIF-8 framework in MOF precursors Co-ZIFx.

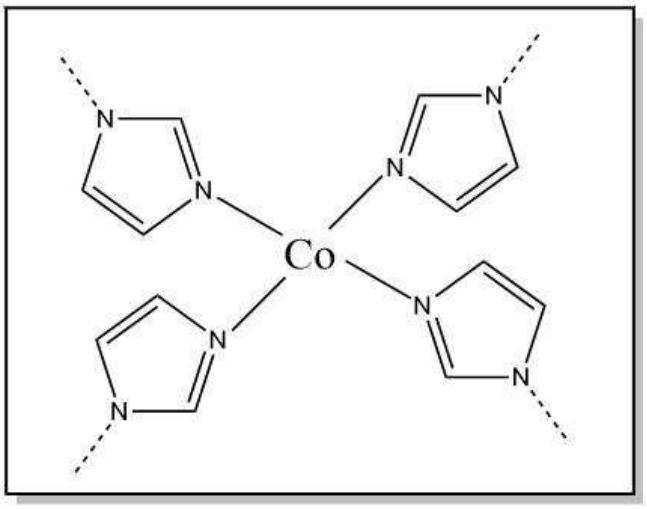

Figure 1. Schematic representation of Cobalt doped in ZIF-8.

Electrochemical Measurements

The cyclic voltammetry measurements were done using a standard three-electrode cell (AB bipotentiostat, Pine Chem USA) system. Ag/AgCl (KCl-saturated) and Pt wire were used as the reference and counter electrodes respectively with 0.1 M $HClO_4$ solution being used as the electrolyte. PineChem glassy carbon electrode (GCE) with 5 mm diameter (0.196 cm^2 surface area) coated with the prepared sample ink used as working electrode. To evaluate oxygen reduction reaction (ORR) of all the samples, the ink is prepared by pre-mixing 5.0 mg of the sample in 212.5 µL isopropyl alcohol (IPA) and 150 µL 5 wt% Nafion solution in required amount of water and ultrasonicating in ice bath for 60 min. 10 µL of the catalyst ink was deposited on the cleaned glassy carbon electrode with catalyst loading of 255.10 µg cm^{-2} and allowed to air dry. ORR activity was determined by cyclic voltammetry (CV) method using a rotating disk electrode (RDE) in oxygen or nitrogen saturated acidic (0.1 M $HClO_4$) electrolyte (33). The oxygen and nitrogen were purged in electrolytic cell, using a syringe nozzle connected from the respective gas bottles, with high purity. The scan rate was set to 100 mVs^{-1} with disc electrode speed of 1600 rpm and potential cycled from -0.150 V to 1 V (vs. Ag/AgCl as reference electrode).

Results and Discussion

Characterization of samples

The synthesized N-GR-Co-ZIF materials were characterized using SEM, EDS, XRD, FTIR, and RAMAN techniques for microstructure, composition and structural information of different phases formed. JEOL JSM 7600F field emission SEM with EDS attachment is used to examine the grain size and other microstructural features along with elemental mapping. Malvern-Panalytical Empyrean diffractometer was used for obtaining powder XRD patterns of the samples at room temperature using Co target (Co-Kα1= 1.78Å) and scanned at a step size of 0.008º with 20.32 scan-points per step. FTIR was carried out using Thermo Science. Nicolet iS 5 FTIR Spectrometer in range 4000 to 400 cm^{-1} for identifying important functional groups present in the catalyst. Raman spectroscopy was carried out using a confocal Laser Raman system (Renishaw InVia Laser Raman Microscope) with a λ= 532 nm excitation laser at a power of 10 mW.

Figure 2 shows SEM images of the N-Gr-Co-ZIF-8 samples to determine the effect of Carbonization and Nitrogen doping in these materials. Figure 2 (a, b, c and d) shows SEM pictures of the samples Gr-Co-ZIF0.9, Gr-Co-ZIF0.9-600, N-Gr-Co-ZIF0.9 and N-Gr-Co-ZIF0.9-600 respectively. It may be observed from figure 2(b) that the carbonization at 600ºC resulted in a relatively more porous Gr-Co-ZIF0.9 compared to figure 2(a). This also appears to have accompanied by an observable reduction in grain size (~20%). A similar carbonization effect was observed in ZIF-8 derived nanoporous carbon samples, by C. Young et al (34). It is also interesting to note that N-Gr-Co-ZIF0.9 samples also showed 20-25% grain size reduction after carbonization at 600ºC in argon atmosphere (figure 2c and d). Comparing figure 2(a and c) indicates the nitrogen doping effect, which shows the increased film density (figure 2c).

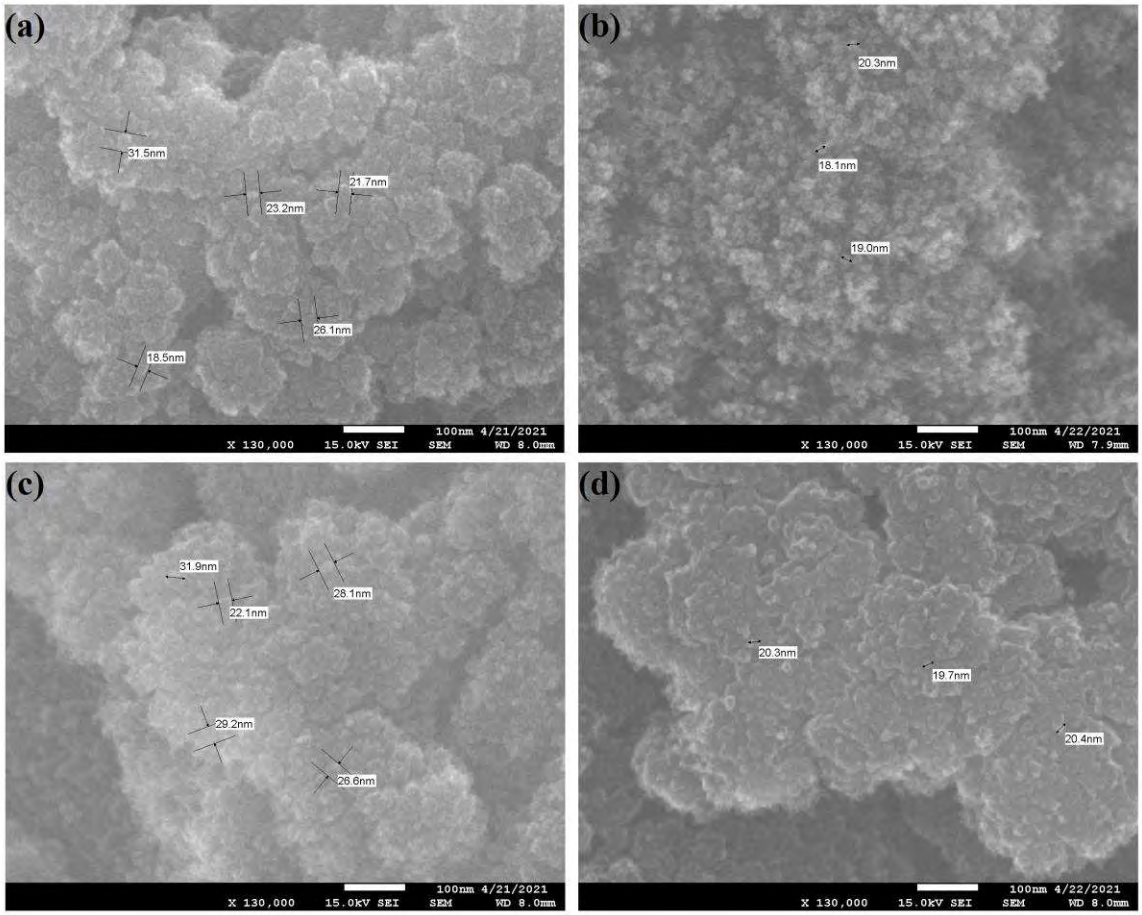

Figure 2. SEM image of (a) Gr-Co-ZIF0.9, (b) Gr-Co-ZIF0.9-600, (c) N-Gr-Co-ZIF0.9 and (d) N-Gr-Co-ZIF0.9-600 samples.

Figure 3 compares FTIR spectra for Gr-Co-ZIF0.9 as-is, doped with nitrogen and carbonized. Note from the Figure that the ring stretch frequency of ZIF-8 was observed in range 1450-1300 cm^{-1} for all the samples along with out of plane bending vibrations at 694 cm^{-1}. C-N stretching vibration is observed at 994 cm^{-1} in all samples, and C=N stretching vibrations is observed at 1550 cm^{-1} in Gr-Co-ZIF0.9, N-Gr-Co-ZIF0.9 and N-Gr-Co-ZIF0.9-600 samples and those can be attributed to imidazole framework. However, the spectra for sample Gr-Co-ZIF0.9-600, the C=N @ 1381, 1550cm^{-1} peaks are quite small, which may be due to the absence of Nitrogen in the sample. Vibrations at 1450 cm^{-1} are assigned to C=C stretching. As expected, the intensity of C=C stretching is higher in reduced graphene samples and can be ascribed to greater degree of unsaturation in the samples. The peak at 1381 cm^{-1} is also attributed to C=N stretching vibrations of either imidazolate or N-Gr and it is most striking in N-Gr-Co-ZIF0.9 sample because of excess nitrogen present.

The IR peaks within 420-425 cm^{-1} region are assigned to Zn-N (ZIF-8) and Co-N stretching frequencies, and these vary with Co to Zn ratios (35). A closer analysis of the Zn-N/Co-N peak in these spectra showed a peak shift from 421.3 cm^{-1} in Co-ZIF0.6 to 422.8 cm^{-1} in Co-ZIF-1.2 (Figure 4). The FTIR results presented here shows that Co is doped into the ZIF network and is incorporated into reduced graphene oxide template. These results are in agreement with our EDS analysis, which showed that the Co to Zn ratio changed from 19:81 to 29:71 for the Co-ZIF0.6 to Co-ZIF-1.2 samples.

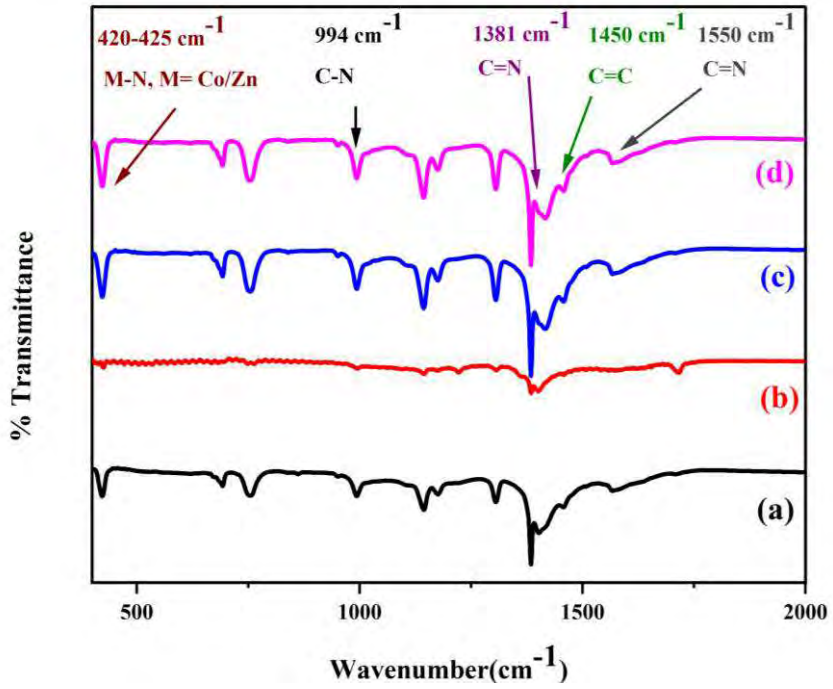

Figure 3. Comparison of FTIR for (a) Gr-Co-ZIF0.9, (b) Gr-Co-ZIF0.9-600, (c) N-Gr-Co-ZIF0.9 and (d) N-Gr-Co-ZIF0.9-600 samples.

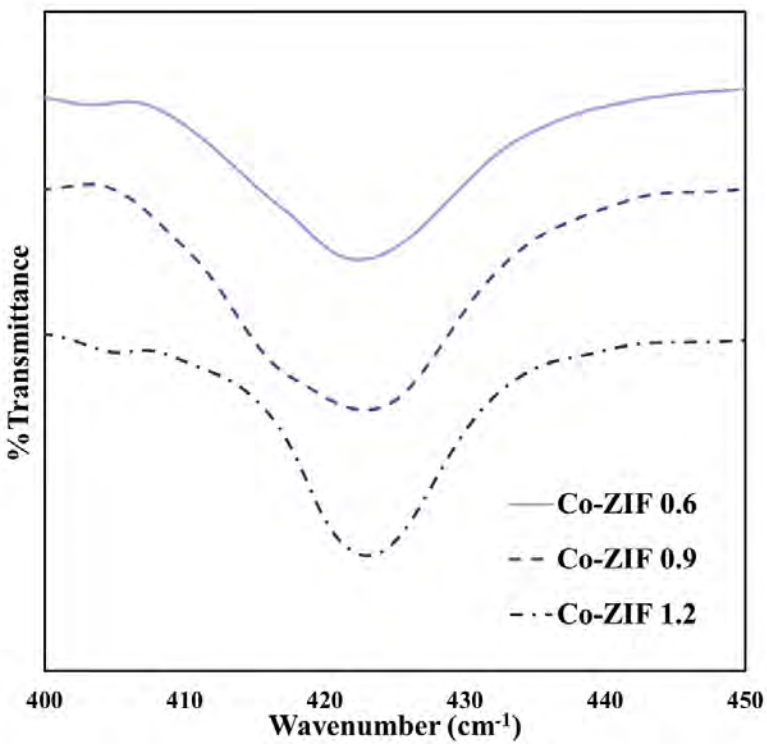

Figure 4. Metal-Nitrogen peak comparison with different loading of Cobalt in FTIR.

Raman Spectroscopy was performed to understand the carbonization and nitrogen doping effects in these samples. Figure 5 illustrates G-band as the ordered graphitic carbon and D-band as the defect band, which were shown at 1330 and 1597 cm^{-1} respectively. Table 1 summarized the peak positions of Raman G and D bands of all samples along with their intensity. As shown in the table, the I_D/I_G value of the synthesized samples varied between 1.29 to 1.13. This indicates the existence of defects in carbon framework and a higher ratio is indicative of more defects in the sample. The N-Gr-Co-ZIF0.9-600 sample represents highest value for I_D/I_G ratio after carbonization. The I_D/I_G ratio is higher for both carbonized samples with and without nitrogen. Though overall I_D/I_G ratios can be correlated to their respective processing conditions as shown in table 1, the lower I_D/I_G ratio of the N-Gr-Co-ZIF0.9 sample requires further understanding.

TABLE 1. G and D bands wavelength and their intensity of the synthesized materials.

	I_D Wavelength (cm^{-1})	I_G Wavelength (cm^{-1})	I_D (a.u.)	I_G (a.u.)	I_D/I_G
N-Gr-Co-ZIF0.9	1315.48	1597.09	963.87	847.76	1.1369
N-Gr-Co-ZIF0.9-600	1337.15	1597.94	399.52	309.65	1.2902
Gr-Co-ZIF0.9	1315.48	1597.09	663.06	546.19	1.2139
Gr-Co-ZIF0.9-600	1303.71	1599.80	1816.52	1419.99	1.2792

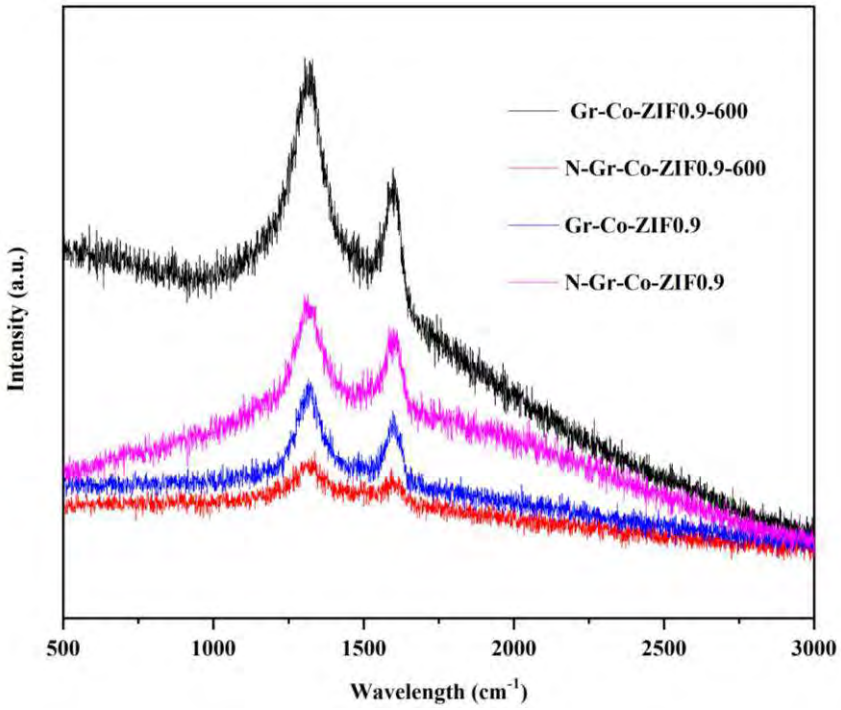

Figure 5. Raman spectra showing D and G bands for synthesized materials, confirming the doping process and pyrolyzing with increasing ID/IG ratios.

Figure 6 represents powder XRD patterns of Co-doped ZIF-8 samples to understand the effect of Nitrogen doping and carbonization. Each peak in XRD patten corresponds to an identified phase belonging to different planes of ZIF-8 represented by (h,k,l) values. Though all of the samples have similar peak pattern, their peak intensities and widths were different based on the composition and processed condition. The XRD patterns for samples Co-ZIF0.9 and Co-ZIF0.9-600 were identical with relative intensities of the peaks of Co-ZIF0.9-600 being lower compared to that of Co-ZIF0.9. This may be attributed to the

carbonization effect, due to decomposition of Zn-N-C phase at 600 ºC (36). As shown in figure 1, with a reduction in grain size and increase in porosity, the crystallinity might have been affected. However, the carbonization at 600 ºC may have a limited effect on the crystallinity of ZIF-8, which may require higher temperature. Nitrogen doping also didn't show a significant effect on its crystallinity.

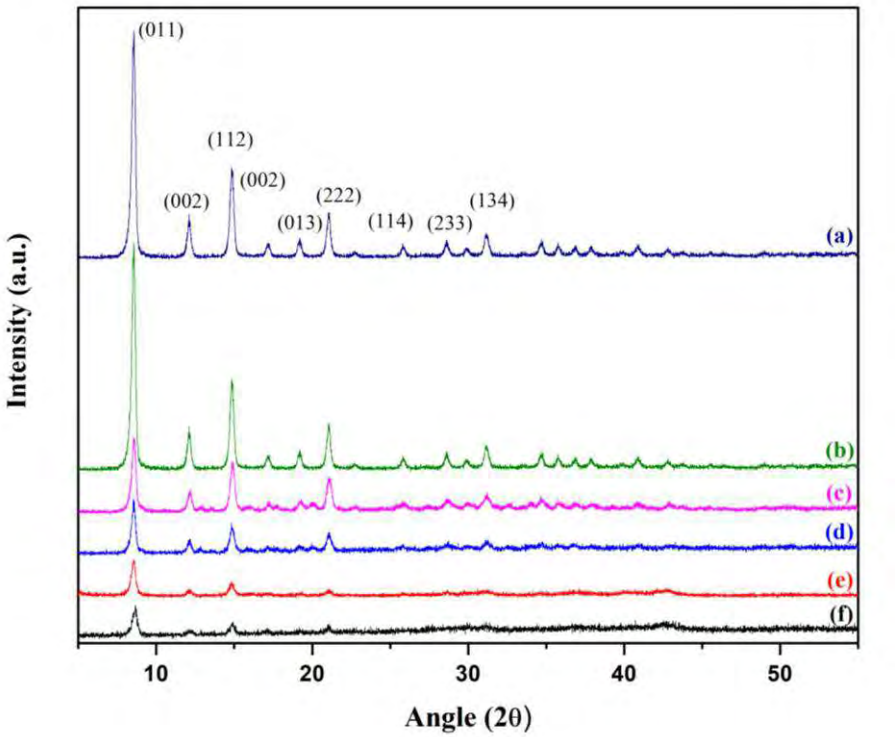

Figure 6. Powder XRD patterns for (a)Co-ZIF0.9, (b)Co-ZIF0.9-600, (c)N-Gr-Co-ZIF0.9, (d)Gr-Co-ZIF0.9, (e)N-Gr-Co-ZIF0.9-600, (f)Gr-Co-ZIF0.9-600 samples.

Oxygen Reduction Reaction

Cyclic Voltammetry studies were performed in oxygen and nitrogen saturated 0.1 M $HClO_4$ acidic solution to evaluate the ORR activity of the synthesized samples. The electrochemical cell was purged with N_2 gas to create inert background conditions for each voltammogram. The solution is saturated with respective gas (O_2 and N_2) with continuous flow of gas into the cell during the entire time of measurement. To ensure that no gas bubbles were attached to the electrode, it is rotated at higher speed (3000 rpm) before start of the measurements. The samples' voltammetric curves were compared with 40 wt% Pt/C catalyst as a reference to compare their relative performances.

Figure 7a illustrates cyclic voltammogram for 40 wt% Pt/C catalyst, which clearly shows a pair of broad redox peaks in N_2 and O_2-saturated conditions. In the presence of oxygen, a relatively larger and clear ORR peak is observed at 342 mV. Figure 7b compares the CV plots for three sets of samples having Co-ZIF0.9, Gr-Co-ZIF0.9 and N-Gr-Co-ZIF0.9, which shows a better ORR peak for N-Gr-Co-ZIF0.9 relative to the other two. In order to understand the effect of carbonization, the CV plots of carbonized samples of the same compositions were also included in Figure 7b. The area under the curve for Gr-Co-ZIF0.9-600 is 55% and 83% higher than N-Gr-Co-ZIF0.9-600 and Co-ZIF0.9-600

respectively. This indicates that the sample Gr-Co-ZIF0.9-600 has highest power density (power per active surface area) of the working electrode. However, the ORR peak is more clearly visible in N-Gr-Co-ZIF0.9-600 and Co-ZIF0.9-600 compared to Gr-Co-ZIF0.9-600. The potentials corresponding to ORR peaks are 234 mV, 280mV and 329 mV for Co-ZIF0.9-600, Gr-Co-ZIF0.9-600, and N-Gr-Co-ZIF0.9-600, respectively. This shows that incorporation of nitrogen doped reduced graphene oxide enhanced the catalytic performance of the investigated samples.

Figure 7c demonstrates the effects of carbonization on CV plots for reduced graphene oxide-MOF samples. It can be concluded from the plots that the area under the curve is 41% higher with an increase of 11 mV in ORR potential after carbonization. Figure 7d represents the carbonization effects on the CV plots for nitrogen doped reduced graphene oxide-MOF samples. An increase in the area under the curve by 23%, with a 58 mV increase of the cathodic potential is observed as a result of carbonization in these samples. Thus, the results from figure 7c and 7d clearly show that carbonization have increased the power per active surface area of the working electrode and the cathodic potential peak.

Figure 7e compares the CV plots of N-Gr-Co-ZIF0.9-600 and Gr-Co-ZIF0.9-600 purged in nitrogen and oxygen. It can be observed that although nitrogen doping decreases area under the CV curve, it makes the ORR peak more visible and at a higher cathodic potential. Moreover, the comparison of the synthesized samples with Pt/C catalyst shows good ORR activity in acidic media. The potentials for N-Gr-Co-ZIF0.9-600 and Gr-Co-ZIF0.9-600 are 23 mV and 63 mV lower than that of Pt/C catalyst respectively. These CV measurements clearly show a qualitative improvement in the catalytic performance of N-Gr-Co-ZIF0.9-600 compared to its base cobalt doped MOF samples.

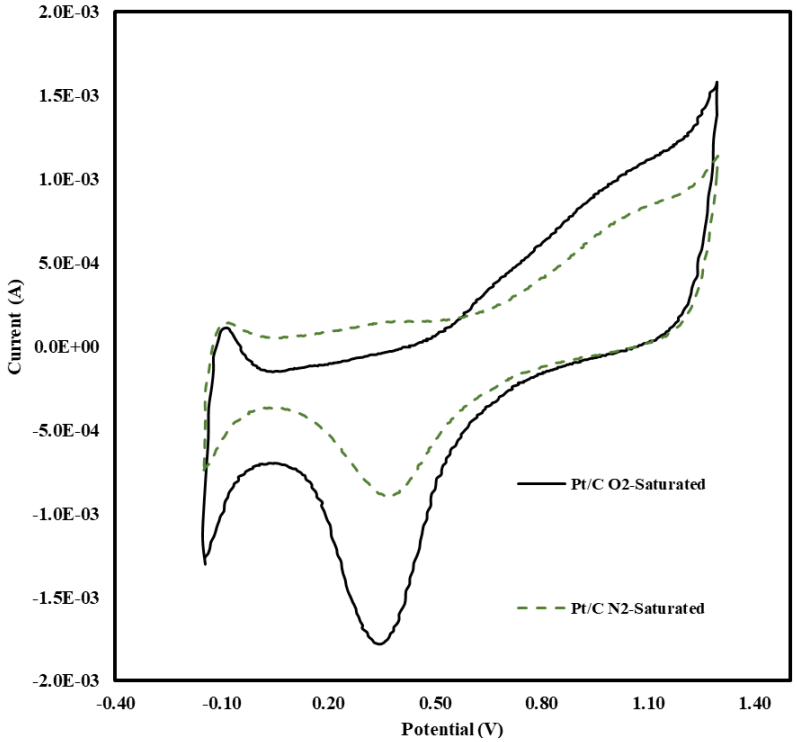

Figure 7a. Comparison of CV plots for 40 wt% Pt/C catalyst purged in nitrogen and oxygen.

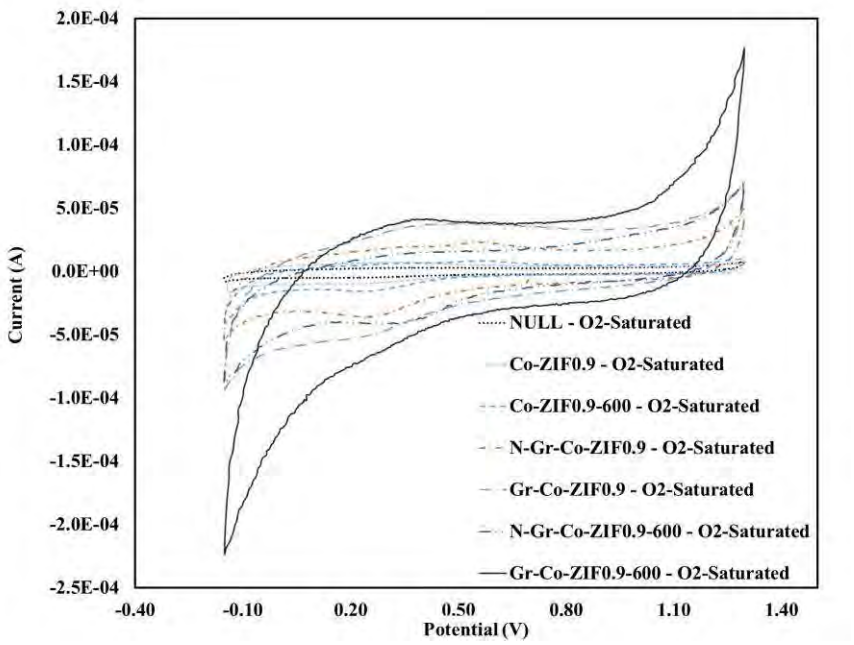

Figure 7b. Comparison of CV plots for different Co-MOF samples purged in oxygen.

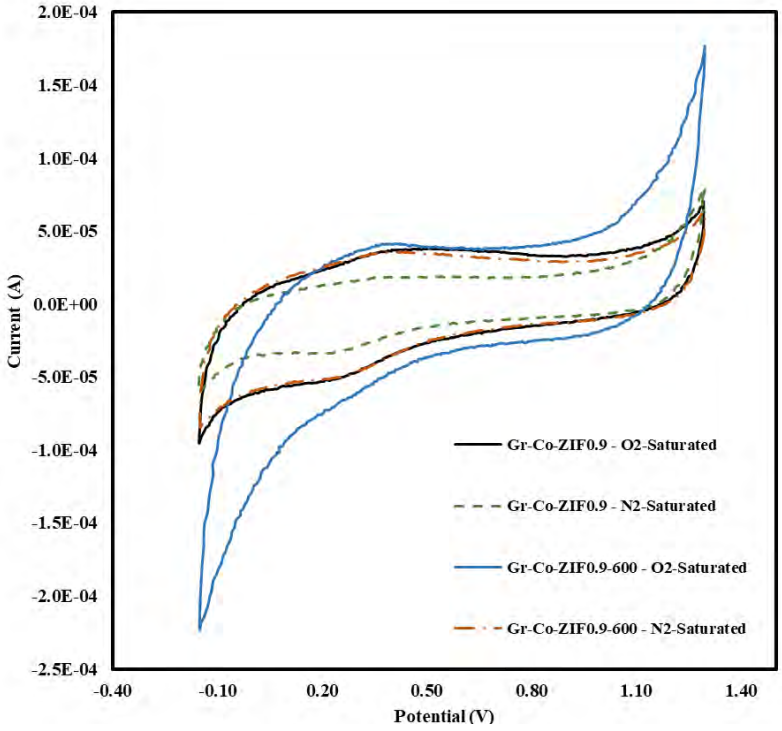

Figure 7c. CV plots of Gr-Co-ZIF0.9 samples before and after carbonization purged in nitrogen and oxygen.

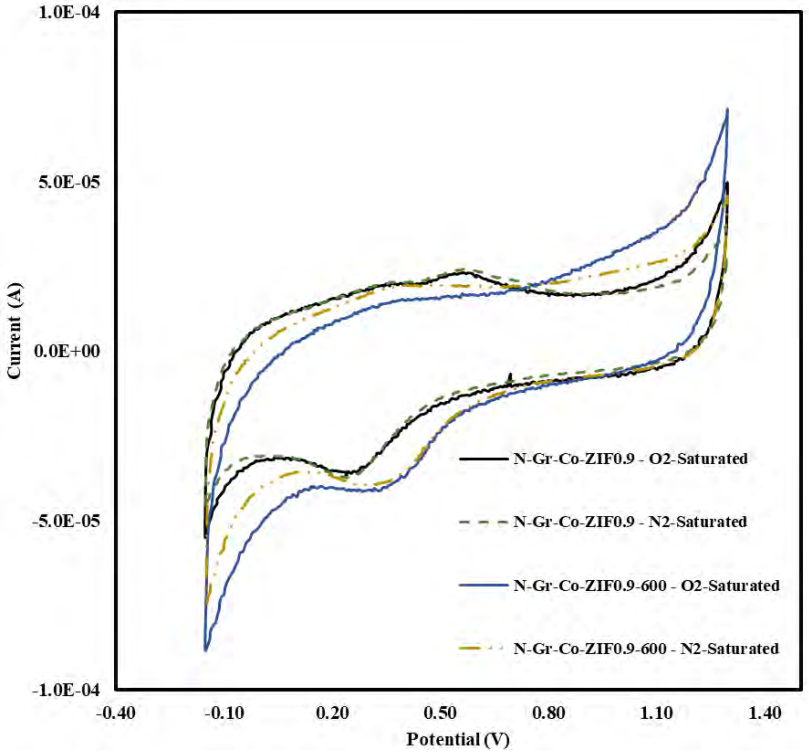

Figure 7d. CV plots of N-Gr-Co-ZIF0.9 samples before and after carbonization purged in nitrogen and oxygen.

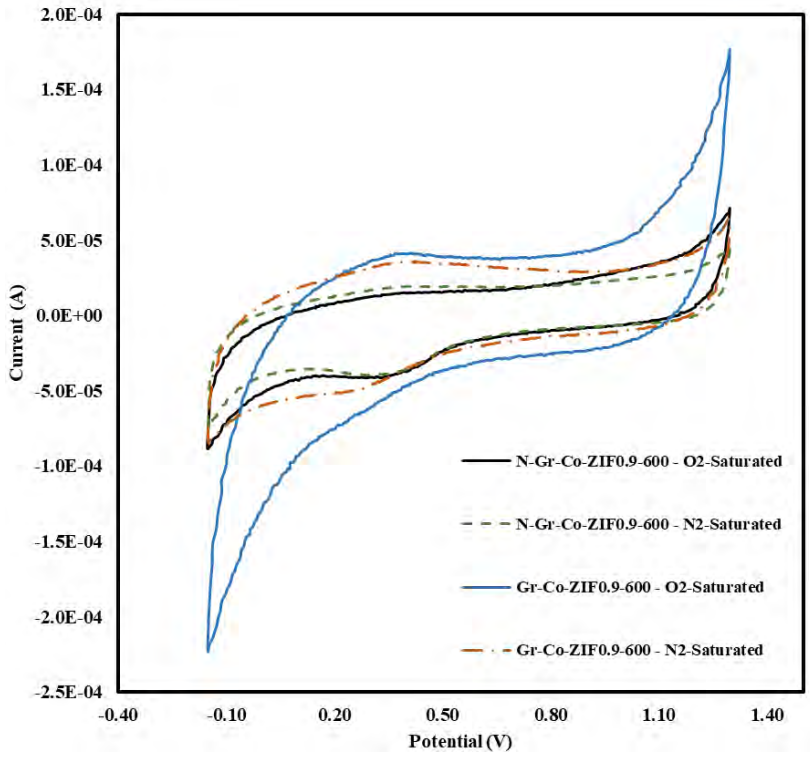

Figure 7e. Comparison of CV plots for N-Gr-Co-ZIF0.9-600 and Gr-Co-ZIF0.9-600 purged in nitrogen and oxygen.

As discussed earlier, SEM results showed that N-Gr-Co-ZIF0.9-600 samples have higher density than Gr-Co-ZIF0.9-600. N-Gr-Co-ZIF0.9-600 showed most striking C=N stretching vibrations in FTIR whereas RAMAN showed highest I_D/I_G value (1.2902) indicating highest number of defects. Powder XRD pattern showed reduced crystallinity too for these samples. All these characteristics of N-Gr-Co-ZIF0.9-600 are pointing to favorable conditions for better ORR catalytic activity in acidic medium.

Conclusion

The synthesis and characterization of nitrogen doped reduced graphene oxide-based Metal organic framework materials for fuel cell catalyst applications is investigated. The effect of Cobalt inclusion within metal organic framework is investigated at different Co/Zn ratios of 0.6, 0.9 and 1.2. All materials were synthesized using wet chemical processes followed by their pyrolysis in argon atmosphere. The structural and chemical properties of the synthesized materials were analyzed using FTIR, SEM, EDS, Raman and XRD Microstructural analysis showed a reduction in grain size and increased porosity after carbonization. The results of ORR activity performance show that incorporation of reduced graphene oxide enhanced the catalytic performance of the investigated samples. Moreover, catalytic performance of the samples is increased with pyrolysis. The as-prepared N-Gr-Co-ZIF0.9-600 showed excellent catalytic activity, long durability, and high selectivity for ORR in acidic medium. The nitrogen doping of reduced graphene oxide metal organic framework materials with Cobalt inclusion after carbonization showed potential for use as a fuel cell catalyst material.

Acknowledgments

Access to facilities at Center for Nanoscale Materials was supported by the U.S. Department of Energy, Office of Science, Office of Basic Energy Sciences, under contract no. DE-AC02-06CH11357.

References

1. U. Eberle, B. Müller, and R. von Helmolt, *Energy Environ. Sci.*, **5**, 8780 (2012).
2. M. Muthukumar et al., *Mater. Today Proc.*, **45**, 1181–1187 (2021).
3. A. G. Olabi, T. Wilberforce, and M. A. Abdelkareem, *Energy*, **214**, 118955 (2021).
4. I. Staffell et al., *Energy Environ. Sci.*, **12**, 463–491 (2019).
5. F.-C. Wang and W.-H. Fang, *Int. J. Hydrogen Energy*, **42**, 10376–10389 (2017).
6. J. Kurtz, S. Sprik, and T. H. Bradley, *Int. J. Hydrogen Energy*, **44**, 12010–12023 (2019).
7. F. Ayatollahi, P. Eskandari, and S. B. Shokouhi, in *2018 4th Iranian Conference on Signal Processing and Intelligent Systems (ICSPIS)*, p. 101–105, IEEE (2018).
8. S. Jahromi, E. Amani, and S. Movahed, *Electrophoresis*, **40**, 1678–1690 (2019).
9. U.S. DRIVE: Fuel Cell Technical Team Roadmap, (2017).
10. C. S. Gittleman, A. Kongkanand, D. Masten, and W. Gu, *Curr. Opin. Electrochem.*, **18**, 81–89 (2019).
11. M. Shao, Q. Chang, J.-P. Dodelet, and R. Chenitz, *Chem. Rev.*, **116**, 3594–3657 (2016).
12. S. T. Thompson and D. Papageorgopoulos, *Nat. Catal.*, **2**, 558–561 (2019).
13. C. Sealy, *Mater. Today*, **11**, 65–68 (2008).

14. A. Serov, I. V. Zenyuk, C. G. Arges, and M. Chatenet, *J. Power Sources*, **375**, 149–157 (2018).
15. J. Wu and H. Yang, *Acc. Chem. Res.*, **46**, 1848–1857 (2013).
16. Y. Wang and P. B. Balbuena, *J. Chem. Theory Comput.*, **1**, 935–943 (2005).
17. A. Morozan, B. Jousselme, and S. Palacin, *Energy Environ. Sci.*, **4**, 1238 (2011).
18. H. Ge et al., in *EFCF 2021*, p. hal-03195353, Lucerne, Switzerland (2021).
19. Y. He, S. Liu, C. Priest, Q. Shi, and G. Wu, *Chem. Soc. Rev.*, **49**, 3484–3524 (2020).
20. X. X. Wang, M. T. Swihart, and G. Wu, *Nat. Catal.*, **2**, 578–589 (2019).
21. S. Sui et al., *J. Mater. Chem. A*, **5**, 1808–1825 (2017).
22. Y.-J. Wang et al., *Chem. Rev.*, **115**, 3433–3467 (2015).
23. B. Saner, S. A. Gürsel, and Y. YÜRÜM, *Fullerenes, Nanotub. Carbon Nanostructures*, **21**, 233–247 (2013).
24. J. J. Slack, R. Wycisk, N. Dale, A. Kumar, and P. N. Pintauro, *ECS Trans.*, **80**, 829–837 (2017).
25. A. R. Setoodeh, H. Badjian, and H. S. Jahromi, *J. Mol. Model.*, **23**, 2 (2017).
26. M. Liu, R. Zhang, and W. Chen, *Chem. Rev.*, **114**, 5117–5160 (2014).
27. M. Reda, H. A. Hansen, and T. Vegge, *Catal. Today*, **312**, 118–125 (2018).
28. A. C. Lloyd, *J. Power Sources*, **86**, 57–60 (2000).
29. Q. Xue, D. Yang, L. Jiang, B. Li, and P. Ming, *Automot. Innov.*, **4**, 119–130 (2021).
30. H. Shirzadi Jahromi, F. Mehdipour, and G. Firoozi, *Mapta J. Mech. Ind. Eng.*, **5**, 18–23 (2021).
31. Q. Wang et al., *Sci. Bull.*, **65**, 1743–1751 (2020).
32. S. Jayabal, G. Saranya, D. Geng, L.-Y. Lin, and X. Meng, *J. Mater. Chem. A*, **8**, 9420–9446 (2020).
33. Y. Garsany, J. Ge, J. St-Pierre, R. Rocheleau, and K. E. Swider-Lyons, *J. Electrochem. Soc.*, **161**, F628–F640 (2014).
34. C. Young et al., *Phys. Chem. Chem. Phys.*, **18**, 29308–29315 (2016).
35. F. Hillman et al., *J. Mater. Chem. A*, **5**, 6090–6099 (2017).
36. D. E. Newbury and N. W. M. Ritchie, *J. Mater. Sci.*, **50**, 493–518 (2015).

Chapter 3

Gas Diffusion Layer

ECS Transactions, 104 (8) 75-82 (2021)
10.1149/10408.0075ecst ©The Electrochemical Society

Insights into the Stability and Formation of Water Droplets Using Operando X-Ray Tomographic Microscopy

T. Dörenkamp[a], M. Sabharwal[a] and J. Eller[a]

[a] Electrochemistry Laboratory, Paul Scherrer Institut, Villigen, Switzerland

Efficient removal of the electrochemically produced water from the gas diffusion layer (GDL) in polymer electrolyte fuel cells (PEFC) is crucial for reducing the mass transport losses and enabling the technology to become a viable energy solution. Understanding the interaction between the water cluster percolation through the GDL and the droplet formation and detachment in the gas channel could enable the design of advanced GDL materials, which provide optimal water management. In this study, a catalyst-coated membrane (CCM) with 8 small, independent active areas (0.0625 mm^2 each) is investigated using operando X-ray tomographic microscopy (XTM) to study the transient development and interaction of multiple percolating water clusters in a GDL and droplet formation and detachment in the channel. The results of the study provide insights into the water removal in PEFC through the development of percolating networks in the GDL. Transient instabilities in the developed percolating water networks associated with break-through and droplet detachment were also observed.

Introduction

Polymer electrolyte fuel cells (PEFCs) are one of the most promising technologies to achieve an environmentally friendly and sustainable energy solution for the future [1]. PEFCs convert hydrogen and oxygen into electric power through an electrochemical reaction. Hydrogen is supplied to the anode, whereas oxygen, usually provided by ambient air is fed to the cathode of the fuel cell. To ensure an ideally homogeneous distribution of the active gases on the surface area of the catalyst layer (CL), porous gas diffusion layer (GDL) is used to distribute the gases from the channel to the CL [2,3]. The performance of PEFCs is limited by the sluggish oxygen reduction reaction (ORR) occurring in the cathode CL with water being a by-product of the reaction. At high current densities, water drainage through the GDL is crucial to avoid flooding of the cathode CL while simultaneously avoiding water accumulation in the GDL pores to prevent blockage of the gas pathways (flooding) [4–6]. Hence, GDLs are typically made of carbon fibers either manufactured as papers, felts or woven materials treated with a certain amount of Polytetrafluoroethylene (PTFE) to increase hydrophobicity in order to improve water management [3,7].

Water transport through the GDL can be distinguished into two phenomenon namely capillary-fingering of liquid water and gas diffusion of water vapor [8]. However, determination of the capillary pressure evolution during the water cluster formation in fuel cell operations is difficult and the in-plane interactions between several water clusters in operando cells make it impossible to predict the percolation of a single water cluster. Moreover the current distribution on the surface area of the catalyst layer is inhomogeneous resulting in an uneven rate of water generation [9].

The developments in 4D X-ray tomographic microscopy (XTM) have enabled to become a versatile tool to image the dynamic processes in GDLs of PEFCs during fuel cell operation [8,10–13]. Recent work on droplet formation and detachment cycle [7,13] has provided insights into the interaction between the percolating water clusters feeding the droplet on the GDL surface and allowed the calculation of the capillary pressure in the water cluster via surface curvature analysis. Mularczyk et. al.[7] observed periodic drainage in the top third of the GDL thickness after droplet detachment, whereas in the bottom two thirds of the GDL the percolation cluster showed much lower fluctuations. It was also shown that the break-through location remained stable during the observation time. In another operando XTM study [13], two distinct modes of droplet filling were revealed after droplet break-through into the channel. At first, a continuous feeding was observed, whereby the water cluster and the droplet in the channel remain connected. After the droplet disconnected from the feeding water cluster the droplet feeding procedure changed to an unstable state where the cluster periodically connected and disconnected from the droplet in the channel. However, the work of Mularzcyk et. al.[13] was limited to the analysis of a single percolating water cluster using only one small active area of 0.005 mm^2. In this study, we aim to improve on the previous work by understanding the water cluster percolation and interactions with 8 independent active areas using operando X-ray tomographic microscopy.

Methodology

Operando Cell and Setup

The cell assembly used for this experiment is shown in Figure 1b (scheme) and 1c (through plane cross section). A catalyst coated membrane (Gore® Primea® A510.1/M815.15/C510.4 with a 15 µm thick reinforced Gore-Select® membrane and anode/cathode Pt loadings of 0.1/0.4 mg/cm^2) was laser ablated to form 8 isolated active areas of (250 x 250 μm^2) which acted as individual water injection sites into the GDL (Toray TGP-H-060, 10 wt% PTFE). The MEA and the GDLs were then sandwiched between two double channel flow fields made of graphite (BMA5, Eisenhuth, Germany) forming the anode side and the cathode side of the cell respectively. On each side Fluoroethylenepropylene (FEP) gaskets were used to seal the gas channels against the environment. According to the depth of the cavity and the thickness of the FEP gaskets (50 µm), the GDL was compressed to 75 % of its original thickness (190 µm). For the experiment, the cell was operated first at OCV and then at a constant current density of 1 A/cm^2 at a temperature of 30 °C with fully humidified gases to avoid evaporation of the electrochemically produced water. The gas flow rates on both the anode and cathode were set to 172.8 Nml/min resulting in a flow velocity of 6 m/s.

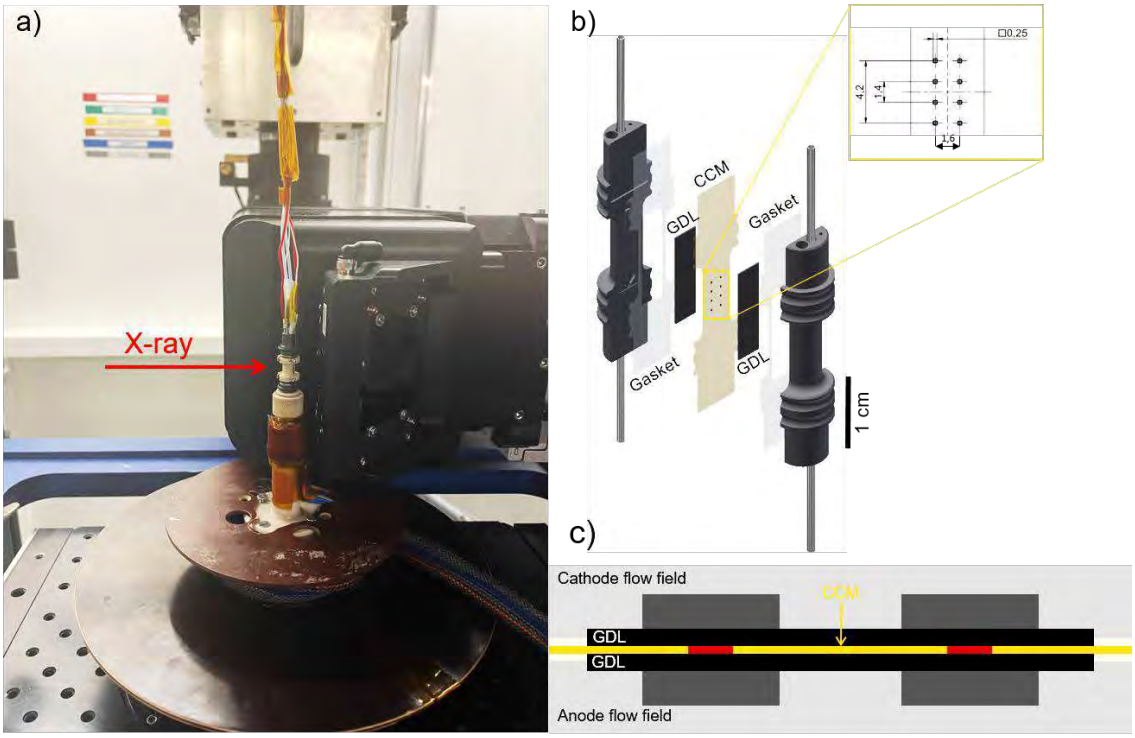

Figure 1: a) Cell mounted on the rotation stage of the Tomcat beamline at the Swiss Light Source (SLS); b) Schematic of the operando double channel fuel cell (CCM, GDLs and gaskets sandwiched between the two flow fields); c) Schematic of the operando fuel cell in the through plane view with the active area (red) under the channels

XTM data acquisition

The cell was mounted in a sample holder at the Tomcat beamline of the Swiss Light Source (SLS) as shown in Figure 1a. The polychromatic X-ray beam emitted by a 2.9 T bending magnet at a ring current of 400 mA was filtered using 20mm of Sigradur to about 5 % of the original power and further hardened by 2 mm of silicon and converted to visible light with a 150 µm LuAg:Ce scintillator and magnified using a 4x optical microscope (Optique Peter). Operando scans were performed during the forward and backward rotation of the sample enabling a scan interval of 1 Hz. For each scan, 401 projections were taken with an exposure time of 0.83 ms resulting in a scan time of 333 ms and a voxel edge length of 2.75 µm. The cell was operated for 180 s and operando scans were recorded at regular intervals of 1 s. Additionally a low quality (LQ) and a high quality (HQ) dry scan of the cell were recorded after drying the cell for wet segmentation via difference imaging and solid segmentation, respectively. While the scan parameters for the LQ dry scan remained the same as for the operando scans, the number of projections for the HQ dry scan was increased to 2001.

Image processing

For the water and the solid segmentation an in-house implemented python pipeline was used. At first the LQ dry scan was aligned to the cartesian coordinates and the operando scans were registered according to the aligned LQ dry scan. The water segmentation is based on subtraction of the dry scan from the wet scan. For segmentation the difference images are denoised and segmented using a two-step thresholding approach. The solid structure is

extracted from the denoised and segmented HQ dry scan. Detailed information about the image processing procedure can be found in Sabharwal et al.[12].

Results and discussion

The operando experiments with a scan frequency of 1 Hz were performed for 180 s starting from a previously dried cell ensuring that water cluster break-through from the GDL interface into the channel occurs just by the water produced according to fuel cell operation. Figure 2 shows two greyscale in-plane slices at the end of the operation demonstrating the water droplet distribution (Figure 2 b)) with respect to the corresponding active area pattern (Figure 2a)). The water produced by the active catalyst area feeds either one (A, E, F, G, H) or two (B, C, D) droplets.

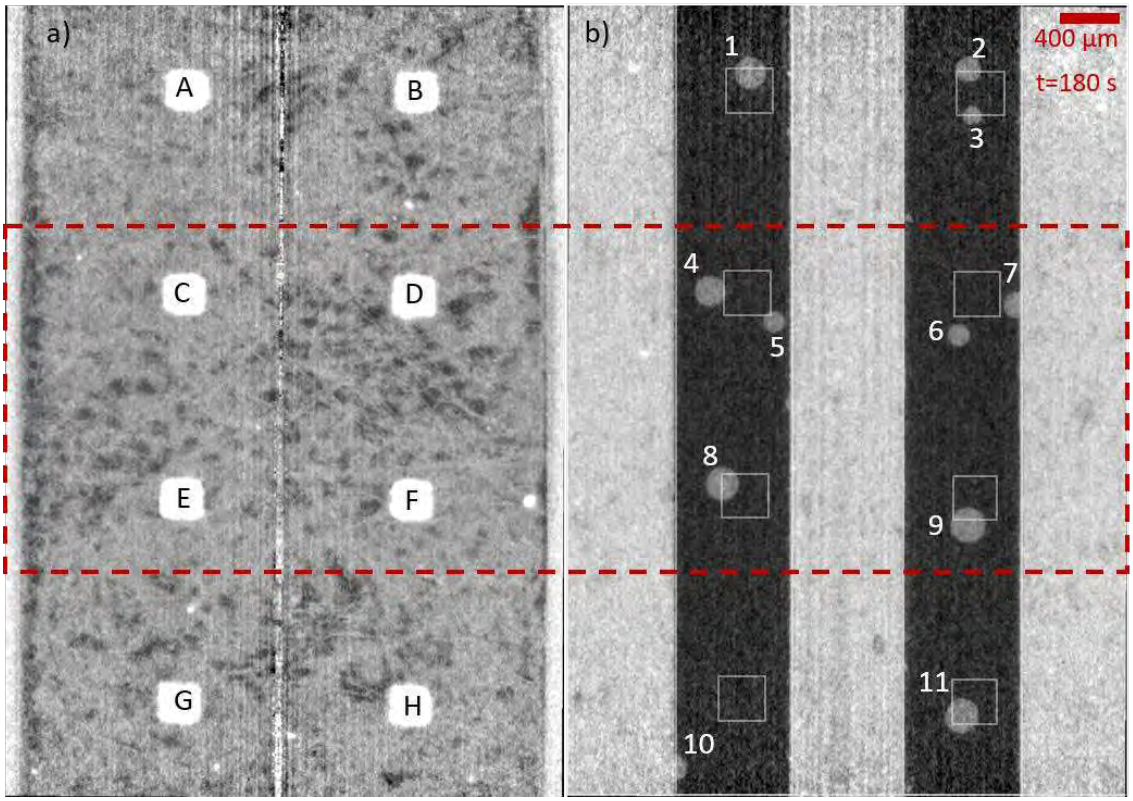

Figure 2: a) In-plane slice at the GDL-catalyst-layer interface with catalyst pattern labeled according to table 1; b) In-plane slice showing the cathode channels with droplets. The water droplets are labeled for further analysis and the active areas are depicted as hollow white boxes.

Table 1 summarizes the general observations for each cluster. For the first droplet (according to numbering on Figure 2b) no instabilities were seen and after break-through into the channel the percolating water cluster in the GDL keeps feeding the droplet continuously until the end of the scan. The second droplet shows a periodic fluctuation since the droplet disconnects and reconnects to the percolating water cluster in the GDL. The droplet disconnects 8 s after break-through and then reconnects after another 17 s and finally disconnects again after 19 more seconds without connecting anymore until the end of the scan. For the third droplet, a different behavior is observed. After break-through into the channel, the droplet and the corresponding water cluster in the GDL change into a static state until the end of the operation.

For further understanding of the different water transport dynamics, Figure 3 shows segmented image data of the water progression at defined timestamps. The images were created by overlaying through plane slices of the segmented water clusters and the segmented solid structure. Note that the clusters are treated as independent and the temporal resolution was chosen according to certain events happening. Due to better image quality, just CCM areas C, D, E and F (highlighted by the red box in Figure 2) were considered. However, all the observed phenomena are captured in these six sequences. The development of each droplet with respect to time is shown from left to right and the droplet number shown in red refers to the labelling Figure 2 b.

TABLE I. Overview of water cluster percolation events during XTM scans according to labels in Figure 1.

Active Area	Droplet	Breakthrough Time [s]	Behavior
A	1	105	After break-through the droplet is connected to the cluster over the entire scan time continuously growing
B	2	128	Cluster disconnects from droplet 8 s after break-through
	3	60	After break-through the droplet stays stable and doesn't grow anymore
C	4	92	Cluster disconnects from droplet 8 s after break-through
	5	141	No instabilities at the GDL surface but cluster disconnects in the GDL structure itself
D	6	113	Cluster disconnects from droplet 40 s after break-through
	7	115	No instabilities detected, droplet continuously fed by water cluster
E	8	75	Cluster disconnects from droplet 39 s after break-through
F	9	31	Cluster disconnects from droplet 93 s after break-through
G	10	163	Cluster disconnects from droplet immediately after break-through
H	11	63	After break-through the droplet is connected to the cluster over the entire scan time continuously growing

At the active region C, again two percolation clusters are observed. The image sequence in Figure 3 also captures the moment of break-through into the channel between 91 s and 92 s. Moreover, instabilities with a low frequency can be seen since the water cluster disconnects from the droplet at 106 s, connects again at 138 s and finally disconnects after 151 s until the end of the scan. Note that close to the shown break-through area of droplet 4 in Figure 3 another droplet already attached the GDL surface was observed from the beginning of the experiment due to insufficient pre-drying (not shown in Figure 3). Considering this circumstance and the fact that the water cluster percolates again into the same direction to break-through into the channel at almost the same spot, one could hypothesize that the water percolation pathways through the GDL are rather stable and follow the least resistant path, which depends on the hydrophobicity and contact angles of the GDL fibers. The instabilities of droplet 5 were not observed on the GDL-channel interface, but in the GDL bulk (see highlighted spots in green in the respective image sequence). It can be seen that water rapidly penetrates the void at the timestamps 114 s and 115 s. Afterwards periodically connecting and disconnecting procedures are observed with a frequency of 1-2 seconds, exemplary illustrated at the timestamps 141 s, 142 s and 143 s.

The active area D also feeds two water droplets (6 and 7) to the channel, one of them (7) attaches to channel wall after break-through. It is observed, that the droplet 7 is continuously fed by the water cluster and grows without showing any instabilities. Both droplets 6 and 7

show a strong in-plane extent from the corresponding active area as can be seen by their relative positions in Figure 2b. It is also observed that the water cluster feeding droplet 6 is not attached to the CCM surface in the shown through-plane slice of the image sequence in Figure 3. This is explained by the displacement of the break-through location of the droplet away from the feeding active area and implies an initial in-plane progression of the water cluster. Apart from this, droplet 6 disconnects from its feeding cluster after growing steadily for 38 s. Afterwards it does not connect again, but considering the images after 153 s and 180 s indicates, that the cluster would have grown again towards the droplet in a long-term operation.

Unlike domain C and D, section E and F only fed one droplet to the channel. Both percolation clusters 8 and 9 showed a similar behavior, starting with a comparably long time of initial droplet growth after break-through (34 s and 92 s respectively) and then ending up in a periodic fluctuation. Noteworthy is here that the duration of the reconnection between the feeding cluster and the water droplets on the GDL surface might last only for 1 s or even shorter and therefore might not be captured sufficiently in the operated scan time resolution (see164 s to 166 s for droplet 8 and 127 s to 129 s for droplet 9). Note that similar to droplet 6 the water cluster feeding droplet 9 starts growing from another location towards the in-plane direction due to displacement between the break-through location and the active area (see Figure 2).

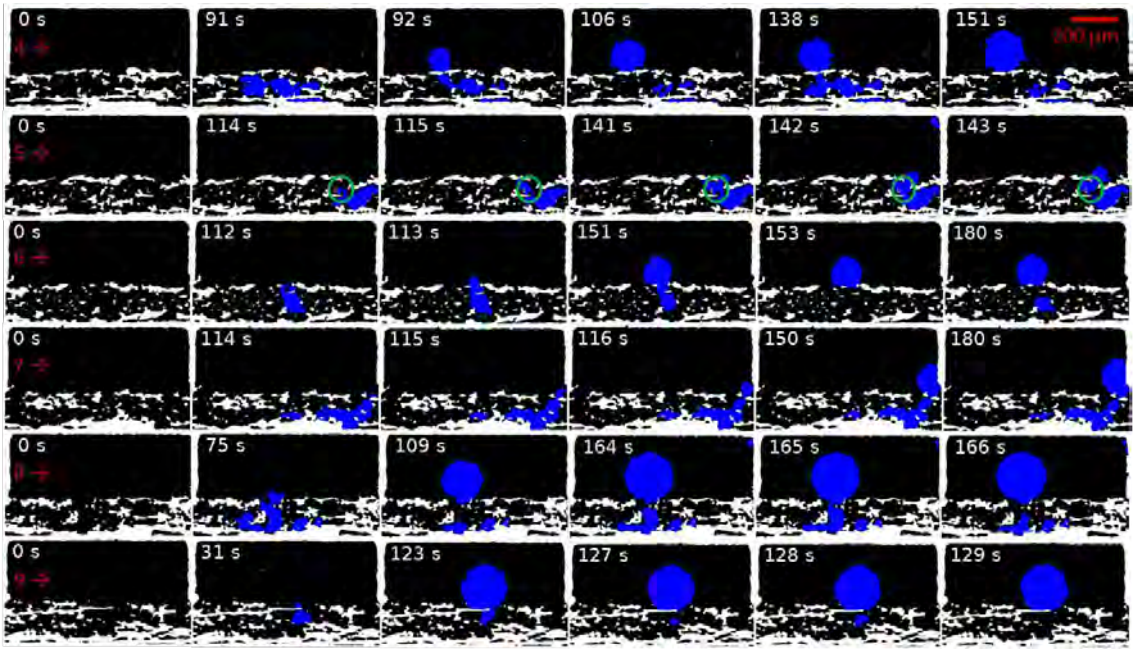

Figure 3: Percolation of water clusters (blue) through the GDL (GDL fibers in white) and droplet growth in the channel (Droplet 4-9 according to Figure 2) for selected timestamps.

The liquid water percolation path from active area G shows the strongest in-plane extent as the droplet breaks through the GDL at the channel border with an in-plane displacement nearly equal to the size of the active area itself. The water cluster first grows directly towards the channel but instead of breaking through continues growing in the in-plane direction towards its final break-through location (see Figure 2 b). The water droplet on the GDL surface corresponding to the active area H continuously grows in the channel after break-through until the end of the scan. However, it cannot be said for sure, if the water cluster would remain stable in a longer observation period.

Conclusion

The findings in this study extend the observations Mularczyk et. al. [13] by showing agreements with their findings as well as several further insights. It was found that after break-through some clusters fall into a state of periodic fluctuations between connection and disconnection to the droplet resulting in an intermittent feeding of the droplet. The frequency of this unstable droplet feeding procedure was different for the individual water clusters and seems to be dependent on the water pathway Furthermore, it is shown that the instabilities do not necessarily appear at the GDL surface but also inside the GDL. One of the emerged droplets showed no instabilities during the conducted investigation. It can therefore not be concluded that instabilities occur always during the water percolation process. Moreover 3 of the 8 catalyst surfaces of $(250\ \mu m)^2$ formed multiple percolating water networks resulting in two droplets breaking through the GDL into the channel. The breakthrough time for the water clusters in the GDL was found to vary from 31 s to 163 s which was likely due to the material properties and stochastic nature of the droplet formation. The instability of water percolation paths to drain water from the CL into the flow-field needs to be considered as being very common for future material development and GDL two-phase modelling.

Acknowledgements

The authors would like to acknowledge Federica Marone, Arnaud Schuller, Michael Striednig and Yen-Chun Chen (all Paul Scherrer Institut) for their support at the beamline. Thomas Gloor (Paul Scherrer Insitut) is acknowledged for his technical support during beamtime preparation. We also thank the Paul Scherrer Institut, Villigen, Switzerland for providing synchrotron radiation beamtime at the TOMCAT beamline of the SLS.

References

1. Sharaf, O. Z.; Orhan, M. F. An Overview of Fuel Cell Technology: Fundamentals and Applications. Renewable and Sustainable Energy Reviews 2014, 32, 810–853. https://doi.org/10.1016/j.rser.2014.01.012.
2. Espinoza-Andaluz, M.; Reyna, R.; Moyón, A.; Li, T.; Andersson, M. Diffusion Parameter Correlations for PEFC Gas Diffusion Layers Considering the Presence of a Water-Droplet. International Journal of Hydrogen Energy 2020, 45 (54), 29824–29831. https://doi.org/10.1016/j.ijhydene.2019.08.144.
3. Mathias, M. F.; Roth, J.; Fleming, J.; Lehnert, W. Diffusion Media Materials and Characterisation. In Handbook of Fuel Cells; American Cancer Society, 2010. https://doi.org/10.1002/9780470974001.f303046.
4. Litster, S.; Sinton, D.; Djilali, N. Ex Situ Visualization of Liquid Water Transport in PEM Fuel Cell Gas Diffusion Layers. Journal of Power Sources 2006, 154 (1), 95–105. https://doi.org/10.1016/j.jpowsour.2005.03.199.
5. Sakaida, S.; Tabe, Y.; Tanaka, K.; Konno, M. Study on Water Transport in Hydrophilic Gas Diffusion Layers for Improving the Flooding Performance of Polymer Electrolyte Fuel Cells. International Journal of Hydrogen Energy 2021, 46 (10), 7464–7474. https://doi.org/10.1016/j.ijhydene.2020.11.202.
6. Ihonen, J.; Mikkola, M.; Lindbergh, G. Flooding of Gas Diffusion Backing in PEFCs : Physical and Electrochemical Characterization. J. Electrochem. Soc. 2004, 151 (8), A1152. https://doi.org/10.1149/1.1763138.
7. Mularczyk, A.; Lin, Q.; Blunt, M. J.; Lamibrac, A.; Marone, F.; Schmidt, T. J.; Büchi, F. N.; Eller, J. Droplet and Percolation Network Interactions in a Fuel Cell Gas

Diffusion Layer. J. Electrochem. Soc. 2020, 167 (8), 084506. https://doi.org/10.1149/1945-7111/ab8c85.

8. Xu, H.; Nagashima, S.; Nguyen, H. P.; Kishita, K.; Marone, F.; Büchi, F. N.; Eller, J. Temperature Dependent Water Transport Mechanism in Gas Diffusion Layers Revealed by Subsecond Operando X-Ray Tomographic Microscopy. Journal of Power Sources 2021, 490, 229492. https://doi.org/10.1016/j.jpowsour.2021.229492.
9. Büchi, F. N.; Geiger, A. B.; Neto, R. P. Dependence of Current Distribution on Water Management in PEFC of Technical Size. Journal of Power Sources 2005, 145 (1), 62–67. https://doi.org/10.1016/j.jpowsour.2004.12.039.
10. Eller, J.; Marone, F.; Büchi, F. N. Operando Sub-Second Tomographic Imaging of Water in PEFC Gas Diffusion Layers. ECS Trans. 2015, 69 (17), 523. https://doi.org/10.1149/06917.0523ecst.
11. Nagai, Y.; Eller, J.; Hatanaka, T.; Yamaguchi, S.; Kato, S.; Kato, A.; Marone, F.; Xu, H.; Büchi, F. N. Improving Water Management in Fuel Cells through Microporous Layer Modifications: Fast Operando Tomographic Imaging of Liquid Water. Journal of Power Sources 2019, 435, 226809. https://doi.org/10.1016/j.jpowsour.2019.226809.
12. Sabharwal, M.; Büchi, F. N.; Nagashima, S.; Marone, F.; Eller, J. Investigation of the Transient Freeze Start Behavior of Polymer Electrolyte Fuel Cells. Journal of Power Sources 2021, 489, 229447. https://doi.org/10.1016/j.jpowsour.2020.229447.
13. Mularczyk, A.; Lin, Q.; Niblett, D.; Vasile, A. V. A.; Blunt, M. J.; Niasar, V.; Marone, F.; Schmidt, T. J.; Büchi, F. N.; Eller, J. Operando Liquid Pressure Determination in Polymer Electrolyte Fuel Cells. ACS Applied Materials and Interfaces 2021.

ECS Transactions, 104 (8) 83-92 (2021)
10.1149/10408.0083ecst ©The Electrochemical Society

Effects of Condensed Water on Oxygen Transport Resistance Components Separated by the Limiting Current Analysis in PEFC

Y. Iizuka, Y. Kitami, S. Uemura, and Y. Tabe

Division of Mechanical and Aerospace Engineering, Hokkaido University,
N13 W8, Kita-ku, Sapporo, Hokkaido 060-8628, Japan

The limiting current analysis was extended to evaluate the effects of condensed water on components of oxygen transport resistance under flooding conditions in this study. By introducing two indices of water accumulation effects, the oxygen transport resistance was separated into resistances inside and outside of the catalyst layer (CL) considering the flooding effects. The results using this extended method showed that increases in the oxygen transport resistance both outside and inside the CL are suppressed at higher temperature. The narrower channel and rib, 0.3 mm, also suppresses the resistance increases, as compared with 1.0 mm wide channel. Further, the observation of water distribution by a freezing method and a cryo-SEM showed that there is ice layer at MPL/CL interface with wider channel even at high temperature, 80°C. This suggests that loose contact causes water accumulation at the MPL/CL interface, resulting in an increase in the oxygen resistance inside the CL.

Introduction

Polymer electrolyte fuel cells (PEFCs) have attracted attention as energy conversion devices with low environmental impact: high efficiency and no carbon dioxide emission during the operation, etc. To increase the power of PEFCs, it is important to control the generated water appropriately and to prevent the flooding (the blockage of the gas supply to the reaction area by the accumulation of water). It has been widely accepted that the water management ability is strongly influenced by the gas diffusion layer (GDL) and micro-porous layer (MPL), but the detailed mechanisms have not been clarified.

Various studies have been conducted on the effects of liquid water on the cell performance. Water in the porous structure was visualized and observed by several advanced methods (1,2). Changes of oxygen transport resistance under flooding conditions were also evaluated using the limiting current method (2-4). Detailed analysis of the transport resistance is possible under dry conditions: the oxygen resistance was separated into two components, a pressure dependent and an independent components (5-7). Under wet conditions, however, the oxygen transport resistance cannot be separated because of increases in the resistance (not constant) by flooding. The relationship between the water distribution and the resistance change still remains not clear.

This study extends the limiting current analysis to investigate the effect of water accumulation on the components of oxygen transport resistance quantitatively under

flooding conditions. The oxygen transport resistance was separated into resistance components inside and outside of the catalyst layer (CL) by introducing two indices of water accumulation effects. Using this extended separation method, we evaluated the effects of operation temperature on increases in the components of oxygen transport resistance due to water accumulation in the cell. Further, the effects of channel width were also examined. To discuss the resistance increase depending on the channel width, the water distribution in the cathode side MPL and CL were observed by using a freezing method and a cryo-SEM (1).

Experimental Apparatus and Methods

Fuel Cell Hardware

In this study, small cells with an active area of 1.8 cm^2 (0.9 cm × 2.0 cm) were used so that the cells could be frozen and disassembled rapidly in the freezing method. To evaluate the effects of non-uniformity of the channel and rib structure, two kinds of separators with 0.3 mm or 1.0 mm wide rib and channel were compared. They are called 0.3 mm separator and 1.0 mm separator, respectively. The channel depth was 0.5 mm. 235 μm thick GDLs with MPLs (SGL Co., Ltd., SIGRACET®28BC) were used for the cathode and anode sides. The catalyst coated membrane (CCM) (Gore, PRIMEA®) had 30 μm thick membrane and the Pt loadings were 0.4 mg/cm^2.

Experimental Methods and Conditions

The experiments consisted of the oxygen transport resistance measurements (limiting current measurements) and observations of water distribution in near the MPL. In the cell operations, mixed gas of oxygen and nitrogen was supplied to the cathode side. The cathode gas flow rate was set very high, 2000 standard cc/min (SCCM, 1.00 standard cc/min = 1.67×10^{-8} m^3/s), to prevent water plugging and flooding in the narrow channels. Hydrogen was supplied to the anode side, and the anode gas flow rate was 100 sccm. The relative humidity of supplied gases was 81%RH, which was controlled by bubbler temperature.

The oxygen transport resistance was evaluated by using the limiting current method (2-6). The oxygen concentration at the platinum surface is assumed zero at the limiting current density, and the total oxygen transport resistance, R_T, is given by Eq. 1.

$$R_{\mathrm{T}} = \frac{4F}{I_{\mathrm{Lim}}} C_0 = \frac{4F x_0^{\mathrm{dry-in}}}{I_{\mathrm{Lim}}} \frac{P - P_w}{RT} \qquad [1]$$

Here, I_{Lim} is the limiting current density [A/m^2], F the Faraday's constant [C/mol], C_0 the oxygen concentration at the channel inlet, $x_0^{\mathrm{dry-in}}$ the dry mole fraction of oxygen, P the total gas pressure, P_{W} the vapor pressure at the channel inlet, R the universal gas constant, and T the absolute temperature. In the limiting current density measurement, the cell voltage was kept constant at 0.1 V, and the current density at steady state for about 5 minutes was measured as the limiting current density. The measurements were conducted at three different temperatures (35°C, 60°C, and 80°C) to investigate the effect of water accumulation in PEFC on the oxygen transport. The dry mole fractions of oxygen and back

pressure on cathode were also varied at each measurement, as in Table I. This is to evaluate the transport resistance components in the next section.

For the cryo-SEM observation, the water in the cell was frozen and immobilized by cooling to −30°C after the operation of the power generation. The cell was disassembled in the thermostatic chamber (−30°C), and the CCM and GDL removed from the cell were quickly put into liquefied nitrogen. The CCM and GDL were cut into pieces perpendicular to the gas flow direction in liquid nitrogen and set on a sample holder. The sample were moved from the liquid nitrogen to the preparation chamber at −100°C in the cryo-SEM (JEOL, JSM-6701F with Gatan, ALTO2500) and cut by a cooled knife. The cut surface of the sample was coated with Au-Pd for clear observations and prevention of the ice sublimation. The sample was moved to the sample chamber of the cryo-SEM at −150°C and observed with an acceleration voltage of 5 kV.

TABLE I. Experiment conditions for oxygen transport resistance measurement.

Experiment condition	
Rib/channel width [mm]	0.3, 1.0
Cell temperature [°C]	35, 60, 80
Relative humidity [%RH]	81
Cathode flow rate [sccm]	2000
Anode flow rate [sccm]	100
Cathode gas	Mixed gas of N_2 and O_2
Anode gas	H_2
Oxygen dry mole fractions [%]	1, 2, 4, 6, 8, 12, 16, 20, 24
Back pressure on cathode [kPa]	110, 140, 180 (abs)
Back pressure on anode [kPa]	Atmospheric pressure

Results and Discussion

Total Oxygen Transport Resistance with the Different Temperature

Figure 1 shows the experimental results of the oxygen transport resistance calculated using Eq. 1 using the cell with 1.0 mm separator at 81%RH and 110 kPa. To evaluate the effects of water condensation on the oxygen transport, the oxygen concentration of the cathode gas was set at nine different values from 0.01 to 0.24, as in Table I. As the limiting current density increases, the oxygen transport resistance at 35°C increases from about 0.3 A/cm^2, and then the gradient becomes smaller between 0.6 A/cm^2 to 1.3 A/cm^2. From 1.3 A/cm^2, the resistance increases sharply again. This behavior is similar to those reported in the literature (2-4). The larger increase means the larger effect of water accumulated in the cell, and the changing trend is estimated to be affected by locations where water accumulates in the cell. At the higher temperature, 60°C and 80°C, the oxygen resistance increases gradually from higher current density regions and the increase is suppressed. At 80°C, the increase in the resistance becomes slight; it was reported that the balance of generated water and heat is kept appropriate at 80°C in this condition (8). However, this results in Fig. 1 is not enough to understand the detailed relationship between the increasing trend of resistance and water distribution in the cell. Next, we try to extend the limiting current analysis and to evaluate the effects of water locations on the oxygen transport resistance.

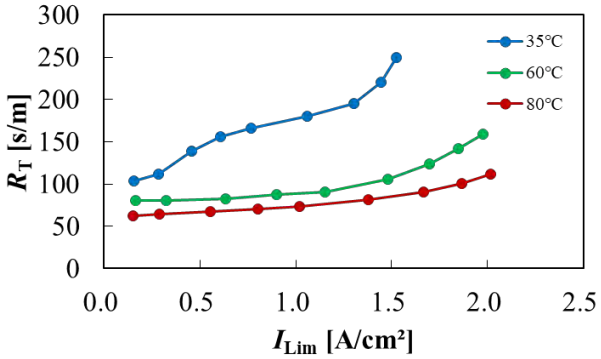

Figure 1. Oxygen transport resistance using limiting current density method at 81%RH and 110 kPa.

Extension of Limiting Current Method to Flooding Conditions

Considering the oxygen diffusion in the cell, the total oxygen transport resistance, R_T, can be divided into two resistances by Eq. 2.

$$R_T = \frac{P}{P_0} R_P + R_{NP} \quad [2]$$

Here, P_0 is the reference pressure, and 100 kPa in this study. The R_P is the pressure dependent oxygen transport resistance at 100 kPa, and corresponds mainly to the oxygen transport resistance in the GDL and the MPL by molecular diffusion. The R_{NP} is the pressure independent oxygen transport resistance, and corresponds approximately to the oxygen transport resistance in the CL: Knudsen diffusion resistance in the pores of the CL, and the transport resistance from the gas in the pores to Pt surface through ionomer. Molecular diffusion is dominant in large pores such as GDL and MPL, and diffusion coefficient is inversely proportional to total pressure. On the other hand, Knudsen diffusion and diffusion coefficient in ionomer don't depend on total pressure. Under dry conditions, the R_P and R_{NP} can be assumed constant because these depend on only the structure of porous media. Therefore, by using the pressure dependency, it is possible to separate the oxygen transport resistance into resistances inside and outside CL. However, under the wet conditions of high humidity and high current density, the R_P and R_{NP} are expected to increase by the effect of water accumulation. Therefore, this method cannot be used directly under flooding conditions; detailed analysis of oxygen transport resistance components is difficult.

Then, this study developed the separation method of oxygen transport resistance for flooding conditions, considering vapor transport and water distribution. In the method, it was assumed that the water production rate dominates the water accumulation inside the CL (pressure independent). The water production rate is proportional to current density. Outside the CL (pressure dependent), it was assumed that the water accumulation was determined by the ratio of the water production rate to the vapor diffusion coefficient D_{Vapor}. The D_{Vapor} is inversely proportional to the total pressure P, and the ratio of the water production rate to D_{Vapor} is expressed by Eq. 3.

$$\frac{I_{\mathrm{Lim}}}{D_{\mathrm{Vapor}}} \propto I_{\mathrm{Lim}}P \qquad [3]$$

Based on these assumptions, the R_{P} and R_{NP} are expressed as a function of each index, as shown in Eq. 4.

$$R_{\mathrm{T}} = \frac{P}{P_0}R_{\mathrm{P}}(I_{\mathrm{Lim}}P) + R_{\mathrm{NP}}(I_{\mathrm{Lim}}) \qquad [4]$$

Oxygen transport resistance measurements were conducted at three back pressures on cathode (110 kPa, 140 kPa, 180 kPa) to separate the total oxygen transport resistance. The R_{P} and R_{NP} were determined by a least square error calculation of actual total oxygen transport resistances (Eq. 1) and calculated values (Eq. 4). The separation was conducted under the restriction that the R_{P} and R_{NP} do not change or increase as the index of water accumulation increases. Further, we set the R_{P} and R_{NP} under dry conditions as minimum values.

Setting the Oxygen Transport Resistances under Dry Conditions

Figure 2 shows the results to determine the R_{P} and R_{NP} in 1.0 mm separator and 0.3 mm separator under little water effect conditions at 80℃ and 81%RH. The measurement with the 0.3 mm separator was also conducted to discuss the effect of channel widths later. As shown in Figs. 2(a) and (b), limiting current densities (I_{Lim}) were measured at three oxygen dry mole fractions (1%, 1.5%, 2%) and three back pressures on cathode (110 kPa, 140 kPa, 180 kPa). The results show linear trends, indicating that the total oxygen transport resistance is constant at each pressure under the dry conditions. To eliminate the oxygen independent current density, I_{Lim}, the gradient of the line was used to estimate the oxygen transport resistance by Eq. 1. From Fig. 2(c), the total oxygen transport resistance is separated into the R_{P} (pressure dependent component corresponding to outside CL) and the R_{NP} (pressure independent component corresponding to inside CL) under the dry conditions using the gradient and the intercept of each line.

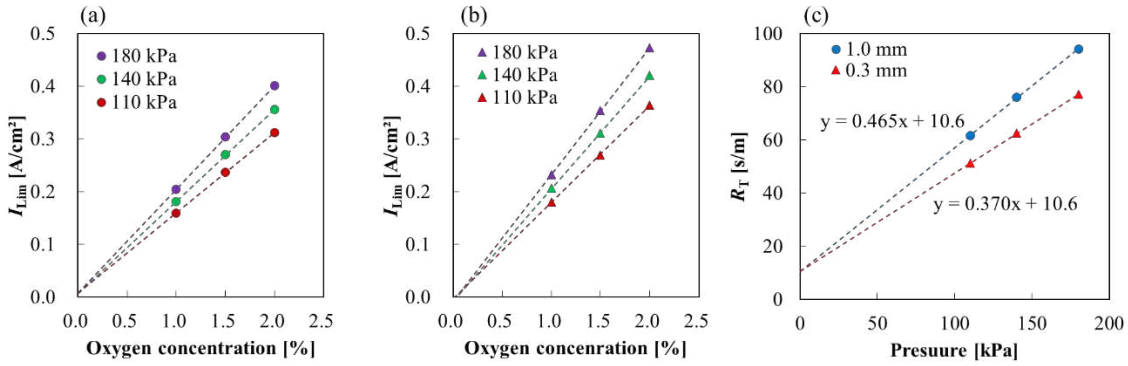

Figure 2. Limiting current density as a function of oxygen dry fraction for (a) 1.0 mm separator and (b) 0.3 mm separator, and (c) oxygen transport resistance as a function of pressure at 80℃ and 81%RH under no water effect condition.

In case of 35℃ and 60℃, the R_{P} and R_{NP} under dry the conditions were determined by using the result of R_{P} and R_{NP} at 80℃ considering the temperature dependency of molecular

diffusion coefficient ($1/D_{\mathrm{M}} \propto T^{1.75}$) for R_{P} and Knudsen diffusion coefficient ($1/D_{\mathrm{K}} \propto \sqrt{T}$) for R_{NP}. The determined values are summarized in Table II. As shown in Table II, the R_{P} with 0.3 mm separator is smaller than with 1.0 mm separator, which indicates that narrower channel produces more uniform diffusion of oxygen and decrease the diffusion resistance. These values were set as minimum values in the oxygen transport resistance separation method under flooding conditions.

TABLE II. Results of oxygen transport resistance separation under no water effect condition at 81%RH.

(a) 1.0 mm separator

Temperature [℃]	R_{P} [s/m]	R_{NP} [s/m]
35	59.0	11.4
60	51.5	10.9
80	46.5	10.6

(b) 0.3 mm separator

Temperature [℃]	R_{P} [s/m]	R_{NP} [s/m]
35	46.9	11.4
60	43.2	10.9
80	37.0	10.6

Analysis of Oxygen Transport Resistance Components with the Different Temperature

Figure 3 shows the determined oxygen transport resistances outside CL, R_{P}, and inside CL, R_{NP}. The R_{P} and R_{NP} are functions of $I_{\mathrm{Lim}}P$ and I_{Lim} respectively, as in Eq. 4. In Fig. 4, the ordinate is the total oxygen transport resistances, R_{T}, and the values calculated from the measured limiting current density using Eq. 1 are shown as filled marks. The open marks represent the values calculated from the results of Fig. 3 using Eq. 4. The resistances in Fig. 4 are similar at each condition, showing the effectiveness of this separation method of the oxygen transport resistance.

From the results of 35℃ in Fig. 3(a), the R_{P} (oxygen transport resistance outside CL) has characteristic trends of water effect: as the index of $I_{\mathrm{Lim}}P$ increases, the R_{P} increases sharply at low index region, forms a plateau between 50 and 250 kPaA/cm^2, and increases again. This trend is estimated because the amount of water accumulated in the GDL and MPL increases and reaches an equilibrium situation in the plateau region. Then, the R_{P} increases due to further water accumulation with much higher $I_{\mathrm{Lim}}P$. On the other hand, as shown at Fig. 3(b), the R_{NP} (oxygen transport resistance inside CL) at 35℃ increases gradually at low current density region and increases sharply from about 1.4 A/cm^2. From these results, in case of 35℃, the increase in the total oxygen transport resistance at low current density region is dominated mainly by the R_{P}, while the increase at high current density region is affected by the R_{NP}. At 60℃, as shown at Fig. 3, the R_{P} and R_{NP} has the similar trend: the transport resistances are maintained nearly constant at low index region and increases gradually at high index region. Therefore, at 60℃, the increase in the total oxygen transport resistance is caused by both the R_{P} and R_{NP} increases. At 80℃, the R_{P} is suppressed even at high index region, as shown at Fig. 3(a), but the R_{NP} increases gradually at high current density region (Fig. 3(b)). So, in case of 80℃, the increase in total oxygen transport resistance at high current density region depends only on the R_{NP}. These results indicate that high temperature basically suppressed water accumulation, but it is difficult to prevent water accumulation inside the CL.

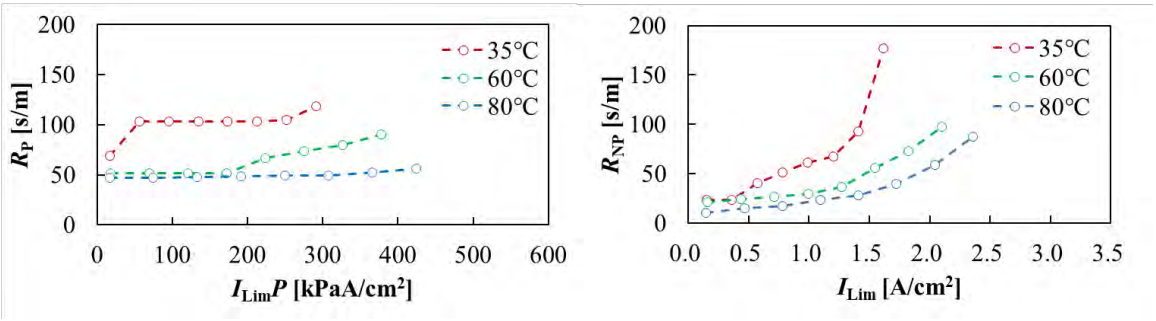

(a) Oxygen transport resistance outside CL (b) Oxygen transport resistance inside CL

Figure 3. The separation of oxygen transport resistances corresponding to inside and outside the CL.

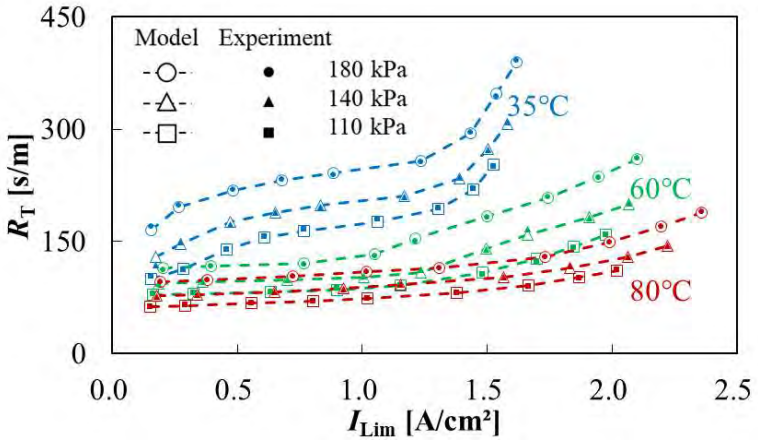

Figure 4. Difference of actual values from theoretical values about oxygen transport resistance at three pressures (110 kPa, 140 kPa, 180 kPa) and three temperatures (35°C, 60°C, 80°C).

Analysis of Oxygen Transport Resistance Components with the Different Channel Width

To investigate the reason why the R_{NP} (oxygen transport resistance inside CL) increases at high current density region even at the high temperature, 80°C, the effect of the difference in the channel width was investigated with 0.3 mm separator. Figures 5 and 6 show the results of oxygen transport resistance in each inside and outside the CL, and the calculated total resistance. From Fig. 6, it is confirmed that the calculation using Eq. 4 with values in Fig. 5 can simulate the experimental results of the oxygen transport resistance pretty well.

As shown in Fig. 6, the behavior of total oxygen transport resistance with 0.3 mm separator is similar to that with 1.0 mm separator (Fig. 1). However, the values are lower than with the 1.0 mm separator. Especially, at 80°C, the total oxygen transport resistance is kept nearly constant even at higher current densities. From the results of Fig. 5(a), the R_P (oxygen transport resistance outside CL) has similar behavior with 1.0 mm separator (Fig. 3(a)), though the values of R_P are smaller. The smaller values may be due to smaller amount of condensed water under narrower rib: it is commonly considered that generated water easily accumulates under ribs. On the other hand, from the result of Fig. 5(b), the R_{NP} has

different behavior from with the 1.0 mm separator depending on temperature: the R_{NP} at 35°C increases sharply from high current density, while the R_{NP} at 80°C is relatively constant. This result suggests that narrower rib and channel suppresses the increase in R_{NP}. It was an unexpected result that channel width has a great influence on R_{NP} rather than R_P. Therefore, observation of water distribution in cathode side MPL and CL was conducted to discuss the reason.

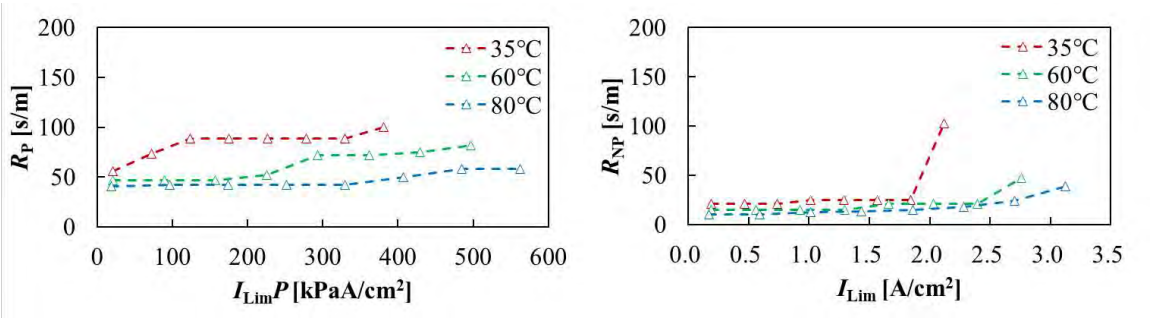

(a) Oxygen transport resistance outside CL (b) Oxygen transport resistance inside CL

Figure 5. The separation of oxygen transport resistances corresponding to inside and outside the CL in case of 0.3 mm separator.

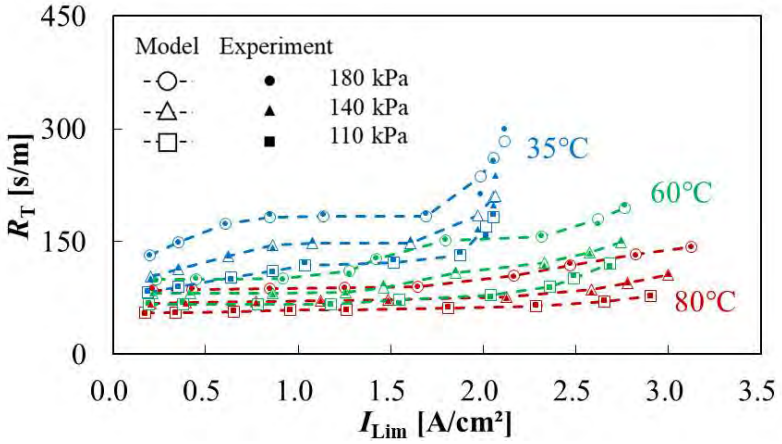

Figure 6. Difference of actual values from theoretical values about oxygen transport resistance in case of 0.3 mm separator at three pressures (110 kPa, 140 kPa, 180 kPa) and three temperatures (35°C, 60°C, 80°C).

Water Distribution in Cathode Side MPL and CL by Freezing Method

Figure 7 shows the water distribution in the vicinity of MPL at just before limiting current condition to discuss reasons why the R_{NP} (oxygen transport resistance inside CL) increases in case of 1.0 mm separator. The cell operation was conducted at 80°C with 24% oxygen concentration. No ice is observed in the MPL and CL for the 0.3 mm separator (Fig. 7(a)). This suggests that there is little water accumulated and the oxygen may reach to the CL directly through the GDL and MPL during the operation, as shown in Fig. 8(a). On the other hand, ice layer is observed at the MPL/CL interface for the 1.0 mm separator, as shown in Fig. 7(b) (It is considered that gaps above and below ice layer were made during creating a

sample after the operation). This can be considered related to the result in Fig. 3(b). The R_{NP} at 80°C increases in high current density region in case of 1.0 mm separator. This study used approximately 235 μm thick GDL with MPL and about 10 μm thick CL. When condensed water is accumulated at the MPL/CL interface as in Fig. 8(b), the water prevents oxygen diffusion to the CL. Considering the thickness of GDL and CL, the effect of increasing diffusion path length is much larger inside the CL. This is a reason why the R_{NP} increases only with 1.0 mm separator. The water accumulation at the interface can be considered due to worse contact of MPL and CL with the wider channel. These results suggest that a tight contact at the MPL/CL interface is important to suppress an increase in the oxygen transport resistance in the CL.

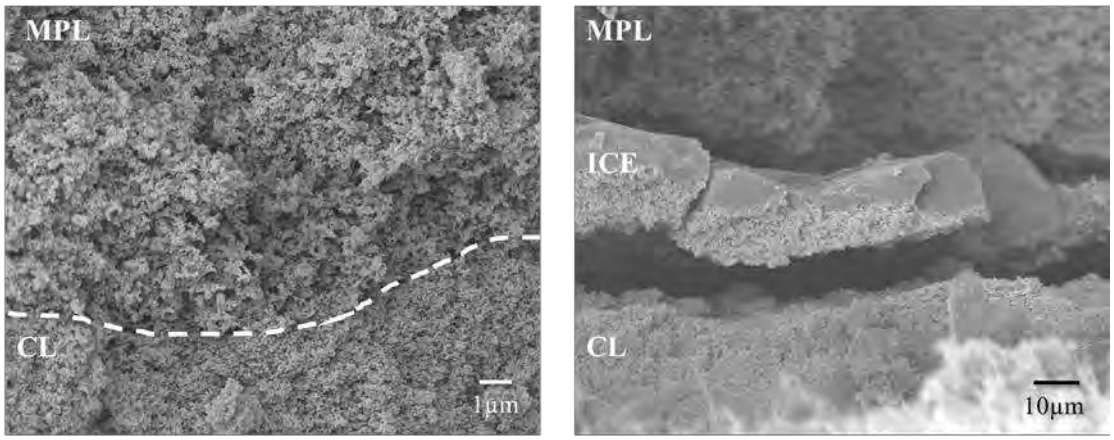

(a) 0.3 mm separator (b) 1.0 mm separator

Figure 7. Cross-Sectional image near the interface between MPL and CL after the operation at limiting current density (O_2 24%).

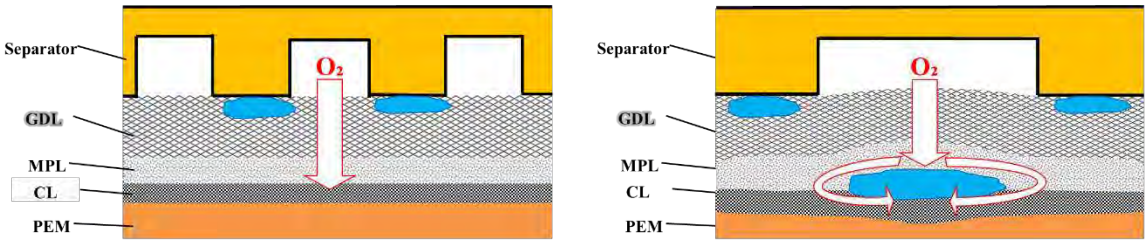

(a) 0.3 mm separator (b) 1.0 mm separator

Figure 8. Image of oxygen transport.

Conclusion

This study extended the limiting current analysis to investigate the effects of water accumulation on components of the oxygen transport resistance under flooding conditions. The oxygen transport resistance was separated into the resistance components inside and outside the CL by introducing two indices of water accumulation effects. The extended method showed that the oxygen transport resistance outside of the CL at 35°C increases sharply from low index region: at low current density and low pressure region. At high temperature of 80°C, the resistance increase is suppressed even at high index region.

However, the oxygen transport resistance inside of the CL increases even at high temperature. This tendency of the resistance increases is for the cell with the 0.1 mm wide channels and ribs. In the cell with the 0.3 mm wide channel/rib, the increases in the oxygen transport resistance inside the CL are suppressed, and at high temperature the resistance inside the CL are relatively constant even at high current density region. Then, the vicinity of MPL and CL was observed by a freezing method and a cryo-SEM. Ice layer (formed by condensed water accumulation) was observed at the MPL/CL interface with wider channel separator. This is attributed to the worse contact of MPL and CL under the wider channel. The observation results suggest that condensed water accumulation at the MPL/CL interface causes mainly the increase in oxygen transport resistance inside the CL.

Acknowledgments

This work was supported by JSPS KAKENHI Grant Number 21H01254.

Reference

1. Y. Aoyama, K. Suzuki, Y. Tabe, and T. Chikahisa, *Electrochem. Commun.*, **41**, 72 (2014).
2. D. Muirhead, R. Banerjee, M. G. George, N. Ge, P. Shrestha, H. Liu, J. Lee, and A. Bazylak, *Electrochimica Acta,* **274**, 250 (2018).
3. J. P. Owejan, T. A. Trabold, and M. M. Mench, *J. Heat and Mass Transfer*, **71**, 585 (2014).
4. D. A. Caulk and D. R. Baker, *J. Electrochem. Soc.*, **157**, B1237 (2010).
5. D. R. Baker, D. A. Caulk, K. C. Neyerlin, and M. W. Murphy, *J. Electrochem. Soc.*, **156**, B991 (2009).
6. N. Nonoyama, S. Okazaki, A. Z. Weber, Y. Ikogi, and T. Yoshida, *J. Electrochem. Soc.*, **158**, B416 (2011).
7. H. Oh, Y. i. Lee, G. Lee, K. Min, J. S. Yi, *J. Power Sources*, **345**, 67 (2017).
8. Y. Kitami, Y. Tabe, and T. Chikahisa, *ECS Trans.,* **92**(8), 213 (2019).

ECS Transactions, 104 (8) 93-99 (2021)
10.1149/10408.0093ecst ©The Electrochemical Society

3D Visualization of Liquid Water Penetration from MPL to Substrate Layer in PEFC Using in-Situ X-Ray Tomographic Microscopy

T. Sugahara, T. Sasabe, H. Naito, M. Kodama, S. Hirai

Department of Mechanical Engineering, Tokyo Institute of Technology,
Tokyo 152-8550, Japan

X-ray tomographic microscopy (XTM) is used to clarify liquid water behavior in polymer electrolyte fuel cell (PEFC). It was difficult to acquire 3D image of liquid water in gas diffusion layer (GDL) by using laboratory-based XTM because the intensity of laboratory-based X-ray is lower than that of synchrotron-based X-ray. By improving the cell, 3D visualization of liquid water in substrate layer and cracks of micro porous layer (MPL) is achieved. It is also shown that liquid water in substrate layer tends to remain in the bigger pore diameter.

Introduction

Polymer electrolyte fuel cell (PEFC) plays an important role in solving environmental problems and energy problems. It is required to perform it at higher current density to achieve the cost reduction. At high current density, however, water which is generated from the electrochemical reaction condenses. Then, cathode gas diffusion layer (GDL) is saturated with liquid water. In other words, water is one of the factors that prevents the oxygen diffusion. That's why clarifying the water management in GDL is essential to perform at higher current density. At present, synchrotron-based X-ray tomographic microscopy (XTM) is the common way to observe water distribution. Its high intensity X-ray makes it possible to acquire high-resolution data by imaging in short exposure time. In 2020, Hong Xu et al. reported that 88% water could be detected accurately by synchrotron-based XTM with a scan time of 0.4s at a voxel size of 3 μm (1). However, it is known that the polymer electrolyte is decomposed by synchrotron radiation. It is crucial to keep cell performance during imaging. In addition, the experiment time using synchrotron radiation facility is limited.

To inspect other ways than synchrotron-based XTM, here we aim to achieve 3D visualization of liquid water penetration in GDL using laboratory-based in-situ XTM. There is no experimental time limit when using laboratory-based XTM. Besides, the polymer electrolyte is not decomposed because the intensity of X-ray is much lower than that of synchrotron-based X-ray. However, the low intensity of X-ray has bad effects on spatial and time resolutions. To improve resolutions, we reduced the active area of fuel cell to prevent X-ray absorption. Jens Eller et al. used the cell with a horizontally aligned membrane electrode assembly (MEA) and an active area of 4.9 mm^2 (2). We used the horizontal cell with an active of 1.0 × 1.0 mm^2. Nevertheless, it takes more than an hour to acquire 3D data. water distribution of XTM may be averaged and different from that of X-ray radiography. To clear the effects of long scan time, we compared the water distribution obtained by 3D visualization and by 2D visualization using X-ray

radiography. Besides, we aim to evaluate the relationship between water distribution and GDL structure.

Experiment Setup

Fig.1 shows the schematics of fuel cell. To acquire high-resolution data, the cell with an active area of 1.0 × 1.0 mm^2 was applied. The cell equipped with Toray TGP-H-060 coated with MPL was used.

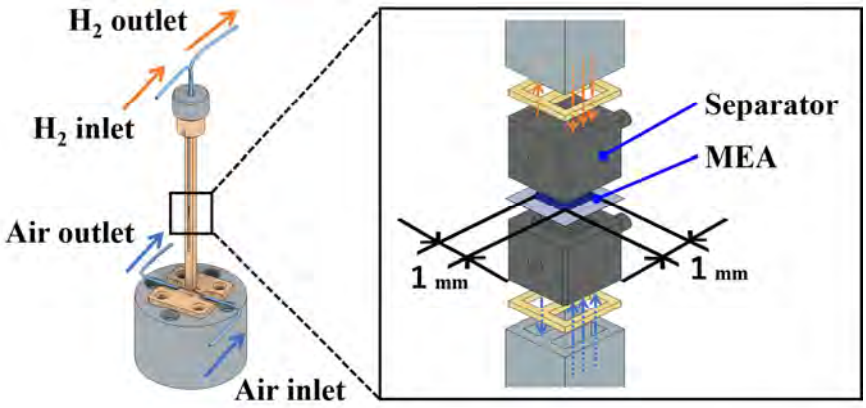

Figure 1. Schematics of fuel cell.

Laboratory-based XTM experiment was conducted by RIGAKU nano 3DX. The Cu target X-ray beam with a tube voltage of 40keV was used. Fig.2 shows the cross-section image of fuel cell obtained by XTM. The pixel size is 2.16 μm.

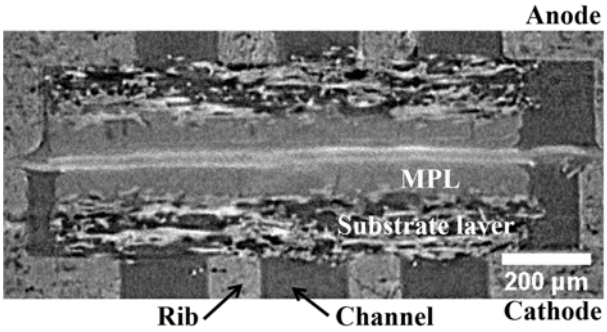

Figure 2. Cross-section image obtained by XTM.

3D visualization experiment

To reduce the exposure time as short as possible, we set the exposure time as 8.0s. The projection number is 850. The total scan time is about 2 hours. Hydrogen and air (O_2: 21%, N_2: 79%) are supplied from the anode and the cathode each other with the frow rate of 30cc/min. The cell temperature is room temperature (about 28℃), and the relative humidity is 80%. The cell was operated at 0.75, 1.0, 1.25, and 1.5 A/cm^2.

Comparative experiment between XTM and X-ray radiography

To get accurate water distribution, we set the exposure time as 14s. The projection number is 900. The total scan time is about 3.5 hours. Hydrogen and air (O_2: 21%, N_2:

79%) are supplied from the anode and the cathode each other with the frow rate of 30cc/min. The cell temperature is room temperature (about 28℃), and the relative humidity is 100%. The cell was operated at 1.0, 1.25, 1.5, 1.75 and 2.0 A/cm^2.

Results

3D visualization experiment

After the raw 3D data was obtained by XTM, the phase retrieval process was applied to conduct segmentations accurately (3). Then, image filtering and morphological operations were performed using ImageJ and MATLAB (4). As a result, we succeeded the segmentation of MPL, Fiber, pore, and liquid water. Fig.3 shows the 3D visualization of the cathode GDL and liquid water at 0.75, 1.0, 1.25, and 1.5 A/cm^2. The width is 900μm, the depth is 950μm, and the height is 214μm. Fig.3 suggests that the bigger current density is, the more water volume increase. Fig.4 shows one droplet of liquid water in the cracks of MPL and substrate layer. It is confirmed that there is a connection between the water in the crack and the water in the pore. It suggests that the crack of MPL is the dominant pathway of liquid water.

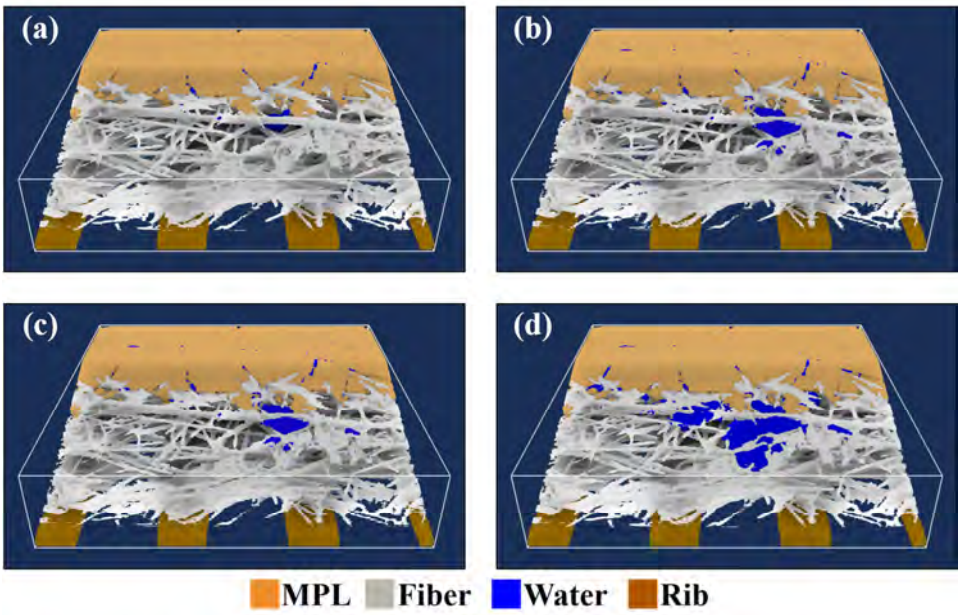

Figure 3. 3D visualization of the cathode GDL and liquid water: (a) 0.75 A/cm^2, (b) 1.0 A/cm^2, (c) 1.25 A/cm^2, (d) 1.5 A/cm^2.

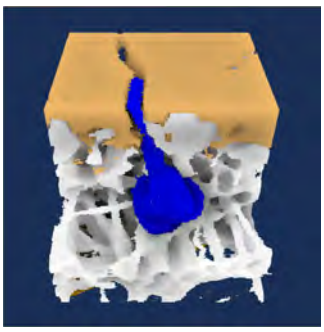

Figure 4. Liquid water in the cracks of MPL and substrate layer.

Fig.5 shows the water volume in each substrate layer. 0μm is the boundary between MPL and substrate layer. Fig.5 suggests that water tends to remain near the boundary.

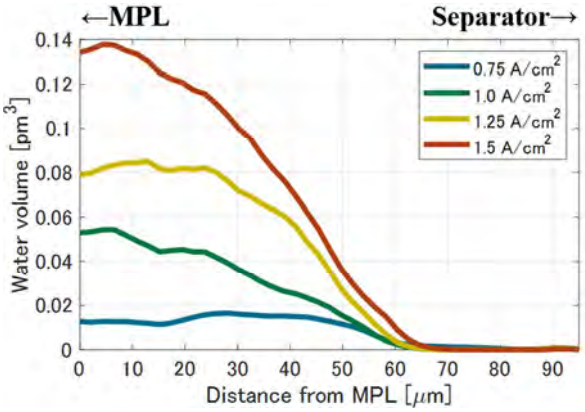

Figure 5. Water volume in each substrate layer

Fig.6(a) is the sliced image of substrate layer. Fig.6(b) is the image whose pore diameter was classified as the size. Effective pore diameter is defined as the 3D distance between pore and fiber. Fig.6(c) is the histogram of the relationship between effective pore diameter and water volume. Fig.6(c) suggests that at low current density such as 0.75 A/cm^2, liquid water tends to remain in the bigger pore diameter. As the current density increase, water tends to remain around the big pore diameter.

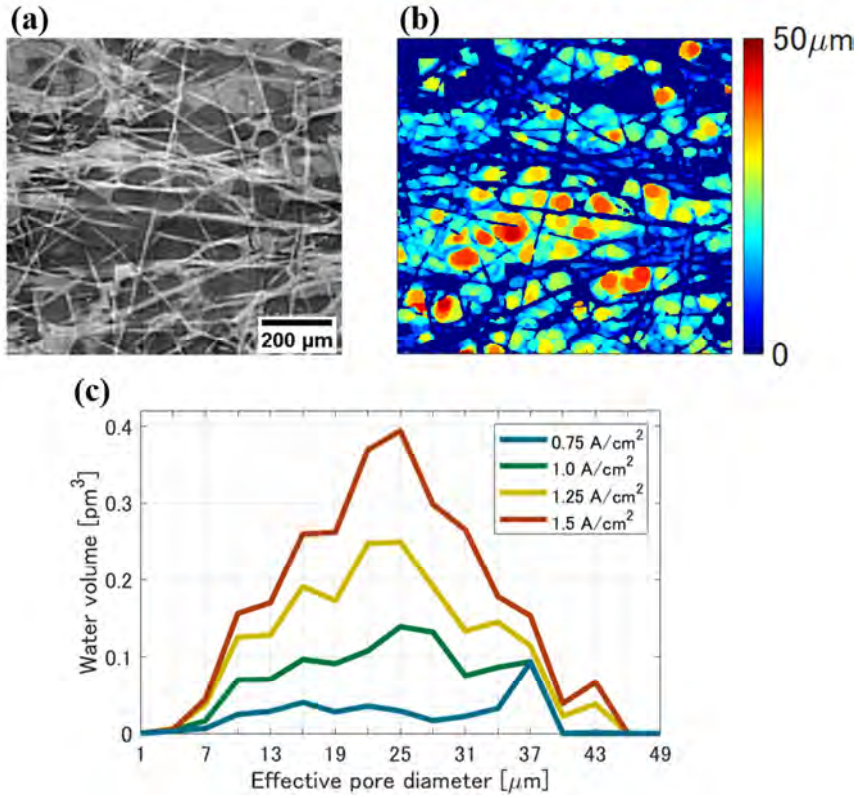

Figure 6. Relationship between effective pore diameter and water volume: (a) a slice of substrate layer, (b) image classified by effective pore diameter, (c) histogram of the relationship between effective pore diameter and water volume.

Comparative experiment between XTM and X-ray radiography

After 3D water distribution was obtained by XTM, it was converted into 2D. Then, it was compared with water distribution obtained by X-ray radiography. Fig.7(a) shows the region of interest of substrate layer. Fig.(1a)-(1e) show the 2D water distribution obtained by X-ray radiography at 1.0, 1,25, 1,5, 1.75, 2.0 A/cm^2. Fig.(2a)-(2e) show the 2D water distribution obtained by XTM at 1.0, 1,25, 1,5, 1.75, 2.0 A/cm^2. There is little difference between water distribution of XTM and X-ray radiography.

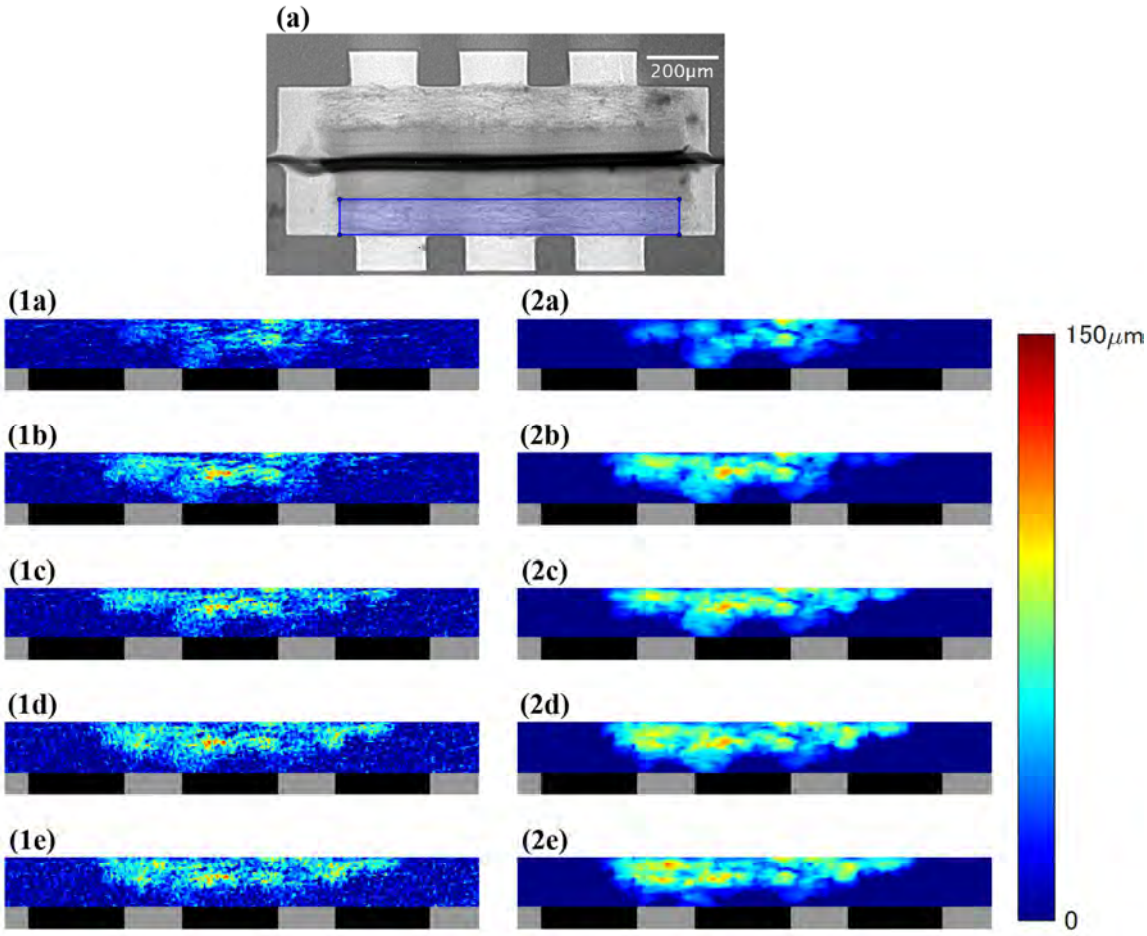

Figure 7. Comparison between water obtained by X-ray radiography and XTM: (a) region of interest of substrate layer, (1a)-(1e) 2D water distribution obtained by X-ray radiography at 1.0, 1,25, 1,5, 1.75, 2.0 A/cm^2, (2a)-(2e) 2D water distribution obtained by XTM at 1.0, 1,25, 1,5, 1.75, 2.0 A/cm^2.

To look closely, water volume in each substrate layer was compared. Fig.8 shows the comparison of water volume. At low current density, water volume obtained by XTM is almost same as that obtained by radiography. As current density increase, water volume near the separator obtained by XTM is lower than that obtained by radiography. This is because water near the separator moves dynamically. Because water volume near MPL is almost same, it is valid to evaluate water distribution in substrate layer near MPL obtained by XTM.

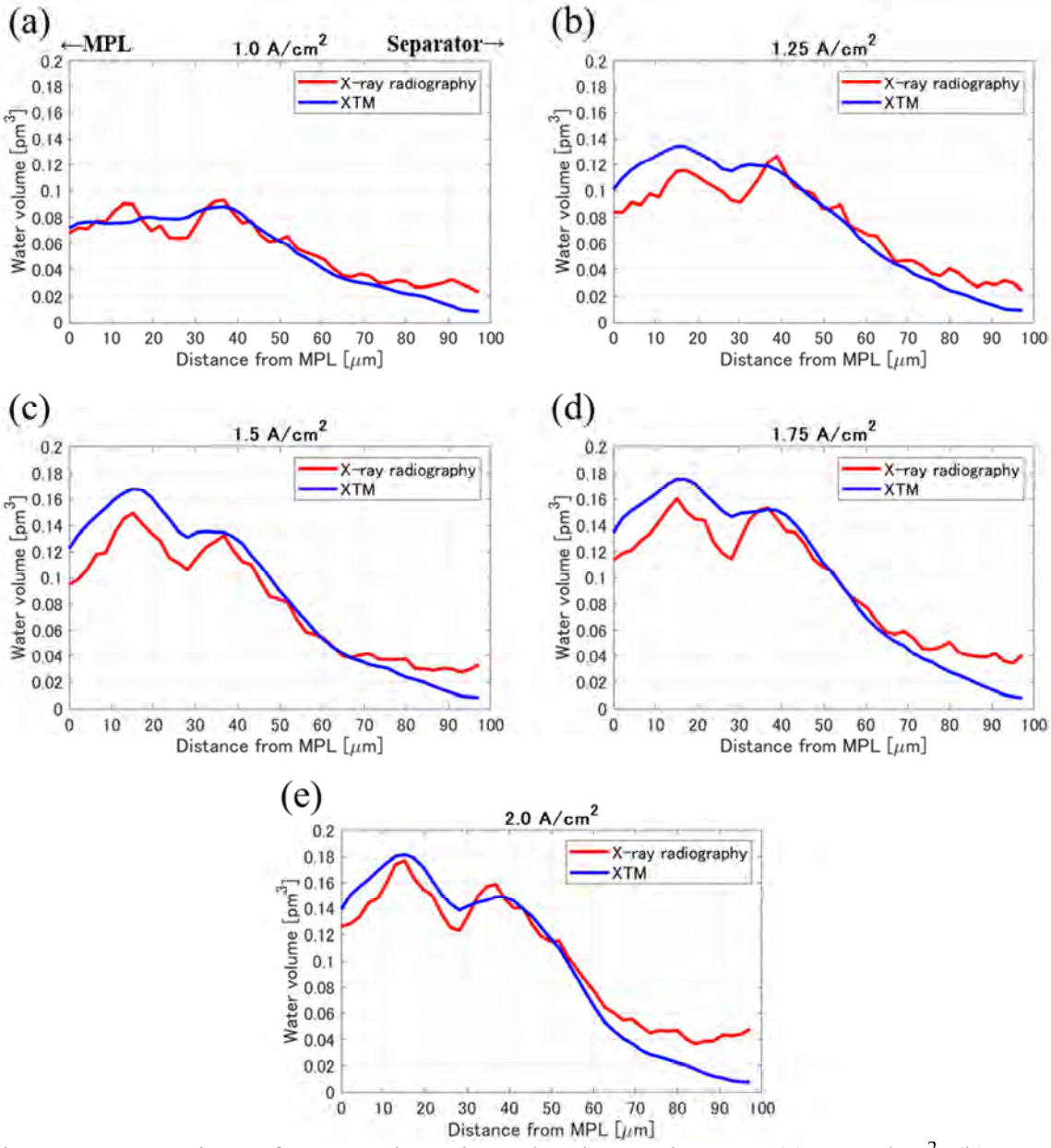

Figure 8. Comparison of water volume in each substrate layer: at (a) 1.0 A/cm^2, (b) 1.25 A/cm^2, (c) 1.5 A/cm^2, (d) 1.75 A/cm^2, (e) 2.0 A/cm^2.

Conclusion

In this study, 3D visualization using laboratory-based XTM was conducted. By improvement of the cell, phase retrieval, and image processing, the segmentations of MPL, fiber, pore, and water were succeeded. In addition, it was confirmed that there was a connection between water in the cracks of MPL and water in pores. It suggests that the crack of MPL is the dominant pathway of liquid water. Moreover, it was observed that water tended to remain in big pores near the boundary between MPL and substrate layer. This water saturation has a strong influence on oxygen transport to the catalyst layer. Then, by comparing water distribution of XTM and X-ray radiography, it is confirmed that water distribution obtained by XTM was valid.

References

1. Hong Xu, Minna Bührer, Federica Marone, Thomas J. Schmidt, Felix N. Büchi, and Jens Eller, *J. Electrochem. Soc.*, 167, 104505 (2020).
2. Jens Eller, Tomas Roén, Federica Marone, Marco Stampanoni, Alexander Wokaun, and Felix N. Büchi, *J. Electrochem. Soc.*, 158, B963-B970 (2011).
3. Dominika Kalasová, Tomáš Zikmund, Ladislav Pína, Yoshihiro Takeda, Martin Horváth, Kazuhiko Omote, and Jozef Kaiser, IEEE Transactions on Instrumentation and Measurement, Vol.69, No.4 (2020), pp.1170-1178.
4. Utku U. Ince, Henning Markötter, Nan Ge, Merle Klages, Jan Haußmann, Martin Göbel, Joachim Scholta, Aimy Bazylak, and Ingo Manke, *J. Hydrogen Energy*, Vol.45, No.21 (2020), pp.12161-12169.

ECS Transactions, 104 (8) 101-107 (2021)
10.1149/10408.0101ecst ©The Electrochemical Society

Optimization of Water Transport in the Gas Diffusion Layer of PEM Fuel Cells

Alexandru Herescu*

*Dpt. of Mechanical, Civil and Environmental Engineering,
Tarleton State University – The Texas A&M University System
Bryan, TX 77807, USA

Present study examines menisci morphology and breakthrough behavior of water through the porous fiber matrix of the Gas Diffusion Layer (GDL), and the transport characteristics of droplets according to the energy landscape of the medium. The hydrophobic GDL, which shows promise for improved water management, can be classified as non-wetting (NW), and mixed-non-wetting (MNW, i.e. PTFE coated). The mixed-non-wetting behavior is caused by the hydrophobic coating which allows parts of the meniscus contact line to deform freely in contact with the fibers, while other parts of the meniscus remain pinned due to coating defects. The MNW meniscus is critical to establishing a high breakthrough pressure and a small characteristic droplet volume, setting it apart from both NW and wetting GDL. The main difference between the two non-wetting media, NW and MNW, is evidenced by the breakthrough pressure which is significantly lower for the former, as shown by existing experimental data. This fact seems to indicate that the main transport mechanism for NW media is by droplet gliding along the fibers, made possible by low adhesion forces. "Clamshell" droplets are energetically favored at high contact angles, optimal design would require small volume droplets yielding low adhesion forces for this morphology. On the other hand, if MNW conditions are present, optimal design should aim for a small droplet volume and high breakthrough pressure as shown in present simulations. The numerical model employed herein captures the meniscus evolution and the corresponding breakthrough pressure for MNW and wetting media, and various degree of pinning. The model predicts up to 50% higher breakthrough pressure when 20% of the meniscus perimeter is pinned, for the MNW medium when compared to the wetting (non-coated) counterpart, results being supported by recent experimental studies.

Introduction

Optimal function of two-phase flow applications depends upon effective fluid management in small passages in which capillary forces act as one of the dominant mechanisms. This type of micro-scale scale system is present in PEM Fuel Cells which require a delicate balance between water production and removal such that the Proton Exchange Membrane is hydrated while the reactant gas is allowed to pass through the

Gas Diffusion Layer (GDL). The operation of the fuel cell can be hindered when a phenomenon referred to as flooding occurs, i.e. when the bipolar plate channels become completely filled with water. This is typically preceded by water accumulation in the GDL, which suggests the need for optimized channels and porous electrodes.

There has been a significant number of studies concerning the characterization and optimization of the bipolar plate channels and of the GDL[3,4,5]. The GDL is a porous medium consisting of carbon fibers and a non-wetting polymer (e.g. PTFE or Nafion) which are assembled into a porous matrix. Liquid water and gas transport through the medium depends on the characteristics of the pores as well as its thermal and electrical properties. At lower temperatures the capillary forces are the driving mechanism, while at higher temperatures both capillary and phase change induced transport occurs.

Continuing previous work aiming to develop design approaches for effective water management in PEM fuel cells, in this study we examine one aspect of the capillary transport through the GDL: the breakthrough pressure of water through multiple fiber-defined pores. The droplets forming through the pores have pinned (non-deforming) and free (deforming) sides, as in the case of non-wetting fibers with coating defects (the Mixed Non-Wetting case, MNW, e.g. PTFE coated). The Laplace pressure across the gas-liquid interface is calculated as a function of the droplet volume. The breakthrough pressure is determined for pores with pinned sides, and for pores with alternating pinned and free sides. These pinning conditions correspond to wetting pores, as well as MNW pores, as usually encountered in GDLs.

Mortazavi and Tajiri[7] examined experimentally the breakthrough of water through uncoated, as well as PTFE and Nafion-coated GDL. They found that the breakthrough pressure is significantly larger for the PTFE-coated versus the uncoated GDL, while for the Nafion-coated the breakthrough pressure was smaller hypothetically explained by a change in wetting properties from non-wetting to wetting. The water wetting behavior of Nafion coated GDL fibers warrants further experimental investigation, considering the wetting hysteresis from wetting in the receding mode to non-wetting in the advancing mode[9].

The stability of liquid droplets on fibers was found to be a function of fiber diameter, droplet volume, and wetting properties (contact angle)[8].

Background and Computational Model

Within the broad scope of micro-technology development an effective approach is to model capillary gas-liquid interfaces in complex geometries and under varied wetting conditions. Using this method we previously predicted liquid holdup through characterization of static plug morphology in square channels of mixed wettability, as the bipolar plate channels are, i.e. differing contact angles on the GDL side and on the bipolar plate walls[6]. We also showed that water can be passively removed from the GDL side of the channel if the bipolar plate walls are made more wetting. In this study we explore the breakthrough and stability behavior of droplets emerging through pores. An energy minimization technique is used via the Surface Evolver (SE) program by Kenn Brakke[1,2].

A pore model is programmed in Surface Evolver to investigate the pressure-volume dependence for a number of pore geometries and contact line pinning configurations along the edge. The pore has a small diameter such that gravity is neglected with respect to surface energy, therefore being considered to be a zero Bond number system ($Bo = \rho g l^2/\sigma$) dominated by capillary forces. Inertia is neglected and the breakthrough pressure

is found from the relation between the volume and pressure, calculated during quasi-steady simulations.

The physical process can be understood if we consider the circular pore geometry. As the fluid is forced through the orifice, the pressure jump across the interface is given by the Young-Laplace equation $\Delta P = \sigma\ (1/R_1 + 1/R_2)$, where σ is the surface tension and R_1, R_2 are the principal radii of curvature of the gas-liquid interface. For the circular geometry the interface is a spherical surface in the absence of gravity and $R_1 = R_2$ is the sphere radius. The pressure increases as the droplet of volume V is being formed reaching a maximum at a certain point defined by the breakthrough pressure P* and the corresponding volume V*. This point marks a bifurcation, if the pressure is further increased there are no stable solutions.

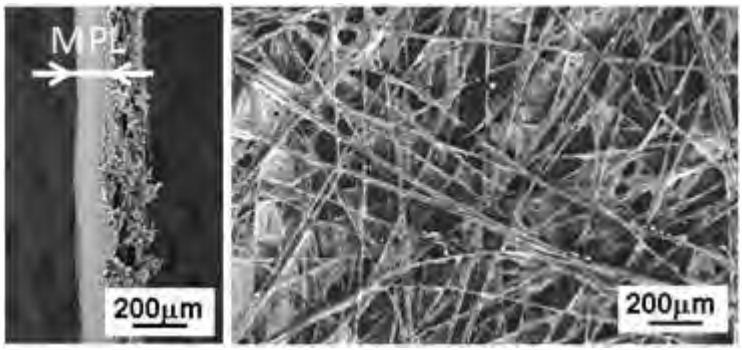

Figure 1. A typical GDL displaying a variety of pores having wetting, non-wetting, or mixed-wetting edges.

A typical non-woven GDL is shown in Figure 1, pores of different sizes having varying number of edges which can be wetting and non-wetting are visible. We are interested in determining the pressure across the gas-liquid interface as the liquid protrudes through pores of varying geometry and wetting/ pinning conditions that mimic the types of pores found in the GDL. The model is set in Surface Evolver as an initial planar surface bound by the edge of the pore as in Figure 3. The octagonal geometry shown represents a mixed non-wetting pore (MNW), the contact line is pinned to the short edges and let free to evolve within the orifice's plane on the remaining edges. The surface consisting of a union of triangles is then evolved towards the minimum energy configuration using a gradient descent method, the free surface energy is minimized under a fixed volume constraint while the edges of the droplet are attached to the pore edges or let free within its plane depending on the case under investigation. Three cases are considered: a circular pore with pinned edge, a square pore with pinned edges and an octagonal pore with alternating pinned and free edges as in Figures 2 and 3.

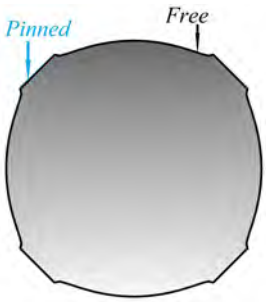

Figure 2. Mixed Non-Wetting Pore, a droplet forming through the pore has pinned and free deforming edges.

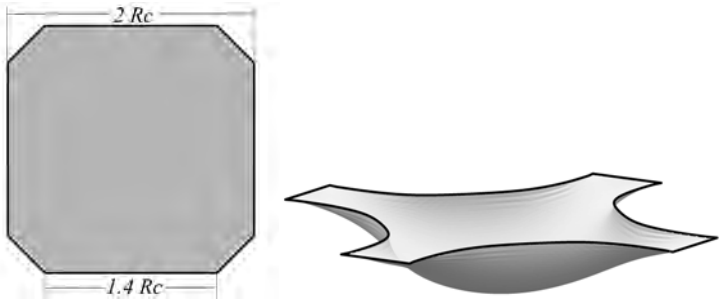

(a) (b)

Figure 3. Pore 2-D Geometry. (a) Initial SE Model: the oblique sides are pinned while the other sides are free to deform within the pore plane, (b) The Minimum Energy Surface of a Droplet of Volume $\widetilde{V}$ = 0.481, evolved from the initial model. The pinned sides are unchanged while the free sides bend under the action of capillary forces.

The simulation is run with non-dimensional parameters $\widetilde{\sigma}=1$ and $\widetilde{R}=1$, the surface tension and pore radius, respectively. The problem is non-dimensionalized as follows:

$$\widetilde{x} = xA^{1/3} \quad [1]$$

$$\widetilde{V} = VA^{-3/2} \quad [2]$$

$$\Delta\widetilde{P} = \frac{\Delta P A^{1/2}}{\sigma} \quad [3]$$

,where the non-dimensional length scale, volume and pressure are $\widetilde{x}$, $\widetilde{V}$, and $\Delta\widetilde{P}$, respectively.

We vary the volume $\widetilde{V}$ beginning with small values and calculate the corresponding pressure for each converged interface solution. In this way the pressure-volume dependence is determined, which leads to the maximum breakthrough pressure values for each pore geometry considered. For the purpose of comparison pores having the same area as a circular pore of radius $\widetilde{R}=1$ are analyzed.

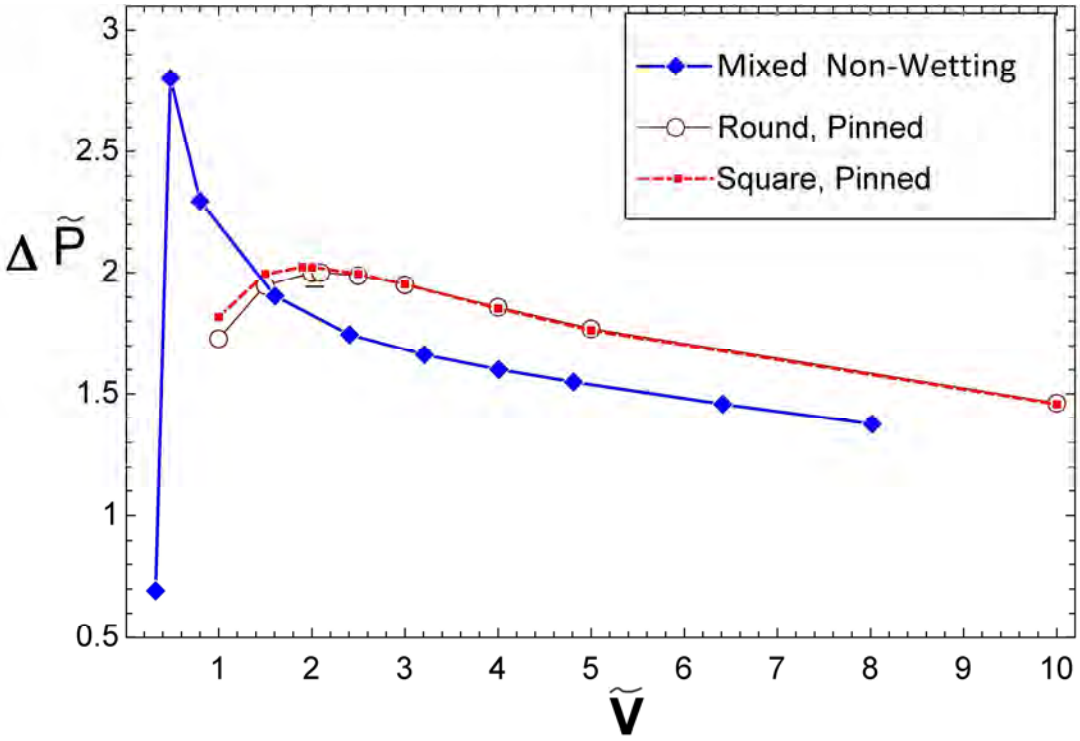

Figure 4. Pressure-volume dependence for a drop breaking through a pore.

Pore Breakthrough Analysis

The code is validated by comparing the breakthrough pressure corresponding to the critical volume, to the theoretical value. The volume is that of a hemisphere with R = 1, V* = 2.094 and the corresponding breakthrough pressure can be calculated using the Young-Laplace equation as P* = 2. Using the SE pore model the breakthrough pressure is calculated to be P* = 2.001.

We simulate gas-liquid interfaces formed at circular and square pores having the contact line pinned along the edges, as well as octagonal pores with alternating free and pinned sides as in Figure 3. All pore geometries have the same area of a circular pore of radius $\widetilde{R} = 1$ and gravity and inertia of are neglected. The Laplace pressure across the interface is plotted as a function of volume in Figure 4. As the volume increases the pressure follows the same trend until a maximum is reached, corresponding to the breakthrough volume V*. With a further increase in volume, the pressure decreases and no stable solutions are possible. The converged interface solutions for a mixed non-wetting pore are shown for three prescribed droplet volumes in Figure 5. Note the change in curvature of the non-wetting (free) edges as the surface energy is minimized.

The breakthrough volume and pressure are determined for the considered pore configurations and are presented in Table I. The octagonal pore requires the largest breakthrough pressure P* = 2.8024 when a volume V* = 0.4809 is reached, beyond this point the pressure decreases if the volume is further increased as seen in Figure 4. Notably approximately 40% larger pressure is required to displace the liquid through the

mixed non-wetting octagonal pore, when compared to the wetting round and square pores. For volumes up to $\widetilde{V}$ = 2.2 a larger pressure is required to displace the same liquid volume through the square pore than through the round. For wetting square and round pores the maximum breakthrough pressure does not differ significantly and it occurs around a volume $\widetilde{V}$ = 2 with a decreasing trend thereafter.

TABLE I. Breakthrough Pressure and Volume for Pore Liquid Protrusion. Geometry and Wetting Types are Varied.

Geometry/ Wetting Type	V^*	P^*
Circular/ Wetting	2.094	2.001
Square/ Wetting	1.9	2.023
Octagonal/ Mixed Non-Wetting	0.4809	2.8024

(a) (b) (c)

Figure 5. Gas-liquid interface evolution in octagonal mixed non-wetting pores, shown as the droplet volume increases: (a) $\widetilde{V}$ = 0.481, (b) $\widetilde{V}$ = 3.206, (c) $\widetilde{V}$ = 4.809. The short edges are pinned while the long edges deform freely in the plane of the orifice having only the end points pinned.

The simulations show that the liquid protrusion process depends on both the geometry and the pinning of the contact line as found in both wetting, and MNW cases. The gas liquid-interface morphology differs between the pore types considered, this fact being reflected in the Laplace pressure variation with changes in volume. Furthermore, the maximum breakthrough pressure differs significantly for the mixed non-wetting pores being higher than for the wetting pores. This implies that the liquid water will pass through a wetting pore and not through a mixed non-wetting pore having the same area. Note that the different view this study brings in comparison with previous studies is that the pore is considered to be a perimeter formed with segments which are the fibers of the medium, and not capillary tubes with varying contact angles. A contact angle is not set in this model, any contact angle can be attained at the fiber contact line. The wettability and pinning effects are captured through the behavior of the contact line in contact with the fibers, which is pinned on the wetting fibers or defects, but it can easily glide and deform on the non-wetting fibers. Fingers can then form as the fluid passes through a pore and moves to the next as it makes contact with the subsequent fiber perimeter.

Discussion

The key results found using the mixed non-wetting pore model are:

1. The breakthrough pressure of water through the pores of a GDL is a function of contact line pinning,
2. The breakthrough pressure through the mixed non-wetting pore considered is 40% larger then through the wetting counterpart, confirmed by the experiments of Mortazavi and Tajiri[7].

The direct implication regarding water management in the GDL is that the in-homogeneity of the non-wetting coating (PTFE) itself can be used to change the breakthrough pressure. The MNW pore considered was 23% pinned, which resulted in a 40% increase in the breakthrough pressure. The high breakthrough pressure is critical to finger formation, therefore to water removal while maintaining reactant access when operating close to the stable displacement regime.

From a surface energy perspective, droplets on fibers are present in two morphologies[8], barrel and clamshell. The available water droplet volumes, the fiber diameter and the contact angle dictate which morphology is favored. At high contact angles, as in the case of non-wetting fibers, lower volume droplets will adopt a clamshell morphology which is beneficial for water removal, due to low adhesion forces which establish a "droplet gliding" along the fibers mechanism.

The two key GDL design elements are therefore:

1. The (high) breakthrough pressure,
2. The (small) droplet volume at breakthrough.

Conclusion

The mixed non-wetting pore model considered in this study shows that the breakthrough pressure is a function of contact line pinning. Therefore, the coating defects, the inhomogeneity of the GDL coating, have direct implications on water management by changing the breakthrough pressure. The MNW droplet considered is 23% pinned along the pore perimeter and presents a breakthrough pressure 40% higher than the wetting (100% pinned) droplet. Moreover, the MNW droplet volume at breakthrough is only 23% of that of the wetting counterpart.

The model can be used to improve water management in the GDL by maximizing the breakthrough pressure while minimizing the droplet volume at breakthrough. These calculations have to account as well for a favorable drop-on-fiber morphology which promotes water removal, i.e. the clamshell morphology in the case of non-wetting fibers.

Acknowledgments

I dedicate this work to my daughters Mara and Ilinca.

References

1. K. Brakke., *Surface Evolver*, Ver. 2.14, (2003).
2. K. Brakke, *Experimental Mathematics,* **1**(2):141, (1992).
3. A. Bazylak, *International Journal of Hydrogen Energy*, **34**(9):3845, (2009).
4. S. Park, et. al., *Int. Journal of Hydrogen Energy*, **37**:5850, (2012).
5. J. Lee, et. al., *Electrochimica Acta*, **236**: 161-170, (2017).
6. A. Herescu, J. Allen, *Journal of Power Sources*, **216**: 337-344, (2012).
7. M. Mortazavi, K. Tajiri, *International Journal of Hydrogen Energy*, **39**(2014).
8. H.B. Eral, F. Mugele, Et. Al., *Soft Matter*, **7** (2011).
9. S. Goswami, S. Klaus, J. Benziger, *Langmuir*, **24** (2008).

ECS Transactions, 104 (8) 109-114 (2021)
10.1149/10408.0109ecst ©The Electrochemical Society

Rapid freezing and Cryo CT Imaging of Liquid Water inside PEFCs

Hiroshi Naito, Yuki Tsubai, Katsuyuki Kawamura,
Takashi Sasabe and Shuichiro Hirai

Department of Mechanical Engineering, Tokyo Institute of Technology,
Tokyo 152-8550, Japan

A cryo CT imaging to observe fixed three-dimensional liquid water structure of PEFC was developed. An operating at 40 ℃ cell temperature and 80 % gas relative humidity was instantaneously frozen, and the CT imaging was performed in low humidity and low temperature gas to prevent condensation from adhering to the MEA. The results of GDL visualization showed that the liquid water in the GDL was connected between the pores and formed a large structure. Moreover, it was found that, from the calculation of effective pore diameter, liquid water mainly accumulates in pores having 7 μm to 16 μm pore diameter. A numerical simulation of oxygen diffusion was also performed to investigate the influence of liquid water accumulation on the oxygen transport to the catalyst layer. The result of computation showed that liquid water accumulation clearly decreased the oxygen concentration inside the catalyst layer just below it.

Introduction

Polymer electrolyte fuel cells (PEFCs) has attracted attention because of the higher energy efficiency and the lower environmental load. Toward the wider use of PEFCs, research and development are being conducted to improve the cell performances. One of factors that degrades the cell performance is liquid water accumulation inside PEFCs. PEFCs generate water by the electrochemical reactions. Some of the generated water condenses and accumulates inside PEFCs. The gas diffusivity of the stagnant liquid water is extremely small, and it prevents the gas transport, resulting in a decrease in the cell performance. In order to mitigate this problem, it is first necessary to understand the phenomena of liquid water formation and accumulation accurately. For this reason, research on visualization of liquid water behavior inside PEFCs has been conducted. Among several visualization methods, X-ray visualization with micron scale spatial resolution is a suitable method which enables to observe liquid water structure between substrates of gas diffusion layer (GDL) (1). Methods of X-ray visualization fall into X-ray radiography (1-10) and computed tomography (CT) imaging (11-13). X-ray radiography is a technique that obtains transmitting image from one direction, and allows relatively short time imaging interval (9). The obtained images, however, shows the attenuation of X-ray through the all transmitting path, and only provide spatially averaged information. CT imaging, on the other hand, is a technique that obtains three-dimensional structure by reconstructing multiple images taken from multiple directions. Three-dimensional structure inside PEFCs can be observed, but, due to large number of images taken, it takes relatively long imaging time. Since liquid water inside PEFCs exhibits unsteady behavior

including repeated accumulation and discharge, uncertainty in handling unsteadiness still remains. Considering these, we developed cryo CT imaging that freezes PEFC instantly and conduct imaging while keeping liquid water structure fixed. High-resolution three-dimensional visualization of the liquid water structure without the effect of unsteadiness was performed, and analysis on the correlation between the pore structure and liquid water accumulation was performed.

Experimental

In this study, membrane electrode assembly (MEA) was instantly frozen, and CT imaging was performed in extremely low partial vapor pressure (low-temperature and low-humidity) condition to prevent condensation of water vapor in atmosphere. Taking into account the heat transfer efficiency, a small size cell having 0.03 cm^2 (0.1 cm in the transmission direction and 0.3 cm in the perpendicular direction) was used (Fig. 1). The rib/channel widths of flow field are 0.5 cm each. SIGRACET® 24BC (SGL Carbon) was used for GDL. The GDL compression level is defined by the thickness of hard type gasket. In this experiment, 235 μm thickness is compressed to 188 μm.The procedure of cryo CT imaging is as follows.

1. Removing the cell operating in thermostatic cell, and freezing instantaneously by immersing the operating cell directly in liquid nitrogen (Gas flow was stopped immediately after confirming that the operation had stopped due to the instantaneous freezing).

2. Disassembly of the cell in a glove box filled with a gas with a dew point of -196 ℃ and a temperature of -20 ℃, removal of the MEA, and mounting on a chamber for cryo CT imaging.

3. Mounting of the chamber to a X-ray CT microscope and CT imaging in dry nitrogen gas cooled to about -50 ℃ by dry ice.

The chamber for imaging is composed of three layers: dry and low temperature nitrogen gas inlet part, outlet part and heat-insulting part (Fig. 2). During the imaging, the chamber surface was continuously blown with dry air to prevent frost adhering to the chamber. The imaging was performed with 1.08 $\boldsymbol{\mu m}$ ×1.08 $\boldsymbol{\mu m}$ resolution. The cell temperature was set to 40 ℃, the anode (H_2) / cathode (air) gas pressure was set to 101 kPa, and the relative humidity was set to 80 %. In the image analysis, the catalyst layer (CL), microporous layer (MPL), and substrate part were identified from the CT values, and the structure of the ice part was extracted from the difference between the CT images of the MEA with ice (wet case) and the dry MEA (dry case).

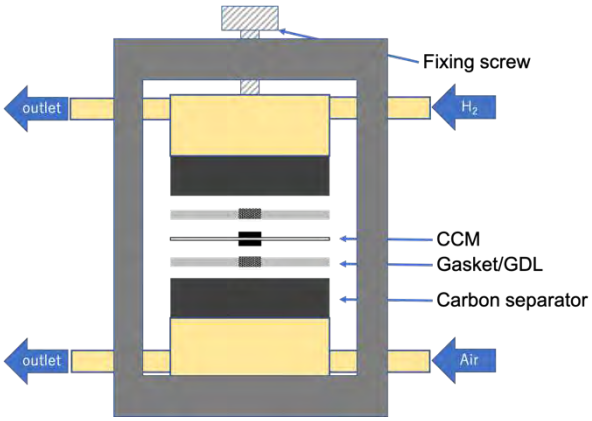

Fig.1 Schematic of fuel cell.

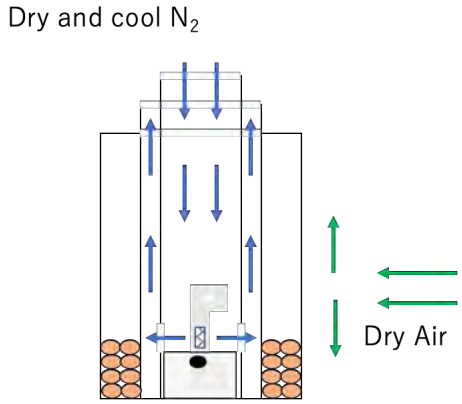

Fig.2 Schematic of chamber for cryo CT imaging

Results

Especially in the high concentration overpotential operation, the liquid water accumulation is considered to have a significant influence on the cell performance. In this study, cryo CT imaging of 0.1 V and 1.7 A/cm^2 case, which shows high concentration overpotential was attempted. The following results of visualization focused on 1 mm × 1 mm region shown in Fig. 4.

Figure 5 shows only the liquid water portion extracted. It can be seen that the accumulated liquid water does not exist dispersedly, but is connected between the pores of the substrates and forms large structures. Figure 6 shows the percentage of area occupied by liquid water at each position in the thickness direction. It can be seen that liquid water is small near the rib and increases in the area near the micro porous layer (MPL). The effective pore diameter, which is the diameter of the largest sphere in contact with the substrate, was calculated and compared between the dry and wet cases. Figure 7 shows the volume fraction of pores belonging to each effective pore diameter. The volume of pores having 7 μm to 16 μm is reduced in the wet case, which indicates that liquid water accumulates in the spaces belonging to this pore diameter range. On the other hand, accumulation of liquid water causes an increase of pore volumes with pore diameter below 7 μm. The effective liquid water diameter was calculated in the same way as effective pore diameter. Figure 8 shows the mean liquid water diameter at each position in the thickness direction. It can be seen that the liquid water diameter increases on the side closer to the MPL same as the volume percentage shown in Fig. 6.

Numerical simulation of oxygen transport was performed to investigate the effects of liquid water accumulation on the gas transport. The computation of the following diffusion equation,

$$\frac{\partial C_{O_2}}{\partial t} = \nabla \cdot \left(D \nabla C_{O_2}\right) + q, \qquad [1]$$

was carried out until the steady state was reached, where q is oxygen consumption per unit time. Second-order central difference was used, and the grid number is $N_x \times N_y \times N_z = 256 \times 96 \times 256$.

The effect of the presence of liquid water on the oxygen transport was investigated by comparing the wet and dry cases. The difference of O_2 concentration in the catalyst layer between the dry case and the wet case (dry case minus wet case) is shown in Figs. 9(a) and 9(b). It is clear from Fig. 9(a) that the oxygen concentration decreases in the area just below where the liquid water accumulates. In particular, a large decrease can be seen in the area where a lot of liquid water accumulates near the catalyst layer (Figure 9(b)). This indicates that the liquid water in the GDL prevents the transport of oxygen to the catalyst layer directly below it.

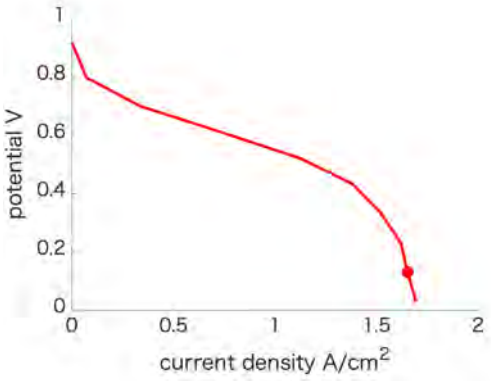

Fig.3 i-V performance curve.

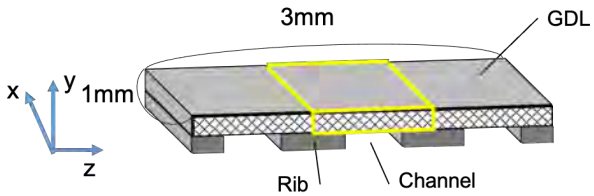

Fig.4 Schematic of visualized part.

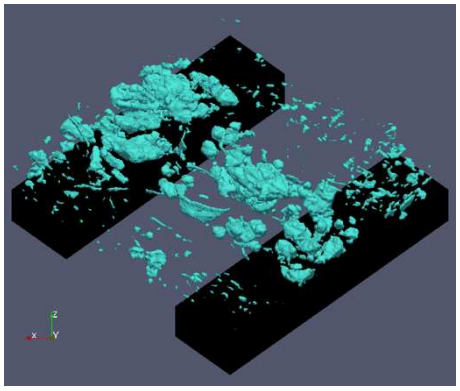

Fig.5 Liquid water distribution.

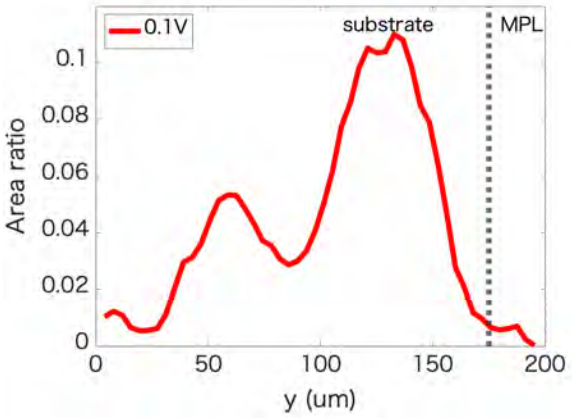

Fig.6 Liquid water profile.

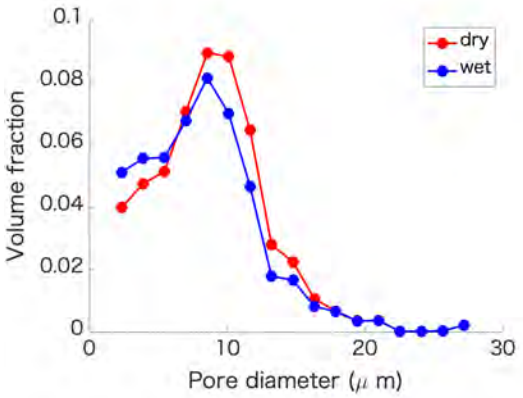

Fig.7 Volume fraction at each pore diameter

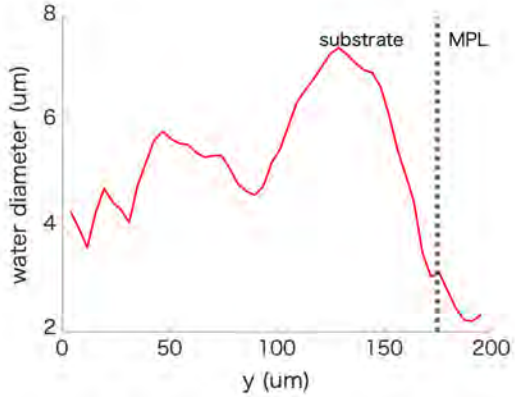

Fig.8 Mean water diameter profile.

(a) (b)

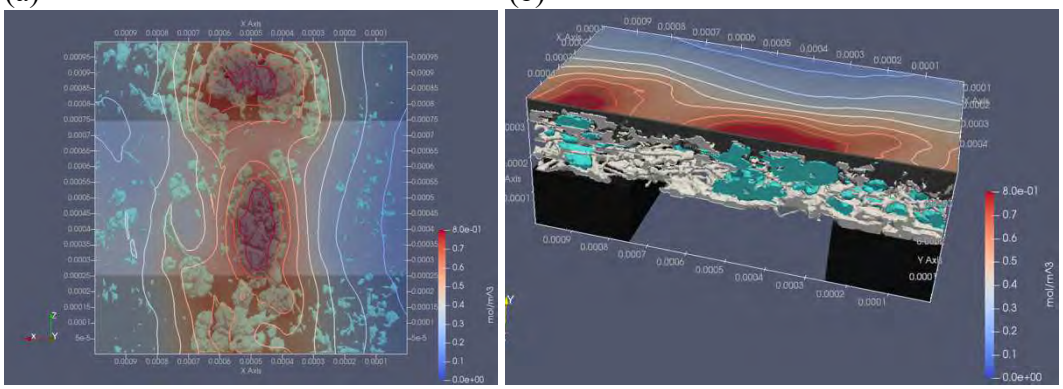

Fig.9 O_2 loss due to liquid water accumulation, $O_{2,\mathrm{dry}} - O_{2,\mathrm{wet}}$: (a) top view, (b) cross sectional view.

Summary

A cryo CT imaging technique was developed to observe the fixed liquid water structure three dimensionally by instant freezing an operating PEFC. The liquid water structure obtained from the imaging was connected between each pore to make a large structure. The distribution of liquid water was found to be less on the rib side and increased near the substrate/MPL boundary. From the calculation of the effective pore diameter distribution, it was found that the liquid water mainly accumulated in the area with the effective pore diameter range of 7 μm to 16 μm. From the simulation of gas transport, it was confirmed that the accumulation of liquid water prevents the transport of oxygen to the catalyst layer directly below it.

Acknowledgments

References

1. C. Hartnig, I. Manke, R. Kuhn, S. Kleinau, J. Goebbels, and J. Banhart, *J. Power Sources*, **188**, 468 (2009).
2. I. Manke, Ch. Hartnig, M. Grünerbel, W. Lehnert, N.Kardjilov, A. Haibel, A. Hilger, J. Banhart and H. Riesemeier, *Appl. Phys. Lett.*, **90**, 174105 (2007.)
3. T. Mukaide, S. Mogi, J. Yamamoto, A. Morita, S. Koji, K. Takada, K. Uesugi, K. Kajiwara, and T. Noma, *J. Synchrotron Radiat.*, **15**, 329 (2008).
4. T. sasabe, S. Tsushima, and S. Hirai, *Int. J. Hydrogen Energy*, **35**, 1119 (2010).
5. T. Sasabe, P. Deevahnhxay, S. Tsushima, and S. Hirai, *J. Power Sources*, **196**, 8197 (2011).
6. T. sasabe, P. Deevahnhxay, S. Tsushima, and S. Hirai, *Electrochem. Commun.*, **13**, 638, (2011).

7. P. Deevanxay, T. Sasabe, S. Tsushima, and S. Hirai, *J. Power Sources*, **230**, 38, (2013).
8. H. Markötter, I. Manke, Ph. Krüger, T. Arlt, T. Haussmann, M. Klages, H. Riesemeier, Ch. Hartnig, J. Scholta, and J. Banhart, *Electrochem. Commun.*, **13** 1001 (2011).
9. R. Banerjee, N. Ge, J. Lee, G. George, S. Chevalier, H. Liu, P. Shrestha, D. Muirhead, and A. Bazylak, *J. Electrochem. Soc.*, **164**, F154 (2017).
10. F. Akitomo, T. Sasabe, T. Toshida, H. Naito, and S. Hirai, *J. Power Sources*, **431**, 205 (2019).
11. H. Markötter, I. Manke, Ph. Krüger, T. Arlt, J. Hauussmann, M. Klages, H. Riesemeier, Ch. Hartnig, J. Scholta and J. Banhart, *Electrochem. Commun.*, **13**, 1001 (2011).
12. Y. Nagai, J. Eller, T. Hatanaka, S. Yamaguchi, S. Kato, A. Kato, F. Marone, H. Xu, and N. F. Büchi, *J. Power Sources*, **435**, 226809 (2019).
13. J. Eller, J. Roth, F. Marone, M. Stampanoni, and N. F. Büchi, *J. Electrochem. Soc.*, **164,** F115 (2017).

Chapter 4

12 MPL & Imaging Methods

ECS Transactions, 104 (8) 117-127 (2021)
10.1149/10408.0117ecst ©The Electrochemical Society

Hydrophilic and Hydrophobic Microporous Layer Coated Gas Diffusion Layer for Enhancing PEFC Performance

P. Wang[a], H. Nakajima[b], and T. Kitahara[b]

[a] Graduate School of Engineering, Kyushu University, 744 Motooka, Nishi-ku, Fukuoka 819-0395, Japan
[b] Department of Mechanical Engineering, Kyushu University, 744 Motooka, Nishi-ku, Fukuoka 819-0395, Japan

The hydrophobic microporous layer (MPL) coated gas diffusion layers (GDLs) have been commonly used to improve water management properties of polymer electrolyte fuel cells (PEFCs). An MPL coated GDL designed to prevent dehydration of the membrane electrode assembly (MEA) under low humidity conditions is generally inferior at reducing flooding under high humidity conditions. Thus, developing an MPL coated GDL to enhance the PEFC performance under low and high humidity conditions is crucial. One method to overcome the defects of pure hydrophobic MPL is to make double and triple MPLs, in which a thin hydrophilic layer is coated on the hydrophobic MPL. Another method is a hydrophobic MPL containing hydrophilic carbon nanotubes (CNTs). Both methods effectively conserve membrane humidity and reduce flooding under high humidity conditions.

Introduction

The polymer electrolyte fuel cell (PEFC), which uses hydrogen fuel directly and efficiently to generate electrical energy with water as the only byproduct, can reduce energy use, pollutant emissions, and dependence on fossil fuel (1). Water management is focused on as the main problem of fuel cell performance improvement. Under low humidity conditions, due to the low proton conductivity caused by membrane dehydration, the PEFC shows inferior performance. Under high humidity conditions, too much water cannot be expelled, which causes insufficient oxygen supply to the catalyst layer. Several investigations have demonstrated that a hydrophobic microporous layer (MPL) coated on a GDL substrate can effectively improve the water management characteristics, enhancing the PEFC performance (2). However, the appropriate design parameters for the MPL coated GDL are different under low and high humidity conditions. An MPL coated GDL designed to prevent dehydration of the membrane electrode assembly (MEA) under low humidity conditions is generally inferior at reducing flooding under high humidity conditions. Thus, developing an MPL coated GDL to enhance the PEFC performance under low and high humidity conditions is essential.

Although the hydrophobic MPL coated GDLs have been commonly used to improve the water management properties of PEFCs, some studies have reported that the hydrophilic MPLs are effective in improving the water management properties of PEFCs (3)-(5). To further improve PEFC performance under high humidity conditions, studies about multiple MPLs and an MPL with hydrophilic CNTs were undertaken (6)-(8).

Additionally, the laser was applied to modify the MPLs areal hydrophilicity, enhancing the performance (9),(10). Moreover, a new method was alternatively arrayed hydrophilic and hydrophobic rows in the in-plane direction to obtain better performance (11).

This study is conducted to evaluate an appropriate hydrophilic, and hydrophobic composite MPL is undertaken. One design is making a hydrophilic layer coated on the hydrophobic MPL. Another design is a hydrophobic MPL containing hydrophilic CNTs. The oxygen transport resistance was assessed based on the limiting current density value of polarization curves to evaluate the ability of the MPL to reduce flooding under high humidity conditions.

Experiments

MPL coated GDLs

The GDL substrate was a carbon paper (SGL SIGRACET® 24BA) loaded with 5 mass% PTFE to impart hydrophobicity. The thickness of the GDL substrate is 190μm, and the areal weight is 54g m^{-2} and 84% porosity. The slurry containing PTFE dispersion liquid, distilled water, carbon black, and a surface-active agent was mixed by an impeller blade-type mixer, then was coated on the substrate by a bar coating machine. The MPL was dried in an oven and then heated at 350°C to remove any remaining solvent and surfactant, sintering PTFE and carbon black onto the substrate. For double MPLs, the PTFE content in the first layer was set to 20 mass%, then a hydrophilic MPL composed of 25 mass% titanium dioxide (T_iO_2), 5 mass% silicon, and carbon black was coated as a top layer with a thickness of 5μm. For triple MPLs coated GDL, the MPL contained PTFE 10 mass% was coated on the substrate as the first layer, and the MPL with PTFE 20 mass% was set as the second layer. Finally, a hydrophilic MPL, with the same ingredients as double MPL, was coated on the previous hydrophobic MPLs to generate triple MPLs, as shown in Figure 1.

Except for the multiple MPL coated GDL, adding the hydrophilic CNTs to the hydrophobic MPL is another method. The MPL coated GDL containing CNTs consisted of a GDL substrate (SGL24BA) coated with an MPL made from 4 mass% CNTs, 76 mass% carbon black, and PTFE. The CNTs were 10-15 nm in diameter and had a length of 1-5 μm. The CNTs got surface modification via an oxidation treatment before utilization, creating functional groups. As a result, the contact angle of a CNT sheet was 30°, demonstrating that the CNT surfaces exhibited relatively high hydrophilicity.

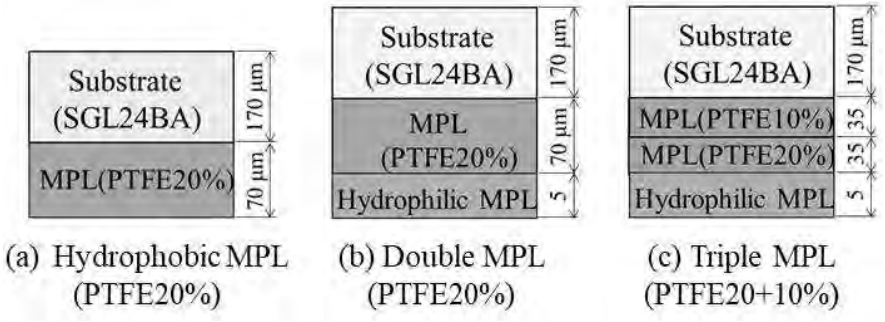

Figure 1. Hydrophobic MPL, double MPL, and triple MPL coated GDLs were used at the cathode.

Air and Water Vapor Permeability, Pore Diameter and Contact angle Measurements

Figure 2. shows the schematic diagram of the test apparatus used to measure the air permeability of the GDL. The GDL sample with a diameter of 13mm is set between cylinder plates and sealed by an o-ring. The compression pressure was imposed on the plates with 1MPa using a clamp screw to intimate the same pressure in typical PEFC. The supplied air pressure was set to 1.23 kPa, which is the same as that used in the Gurley method (12). The air permeance q_a is defined as the flow rate divided by the supplied pressure and permeable cross-sectional area with a diameter of 5mm.

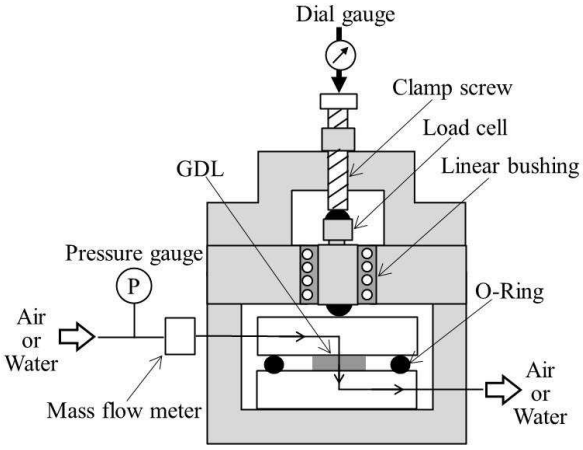

Figure 2. Schematic diagram of the air permeability test apparatus.

Relied on the ASTM (F316-86) standard test method, the maximum pore diameter d_{max} and mean pore diameter d_m of MPL coated GDL can be measured using the same apparatus shown in Figure 2. The tested sample is immersed in low surface tension liquid (γ=0.0159N m^{-1}) with a contact angle of 0° under vacuum conditions to fill out the pores. Supplying through-plane air flow rate to the saturated sample, when the liquid in the maximum pore was blown out, according to the relationship between pore diameter and liquid blew out the minimum supply air pressure, the maximum pore diameter can be calculated. Continually increasing air pressure, all the fluid in other pores will be gradually expelled, and the wet flow curve can be obtained. Meanwhile, the dry flow curve representing the relationship between air pressure and airflow rate can also be measured by applying a dry sample. The mean flow pore diameter is calculated using the mean flow pressure corresponding to the intersection point of the wet flow and half-dry flow curves.

$$d = -\frac{4\gamma\cos\theta}{P} \quad [1]$$

where d is the pore diameter, γ and θ are surface tension and contact angle of the wetting liquid, and P is the air pressure.

For measurement of the contact angle in the GDL pores, a water permeability test was conducted in the through-plane direction of the GDL using the same apparatus shown in Figure 2. When the water began to flow through the largest pores of the GDL, the minimum water-supplied pressure was defined as the water breakthrough pressure, P_w. Meantime,

assuming that the maximum pore diameter in the water permeability test was equal to that obtained from the air permeability test. The contact angle in the largest pores of the GDL could be calculated from Eq. [1]. The surface tension of water at 25 °C was set as 0.0720 N m^{-1}.

The water vapor permeance test apparatus is shown in Figure 3. The MPL coated GDL was sandwiched between two stainless steel plates with a flow channel that was 1 mm wide, 20 mm long, and 1 mm deep. Dry air and water were supplied to the upper flow channel and lower flow channel, respectively. Water supply pressure was set at 5 kPa, which was lower than the water breakthrough pressure to prevent water from flowing through the GDL. The test was conducted under 25 °C, and the amount of water vapor transported through the GDL was obtained from relative humidity (RH) measurements of the inlet and outlet air. The water vapor permeance q_w is defined as the water vapor flow rate divided by the permeable cross-sectional area of the MPL coated GDL.

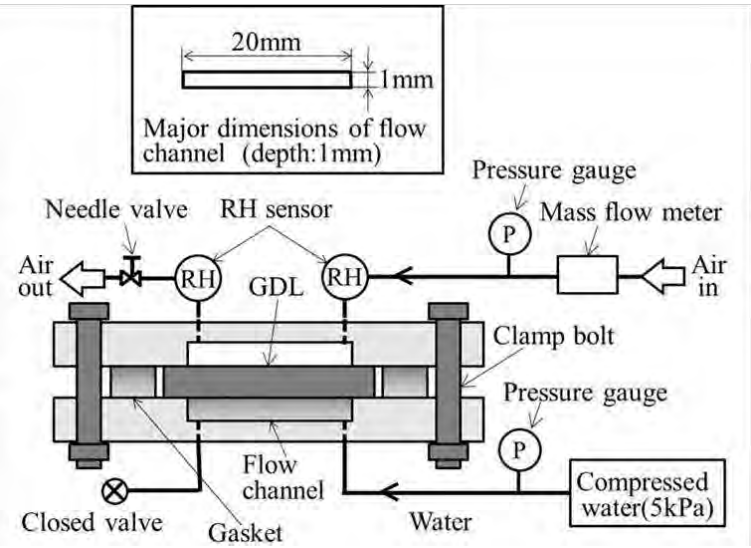

Figure 3. Schematic diagram of the water vapor permeance test apparatus.

Oxygen Transport Resistance as decide from Polarization Curves

To assessing the oxygen transport resistance of the MPL coated GDL, it is necessary to measure the limiting current density in polarization curves. During the tests, the commercial MEA (GORE PRIMEA® 5580) and MPL coated GDLs were clamped by separators and end plates with 3 Nm torque. The active area of the MEA was 1.0 cm^2. The cell temperature was kept at 35 °C by a cooling water system. Pure hydrogen and diluted oxygen (2 vol% O_2 and 98 vol% N_2) gases were supplied at the anode and cathode in a cross-flow orientation, respectively. Flow rates were set at 1000 cm^3 min^{-1}. The RH values of gases supplied to anode and cathode were varied between 50 and 200%, and the gases backpressure was set to zero. Figure 4. shows polarization curves obtained with the GDL substrate (SGL 24BA), hydrophobic MPL coated GDL, and triple MPL coated GDL. Based on the limiting current density values, the following equation was used to calculate the oxygen transport resistance (13),(14).

$$R_{O2} = \frac{4FP_{O2}}{RTi_{lim}} \quad [2]$$

where the i_{lim} is the limiting current density, F is the Faraday constant(96,485 C mol^{-1}), R is the gas constant (8.314 J (mol K)$^{-1}$), T is the absolute temperature of the cell, and P_{O2} is the average oxygen partial pressure in the inlet and outlet gases.

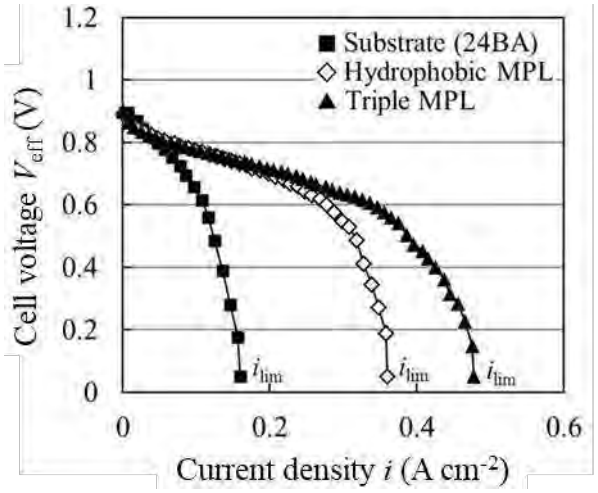

Figure 4. Polarization curves were obtained for SGL24BA, hydrophobic MPL, triple MPL coated GDLs under conditions of 200 % RH, a gas flow rate of 1000 cm^3 min$^{-1,}$ and a 35°C cell temperature.

Results and Discussion

Effect of the Multiple MPLs on the PEFC Performance

The surface scanning electron microscopy (SEM) micrographs of the SGL 24BA substrate and hydrophilic MPL in triple MPL are shown in Figure 5. The mean pore diameter d_m of the substrate was 42μm. The d_m of hydrophobic MPL in the double MPL and triple MPL is 3μm, the d_m of the hydrophilic MPL in the triple MPL was 2μm.

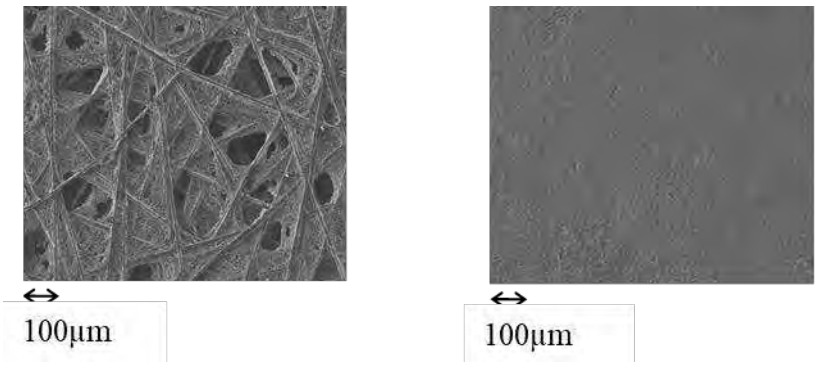

(a) GDL substrate (b) Hydrophilic MPL in triple MPL

Figure 5. Surface SEM micrographs of the substrate (SGL24BA) and the hydrophilic MPL in the triple MPL coated GDL.

Figure 6 summarizes the contact angles obtained with hydrophobic and hydrophilic MPLs. The contact angle value was 127° when the PTFE content in the hydrophobic MPL was 10%. With the PTFE content raised to 40%, the contact angle value also became larger. As for hydrophilic MPL, the contact angle was less than 90° and much lower than hydrophobic MPL, which represents strong hydrophilicity.

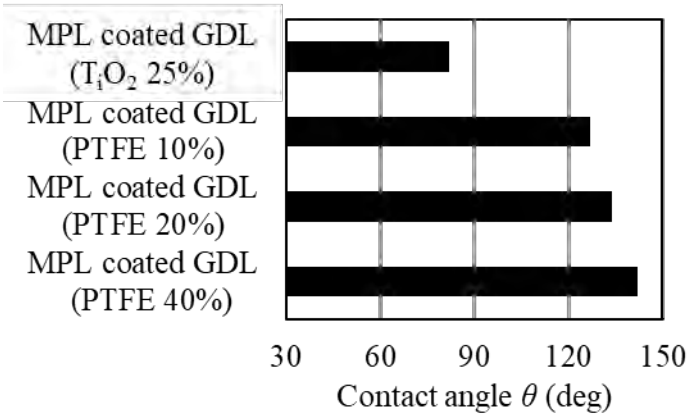

Figure 6. Contact angles of the hydrophobic and hydrophilic MPLs.

Figure 7 presents the influence of the RH value on the oxygen transport resistance, R_{O2}, obtained with the substrate, hydrophobic MPL, and double MPL. The R_{O2} among the three GDLs were similar values when the RH was less than 80%. Flooding occurred once relative humidity was higher than 80% RH and water occupied the pores in the substrate, so the R_{O2} suddenly increased but finally kept constant. However, for GDLs with MPL, the R_{O2} values are much lower than the substrate, so the MPL was proved effective at reducing flooding and guaranteeing oxygen transportation. Furthermore, the double MPL showed lower oxygen transport resistance than hydrophobic MPL.

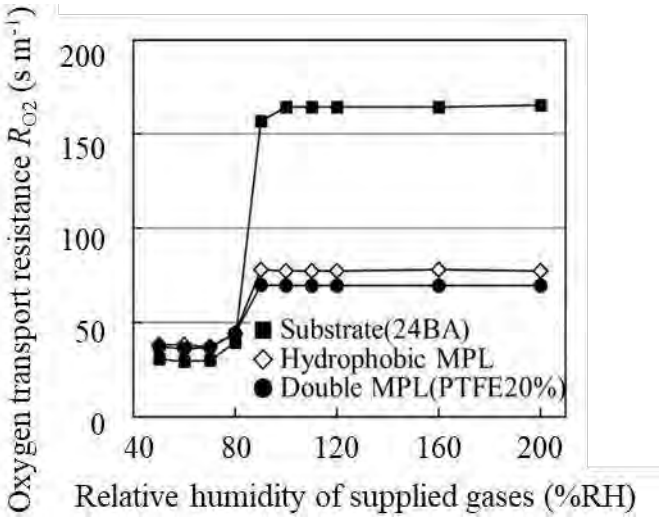

Figure 7. Variations in the oxygen transport resistance with increasing RH of the supplied gases at the anode and cathode for SGL24BA, hydrophobic MPL, and double MPL coated GDLs.

The water vapor permeance q_w obtained with hydrophobic MPL and double MPL are shown in Figure 8. The air velocity U is defined as the flow rate divided by the crosssection of the airflow channel. Generally, the q_w of both MPL coated GDLs increased with increasing air velocity. However, the increment was not significant when U increased to more than 8m s^{-1}. Under low air velocity, the water vapor permeance was relatively low, which indicated high water vapor transport resistance at the GDL/air interface. The water vapor permeance increased with faster air velocity, representing that the water vapor transport resistance at the GDL/air interface decreased. As for hydrophobic MPL coated GDL, the water was hard to be introduced into the tiny pores, which led to worse water vapor permeability. On the contrary, the hydrophilic layer on double MPL coated GDL can readily introduce water into the small pores, which resulted in higher water vapor permeance than that for the hydrophobic MPL. Therefore, a double MPL coated GDL with high water vapor permeability could effectively discharge excess water from the catalyst layer during PEFC operation under high humidity.

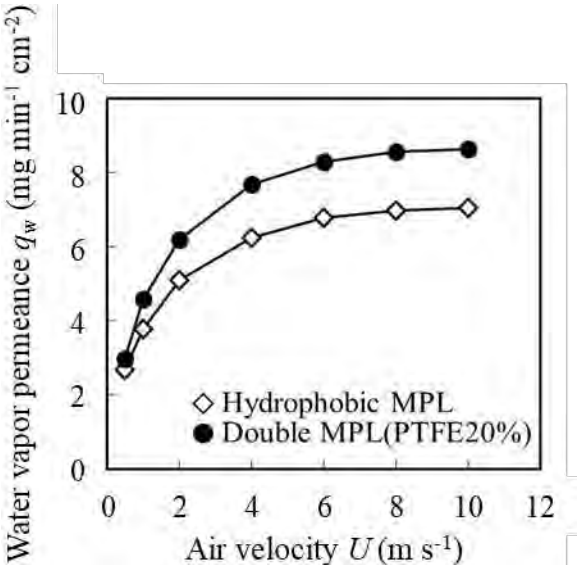

Figure 8. Variations in the water vapor permeance increased air velocity for the hydrophobic MPL, and the double MPL (PTFE: 20 mass%) coated GDLs.

Figure 9. demonstrates the details of the effect of the triple MPL coated GDL on the R_{O2}. Under 80% RH, the R_{O2} of the hydrophobic MPL, double MPL, and triple MPL were almost the same, about 38 s m^{-1}. From 90-200% RH, the R_{O2} of all the samples kept a constant value. The pure hydrophobic MPL indicated the highest R_{O2} value above double MPL and triple MPL. As for the double MPL, the R_{O2} was reduced to 70 s m^{-1} by introducing the hydrophilic layer. In the triple MPL coated GDL, the different PTFE content layers possessed a gradient of hydrophobicity, which helped expel excess water from the catalyst layer. This significantly reduced the R_{O2} to 58 s m^{-1}.

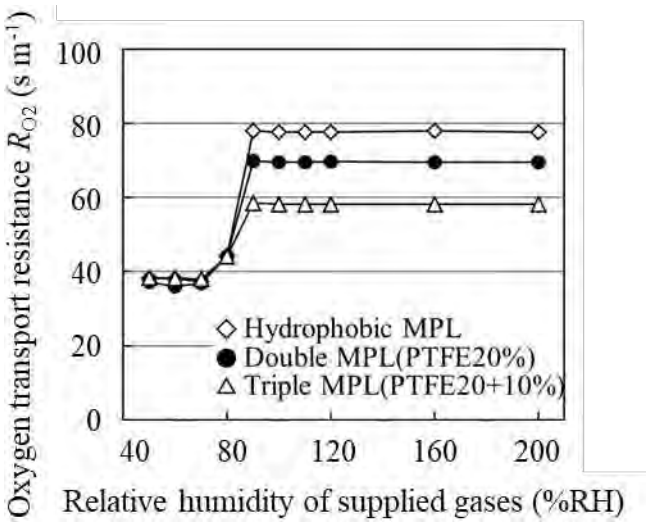

Figure 9. Effect of the triple MPL coated GDL on the oxygen transport resistance.

Effect of MPL containing hydrophilic CNTs on the PEFC Performance

Figure 10. shows the close-up micrographs of the MPL with and without CNTs. The CNTs were 10-15 nm in diameter and had a length of 1-5 μm.

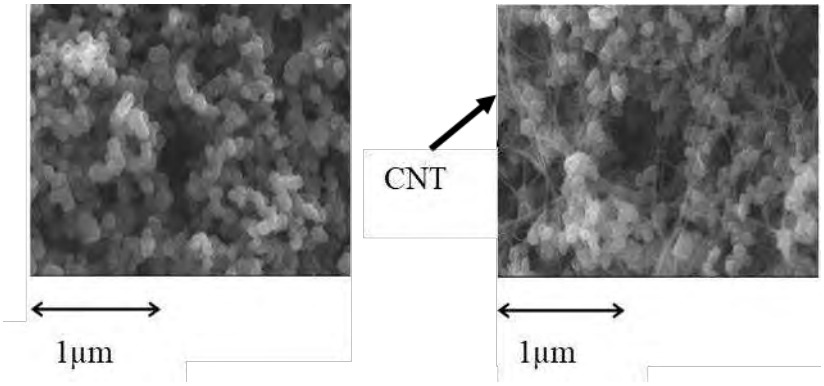

(a) MPL without CNTs (0%) (b) MPL with CNTs (4%)

Figure 10. Close-up surface SEM micrographs of MPLs with and without CNTs.

Figure 11 demonstrates the through-plane air permeance of the GDL substrate and MPL coated GDLs with and without CNTs. The largest permeance was shown by substrate (24BA) because it was without MPL and possessed a considerable pore size. Among the hydrophobic MPL coated GDLs, the air permeance gradually decreased with the decreasing d_m from 10 to 2 μm. As for MPL containing CNTs, it exhibited the same air permeance as the hydrophobic MPL with the same pore size, so pore size was the only factor to change the air permeance value, and the CNTs did not influence the air permeance.

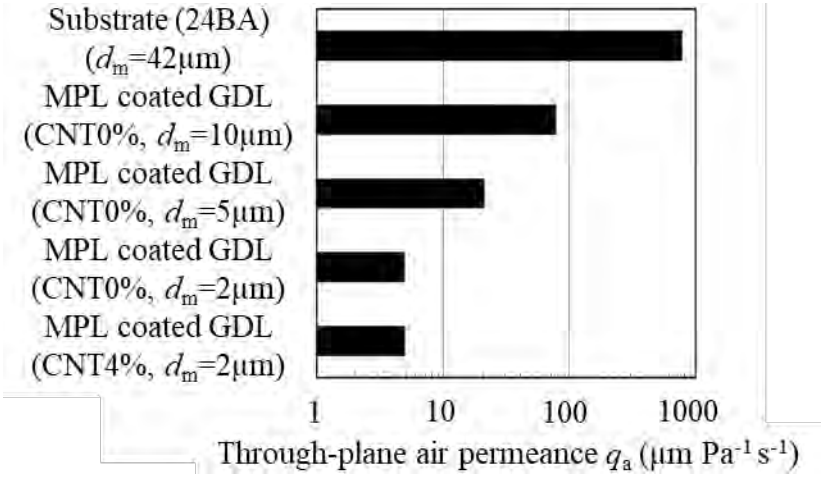

Figure 11. Through-plane air permeance of GDLs with and without CNTs.

Figure 12 shows the water breakthrough pressures obtained from MPL coated GDLs with and without CNTs. For the MPL without CNTs, with the d_m decreasing from 10 to 2 μm, the water breakthrough pressure significantly increased. As for the MPL with CNTs, liquid water was more readily introduced into the less hydrophobic pores containing hydrophilic CNTs. Therefore, the water breakthrough pressure for the MPL with CNTs can be significantly reduced, even when d_m was as low as 2 μm.

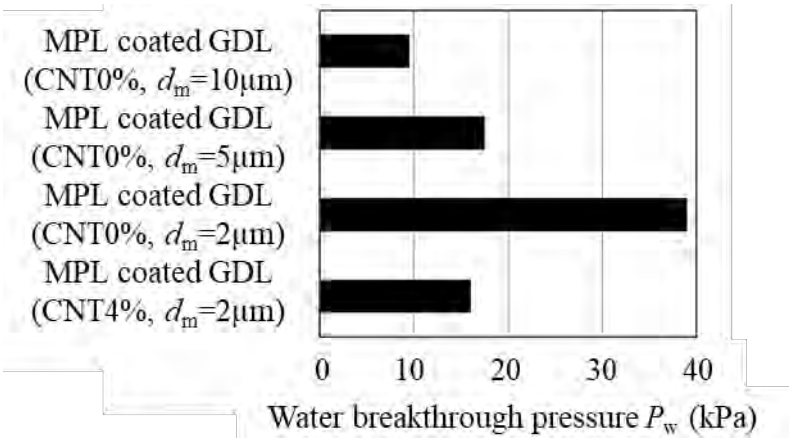

Figure 12. Water breakthrough pressure of GDLs with and without CNTs.

Figure 13 shows the effect of the pore size and the CNTs addition on the R_{O2}. The difference between the R_{O2} of all four samples was insignificant when the RH was less than 80%. When the RH increased to more than 80%, the flooding occurred and resulted in a sharp increment of R_{O2}. Among the hydrophobic MPLs, when the d_m was 10μm, the water was accumulated in the large pores and blocked the oxygen transportation. Reducing the d_m to 5μm could helpfully lower the oxygen transport resistance. However, continuing to decrease pore size to 2μm, the water breakthrough pressure was raised. Thus, the water could not flow through the MPL and accumulated between the MPL and catalyst layer, further deteriorating oxygen transportation ability. Hence, the appropriate pore sizes for enhancing oxygen transportation under high and low humidity conditions were different.

Under high humidity conditions, the MPL with CNTs displayed better performance than pure hydrophobic MPL. Even when d_m was 2 μm, the MPL with CNTs significantly lowered the water breakthrough pressure, as shown in Figure 12. The added hydrophilic CNTs in the MPL could generate weak hydrophobicity pores to reduce the water breakthrough pressure, which effectively expelled excess water from the catalyst layer to the GDL substrate. Besides, the small hydrophobic pores composed of fewer CNTs also existed in the MPL with CNTs, as shown in Figure 10. These hydrophobic pores prevented water penetration and maintained sufficient oxygen flow pathways. The combination of tiny hydrophobic pores and weak hydrophobic pores enhanced the ability of the MPL with CNTs to reduce the oxygen transport resistances under high humidity conditions.

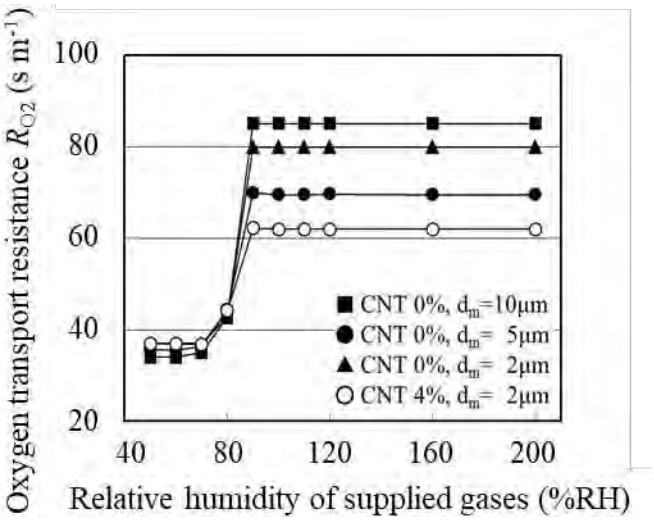

Figure 13. Effect of the MPL coated GDL with and without CNTs on the oxygen transport resistance.

Figure 14 summarizes the R_{O2} values obtained with the different types of MPLs under the 200RH% condition. Compared with the pure hydrophobic MPL, the composite MPLs could effectively discharge water from the catalyst layer and promoted oxygen transportation. Among the composite MPLs, the double MPL slightly reduced the oxygen transport resistance compared to the hydrophobic MPL. Both the triple MPL and the MPL with CNTs significantly lowered the resistance and showed almost the same performance.

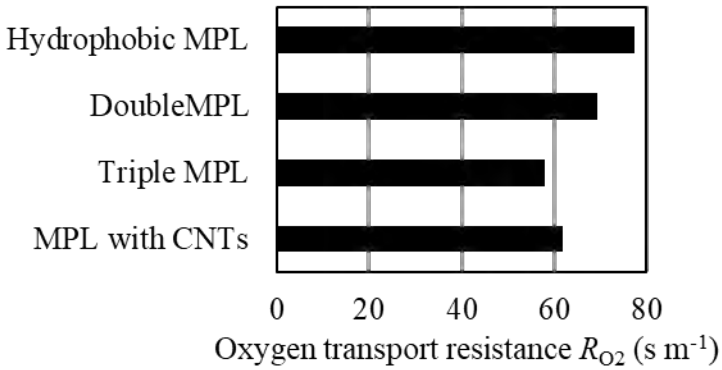

Figure 14. The oxygen transportation resistances of the different types MPLs under conditions of 200% RH, a gas flow rate of 1000 cm^3 min$^{-1,}$ and a 35 °C cell temperature.

Conclusions

(1) The hydrophobic MPL coated GDL designed to prevent dehydration of the MEA under low humidity conditions is inferior at reducing flooding under high humidity conditions. Thus, it is vital to develop a hydrophilic and hydrophobic MPL coated GDL to enhance the PEFC performance under low and high humidity conditions.

(2) The double MPL, in which the thin hydrophilic layer coated on the hydrophobic MPL, effectively enhances the performance under low and high humidity conditions. The triple MPL achieves further enhancement of the performance under high humidity conditions.

(3) The hydrophobic MPL containing hydrophilic CNTs reduces the water breakthrough pressure. Comparing with hydrophobic MPL coated GDL, this MPL enhances the performance under low and high humidity conditions by decreasing pore diameter and adding hydrophilic CNTs.

Acknowledgments

This work was supported in part by JSPS KAKENHI Grant Number 21H01549.

References

1. Y. Wang, K. S. Chen, J. Mishler, S. C. Cho, and X. Cordobes, *Applied Energy*, **88**(4), (2011).
2. T.Kitahara, T.Konomi and H.Nakajima, *J. Power Sources*, **195**(2202), (2010).
3. Schweiss R, Steeb M, and Wilde PM, *Fuel Cells*, **10**(6), (2010).
4. M. Ahn, Y. H. Cho, Y. H. Cho, J. Kim, N. Jung, and Y. E. Sung, *Electrochim Acta*, **56**(5), (2011).
5. T. Tanuma, *J. Electrochem. Soc.*, **157**, B1809, (2010).
6. T.Kitahara, H.Nakajima, M.Inamoto and M.Morishita, *J. Power Sources*, **234**(129), (2013).
7. T.Kitahara, H.Nakajima and K.Okamura, *J. Power Sources*, **283(**115), (2015).
8. J. H. Chun, K. T. Park, D. H. Jo, J. Y. Lee, S. G. Kim, S. H. Park, E. S. Lee, J. Jyoung, and S. H. Kim, *J. International Journal of Hydrogen Energy*, **36**(14), (2011).
9. A. Tiliakos, A. M. I. Trefilov, E. Tanasă, A. Balan, and I. Stamatin, *Applied Surface Science*, **504**, (2020).
10. M. P. Manahan, J. T. Clement, A. K. Srouji, S. W. Brown, T. Reutzel, and M. M. Menchet, *J. Electrochem. Soc.*, **161**, F1061 (2014).
11. G. Wang, Y. Utaka, and S. Wang, *Journal of Power Sources*, **437**, (2019).
12. *Japanese Industrial Standards Committee*, p. 1, (1998).
13. N. Nonoyama, S. Okazaki, A. Z. Weber, Y. Ikogi, and T. Yoshida, *J. Electrochem. Soc.*, **158**, B416 (2011).
14. D. R. Baker, D. A. Caulk, *ECS Trans*., **50**(2), 35 (2012).

ECS Transactions, 104 (8) 129-135 (2021)
10.1149/10408.0129ecst ©The Electrochemical Society

Mass Transfer in Microporous Layers for Polymer Electrolyte Fuel Cells Analyzed with Pore Network Modeling

Hironori Nakajima[a,b], Shintaro Iwasaki[b], and Tatsumi Kitahara[a,b]

[a] Department of Mechanical Engineering, Faculty of Engineering
[b] Department of Hydrogen Energy Systems, Graduate School of Engineering
Kyushu University
744 Motooka, Nishi-ku, Fukuoka 819-0395, Japan

The application of a microporous layer (MPL) to the catalyst layer (CL) side of the gas diffusion layer substrate of a polymer electrolyte fuel cell (PEFC, PEMFC) is effective to mitigate liquid water accumulation at the CL that inhibits oxygen transport to the cathode CL (Flooding). To elucidate the effects of two-phase flow on the oxygen transport in an MPL for its optimized designs, we have modeled three-dimensional porous structures of in-house hydrophobic MPLs with pore network models (PNMs) for convective air permeation and oxygen diffusion with liquid water saturation. Pore diameter distributions derived by a focused ion beam scanning electron microscope (FIB-SEM) are used to construct the PNMs. Oxygen diffusion measurements by using gas chromatography with changing wetting liquid saturation, as well as air permeation measurements, validate the PNMs.

Introduction

Polymer electrolyte fuel cells (PEFCs, PEMFCs) are promising as zero-emission power sources for future automobiles and houses. However, proper water management among the catalyst layer (CL), gas diffusion layer (GDL), and flow channels of a PEFC is necessary to improve its performance. In particular, excess liquid water is generated in a high current density region. The liquid water may cause clogging in the CL and GDL, resulting in performance deterioration due to inhibition of transport of the reactant oxygen in the cathode (Flooding). To enhance the drainage in the GDL, the application of a microporous layer (MPL) is effective to the CL side of a GDL (1-4).

In this research, we focus on mass transfer in the three-dimensional porous structure of MPLs. Pore diameter distributions of our in-house MPLs given by a focused ion beam scanning electron microscope (FIB-SEM) have been employed in pore network models (PNMs) (5)(6) with convective air permeation and oxygen diffusion. Gas permeation measurement for air permeabilities as well as gas chromatography for oxygen diffusivities was also carried out to validate the models. Oxygen diffusivities were evaluated for dry MPLs and those with a wetting liquid of different liquid saturations. The aim of this research is thereby to develop reliable and practical numerical models validated with experiments taking into account liquid saturation for the optimized design of the MPLs, elucidating the effects of two-phase flow and water clogging on oxygen transport in an MPL.

Experimental

MPL preparation

Slurries for the hydrophobic MPL of carbon black (80wt%, Denka Black HS-100, Denka, Japan) with PTFE (20wt%, POLYFLON PTFE D-210C, Daikin Industries, Japan) and dispersant (0.5-1.0wt%, TritonX-100, Nacalai Tesque Inc., Japan) were applied to a commercial GDL having a thickness of 100 μm (TGP-H-030: 5wt% PTFE, Toray, Japan) as a GDL substrate with changing added water amount to the slurries so that the MPL has a thickness of ca. 60 μm and maximum pore diameter, d_{max}, of ca. 5 μm. The pore contact angle was 137°. Details of the MPL application as well as the maximum pore diameter and pore contact angle determinations were described elsewhere (2). The penetration depth of the MPL slurry into the GDL was indicated to be negligible by cross-sectional scanning electron microscope (SEM) observation (SU3500, Hitachi High-Tech Corporation, Japan) in contrast to a commercial GDL, SIGRACET 24BA (SGL carbon Inc., Germany) (2). The porosity of the MPL was estimated to be 0.37 with the Archimedes method by immersing the MPL-coated GDL in a non-volatile wetting liquid (GALWICK, Porous Materials Inc., USA) having a sufficiently small surface tension.

FIB-SEM observation for the PNM

Three-dimensional structural analysis of the MPL was performed using an FIB-SEM (Helios NanoLab 600i, FEI, USA) at a slice number of 100 to determine porosities and pore diameter distributions by image binarization followed by watershed segmentation (Amira 6.3, FEI, USA). The porosity and pore diameter distribution were derived for a three-dimensional image at a magnification of 2000 and a slice thickness of 300 nm. The contribution of pores from higher resolution images was small for the permeability and diffusivity in the PNM. The PNM (OpenPNM 1.2) (5)(6) empirically constructed using Weibull distribution fitted with the porosity and pore diameter distribution as presented in Fig. 1 gives air permeability and oxygen diffusion resistances with the porosity and tortuosity of 0.39 and 2.0, respectively.

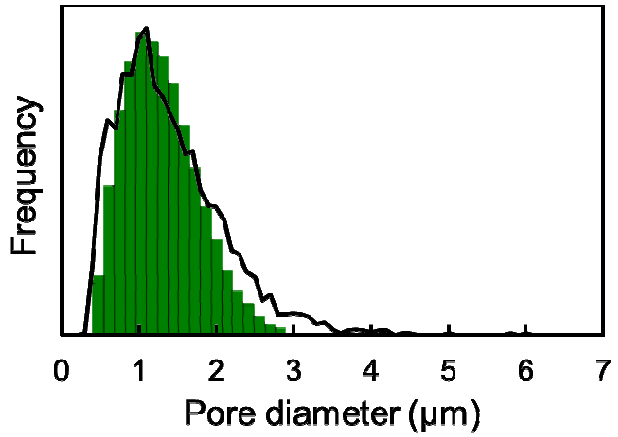

Figure 1. Pore diameter distribution from the FIB-SEM analysis fitted with the empirical Weibull distribution for the PNM construction.

Air permeability measurement

Air permeability (permeance) was measured with equipment of stainless steel shown in Fig. 2 at 25 °C from volumetric air flow rates (Model 3760, KOFLOC, Japan) through the GDL divided by the air-permeable cross-sectional area for a diameter of 5 mm and the pressure difference of ΔP = 1.23 kPa (2) between the inlet (FP101-S31, Yokogawa, Japan) and outlet. A mass flow controller (SEC-40, Horiba STEC, Japan) was controlled by a personal computer with LabView 8.6 (National Instruments Inc., USA) via an I/O device (USB-3106, Measurement Computing, USA) for the air supply.

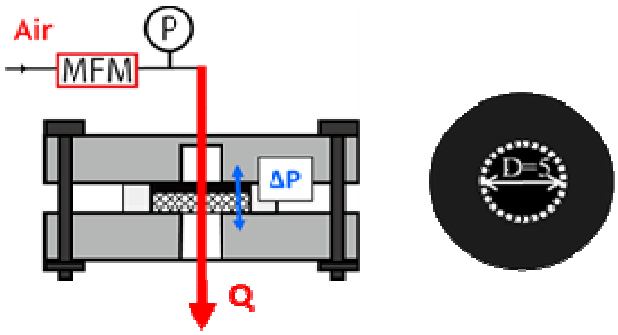

Figure 2. Schematic of the air permeability measurement.

Oxygen diffusivity measurement

Figure 3 shows an experimental set-up of stainless steel for ex-situ measurement of the oxygen diffusivity of the GDL between air and nitrogen (99.99% purity, each) flow channels (22 mm length, 1 mm width and depth). Their inlet flow rates were controlled similarly to the air permeability measurement. GDL samples (30 mm length, 5 mm width) were installed with a silicone rubber gasket between a fixture having the above flow channels. Oxygen concentration in the outlet gas from the nitrogen flow channel was determined by a gas chromatograph (GC) (GC7100T, thermal conductivity detector, J-Science Lab, Japan). Differential pressure between the flow channels was minimized by a back pressure valve at the outlet of the air flow channel with monitoring pressure gauges (FP101-S31, Yokogawa, Japan) at the inlets of both flow channels.

Oxygen diffusion flux in the GDLs at 60°C for dry and wet conditions was derived by the outlet oxygen concentration (GC) and the outlet gas flow rate (SEF-8440F, Horiba STEC, Japan) of the nitrogen flow channel. The flux was divided by the difference of the

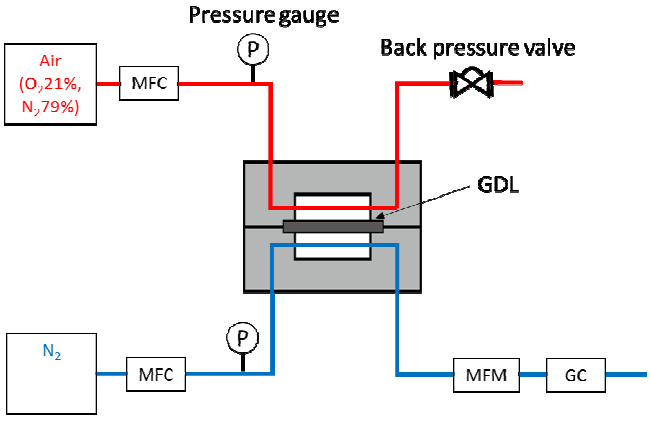

Figure 3. Schematic of the oxygen diffusivity measurement.

logarithmic mean concentration of oxygen (7), which involves the mass conservation, between the GDL surfaces to obtain the oxygen diffusion resistance, $R_{O2} = \delta_{GDL} / D^{eff}_{O2}$, where δ_{GDL} and D^{eff}_{O2} are the thickness of the GDL and the effective oxygen diffusion coefficient of the GDL, respectively, for the oxygen diffusivity (4).

For measurement under wet conditions, a GDL fully impregnated with the wetting liquid (GALWICK) was discharged by increasing differential air pressure in the GDL, which corresponds to the capillary pressures between air and the wetting liquid, every 20 kPa to reduce liquid saturation from unity because ex-situ control of liquid saturation in hydrophobic pores using the wetting liquid is more reliable than that with water in terms of equilibrium of forces. We assume that the liquid saturation in the GDL substrate of the MPL-coated GDL is zero at pressures higher than that the wetting liquid in the pore of the MPL is discharged because the minimum pore diameter of the GDL substrate is larger than the maximum pore diameter of the MPL.

We also confirmed that the thickness of the MPL-coated GDL between the flow channels was 165±5 μm with cross-sectional X-ray microscopy images (Skyscan 1272, Bruker, USA) for the GDLs installed in an acrylic fixture with flow channels having the same dimensions and compression pressure as above. Thus the deformation of the MPL-coated GDLs between the flow channels was negligibly small.

The oxygen diffusion resistance includes a resistance with the concentration boundary layers at both surfaces of a GDL with the viscous flows. The resistance was determined by the least-squares fitting of the oxygen diffusion resistances for one, two, and three-ply GDLs of the TGP-H-030.

Results and Discussion

Air permeability

Air permeance of the MPL-coated GDL measured for the dry condition was 3.7 μm /(Pa·s) while the PNM gives 3.0 μm/(Pa·s), corresponding to the air permeabilities of 4.0×10^{-15} m^2 and 3.2×10^{-15} m^2, respectively, for negligible pressure drop in the GDL substrate compared with the MPL of the thickness of 60 μm, exhibiting good agreement between them.

Diffusion resistance

Oxygen diffusion resistance for the concentration boundary layers of 26.5 s/m for TGP-H-030, respectively, is derived by the least-squares fitting of the oxygen diffusion resistances presented in Table I at the inlet flow rates of the air and nitrogen of 150 cm^3/min (25°C, 1atm) and 60°C. Thereby, the oxygen diffusion resistance for the GDL used for the substrate is 16.9 s/m from the gradient.

Oxygen diffusion resistance of the MPL-coated GDL for the dry condition without the resistance for the concentration boundary layers and the substrate is thus 14.8 s/m while the PNM gives 12.2 s/m for the MPL, which are consistent with each other. They provide the diffusion coefficients of 4.1×10^{-6} $m^2 s^{-1}$ and 4.9×10^{-6} $m^2 s^{-1}$, respectively, for the MPL thickness of 60 μm.

TABLE I. Oxygen diffusion resistances of the GDLs with the concentration boundary layer at the inlet flow rates of air and nitrogen of 150 cm^3/min (25°C, 1atm) and 60°C.

Sample	Number of the GDLs	Thickness (μm)	O_2 diffusion resistance (s/m)
TGP-H-030 (Toray)	1	100	43.4
	2	200	60.3
	3	300	77.2

On the other hand, in the MPLs impregnated with the wetting liquid (GALWICK), the oxygen diffusion resistance decreased when the liquid saturation decreased with the discharge of the wetting liquid as shown in Fig. 4, where oxygen diffusion resistance is evaluated with reference to the dry condition as relative resistivity, R_{dry}/R_{wet}. Because the trend of the PNM is consistent with the experiment, the change in the oxygen diffusion resistance with the liquid saturation of the wetting liquid is successfully reproduced by the PNM.

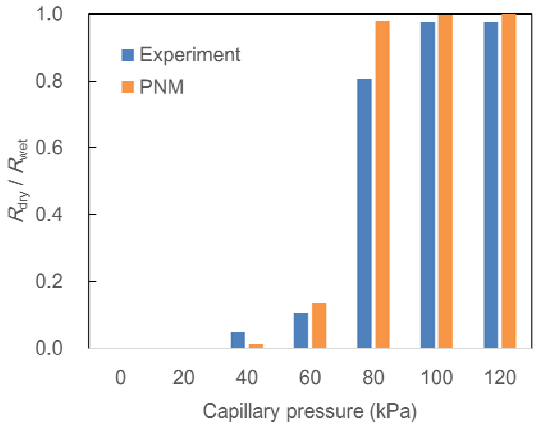

Figure 4. Relative diffusion resistance for the MPL (d_{max} = 5 μm) impregnated with the wetting liquid against the caplillary pressure between air and the wetting liquid for the minimum diameter of the pores where the wetting liquid is discharged.

It would be worth comparing the PNM and the conventional analysis with the Leverett function (8)(9). Figure 5 presents the derived capillary pressures with liquid water saturation by the PNM and Leverett function with the contact angle, permeability, and porosity of the PNM. The Leverett function exhibits significant deviation from the PNM both at low and high saturations. Thus the PNM is more reliable for the MPL analysis than the Leverett approach proposed for fluid flow through packed soil beds.

Figure 6 shows the relative permeabilities (9)(10) of liquid water and air predicted by the PNM. Empirical fit for those relative permeabilities indicates high-order power-law dependence, indicating a wide pore diameter distribution (10).

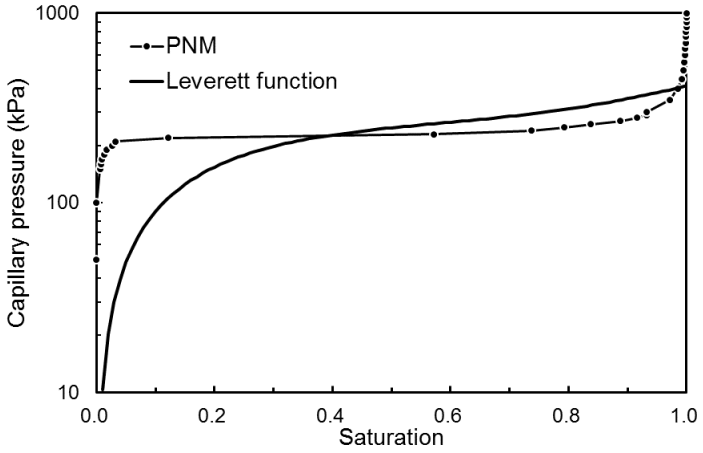

Figure 5. Capillary pressures between air and liquid water for the MPL (d_{max} = 5 μm) predicted by the PNM and the Leverett function.

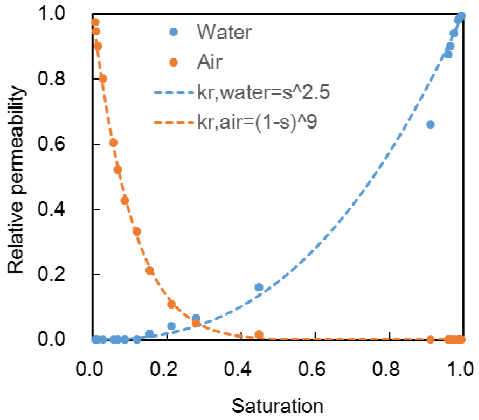

Figure 6. Gas and liquid water relative permeability with saturation from the PNM of the MPL.

Conclusions

Air permeability and oxygen diffusion resistances for the dry and wet conditions of the MPL agree well between the PNM and experiment. Thus PNM is validated and useful to model oxygen and water transports in MPLs with employing wettability (contact angle) of the pores. Numerical models with the PNM for optimized designs of MPLs are feasible.

Acknowledgments

The authors are indebted to graduate students, Messrs. Yuhang Liu, Kentaro Harano, Yuki Monde, and Dingfeng Chen for help in the modeling and experiments. Thanks are offered to Professor Kohei Ito of Kyushu University for valuable discussions. The authors acknowledge Ms. Chie Uryu of the International Research Center for Hydrogen Energy, Kyushu University for operating the FIB-SEM. The SEM and X-ray CT observations were performed at the Center of Advanced Instrumental Analysis, Kyushu

University with the help of Akiko Inada of the Center for Co-Evolutional Social Systems, Kyushu University.

References

1. H. Nakajima, T. Konomi, and T. Kitahara, *J. Power Sources*, **171**, 457 (2007).
2. T. Kitahara, T. Konomi, and H. Nakajima, *J. Power Sources*, **195**, 2202 (2010).
3. T. Kitahara, H. Nakajima, and K. Okamura, *J. Power Sources*, **283**, 115 (2015).
4. T. Kitahara and H. Nakajima, *Int. J. Hydrogen Energy*, **41** (22), 9547 (2016).
5. J. Gostick, M. Aghighi, J. Hinebaugh, T. Tranter, M.A. Hoeh, H. Day, B. Spellacy, M.H. Sharqawy, A. Bazylak, A. Burns, W. Lehnert, and A. Putz, *Comput. Sci. Eng.*, **18**, 60 (2016).
6. http://openpnm.org/. Accessed on Jury 14 (2021).
7. R. B. Bird, W. E. Stewart, and E. N. Lightfoot, *Transport Phenomena*, *Revised 2nd Edition*, John Wiley & Sons, Inc., Hoboken, New Jersey (2006).
8. E. C. Kumbur, K. V. Sharp, and M. M. Mench, *J. Electrochem. Soc.*, **154**(12), B1295 (2007).
9. M. M. Mench, *Fuel Cell Engines*, John Wiley & Sons, Inc., Hoboken, New Jersey (2008).
10. A. Weber, *J. Power Sources*, **195**, 5292 (2010).

ECS Transactions, 104 (8) 137-153 (2021)
10.1149/10408.0137ecst ©The Electrochemical Society

Evaluation of Automatic Microstructural Analysis of Energy Dispersive Spectroscopy (EDS) Maps via a Python-Based Data Processing Framework

Mariah Batool[a], Richard Andres Ortiz Godoy[a,b], Martin Birnbach[b], Dario R. Dekel[c], Jasna Jankovic[a,b]

[a] Institute of Materials Science, University of Connecticut, 97 North Eagleville Road, Unit 3136, Storrs, CT 06269-3136

[b] Department of Materials Science & Engineering, University of Connecticut, 97 North Eagleville Road, Unit 3136, Storrs, CT 06269-3136

[c] The Wolfson Department of Chemical Engineering, and The Nancy & Stephen Grand Technion Energy Program (GTEP); Technion – Israel Institute of Technology, Haifa 3200003, Israel

Abstract

Computer-aided data acquisition, analysis and interpretation have been employed in various research areas generating useful information. Among these, image processing is most often implemented for post-processing of material characterization data. However, to tackle ambiguity of multi-component materials analysis, spectral data analysis can be used instead. The current study introduces a unique Python-based data processing method for in-depth analysis of energy dispersive spectroscopy (EDS) elemental maps to analyze agglomerate size distribution, average area of each component and their overlap. The framework developed in this study is applied to examine interaction of Cerium (Ce) and Palladium (Pd) particles in membrane electrode assembly (MEA) of Anion-Exchange Membrane Fuel Cell (AEMFC) and investigate if this approach can be utilized to predict the fuel cell's electrochemical behavior. The study concludes that the developed framework is a promising method for automatic data extraction and can be beneficial for use in a variety of clean energy applications.

Introduction

With the progression of materials from being discovered coincidentally to being designed and optimized strategically, there has been an imminent need to analyze and model materials for specific applications. This process can nowadays be facilitated by the power of microscopy and image processing (1). Image processing has found a plethora of applications in the field of materials science ranging from detailed morphological and structural analysis of materials to the study of their degradation and failure, including fuel cells (2–7). Image processing is most widely implemented to extract valuable information from a larger set of materials characterization data to better understand and predict material features, properties, and behaviors at multiple scales. To ensure accuracy of results obtained from image processing, it is vital for it to have a systematic recognition of volumetric data and the ability to process it swiftly, for an efficient analysis.

Unfortunately, image processing also comes with complications and challenges since microstructural images have a series of inherent properties that can cause analysis to be difficult for manual and automated techniques. Microscopic images are influenced by noise which is the inclusion of random and false signals due to external conditions produced by sensors, detectors, amplifiers etc., (8,9), and can make features like grain boundaries or materials interfaces difficult to perceive or can create the appearance of features that are not real. Consequently, it is appropriate to state that manual image processing is subjected to human error, experience and bias due to varying opinions on what constitutes a grain, grain boundary, defect, etc. within a microstructure. As a result, ensuing measurements are objective and statistically representative requires repetition of the measurements, which becomes a burdensome and time-consuming task. Manual methods are therefore very slow and laborious (10). With automation, microstructural analysis and measurements are conducted within seconds, can be repeated without any inter-operator variation, and human error is reduced. One of the most difficult tasks of automated image processing is guaranteeing that the software is representing the material features accurately. However, although computer-based automated image processing has its challenges, it is far more superior and has unarguably overshadowed manual image processing techniques in the recent decades.

The main process involves digitization of the image (11,12) which can be graphically represented by Figure 1.

Figure 1: A graphical representation of how image processing works.

Such favorable characteristics of image processing led researchers to realize its potential for providing valuable microstructural information in the process of improving performance and efficiency of clean energy systems (13–15). Particularly, inspecting individual and collective characteristics of microstructural features of materials constituting a fuel cell such as electrodes, catalysts and electrolyte membranes can help predict electrochemical behavior down to nanometric scale (16). Beside composition, fuel cell performance and durability are known to depend on the electrode microstructure and component distribution. Therefore, to facilitate the development of efficient fuel cells and establish statistically relevant correlations between the microstructure and performance, automated image processing is required. Typically, the automated image processing for fuel cells involves particle or pore size distribution using Transmission Electron Microscopy (TEM) or Scanning Electron Microscopy (SEM), without taking into account elemental composition (17,18). However, using greyscale TEM and SEM images often makes it challenging to differentiate between various components in the material. Utilization of Scanning Transmission Electron Microscopy with Energy Dispersive Spectroscopy (STEM-EDS) provides elemental maps with spatial component distribution, enabling this differentiation and offering a whole range of new possibilities for automated sample analysis.

Several data processing approaches using EDS data, mainly in conjunction with SEM have been developed and reported for a wide range of applications such as automatic particle size analysis of nano-materials, mineral constituents in rocks, inclusions in metals, contaminants in pharmaceutical products, air or water particulates, gun-shot residue in forensic science, pathological tissue in biomedical research, automated identification of different phases and calculation of area, perimeter or compactness in a sample (19–26). Combined with machine and deep learning algorithms, SEM-EDS data have been used to automatically investigate the microstructural features, morphology, orientation and symmetry in samples and count, aspect ratio and dimensions of the features in the materials. However, apparently no such automated approach has been adopted and documented for anion exchange membrane fuel cells (AEMFCs) related research yet, especially not when using STEM-EDS.

In this study, a python-based data processing interface was developed and subsequently utilized to investigate STEM-EDS maps for Palladium (Pd)-based electrodes of AEMFCs. Pd based catalysts are known low-cost alternatives to expensive Platinum (Pt) catalysts used in lower operating temperature range fuel cells such as AEMFCs. However, this catalyst suffers from reduced hydrogen oxidation reaction (HOR) kinetics (27). It is reported that this problem could be potentially avoided by combining Pd with Cerium oxide (CeO_x) and ensuring sufficient Pd-CeO_x interaction for increase in catalytic activity (28,29). In this work, we report testing of an in-house developed python-based code (30) to process Pd and Ce EDS maps for AEMFC catalyst layers, and determine Pd and Ce particle/agglomerate size distribution, as well as overlap area between Pd and Ce particles. The python interface uses microscopy and EDS elemental maps data of Pd-CeO_x based catalyst to produce visual and numerical results with potential to predict the electrochemical performance and durability of the AEMFCs.

Methodology

The script for the data processing framework developed in this study was written in Python programming language. The idea was built around the fact that materials characterization data about Pd-CeO_x based catalyst, although can be a source of vast amount of information, it requires a rigorous analysis procedure to get “concealed” or underlying information not visible to the naked eye such as percentage of area where Pd and CeO_x overlap (contact area, which is expected to benefit the HOR activity). Thus, three different catalyst samples, i.e., n CeO_x-Pd/C with varying compositions (where n denotes bulk atomic fraction of Ce/Pd) 0.24 CeOx-Pd/C, 0.38 CeOx-Pd/C and 0.59 CeOx-Pd/C labelled as DD08, DD09 and DD16, respectively were taken into consideration and three different maps of each sample were analyzed using the data processing interface. A graphical overview of the whole process is shown in Figure 2 and discussed below. A detailed description of the samples, their fabrication and testing are described in a study by Singh. et al (31).

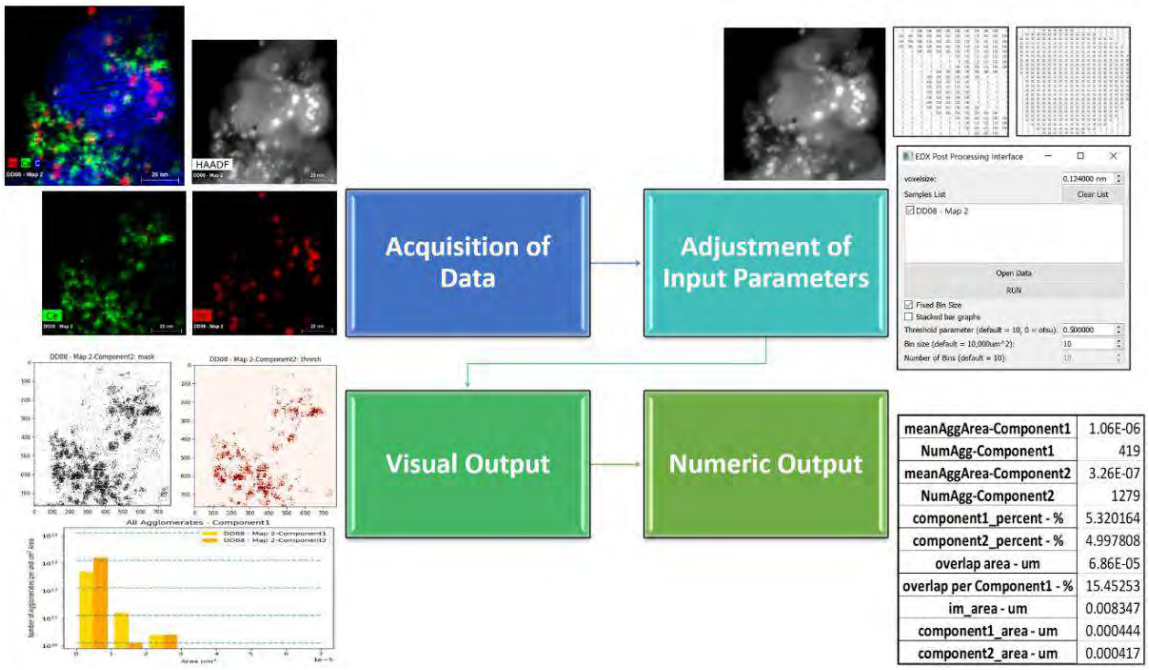

Figure 2: A graphical step-by-step overview of the data processing methodology

Acquisition and Processing of Raw Data

STEM-EDS mapping was used to take elemental maps of the MEA electrode cross-section. Images were obtained at a constant magnification of 910,000X using high-angle annular dark field (HAADF) imaging technique. This technique was combined with the EDS to get elemental maps. The type of raw maps that are obtained are shown in Figure 3. The raw maps were processed using the software Esprit (Version 1.9) to remove background and deconvolute the spectral peaks. The processed individual elemental maps of EDS X-ray net intensities of Ce and Pd were obtained and saved as text file in ASCII format. The software allocates a specific numeric value in the text file according to the X-ray net intensity data for each pixel of the map. However, the processing of the elemental maps can be performed using different binning (resolutions): e.g., with the resolution 1, each pixel is separately processed, and its processed value is assigned to the same pixel; with the resolution 0.5 (1/2), four pixels are averaged; with the resolution 0.125 (1/8), sixteen pixels are averaged; etc. Consequently, resulting net count values of same pixels (e.g., ascribed to a particle) in text files of the same map at different resolutions are very different. The net count values are smaller for lower resolution maps as compared to higher resolution maps. An example of different net count values at different map resolutions is shown in Figure 4. The name of all the text files for Pd were labelled as _component1.txt and all the text files for Ce were labelled as _component2.txt and saved in separate folders with each sample's name and map number. Furthermore, the STEM image for each map taken with HAADF imaging was saved in the same folder in TIFF format and labelled as Mask. The specific labelling was done to be traceable by the code as well as to be able to be used with any two components at any time.

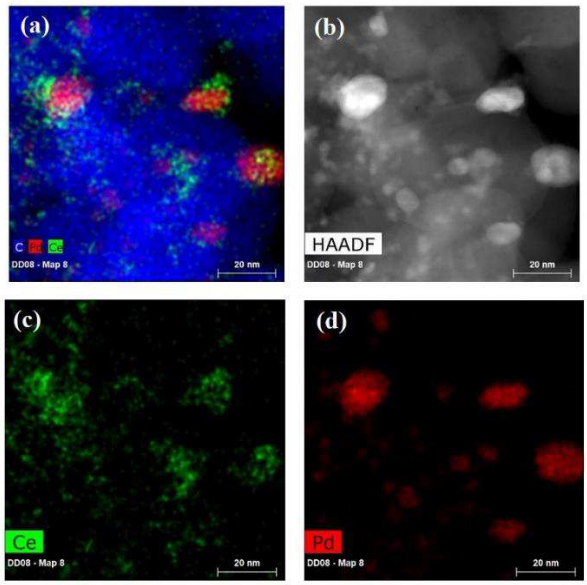

Figure 3: (a) Raw STEM/EDS elemental map of C, Ce & Pd (b) HAADF image (c) Raw Ce elemental map (d) Raw Pd elemental map

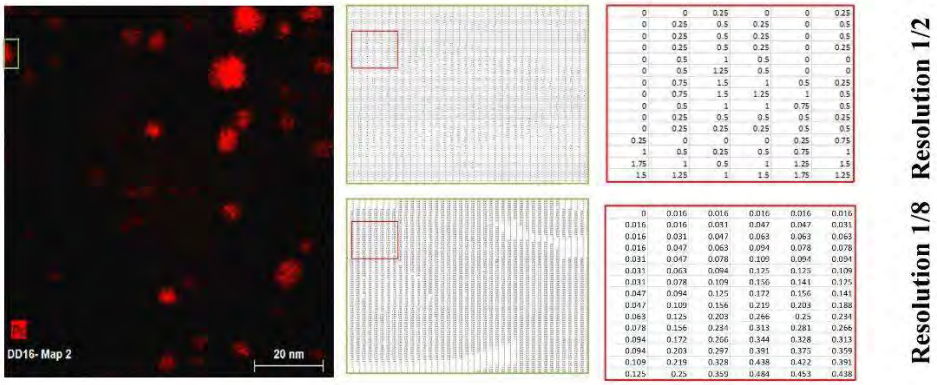

Figure 4: An example of magnified net count data from same region of same EDS map at two different processed map resolutions i.e., 1/2 and 1/8

Adjustment of Input Parameters

The text files of the required components were selected using the main window of the data processing interface as shown in Figure 5. The window allows user to change different parameters including pixel value (from raw images/maps), threshold value (to remove the noise), bin size and number of bins (for the area size histogram display) and type of output that is required (image, labels, histogram). The pixel size needs to be adjusted according to the pixel size of the raw map while appropriate threshold value needs to be selected to ensure that the code considers only the specified component's true signal and disregards any noise the map might contain. Appropriate bin size and number of bins needs to be selected for an appropriate representation of area (agglomerate, particle, etc.) size distribution histograms. The code automatically takes into account all the text files and mask image contained in a specific folder. Once the text file is selected and loaded, the

analysis is allowed to run. The input parameters selected to carry out the analysis of all the samples are given in Table 1.

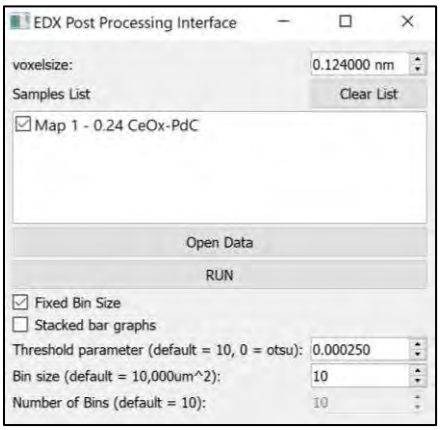

Figure 5: Overview of the EDS Post Processing Interface

Image Magnification	Map Resolution	Map Filter	Image Filter	Pixel size	Threshold values (T)	Bin size
910kx	0.5	Automatic	None	0.124 nm	T = 0.00025 & T = 0.50	10

Table 1: Input Parameters

Post Processing Analysis

Once the parameters are set and the EDS Post Processing Program is allowed to run, the code runs the text files and scans through all the numeric values listed in the text file of each component and runs the thresholding algorithm. The Otsu and watershed algorithms (32,33) are used to threshold and segment both Pd and Ce maps, producing binarized masks. The mask is a binary image which has assigned zero (black color) to all pixels below the threshold value and 255 (white color) to all pixels above the threshold value. The code also eliminates the noise according to the user-defined threshold value and produces the final individual thresholded images. The program creates histograms for agglomerate size distribution of each component individually and collectively. It calculates the individual area occupied by each component, their overlap area, overlap percentage and the number and size of agglomerates. This information is automatically saved in an excel file at the completion of the analysis in the same directory. By default, all the measurements are carried out in unit of micrometer. For each map, two different net count threshold values (T) were selected i.e., T = 0.00025 and T = 0.5. These values were selected keeping in view the range of numerical values in input text files. The threshold value of 0.00025 is the lowest possible value no matter which map resolution is selected and therefore, includes all net intensity signals from a map (refer to Figure 5). However, there is at least one value lesser than 0.5 i.e., 0.25 in the text file for maps processed at resolution of 0.5 (input resolution), therefore it was chosen to selectively eliminate some of background signals or noise (having net count value of 0.25) from the thresholded image.

Results and Discussion

As mentioned above, data processing method introduced in this study generates mainly two different forms of outputs: graphical and numerical. The different results that were obtained for each concentration of the catalyst samples under observation are therefore presented using these outputs. It can be aptly implied that the variety of outputs generated by the developed program in the form of masks, thresholded images, agglomerate size distribution charts, component area overlap, and calculation datasheet offers a wide range of result dataset which can be crucial for comprehensive study of any sample under consideration. Such comprehensive approach in data analysis, obtained by one imaging/spectroscopy method and data post-processing has not been reported for electrochemical systems, as per the authors' knowledge.

To evaluate the use of the discussed automatic EDS analysis interface, we investigated the effect of several parameters which are set before feeding the input data to the program. These parameters are associated with EDS map processing software Esprit and some of these parameters greatly influence the output given by the developed interface and might contribute to errors. The effect of a few of such parameters is discussed below:

Effect of Different Parameters

Map Resolution. The effect of different map processing resolutions upon the graphical and numerical results is significant, an example of which is shown in Figure 6. There are four options for map resolutions in Esprit to choose from depending upon the pixel quality and processing time. The highest resolution is 1 and the lowest is 0.125. The lowest threshold value of 0.00025 was chosen to ensure inclusion of all signals from all the maps processed at different resolutions. The code did not work out the calculations for map resolution of 1 accurately and in most cases, it did not work at all with maps containing low intensity signals possibly because the developed program is not sensitive to the finer quality signals, and it eliminates many real signals along with noise. On contrary, the lowest map resolution blurred the real signals causing confusion between agglomerates and individual particles which contributed towards greater overlap values and incorporated plenty of noise thereby confirming that it is also not a good selection to begin with. Therefore, it was deduced that a reasonable selection to carry out the main calculations without compromising on the pixel quality was map resolution of 0.5. It must be noted here that the user must be extra cautious while choosing the threshold value when dealing with lower resolution maps since the low quality of image is prone to inclusion of more noise.

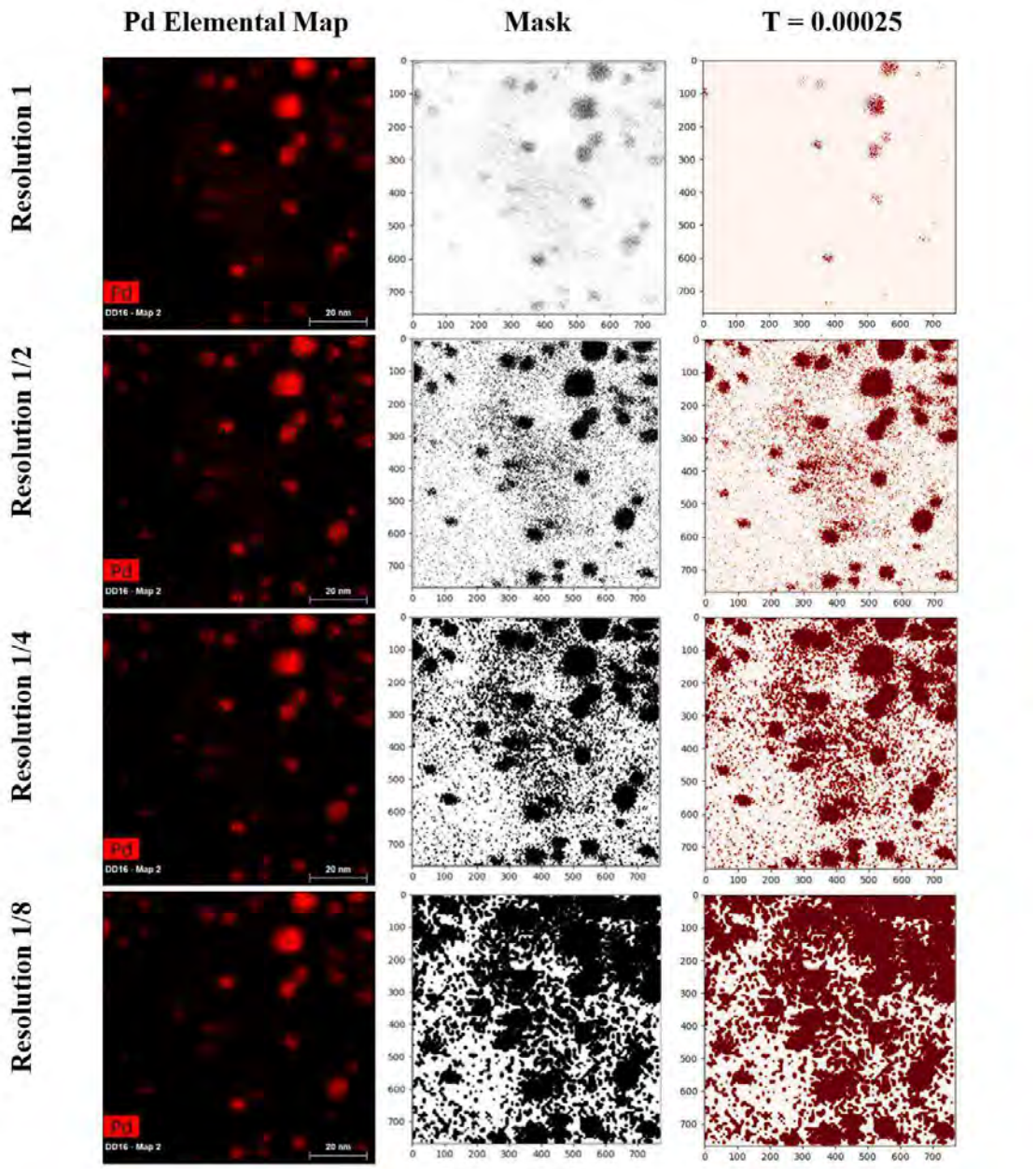

T = 0.00025	Resolution 1	Resolution 1/2	Resolution 1/4	Resolution 1/8
Pd Area (nm^2)	82.62	1759.71	3637.27	5561.90

Figure 6: Effect of different map resolutions upon graphical and numerical results

Map and Image Filters. Esprit also allows users to choose a map and image filter out of different options. Map filter is applied directly on the net count signals contained in the map while image filter is applied only to the overlay image to enhance visibility of features. The name and effect of different map and image filters is demonstrated in Figure 7 and Figure 8, respectively. It can be clearly deduced from the Figure 7 that the effect of smooth and average map filter is quite comparable with same calculated results. However, the results for the automatic map filter are different and can be considered the best choice among the rest because it is based on local noise removal instead of uniform noise removal as in case of smooth and average filter.

However, it is very noticeable from Figure 8 that the different image filters have either no effect upon the results or the difference is too minimal to cause any change in the results. Since the effect of image filters is not as pronounced as the effect of map resolution and map filters, therefore, to carry out the analysis, the image filter was set to None.

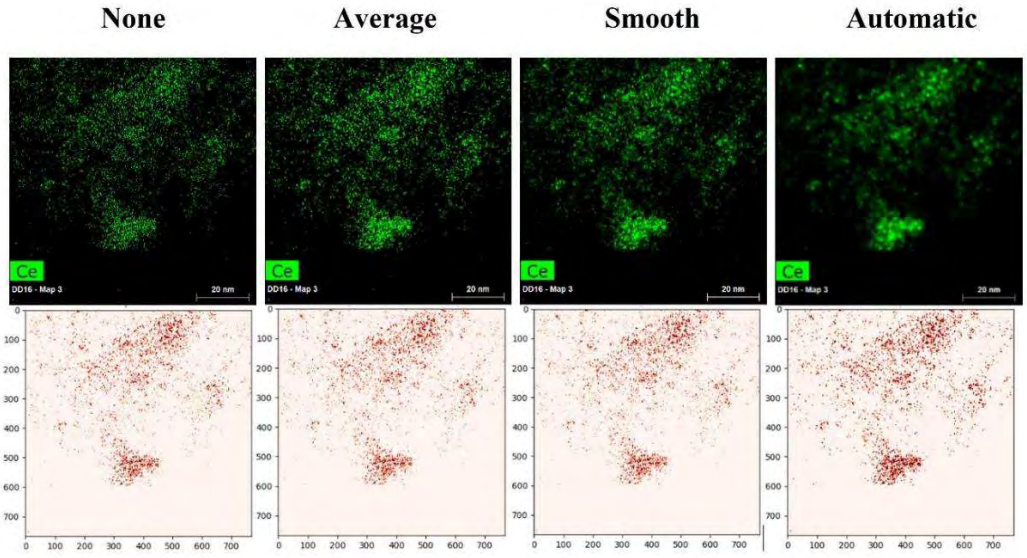

T = 0.00025	None	Average	Smooth	Automatic
Ce Area (nm^2)	296.77	296.77	296.77	404.40

Figure 7: Effect of different map filters upon graphical and numerical results

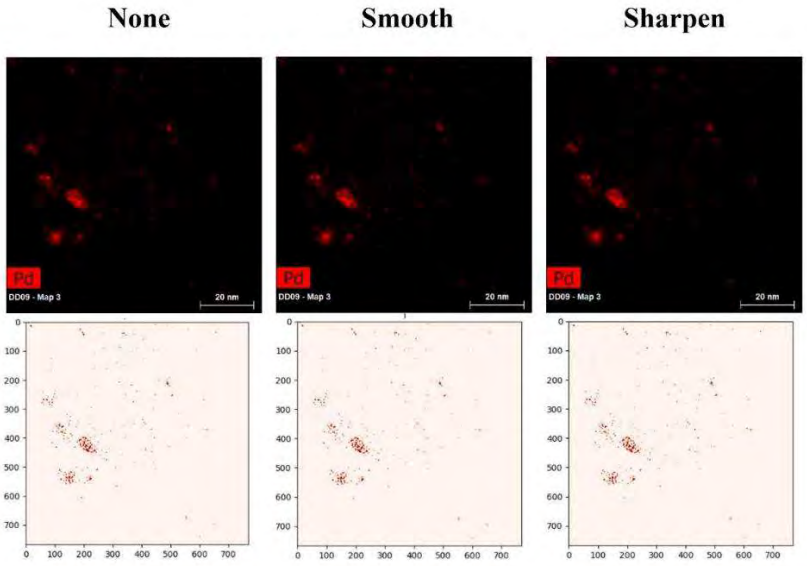

T = 0.00025	None	Smooth	Sharpen
Pd Area (nm^2)	42.24	42.24	42.24

Figure 8: Effect of different image filters upon graphical and numerical results

Threshold value. The thresholding methods reported in the literature mostly rely upon the Otsu thresholding for image processing of greyscale values, which despite having many advantages, face certain limitations especially when dealing with images having large variance discrepancy and low contrast (34–37). Moreover, using greyscale images often complicates component differentiation, as one relies on greyscale contrast to differentiate between the components. To avoid such issues in this work, the differentiation between components (elements) is completed based on the spectral data, where spectral distribution maps of each element can be separately processed and thresholded. The introduced method uses a two-step noise removal, i.e., Otsu and a user-selected thresholding value for a finer noise removal. The user-selected thresholding value should be selected based on the lowest EDS spectra X-ray net count signal that is determined by Esprit software algorithm to be the background noise.

Three maps of each sample were run through the code using two different threshold values (T) i.e., 0.00025 and 0.50 and all the other input parameters were set to the same values as mentioned in Table 1 to investigate effect of thresholding upon the results. For the processed map resolution of 0.5, the lowest value in the net count data was found to be 0.25 indicating that anything lower than this value such as 0.00025 automatically includes all the net count signals within a map. It was also observed that no other net count value exists between 0.25 and 0.5 implying that the threshold value of 0.5 only excludes the minimum value signals of 0.25 and keep account of the rest. The resulting visual outputs of one map of each sample in the form of combined and individual elemental maps, masks and thresholded images and agglomerate size distribution charts are shown in Figure 9, 10 and 11, respectively.

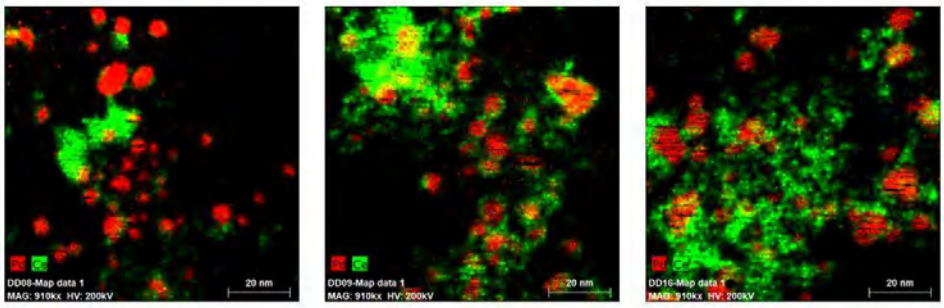

Figure 9: Processed elemental maps with map resolution of 1/2 showing overlap of Ce and Pd for sample (a) DD08 (b) DD09 (c) DD16

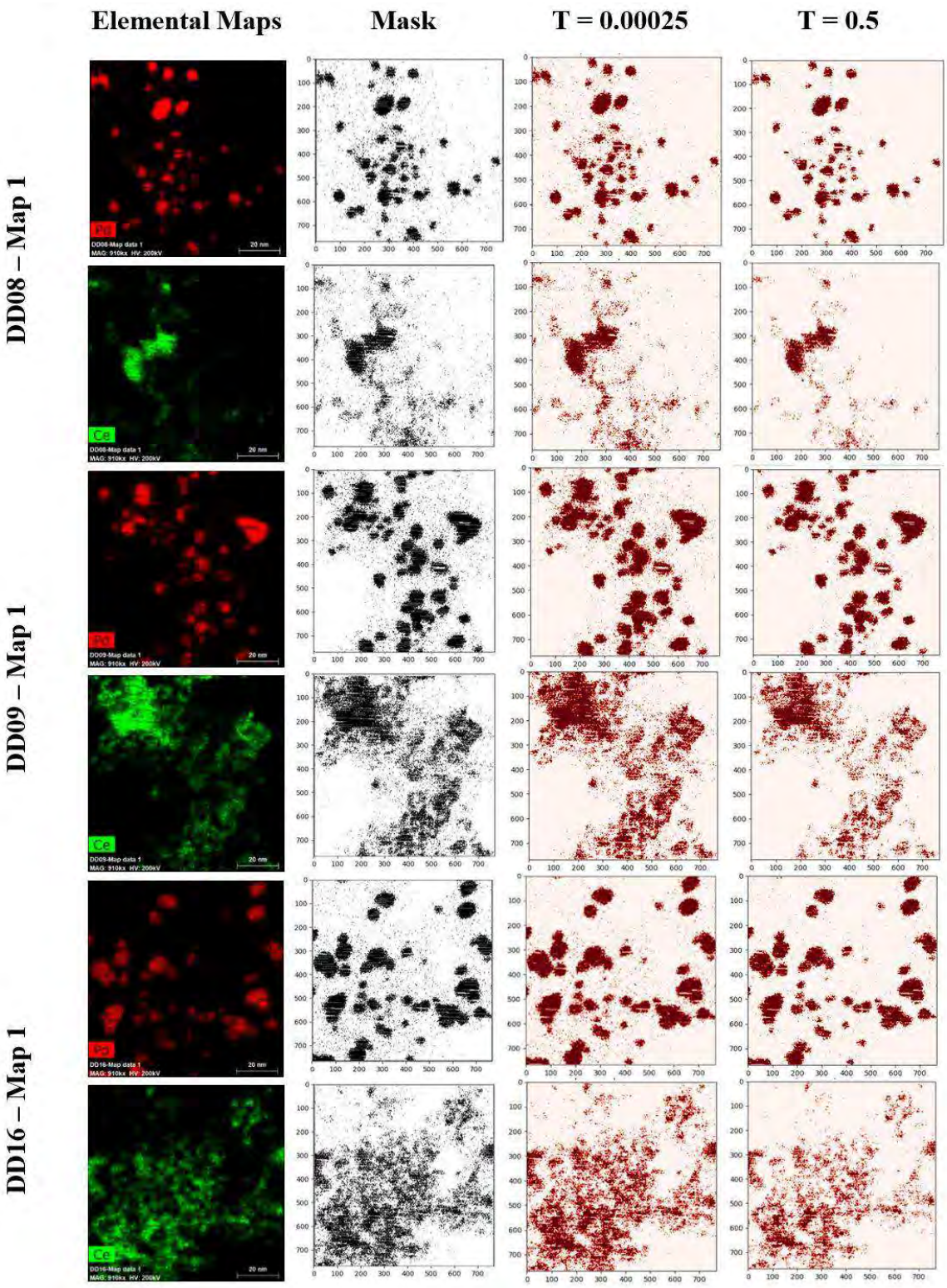

Figure 10: Elemental maps of Ce and Pd and corresponding mask and thresholded images with threshold values: T = 0.00025 and T = 0.5

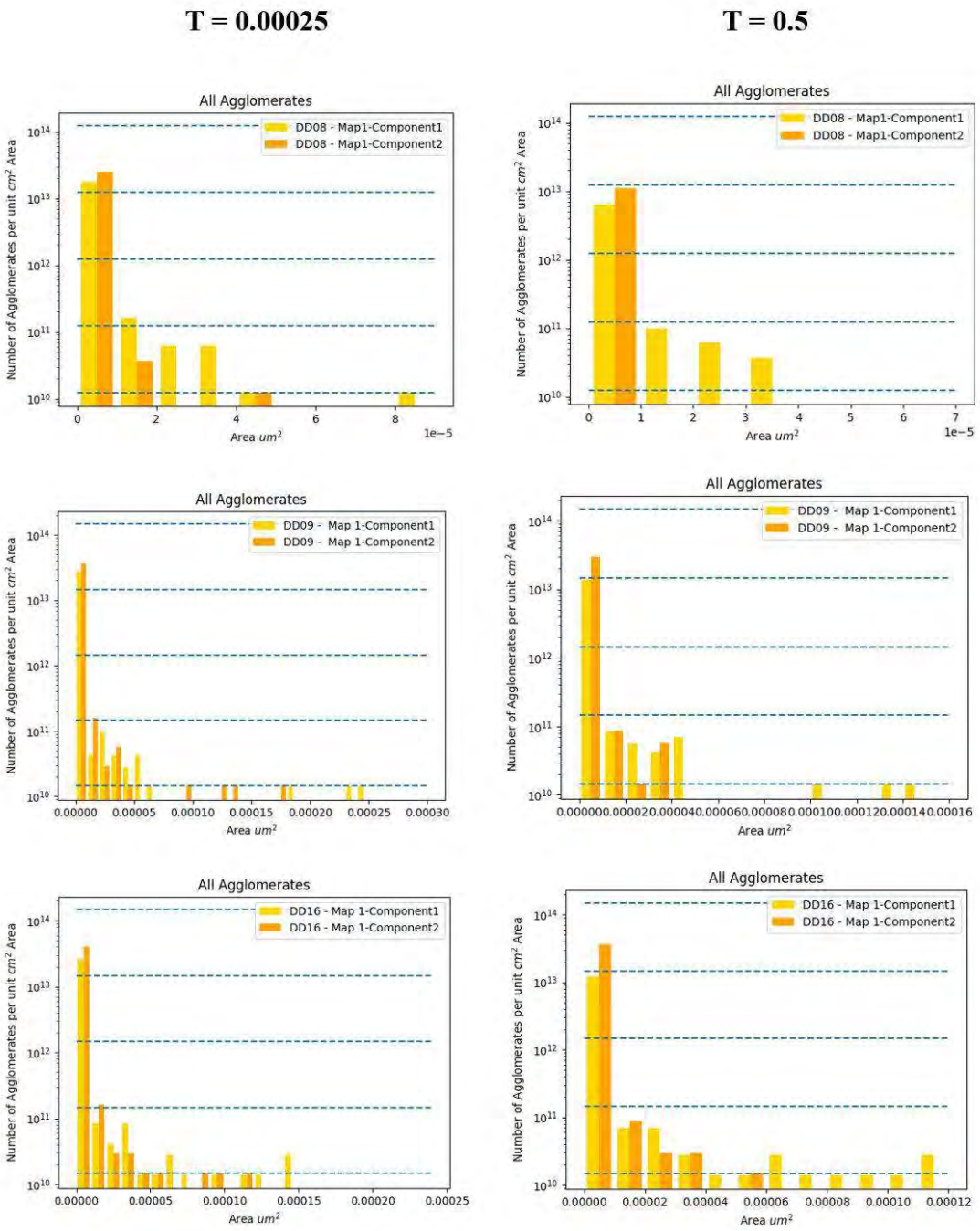

Figure 11: Agglomerate size distribution charts for T = 0.00025 and T = 0.5 map of each sample in Figure 9

All the calculations carried out by the code for the specified threshold values are compiled in Table 2. A graphical representation of average percentage of Pd in contact with Ce (Pd-Ce overlap) for each threshold value and each sample is shown in Figure 12. The analysis of the component overlap presented here is, in the authors' opinion, a novel approach, which has not been reported in the previous literature (38–41).

Samples (T = 0.00025)	Average Pd Area (nm^2)	Average Ce Area (nm^2)	Average Overlap Area (nm^2)
DD08	626	576	164
DD09	655	736	370
DD16	1639	2266	652

Samples (T = 0.5)	Average Pd Area (nm^2)	Average Ce Area (nm^2)	Average Overlap Area (nm^2)
DD08	410	279	55
DD09	481	431	194
DD16	1155	1528	258

Table 2: Computed results for threshold value T = 0.00025 and T = 0.5

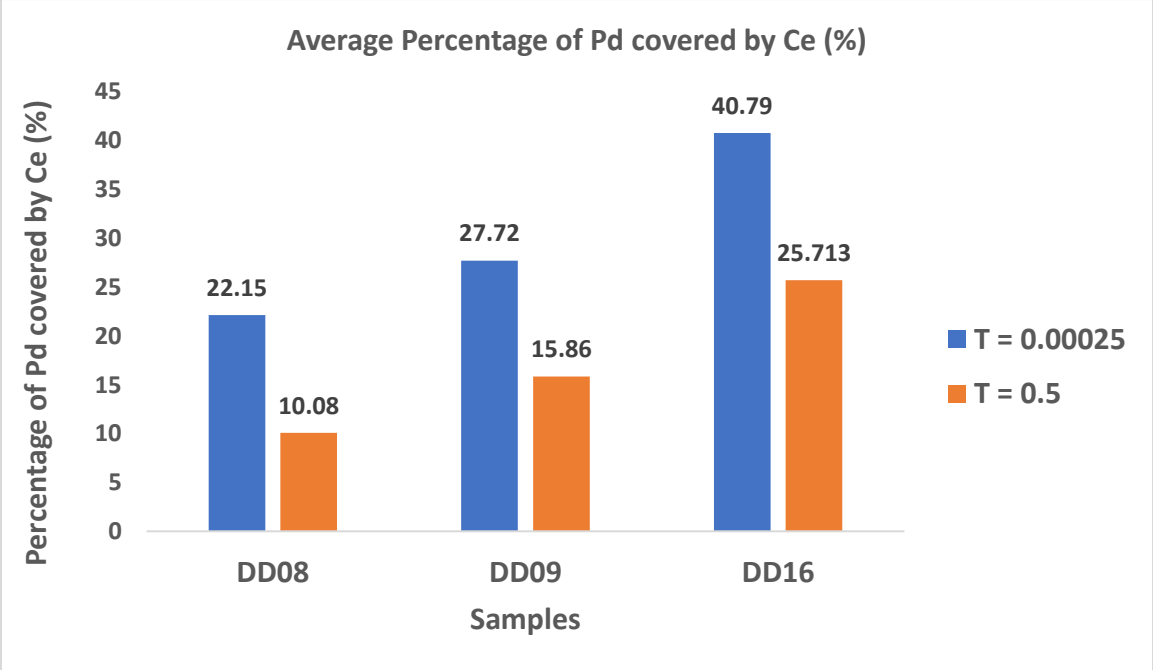

Figure 12: Results for average percentage of Pd covered by Ce by each sample with threshold value of T = 0.00025 and T = 0.5

As evident from the results, sample DD16 shows the highest average Pd area among the rest which also signifies that sample DD16 has relatively larger Pd particles as compared to the other samples. Furthermore, as expected, with increasing concentration of Ce, a considerable increase in Pd area percentage in contact with CeO_x (overlap percentage) can be observed. It can also be inferred that the thresholding value has a very pronounced effect upon all the calculations showing a decrease of about 40-54% in the overlap percentage with the increase in thresholding value from 0.00025 to 0.5. Besides, comparing specific regions of original maps with the thresholded maps and their EDS spectra also represents that maps thresholded with 0.00025 show more signs of inclusion of noise but the maps

thresholded with 0.5 are relatively cleaner and hence can be used to acquire more accurate results.

Generally, most studies involving data processing have computed and reported results based upon the imaging data alone (42–47). On contrary, extraction of microstructural information from STEM in combination with elemental map data from EDS is what gives this method its distinctiveness. Furthermore, automatic computation of agglomerate size distribution and overlap area of the particles has not been reported before, further promoting exclusivity of the developed method.

Conclusion

The data processing framework introduced in this study is a unique, automated, and promising method for an automatic post processing of STEM-EDS data. The code runs pixel by pixel numerical analysis keeping into account distinct particles in the maps which might be overlooked during manual analysis, thus, it can effectively resolve problems associated with extensive and exhaustive analysis of larger data sets. However, it can be concluded that the calculations also depend heavily upon the EDS map processing software used to extract data for the code. The study also points out that the selection of an appropriate threshold value is vital to ensure good precision of results generated by the program. Minor improvements such as automatic selection of local threshold values and optimizing the code to work with more than two components at the same time can help extend the serviceability of the developed script. Furthermore, the code can be tailored to detect and analyze other microstructural features and can be optimized to be used with other formats of materials characterization data. Experimentally derived electrochemical performance data of the samples investigated in this study can be used to verify the accuracy of the developed method. Such information can be of paramount importance to research focusing on improving the efficiency of Pd-CeO_x based catalysts for AEMFCs by relating the overlap area to the electrochemical performance.

Acknowledgements

We are immensely grateful to the U.S. Fulbright Foreign Scholarship program for providing the opportunity and funding to carry out this research work.

References

1. Duval L, Moreaud M, Couprie C, Jeulin D, Talbot H, Angulo J. Image processing for materials characterization: Issues, challenges and opportunities. 2014 IEEE Int Conf Image Process ICIP 2014. 2014;4862–6.
2. Xia D, Song S, Tao L, Qin Z, Wu Z, Gao Z. Journal of Materials Science & Technology Review-material degradation assessed by digital image processing : Fundamentals , progresses , and challenges. J Mater Sci Technol [Internet]. 2020;53:146–62. Available from: https://doi.org/10.1016/j.jmst.2020.04.033
3. Hou Y, Li Q, Zhang C, Lu G, Ye Z, Chen Y, et al. The State-of-the-Art Review on Applications of Intrusive Sensing, Image Processing Techniques, and Machine Learning Methods in Pavement Monitoring and Analysis. Engineering [Internet].

2021;7(6):845–56. Available from: https://doi.org/10.1016/j.eng.2020.07.030
4. Bae SM, Jung HY, Lee JH, Hwang JH. Microstructural characterization of composite electrode materials in solid oxide fuel cells via image processing analysis. J Korean Ceram Soc. 2010;47(1):86–91.
5. Jankovic J, Zhang S, Putz A, Saha MS, Susac D. Multiscale imaging and transport modeling for fuel cell electrodes. J Mater Res. 2019;34(4):579–91.
6. Sabharwal M, Putz AMV, Susac D, Jankovic J, Secanell M. Improving FIB-SEM Reconstructions by Using Epoxy Resin Embedding. ECS Trans. 2017;77(11):1337–49.
7. Sabharwal M, Pant LM, Putz A, Susac D, Jankovic J, Secanell M. Analysis of Catalyst Layer Microstructures: From Imaging to Performance. Fuel Cells. 2016;16(6):734–53.
8. Kumar Boyat A, Kumar Joshi B. Signal & Image Processing. An Int J. 2015;6(2).
9. Patidar P, Gupta M, Srivastava S, Nagawat AK. Image De-noising by Various Filters for Different Noise. Int J Comput Appl. 2010;9(4):45–50.
10. Campbell A, Murray P, Yakushina E, Marshall S, Ion W. New methods for automatic quanti fi cation of microstructural features using digital image processing. Mater Des [Internet]. 2018;141:395–406. Available from: https://doi.org/10.1016/j.matdes.2017.12.049
11. Biswal SR, Sahoo T, Sahoo S. Prediction of grain boundary of a composite microstructure using digital image processing: A comparative study. Mater Today Proc [Internet]. 2021;41:357–62. Available from: https://doi.org/10.1016/j.matpr.2020.09.559
12. Soosai MR, Joshya YC, Kumar RS, Moorthy IG, Karthikumar S, Chi NTL, et al. Versatile image processing technique for fuel science: A review. Sci Total Environ [Internet]. 2021;780:146469. Available from: https://doi.org/10.1016/j.scitotenv.2021.146469
13. Chen Z, Wu X. Research on regional energy efficiency based on GIS technology and image quality processing. J Vis Commun Image Represent [Internet]. 2019;62:410–7. Available from: https://doi.org/10.1016/j.jvcir.2019.06.008
14. Cai W, Wen X, Wang S, Wang L. A real-time detection method of building energy efficiency based on image processing. J Vis Commun Image Represent [Internet]. 2019;60:295–304. Available from: https://doi.org/10.1016/j.jvcir.2019.02.032
15. Salamanca S, Merchán P, Adán A, Pérez E. An appraisal of the geometry and energy efficiency of parabolic trough collectors with laser scanners and image processing. Renew Energy. 2019;134:64–77.
16. Shin HS, Kwon OJ, Oh BS. Correlation between performance of polymer electrolyte membrane fuel cell and degradation of the carbon support in the membrane electrode assembly using image processing method. Int J Hydrogen Energy [Internet]. 2018;43(45):20921–30. Available from: https://doi.org/10.1016/j.ijhydene.2018.09.016
17. Klingele M, Zengerle R, Thiele S. Quantification of artifacts in scanning electron microscopy tomography: Improving the reliability of calculated transport parameters in energy applications such as fuel cell and battery electrodes. J Power Sources [Internet]. 2015;275:852–9. Available from: http://dx.doi.org/10.1016/j.jpowsour.2014.11.053
18. Cetinbas FC, Ahluwalia RK, Kariuki N, De Andrade V, Fongalland D, Smith L, et al. Hybrid approach combining multiple characterization techniques and simulations for microstructural analysis of proton exchange membrane fuel cell

electrodes. J Power Sources [Internet]. 2017;344:62–73. Available from: http://dx.doi.org/10.1016/j.jpowsour.2017.01.104
19. Muto H, Shimada A, Kaneko T, Erdman N, Nielsen C. SEM-EDS Automated Particles Analysis— " INCA Mineral " — Mineral Compositions of Koujaku Granite and Hakkoda Pyroclastic Flow Deposition. J Geol Soc Japan Earth Sci (Chikyu Kagaku) J Geogr. 1972;78(1):2–3.
20. Anderhalt R, Swenson L. Applications for Automated Particle Analysis. Micros Today. 2006;14(5):22–7.
21. Lang C, Hiscock M. Automated Analysis of EDS Maps. Microsc Microanal. 2016;22(S3):122–3.
22. Information P. ZEISS SmartPI Your Automated SEM Particle Analysis and Classification Solution Detect , Analyze and Classify Particles. :1–19.
23. Note A. ZEISS SmartPI Automated Identification of Asbestos ZEISS SmartPI Automated Identification of Asbestos.
24. Scimeca M, Bischetti S, Bonanno E. Energy Dispersive X-ray (EDX) Microanalysis in Biomedical Research. Lett Heal Biol Sci. 2016;1(1):10–1.
25. Jany BR, Janas A, Krok F. Automatic microscopic image analysis by moving window local Fourier Transform and Machine Learning. Micron [Internet]. 2020;130(July 2019):102800. Available from: https://doi.org/10.1016/j.micron.2019.102800
26. Biswas S. Automated Asbestos Analysis using Semantic Segmentation. 2020;(March).
27. Zhang J, Zhu W, Huang T, Zheng C, Pei Y, Shen G, et al. Recent Insights on Catalyst Layers for Anion Exchange Membrane Fuel Cells. Adv Sci. 2021;2100284:1–26.
28. Cao Y, Ran R, Wu X, Zhao B, Wan J, Weng D. Comparative study of ageing condition effects on Pd/Ce0.5Zr 0.5O2 and Pd/Al2O3 catalysts: Catalytic activity, palladium nanoparticle structure and Pd-support interaction. Appl Catal A Gen. 2013;457:52–61.
29. Kolli T, Rahkamaa-Tolonen K, Lassi U, Savimäki A, Keiski RL. Comparison of catalytic activity and selectivity of Pd/(OSC + Al 2O3) and (Pd + OSC)/Al2O3 catalysts. Catal Today. 2005;100(3–4):297–302.
30. Darija S et al. Towards Understanding of the Anode Catalyst Layer Structure for Extended Reversal Tolerance: An Advanced Characterization Approach. ECS Meet Abstr [Internet]. 2016;MA2016-02(2593). Available from: http://dx.doi.org/10.1149/MA2016-02/38/2593
31. Singh RK, Davydova ES, Douglin J, Godoy AO, Tan H, Bellini M, et al. Synthesis of CeOx-Decorated Pd/C Catalysts by Controlled Surface Reactions for Hydrogen Oxidation in Anion Exchange Membrane Fuel Cells. Adv Funct Mater. 2020;30(38).
32. Hoang ND. Detection of Surface Crack in Building Structures Using Image Processing Technique with an Improved Otsu Method for Image Thresholding. Adv Civ Eng. 2018;2018.
33. Salman N. Image Segmentation Based on Watershed and Edge Detection Techniques. Int Arab J Inf Technol. 2006;3(2):104–10.
34. Stuckner J, Frei K, McCue I, Demkowicz MJ, Murayama M. AQUAMI: An open source Python package and GUI for the automatic quantitative analysis of morphologically complex multiphase materials. Comput Mater Sci [Internet]. 2017;139:320–9. Available from:

http://dx.doi.org/10.1016/j.commatsci.2017.08.012
35. Bourrous S, Ribeyre Q, Lintis L, Yon J, Bau S, Thomas D, et al. A semi-automatic analysis tool for the determination of primary particle size, overlap coefficient and specific surface area of nanoparticles aggregates. J Aerosol Sci [Internet]. 2018;126(September):122–32. Available from: https://doi.org/10.1016/j.jaerosci.2018.09.001
36. Filho PPR, Da Silveira Cavalcante T, De Albuquerque VHC, Tavares JMRS. Brinell and Vickers hardness measurement using image processing and analysis techniques. J Test Eval. 2010;38(1).
37. Garrido I, Lagüela S, Sfarra S, Madruga FJ, Arias P. Automatic detection of moistures in different construction materials from thermographic images. J Therm Anal Calorim. 2019;138(2):1649–68.
38. White RT, Wu A, Najm M, Orfino FP, Dutta M, Kjeang E. 4D in situ visualization of electrode morphology changes during accelerated degradation in fuel cells by X-ray computed tomography. J Power Sources. 2017;350:94–102.
39. Xu H, Bührer M, Marone F, Schmidt TJ, Büchi FN, Eller J. Optimal Image Denoising for In Situ X-ray Tomographic Microscopy of Liquid Water in Gas Diffusion Layers of Polymer Electrolyte Fuel Cells. J Electrochem Soc. 2020;167(10):104505.
40. Satija R, Jacobson DL, Arif M, Werner SA. In situ neutron imaging technique for evaluation of water management systems in operating PEM fuel cells. J Power Sources. 2004;129(2):238–45.
41. Kneer A, Jankovic J, Susac D, Putz A, Wagner N, Sabharwal M, et al. Correlation of Changes in Electrochemical and Structural Parameters due to Voltage Cycling Induced Degradation in PEM Fuel Cells. J Electrochem Soc. 2018;165(6):F3241–50.
42. Codaro EN, Nakazato RZ, Horovistiz AL, Ribeiro LMF, Ribeiro RB, Hein LRO. An image processing method for morphology characterization and pitting corrosion evaluation. Mater Sci Eng A. 2002;334(1–2):298–306.
43. Bescond A, Yon J, Ouf FX, Ferry D, Delhaye D, Gaffié D, et al. Automated determination of aggregate primary particle size distribution by tem image analysis: Application to soot. Aerosol Sci Technol. 2014;48(8):831–41.
44. Bessa IS, Castelo Branco VTF, Soares JB. Evaluation of different digital image processing software for aggregates and hot mix asphalt characterizations. Constr Build Mater [Internet]. 2012;37:370–8. Available from: http://dx.doi.org/10.1016/j.conbuildmat.2012.07.051
45. Scozzafava A, Tomesani L, Zucchelli A. Image analysis automation of spheroidal cast iron. J Mater Process Technol. 2004;153–154(1–3):853–9.
46. Sochan A, Zieliński P, Bieganowski A. Selection of shape parameters that differentiate sand grains, based on the automatic analysis of two-dimensional images. Sediment Geol. 2015;327:14–20.
47. Liu C, Shi B, Zhou J, Tang C. Quantification and characterization of microporosity by image processing, geometric measurement and statistical methods: Application on SEM images of clay materials. Appl Clay Sci [Internet]. 2011;54(1):97–106. Available from: http://dx.doi.org/10.1016/j.clay.2011.07.022

Chapter 5

Poster Session

ECS Transactions, 104 (8) 157-160 (2021)
10.1149/10408.0157ecst ©The Electrochemical Society

Pore Network Modeling of Hydrophilic / Hydrophobic Composite Microporous Layers for Polymer Electrolyte Fuel Cells

Shintaro Iwasaki[a], Hironori Nakajima[a, b], and Tatsumi Kitahara[a, b]

[a] Department of Hydrogen Energy Systems, Graduate School of Engineering, Kyushu University, 744 Motooka, Nishi-ku, Fukuoka 819-0395, Japan
[b] Department of Mechanical Engineering, Faculty of Engineering, Kyushu University, 744 Motooka, Nishi-ku, Fukuoka 819-0395, Japan

Liquid water accumulated in the catalyst layer (CL) and gas diffusion layer (GDL) of a polymer electrolyte fuel cell (PEFC, PEMFC) results in performance deterioration due to the inhibition of oxygen transport to the cathode CL (Flooding). To enhance the drainage in the GDL, a microporous layer (MPL) employed at the CL side of the GDL substrate is effective. Hydrophilic/hydrophobic composite MPLs in-house applied have mitigated the flooding, while the mechanism was not well clarified. A pore network model (PNM) of our in-house hydrophobic MPLs is modified for the analysis of the composite MPL.

Introduction

One of the technical problems of polymer electrolyte fuel cells is the flooding phenomenon that the product water accumulates in the catalyst layer (CL), Gas diffusion layer (GDL), and flow channels, which hinders the supply of oxygen to the CL. Many studies have reported that hydrophobic microporous layer (MPL) coated GDL improves the flooding in PEFCs (1, 2). So far, we have developed hydrophilic / hydrophobic composite MPLs (3, 4), in which carbon nanotubes (CNTs) with surface modification by an oxidation treatment to give high hydrophilicity was introduced. We showed that the hydrophilic / hydrophobic composite MPL improves the flooding compared with the conventional hydrophobic MPLs (4). However, the mechanism was not clarified well. In this study, we investigate the mechanism of hydrophilic / hydrophobic composite MPL by using a pore network model (PNM) (5, 6) for gas-liquid transport.

Numerical Modeling

In a hydrophobic pore, the contact angle, θ, is larger than 90 degrees between air and water with the surface tension, γ, so that the capillary pressure and outer water pressure are in a balanced relationship as presented in Fig. 1. In contrast, in a hydrophilic pore, the contact angle is smaller than 90 degrees, so that the pores are always filled with liquid water (Fig. 1). Thus, by combining gas-liquid two-phase transport in hydrophobic pores and liquid water single-phase transport in hydrophilic pores, the transport rates of water and oxygen in the hydrophilic / hydrophobic composite MPL are calculated as presented in Table I, where the volumetric ratio of the hydrophilic pores, X %, is introduced.

A PNM of a hydrophobic MPL having a thickness of 60 μm and a maximum pore diameter of 5 μm is adopted for the hydrophobic and hydrophilic pores (7, 8). An equivalent capillary pressure to a liquid water saturation is employed to establish the saturation in the PNM for the hydrophobic pores. However, this saturation can result from liquid water condensation in an actual cell (9). On the other hand, liquid saturation of unity is applied to the hydrophilic pores. For the estimation of the limiting current densities, we compare the viscous liquid water transport rates and diffusive oxygen transport rates determined at varying saturations by the PNM. Then we find saturations that obey the relation between the water production rate (g/s) and oxygen consumption rate (g/s) with their molecular weights, M, $Q_{\mathrm{w}} = (2M_{\mathrm{H2O}}/M_{\mathrm{O2}})\ Q_{\mathrm{O2}}$, for zero oxygen concentration at the CL side. Thereby a limiting current density is derived at a saturation for a pressure loss for the viscous liquid water transport and a volumetric ratio of the hydrophilic pore.

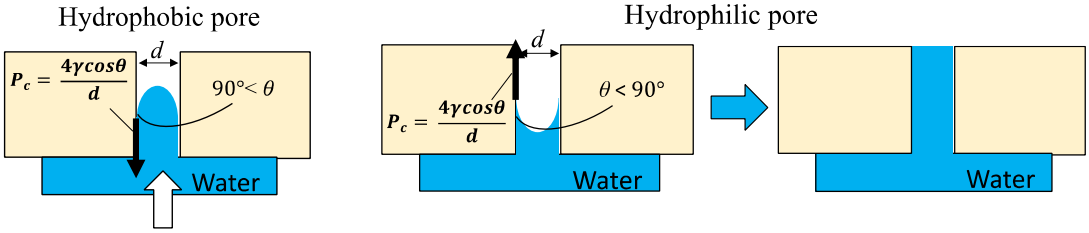

Figure 1. Water intrusion in the hydrophobic and hydrophilic pores.

TABLE I. Numerical calculation for hydrophobic and hydrophilic MPLs.

	Hydrophobic MPL ($90° < \theta$)	**Hydrophilic MPL ($\theta < 90°$)**	**Composite MPL (Hydrophilicity ratio is X%)**
Water transport rate Q_{w}	Gas and liquid Hagen-Poiseuille equation, Q_{dry}	Only liquid Hagen-Poiseuille equation, Q_{wet}	$Q_{\mathrm{w}} = \frac{(100-X)}{100} Q_{\mathrm{dry}} + \frac{X}{100} Q_{\mathrm{wet}}$
Oxygen transport rate Q_{O2}	Gas and liquid Fick's law, Q_{dry}	Only liquid 0	$Q_{\mathrm{O2}} = \frac{(100-X)}{100} Q_{\mathrm{dry}}$

Results and Discussion

Figure 2 represents the relation among the volumetric ratio of the hydrophilic pore, the pressure loss for the viscous water transport, and the limiting current density. The limiting current density increase with a decrease in the volumetric ratio of the hydrophilic pore, and with an increase in the pressure loss. A decrease in the liquid water saturation of the MPL improves the diffusion transport of oxygen and increases the limiting current density. Figure 3 illustrates the relation among the volumetric ratio of the hydrophilic pore, the pressure loss for the viscous water transport, and the liquid water saturation. It can be seen that the increase in the limiting current density in Fig. 2 is in accordance with a decrease in the saturation level in Fig. 3.

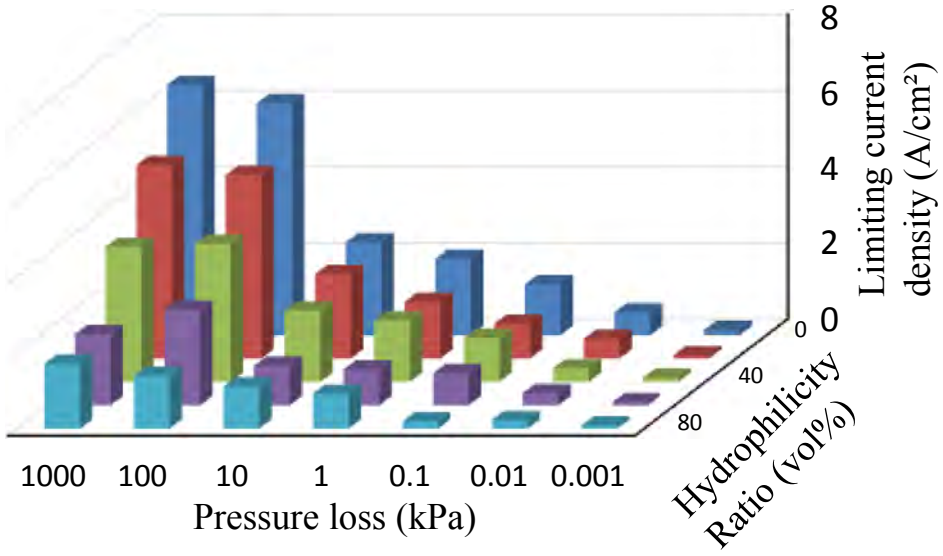

Figure 2. Relation among the limiting current density, volumetric ratio of hydrophilic pore, and pressure loss.

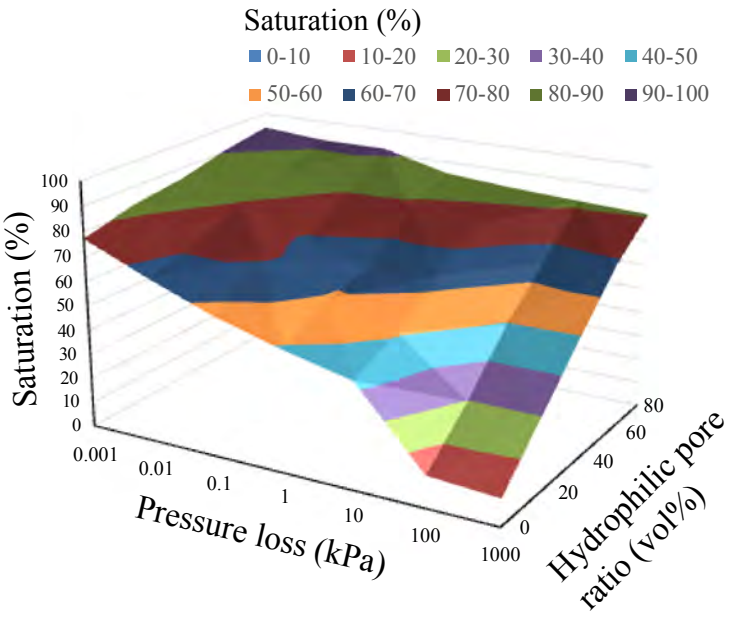

Figure 3. Relation among saturation, the volumetric ratio of hydrophilic pore, and pressure loss.

In addition, we compare the PNM with experimental limiting current densities for the hydrophilic / hydrophobic composite MPLs containing CNTs of 0wt%, 2wt%, 4wt%, and 8wt% at 200%RH, 1.00 NL/min air flow rate, and 35°C (4). The composite MPL having a maximum pore diameter of 5 μm was composed of carbon black (80wt%), CNTs (10-15 nm diameter, 1-5 μm length, and 30 degrees contact angle) with the surface hydrophilic modification, and PTFE (20wt%). Because the experimental limiting current density increased in the order of the CNTs of 0wt% (1.1 A/cm^2), 2wt% (1.5 A/cm^2), 8wt% (1.9 A/cm^2), 4wt% (2.0 A/cm^2) (4), the hydrophilic material improves the limiting current density up to an optimal mixing ratio. The trend of this relationship between the

CNT ratio and the limiting current density is compared with that between the volumetric ratio of the hydrophilic pore and limiting current density in Fig. 2.

Although the maximum limiting current density for the composite MPL was reported to be 2.0 A/cm^2 with the CNTs of 4wt%, the limiting current densities above 2.0 A/cm^2 are obtained in Fig. 2 by the PNM. Thus, there is possibly a limitation of an increase in the limiting current density and decrease in the liquid water saturation in the actual composite MPL depending on the saturation in the CL and the MPL-CL interface. Therefore, in the future, we will develop a coupled PNM of the composite MPL and CL.

Conclusions

By using the PNM, we investigated the two-phase transport for the hydrophilic / hydrophobic composite MPL. As a result, we obtained the following conclusions.

(1) The limiting current density increases with a decrease in the volumetric ratio of the hydrophilic pore, and with an increase in the pressure loss. A decrease in the liquid water saturation of the MPL improved the diffusion transport of oxygen and increased the limiting current density.

(2) There is a limit to the minimum of the liquid water saturation in MPL possibly depending on the saturation in the CL and MPL-CL interface. Thus, the development of a coupled PNM of the composite MPL and CL is our future work.

Acknowledgments

Thanks are offered to Professor Kohei Ito of Kyushu University for valuable discussions.

References

1. H. Nakajima, T. Konomi, and T. Kitahara, *J. Power Sources*, **171**, 457 (2007).
2. T. Kitahara, T. Konomi, and H. Nakajima, *J. Power Sources*, **195**, 2202 (2010).
3. T. Kitahara and H. Nakajima, *Int. J. Hydrogen Energy*, **41**, 9547 (2016).
4. T. Kitahara, H. Nakajima, and K. Okamura, *J. Power Sources*, **283**, 115 (2015).
5. J. Gostick, M. Aghighi, J. Hinebaugh, T. Tranter, M.A. Hoeh, H. Day, B. Spellacy, M.H. Sharqawy, A. Bazylak, A. Burns, W. Lehnert, and A. Putz, *Comput. Sci. Eng.*, **18**, 60 (2016).
6. http://openpnm.org/. Accessed on July 14 (2021).
7. S. Iwasaki, H. Nakajima, and T. Kitahara, *ECS Meeting Abst.*, **MA2020-02**, 3841 (2020).
8. H. Nakajima, S. Iwasaki, and T. Kitahara, *ECS Trans.*, in press (2021).
9. S. Kato, S. Yamaguchi, W. Yoshimune, Y. Matsuoka, A. Kato, Y. Nagai, and T. Suzuki, *Electrochem. Commun.*, **111**, 106644 (2020).

Chapter 6

Catalyst Layer 1

ECS Transactions, 104 (8) 163-171 (2021)
10.1149/10408.0163ecst ©The Electrochemical Society

Improvement of Multilayer Applying Method for Catalyst Layer of PEFC Using Inkjet Coating Printer

I. Otake and K. Sugiura

Osaka Prefecture University College of Technology
26-12 Saiwai-cho, Neyagawa, Osaka, 5728572, Japan

Polymer electrolyte fuel cells are expected to be widly used as clean energy source. Generally, because a catalyst layer of the membrane electrode assembly in PEFC is manufactured by a doctor blade method, it has problems such as a bad dispersibility of Pt catalyst and a difficult thickness control in precisely. Our laboratory proposes applying an inkjet coating printing to the CL manufacturing process to solve these problems. Because the CL applied by an inkjet coating printing is extremely thin, a multilayer applying is necessary to obtain enough thickness. However, the cell performance of CL composed of a multilayer was lower than that of single layer. The reason was to have obstructed the electron transport property by separating ionomer and Pt in the catalyst ink. The cell performance has been enhanced by the formation of the CL where I/C ratio was changed from GDL to the direction of the membrane.

Introduction

Today, switching over to decarbonized and sustainable society is hoped worldwide. In Japan, hydrogen is attracting as a new energy resource that can be used to eliminate nuclear power, and development is underway in various fields to realize a hydrogen society. The polymer electrolyte fuel cell (PEFC) has been attracting as a device to generate electricity directly from hydrogen, and is expected to be widely spread in society because it does not emit greenhouse gases during power generation, can be easily downsized, and can achieve high thermal efficiency by co-generation. In order to further promotion of PEFC, reducing the amount of using Pt is essential while maintaining and improving the cell performance of PEFC. The doctor blade method, which is general MEA fabrication method, has been found to have the following problems: (A) thickness of the catalyst layer (CL) is difficult to control in precisely, (B) dispersion of the Pt catalyst and ionomer in the CL is poor, and (C) a large amount of catalyst slurry is disposed of during the MEA fabrication process. In order to reduce the amount of Pt catalyst while maintaining performance, applying inkjet coating method (IJP method) have been studying recently (1-4). Although the IJP method can produce thin CLs, stacked CLs is necessary to secure a certain layer thickness to prevent gas cross leakage (1). However, our previous research has confirmed that the performance of the MEA with stacked CL was lower than that of the MEA with single CL. In order to verify the reason for this, this paper aimed to examine the ink components used during CL layering and examine the effect of the additive amount of ionomer on cell performance.

Experimental Apparatus and Methods

Manufacturing Method of MEA

The catalyst ink is composed of Pt catalyst (TEC10V40E, 38.0wt% Pt/CB, Tanaka Kikinzoku Kogyo), pure water, ethanol, and Nafion® solution (DE2021CS, 20%Nafion dispersion, Wako Pure Chemical Industries). TABLE I shows the composition of the inks in mainly used ionomer/catalyst ratio (I/C ratio). These were mixed in a screw vial and was stirred by a rotor for 12 h. Before printing, the solid materials in the catalyst ink were dispersed by 20 W of a homogenizer for 180 s, and it was degassed by a vacuum stir machine for 5 min.

In this experiment, the Micro Jet Labojet-500 with a piezo-electric type exhaling device was used as an inkjet printer. The catalyst ink was discharged by the pressure wave caused by contraction and expansion. In inkjet parameters, the drive voltage was 34 V, the 1st pulse width was 100 µs, frequency was set to 100 Hz and the ink ejection speed was set to about 6 m/s.

TABLE I. Catalyst ink composition corresponding to I/C ratio.

Item	I/C = 1/3	I/C = 2/3	I/C = 3/3 (Standard)	I/C = 4/3
TEC10V40E 38.0wt% Pt/CB [g]	0.50	0.50	0.50	0.5
Pure water [g]	8.02	7.51	7.00	6.49
Ethanol [g]	2.75	2.75	2.75	2.75
DE2021CS, 20%Nafion dispersion [g]	0.51	1.02	1.53	2.04

The CLs were applied to the micro porous layer (MPL) side of the gas diffusion layer (GDL22BB, SGL group) cut out to 3 cm × 3 cm. The inkjet program used is shown in Fig.1 (a). This inkjet program was set to a pitch of 200 µm. In the first coating process, only point 1 is coated every 200 µm, and the same process is repeated three times in the order of point 2, point 3 and point 4 to complete one catalyst layer. The program then discharged the third and fourth layers in turn. In this program, droplet agglomeration can be suppressed than uniformly discharging at a pitch of 100 µm. As a result, CL was generally applied evenly though there were small cracks on the CL surface as shown in Fig. 1 (b). Finally, a membrane (Nafion® NRE-212, Sigma-Aldrich) was placed between the two CLs, and attached to the GDLs with a hot press at 123°C and 8 MPa for 5 min.

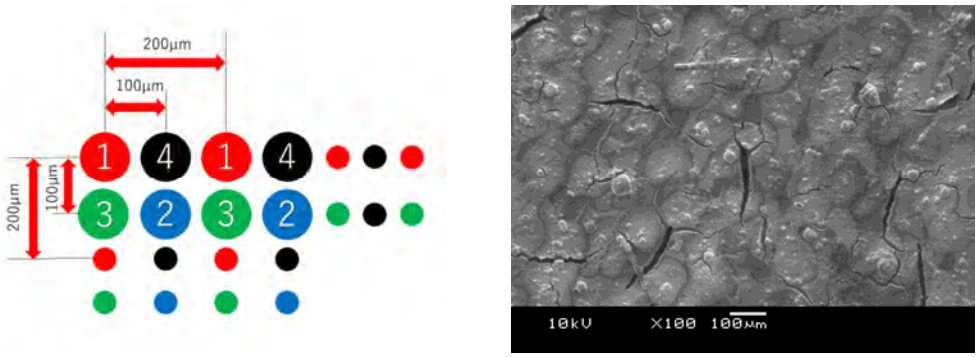

(a) Schematic diagram of inkjet program (b) SEM image of catalyst layer surface

Figure 1. Drawing pattern of inkjet program and SEM image of CL surface.

Experimental Apparatus

Figure 2 shows the configuration of the cell that evaluates the 3 cm × 3 cm MEA. As shown in this figure, the evaluation cell had a structure in which the MEA was sandwiched between a separator and an end plate. A gas channel on the separator was a serpentine channel with a size of 1.8 mm^W × 1.2 mm^D and a rib width of 1mm.

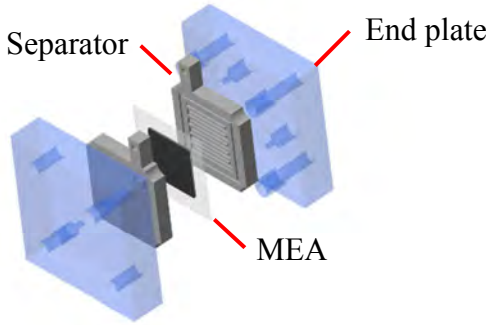

Figure 2. Schematic diagram of cell structure of 3 cm × 3 cm.

Figure 3 shows the schematic diagram of the experimental apparatus. The cell performance was evaluated by I-V characteristic curve and Cole-Cole plot using an impedance meter for fuel cells (KFM2030, Kikusui Electronics Corp.). The experimental conditions and humidification conditions are shown in TABLE II. The catalyst layer structure was evaluated with and without humidification, and especially since the ionomer content was changed in the thickness direction in this study, we consider that the behavior of the ionomer can be confirmed with or without humidification.

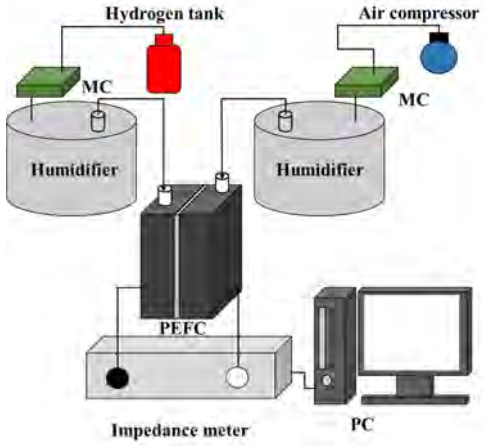

Figure 3. Schematic diagram of experimental apparatus.

TABLE II. Experimental conditions for fuel cell operation.

Item	Standard Conditions	Advanced Conditions
Quantity (H_2/Air) [ml/min]	38.4/160.2 (70%/40%)	38.4/160.2 (70%/40%)
Gas Temperature [℃]	80	20
Gas Humidity [%RH]	100	H_2:0, Air:0.5~0.7
Cell Temperature [℃]	80	20
Operating pressure [kPa]	101.3	101.3

Experimental Parameters

Examination of I/C Ratio in the Direction of CL Thickness

Figure 4 shows the SEM image of the ionomer aggregated on the catalyst surface. The degradation of cell performance due to the stacking of CLs was attributed to the separation of Pt catalyst and ionomer during the drying process of the catalyst ink, consequently the formation of only ionomer layer. The presence of this ionomer-only layer inhibits electron transport and degrades performance. In order to improve this problem, an MEA with a gradation CL in which I/C ratio gradually increased by gradually increasing the amount of ionomer added from GDL side to the membrane side was fabricated as shown in Fig. 5 and TABLE III.

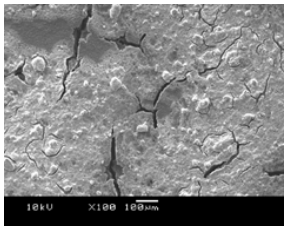

Figure 4. Aggregated ionomer.

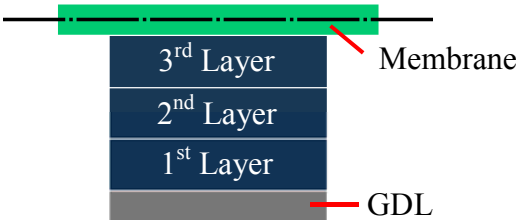

Figure 5. Schematic diagram of CL stacking.

TABLE III. I / C ratio of each layer.

Layer Number	I/C Ratio
1st Layer	1/3
2nd Layer	2/3
3rd Layer	3/3

Influence of the Amount of Ionomer Added on Cell Performance

The ionomers used in catalyst ink consist of a hydrophobic Teflon backbone and sulfonic acid groups. If an excessive amount of ionomer is added to a Pt catalyst, the ionomer will aggregate at or near the air-liquid interface of the ink due to hydrophobic interactions. Excessive ionomer addition has also been reported to clog the primary and secondary pores of the catalyst (5). Since it has been reported that the aggregation of Pt catalyst and ionomer depends on the amount of ethanol and water added (6), we conducted experiments to evaluate the performance of different amounts of ionomer in catalytic inks tailored for inkjet applications. Here, to focus on the effect of I/C ratio on the performance, only one catalyst layer was applied.

Influence of I/C Ratio Distribution in CL Thickness Direction on Cell Performance

In order to investigate the influence of I/C ratio distribution in CL thickness direction on the cell performance, two new combinations of catalyst layers with different I/C ratios in each layer were manufactured and evaluated as cells as shown in TABLE IV. Here, Gradation A is a model in which the amount of ionomer in each CL is reduced from the membrane side to the GDL side (Same as the previous section). Gradation B is a model with an increased amount of ionomer in the CL on the GDL side, and Gradation C is a model in which a thin ionomer layer is placed between each CL layer.

TABLE IV. Combinations of catalyst layers with different I/C ratios in each layer.

Layer Number	I/C (Gradation A)	I/C (Gradation B)	I/C (Gradation C)
1st Layer	1/3	2/3	2/3
2nd Layer	2/3	2/3	2/3
3rd Layer	3/3	3/3	2/3

Results and Discussion

Examination of I/C Ratio in the Direction of CL Thickness

Figure 6(a) and (b) show a comparison of the I-V characteristics and Cole-Cole plot of the MEAs with gradation 3CLs under standard experimental conditions. This figure shows that the cell voltage of the MEA with the gradation 3CLs is higher than that of the MEA with normal 3CLs and the MEA with a single CL in all of current density range, and the polarization resistance is 70 mΩ, which is about 25 mΩ lower than the 95 mΩ of the MEA with normal 3CLs. Generally, the polarization resistance is composed of the proton conduction resistance, the reaction resistance (ORR) and the gas diffusion resistance. If the mixing ratio of the Pt catalyst/ionomer mixed layer is the same, this performance difference is related to the ratio of the ionomer layer to the mixed layer separated during the drying process. As shown in Fig. 7(a), in the MEA with normal 3CLs, as three layers are stacked with the state of the separation of Pt catalyst ionomer, it consists of alternating layers of ionomer layer and Pt catalyst/ionomer mixture layer. The layer of only ionomers interfere with the electron transport from the Pt/ionomer mixed layer, which is located inside the ionomer layer, and deteriorate the cell performance. Therefore, the layer of only ionomers outside the Pt catalyst/ionomer mixed layer should be removed. On the other hand, as shown in Fig. 7(b), in the MEA with gradation 3CLs, as the layer of only ionomers on the outside didn't exist, electron transports smoothly from the GDL to the cathode electrode and from the anode electrode to the GDL, the cell performance is improved. However, the ohmic resistances of the three catalyst layers are different, it is possible that the ohmic resistance relates to the ionomer content.

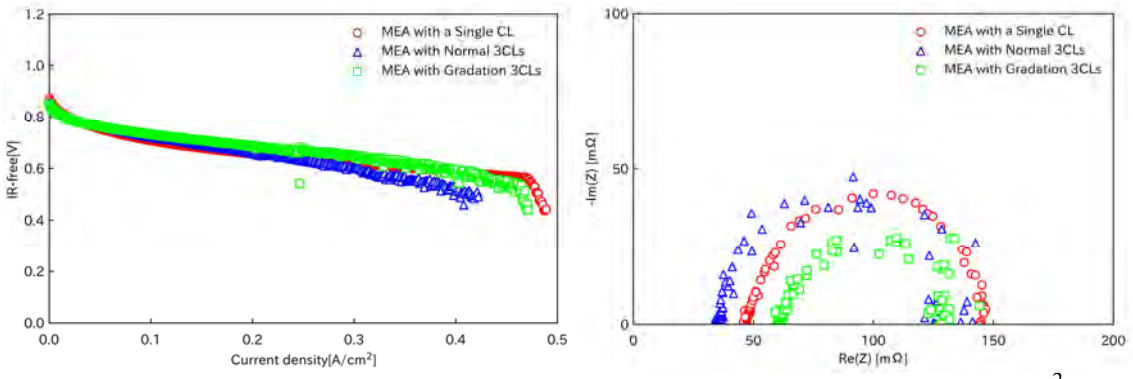

(a) I-V performance (b) Cole-Cole plot (0.1[A/cm^2])

Figure 6. Influence of catalyst layer stacking method on cell performance.

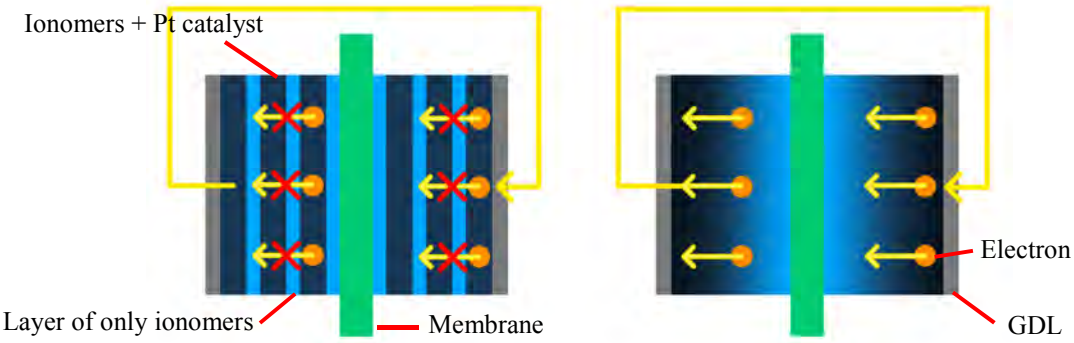

Figure 7. Schematic diagram of an electronic transport.

Influence of the Amount of Ionomer Added on Cell Performance

Figure 8(a) and (b) show a comparison of I-V characteristics and Cole-Cole plot of the MEAs with various I/C ratios under standard experimental conditions. From Fig. 8(a), in the current density range up to 0.4 A/cm^2, although the performances of the MEAs with 2/3 and 3/3 of I/C ratio hardly change, that of the MEAs with 4/3 of I/C ratio is greatly worse. Since these differences are largely reflected in the Cole-Cole plots, the ohmic resistance and activation resistance are extracted and rearranged them as shown in Fig. 9. The ohmic resistance, which indicates the proton transfer resistance of the membrane, strongly depends on the amount of ionomer added to the CL, and is smallest when I/C ratio is 2/3 as shown in Fig. 9 (a). Since the I/C ratio is set by changing the amount of ionomer while keeping the amount of platinum fixed, the thickness of CL increases with the increase of I/C ratio, and the ionomer layer also increases. Since this ionomer layer is connected to the membrane, the membrane is thickened by the ionomer layer. Therefore, the ohmic resistance increases when I/C ratio exceeds 2/3. Oppositely, we consider that the ionomer content in the Pt catalyst/ionomer mixed layer decreases when I/C ratio becomes 2/3 or less, the interface resistance between the membrane and CL increases, and consequently the ohmic resistance increases. On the other hand, the polarization resistance increases gradually when I/C ratio exceeds 2/3, it increases drastically when I/C ratio exceeds 3/3. When the ionomer in the CL is insufficient, although the proton conduction resistance in the CL is almost unaffected, that of the membrane (ohmic resistance) is affected. Oppositely, if the CL contains an excess of ionomer, the percentage of the ionomer-only layer increases and the ionomer in the Pt catalyst /ionomer mixed layer also increases as shown in Fig. 10. As this ionomer layer cannot transport electron, the electron transport resistance in the CL increases. Moreover, the excessive ionomer begins to submerge the platinum catalyst by retaining excess water under standard conditions, and flooding phenomenon occurs when I/C ratio exceeds 1. Consequently, the cell performance is deteriorated by increasing a diffusion polarization. Therefore, when I/C ratio exceeds 1, the cell performance is greatly deteriorated due to the increase of the ohmic resistance, the electron transport resistance and gas diffusion resistance.

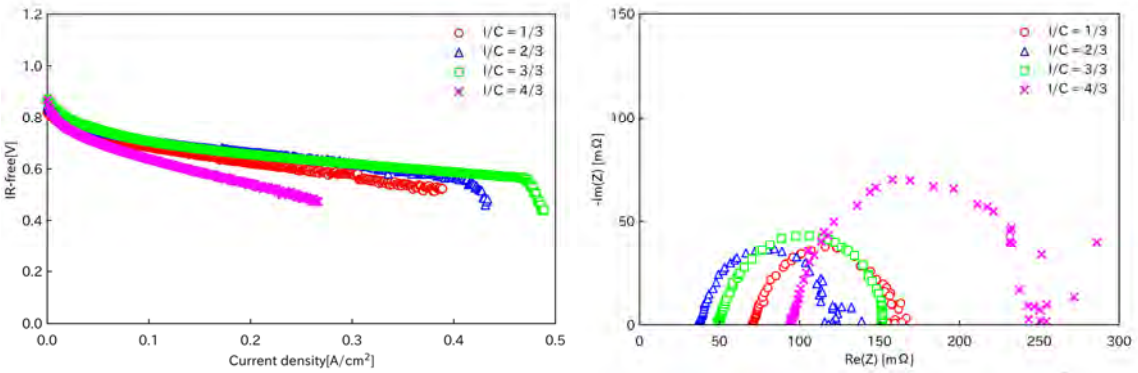

(a) I-V performance (b) Cole-Cole plot (0.1[A/cm^2])

Figure 8. Influence of ionomer addition amount on cell performance.

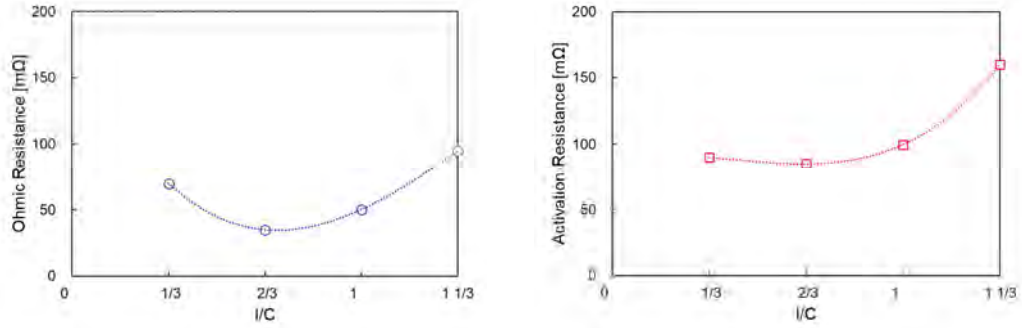

(a) ohmic resistance (b) activation resistance

Figure 9. Influence of I/C ratio on ohmic and polarization resistances.

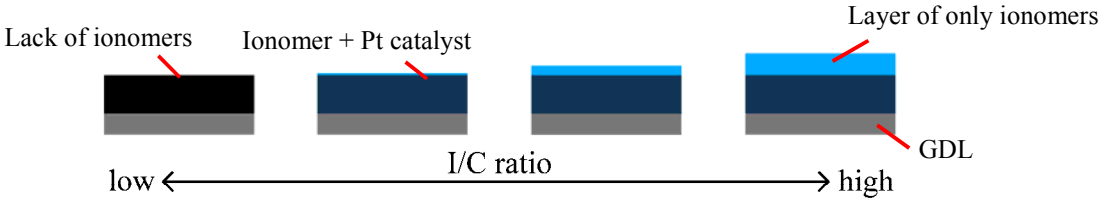

Figure 10. Influence of I/C ratio change on catalyst layer formation.

Influence of I/C Ratio Distribution in CL Thickness Direction on Cell Performance

Figure 11 shows the influence of I/C ratio distribution in CL thickness direction on the cell performance under advanced experimental conditions. Although the ohmic resistances of all cells are almost the same, the voltage of Gradation B is lower than that of Gradation A in all current density region, and the polarization resistance has deteriorated from 100 mΩ to 130 mΩ. As shown in Figure 12, the layer of only ionomer in the CL close to the gas flow path in Gradation B compared to Gradation A inhibits the electron transfer. From Fig. 11 (a), Gradation C composed of only 2/3of I/C ratio has a lower voltage than Gradation A and B in all current density region, and the polarization resistance is 130 mΩ as same as Gradation B as shown in Fig. 11 (b). However, since the arc diverges in the low frequency region, it is clear that the diffusion polarization on the cathode side increases. On Gradation C, as I/C ratio of the CL on the GDL is 2/3, proton

cannot through at the interface smoothly since the interface with the GDL is not an ionomer layer but a mixed layer of Pt catalyst and ionomer. Moreover, since there is enough ionomer in each CL and a thin ionomer layer at each CL interface, there is excess ionomer in the entire catalyst layer. Consequently, even under non-humidified and non-heated conditions, flooding is caused by which a lot of ionomer in the catalyst layer retain water generated by the cell reaction. Especially, because water formed like film at the interface between GDL and the 1st CL prevents the diffusion of the cathode gas, the diffusion polarization increases furthermore, and the cell performance is deteriorated drastically.

These results indicate that ionomer with proton conductive not only causes flooding phenomena but also fail to transport electrons, depending on the amount of ionomer added and the humidified operating conditions. Therefore, we have proposed a self-water management catalyst layer, which can solve these problems by adding carbon grains to the catalyst layer, which can control the produced water without containing water and can also pass electrons (8).

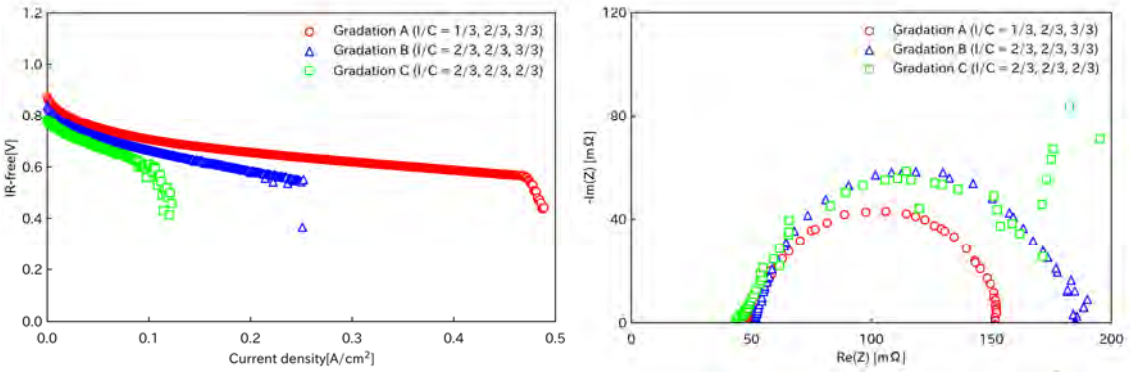

(a) I-V performance (b) Cole-Cole plot (0.1[A/cm^2])

Figure 11. Influence of I/C ratio distribution in CL thickness direction on cell performance.

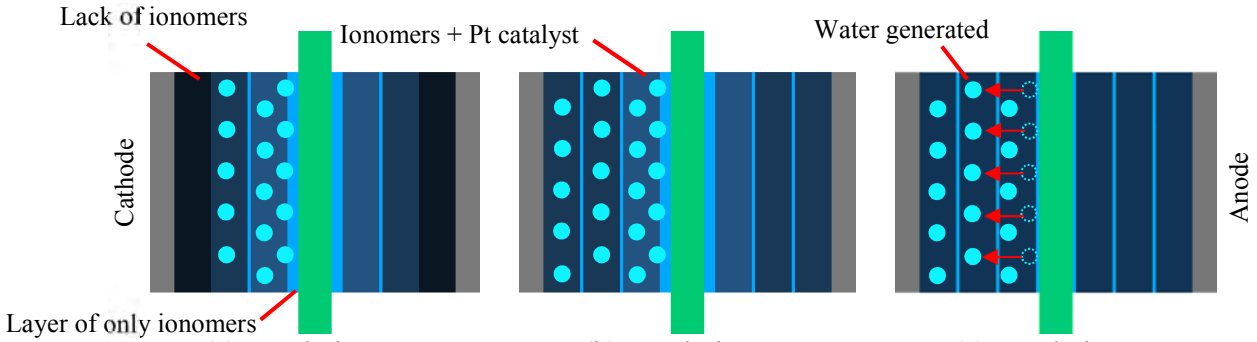

(a) Gradation A (b) Gradation B (c) Gradation C

Figure 12. Schematic diagram of layering composition.

Conclusion

The objective of this study is to examine the ink components used during CL layering and examine the effect of the additive amount of ionomer on cell performance. The results obtained in this study are summarized as follows.

(1) By adjusting the I/C ratio of the ink during the CL layering process, we were able to create gradation CLs that enabled smooth electron and proton transport and improved cell performance.
(2) If I/C ratio exceeds 1, the cell performance is greatly deteriorated due to the increase of the ohmic resistance, the electron transport resistance and gas diffusion resistance.
(3) For CL with only one layer by ink-jet coating method, the optimum I/C ratio is 2/3.
(4) Ionomer with proton conductive not only cause flooding phenomena but also fail to transport electrons, depending on the amount of ionomer added and the humidified operating conditions.
(5) By gradually decreasing the ionomer concentration in the CL thickness direction from the membrane side to the GDL side, proton transport, electron transport, and gas diffusivity are improved, and as a result, cell performance is enhanced.

Acknowledgements

This work was supported by JKA and its promotion funds from AUTO RACE (2017M-116).

References

1. K. Morioka and K. Sugiura, *J. Mech. Eng. Res. Dev.* **43,** 20 (2020).
2. S. Shukla and K. Domican, *Electrochim. Acta*, **156**, 289 (2015).
3. S. Shukla and J. Stumbper, *J. Electrochem. Soc.,* **163**, 667 (2016).
4. U. Tamaki and K. Sugiura, *Polymers*, **13**, 899 (2021).
5. K. Kakinuma, K. Masako, T. Kayoko, Y. Miho, H. Satoru, I. Akihiro, and U. Makoto, *J. Electrochem. Soc.*, **168** 054510 (2021).
6. N. Kumano, K. Kudo, Y. Akimoto, M. Ishii, and H. Nakamura, *Carbon*, **169**, 429 (2020).
7. W. Vielstich, H. A. Gasteiger, and A. Lamm, *Fuel Cell Technology and Applications*, **3**, 597 (2003).
8. K. Sugiura and S. Teramae, *Proc. EFCF2021,* p.237 (2021).

Chapter 7

22 Catalyst Layer 2

ECS Transactions, 104 (8) 175-183 (2021)
10.1149/10408.0175ecst ©The Electrochemical Society

Experimental Evaluation of PEFC Catalyst Layer Structure to Reduce Oxygen Transport Resistances

S. Mizuno[a], S. Uemura[a], and Y. Tabe[a]

[a] Division of Mechanical and Aerospace Engineering, Hokkaido University, N13 W8, Kita-ku, Sapporo, Hokkaido 060-8628, Japan

To increase the output power of polymer electrolyte fuel cells (PEFCs), it is important to reduce the oxygen transport resistance in the cathode catalyst layer (CL). The authors have been conducted detailed analysis of the oxygen transport resistance elements: the diffusion resistances in the CL pores, the dissolution resistance into the ionomer, and the transport resistance at the Pt surface. This study improved the method of fabrication of CL and measurement of limiting current for reliable evaluation of oxygen transport resistance in the CL. Using the experimental results, the oxygen transport resistance elements were evaluated, and the transport resistance at Pt surface was confirmed to be dominant even in the improved methods. However, the difference between the model analysis and experimental values became large at CLs with low Pt loadings. To elucidate appropriate structures of the low Pt CLs with smaller oxygen transport resistance, further detailed study is needed.

Introduction

The polymer electrolyte membrane fuel cell (PEFC) is expected as a power source for automobiles and stationary distributed power supply systems with high efficiency and zero CO_2 emission in operation. For the practical use of PEFC, many issues remain to be solved, and one is high cost because of the expensive components such as Pt catalyst and polymer membrane. In the PEFC, the catalyst layer (CL) of the cathode needs a large amount of Pt because of the slow oxygen reduction reaction. Since electron, proton, and oxygen are necessary to the cathode reaction, achieving the optimum structure of CL and the efficient transport of the reactants is significantly effective to reduce the usage of Pt catalyst.

Some studies investigated the relationship between the CL structures and the oxygen transport resistances (1, 2), while the appropriate structures to reduce the resistance are not clear especially at low Pt loading. In our previous research, we have analyzed the three dominant oxygen transport resistances in the CL by using fabricated CLs with various structure: the oxygen diffusion resistances in the CL pores, the oxygen dissolution resistance into the ionomer, and the oxygen transport resistance at the Pt surface (3). The experimental analysis showed that the oxygen transport resistance at the Pt surface was particularly large among the resistances inside the CL (4). However, there are some problems of the analysis to determine limiting current densities and the method of fabrication process of the CLs.

This study improved some methods for reliable evaluation of oxygen transport resistance in the CL. In the experimental analysis, the improved method to fabricate CLs was applied to ensure consistent quality of CLs for accurate estimation the oxygen transport resistances in the CLs. Catalyst coated membranes (CCMs) with various structures, such as various thicknesses and densities of Pt catalyst on carbon, were fabricated by decal transfer method. To distinguish the oxygen transport resistance in the CL from the other resistances in gas diffusion layers (GDLs) and channels, IV characteristics were measured with different total pressures, and the limiting current method (5, 6) was applied with the improved method. Using the estimated oxygen transport resistance in the CL and a model analysis (7, 8), the contributions of resistance elements for oxygen transport were evaluated individually. Further, we try to propose appropriate structure of CL that can reduce the oxygen transport resistance at low Pt loadings.

Experimental Apparatus and Methods

Fabrication of Catalyst Coated Membrane

CCMs were fabricated by decal transfer method. The catalyst ink consisting of 10 wt% Nafion solution (Sigma-Aldrich), Pt-supported carbon (Tanaka Kikinzoku, TEC10E30E, TEC10E50E, TEC10E70TPM), water, and ethanol was mixed with the ball mill, and applied to a polytetrafluoroethylene (PTFE) sheet by using a doctor blade. To prevent the aggregation of Nafion in the solution before the mixing, the reagent was kept spinning by a roller. In our previous research without the spinning, it was possible that the ionomer/carbon (I/C) ratio was not set correctly due to non-uniform solution. The CLs dried at 20 °C on the PTFE sheets were cut into 1 cm × 5 cm pieces, and transferred to both sides of a Nafion membrane (NR-211) by hot-pressing with 2.0 MPa at 150 °C for 10 min. This study focused on two structural parameters, the CL thickness and the Pt density on carbon, and fabricated CLs with various structures changing each of the parameters on the cathode side. On the anode side CL, the Pt loading was 0.2mg/cm^2 and the Pt density Pt-supported carbon was 46.9%. The I/C ratios were 0.8 on both sides.

Evaluating Method of Oxygen Transport Resistance in the CL

A single cell was used to measure the cell performance with the fabricated CCMs. Bipolar plates with straight channels were used on the anode and cathode. The widths of the channels and lands were 1 mm on the anode and cathode. The channel height was 0.5 mm. 0.2 mm thick gas diffusion layers (GDLs) with micro porous layers (SIGRACET GDL 28BC) were used on both sides. To reduce the variation of the oxygen transport resistance in the GDLs, the compression ratio of the GDL was set to about 0.8 with PET sheet. In the previous study by the authors, the GDL compression was managed with the cell's bolt tightening torque (3, 4). The cell was operated at 80°C with pure hydrogen (100 ml/min) and oxygen-nitrogen mixtures (2000 ml/min). The relative humidity of supplied gases was set 80%, and we set three different oxygen concentrations (1%, 1.5%, 2%) were used. The pressures of supplied gases were set 0.11 MPa, 0.13 MPa, 0.15 MPa and 0.17 MPa for the anode and cathode side. These conditions were selected to measure the limiting current densities without the effects of flooding.

The limiting current method (5, 6) was applied to evaluate the oxygen transport resistances. The total oxygen transport resistance, R_{O2}^{total}, can be expressed by Eq. 1.

$$R_{O2}^{total} = C_{O2}^{ch} \frac{4F}{I^{lim}} \quad [1]$$

C_{O2}^{ch} is the oxygen concentration in the channel, F is Faraday's constant, and I^{lim} is the limiting current density. The previous study by the authors applied current scanning to measure the limiting current from IV curve. In the present study, voltage scanning was used for accurate measurement of I^{lim} because it became easier to measure the limiting current where the cell voltage drops vertically.

Further, the R_{O2}^{total} can be divided into two components by Eq. 2.

$$R_{O2}^{total} = R_{O2}^{P,dep} + R_{O2}^{P,ind} \quad [2]$$

Here, $R_{O2}^{P,dep}$ is the pressure dependent resistance, and $R_{O2}^{P,ind}$ is the pressure independent resistance. It can be considered that the $R_{O2}^{P,dep}$ is the oxygen transport resistance in the GDL and the channel. This is because molecular diffusion, that is inversely proportional to pressure, is dominant in the gas diffusion in these two regions. The $R_{O2}^{P,ind}$ can be considered to be the oxygen transport resistance in the CL; in the gas diffusion in the CL, the diffusions which are not affected by pressure, such as Knudsen diffusion in the pores and the diffusion in the ionomer, are dominant. Using this relation and the limiting current densities with several cathode pressures from experiments, the oxygen transport resistance in the CL was distinguished from that in the GDL and the channel.

Evaluation Method of Electrochemical Surface Area in the CL

To estimate electrochemical surface area (ECSA) of Pt in the CL, cyclic voltammetry measurement (CV measurement) was conducted. In the CV measurement, the potential was held at a starting potential of 0.05 V for 10 seconds, and then increased to 0.90 V and decreased to 0.05 V at 50 mV/s. The ECSA was calculated from the proton adsorption amount. The measurement was conducted with N_2 atmosphere at the cathode, and pure hydrogen (100 ml/min) at the anode. The relative humidity of both gases was 100% with the cell temperature of 80°C.

Analysis Model and Formulation

The agglomerate model (7) was applied as the three-phase boundary model of the cathode CL. A Pt-supported carbon agglomerate is assumed to be covered with a uniform thick ionomer and the cathode reaction occurs by only oxygen dissolved in the ionomer film. The carbon agglomerates with the ionomer film are dispersed uniformly in the CL. Since the overpotential in the cathode is much larger than that in the anode, the phenomena in the cathode CL were analyzed under the following assumptions, (i) the CL and the GDL are isothermal, isobaric, and at steady state, (ii) the electric potential of the carbon agglomerate is constant, (iii) the generated water is in the gas phase. The oxygen transport resistance in the CL can be expressed by the Eq. 3 by using the above agglomerate model (3).

$$R_{O2}^{CL} \approx R_{Pt} + R_{diss} + R_{pore} = \frac{1}{\delta_{CL} S_{Pt} \gamma k_{Pt}} + \frac{1}{\delta_{CL} S_{ion} \gamma k_{diss}} + \frac{\delta_{CL}}{3 D_{O2}^{CL,eff}} \quad [3]$$

The oxygen transport resistance in the CL, R_{O2}^{CL}, is composed of three elements, oxygen diffusion resistance in the CL pores, R_{pore}, oxygen dissolution resistance into the ionomer, R_{diss}, and oxygen transport resistance at the Pt surface, R_{Pt}. Here, the effect of the oxygen diffusion resistance in the ionomer, R_{diff}, is assumed negligible because of the less contribution reported in the recent researches (3), (10). δ_{CL} is the thicknesses of the CL and ionomer film surrounding the carbon agglomerate, S_{Pt} and S_{ion} are the surface areas of the Pt and the ionomer, γ is the ratio of the oxygen concentration in the ionomer to that in the CL pores at equilibrium state, k_{Pt} and k_{diss} are the oxygen transfer rate at the Pt surface and the dissolution rate into the ionomer, and $D_{O2}^{CL,eff}$ is the effective oxygen diffusion coefficients in the CL pores. Eq. 3 suggests that the transport resistance at the Pt surface, R_{Pt}, and the dissolution resistance into the ionomer, R_{diss}, are inversely proportional to the surface areas of the Pt and the ionomer respectively, and the diffusion resistance in the CL pores, R_{pore}, is proportional to the CL thickness. The contributions of these resistances are determined from the values, the oxygen transfer rate at the Pt surface, k_{Pt}, the dissolution rate into the ionomer, k_{diss}, and the effective oxygen diffusion coefficient in the CL pores, $D_{O2}^{CL,eff}$. In this study, we changed the cathode CL structure related to each resistance, and mainly evaluated the contributions of two resistances (R_{pore} and R_{Pt}) individually.

Results and Discussion

Evaluation of the Diffusion Resistance in the CL Pores

Table I shows measured parameters of CLs fabricated with three different thicknesses. The Pt density on carbon used here was 46.9wt%. The porosity of the fabricated CL was determined from measurements of pore size distribution (PSD) using nitrogen physisorption method. The measured PSDs in the CLs in Fig. 1 are very similar and the porosities in Table I are also similar around 0.56. Using the porosity and the materials used for fabricating, the thickness of the CLs was estimated in Table I. These results indicate that the microporous structures of the fabricated CLs are almost same and only the thicknesses are different with different Pt loadings. Figure 2 shows the polarization curves for the cell with these CLs. The polarization curves for the cell with these CLs were measured at three different total pressures, and the oxygen transport resistances were separated into two resistances, as in Eq. 2, using the limiting current method. The estimated resistances for the CL in Table I are shown in Fig.3. It can be considered that the pressure independent resistance, $R_{O2}^{P,dep}$, corresponds to the oxygen transport resistance in the GDL and the channel, and the pressure independent resistance, $R_{O2}^{P,ind}$, corresponds to the oxygen transport resistance in the CL. As shown Fig. 3, the $R_{O2}^{P,dep}$ of each CLs are similar, indicating that the separation of the oxygen transport resistances is working well. The $R_{O2}^{P,ind}$ decreases with thicker CL because the amount of Pt increases.

By multiplying both sides of Eq. 3 by the CL thickness, δ_{CL}, the following equation is obtained.

$$R_{O2}^{CL} \times \delta_{CL} \approx \left(R_{Pt} + R_{diss} + R_{pore}\right) \times \delta_{CL} = \frac{1}{S_{Pt}\gamma k_{Pt}} + \frac{1}{S_{ion}\gamma k_{diss}} + \frac{\delta_{CL}^{2}}{3D_{O2}^{CL,eff}} \quad [4]$$

This model equation means that change in the oxygen diffusion resistance in the CL pores, R_{pore}, can be evaluated by multiplying the transport resistance (the pressure independent resistance) by the CL thickness. Here, the product of the transport resistance at the Pt surface, R_{Pt}, and the CL thickness is not affected by the change in the thickness, as well as the product of the dissolution resistance into the ionomer, R_{diss}, and the thickness. Figure 4 shows the product of the measured pressure independent resistance, $R_{O2}^{P,ind}$, and the carbon weight in the CL, W_c, which is proportional to the CL thickness. The horizontal axis is the square of the CL thickness, δ_{CL}^2. The plots are on a line, and this suggests that the model developed in this study is valid. The gradient of the line corresponds to change in the product of the diffusion resistance in the CL pores and the carbon weight, as shown by Eq. 4. The intercept also corresponds to the product of the other resistances and the carbon

TABLE I. Measured parameters of CLs with different thicknesses.

Pt loading [mg/cm^2]	0.066	0.125	0.223
Carbon weight [mg]	0.37	0.71	1.26
Porosity	0.58	0.55	0.56
Thickness [μm]	1.7	3.0	5.5

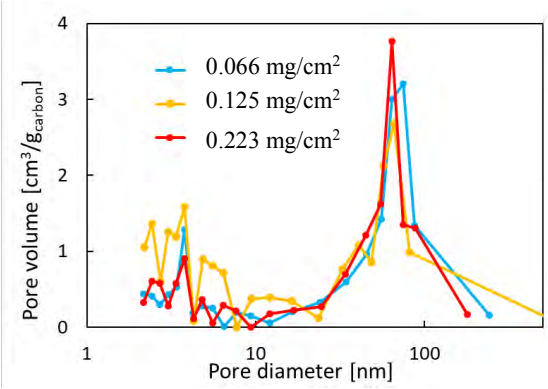

Figure 1. Measured pore size distributions of CLs with different CL thicknesses.

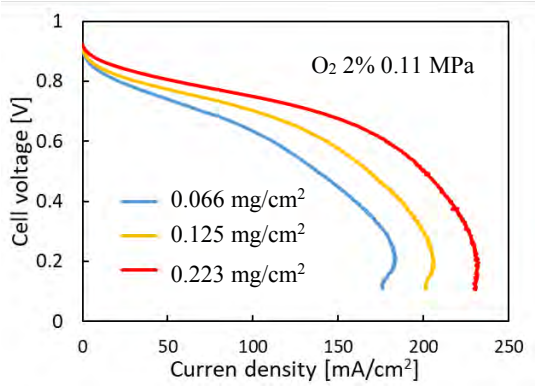

Figure 2. Polarization curves with different CL thicknesses.

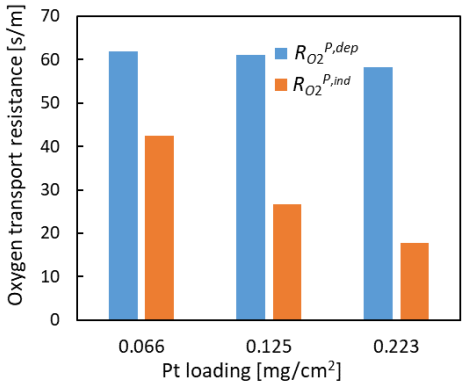

Figure 3. Oxygen transport resistances with different CL thicknesses.

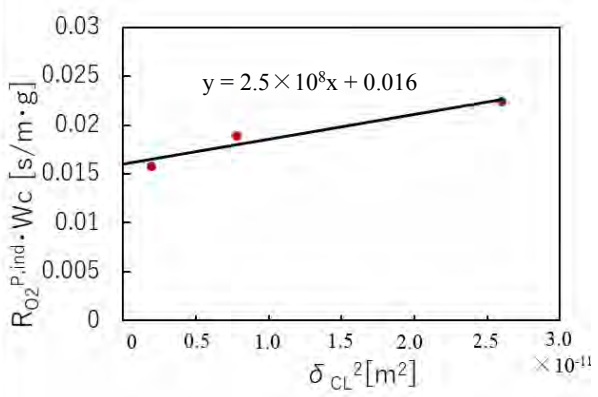

Figure 4. Analysis of the contribution of oxygen transport resistance in the CL pores.

weight. Using the gradient and Eq. 4, the effective oxygen diffusion coefficient in the CL pores was estimated: $D_{O2}^{CL,eff} = 2.7\times10^{-7}$ m^2/s. This is slightly lower than that in our previous research $D_{O2}^{CL,eff} = 3.1\times10^{-7}$ m^2/s (4), which is considered to be attributed to the decrease in the porosity.

Evaluation of the Transport Resistance at the Pt Surface

The measured structural parameters of the fabricated CLs with three different Pt loadings are shown in Table II. Here, to evaluate the transport resistance at the Pt surface, R_{Pt}, Pt-supported carbons with three different Pt densities were used. The weights of carbon were set to be similar, and I/C ratios were 0.8. Then the Pt loadings of the CLs were 0.101, 0.223, and 0.475 mg/cm^2, and the estimated Pt surface areas with CV measurements were 101, 148, and 250 m^2-$_{Pt}$/m^2-$_{CL}$, respectively. Figure 5 shows the PSDs in the CLs measured by nitrogen physisorption method for these CLs. The PSDs are similar, indicating similar microporous structure of the CLs. The measured porosities were also similar around 0.55, and the CL thicknesses were estimated around 5 μm, as shown in Table II. These similar structures indicate that the difference in oxygen transport resistances for these CLs is mainly caused by the different Pt loadings with different Pt surface areas.

Eq. 3 is transformed into Eq. 5 using the Pt surface area per unit area of the CL, $A_{Pt} = \delta_{CL} S_{Pt}$ [m^2-$_{Pt}$/m^2-$_{CL}$] and the ionomer surface area per unit area of the CL, $A_{ion} = \delta_{CL} S_{ion}$ [m^2-$_{ion}$/m^2-$_{CL}$].

$$R_{O2}^{CL} \approx \frac{1}{A_{Pt}\gamma k_{Pt}} + \frac{1}{A_{ion}\gamma k_{diss}} + \frac{\delta_{CL}}{3D_{O2}^{CL,eff}} \qquad [5]$$

TABLE II. Measured parameters of CLs with different Pt densities on carbon.

Density of Pt [wt %]	28.3	46.9	66.9
Carbon weight [mg]	1.28	1.26	1.18
Pt loading [mg/cm^2]	0.101	0.223	0.475
ECSA [m^2/g$_{Pt}$]	101	66	53
Pt surface area [m^2-$_{Pt}$/m^2-$_{CL}$]	101	148	250
Porosity	0.57	0.56	0.52
Thickness [μm]	5.4	5.5	4.9

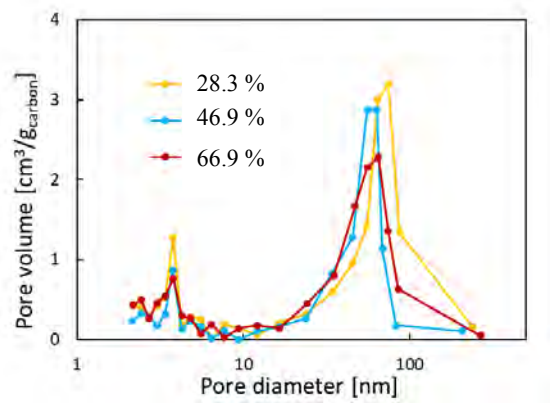

Figure 5. Measured pore size distributions of CLs with different Pt surface areas.

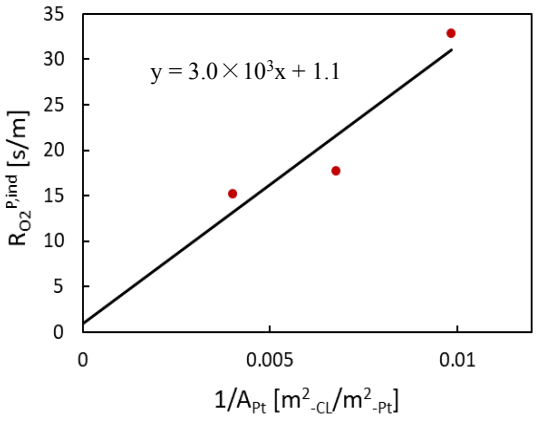

Figure 6. Analysis of the contribution of oxygen transport resistance at the Pt surface.

The oxygen transport resistances in the CL separated using the limiting current method are plotted in Fig. 6. The vertical axis is the pressure independent resistance corresponding to the oxygen transport resistance in the CL, and the horizontal axis is the inverse of the Pt surface area. From Eq. 5, the oxygen transport resistance at the Pt surface is inversely proportional to the Pt surface area, and the result in Fig. 6 shows that this analysis model is valid. The gradient corresponds to change in the transport resistance at the Pt surface, and the intercept corresponds to the sum of the other resistances. This result shows that the contribution of transport resistance of the Pt surface is very large and from the gradient and Eq. 5, the oxygen transfer rate at the Pt surface was estimated with γ = 0.093: $k_{Pt} = 3.6\times10^{-3}$ m/s. These values were similar to the previous researches, $k_{Pt} = 3.7\times10^{-3}$ m/s (3), and $k_{Pt} = 4.1\times10^{-3}$ m/s (4).

Evaluation of the Oxygen Transport Resistance at Low Pt Loading

We evaluated the diffusion resistance in the CL pores and the transport resistance at the Pt surface above, while the contribution of the dissolution resistance into the ionomer was not clear (4). At low Pt loading, the transport resistance at the Pt surface is expected to be so large because the Pt surface area decreases. To validate an availability of the model analysis in the present study to CLs with low Pt loadings, we fabricated the CL with similar Pt surface area with the Pt density 28.3% as the previous one in Table I (Pt loading 0.066 mg/cm^2 with Pt density 46.9%) and compared the oxygen resistances calculated from experiments and the model analysis. Table III shows measured parameters of the fabricated CLs (the CL with Pt density 46.9% is the same as that in Table I). In Fig. 7, the plots show the experimentally-estimated $R_{O2}^{P,ind}$ of the fabricated CLs, and the bar charts show the R_{CL} calculated using the model with the constants determined above ($D_{O2}^{CL,eff}$, γ and k_{Pt}). Here, the dissolution resistance into the ionomer in Eq. 5 is not included in calculation. There is

TABLE III. Measured parameters of CLs with low Pt loading and similar Pt surface areas.

Density of Pt [wt %]	28.3	46.9
Carbon weight [mg]	0.55	0.37
Pt loading [mg/cm^2]	0.043	0.066
Pt surface area [m^2-$_{Pt}$/m^2-$_{CL}$]	43.6	43.6
Thickness [μm]	2.3	1.7

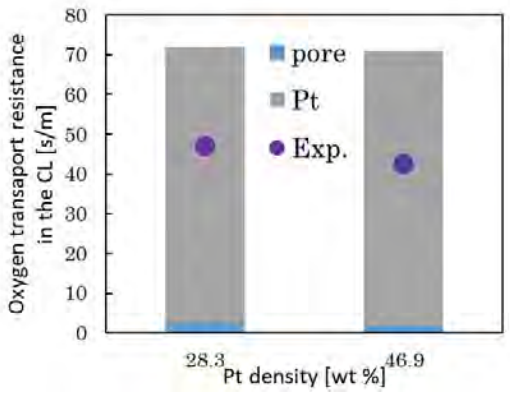

Figure 7. Measured and estimated oxygen transport resistances of CLs at low Pt loading.

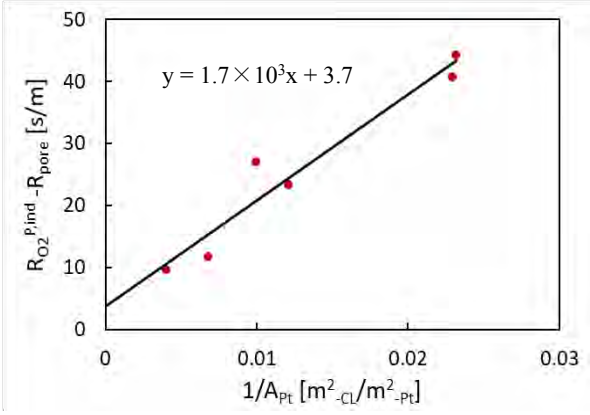

Figure 8. Analysis of the contribution of oxygen transport resistance at the Pt surface.

no significant difference between the two CLs when we compare only the experimental results or the calculated results, but the difference between the model values and the experimental results are very large. This may be due to an over-estimation of the transport resistance at the Pt surface in the model calculation, suggesting that the model using the constants determined above (γ and k_{Pt}) are not appropriate for low Pt loading CLs. Figure 8 shows the results summarizing all of the fabricated CLs in this study with the same horizontal axis as Fig. 6. Since the thicknesses of the added CLs are different respectively, the vertical axis is modified $R_{O2}^{P,ind}$ minus the diffusion resistance, R_{pore}. The gradient of line is smaller than Fig. 6, then the oxygen transfer rate at the Pt surface becomes higher: $k_{Pt} = 5.8\times10^{-3}$ m/s. Using this value, the oxygen transport resistances in the CL calculated by the model become closer to the experimental results. This may indicate that a wider range of Pt surface areas is needed to determine the constant, k_{Pt}. It may be also indicated that the model to determine the transport resistance at the Pt surface with the inverse of the Pt surface area and the dissolution resistance with the inverse of the effective ionomer surface area in Eq. 3 is inappropriate. The dissolution resistance into the ionomer is reported to be large at low Pt loadings (11). The dissolution resistance into the ionomer near the Pt particles may complicatedly affect the transport resistance at the Pt surface. Further detailed study is needed to improve the model and discuss appropriate structures of the CLs with low Pt loadings.

Conclusions

This study improved the method to fabricate the CLs and to determine the limiting current density for reliable calculation of the oxygen transport resistance. The CLs with various structures were fabricated and the contributions of the diffusion resistance in the CL pores and the transport resistance at the Pt surface were evaluated. It was shown that the transport resistance at the Pt surface is dominant in the CL, as in the previous study. However, for CLs with low Pt loadings, the oxygen transport resistances calculated using the model with the constants determined by the previous method become much larger than those of the experimental results. This suggests that the experimental conditions used to determine the constants or the model itself is inadequate. To elucidate the appropriate structure of the low Pt loading CLs with low oxygen transport resistance, further detailed study is needed.

Acknowledgments

This work was supported by JSPS KAKENHI Grant Number 21H01254.

References

1. N. Ramaswamy, W. Gu, J. M. Ziegelbauer and S. Kumaraguru, *J. Electrochem. Soc.*, **167**, 064515 (2020).
2. T. Schuler, A. Chowdhury, A. T. Freiberg, B. Sneed, F. B. Spingler, M. C. Tucker, K. L. More, C. J. Radke, and A. Z. Weber, *J. Electrochem. Soc.*, **166**, F3020 (201).
3. Y. Tabe, T. Satake, T. Iiri, T. Hayashi and T. Chikahisa, *ECS Trans*., **80**(8), 205 (2017).

4. T. Iiri, T. Satake, M. Kabeya, Y. Tabe, T. Chikahisa, *56th Heat Transfer Symposium of Japan* (2019), C124.
5. J. P. Owejan, J. E. Owejan, and W. Gu, *J. Electrochem. Soc.*, **160**, F824 (2013).
6. D. R. Baker, D. A. Caulk, K. C. Neyerlin, and M. W. Murphyc, *J. Electrochem. Soc.*, **156**, B991 (2009).
7. Y. Tabe, M. Nishino, H. Takamatsu, and T. Chikahisa, *J. Electrochem. Soc.*, **158**, B1246 (2011).
8. T. Hayashi, Y. Tabe, and T. Chikahisa, *ECS Trans.*, **75**(14), 373 (2016).
9. Y. Tabe, T. Hayashi, and T. Chikahisa, *Asian Conference on Thermal Sciences 2017 (1st ACTS)*, ACTS-P00228 (2017).
10. K. Kudo, R. Jinnouchi, and Y. Morimoto, *Electrochim. Acta*, 209, 682 (2016).
11. N. Nonoyama, S. Okazaki, A. Z. Weber, Y. Ikogi, and T. Yoshida, *J. Electrochem. Soc.*, **158**, B416 (2020).

ECS Transactions, 104 (8) 185-190 (2021)
10.1149/10408.0185ecst ©The Electrochemical Society

Soft X-ray Imaging of Polymer Electrolyte Fuel Cells Using Different Support Materials for Catalyst Layers

K. Kinose[a], T. Suzuki[a], K. Kakinuma[b], M. Uchida[b], A. Iiyama[b], and S. Tsushima[a]

[a] Department of Mechanical Engineering, Osaka University, 2-1 Yamadaoka, Suita, Osaka 565-0871, JAPAN
[b] Fuel Cell Nanomaterials Center, University of Yamanashi, 6-43, Miyamae, Kofu, Yamanashi 400-0021, Japan

Water management in polymer electrolyte fuel cells (PEFC) is an important factor for improving cell performance. It is necessary to understand the liquid water behavior in the porous layer during power generation. In this study, we prepared PEFCs using carbon and tin oxide as the support materials for the catalyst layer, respectively. Although tin oxide supports have high durability, their wettability differs greatly from that of carbon supports, and there is concern that flooding is likely to occur. Liquid water in the two types of PEFCs during power generation was observed by soft X-ray radiography. It was shown that the distribution of liquid water in the porous media was different between the carbon support and tin oxide support catalyst layers due to the differences in support materials and structures of the catalyst layers.

Introduction

The polymer electrolyte fuel cell (PEFC) is a type of fuel cell that has been developed due to its advantages such as low operating temperature and compact size. The PEFC is assembled by putting a membrane electrode assembly (MEA), which consists of the polymer electrolyte membrane (PEM) with the catalyst layers (CL) and the gas diffusion layers (GDL) on both sides, between separators. Pt nanoparticle catalysts supported on carbon black (Pt/C) are usually used for the CLs. However, there is a problem that the CLs deteriorates due to oxidative corrosion of the carbon supports. Pt supported on tin oxide (Pt/Nb-SnO_2) have been studied as an alternative material for the CLs (1,2). However, SnO_2 supports are more hydrophilic than carbon supports, and it is not clear how this characteristic affects the liquid water behavior during power generation. There is a concern that the hydrophilicity of the material may cause excessive liquid water accumulation (flooding), inhibiting gas supply and degrading the performance of the cell. In order to realize high current density operation, it is essential to clarify the liquid water transport phenomena in the PEFC. Soft X-ray radiography is one of the methods to visualize the liquid water in the PEFC. (3) In this study, we attempted to analyze and compare the liquid water generation behavior of PEFCs of conventional (carbon support) and SnO_2 support catalyst layers by high-resolution soft X-ray radiography.

Experimental method

Configuration of the PEFCs for in-situ observation

Catalyst inks were prepared by dispersing platinum supported substrate and Nafion solution into an alcohol-based dispersion media. The carbon support CL was prepared by spreading the catalytic ink on the substrate using the doctor blade method. Catalyst coated membrane (CCM) using the carbon supports was made by transferring the CL onto the PEM (Nafion®212) by hot pressing. The SnO_2 supports CCM was made by the pulse swirl spray (PSS) method. We constructed two types of PEFCs with a reaction area of 5×8 mm^2 by layering each CCM, GDL (SIGRACET®24BC) with micro porous layer (MPL), gaskets, and separators, respectively. Polypropylene with a low attenuation coefficient was used as the gasket material, and the X-ray transmission length of the MEA was 5 mm.

Power generation conditions

Fully humidified hydrogen and air were supplied to the anode and the cathode, respectively. The cell we developed was operated at room temperature (ca. 25°C). The polarization curves of the two types of PEFCs were investigated by measuring the voltage at current densities of 0.1 to 0.8 A/cm². After a sufficient time for the generated water to dry, the current density was kept at 0.8 A/cm² and power generation was carried out for 20 minutes.

Soft X-ray radiography.

The soft X-ray imaging system (TUX-9000D, Mars-Tohken X-ray Inspection) used in this study detected the liquid water behavior in PEFCs because light elements have large mass attenuation coefficient by irradiating X-rays below 10 keV. The magnified X-ray transmission images which contain both the area under the rib and under the channel were obtained. The PEFCs were observed in the through-plane direction when the current density was kept at 0.8 A/cm^2, and an image was taken every 30 seconds.

Results and Discussion

Cell performance

Figure 1 shows the polarization curves of two PEFCs with different support materials. It was suggested that the hydrophilicity of the SnO_2 support caused more flooding, resulting in a larger overvoltage in the high current density region, although the SnO_2 support catalyst layer showed higher performance than carbon support catalyst layer in the low current density region.

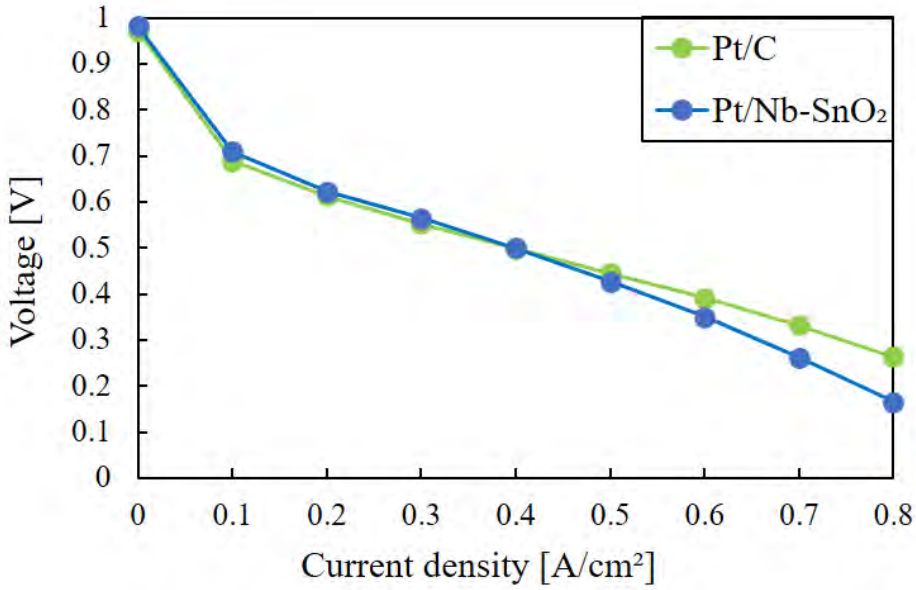

Figure 1. Polarization curves Polarization curves of PEFC using Pt/C and Pt/Nb-SnO_2 as catalyst layers. The cell was operated at room temperature (ca. 25°C).

X-ray radiography

A soft X-ray imaging system was used to visualize the inside of PEFCs that were operated at 0.8 A/cm^2. Figure 2(a), and 3(a) show the X-ray radiographs of the MEA at open-circuit voltage. The right side of the figure shows the cathode and the left side shows the anode. The generated water during the power generation was identified by image processing that subtracted the image taken after operation from the image taken under open-circuit voltage conditions (Figure 2(b), and 3(b)). Liquid water is shown as bright parts in the subtracted image.

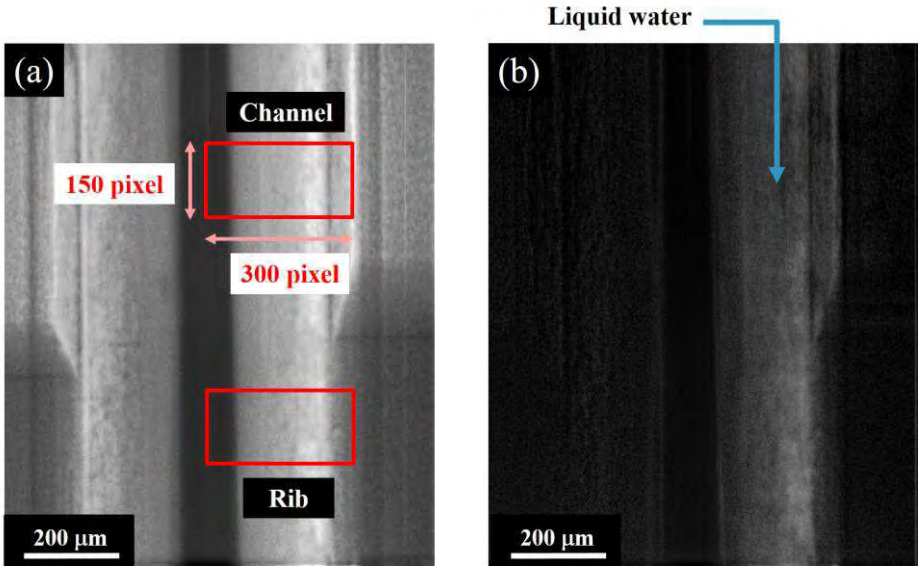

Figure 2. Soft X-ray radiograph of the MEA using Pt/C
(a) 0 s (Original image), (b) 1200 s (Subtracted image).

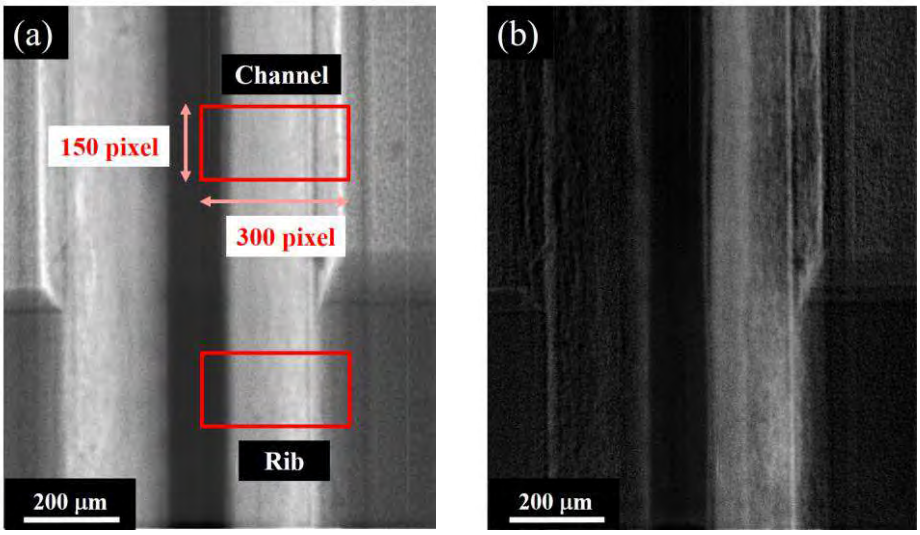

Figure 3. Soft X-ray radiograph of the MEA using Pt/Nb-SnO_2
(a) 0 s (Original image), (b) 1200 s (Subtracted image).

For the image after the subtraction process, two areas, the cathode under the channel and that under the rib, were cropped (red lines in Figures 2 (a) and 3 (a)), and through-plane one-dimensional water distribution at each cell operating time was analyzed as shown in Figures 4 and 5. The amount of liquid water retention increases by the progress of the time. The retention of liquid water was faster and the amount of retention was larger at the area under the rib than under the channel.

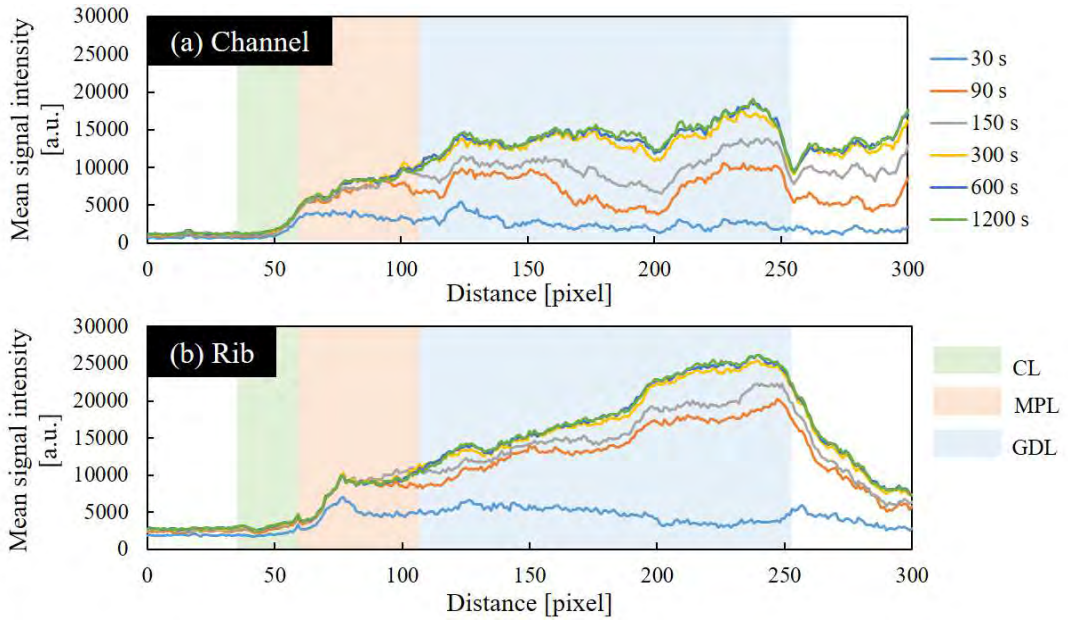

Figure 4. Change in mean signal intensity by operating time of the PEFC using Pt/C
(a) under the cannel, (b) under the rib.

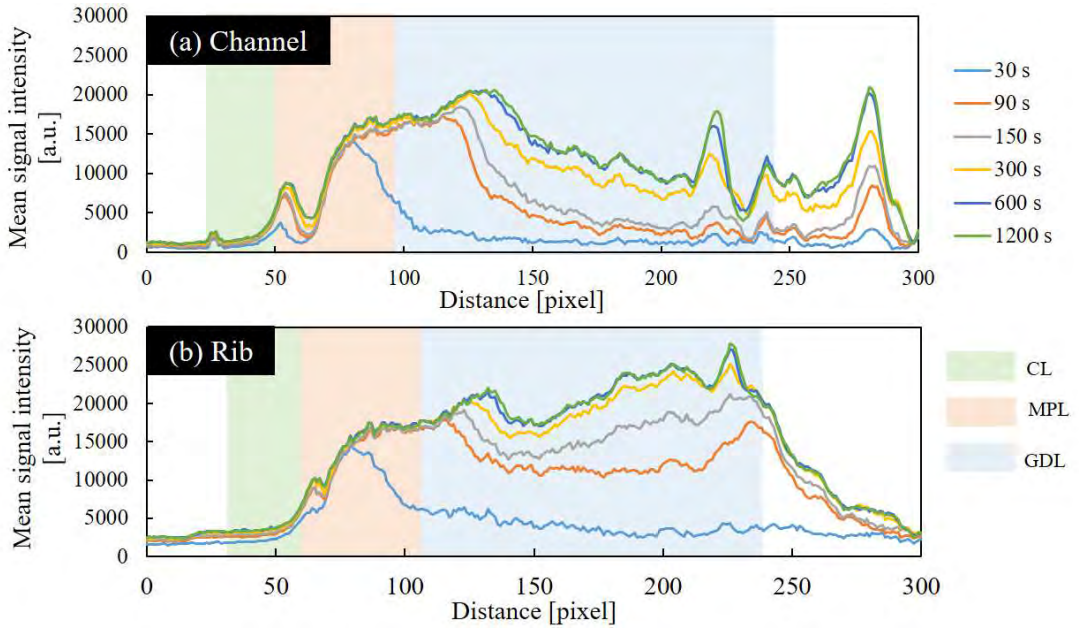

Figure 5. Change in mean signal intensity by operating time of the PEFC using Pt/SnO_2 (a) under the cannel, (b) under the rib.

In the Pt/C cathode, the mean signal intensity was largest near the separator wall, and there was little change in the mean signal intensity at the MPL. This result implies that the insertion of the MPL efficiently discharged the liquid water near the CL and maintained the supply of reactant gas to the CL.

In the $Pt/Nb\text{-}SnO_2$ cathode, the gradient of the profile was different from that of the carbon support cathode. Water content changed from higher near MPL to lower near the separator. The change in mean signal intensity was large even in the MPL. It was observed that the liquid water spread inside the porous material as if sticking to the hydrophilic CL surface. It is thought that this liquid water interferes with the supply of the reactant gas and causes the concentration overvoltage to increase. In addition, there is a peak in the mean signal intensity near the boundary between CL and MPL. This may be due to the hydrophilic CL increasing the amount of liquid water near the PEM, swelling the PEM, and pushing the CL toward the MPL. The change in the mean signal intensity with the operating time of the SnO_2 support CCM region obtained from raw images is shown in Figure 6. The width of the CCM with a large attenuation coefficient increased as time went by.

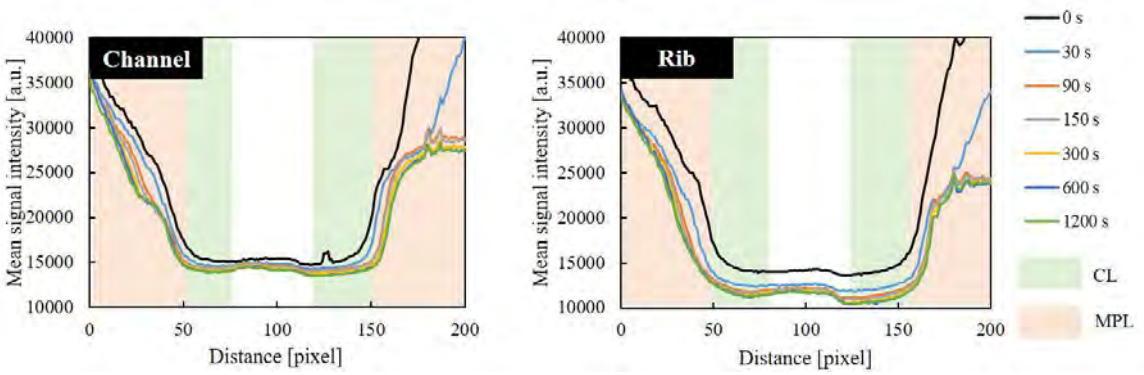

Figure 6. Change in mean signal intensity of the CCM area obtained from raw images.

Conclusions

In this study, the liquid water generation behavior of PEFCs using carbon and SnO_2 supports for catalyst layers was observed by the soft X-ray imaging system, and the following findings were obtained.

The PEFC using SnO_2 support catalyst layers showed larger overvoltage in the high current density region than the PEFC using carbon support catalyst layers, because the hydrophilicity of the SnO_2 support easily caused the retention of liquid water.

In the Pt/C cathode, the liquid water retention was highest near the separator wall, suggesting that the liquid water was discharged along the separator wall. The insertion of the MPL suppressed the retention of liquid water near the CL. The Pt/Nb-SnO_2 cathode showed higher concentration overvoltage in the high current density region than PEFC using carbon support catalyst layers. Liquid water accumulated in the MPL area, sticking to the hydrophilic CL surface. In addition, it was observed that the CL was pushed to the MPL side by the swelling of the PEM.

Acknowledgments

The catalyst with Tin oxide support material used in this study was provided by NEDO ECCEED'30. The authors would like to acknowledge their assistance in assembling PEFCs for visualization study.

References

1. Y. Chino, K. Taniguchi, Y. Senoo, K. Kakinuma, M. Hara, M. Watanabe, and M. Uchida, ***Journal of The Electrochemical Society***, **162** (7) F736-F743 (2015).
2. Y. Senoo, K. Taniguchi, K. Kakinuma, M. Uchida, H. Uchida, S. Deki, and M. Watanabe, ***Electrochemistry Communications***, **51**, 37-40 (2015).
3. P. Deevanhxay, T. Sasabe, S. Tsushima, and S. Hirai, ***Journal of Power Sources***, **230**, 38-43 (2013).

ECS Transactions, 104 (8) 191-196 (2021)
10.1149/10408.0191ecst ©The Electrochemical Society

Impact of Solvent Decomposition on Dispersion Structure of PEFC Catalyst Ink

T. Sasabe[a], K. Iida[a], K. Sakai[a], S. Uemura[b], K. Shinohara[c], and S. Hirai[a]

[a] Department of Mechanical Engineering, Tokyo Institute of Technology, Meguro-Ku, Tokyo 152-8550, Japan
[b] School of Engineering, Hokkaido University, Sapporo, Hokkaido 060-8628, Japan
[c] Fuel Cell Cutting-edge Research Center (FC-Cubic), Technology Research Association, Koto-ku, Tokyo 135-0064, Japan

To achieve high current density operation of polymer electrolyte fuel cells (PEFCs), high performance catalyst layer is requested. Though dispersion structure of catalyst ink strongly affects the catalyst layer structure, dispersion mechanism of the catalyst ink has not been understood. In this study, to understand the impact of solvent decomposition on the dispersion of the catalyst ink, the decomposition products of the ethanol were artificially added to the catalyst ink, and the impacts of each decomposition products on rheology characteristics and ionomer adsorption rate on platinum supported carbon (Pt/C) of the catalyst inks were investigated. The results showed that the aldehyde lower the ionomer adsorption rate and increased viscosity. Because the ionomer works as surfactant within the catalyst ink, lower ionomer adsorption rate might cause aggregation of the Pt/C, and further understanding about the impacts of decomposition products are important to control the dispersion structure of the catalyst ink.

Introduction

A polymer electrolyte fuel cell (PEFC) is an energy device that generate electricity from the electrochemical reaction of hydrogen and oxygen and has been expected to be used as an automotive power source. Though the performance of the PEFC has been improved a lot, further cost reduction and downsizing of PEFC system is needed, and higher performance catalyst layer with lower oxygen transport resistance, proton transport resistance, and electron transport resistance is essential.

The catalyst layer (CL) is nano-porous layer and composed of platinum-supported carbon (Pt/C) and ionomer. Because the electrochemical reaction occurs only on Platinum surface, structure of the CL greatly affects PEFC performance, and control of the CL structure is important to realize the high-performance CL. The CL is fabricated by coating and drying a catalyst ink in which the Pt/C and the ionomer are dispersed in a mixed solvent of water and ethanol. Therefore, dispersion structure of the catalyst ink strongly influences the CL structure, and understanding the relationship between the dispersion structure and the CL structure is highly important.

It is reported that the solvent composition of the catalyst ink strongly affects the structure and performance of the CL (1), and Uemura et al. reported that the decomposition of

ethanol within the catalyst ink strongly affect its dispersion (2, 3), but its mechanism was not fully understood yet.

In this study, to understand the effects of solvent composition of the catalyst ink on the dispersion structure, three catalyst inks with different ethanol/water ratio (EtOH ratio) were prepared, and the dispersion structure (viscosity characteristics, particle size distribution, and ionomer adsorption rate) of the catalyst inks were measured without dilution. Furthermore, impact of solvent decomposition on the dispersion of the catalyst ink was investigated by adding the decomposition products to the catalyst ink.

Experimental

To investigate the effects of EtOH ratio and the solvent decomposition on dispersion structure, the catalyst inks with three different EtOH ratio (20, 46, 60 wt%) were prepared, and the dispersion structure of the catalyst inks were investigated by rheology measurement technique, particle size measurement technique, and ionomer adsorption measurement technique.

In addition, to investigate the influence of solvent decomposition on the dispersion structure, decomposition products were added to the catalyst ink. Because ethanol within the solvent was decomposed based on the following reactions ([1]-[3]), influence of aldehyde, acetic acid, and ethyl acetate were added to the catalyst ink (EtOH ratio: 20 wt%) one by one.

$$C_2H_5OH + \frac{1}{2}O_2 \rightarrow CH_3OH + H_2O \quad [1]$$

$$CH_3OH + \frac{1}{2}O_2 \rightarrow CH_3COOH \quad [2]$$

$$CH_3COOH + C_2H_5OH \rightarrow CH_2COOC_2H_5 + H_2O \quad [3]$$

Catalyst Ink

The catalyst inks were fabricated by mixing platinum-supported carbon (TEC10V30E, Tanaka Kikinzoku), ionome solution (DE1021, Sigma-Aldrich), and mixed solvent of ethanol and water. The ethanol/water ratio, the ionomer/carbon ratio and the solid content of the catalyst ink were kept 46wt%, 0.75 and 10%, respectively.

To investigate the influence of solvent decomposition, aldehyde, acetic acid, and ethyl acetate were added to the catalyst ink (EtOH ratio: 20 wt%) one by one. The concentration of aldehyde, acetic acid, and ethyl acetate were adjusted to 5%, 10%, and 10%, respectively.

Rheology Measurement

A rotating rheometer (MCR302, Anton-Paar) was used to measure the rheology characteristics of the catalyst inks. The viscosity was measured at each shear rate in the range of 0.01 to 1000 s^{-1}. To minimize evaporation of the catalyst ink, the sample chamber was used and temperature of the catalyst ink was kept to 25°C during measurement.

Particle Size Distribution Measurement

A laser diffraction particle size distribution analyzer (LA-960V2, HORIBA), which uses the Mie scattering theory as the measurement principle (4), was used to measure the particle size within the catalyst inks. In order to increase the laser transmittance to the catalyst ink, the catalyst ink was sealed within the interval of 2 μm created between glass plates, and the laser was irradiated from vertical to the glass plate, and the particle size distribution was calculated from diffracted light through the thin catalyst ink film. By using this glass plates holder, the particle size distributions of the catalyst ink were able to measure without any dilution.

Ionomer Adsorption Rate Measurement

To investigate the dispersion structure of the catalyst ink, ionomer adsorption rate on the Pt/C was measured by centrifugal separation technique. The ionomers adsorbed on the Pt/C settled out together with the Pt/C particle by centrifugation, while the ionomers not adsorbed on the Pt/C keep floating. Therefore, the ionomer adsorption rate can be calculated by measuring the concentration of the ionomer solution after the centrifugation.

Results and Discussion

The effects of EtOH ratio and the solvent decomposition on dispersion structure of the catalyst inks were investigated.

Effects of EtOH/Water Ratio on Dispersion

Figure 1 showed the rheology characteristics of the catalyst inks with different EtOH ratio. It was clearly observed that the catalyst ink was non-Newtonian fluid and viscosity decreased with increasing shear rate (shear-thinning fluids). In addition, compared to the catalyst ink with low ethanol ratio (low EtOH ink), the catalyst ink with high ethanol ratio (high EtOH ink) showed higher viscosity.

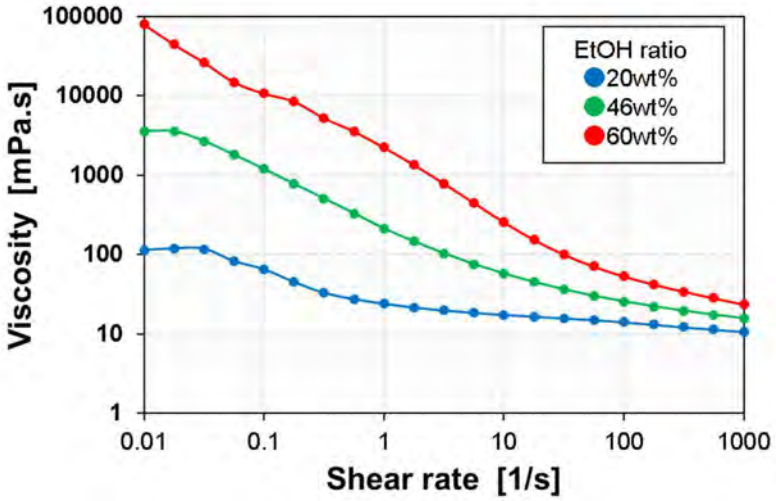

Figure 1. Rheology characteristics of catalyst inks with different EtOH ratio.

Figure 2 showed the particle size distribution of the catalyst inks with different EtOH ratio. The catalyst ink with higher EtOH ratio showed larger particle size. It is said that the change of viscosity reflects the change of aggregation size within the sample. Therefore, these results suggested that the ink with high ethanol ratio had more aggregated structure, and the aggregates of the Pt/C was broken up into smaller aggregates under high shear rate region (5-6).

To understand the difference of the dispersion structure between the inks, the ionomer adsorption rate was evaluated. In Figure 3, the ionomer adsorption rate was obtained as a function of centrifuge time, and the low EtOH ink showed higher value than the high EtOH ink. Because the ionomer works as the surfactant within the catalyst ink, it was suggested that the ionomer adsorbed on the Pt/C suppressed aggregation of the Pt/C and the high EtOH ink was easily aggregated.

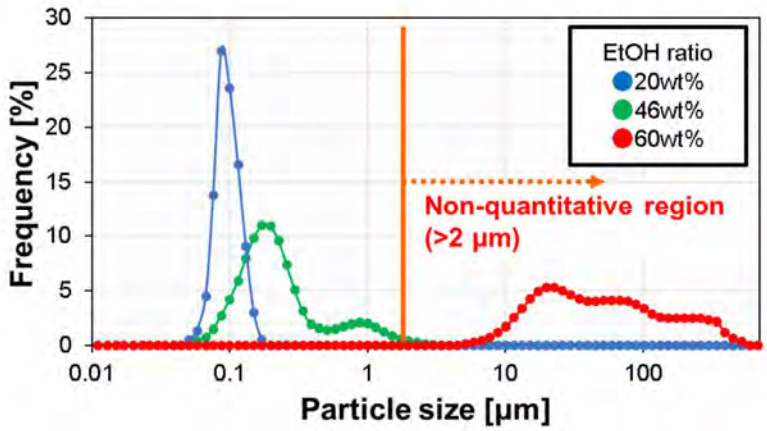

Figure 2. Particle size distribution of catalyst inks with different EtOH ratio.

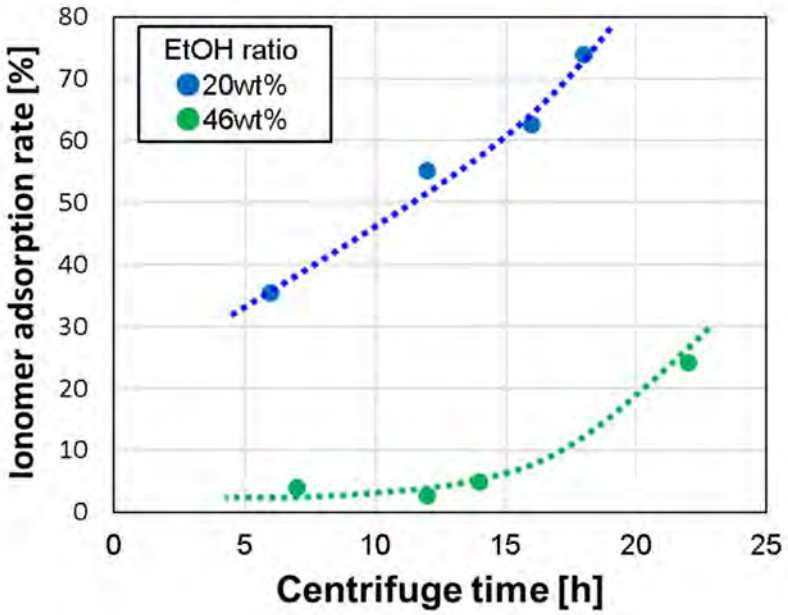

Figure 3. Effects of EtOH ratio on ionomer adsorption rate.

Effects of Decomposition Products on Dispersion

Based on the reaction [1]-[3], aldehyde, acetic acid, and ethyl acetate could be generated on the Platinum catalyst surface, and Figure 4 showed the influence of each decomposition products on the rheology characteristics. Though the effects of ethyl acetate on the viscosity was small, acetic acid and aldehyde influenced the viscosity. Because the high EtOH ink showed larger viscosity than the low EtOH ink, it was suggested that aldehyde was generated and influenced the viscosity of the high EtOH ink.

In addition, effects of aldehyde on the ionomer adsorption rate was investigated (Figure 5), and it was clearly observed that the aldehyde reduced the ionomer adsorption rate. Therefore, these results suggested that the ionomer adsorption rate strongly affect the dispersion structure of the catalyst ink, and further understanding about the influence of each decomposition products on the dispersion structure is important.

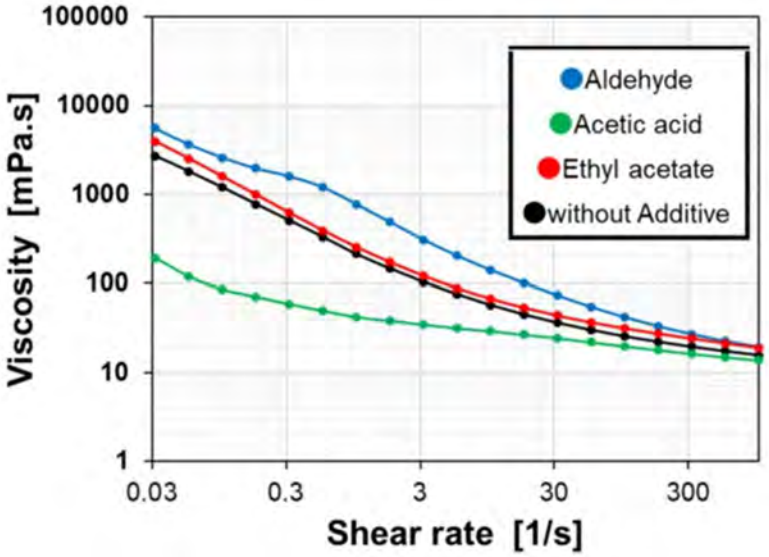

Figure 4. Rheology characteristics of catalyst inks with different decomposition products (EtOH ratio: 20wt%)

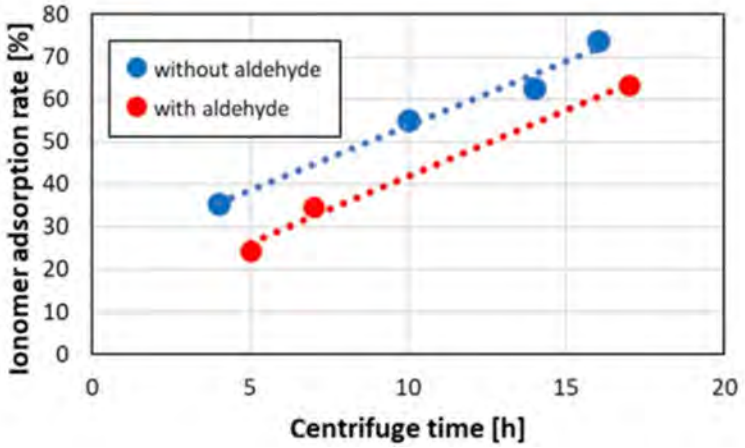

Figure 3. Effects of aldehyde on ionomer adsorption rate.

Conclusions

To understand the impact of solvent decomposition on the dispersion structure of the catalyst ink, the decomposition products of the ethanol were artificially added to the catalyst ink, and the impacts of each decomposition products on rheology characteristics and ionomer adsorption rate were investigated.

The results showed that the aldehyde lower the ionomer adsorption rate and increased the viscosity. Because the ionomer works as surfactant within the catalyst ink, lower ionomer adsorption rate might result in aggregation of the Pt/C, and further understanding about impacts of decomposition products are important to control the dispersion structure of the catalyst ink.

Acknowledgments

The part of results reported in this research were obtained under the PEMFC Research and Development Program for “Highly-Coupled Analysis of Phenomena in MEA and its Constituents and Evaluation of Cell Performance,” commissioned by the New Energy and Industrial Technology Development Organization (NEDO).

References

1. Y. Mori et al., *J. Jpn. Soc. Precision Engineering*, 54, 2132 (1988).
2. S. Uemura et al., *J. Electrochem. Soc.* 166 F89 (2019).
3. K. Iida et al, *ECS Trans.* 98 497 (2020).
4. M. Kishi et al., *J. Soc. Powder Technol.*, 55, 366 (2018).

ECS Transactions, 104 (8) 197-202 (2021)
10.1149/10408.0197ecst ©The Electrochemical Society

Characterization of Agglomerated Particles in a PEFC Electrode Slurry by Soft X-ray Radiography

Y. Tokunaga[a], T. Suzuki[a], and S. Tsushima[a]

[a] Department of Mechanical Engineering, Osaka University, 2-1 Yamadaoka, Suita, Osaka 565-0871, JAPAN

Controlling the porous structure of the catalyst layer in polymer electrolyte fuel cells (PEFCs) is one of the important challenges to improve the cell performance. Dispersed particles in the electrode slurry (catalyst ink) agglomerate and affect both the fabrication process of the catalyst layers and the resultant porous structure. Therefore, it is necessary to thoroughly understand the state of particles in electrode slurry. In this study, we carried out a time-series visualization of the electrode slurry by a soft X-ray radiography system to clarify the agglomeration/dispersion state and migration phenomena of particles in the electrode slurry. We prepared four types of electrode slurries with different non-volatile ratios for observation. Sedimentation behaviors of the agglomerated particles were observed in all electrode slurries. The sedimentation rate decreased with the increase of non-volatile ratio. The effective density of the agglomerated particles was estimated from captured images.

Introduction

Polymer electrolyte fuel cells (PEFCs) have been commercialized for various applications, such as automobiles and household power sources, because of their low operating temperature and high power density. A PEFC has multilayer porous electrodes consisting of a catalyst layer and a gas diffusion layer. The catalyst layer plays a role as an electrochemical reaction field and is generally prepared by mixing platinum-supported carbon and ionomer in a solvent to make a suspension (electrode slurry), which is then coated on a substrate and dried. The electrode material particles agglomerate in the electrode slurry, the state of agglomeration changes the porous structure of the catalyst layer. In order to realize high cell performance of PEFCs, clarifying the aggregation and dispersion state of particles in the electrode slurry and thoroughly understanding the formation mechanism of the porous structure of the catalyst layer are required. Some studies for understanding and characterizing electrode slurries have been conducted (1-2).

The objective of this study is to investigate and evaluate the agglomeration/dispersion state and migration phenomena of particles in the electrode slurry. Therefore, we visualized the electrode slurry by a soft X-ray radiography system. X-ray is effective to observe PEFC electrode slurries which are black opaque suspensions. We quantitatively characterized sedimentation rates in the slurry by processing the captured images. Also, the estimation method for the effective density of agglomerated particles in the electrode slurry using the images was examined.

Materials and Experimental Methods

Preparation of Electrode Slurry

The electrode slurries were prepared by dispersing platinum-supported carbon (Pt/C, TEC10E50E, Tanaka Kikinzoku Kogyo) and ionomer dispersion (DE2020, Sigma-Aldrich) into a disperse medium that consists of purified water and n-propyl alcohol (NPA). The weight ratio of ionomer and carbon (I/C) and the volume ratio of water to NPA was 1.0. In order to investigate the effect of interaction between particles, four types of electrode slurries with different non-volatile ratios (NV: 7.0, 0.70, 0.40, and 0.11%) were prepared. The dispersions were stirred by a planetary centrifugal mixer (ARE-250, Thinky) for 30 minutes (2000 rpm for the revolution and 800 rpm for the rotation) just before soft X-ray visualization.

Soft X-ray Radiography

In this study, we used the soft X-ray radiography system (Mars-Tohken X-ray Inspection, TUX-9000D). It uses X-rays in a lower energy range than common X-ray imaging systems. In order to observe the electrode slurry by soft X-ray radiography, we used an in-house PTFE container. The thickness of a content (the length of the transmission light path through the slurry) was 0.2 mm.

The PTFE container was placed on the sample stage of the soft X-ray imaging system and captured an image of the empty container as a background image. After that, 9.5 ml of electrode slurry was filled into the container. The container with electrode slurry was sealed to prevent drying and observed by X-ray radiography. In addition, a time-series visualization of the electrode slurry was conducted for several hours. The observation area was the horizontal center of the electrode slurry filling part including the bottom of the container. The observation area was 0.86 mm square (Figure 1).

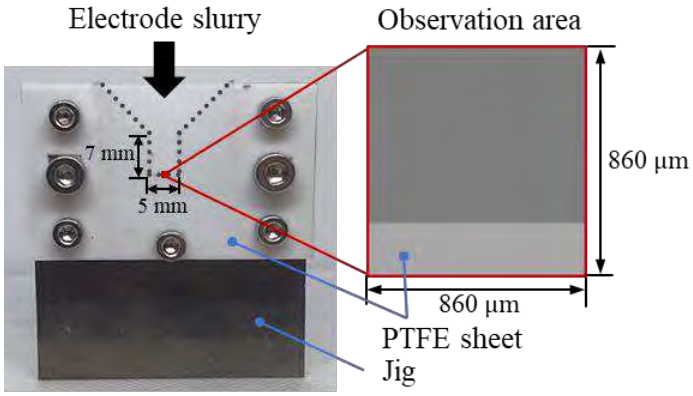

Figure 1. Container and observation area.

Results and Discussion

Agglomerated Particles in Electrode Slurry

The background image (only the container) and the observation image with electrode slurry were processed by subtraction, black/white inversion, and contrast adjustment (Figure 2). All images showed a spatial variation of X-ray absorption in the electrode slurry. High X-ray absorption (dark) regions correspond to high density regions in the slurry,

attributed to agglomerates of platinum-supported carbon particles and ionomers. Their diameters were about 10 – 40 μm regardless of the non-volatile ratio of the electrode slurry. However, the number of agglomerated particles varied depending on the non-volatile ratio of the electrode slurry. The less the non-volatile ratio was, the less the number of observed agglomerated particles was. Here, note that there was vertically linear noise at both ends and in the center of the image.

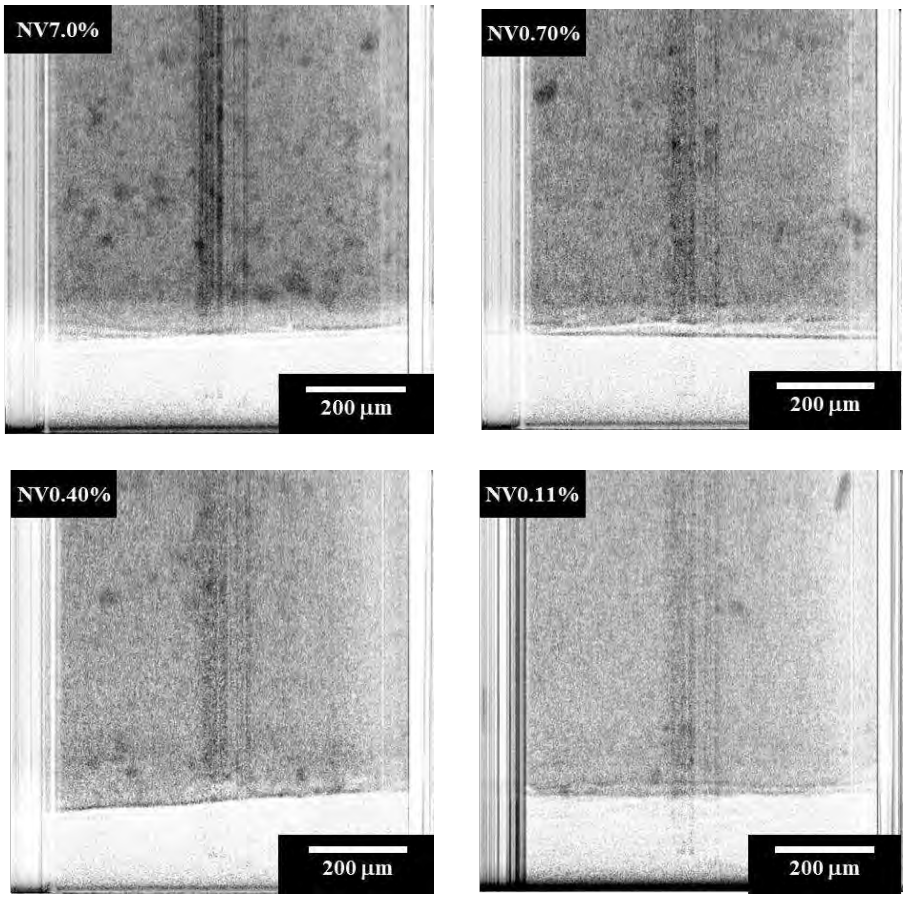

Figure 2. Agglomerate particles in electrode slurries.

Observation of Sedimentation and Calculation of Sedimentation Rate

We performed a time-series visualization of the electrode slurry placed in the X-ray radiography system for 7206 seconds. Sedimentation behaviors of the agglomerated particles were observed in all electrode slurries. The captured images were processed to quantitatively characterize sedimentation rates of selected particles in the slurry (Figure 3). The sedimentation rate of the agglomerated particles was decreased with the increase of non-volatile ratio.

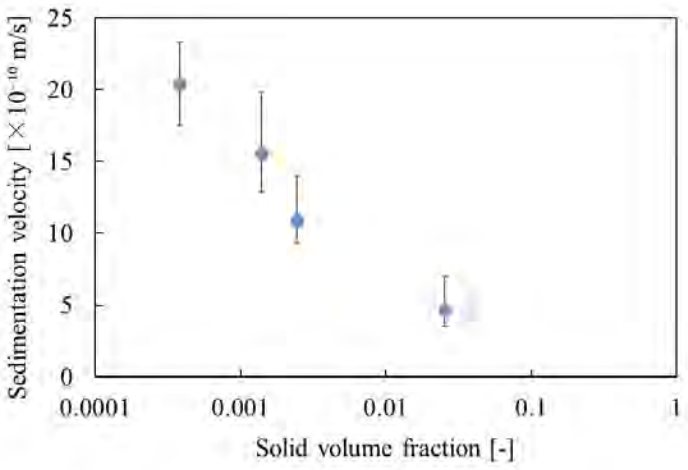

Figure 3. Sedimentation rate of agglomerate particles.

Examination of the Calculation for the Effective Density of Agglomerated Particles

In order to investigate the factors related to the aggregation state and sedimentation behavior of aggregated particles, we attempted to calculate the effective density. We considered a method using Lambert-Beer's law with the following assumptions: the intensity of the irradiated X-rays is constant, the agglomerated particles are spherical, the unoccupied region of the platinum-supported carbon contains ionomers, H_2O and NPA with the same composition as that of the electrode slurry, and the region around the agglomerated particles is uniformly dispersed.

The absorption coefficients are specific to each element, and those of compounds are determined by the absorption coefficients and composition of its constituent elements. Therefore, if we can obtain the absorption coefficients of the agglomerated particles from the images captured by the soft X-ray imaging system, the composition of the agglomerated particles can be estimated conditionally, and the effective density of the agglomerated particles can be calculated. In order to take the time variation of the X-ray irradiated intensity into consideration, we introduced a correction term using the outer edge of the container included in the observation area as a reference area and devised a method to calculate the effective density of agglomerated particles.

Calculation of Effective Density of Agglomerated Particles

The effective density of the agglomerated particles, which we examined the sedimentation rates, were calculated. Figure 4 shows the results of the non-volatile ratio of the electrode slurry 7.0 % and 0.11 %, where t=0 s is the time when we started the observation of sedimentation processes and t=7206 s is the time when the measurement was terminated.

In all the electrode slurries, the effective density tended to increase with decreasing particle diameter. The effective density after the sedimentation (t=7206 s) was larger than that in the initial state. This can be due to the progress of agglomeration with time and the increase of the number of platinum-supported carbon particles that compose the agglomerated particles. Furthermore, the effective density of agglomerated particles slightly decreased with the decrease of the non-volatile ratio. This can be because of the

decrease in the number of particles that compose an agglomerate by decreasing the non-volatile ratio.

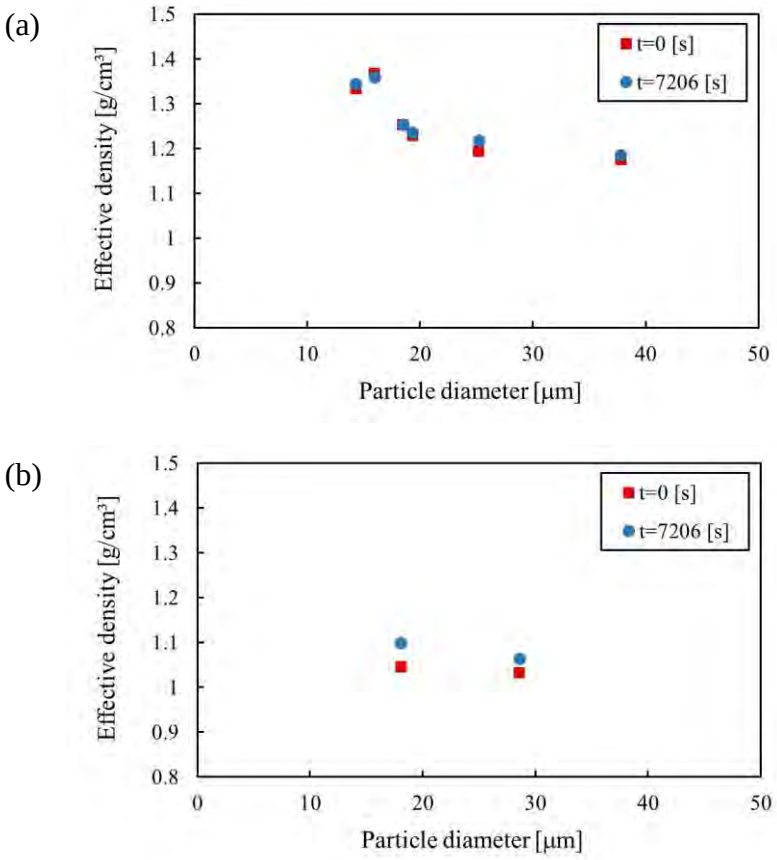

Figure 4. Effective density of agglomerate particles with non-volatile ratio (a) 7.0%, (b) 0.11%.

Effective Density and Sedimentation Rate of Agglomerated Particles

Figure 5 shows sedimentation rate as a function of the effective density of the agglomerated particles in the slurries with various non-volatile ratios. According to Stokes' law, the sedimentation rate is proportional to the square of the particle diameter and the difference between the particle density and the fluid density in dilute dispersions. However, the relation between the effective density and the sedimentation rate in the electrode slurries seems to be affected by the non-volatile ratio as shown in Figure 5. The viscosity of the electrode slurries was drastically increased with the increase of non-volatile ratio. Therefore, particle–particle interaction significantly affected high concentration electrode slurries and the sedimentation was suppressed by hindered settling.

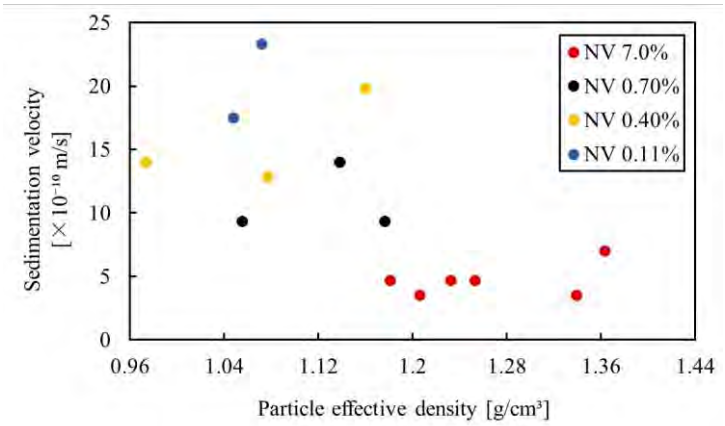

Figure 5. Effective density and sedimentation rate.

Conclusions

In this study, in order to clarify the agglomeration/dispersion state and migration phenomena of particles in the electrode slurries, a time-series visualization by a soft X-ray radiography system was carried out for electrode slurries with various non-volatile ratios. It was found that there were agglomerated particles of about 10 – 40 μm in the electrode slurry. The number of agglomerated particles observed in an image decreased with decreasing the non-volatile ratio. In addition, the sedimentation rate decreased as the increase of the non-volatile ratio. We estimate the effective density of agglomerated particles by introducing Lambert-Beer's law, and it was found that the effective density increased with decreasing particle diameter, the effective density at the end of sedimentation was larger than at the beginning. In addition, the less the non-volatile ratio, the slightly smaller the effective density of agglomerated particles. Furthermore, the sensitivity of the sedimentation rate to particle diameter and density varied depending on the non-volatile ratio of the slurry.

Acknowledgments

This work was supported by JSPS KAKENHI Grant Number 18K13702 and 21H04540.

References

1. T. Suzuki, S. Okada, and S. Tsushima, *ECS Trans.*, **86**, 193 (2018).
2. S. Khandavalli, J. H. Park, N. N. Kariuki, D. J. Myers, J. J. Stickel, K. Hurst, K. C. Neyerlin, M. Ulsh, and S. A. Mauger, *ACS Appl. Mater. Interfaces*, **10**, 43610 (2018).

Chapter 8

32 Cell Level Characterization

ECS Transactions, 104 (8) 205-220 (2021)
10.1149/10408.0205ecst ©The Electrochemical Society

Performance of PEFC under Different Gas-mixing Conditions

Yulei Ma, Miho Kageyama, and Motoaki Kawase

Department of Chemical Engineering, Kyoto University, Kyotodaigaku-Katsura, Nishikyo-Ku, Kyoto 615-8510 Japan

For PEFCs' grand-scale commercialization, their performance should be further improved. The performance of PEFC is the results of the distribution of local current density and materials concentration, especially oxygen and water. In addition, the in-plane transport of reactant gas in the gas diffusion layer (GDL), which is difficult to measure, affects the distribution of oxygen partial pressure and relative humidity (RH) by mixing the gas with different residence time. In this study, the distribution of local current density as well as oxygen partial pressure and RH was estimated by varying active area and gas flow rate. Furthermore, two kinds of different gas channels, parallel and serpentine, were utilized to estimate the effect of gas mixing in the GDL. The concept of space time was used to discuss the effects of gas mixing in the perspective of chemical engineering. The results may provide a theory basis for a cell design procedure.

Introduction

Polymer electrolyte fuel cells (PEFC) offer zero-emission energy conversion. However, for PEFCs' grand-scale commercialization, their performance should be further improved. The performance of PEFC is determined by the local current density or the oxygen reduction reaction (ORR) rate. Extensive studies have been carried out on explorations of the effect of factors such as temperature (1), total pressure (2), oxygen partial pressure (3), relative humidity (RH) (4) on the ORR rate as well as mass transfer rate. However, these parameters have distributions even in a single cell, and they may be dependent on each other, so that the effects of a single factor in the cell are complicated and uneasy to be clarified.

The ORR in PEFC is an exothermal reaction, so that the temperature profile exists in a cell in the through-plane and in-plane directions. The temperature at cathode catalyst layer surface is 1–2 ^{o}C higher than the temperature at gas channel, when the current density is 0.8 A/cm^2 and the cell temperature is 80 ^{o}C (5,6). On the other hand, the temperature distribution in the in-plane direction is more ununiform than that in the through-plane direction. The difference of the highest and lowest temperature in the electrode was less than 10 ^{o}C at 0.8 A/cm^2 in a cell with 50 mm × 50 mm active area observed by thermograph (7).

The total pressure also has a distribution in a cell due to the pressure drop along the gas channel. The pressure drop of the cell with 14.4 cm^2 active area and serpentine gas channel,

whose depth, width, and total length are 1.0 mm, 1.0 mm and about 700.0 mm, is about 0.3 kPa, fed with 200 mL/min of N_2 at room temperature under atmospheric pressure (8).

The partial pressure profile of oxygen and water vapor affect the ORR rate distribution. On the other hand, the ORR can change the composition of the reactant gas, i.e. the molar fraction of oxygen and water vapor, so that the performance can also be affected by reactant conversion (9). Furthermore, gas flow pattern distributes the reactant gas in the in-plane direction, which also affect the cell performance (10). Since the pressure gradients and concentration gradients exist in the porous gas diffusion layer (GDL), the reactant gas can cross to the neighboring channels and the gas with different compositions are mixed, so that the gas composition distribution is also affected by the cross-flow phenomenon (11).

The distributions of properties, especially gas composition inside the cell, are difficult to be measured precisely without expensive equipment and high experimental techniques. Technologies such as gas chromatograph and laser absorption spectroscopy can be used to analyze the gas composition inside the cell (12). However, these ex-situ characterizations only yield the effective properties of the whole layer and do not resolve the local impact of morphological heterogeneity (13). By inserting an oxygen sensor, such as optical fiber covered by oxygen-sensitive dye film (14), microelectrochemical cell (15), into a specific location in a cell, the oxygen partial pressure can be measured *in-situ*. Micro-gas-chromatograph and tunable diode laser absorption spectroscopy techniques can be utilized to measure the water vapor partial pressure *in-situ* (12). Additionally, liquid water distribution can be measured by neutron and X-ray imaging (16,17).

The cell performance can be analyzed and predicted by numerical methods, which have been discussed extensively in the literature. Although many 3-dimensional, non-isothermal, multi-phase models have been reported (18, 19), most of the models are complicated with heavy computation load, and difficult to separate the effects of fluid dynamic, heat transfer, proton/electron transfer and electrochemical phenomenon. A computationally inexpensive method to summarize and understand the distributions of properties in the cell is lack of reporting. To clarify the effects of gas composition inside the cell, the concept of gas mixing and residence time distribution (RTD) in the perspective of chemical reaction engineering can be helpful.

The objective of this study is to demonstrate a method to evaluate the gas mixing property of gas channels, and to predict the cell performance. The RTD can be simulated by numerical method, so that the macromixing of gas with different space times can be evaluated. By regarding the PEFC as a reactor, the cell performance can also be predicted according to the reactor model which has similar RTD as the simulation results.

In addition, the cell performance under different space time conditions can be measured experimentally by changing the active area and gas flow rate, so that the gas composition profile can also be evaluated. The results are expected to provide a methodology to understand the gas macromixing in different shape of gas channels, and may be helpful for the cell design.

Numerical Calculation

In this study, a 3-dimensional computational fluid dynamics (CFD) model was developed to simulate the velocity and pressure fields in the cathode gas channels and GDLs. To get the RTD of the gas channel, a kind of tracer which is a stepwise change in a special physical property, e.g., concentration, electrical conductivity, temperature, was supplied to the gas inlet continuously. Then the step responses at the gas channel outlet were simulated by solving time-dependent advection equations of the specific physical property. The calculation was achieved by finite volume method by using an open source toolbox OpenFOAM 8.

Model geometry

The geometries and meshes applied for parallel and serpentine channels in the calculation are shown in Figure 1. The gas flows from the inlets to the outlets, through the GDLs which were implemented as porous medias. The width and depth of gas channels are 1 mm, and the width of the ribs between the channels was 1 mm. The size of the GDLs were 22 mm in X direction, 21 mm in Y direction, and 0.190 mm in Z direction. The meshes of manifolds in parallel channels, bended part in serpentine channels, and GDLs were denser than that in other parts. The total number of cells applied in simulation was 383 000 for parallel gas channel and 373 000 for serpentine gas channels.

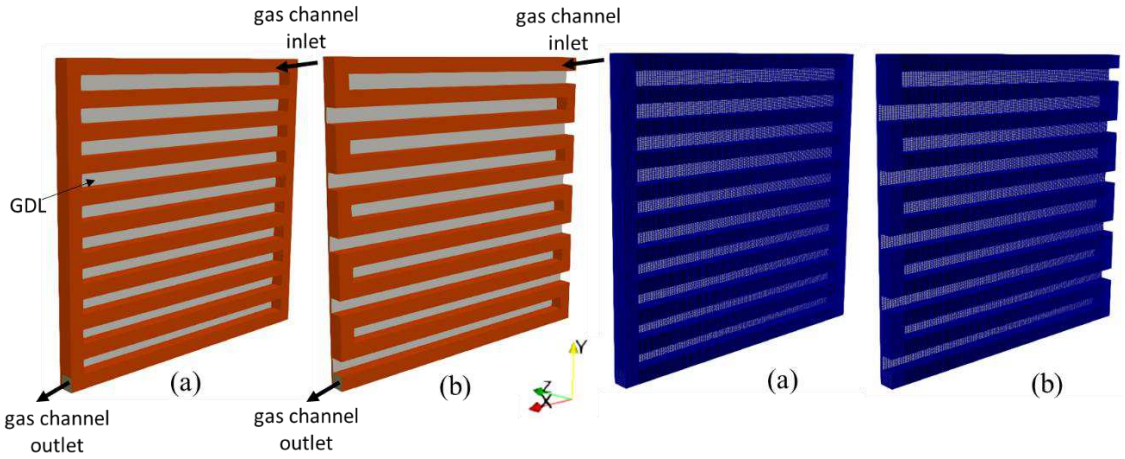

Figure 1. Geometries (left) and meshes (right) of flow fields ((a) parallel, (b) serpentine)

Assumptions

Steady state was assumed. The gas flow was incompressible laminar due to low velocities. Isotropic and homogeneous ideal gas which has uniform temperature, density, and viscosity was assumed. The GDL was regarded as a uniform porous medium. No liquid water condensed in the gas channel.

The tracer which has negligibly small diffusivity in the reactant gas was assumed. In another word, the convection of the tracer is great enough so that the diffusion of the tracer can be ignored.

CFD simulation

Governing equations applied to calculate the velocity and pressure fields are expressed by Eqs. [1] and [2]

Mass conservation:

$$\nabla \cdot (\rho \boldsymbol{U}) = 0 \quad [1]$$

Momentum conservation:

$$\nabla \cdot (\rho \boldsymbol{U}\boldsymbol{U}) - \nabla \cdot (\mu \nabla \boldsymbol{U}) = -\nabla P + \boldsymbol{S_m} \quad [2]$$

where $\boldsymbol{U}$ represents the velocity vector, ρ and μ represent the density and viscosity of the reactant gas respectively. P is the total pressure, and $\boldsymbol{S_m}$ is the momentum source term, which equals 0 in the gas channels and satisfies the Darcy's law in the GDLs given by Eq. [3].

$$\boldsymbol{S_m} = -\frac{\mu}{K}\boldsymbol{U} \quad [3]$$

The operating conditions and physical constants are listed in Table 1. The inlet Re number is 127 so that the gas flow can be regarded as laminar.

Table 1. Operating conditions and physical constants (353 K)

Variable	Symbol	Value
Total pressure at gas channel outlet	P_L	101325 Pa
Cell temperature	T	353 K
Velocity at gas channel inlet	$\lvert\boldsymbol{U}\rvert$	2.6658 m s^{-1}
Inlet molar fraction of O_2	y_{O0}	0.7532
Inlet molar fraction of H_2O	y_{S0}	0.2468
Density	ρ	0.9850 kg m^{-3}
Viscosity	μ	2.0675 × 10^{-5} Pa s (20,21)
Permeability of GDL (in-plane direction)	K_x, K_y	1.30× 10^{-11} m^2 (22)
Permeability of GDL (through-plane direction)	K_z	8.99× 10^{-12} m^2 (22)

RTD simulation

The transport equation of the tracer is given by Eq. [4].

$$\frac{\partial \varphi}{\partial t} + \nabla \cdot (\varphi \boldsymbol{U}) - \nabla \cdot (\Gamma \nabla \varphi) = S_\varphi \quad [4]$$

where φ represents the specific physical property of the tracer, Γ represents the diffusivity of property, and S_φ represents the source term. $\boldsymbol{U}$ is the velocity field calculated by CFD simulation mentioned above.

For example, when the φ represents the temperature, the Γ represents the heat diffusivity. In this study, Γ and S_φ equal 0, so that the Eq [4] can be simplified to a time-dependent advection equation, which means when the φ represents the temperature, the thermal conductivity is 0, and the heat can only be transferred by convection.

When setting the φ equals 1 at the vessel inlet and 0 in the whole vessel from the start time, the tracer is carried in the flow field until it fulfills the whole vessel. Then by monitoring the φ at the vessel outlet, the time variation can be described as a cumulative RTD function, $F(t)$.

$$F(t) = \bar{\varphi}_L(t)/\bar{\varphi}_0(0) \quad [5]$$

where $\bar{\varphi}$ represents the integrated average value at inlet or outlet face, the arguments 0 and L represent the gas channel inlet and outlet, respectively. And the RTD function $E(t)$ and the mean residence time $\bar{t}$ can be obtained by Eqs. [6] and [7].

$$E(t) = \frac{d}{dt}F(t) \quad [6]$$

$$\bar{t} = \int_0^\infty tE(t)dt \quad [7]$$

Reactor design equations

The ORR kinetics can be expressed as Eq. [8].

$$-r_{\mathrm{SO}} = k_{\mathrm{gc}}p_{\mathrm{O}} \quad [8]$$

where p_{O} is the local oxygen partial pressure [Pa], and $-r_{\mathrm{SO}}$ is the oxygen consumption rate per active area [mol/(m^{2}s)], which was experimentally proved to be 1st-order to the oxygen partial pressure (23). k_{gc} represents the partial-pressure-based apparent kinetics constant [mol/(Pa·m^2·s)] which is the function of cathode electromotive force and RH at a fixed temperature (24).

By assuming the kinetics constant k_{gc} is linear to the activity of the water vapor a_{w} which is equal to RH, and the water permeation flux through the membrane is 0, the oxygen partial pressure and the activity of the water vapor can be calculated from the oxygen conversion x_{O} by Eqs. [9] and [10], according to the material balance.

$$p_{\mathrm{O}} = \frac{Py_{\mathrm{O0}}(1 - x_{\mathrm{O}})}{1 + y_{\mathrm{O0}}x_{\mathrm{O}}} \quad [9]$$

$$a_w = \frac{P}{p_{\mathrm{S}}^{\mathrm{sat}}}\frac{y_{\mathrm{S0}} + 2y_{\mathrm{O0}}x_{\mathrm{O}}}{1 + y_{\mathrm{O0}}x_{\mathrm{O}}} \quad [10]$$

where y_{S0} and y_{O0} represents the water vapor and oxygen molar fraction of the inlet gas, $p_{\mathrm{S}}^{\mathrm{sat}}$ represents the saturated water vapor pressure at the cell temperature, P is the total pressure in the gas channel.

When the GDL is thick enough, the continuous oxygen partial pressure and RH distribution on the CL surface can be assumed independent on the location under gas channels and ribs. Therefore, the PEFC can be regarded as a continuous reactor, which has the gas-mixing behavior between plug flow reactor (PFR) and perfectly mixed flow reactor (CSTR), whose design equations can be written as Eqs. [11] and [12].

$$-r_{\mathrm{SO}}d(A/v_0) = C_{\mathrm{O0}}dx_{\mathrm{O}} \quad [11]$$

$$-r_{\mathrm{SO}}(A/v_0) = C_{\mathrm{O0}}x_{\mathrm{O}} \quad [12]$$

where A is the active area from the gas inlet [m^2], v_0 is the inlet gas volumetric flow rate [m^3/s], C_{O0} is the oxygen concentration in the inlet gas [mol/m^3], and x_O is the oxygen conversion. A/v_0 can be regarded as the space time of the reactant gas in the cell. By solving the Eqs. [8], [9], [10] and the design equation, the distributions of oxygen conversion, as well as the oxygen partial pressure and RH, can be estimated.

Experimental

A Japan Automobile Research Institute (JARI) type cell was used in the experiments. The active area was reduced to 2.0 cm×2.0 cm so that the temperature distribution is less ununiform in the in-plane direction. Two kinds of gas channels, i.e. parallel and serpentine, were used in the cell. The width and depth of gas channels are 1 mm, and the width of the ribs between the channels was 1 mm. The membrane electrode assembly (MEA) was consisted of the catalyst layers made of 50 wt% Pt/carbon black catalyst particles with ionomer and the membrane (Chemours NR-212). Ionomer/carbon weight ratio was 1.0, and the catalyst layers (CL) thicknesses of anode and cathode were 10 μm. Carbon paper (Toray TGP-H-060) without microporous layer (MPL) was used as GDL.

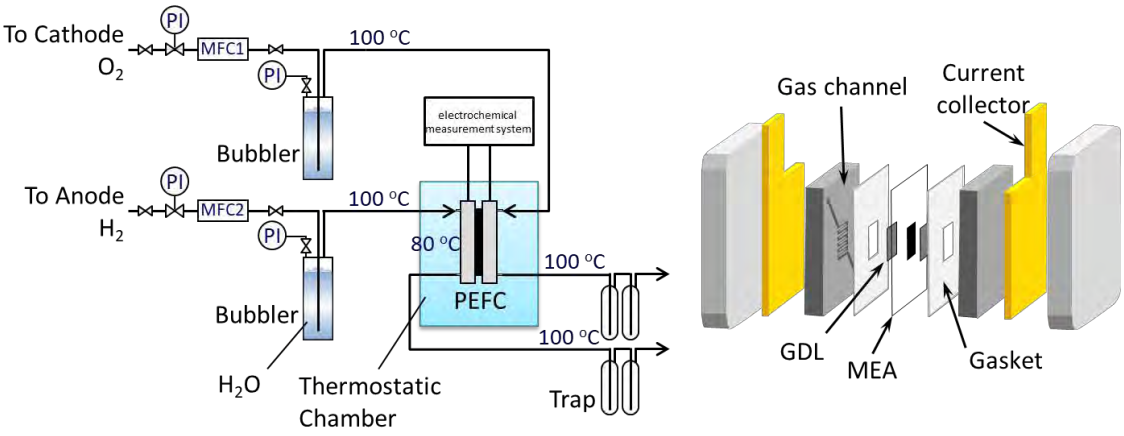

Figure 2. Experiment apparatus and cell structure

The MEAs with the same thickness and catalyst of CL were used in the experiment. On the other hand, the gaskets made of PTFE, which can block the mass transfer and electron conduction, had different opening area to obtain different active areas. The sizes of the gaskets opening were 2.0 cm×2.0 cm, 2.0 cm×1.5 cm, 2.0 cm×1.0 cm, and the GDLs which

had the same size of the gaskets opening were utilized in each experiment, as shown in Figure 3. Since the small active areas were applied, the distributions of the temperature and the total pressure in the gas channels were neglected.

The cell was operated in a thermostatic chamber whose temperature was controlled to maintain the temperature at the center of the cathode gas channel at 80 °C. The pressure at the cell outlet was 1 atm. Pure H_2 and O_2 were humidified in bubblers at 65–75 ˚C. H_2 flow rate was 60–200 cm^3/min (20 °C, 1 atm) on dry basis. The stoichiometry of H_2/O_2 was 2.

Polarization curves and electrochemical impedance spectra were obtained using an electrochemical measurement system (Hokuto Denko Corp., HZ-7000). The polarization curves were obtained by measuring the current at each cell voltage (0.005 V – OCV). The impedance spectra were measured in a range of frequency from 100 mHz to 100 kHz. A standard equivalent circuit model was employed to determine the high frequency resistance (HFR) (25). The cell voltage was corrected by the HFR results.

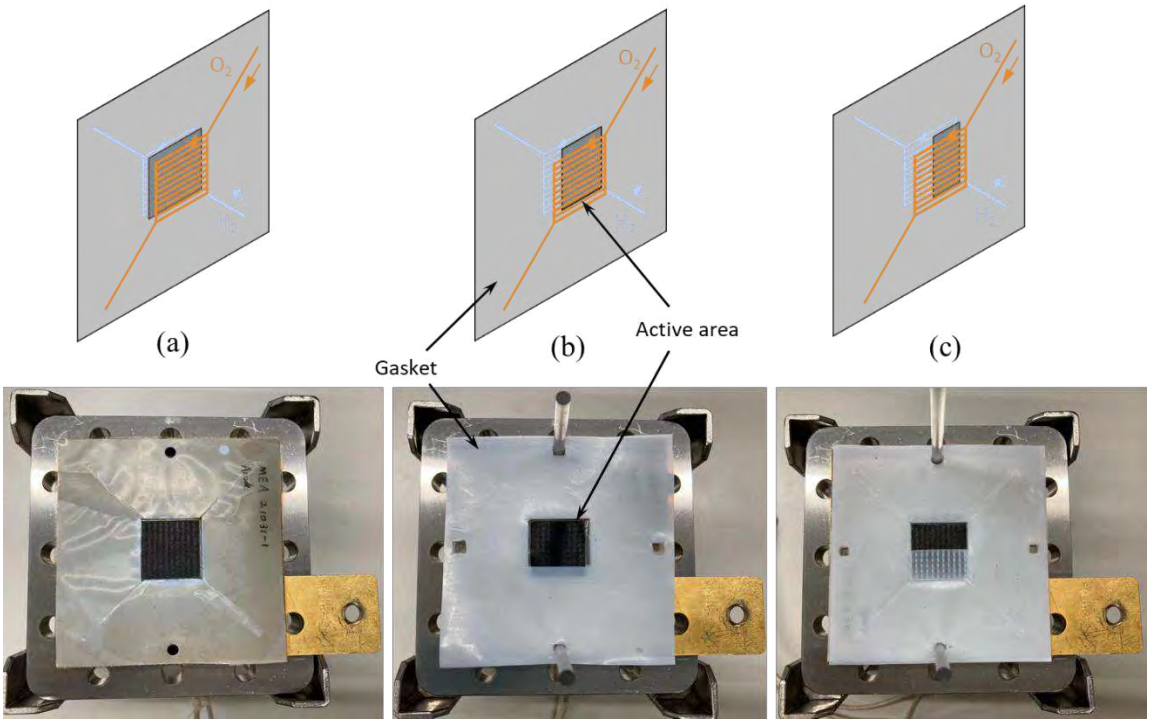

Figure 3. Different active areas utilized in the experiments
((a) 2.0 cm×2.0 cm, (b) 2.0 cm×1.5 cm, (c) 2.0 cm×1.0 cm)

Results and Discussion

Numerical calculation results

The velocity and pressure distributions of parallel and serpentine gas channels simulated by OpenFOAM 8 are shown in Figure 4. As shown in the velocity field in the gas channels (z = 0.5 mm), since the gas flow is separated into several channels in case of parallel channels, the gas velocity in each channel is much lower than that in 1-serpentine channel, and the pressure gradient of the serpentine channel is much higher than that of parallel

channel. As a result, a large amount of gas flows across the rib to the neighbor channel in case of the serpentine channel, especially away from the bended parts where the neighbor gas channels are connected, and nearly no cross-flow gas was found in case of parallel channel as shown in the velocity field in the GDL (z = 1.095 mm).

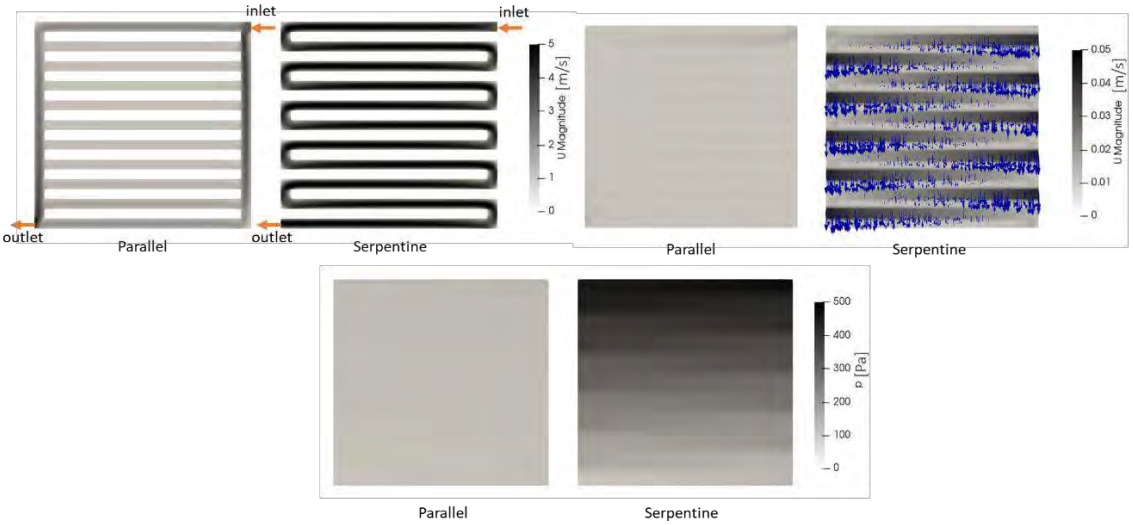

Figure 4. Velocity and pressure field in the center sections of gas channels and GDLs (top left: velocity at z = 0.5 mm, top right: velocity at z = 1.095 mm, bottom: gauge pressure at z = 1.0 mm)

Figure 5 shows the distribution of the property of the tracer, changing over time after starting the continuous feed of the tracer to the inlet. In case of the parallel channel, the property convection rate in the channels near the inlet and outlet is 2–4 times higher than that in the medium channels, due to the nonuniform velocity distribution. Since a part of the gas flows to the outlet quickly, the tracer can be detected earlier than the case of serpentine. After 1 second from feeding the tracer, it nearly fulfilled the whole gas channel, and the concentration in the GDL of parallel channel is still much lower than that of the serpentine channel, which also indicates the cross-flow in GDL under the parallel channel is much weaker than that of the serpentine channel.

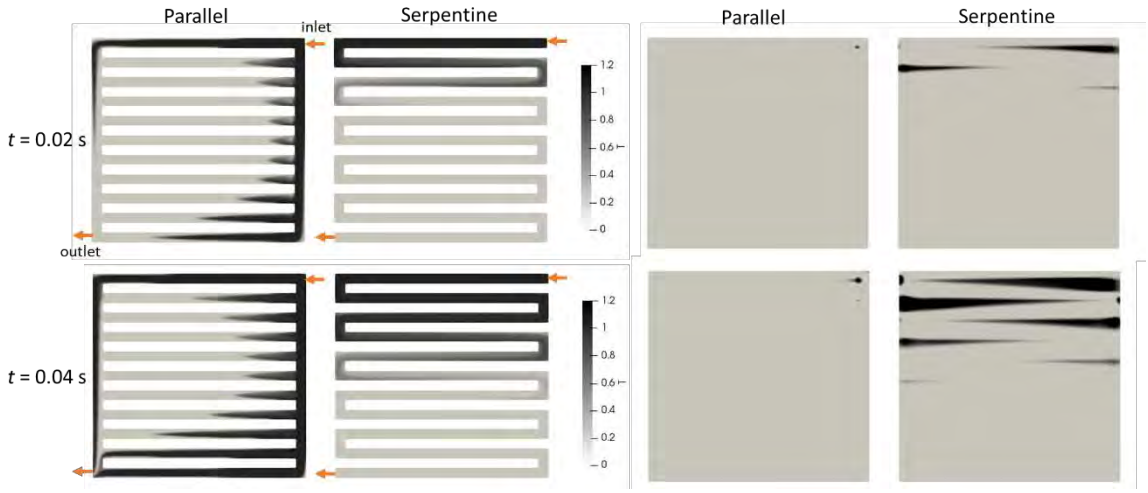

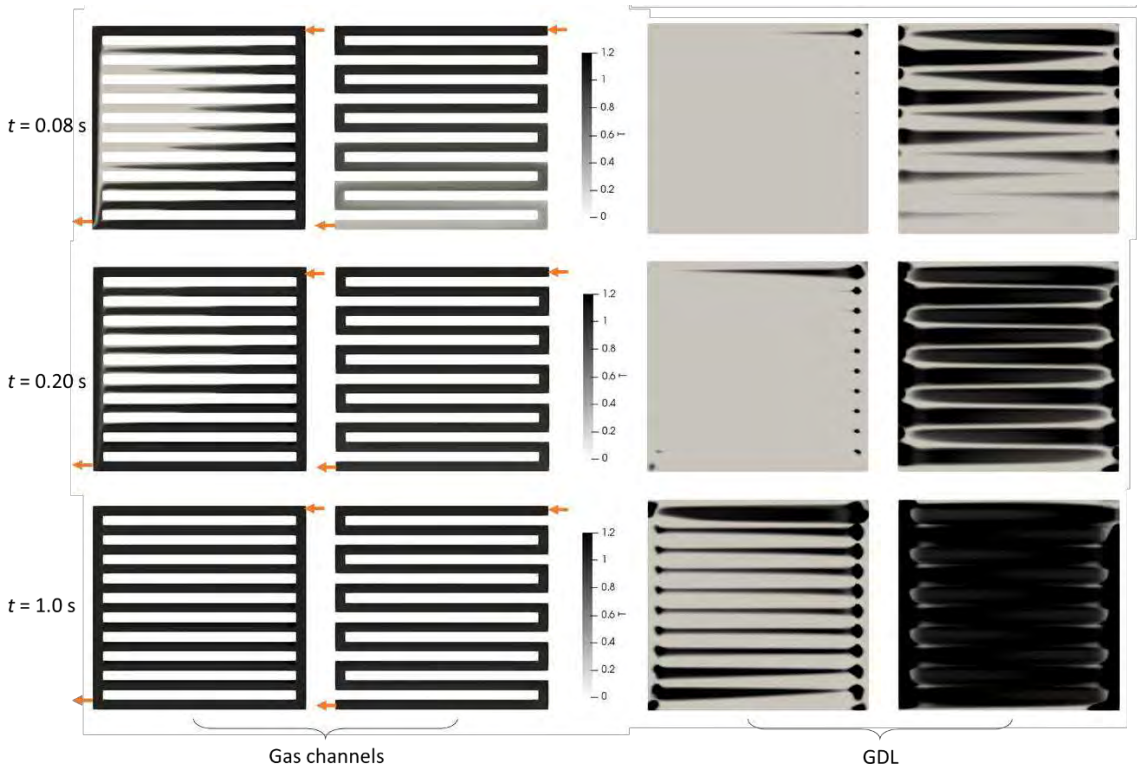

Figure 5. Time variation of the property of the tracer in the center sections of gas channels and GDLs (left: z = 0.5 mm, right: z = 1.095 mm)

By analyzing the time variation of integrated average property of the tracer in the outlet faces, the RTD can be obtained, as shown in Figure 6. The mean residence time, variance and skewness are also shown in Figure 6. The mean residence time of parallel is shorter than the serpentine channel, which indicates some dead volume may exist in the GDL in case of parallel channel. Some oscillation of RTD function of the parallel channels can be detected, due to the nonuniform distribution of the velocity.

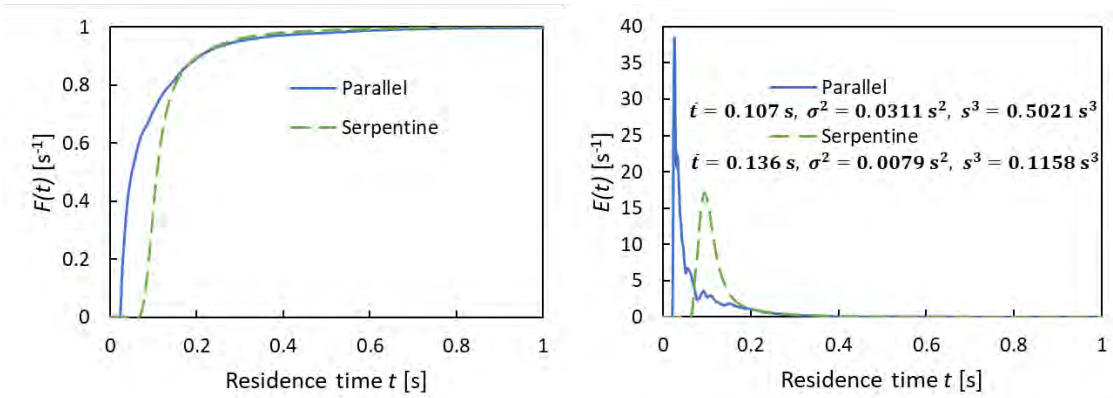

Figure 6. Residence time distribution of parallel and serpentine channels

By normalizing the residence time by the mean residence time, the RTD functions of dimensionless residense time can be derived, as shown in Figure 7. The RTD functions of CSTR, PFR and laminar flow reactor (LFR) plotted in Figure 7 were calcutaled by equations listed in Table 2.

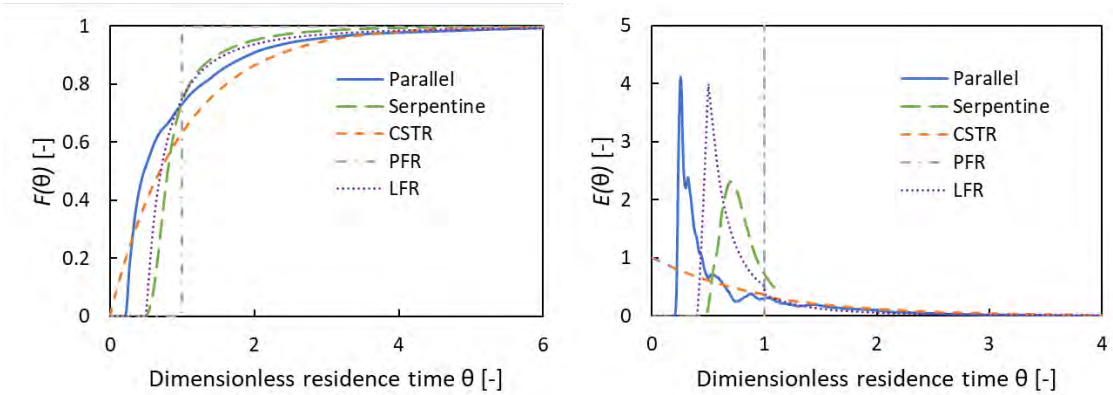

Figure 7. Dimensionless-residence-time distributions of different channels and models

Table 2. Dimensionless-residence-time-based RTD function of different model ($\boldsymbol{\theta = t/\bar{t}}$)

Model	$\boldsymbol{F(\theta)}$	$\boldsymbol{E(\theta)}$
CSTR	$1-\exp(-\theta)$	$\exp(-\theta)$
PFR	$U(\theta-1)$ (Step function)	$\delta(\theta-1)$ (Dirac delta function)
LFR	$\begin{cases} 0 & (0 \le \theta < 0.5) \\ 1-1/(4\theta^2) & (\theta \ge 0.5) \end{cases}$	$\begin{cases} 0 & (0 \le \theta < 0.5) \\ 1/(2\theta^3) & (\theta \ge 0.5) \end{cases}$

The response of the parallel channels is similar to PFR for the short residence time components and CSTR for the long residence time components. The mixing of the gas near the inlet of the parallel gas channels is not obvious, since the pressure gradient between neigbor gas channels is gentle. On the other hand, the gas mixes near the outlet of the parallel gas channels. Consequently, the PFR followed by CSTR model can be considered to simulate the performance with parallel channels, shown as Figure 8.

On the other hand, in case of serpentine channels, the gas near the inlet is mixed with the gas in the neigbor channels, and then flows like in PFR, since the cross-flow is remarkable near the gas inlet and weak near the bended parts. Therefore, the CSTR followed by PFR model can be considered to simulate the performance with serpentine channels. More accurrate model such as CSTR followed by PFR in several parallel line can also be considered. Both of the PFR followed by the CSTR and CSTR followed by PFR has the same RTD function which can be written as Eq. [13].

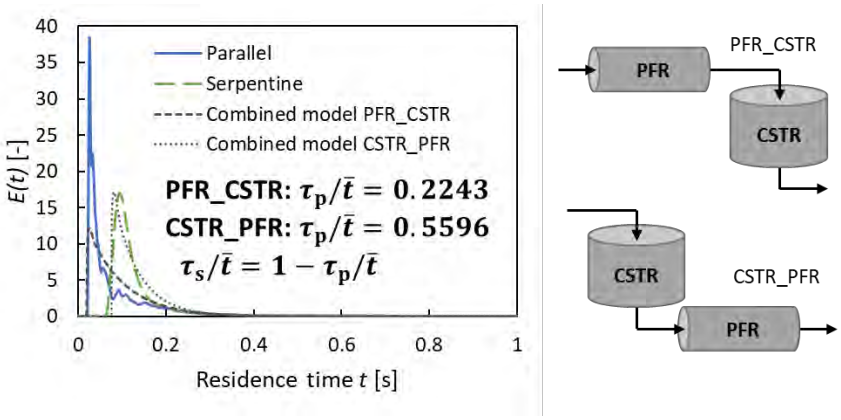

Figure 8. The RTD functions of parallel gas channels and compartment model

$$E(t) = \begin{cases} 0 & (t < \tau_p) \\ \dfrac{\exp\left(-\dfrac{t-\tau_p}{\tau_s}\right)}{\tau_s} & (t \geq \tau_p) \end{cases} \quad [13]$$

where $\bar{t}$ is the mean residence time, τ_p and τ_s are the space time of PFR and the space time of CSTR. The macromixing in the gas channel and GDL can be represented by these two space times, τ_p and τ_s. The serpentine channel exhibited $\tau_p/\bar{t} = 0.56$ which is closer to the plug flow than the parallel flow exhibiting $\tau_p/\bar{t} = 0.22$.

Experimental results

Figures 9 shows the experimental polarization curves of different active areas and inlet gas flow rates in case of parallel gas channels, where the cell voltages are corrected by experimental HFR results. In case of large active area, higher current density was observed under high cell voltage, which resulted from the relatively high average RH of gas due to humidification by the water produced in ORR, and the decrease of oxygen partial pressure is little which cannot overtake the effects of the humidification. It infers that the ORR has the similar behavior of the self-catalytic reaction. The humidification of the water increases the ORR rate at low oxygen conversion, on the other hand, the decreasing oxygen partial pressure reduces the ORR rate at high conversion.

However, the limited current density is higher in case of the 2 cm×1 cm, and limited current densities in cases of the 2 cm×1.5 cm and 2 cm×2 cm are nearly equal. The reason may be the flooding occurs in case of the larger active area, so that the oxygen transfer resistance increases due to the presence of liquid water. On the other hand, the difference in limited current density between 2 cm×1 cm and other cases is smaller in case of gas flow rate of 2.69 mL/s, comparing to 1.35 mL/s, which infers that the humidification of the produced water is less effective in case of the high gas flow rate, so that the flooding is less remarkable. The results also indicate that the flooding occurs at the 1/2–3/4 length of the gas channel from the inlet.

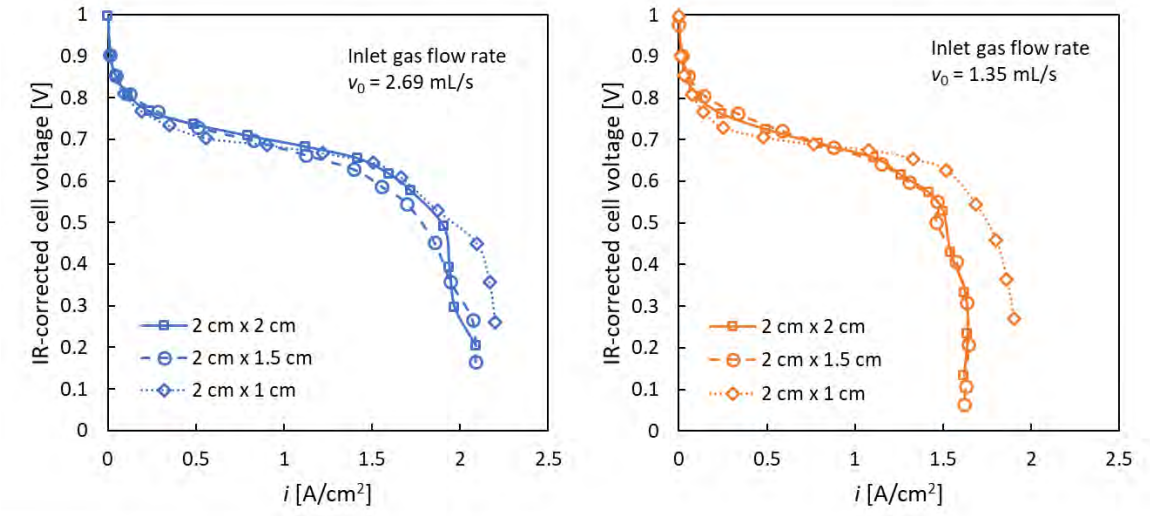

Figure 9. Polarization curves of different active areas (parallel gas channel)

Figure 10 shows the polarization curves of different inlet gas flow rates in the fixed active area in case of the parallel gas channels. The performances are the same when the current density is lower than 0.6 A/cm^2, which indicates that the effect of the water humidification compensated the effects of the oxygen consumption. However, the limited current density is lower in cases of low inlet gas flow rate. The oxygen conversion and oxygen partial pressure at the limited current density are about 0.66 and 17.0 kPa in case of the gas flow rate of 0.81 mL/s, and 0.312 and 27.3 kPa in case of the gas flow rate of 2.69 mL/s, which indicated that the insufficient oxygen supply causes the low oxygen partial pressure so that the oxygen mass transfer resistance increases near the limited current density.

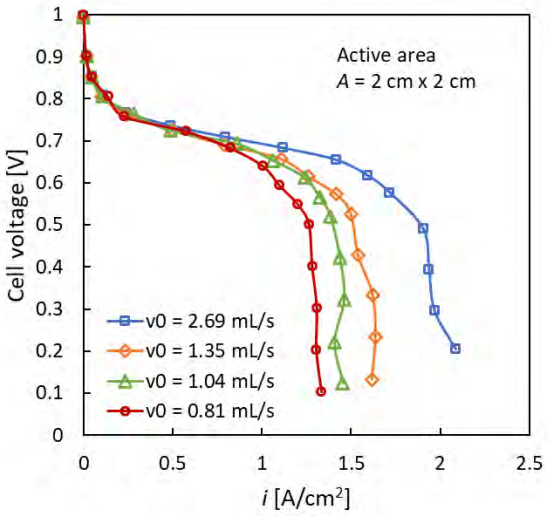

Figure 10. Polarization curves of different inlet gas flow rates (parallel gas channel)

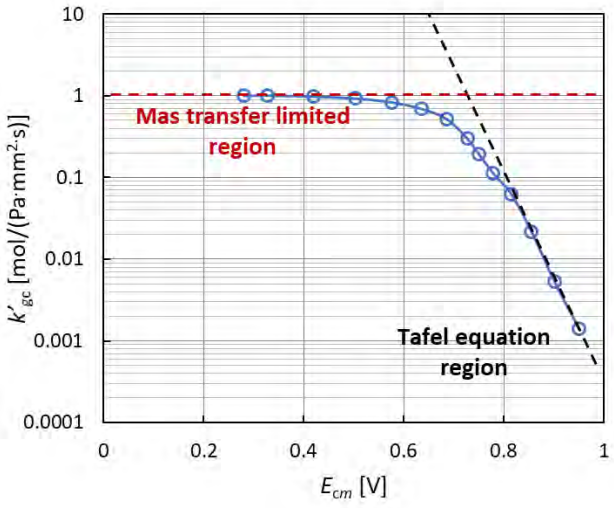

Figure 11. Kinetics data measured by differential reactor
(Gas channel: serpentine, humidified temperature: 75 °C, H_2 flow rate: 600 cm^3/min (20 °C, 1 atm), O_2 flow rate: 300 cm^3/min (20 °C, 1 atm))

To measure the kinetics data of the ORR, the polarization curve of MEA with the equal Pt-loading and catalyst layer thickness was measured under the high flow rate, where the oxygen conversion was 0.10 at 0.64 V of the IR-corrected cell voltage. Since the

conversion is low, the cell can be regarded as a differential reactor, whose design equation can be written as Eq. [14], where k'_{gc} represents the partial-pressure-based apparent kinetics constant [mol/(Pa·m^{2}s)] at RH = 1, and $\bar{x}_O$ represent the average oxygen conversion throughout the gas channel. Consequently, the observed ORR kinetics which contain the effectiveness factors can be calculated simply, as shown in Figure 11.

$$\frac{x_O}{A/v_0} = k'_{gc}\frac{RTP}{p_S^{sat}}\frac{(1-\bar{x}_O)(y_{S0}+2y_{O0}\bar{x}_O)}{(1+y_{O0}\bar{x}_O)^2} \quad [14]$$

By applying the combined PFR followed by CSTR model to parallel gas channels, and the ORR kinetics measured by experiments, the performance of the cell voltage can be calculated by Eqs. [10] and [11]. Figure 12(a) and (b) shows the oxygen conversion under different ratios of active area to the inlet gas volume flow rate, which is regarded as the space time. Since the ORR has a similar behavior to the self-catalytic reaction, the oxygen conversion, which is proportional to the current density, of CSTR is higher than that of PFR at little space time, and lower than PFR at high space time. In case of low IR-corrected cell voltage, the critical space time, at which the CSTR and the PFR have the same performance, is longer than that in case of high IR-corrected cell voltage. However, the difference of the CSTR and PFR is not obvious at short space time. The compartment model has an intermediate performance between PFR and CSTR, and is close to the CSTR at long space time, which indicates the gas mixing in the parallel channel is more obvious at long space time.

On the other hand, the CSTR followed by PFR model, which is considered to characterize the serpentine channel, is closer to the PFR model. The calculation results indicate that the serpentine has better performance than the parallel at high oxygen conversion, since the effect of oxygen consumption is greater than water humidification, so that the gas mixing is not beneficial here.

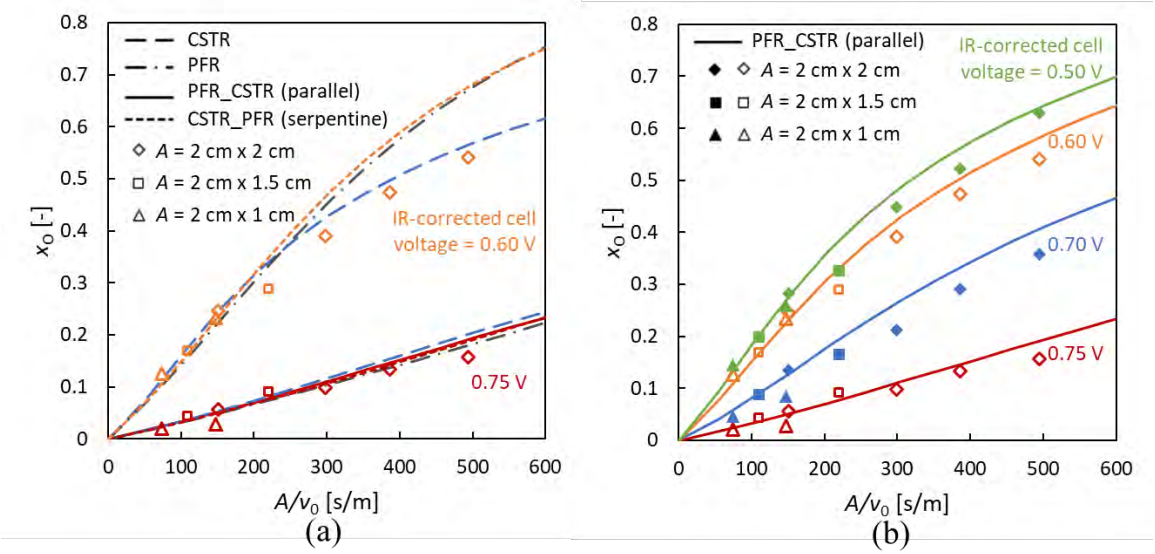

Figure 12. Relationship of oxygen conversion and space time at constant IR-corrected cell voltage (points: experimental results of parallel channels, curves: calculated results (a) CSTR, PFR, compartment models, (b) PFR_CSTR model)

Figure 12(b) shows the experimental data in case of parallel channel with calculated curve by the compartment model. The compartment model fits well with the experiment results at short space time. At long space time, the predicted oxygen conversion is higher than the experimental results. The reason may be that when calculating the ORR kinetics at high oxygen conversion, the reaction rate occurs near the outlet of the gas channel is higher due to the self-catalytic behavior, and the average conversion may be lower than the arithmetic mean of the conversion, so that the kinetics data may be overestimated.

In addition, in this study, the RTD is simulated without the reaction. However, since the gas composition changes due to the reaction, the total molar flow rate cannot be considered as a constant, especially when the oxygen conversion is high, and the real RTD may diverge from the simulated results in this study. Furthermore, the temperature and total pressure distributions are also not negligible at high oxygen conversion. In a word, the compartment model needs to be modified at high conversion.

Conclusions

The method in the perspective of chemical engineering was applied to evaluate the PEFC, which can be regarded as a continuous reactor which has the gas mixing behavior between PFR and CSTR. To characterize the gas mixing behavior, the RTDs of parallel and serpentine gas channels were simulated by numerical method. The cross-flow of the serpentine channels is much more remarkable than that of parallel channel, since the pressure gradient between the neighbor channels is steep in case of the serpentine. The ununiform velocity distribution in the parallel channels, that is the gas has high velocity in the channels near the inlet and outlets, was confirmed. As the results, some gas with long residence time mixes with the gas with short residence time near the gas outlet, so that the PFR followed with CSTR model can be considered. On the other hand, the serpentine has obvious cross-flow where the pressure gradient is steep, *vice versa*, the CSTR followed by PFR model can be considered.

The polarization curves of different ratios of the active area to the gas inlet flow rate, which can be regarded as the space time, were measured experimentally with the parallel gas channel. Lower oxygen conversion obtained in the narrower active area and higher flow rate, i.e. shorter space time, at the identical IR-corrected cell voltage. The phenomenon indicates that the ORR has a similar behavior to the self-catalytic reaction, which is affected by the water humidification and oxygen consumption simultaneously.

According to the calculation results, the serpentine channel has better performance than the parallel channels at long space time, when the IR-corrected cell voltages are fixed. The reason is that the serpentine has similar performance to the PFR, and the effect of oxygen consumption is greater than water humidification, which means the gas mixing is not beneficial at long space time.

The compartment model of PFR followed by CSTR, which is expected to characterize the cell performance with the parallel channel, reproduces the experiment results well at short space time or low oxygen conversion. In the future, more accurate kinetics data and model should be used, and the effects of the ununiform distribution of temperature and total pressure should also be concerned to eliminate the deviation of the model from the

experimental results. The method mentioned in this study can be applied to other shapes of gas channels to understand the gas macromixing, and may be helpful for the cell design.

Acknowledgments

This work was supported by the FC Platform Program: Development of design-for-purpose numerical simulators for attaining long life and high performance project (FY 2020–FY 2022) conducted by the New Energy and Industrial Technology Development Organization (NEDO), Japan.

References

1. Y. Qi, X. Li, S. Li, T. Li, M. Espinoza-Andaluz, P. Tunestål, and M. Andersson, *Int. J. Energy Res.*, **44**, 4352–4365 (2020).
2. F. Akitomo, T. Sasabe, T. Yoshida, H. Naito, K. Kawamura, and S. Hirai, *J. Pow. Sour.*, **431**, 205–209 (2019).
3. K. Takanohashi, T. Suga, M. Uchida, T. Ueda, Y. Nagumo, J. Inukai, H. Nishide, and M. Watanabe, *J. Pow. Sour.*, **343**, 135–141 (2017).
4. H. Nakajima, and K. Matsutani, *ECS Trans.*, **64**(3), 763–769 (2014).
5. M. Kawase, M. Nagayoshi, G. Inoue, and M. Kageyama, *ISCRE 23 & APCRE 7, Bangkok*, Sep. 8, OE03 (2014).
6. A. Nishimura, K. Yamamoto, T. Okado, Y. Kojima, M. Hirota, and M. L. Kolhe. *Energy*, **205**, 117875 (2020).
7. A. Nishimura, K.Shibuya, A. Morimoto, S. Tanaka, M. Hirota, Y. Nakamura, M, Kijima, and M. Narita, *J. Environ. Eng.*, **6**, 1–16 (2011).
8. F. Liu, M. Kvesić, K. Wippermann, U. Reimer, and W. Lehnert, *J. Electrochem. Soc.*, **160**, F892 (2013).
9. A.A. Kulikovsky, *Electrochim. Acta*, **49**, 617–625(2004).
10. G. Inoue, T. Yoshimoto, Y. Matsukuma. M. Minemoto, H. Itoh, and S. Tsurumaki, *J. Pow. Sour.*, **162**, 94–104 (2006).
11. J. Park and X. Li, *Int. J. Energy Res.* **35**, 583–593 (2011).
12. K. Nishida, R. Nakauchi, Y. Maeda, T. Umekawa, and M. Kawasaki, *ECS Trans.*, **80** (8) 527–534 (2017).
13. C. Chan, N. Zamel, X. Li, and J. Shen, *Electrochim. Acta*, **65**(30), 13–21 (2012).
14. Y. Kakizawa, T. Kobayashi, M. Uchida, T. Ohno, T. Suga, M. Teranishi, M. Oneda, T. Saiki, H. Nishide, M. Watanabe, A. Iiyama, and J. Inukai, *J. Surf. Finish. Soc. Jpn*, **72**, 230–237 (2021).
15. W. K. Epting and S. Litster, *Int. J. Heat Mass Transf.*, **306**, 674–684 (2016).
16. O. Panchenko, E. Borgardt, W. Zwaygardt, F. J. Hackemüller, M. Bram, N. Kardjilov, T. Arlt, I. Manke, M. Müller, D. Stolten, and W. Lehnert, *J. Pow. Sour.*, **390**, 108–115 (2018).
17. K. Nishida, R.Funaok, T. Furukawa, and Y. Kono, *ECS Trans.*, **98** (9) 89–96 (2020).
18. T. Berning, N. Djilali, and *J. Electrochem. Soc.*, **150**, 1589–1598 (2003).
19. S. Zhang, S. B. Beale, U. Reimer, M. Andersson, and W. Lehnert, *Int. J. Hydrog. Energy*, **45**, 19761–19777 (2020).
20. P. D. Neufeld, A. R. Janzen, and R. A. Aziz, *J. Chem. Phys.*, **57**, 1100 (1972)
21. C. R. Wilke, *J. Chem. Phys.*, **18**, 517 (1950)

22. J. T. Gostick, M.W. Fowler, M. D. Pritzker, M. A. Ioannidis, and L. M. Behra, *J. Pow. Sour.*, **162**, 228–238 (2006).
23. M. Kawase, K. Yamaguchi, M. Kageyama, K. Sato, and G. Inoue, *ECS Trans.*, **75**(14), 147–156(2016).
24. M. Kawase, K. Sato, R. Mitsui, H. Asonuma, M. Kageyama, K. Yamaguchi, and G. Inoue, *AIChE J*. **63**, 249–256 (2017).
25. S. Cruz-Manzo and R. Chen, *J. Electroanal. Chem.*, **694**, 45–55 (2013).

ECS Transactions, 104 (8) 221-231 (2021)
10.1149/10408.0221ecst ©The Electrochemical Society

Liquid Transport in Superhydrophobic Walled Minichannels for Polymer-Electrolyte Fuel Cell Flow-Fields

A. D. Santamaria[a], M. Mortazavi[a], V. Chauhan[a], J. Benner[a], R. Clemente[a], T. Koyanagi[b], C. Ling[c], H. Jia[c]

[a]Department of Mechanical Engineering, Western New England University, Springfield, MA 01119, USA
[b]Toyota Motor Corporation, Higashifuji Technical Center
1200, Mishuku, Susono, Shizuoka, 410-1193 Japan
[c]Toyota Research Institute of North America, Ann Arbor, MI 48105, USA

This work explores the impact of a superhydrophobic sidewall coating on liquid build up and pressure drop in polymer-electrolyte fuel cell minichannels. Using ex-situ experimental methods and optical imaging, time series liquid water distributions were captured along with pressure drop in a transparent test channel. The minichannel sidewalls were treated with a commercial superhydrophobic coating to achieve a contact angle of ~150º. The liquid was injected at a single point through the gas-diffusion layer to simulate liquid transport from the catalyst layer to the GDL surface. During the tests the liquid injection was cycled on and off to capture a diverse dataset including purge and start up scenarios. Two minichannels with identical widths but different heights were probed. The superhydrophobic walls, while resulting in higher pressures, were observed to reduce the water content (especially during purging) for the thicker channel, while achieving mixed results in the thinner.

Introduction

Flow-field design remains an active area of research in the PEFC community due to its significant impact on power density and overall system efficiency [1-5]. PEFCs produce water in the cathode catalyst layer which must be removed via flow channels to prevent flooding [6, 7]. Aerodynamic drag forces, caused by reactant gas flow, are one of the primary means by which liquid phase water is removed [8-10]. The most common channel based flow-field patterns: serpentine, parallel, and interdigitated have been investigated by many groups [11, 12]. More recently, Toyota has utilized titanium mesh plates on the cathode of the Mirai fuel cell stack, while still using channels on the anode [13]. The use of hydrophobic and hydrophilic coatings on channel walls and GDL surfaces has been proposed as a means to reduce the barrier to water removal [14]. This work adds to these efforts by investigating the effect a superhydrophobic (SH) coating has on two-phase behavior in a PEFC minichannel.

Liquid-gas two-phase flow management is a primary challenge for PEFC reactant channel design [15, 16]. Depending on the channel size, different forces can affect the transport mechanism of such flow [17]. Kandlikar [18] proposed dividing flow channels

into three classifications: (i) conventional channels with hydraulic diameters greater than 3 mm, (ii) minichannels with hydraulic diameters between 200 µm and 3 mm, and (iii) microchannels with hydraulic diameters between 10 µm and 200 µm. In the smaller channels associated with modern PEFCs (usually 250 µm - 1mm), flow is dominated by gas phase while liquid is distributed as droplets and slugs [19]. Smaller channels, while beneficial due to reduced diffusion lengths and the potential for thinner bipolar plate packaging, also lead to larger pressure drops. Cooper et al. [2, 3] conducted extensive experimental testing over a wide range of channel depth and width dimensions ranging from 0.25 mm to 1 mm. They concluded that optimal performance, accounting for pumping power at higher pressures, is achieved at a hydraulic diameter of ~0.4 mm for certain ranges of stoichiometry.

Two-phase transport behavior in flow-field's may be evaluated using imaging methods which include: neutron radiography, x-ray synchrotron, and optical techniques [20]. Neutron and x-ray imaging can allow for 3D tomographic reconstruction of liquid distributions, however, these require access to advanced facilities [21-25]. All of these methods may be employed for both in-situ and ex-situ testing. Optical methods, the focus of this work, while more limiting in some aspects, are the simplest and have been demonstrated in the collection of 2D water distributions allowing for correlation between pressure drop and water buildup [26-28]. In prior work, Santamaria et al. applied optical imaging to larger 3 mm wide channels to collect two-phase data for machine learning applications; these methods have been adopted for smaller channels [29-31]. Hussaini and Wang studied cathode flooding using optical methods by using 2D water images to calculate a wetted area ratio, Ø, defined as the area of water divided by the total area in a specially designed transparent fuel cell flow-field consisting of seven parallel channels [32]. They determined that this ratio could be useful for correlating flooding with overvoltage.

Hydrophobic coatings have been demonstrated to enhance liquid mobility by increasing the static contact angle and reducing the maximum contact angle hysteresis [33]. Cai et al. used numerical modeling to show that water can move faster on a hydrophobic surface while a hydrophilic channel side-wall with a hydrophobic GDL surface could avoid water accumulation on the GDL surface [34]. Zhu et al. experimented with graphite hydrophobic and hydrophilic flow channels using Micro CT imaging finding differences in liquid water distributions between the two. They concluded that adding hydrophobic coatings can have a significant impact on water patterns in flow-fields [35]. Tang et al. [22] compared SH and superhydrophilic coatings for water removal from flow-field channels during purging using neutron imaging. The SH channels lead to small droplet formation and a lower water content while the superhydrophilic case resulted in slightly higher water content in the form of a film. The SH case, however, lead to higher water content under the land areas comparatively.

In the following work, minichannels with SH coated walls were compared to untreated channels to investigate the impact on liquid transport for potential design improvement. Using a transparent ex-situ test channel and optical imaging setup, pictures of the liquid distribution were collected and used to calculate the total wetted area in the channel. The relationship between pressure drop and wetted area is probed as well as the effect of variable flow rate and channel thickness.

Experimental Methods

An ex-situ reaction channel was designed to simulate the two-phase flow conditions in a PEFC reactant channel. Two different 3 cm long rectangular channel geometries were tested with cross sectional dimensions of 0.4 mm (width) x 0.6 mm (height) for the thick one and 0.23 mm (width) x 0.6 mm (height) for the thin one. The channels were made of stainless steel and cut using wire EDM. Employing EDM method was necessary to remove any roughness-induced water pinning sites on the side-wall of the channel. For the SH treatment, commercially available NeverWet was applied to the stainless steel surfaces (~10 µm thickness) as shown in Fig. 1. The top of the channel was covered using a 12.7 mm thick transparent polycarbonate plate (wetting contact angle ~81°) while the bottom was mated to a plate covered with a Sigracet 29 BA GDL, rubber O-rings were used to seal the interfaces. The clear polycarbonate allows for images of the water in the channel to be collected. Liquid water was injected through the bottom plate and GDL via a 250 µm capillary using a digital syringe pump (NE-300); this bottom injection method has been shown to better replicate in-situ PEFC conditions [36]. Air flow rate through the channel was monitored using a digital flow meter (Omega FLR1005-D). Pressure taps were machined 3 cm apart through the polycarbonate to record the pressure drop down the channel using a pressure transducer with 125 Pa pressure measurement range (Omega PX-653) and recording at 5 Hz. A 1.4-megapixel monochrome CCD camera (1501 M Thorlabs) positioned directly above the clear side of the channel was used for image capture at 5 FPS. A zoom lens (Thorlabs, MVL6X12Z) was used to provide proper resolution and pixel count in the width of the flow channel. The camera and data acquisition system were synced by externally triggering them with a function generator. Lighting was supplied by two flexible mounted LEDs. Fig. 2 presents an overview of the setup and key components. Prior to two-phase flow experiments, the test section was tested by gas single-phase experiments to ensure proper sealing in the channel. The gas single-phase pressure drop values obtained from experiments corresponded to the pressure drop calculated based on the laminar flow theory, suggesting an appropriate sealing in the test section.

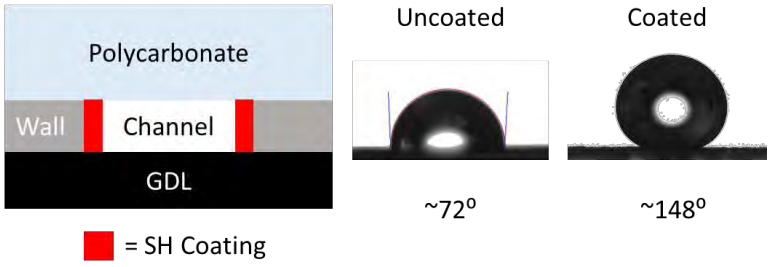

Figure 1. Cross sectional schematic of SH coated walls. Inside wetting angle was measured using a goniometer (Ramé-Hart P/N 290-U4) on untreated and SH treated stainless. The polycarbonate was measured to have a ~81° wetting angle.

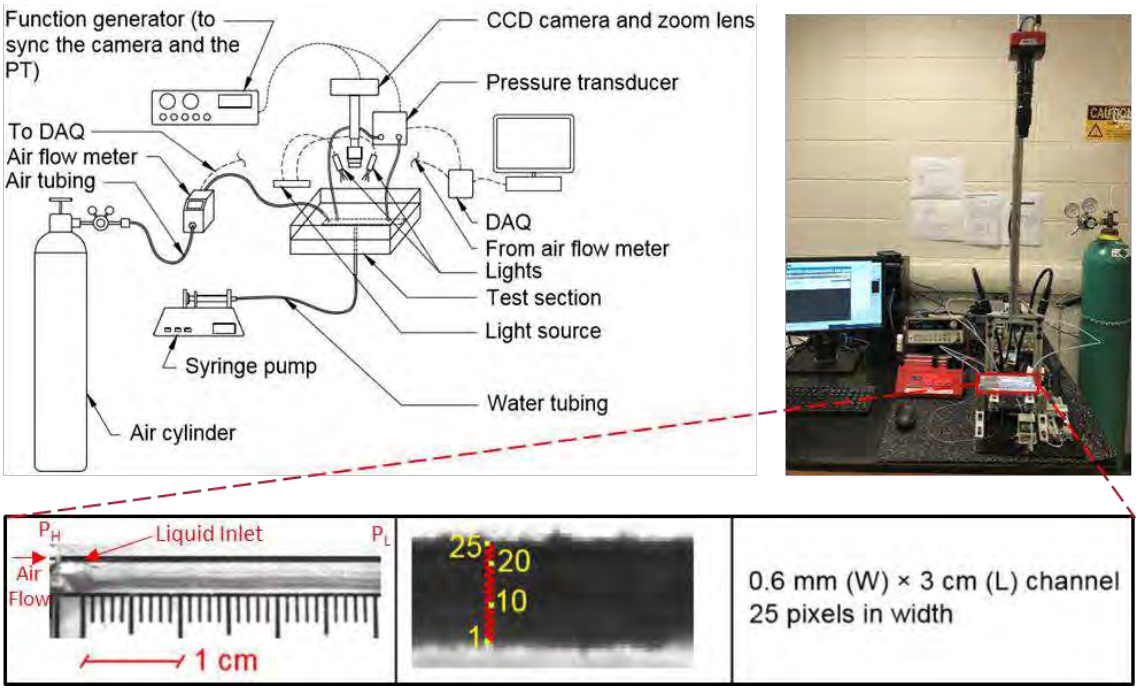

Figure 2. Schematic and picture of experimental setup highlighting key components. The close up shows the ex-situ channel and number of pixels captured during imaging.

Data Collection

An overview of the experimental conditions tested is presented in Tables I & II. The corresponding superficial air velocities are presented in Table I along with liquid injection rates. The protocol for each run is as follows: 1.) First the air flow was turned on, 2.) Then a circuit was turned on which triggered the pressure transducer and camera to begin data recording simultaneously, using a function generator (Hewlett Packard, 33120A), to ensure synchronized 5 Hz collection, 3.) Finally, the liquid water injection was initiated. LabVIEW was used to collect the pressure and flow rate data while Thorlabs software was used to operate the camera. During each run, in order to collect a more diverse set of liquid behavior attributed to startup or purging processes, the liquid injection flow rate was cycled off every 60 min for 30 min. Overall, each test was approximately 5 hours in length. The liquid injection rates for the low air flow rate cases needed to be reduced to prevent liquid back flow toward the transducer port; a result of the reduced ability to move water forward with low gas velocity.

TABLE I: Flow rates.

Channel Thickness	**Air Velocity (m/s)**			**Liquid Flow Rate (µL/hr)**		
	L	M	H	L	M	H
0.40 mm	3.47	6.94	13.19	200	300	300
0.23 mm	3.02	9.06	15.10	150	200	200

TABLE II: Experimental test matrix.

Channel Thickness		Air Vel./Liq. Rate			Wall Treatment	
0.40 mm	0.23 mm	L	M	H	None	SH
X		X			X	
X		X				X
X			X		X	
X			X			X
X				X	X	
X				X		X
	X	X			X	
	X	X				X
	X		X		X	
	X		X			X
	X			X	X	
	X			X		X

Image Processing & Feature Extraction

MATLAB was used for the image processing and calculation of the wetted area; Fig. 3 shows processed images capturing the emergence of GDL water as an example. The following is a summary of the processing steps:

1. A mask image, the same size as the input image, was created depicting the fuel cell channel area as white pixels and the rest of the background details as black pixels, the white channel area is defined as the Region of Interest (ROI).
2. Non-changing details were removed using background subtraction.
3. Noise removal was implemented on the subtracted image to reduce noise resulting from variations in illumination, minor workbench vibrations, and motion blur.
4. The resulting image was then binarized using thresholding.
5. The segmented image was processed using morphological opening and closing operations to account for any discrepancies caused by lighting.
6. The processed image was then masked using logical AND operation to retain the contents of only the ROI. Total wetted area was calculated after this step.

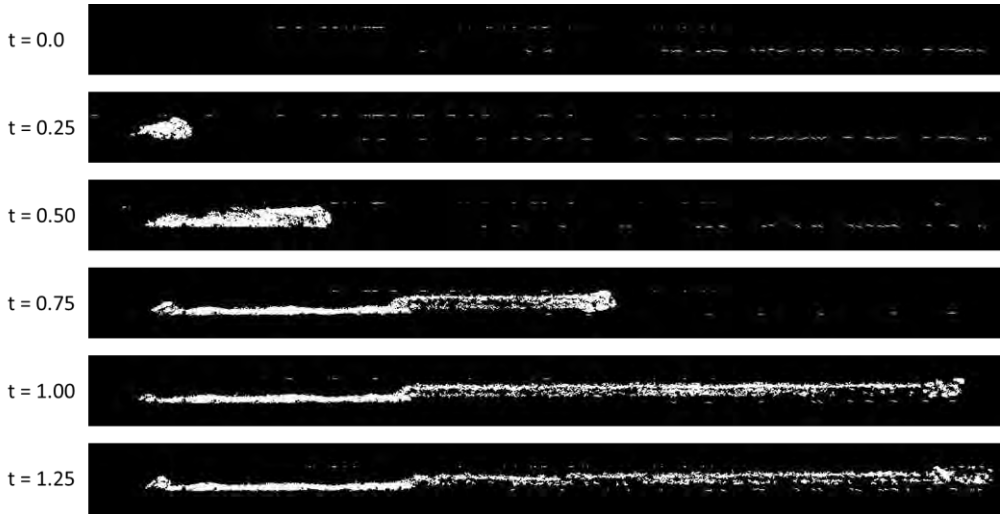

Figure 3. Example of time series ROI binary images depicting liquid emergence, white represents liquid water while black is background. Liquid area was calculated from images such as these.

Results & Discussion

Two-phase pressure and wetted area with respect to time for each run are displayed in Fig. 4 for the 0.4 mm thickness channel and in Fig. 5 for the 0.23 mm thickness. The three periodic drops in pressure and area observed in all the data sets (some clearer than others) are due to the liquid injector cycling off as discussed in the experimental section. At the beginning of each test the channel is completely clear of liquid water. As water begins to form on the GDL surface, the pressure and area signals rise abruptly reaching a plateau. When the liquid injection switches off the channel enters what may be considered a purge scenario and pressure and liquid area decrease. While this behavior was observed in most cases, it was not as clear in some of the 0.23 mm cases. During the purge stage, while the liquid area was observed to fall dramatically in nearly all cases, it almost never returned to 0 which is attributed to some water remaining at the GDL/wall and or GDL/polycarbonate interface as well as in the pores of the GDL injection site. A longer purge cycle would potentially have further reduced this remaining water, however, extending this step would have exceeded the practical experimental duration (already over 5 hours per run with setup). Overall, one clear trend observed in the general data is the significantly lower wetted area achieved in the SH channel during the drying stages. In nearly all cases the measured area in the SH channel is less than the UT channel. This benefit of SH coatings during purging has been previously reported on during in-situ testing for larger channels [22].

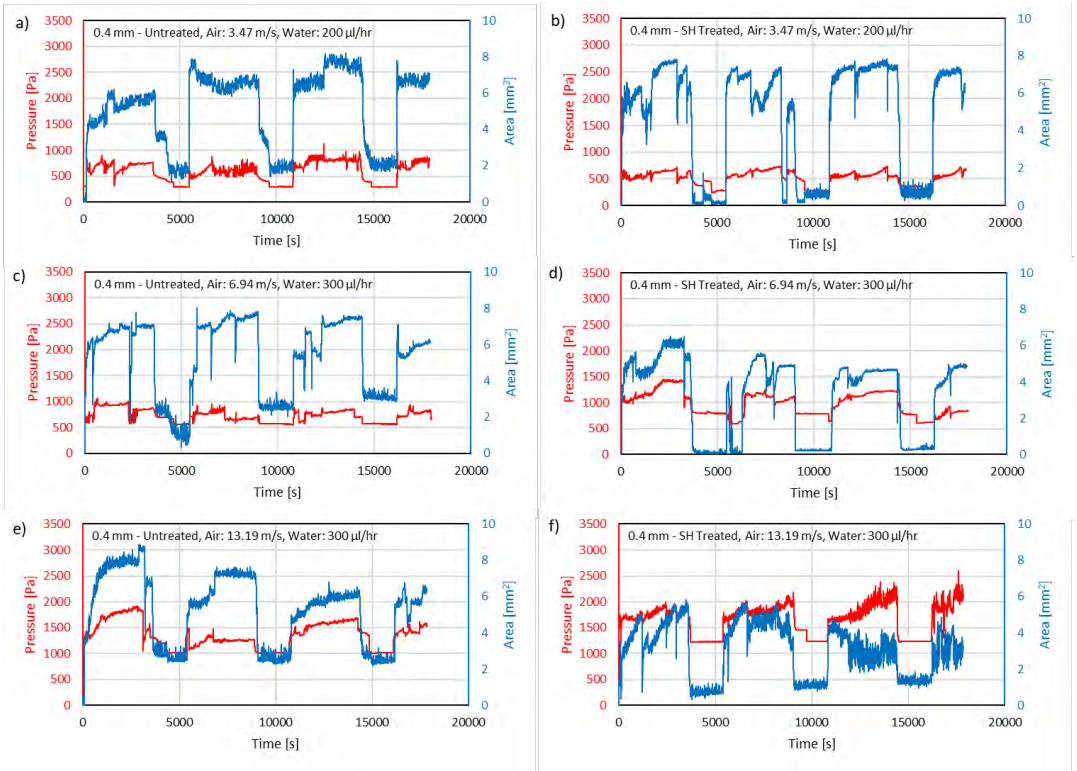

Figure 4. Time series pressure and wetted area data for the 0.4 mm thick channel. Left column plots (a), (c), & (e) are untreated while right column (b), (d), & (f) are SH treated.

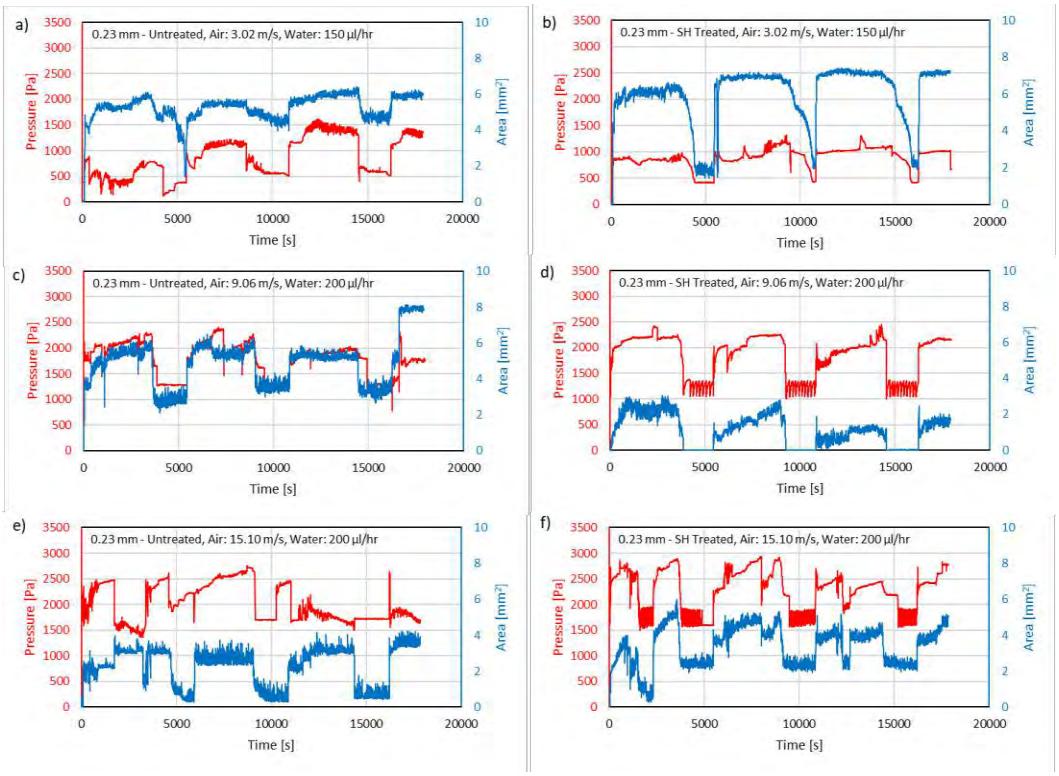

Figure 5. Time series pressure and wetted area data for the 0.23 mm thick channel. Left column plots (a), (c), & (e) are untreated while right column (b), (d), & (f) are SH treated.

Reviewing each of the test results, two discrepancies in the data were noticed and are here addressed. First, in Fig. 5a, the pressure readings at the beginning of the test were unusually low which is attributed to some moisture buildup in the transducer tubing. This was cleared during the purge stage and no longer caused an issue. Because of this, the pressure data for 0-3600s from this case was omitted from later analysis. Second, in Fig 5d, the area measured during the purge stage was much lower than other cases. Review of the images did not reveal any issues with collection and therefore this data was used in further analysis though no clear explanation as to why there was lower area measured.

Average pressure and wetted area behavior as a function of air velocity are presented in Fig. 6. These plots show the averages for the entire test duration including both liquid injection on/off stages. Future analysis may separate the data between the two on/off injection stages, however, that is out of the scope of this short transaction. For both channels, pressure drop increases with respect to flow rate as expected. For the 0.4 mm channel case, the SH treated channel exhibited reduced wetted area while producing a higher pressure drop. The wetted area in the more hydrophilic untreated channel was relatively invariant with flow rate. In the 0.23 channel testing the SH cases also lead to higher pressure drop. The average wetted area in the SH case was higher than the uncoated case, except in the M flowrate test where the lower areas were measured. To dig deeper into these trends, liquid saturation and two-phase pressure amplification were calculated and plotted in Fig 7. Saturation, α, is defined as the ratio of the measured projected wetted area, A_w, divided by the total projected channel area, A_{tot}:

$$\alpha = A_w/A_{tot} \quad [1]$$

where the total is equal to the channel length (30 mm) multiplied by the width (0.6 mm). Pressure amplification, Φ^2, is the ratio of the two-phase pressure drop, ΔP_{TP}, divided by the single phase (gas only) pressure drop, ΔP_g:

$$\Phi^2 = \Delta P_{TP}/\Delta P_g \quad [2]$$

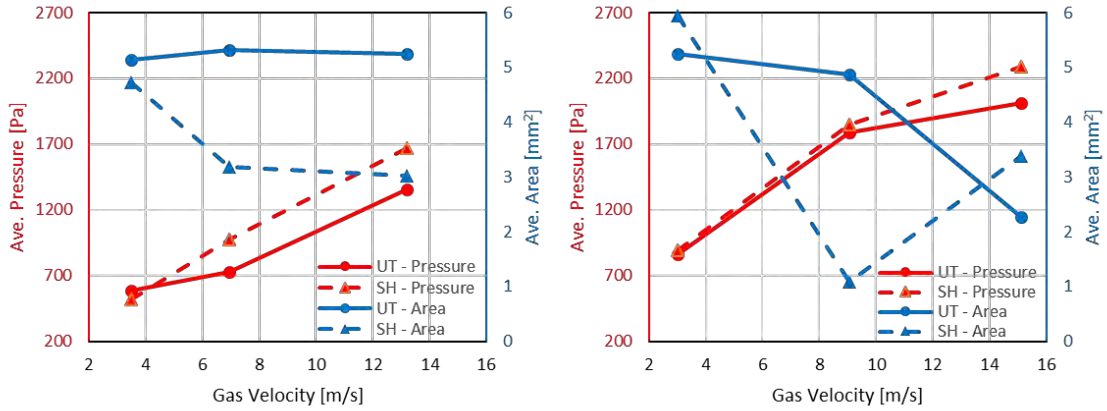

Figure 6. (Left) Average pressure and wetted area for the 0.4 mm thick channel. (Right) Average pressure and wetted area for the 0.23 mm thick channel. UT = untreated.

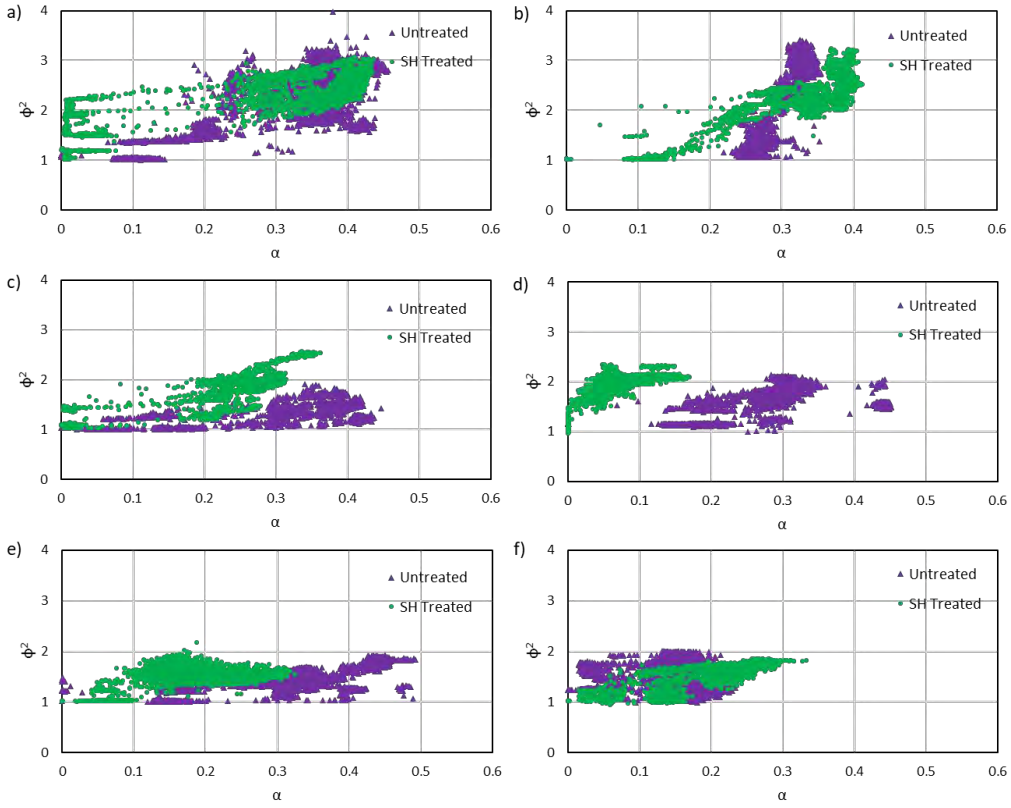

Fig. 7 Liquid saturation and pressure amplification for each test case. Left column plots (a), (c), & (e) are 0.4 mm data while right column (b), (d), & (f) are 0.23 mm.

The resulting graphs show a complex relationship between saturation and pressure amplification. While there is some correlation between wetted area and pressure drop, there is a lot of variation especially in the untreated cases. Wetted area, while useful, does not take into account the liquid distribution (such as droplets vs. corner film flow) which can greatly impact pressure readings. Hydrophobic surfaces have been shown to cause liquid droplets to bead onto the GDL surface while hydrophilic channels have been shown to form liquid films; the former may cause higher pressure drop while the later reduces it [22]. This scenario may account for the higher average pressure drop measured in the SH datasets.

Next steps for this work include a deeper analysis of the imaging data sets as well as collecting data using hydrogen gas. Identifying the difference between the SH and untreated channel liquid distributions will shed light on the complex pressure drop behavior. Additionally, liquid behavior in the anode, where hydrogen is the flow gas, may be quite different than in air due to much lower density which effects the aerodynamic drag force.

Conclusions

Management of two-phase flow in PEFC reactant channels is critical to maintaining their stable and efficient operation. Minichannels with SH coated walls were investigated to understand their impact on liquid transport for potential design improvement in future PEFC systems. Using a transparent ex-situ test channel and optical imaging setup, pictures of the liquid distribution were collected and used to calculate the wetted area in the channel. By comparing these measurements to the simultaneously recorded pressure drop, pressure amplification due to liquid saturation was mapped for a host of flow conditions. The core findings of this ongoing work are summarized as follows:

i.) During the “purge” stage, the SH treated channels achieved significantly lower wetted area for most cases.
ii.) For the 0.4 mm channel thickness data, SH treated channels produced higher pressure drops while resulting in lower wetted areas.
iii.) The 0.23 mm thickness channel tests were less clear in determining the impact of the SH treatment.
iv.) The increase in pressure drop with simultaneous decrease in wetted area in the 0.4 mm thickness data may be due to liquid distribution (droplet vs. film) which will be analyzed in future work.

Acknowledgments

This work was supported by funding from Toyota Motor Engineering & Manufacturing North America (TEMA).

References

1. J. Wang, *Appl. Energy*, **157**, 640-663 (2015).
2. N.J. Cooper, A.D. Santamaria, M.K. Becton, and J.W. Park, *Energ. Convers. Manage.*, **136**, 307-317 (2017).
3. N.J. Cooper, T. Smith, A.D. Santamaria, and J.W. Park, *Int. J. Hydrog. Energy*, **41** (2), 1213-1223 (2016).
4. M. Mortazavi and K. Tajiri, *Renew. Sust. Energ. Rev.*, **45**, 296-317 (2015).
5. M. Mortazavi, M. Heidari, and S.A. Niknam, *Heat Transfer Eng.*, 1-16 (2019).
6. F.Y. Zhang, X.G. Yang, and C.Y. Wang, *J. Electrochem. Soc.* **153** (2), A225-A232 (2006).
7. E.C. Kumbur, K.V. Sharp, and M.M. Mench, *J. Power Sources*, **161** (1), 333-345 (2006).
8. S.C. Cho, Y. Wang, and K.S. Chen, *J. Power Sources*, **206**,119-128 (2012).
9. A. Theodorakakos, T. Ous, M. Gavaises, J.M. Nouri, N. Nikolopoulos, and H.Yanagihara, *J. Colloid Interface Sci.*, **300** (2), 673-687 (2006).
10. A.D. Santamaria, P.K. Das, J.C. MacDonald, and A.Z. Weber, *J. Electrochem. Soc.*, **161** (12), F1184 - F1193 (2014).
11. T.A. Trabold, J.P. Owejan, D.L. Jacobson, M. Arif, and P.R. Huffman, *Int. J. Heat Mass Transf.*, **49** (25–26), 4712-4720 (2006).
12. J.P. Owejan, J.J. Gagliardo, J.M. Sergi, S.G. Kandlikar, and T.A. Trabold, *Int. J. Heat Mass Transf.*, **49** (25–26), 4721-4731 (2006).
13. T. Yoshida and K. Kojima, *J. Electrochem. Soc. Interface* **24** (2), 45-49 (2015).
14. C. Lim and C.Y. Wang, *Electrochim. Acta*, **49** (24), 4149-4156 (2004).
15. L. Hui, Y. Tang, Z. Wang, Z. Shi, S. Wu, D. Song, J. Zhang, K. Fatih, J. Zhang, H. Wang, Z. Liu, R. Abouatallah, and A. Mazza, *J. of Power Sources*, **178**, (1), 103-117 (2008).
16. S. Niknam, M. Mortazavi, and A.D. Santamaria, *Results in Eng.*, **5**, 100071 (2020).
17. M. Mortazavi, A.D. Santamaria, M. Heidari, M.P. Doyle, M.A. Schrader, and E.R. Rizk. *J. Electrochem. En. Conv. Stor.* **18** (3), 031013 (2021).
18. S.G. Kandlikar and W.J. Grande, *Heat Transf. Eng.*, **24** (1), 3-17 (2003).
19. K.A. Triplett, S.M. Ghiaasiaan, S.I. Abdel-Khalik, and D.L. Sadowski, *Int. J. Multiphase Flow*, **25** (3), 377-94 (1999).
20. A. Bazylak., *Int. J. Hydrog. Energy*, **34** (9), 3845-3857 (2009).
21. H.Y. Tang, A.D. Santamaria, J. Kurniawan, J.W. Park, T.-H. Yang, and Y.-J. Sohn, *J. Power Sources*, **195** (19), 6774 - 6781 (2010).
22. H.Y. Tang, A.D. Santamaria, J.W. Park, C. Lee, and W. Hwang, *J. Power Sources*, **196** (22), 9373 - 9381 (2011).
23. J. Bachman, M. Charvet, A.D. Santamaria, H.-Y. Tang, J.W. Park and R. Walker, *Int. J. Hydrog. Energy*. **37** (22), 17172-17179 (2012).
24. A.D. Santamaria, M.K. Becton, N.J. Cooper, A.Z. Weber, and J.W. Park, *J. Power. Sources*, **293** (20), 162-169 (2015).

25. I.V. Zenyuk, D.Y. Parkinson, G. Hwang, and A.Z. Weber, *Electrochem. Commun.*, **53**, 24-28 (2015).
26. E.F Medici, and J.S. Allen, *J. Pow. Sources*. **191** (2), 417-27 (2009).
27. M. Mortazavi, A.D. Santamaria, J.Z. Benner, and V. Chauhan, *J. Electrochem. Soc.*, **166**, F3143-F3153 (2019).
28. M. Mortazavi, A.D. Santamaria, V. Chauhan, J. Z. Benner, M. Heidari, and E.F. Médicic, *J. Power Sources Advances*, **1**, 100001 (2020).
29. V. Chauhan, M. Mortazavi, J.Z. Benner, and A.D. Santamaria. *Energy Reports.* **6** 2713-2719 (2020).
30. A.D. Santamaria, M. Mortazavi, V. Chauhan, J. Benner, O. Philbrick, R. Clemente, H. Jia, and C. Ling. *ECS Transactions*. **98** (9), 279 (2020).
31. A.D. Santamaria, M. Mortazavi, V. Chauhan, J. Benner, O. Philbrick, R. Clemente, H. Jia, and C. Ling. *J. Electrochem. Soc*. **168** (5), 054505 (2020).
32. I.S. Hussaini and C.Y. Wang, *J. Power Sources*, **187** (2), 444-451 (2009).
33. A. Turhan, S. Kim, M. Hatzell, and M.M. Mench, *Electrochim. Acta*, **55** (8), 2734-2745 (2010).
34. Y. Cai, J. Hu, H. Ma, B. Yi, and H. Zhang. *J. Power Sources*, **161** (2) 843-848 (2006).
35. W. Zhu, Z. W. Dunbar and R. I. Masel. *ECS Transactions*, **16** (2) 995-1000 (2008).
36. P.K. Das, A. Grippin, A. Kwong, and A.Z. Weber, *J. Electrochem. Soc.* **159** (5), B489-96 (2012).

ECS Transactions, 104 (8) 233-240 (2021)
10.1149/10408.0233ecst ©The Electrochemical Society

Measurement Technique of Oxygen Concentration in Narrow Channels of PEFCs Based on Transmission Laser Absorption Spectroscopy

K. Nishida[a], R. Nakauchi[b], Y. Maeda[b], T Umekawa[c], and M. Kawasaki[d]

[a] Faculty of Mechanical Engineering, Kyoto Institute of Technology, Sakyo-ku, Kyoto 606-8585, Japan
[b] Department of Mechanophysics, Kyoto Institute of Technology, Sakyo-ku, Kyoto 606-8585, Japan
[c] Plumtec Co., Ltd., Joyo-shi, Kyoto 610-0121, Japan
[d] Research Institute for Humanity and Nature, Kamigamo, Kita-ku, Kyoto 603-8047, Japan

The oxygen transport on the cathode side of polymer electrolyte fuel cells (PEFCs) is an important factor that determines their performance. This study presents a fiber-optic gas sensing technique for monitoring the oxygen concentration in flow channels of operating PEFCs based on transmission tunable diode absorption spectroscopy (TDLAS). As the first stage, the fiber-optic transmission TDLAS system was developed and applied to the ex-situ measurement of oxygen concentration in the narrow channels of a simulated flow cell. It was found that the second-harmonic (2f) absorption spectra of oxygen can be clearly detected without optical noises even though the channel width is narrowed to 1.0 mm. The calibration results obtained from the TDLAS measurements enable to accurately estimate the oxygen mole fraction within the flow cell. The fiber-optic transmission TDLAS is applicable for the oxygen monitoring in submillimeter-scale channels of actual PEFCs.

Introduction

The oxygen transport at the cathode of polymer electrolyte fuel cells (PEFCs) is one of the key factors for determining their power generation performance. Especially, the increase of concentration overpotential due to the insufficient oxygen supply induces the severe voltage deterioration. To maintain the adequate supply of oxygen throughout the cell, it's essential to establish a technique for real-time monitoring of oxygen concentration in the cathode flow field of operational cells. In the previous works, the measurements of oxygen distribution within flow channels and diffusion media of working PEFCs have been conducted by micro gas chromatograph (GC) (1–6), oxygen-quenching of fluorescence and phosphorescence (7–11), electrochemical microsensor (12) and tunable diode laser absorption spectroscopy (TDLAS) (13). GC techniques provide better accuracy for gas detection, however, it takes a long time (at least a few minutes) to collect a gas sample and identify a species. The oxygen visualization method based on luminescence quenching (7–10) is easy to use without specialized equipments, but has several limitations. To allow optical access, a part of cell materials should be replaced by transparent substitutes. Moreover, an oxygen-quenchable luminescent dye must be coated on the electrode surface or channel wall. Several probe-type microsensors (11, 12) have also been developed as a

powerful tool for investigating the oxygen concentration inside porous electrodes. However, their invasive insertion into diffusion media might negatively affect the oxygen supply and water removal. On the other hand, TDLAS enables the non-invasive in-situ monitoring of chemical species inside fuel cells with a high time resolution of 100 milliseconds. Fujii et al. (13) applied the single-ended TDLAS sensor to measure the oxygen concentration in a PEFC channel. In their experiments, since the laser beam is injected perpendicular to the flow direction, the optical path length is extremely short and the detection sensitivity is insufficient. The sensitivity of O_2-TDLAS is relatively lower than those of other species due to the weak infrared absorption of oxygen molecule at 760 nm. To measure its concentration with high accuracy, the optical path needs to be lengthened inside the narrow channel.

To solve the above-mentioned problem, this study developed the fiber-optic transmission TDLAS system and applied it to the ex-situ measurement of oxygen concentration in the narrow channels of a simulated serpentine flow cell. In this measurement system, the laser beam from a DFB laser diode was directly injected into the gas channel along the flow direction. Therefore, the optical path can be lengthened to 50 or 100 mm and the detection sensitivity of oxygen is remarkably improved. Based on the measurement results, we verified whether the fiber-optic transmission TDLAS can be applied to the oxygen monitoring in operational PEFCs.

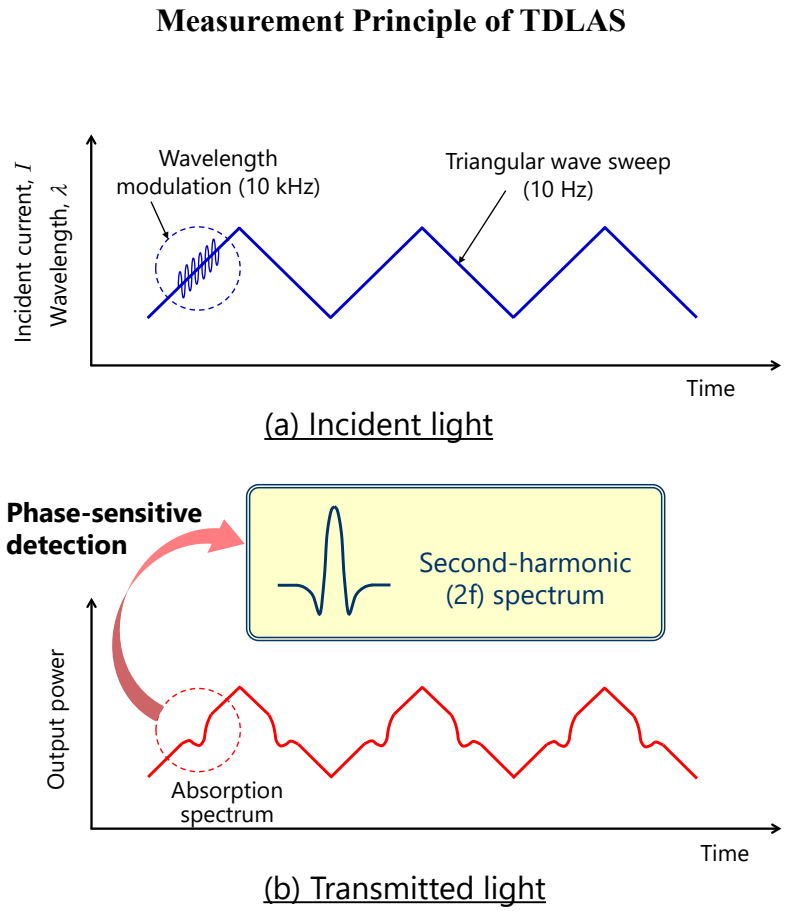

Figure 1. Principle of wavelength modulation spectroscopy (WMS).

Some molecules such as water vapor, methane and oxygen have the property of absorbing infrared lights at specific wavelengths. TDLAS is one of the high-sensitive absorption spectroscopy techniques which measure the absorbance of a chemical species and identify its concentration using infrared diode laser. The infrared absorption due to a species is based on Lambert-Beer's law. In this experiment, wavelength modulation spectroscopy (WMS) technique shown in Figure 1 was adopted for high-sensitive spectral analysis. To detect an absorption spectrum of oxygen, the incident laser wavelength is swept across the selected absorption line by tuning the laser drive current with a 10 Hz triangular waveform. The wavelength sweeping at 10 Hz enables to detect a target gas with a time resolution of 100 ms. Additionally, the high-frequency wavelength modulation of 10 kHz is superimposed on the triangular wave and the harmonic signals are extracted from the output signal by phase-sensitive detection. The peak-valley (PV) height of the even-order harmonic (nf) spectra closely correlates with the concentration of a target species. This WMS approach enables high-sensitive gas monitoring without being affected by noise and other species even if the absorbance of a species is weak. Figures 2(a) and 2(b) show

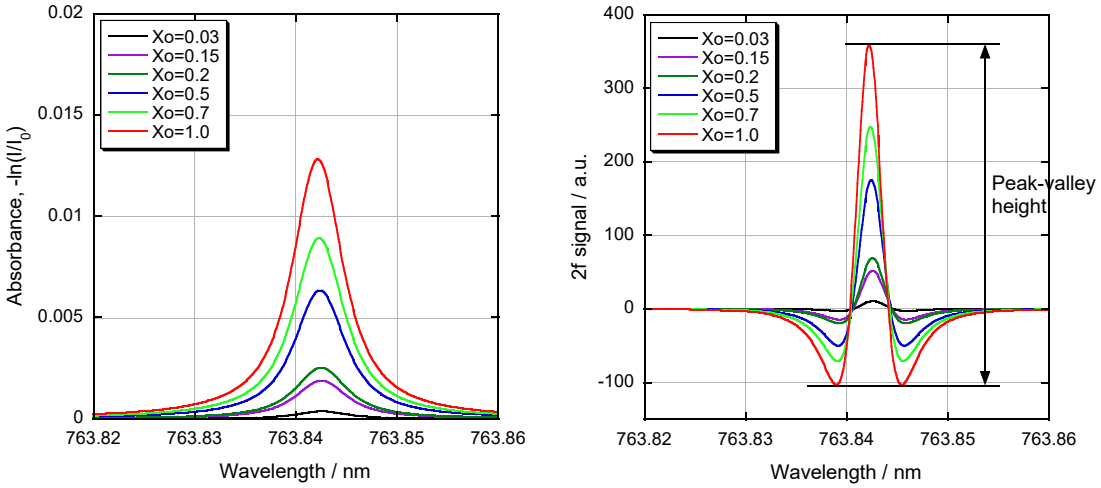

(a) Absorbance (b) 2f signals

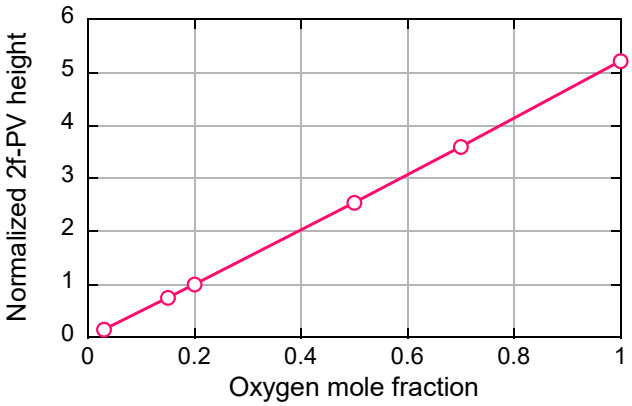

(c) Relationship between oxygen mole fraction and 2f peak-valley height

Figure 2. Theoretical absorption spectra and 2f signals of oxygen at 764 nm calculated by HITRAN database.

the theoretical absorption spectra (absorbance) and 2f signals of oxygen at the laser wavelength of 764 nm, which were calculated by HITRAN database. The temperature, pressure and optical path are 300 K, 1 atm and 100 mm, respectively. The oxygen mole fraction was changed from 0.03 to 1.0 mol/mol. It can be confirmed that the peak-valley (PV) height of 2f spectrum is increased with an increase in oxygen concentration. Figure 2(c) shows the relationship between the oxygen concentration and the normalized 2f-PV height. The 2f-PV height approximately increases in proportion to the oxygen mole fraction.

Experimental

The ex-situ measurements of oxygen in the narrow channels of a simulated serpentine flow cell were conducted based on the fiber-optic transmission TDLAS, and the accuracy of the measurement system was verified under various oxygen concentrations. Figure 3(a) and 3(b) present the schematic diagram of the TDLAS system and the photo images of the

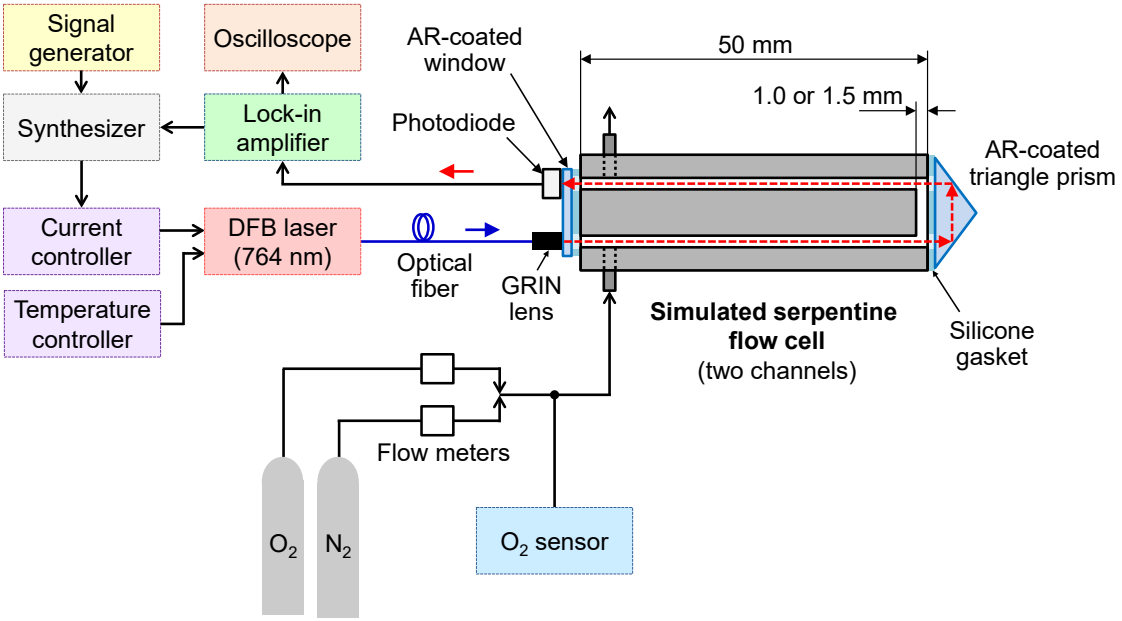

(a) Schematic diagram of the fiber-optic transmission TDLAS system

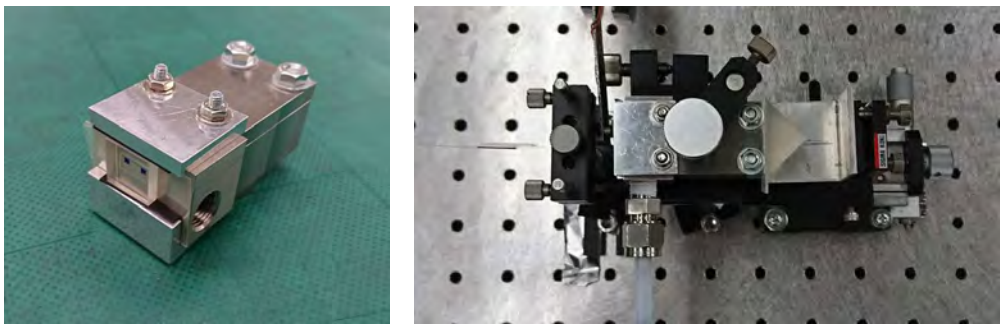

(b) Photo images of the experimental flow cell

Figure 3. Experimental apparatus for measuring oxygen concentration in the simulated serpentine flow cell using the fiber-optic transmission TDLAS system.

experimental cell, respectively. This serpentine flow cell made of stainless steel has two channels (width and depth: 1.0 or 1.5 mm, length: 50 mm) and one bend section (length: 5 mm). The triangular modulated beam emitted from a DFB laser diode (Eagleyard Inc., wavelength: 764 nm) was directly injected into the first channel through the single-mode optical fiber. To collimate the laser beam at the channel inlet, a GRIN lens was attached at the top of the pitch fiber. The injected beam passes one or two channels along the flow direction. In the case of passing two channels (optical path: 100 mm), the beam transmitted through the first channel was turned 180 degrees by a triangular prism at the bend section. The returned beam is passed through the second channel and detected at a photodiode. In the case of one channel (optical path: 50 mm), the reflective prism was removed out and the detector was set at the end of the first channel. The output signal is transmitted to a lock-in amplifier, and then the 2f absorption spectrum can be obtained by phase-sensitive detection. In the experiments, the mixed gas of oxygen and nitrogen was supplied to the first channel at 100 ml/min. In the case of the 100 mm path measurement, the gas flow from the first channel was turned to the second channel at the bend section. The oxygen mole fraction in the channels was adjusted to 0 to 1.0 mol/mol by controlling each gas flow rate and calibrated using an optical oxygen sensor (BAS, Firesting). This measurement was performed at 25 ºC and 1 atm.

Results and Discussion

Figure 4(a) shows the second-harmonic (2f) absorption spectra of oxygen in the 1.5 mm width channels of the simulated flow cell measured by the fiber-optic transmission TDLAS. The optical path is 100 mm long. The oxygen mole fraction in the channels was varied from 0 to 1.0 mol/mol. When the TDLAS is performed in submillimeter-scale or micro channels, the deterioration of S/N ratio due to fringe noises cannot be ignored. The interference fringes are likely to be caused by the laser beam reflection at the channel walls. Although the laser spectroscopy of this experiment was conducted in the narrow channels of 1.5 mm width, the 2f spectra were clearly observed without being affected by fringe

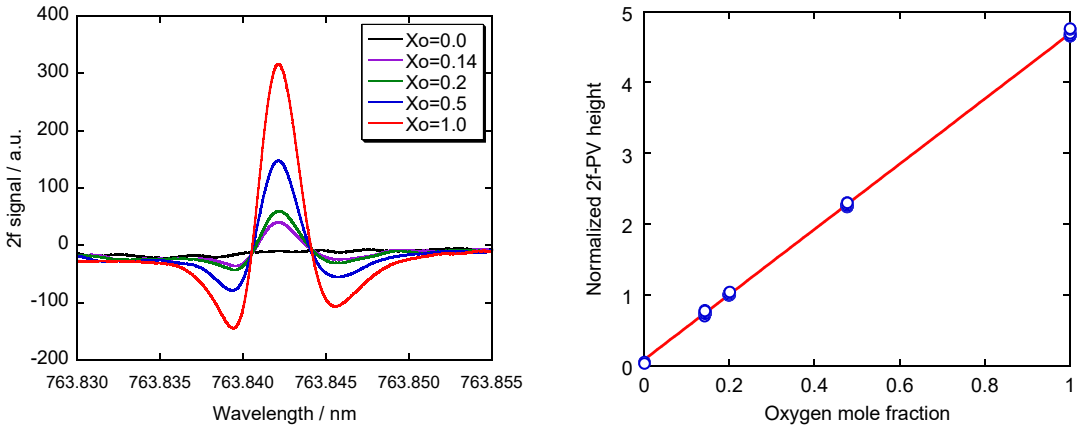

(a) 2f absorption spectra (b) O_2 concentration vs 2f-PV height

Figure 4. The second-harmonic (2f) absorption spectra of oxygen in the 1.5 mm width channels of the simulated flow cell (optical path: 100 mm). The oxygen mole fraction is changed from 0 to 1.0 mol/mol.

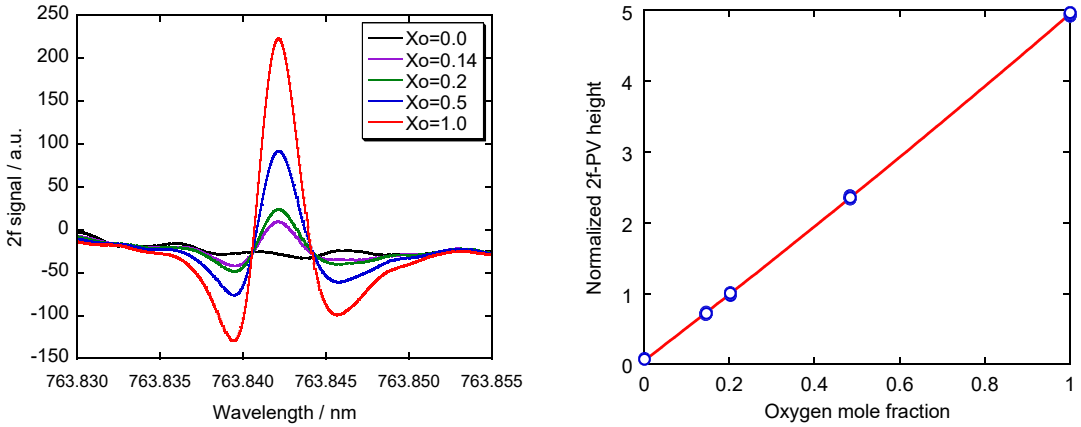

(a) 2f absorption spectra (b) O_2 concentration vs 2f-PV height

Figure 5. The 2f spectra of oxygen in the first channel of the simulated flow cell (channel width: 1.5 mm, optical path: 50 mm).

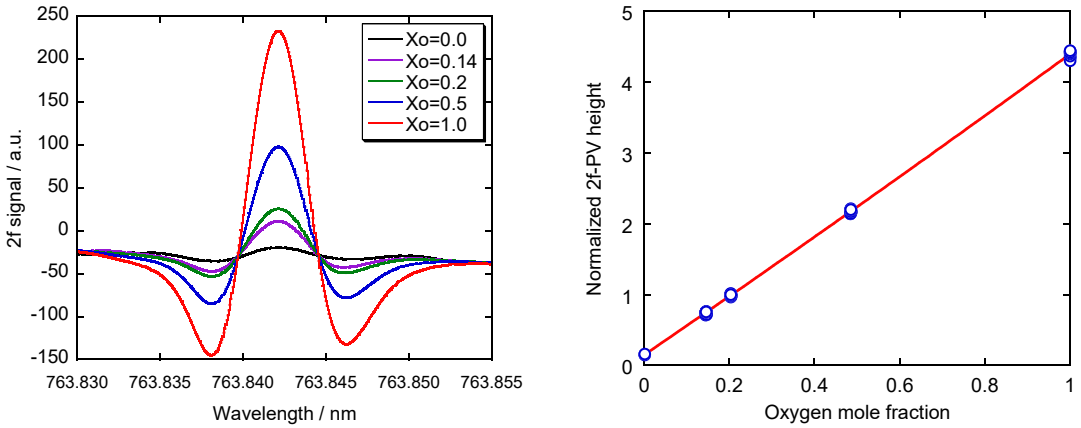

(a) 2f absorption spectra (b) O_2 concentration vs 2f-PV height

Figure 6. The 2f spectra of oxygen in the 1.0 mm width channel of the simulated flow cell (optical path: 50 mm).

noises. Furthermore, it was confirmed that the PV height of 2f signal increases with an increase in the oxygen concentration. Figure 4(b) displays the relationship between the oxygen concentration and the normalized 2f-PV height. The 2f-PV height is approximately proportional to the oxygen mole fraction, which is similar to the calculation result shown in Figure 2(c). This calibration curve obtained from the transmission TDLAS can be used for quantitatively estimating the oxygen concentration in the flow cell. The accuracy of the TDLAS-based oxygen measurement is ±0.012 mol/mol which is much better than that for the electrochemical sensor (12). However, it doesn't reach ±0.5 mol% of a GC method (3).

This study also investigated the effects of optical path length and channel width on the oxygen measurement in the simulated flow cell. Figure 5(a) shows the 2f spectra of oxygen in the first channel when the optical path was shortened to 50 mm. The oxygen concentration was changed from 0 to 1.0 mol/mol. Since the absorbance of oxygen is

reduced with a decrease in the optical path, the 2f peak value of the 50 mm path becomes slightly lower as compared to that of the 100 mm path in Figure 4(a). Despite the short optical path and the weak absorption, the 2f spectra can be clearly measured by the transmission TDLAS. As seen in Figure 5(b), the calibration result reveals that the 2f-PV height grows monotonically to the oxygen mole fraction. Since the simple optical system without the beam return reduces the fringe noises, the measurement accuracy of oxygen concentration is improved to ±0.008 mol/mol which can compare with that of the GC method. Figure 6(a) shows the 2f spectra of oxygen within the 1.0 mm width channel in the concentration range of 0 to 1.0 mol/mol. The optical path is 50 mm long. It can be seen that the broadening of 2f spectra is caused because the gas pressure in the 1.0 mm width channel becomes higher than that in the 1.5 mm width channel. Therefore, the 2f-PV height tends to be decreased due to the spectral broadening. Although the channel width was narrowed to from 1.5 to 1.0 mm, the waveforms of 2f signals were clearly detected without the effect of fringe noises. As shown in Figure 6(b), the 2f-PV height increases in proportion to the oxygen mole fraction. The accuracy of the oxygen measurement is ±0.010 mol/mol. It was noted that the fiber-optic transmission TDLAS developed in this work is applicable for the oxygen measurement in submillimeter-scale channels of actual PEFCs.

Conclusions

The fiber-optic transmission TDLAS system has been developed to measure the oxygen concentration in narrow channels of operating PEFCs. In this study, to verify its practical possibility, the ex-situ measurement of oxygen in the narrow channels of a simulated flow cell was conducted using a prototype system. It was confirmed that the 2f absorption spectra can be clearly observed without the influence of fringe noises, even though the channel width is narrowed to 1.0 mm. Furthermore, the peak-valley (PV) height of 2f spectrum increases in proportion to the oxygen concentration. The calibration results obtained from the TDLAS measurements enable to quantitatively estimate the oxygen mole fraction in the flow cell. The measurement accuracy of oxygen concentration is ±0.010 mol/mol. These results suggest that the fiber-optic transmission TDLAS has the ability to accurately monitor the oxygen concentration in submillimeter-scale channels of actual PEFCs.

References

1. M. M. Mench, Q. L. Dong, and C. Y. Wang, *J. Power Sources*, **124**, 90 (2003).
2. Q. Dong, M. M. Mench, S. Cleghorn, and U. Beuscher, *J. Electrochem. Soc.*, **152**(11), A2114 (2005).
3. Q. Dong, J. Kull, and M. M. Mench, *J. Power Sources*, **139**, 106 (2005).
4. X. G. Yang, N. Burke, C. Y. Wang, K. Tajiri, and K. Shinohara, *J. Electrochem. Soc.*, **152**(4), A759 (2005).
5. F. Q. Liu, G. Q. Lu, and C. Y. Wang, *J. Memb. Sci.*, **287**, 126 (2007).
6. G. Q. Lu, F. Q. Liu, and C. Y. Wang, *J. Power Sources*, **164**, 134 (2007).
7. S. Inagaki, H. Nagai, and K. Asai, *Proc. 2007 ASME-JSME Therm. Eng. Summer Heat Transf. Conf.*, , HT2007 (2007).

8. J. Inukai, K. Miyatake, K. Takada, M. Watanabe, T. Hyakutake, H. Nishide, Y. Nagumo, M. Watanabe, M. Aoki, and H. Takano, *Angew. Chem. Int. Ed.*, **47**(15), 2792 (2008).
9. K. Takada, Y. Ishigami, J. Inukai, Y. Nagumo, H. Takano, H. Nishide, and M. Watanabe, *J. Power Sources*, **196**(5), 2635 (2011).
10. S. Hirano, J. Chen, M. Potocki, and G. Saloka, *ECS Trans.*, **69**(17), 1331 (2015).
11. S. Uemura, T. Yoshida, T. C. Jao, T. Sasabe, and S. Hirai, *ECS Trans.*, **75**(14), 355 (2016).
12. W. K. Epting and S. Litster, *J. Power Sources*, **306**, 674 (2016).
13. Y. Fujii, S. Tsushima, and S. Hirai, *ECS Trans.*, **11**(1), 451 (2007).

Chapter 9

Stacks

ECS Transactions, 104 (8) 243-254 (2021)
10.1149/10408.0243ecst ©The Electrochemical Society

Examination on Water Management Method in the Same Electrode in PEFC

Nanami Shibutani[1], Kimihiko Sugiura[1], Akihisa Tanaka[2] and Keisuke Nagato[2]

[1] Department of Mechanical Engineering, Osaka Prefecture University College of Technology, 26-12 Saiwai-cho, Neyagawa, Osaka, 572872, Japan
[2]Department of Mechanical Engineering, Graduate School of Engineering, The University of Tokyo, 7-3-1 Hongo, Bunkyo-ku, 113-8656 Tokyo/Japan

Our group has proposed a Self-Water Management Separator (SWMS) and a Self-Water Management Catalyst layer (SWMC) to aim cost down of Polymer Electrolyte Fuel Cells. SWMS can manage moisture in the same cell by moving excess water from gas outlet to inlet through a bypass channel installed in a standard separator. Polyvinyl alcohol (PVA) sponge, diatomite powder, cellulose fiber insulation, and EM diatomite grain were prepared as water absorption materials of a bypass channel. Therefore, we selected PVA from viewpoints of cell performance and handling ability. SWMC is composed of the addition of the carbon (graphite rubbish, carbon black, spheroidal carbon) to control the movement of generation water in the catalyst layer. It was confirmed that the performance was improved using only one type of added carbon on the anode side and two types on the cathode side and, by combining hydrophilic and hydrophobic materials.

Introduction

Recently, Polymer Electrolyte Fuel Cells (PEFCs) are beginning to be used in various fields as a clean energy source because of emitting carbon dioxide during operating. Because Japanese Prime Minister SUGA announced the “Green Growth Strategy for Carbon Neutrality in 2050” in December 2020, PEFCs is expected as a high efficiency and a low temperature clean power source. However, in order to further promote PEFC, several issues need to be resolved. For example, (A) reduction of manufacture cost by reducing platinum catalyst of both electrodes, (B) reduction of system cost and operating cost by removing accessory equipment, (C) solution of water management issues such as a drying membrane, flooding and plugging phenomenon (1)-(2). Although a membrane of MEA has proton permeability only wet condition, a cell is heated with power generation because a cell reaction is exothermic reaction. This heating dries an electrolyte membrane, and consequently a proton permeability of the membrane is deteriorated. Generally, PEFC maintains wet condition by supply gas humidified. However, since the partial pressure of water vapor in the cathode gas increases due to the consumption of oxygen and the production of water by the power generation reaction, it becomes supersaturated near the gas outlet and condensate is generated. If this condensation occurs in the catalyst layer or inside the gas-diffusion layer (GDL), a degradation phenomenon called flooding occurs due to the reduction of the triple phase boundary. If this condensation occurs in the gas channel, a degradation phenomenon called plugging occurs due to inhibit gas supply to the electrode. Thus, PEFC has conflicting water management issues. Generally, the reason why

PEFC can operating low temperature in fuel cell is used platinum catalyst usable low temperature and low pressure. However, a high cost of platinum catalyst disturbs the reducing of PEFC cost. Because an electrode catalyst is occupying about 46% of all cost, reducing the amount of platinum used while maintaining performance is a shortcut to cost reduction (3)-(4). Therefore, our laboratory has proposed a Self-Water Management Catalyst (SWMC) in membrane electrode assembly (MEA) (5). Since the SWMC contains carbon powder with porous in a catalyst layer (CL), it can manage water itself in MEA. Graphite rubbish, carbon black and spheroidal graphite were evaluated as an addition carbon to the CL. If water generated by the cell reaction was used effectively by SWMC, the humidifier is unnecessary. The previous study clarified that SWMC added only 27.4 wt.% of graphite rubbish obtained the best cell performance in spite of a little Pt catalyst amount. However, not only graphite rubbish but also carbon black and spheroidal graphite was also able to reduce the amount of platinum while maintaining the cell performance. We consider that further reduction of the amount of platinum may be achieved by changing the carbon species added depending on the location in the same electrode. Therefore, this study aims to select the optimum combination of carbon powder in MEA. On the other hand, we propose to reduce the system cost and solve the water management issues by operating the system without humidification at room temperature by removing the humidifier and heater. Therefore, our laboratory has proposed a Self-Water Management Separator (SWMS) (6). The SWMS has a bypass channel connecting the gas outlet and gas inlet in the separator, and the bypass channel is filled with a water-absorbing material that absorbs excess water by capillary action. Since this water-absorbing material moves water by the difference of water concentration between the gas inlet with low humidity and the gas outlet with condensate, it need to have both absorbency and water drainage ability. The previous study clarified that the bypass position depended on the operating condition, and the optimum bypass position under non-humidifying and non-heating conditions (w/o humidifier and heater) was at gas inlet. Therefore, this study aims to select the optimum water absorption material for SWMS.

Experimental

Self-Water Management Separator

General graphite flow field was applied to an anode side and the SWMS was applied to a cathode side respectively as shown in Figure 1, and a single serpentine was applied to both separators as a gas channel. The bypass inlet was located at the gas outlet, and there are four bypass outlets to choose from: at the gas inlet, upstream of the cell, in the middle, and near the outlet. In this study, the bypass outlet is set at the upstream of the cell based on the results of the previous study. The specification demanded for the water absorption material is absorbency, drainage ability and handling ability. We

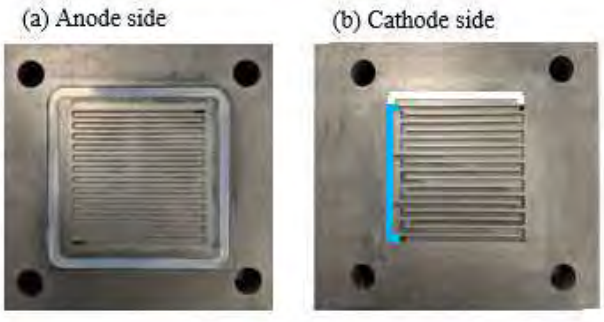

Figure 1. Photograph of each separator

prepared four water absorption materials such as polyvinyl alcohol (PVA) sponge, diatomite powder, cellulose fiber insulation (CFI), and EM diatomite grain offered from OKUTA Co., Ltd. Here, the cellulose insulation is a wood fiber insulation material.

Self-Water Management Catalyst layer

The carbon powder used to make SWMC is graphite rubbish offered from Anaori Carbon Co., Ltd, carbon black and spheroidal carbon as shown TABLE I, and added carbon mass fraction is shown TABLE II. Here, graphite rubbish is the cutting waste produced when cutting graphite kettles. The graphite rubbish and the spheroidal graphite have a hydrophobic, and the hydrophobic of the spheroidal graphite is a little weaker than the graphite rubbish. On the other hand, the carbon black has a weak hydrophilic. The previous study clarified that graphite rubbish with an average particle size of 74 μm or less, carbon black with an average particle size of 56.5 μm and spheroidal carbon with an average particle size of 27.8 μm, in that order, improved cell performance while reducing the amount of platinum. Here, the optimum addition rate for all carbons was 27.4 wt.%. Therefore, one type of carbon was uniformly added to the CL in the previous study. However, if the location of the addition inside the cell can be optimized by considering the characteristics of each carbon species, further reduction of platinum usage may be possible. This study aims to select the optimum combination of carbon powder in MEA. Each carbon was added in combination to the upstream and downstream portions of both electrodes as shown in TABLE III. SWMC attempts to use the properties of carbon to move the water generated by the cell reaction inside the MEA as intended. We expect the following behaviors for each carbon. (A) Since the graphite rubbish has a strong hydrophobic property and is the largest, it penetrates the CL like a pillar to connect a membrane-CL-GDL. Because it is scattered in the CL at the addition ratio of 27.4 wt.%, moves water generated laterally in the CL, and also serves as a pathway for electron transport from the GDL side. (B) The carbon black has a hydrophilic property and is used as a catalyst carrier. The size is a little larger than the CL thickness, so there will be scattered columns penetrating the CL as same as the graphite rubbish. Since this column is hydrophilic, it is expected to move water in the membrane and water generated in the CL between the gas flow path and the membrane. Moreover, it also serves as a pathway for electron transport from the GDL side. (C) Since the spheroidal graphite with a weak hydrophobic property is the smallest, exist on the GDL side like a film. Therefore, it can be expected that the water in the CL will be retained without draining.

TABLE I. Specification of Each Carbon Powder

Kind of Carbon	Graphite Rubbish	Carbon Black	Spheroidal Graphite
Average Particle Size	74μm or less	56.5μm	27.8μm
Image of SEM	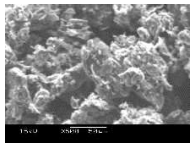	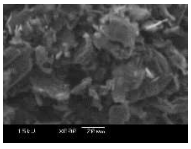	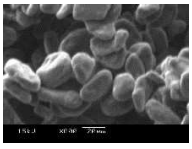
Average Contact Angle	134.2°	55.0°	79.3°
Image of Contact Angle	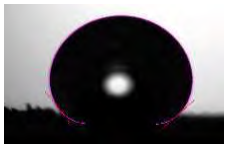		

The additive amount of each carbon powder to catalyst slurry was 0.3 g, and I/C ratio was 0.601. The catalyst slurry that added the carbon powder had stirred using a mix rotor at 24 hr or more, and it was dispersed by an ultrasonic crusher (Thai Tech CO., Ltd.: VP-50; homogenizer) under 40% of output for 60 s. Thereafter, it was applied to gas diffusion layer (GDL: 29BC made by SIGRACET®) using a doctor blade method after it was stirred by a mix rotor for one hour. This CL on the GDL was dried by 80 ℃ of an oven, thereafter the MEA were prepared by sandwiching the membrane (Nafion® 212) between GDLs coated with a CL and hot-pressing them together at 123 ℃ and 8 MPa.

TABLE II. Mass Fraction.

	Standard	**SWMC**
Mass Fraction of Pt	23.7wt%	17.2wt%
Mass Fraction of Additive Carbon	-	27.4wt%

TABLE III. Carbon Combination

	Anode		**Cathode**	
	upstream	**downstream**	**upstream**	**downstream**
1	standard			
2	w/o bypass standard			
3	graphite rubbish(GR)		carbon black(CB)	
				
4	carbon black(CB)		spheroidal graphite(SG)/graphite rubbish(GR)	
				
5	carbon black(CB)/spheroidal graphite(SG)		spheroidal graphite(SG)/graphite rubbish(GR)	
			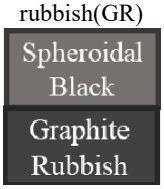	
6	graphite rubbish(GR)/spheroidal graphite(SG)		carbon black(CB)	
				
7	spheroidal graphite(SG)		graphite rubbish(GR)/carbon black(CB)	
				

Experimental apparatus and conditions

The PEFC single cell consists of an anode separator, a cathode separator, a current collector plate, a heater plate. In order to keep electrical insulation, polytetra-fluoro ethylene (PTFE) sheet was put between a current collector plate and a heater plate. The general graphite flow field was applied to an anode side and the SWMS was applied to a cathode side respectively, and a single serpentine was applied to both separators as a gas channel. Figure 2 shows the experimental apparatus. Each gas controlled by mass flow controller was supplied to PEFC. In this study, although the experiments were conducted without humidifier or heater at room temperature and without humidification, the cell temperature was set at 30 ℃ to correspond to the seasonal variation. The cell performance was evaluated by I-V performance and Cole-Cole plots of AC impedance method by the fuel cell impedance meter (KIKUSUI KFM2030). The cell resistance was measured by a milliohm meter with four AC probes. TABLE IV shows the experimental conditions. The cell temperature, the fuel gas flow rate and the air flow rate were set at 30 ℃ , 80 ml/min and 334 ml/min respectively on all experimental conditions. The gas utilization of the evaluation experiment of the SWMS was set at Uf/Uox=70%/40% (based on 0.3 A/cm^2 of current density), and that of the SWMS-Durability and SWMC was Uf/Uox=45%/25% (based on 0.2 A/cm^2 of current density). Here, after the MEA was fabricated and assembled, it was not possible to generate power immediately, so the evaluation experiment was started after approximately 8 hr of break-in (aging).

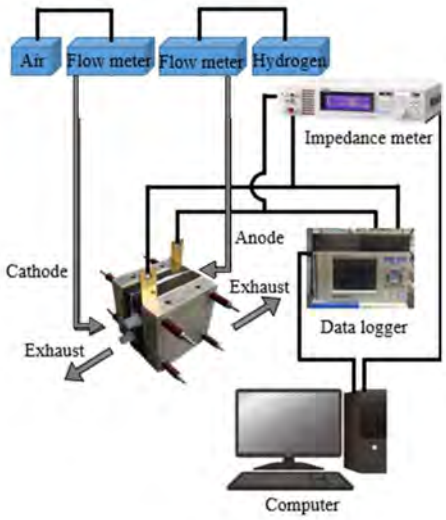

Figure 2. Schematic Diagram of Experimental Apparatus

TABLE IV. Experimental conditions

Condition	SWMS	SWMS-Durability	SWMC
Fuel Flow[ml/min]		80	
Fuel Gas Utilization[%]	70		45
Air Flow[ml/min]		334	
Oxidant Gas Utilization[%]	40		25
Cell Temperature[℃]		30	
Cell Pressure[Pa]		Atmosphere	
Current Density[A/cm^2]	0.3		0.2

Results and Discussions

Selection of water absorbing materials for SWMS

Figure 3 shows the result of (a) I-V performance as IR-Free and (b) AC impedance of a cell filled with each water-absorbing material into the SWMS. Here, the w/o bypass in this graph means that the bypass channel of the SWMS was blocked by PTFE tape. Because the triple phase boundary (TPB) is difficult to form due to non-humidified operating, the arcs of the Cole-Cole plot of all cells begins to separate by increasing of the gas diffusion polarization as shown in Figure 3 (b). Generally, the voltage drop due to the IR-free slope indicates an activation overvoltage, and the voltage deviating from the slope in the high current density region indicates a diffusion overvoltage. Although the slope of the cell without the bypass channel is generally stable in all current density region, that of the cell with the bypass channel is changed with the increase of the current density. Although the water generated by the cell reaction essentially moistens the membrane, any excess water collected at the gas outlet is bypassed and moved to the gas inlet, and the membrane is moistened. On I-V performance, as the amount of produced water increases with the increase of power generation, the TPB in the upper part of the cell increases, and consequently the activation overvoltage decreases. However, although the ohmic resistances of diatomite powder and EM diatomite grain with a high absorbency and low water holding capability are smallest, I-V performances gradually decrease with the increase of the current density and decrease drastically when the current density exceeds 0.3 A/cm^2. Especially, diatomite powder with low water holding capacity may have caused flooding phenomenon by draining water that could not be stored at the inlet and outlet of the bypass. Since the diffusion polarization of EM diatomite grain also increases when the current exceeds 0.32 A/cm^2, we consider that the same phenomenon basically occurs in diatomite powder as EM diatomite grain. On the other hand, it is possible that CFI with a high absorbency increased the ohmic resistance by absorbing water up to the water of the membrane. However, because the polarization resistance of CFI is almost the same as that of the w/o bypass channel and the arc of low frequency region is smaller, we consider that the cathode of the upper stream is supplied a little water by the bypass channel. The effect of SWMS is investigated by which the AC impedance of Figure 3 (b) be analyzed by the distribution of relaxation times (DRT) analysis using Z-Assist (TOYO Corporation) (7). Here, DRT analysis is a method of separating the polarization resistance into components. The relationship between the frequency of the peak in this analysis and the resistance

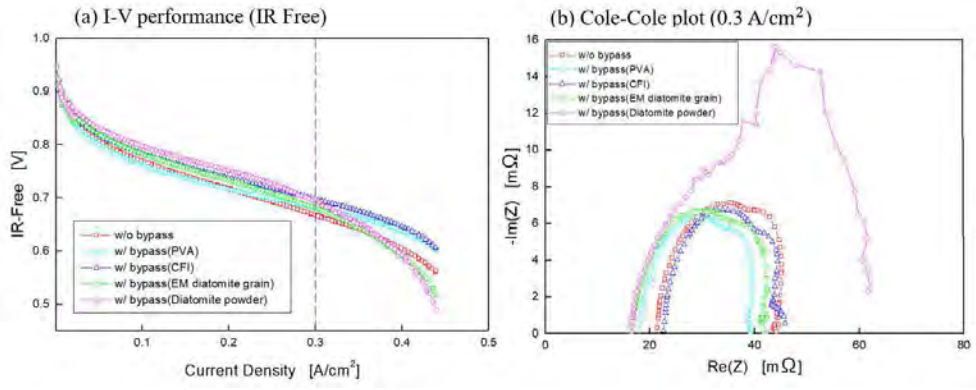

Figure 3. Selection of water absorbing Material for SWMS

TABLE V. DRT Peak Frequency and Elementary Reaction Process of PEFC

Peak	Electrode	Physicochemical Origin
P0	Anode	Gas diffusion process in the anode
P1	Cathode	Oxygen surface exchange and diffusion processes in the cathode
P2	Cathode	Charge transfer in the ORR
P3, P4		Proton conduction process in the mixed ionic-electronic conductor

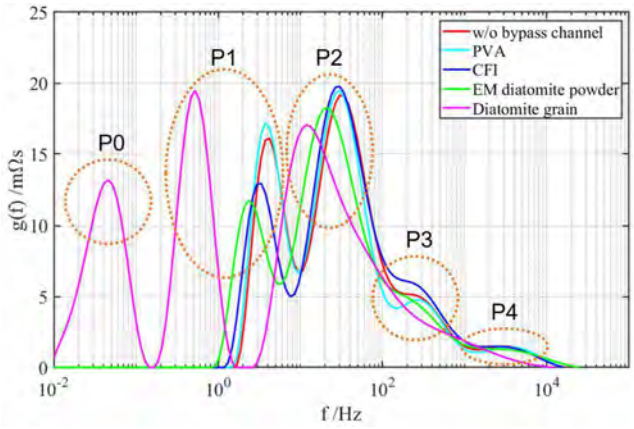

Figure 4. DRT analysis results of all water absorbing materials

component in the cell reaction is shown in TABLE V. Figure 4 shows the DRT analysis results of all water absorbing materials. Although the peak height and peak frequency differed slightly depending on the water absorbing material, the trend of all peaks was the same except for diatomite powder as same as Figure 3 (b). Especially, since the peak around 10 Hz, which indicates the polarization resistance of the oxygen reduction reaction (ORR), is almost the same, it can be judged that the TPB is formed in the same way. However, on the peak around 2 - 4 Hz which indicates the cathode gas diffusion polarization, since the peak heights of CFI and EM diatomite grain decrease, water supply from the bypass channel increases the TPB. However, since these peaks are shifted to the lower frequency side, further water supply may cause gas diffusion polarization. On the DRT analysis result of diatomite powder, the peak indicating the diffusion polarization of the cathode shifted to the lower frequency side and increased in height. Moreover, since a high peak near 0.05 Hz, which indicates the anode gas diffusion polarization, appears even though it does not appear in other water-absorbing materials, we consider that the flooding phenomenon occurs at both electrodes as the above-mentioned.

The durability of each water absorbing material was evaluated for 108 hr under the durability mode condition according to TABLE IV. Figure 5 shows the Cole-Cole plot of each material at the beginning, after 48 hr, and after 108 hr of testing. On the w/o bypass channel, because the ohmic resistance decreases slightly with time, it takes about two days for the membrane to be sufficiently moistened by the water produced by power generation under non-humidifying and non-heating conditions (w/o humidifier and heater). However, because the polarization resistance increases slightly with time, electrons have accumulated in the electron double layer and are not able to move, we consider that a sufficient TPB has not been formed due to the lack of water. On the other hand, the ohmic resistance of the SWMS (all water absorbing materials) is smaller than that of the w/o bypass channel, and it decreases slightly with time as same as the w/o bypass channel. Moreover, the

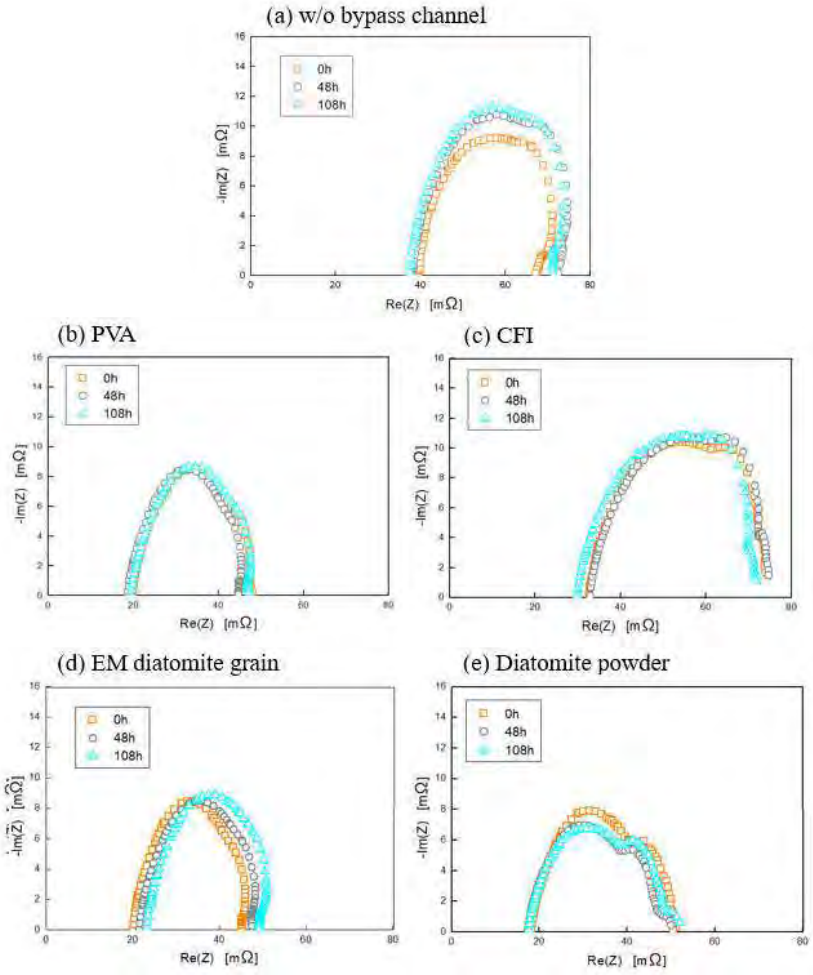

Figure 5. Durability of each water absorbing material (0.2 A/cm2)

polarization resistance of the SWMS hardly changes or decreases over time. Therefore, because the membrane is wetted and the TPB is formed by the water supply from the bypass, the effectiveness of the SMWS is able to be confirmed. Especially, not only the ohmic resistance but also the polarization resistance of PVA is the lowest, and there is little change in these resistances over time. Moreover, the price of PVA is the lowest in the water absorbing materials. From these results, PVA was determined to be the best water-absorbing material for SWMS in terms of performance and cost.

Influence of combination of each added carbon powder on cell performance

Figure 6 shows the influence of combination of each added carbon powder on cell performance. Here, the legend in figure refers to Anode(upperstream)/(downstream)-Cathode(upperstream)/(downstream). I-V performance of all the SWMCs installed into the SWMS was better than that of the standard cell as shown in Figure 6 (a), especially the polarization resistance of all the SWMCs except GR/SG-CB was smaller than that of the standard cell even though the amount of platinum is 6.5 wt.% less than the standard cell as

shown in Figure 6 (b). Figure 7 shows the results of extracting the ohmic and polarization resistances from Figure 6 (b). The effectiveness of the SWMS can be confirmed by comparing the presence or absence of bypass of the standard cells. The ohmic and the polarization resistances of the SWMS are smaller than that of the w/o bypass channel. As mentioned in the previous section, it is clear that the circulation of water generated by the

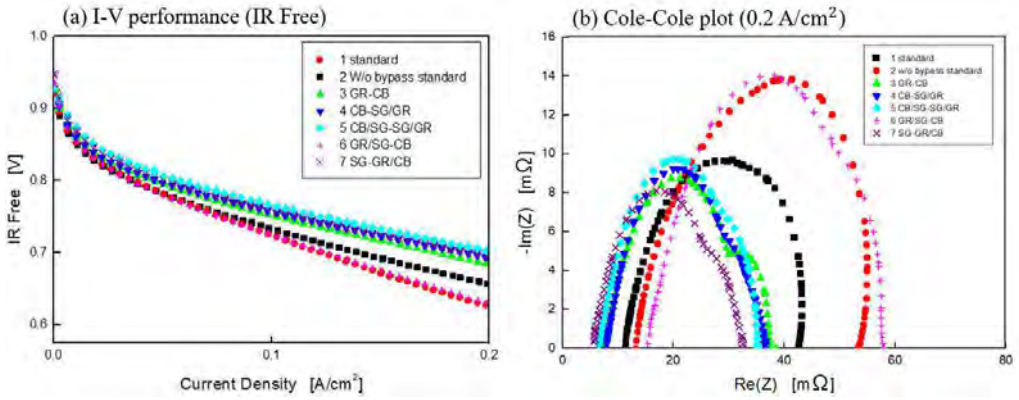

Figure 6. Influence of combination of each added carbon powder on cell performance

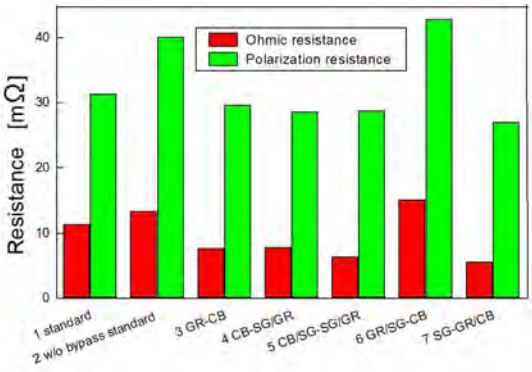

Figure 7. Comparison of ohmic and polarization resistances for each SWMC combination

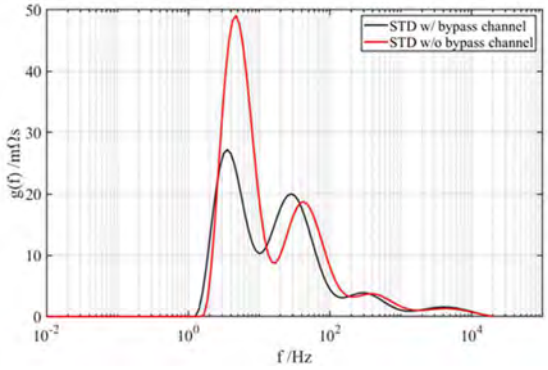

Figure 8. Comparison of DRT analysis results with and without bypass channel

cell reaction in the same electrode by bypass is effective. In order to confirm this reason, these two were subjected to DRT analysis, and the result is shown in Figure 8. Although both peak heights of the proton conduction resistance are almost the same, the peak height of ORR of the w/ bypass channel is greatly reduced compared with the w/o bypass channel. Therefore, the cathode reaction is improved by increasing the TPB of the whole cell by supplying water from the downstream to the upstream of the cell through the bypass channel, since the gas supply was hardly disturbed under the operation under non-humidified condition. Therefore, because the effectiveness of the SWMS was able to be confirmed in spite of operating under non-humidified condition, it could be suggested that the removal of the humidifier and heater from the PEFC system could reduce the system cost and improve the system efficiency.

On the combination of each added carbon powder in the SWMC, although the arc of the standard cell regardless of the presence or absence of bypass are generally one, it with each carbon added begin to separate into two as shown in Figure 6 (b). Figure 9 shows the comparison of the DRT analysis of combination of each carbon added powder. The peak of ORR is shifted to the higher frequency side than the standard cell though the peak height hardly changes as same as the arc diameter of the Cole-Cole plot. Moreover, although there was a peak of the proton conduction resistance in the standard cell, this peak became much smaller with the addition of carbon. The added carbon complements proton conduction instead of ionomer by moving water generated by the cell reaction in the CL. Moreover, because the added carbon also conducts electrons unlike ionomers, we consider that the cathode reaction becomes faster and the ORR peak shifts to the high frequency side though the amount of platinum is reduced by the addition of carbon. On the other hand, the peaks around 1 Hz which indicates the cathode gas diffusion resistance that did not appear in the standard cell appear in the cell with the SWMC. We consider that the presence of carbon in the CL, whose gas permeability is worse than that of the CL, increased the gas diffusion resistance. However, since carbon added occupies a small percentage of the CL space, this carbon addition does not lead to a decrease in the cell performance.

Only the GR/SG-CB has difference positions and highs for each peak. The ORR peak and the gas diffusion peak are higher than others. Because the carbon black with a hydrophilic is added to the entire cathode CL, water generated by the cell reaction is easily drained to the gas flow channel. The ORR resistance is lower than that of the standard cell without the bypass channel because the TPB of the upstream of the cathode electrode increases when water drained into the gas channel is carried upstream of the cell by the bypass channel. However, the graphite rubbish with a strong hydrophobic and the spheroidal graphite with a weak hydrophobic are added to the upper stream and the downstream of the anode CL respectively, water is difficult to be supplied to the anode CL from the membrane. Consequently, as the TPB of the anode electrode is not formed enough, the cell performance is worse than that of the standard cell with the bypass channel.

The ohmic and polarization resistances and the ORR peak of other carbon added cells are almost the same as shown in Figure 7 and Figure 9. On the GR-CB, the cathode side is a system that drains water generated from the CL into the gas flow channel and returns that water to the upstream by the bypass channel, while the anode side is a system that prevents to enter water from the membrane. However, we consider that since the graphite rubbish occupies a small percentage of the anode electrode and it is added to the entire electrode,

water can enter the anode side avoiding the graphite rubbish. Consequently, as the TPB of the anode electrode increases slightly, the performance is better than that of GR/SG-CB.

On the CB-SG/GR, the CB/SG-GS/GR and the SG-GR/CB, the ohmic and polarization resistances as shown in Figure 7 and the ORR and cathode gas diffusion peaks as shown in Figure 9 are almost the same, but the peak appears at around 0.1 Hz on the CB-SG/GR and the SG-GR/CB. On the CB-SG/GR, the anode side is a system in which hydrophilic carbon black draws water from the cathode side through a membrane. On the cathode side, water returned to the upstream of the cell by the bypass channel is pushed to the anode side by the spherical graphite, and on the downstream side, the graphite rubbish makes water generated move laterally in the CL and toward the gas flow channel and the membrane. Although there is a difference in the amount of water supply between the upstream and downstream sections, the system is such that water is easily supplied from the cathode to the entire anode side. Therefore, although the cell performance is enhanced by increasing the TPB of the anode electrode, the water supplied to the anode is rather high and the gas diffusion may have started to be inhibited by the water formed on the carbon black in the anode CL, and consequently we consider that the peak around 0.1 Hz appears. On the SG-GR/CB, the anode side is a system that maintains water supplied in the CL by the spheroidal graphite. On the cathode side, water drained into the gas channel by the carbon black in the downstream part is moved to the upstream part of the cell by the bypass channel, and the moved water is pushed out laterally in the CL and to the anode side by the graphite rubbish at the upstream part. Therefore, the water supply to the anode side is only from the upstream part of the cell. However, we consider that since the spheroidal graphite exists between the anode GDL and the CL like a film, the gas diffusion resistance increases slightly and the peak around 0.1 Hz begins to appear.

From these results, the SG-GR/CB is the best combination to reduce the ORR resistance and improve the performance with less platinum, and it is able to confirm that the manufacturing cost was able to reduce using the combination of the SWMS and the SWMC.

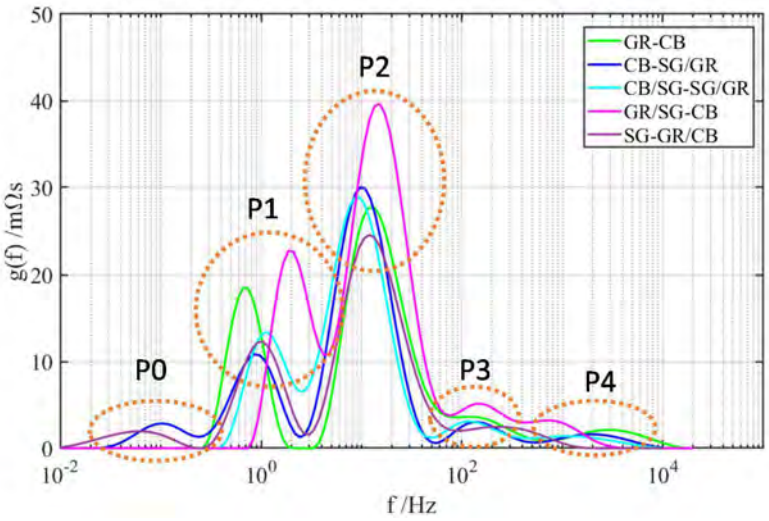

Figure 9. Comparison of DRT analysis results with difference combinations of added carbon

Conclusion

The objective of this study is development of cell separator and MEA with self-water management on PEFC for the cost reduction. The results obtained in this study are summarized as follows.

1. The effectiveness of the SWMS was able to be confirmed from the viewpoint of the enhancement of the cell performance.
2. The best filling water-absorption material in the bypass channel for the SWMS was PVA sponge from the viewpoint of the cell performance and the cost.
3. The effectiveness of the addition of the carbon powder as the water management grain to the CL was able to be confirmed under the non-humidifying condition.
4. The SWMC was found to be effective in reducing ohmic resistance, proton conduction resistance, and ORR resistance.
5. It was found that it is possible to both reduce the manufacturing cost and improve the cell performance by optimizing the addition position of each carbon in the electrode according to the characteristics of each carbon.

Acknowledgments

This work was supported by JKA and its promotion funds from AUTO RACE (2017M-116). We wish to express our gratitude to OKUTA Co., Ltd. that offers the diatomite sample and Anaori Carbon Co., Ltd. that offers the carbon sample.

References

1. Y.Sato, K.Fujii, N.Mitani, A.Matsuura, T.Kakigi, F.Muto, J.Li, A.Oshima, and M.Washio, *Nuclear Instruments and Methods in Physics Research*, Section B: Beam Interactions with Materials and Atoms, **265(1)**, p. 213-216 (2017).
2. Hubert A. Gasteiger, Mark F. Mathias, *ECS Proceedings*, **2002-31** (2002).
3. K. Uda, Z. Noda, M. Nagayama, K. Sasaki, and A. Hayashi, *ECS Transactions*, **86**, p. 497-506, ISBN 9781607685395 (2018).
4. Prakash C.Ghosh, *Clean technologies and environmental policy*, **19**, p. 595-601 (2017).
5. K. Sugiura and S. Teramae, *Proceeding of EFCF 2021*, A0708 (2021).
6. Y. Yanagisawa and K. Sugiura, *Journal of Mechanical Engineering Research and Developments*, **43**, No. 2, p. 11-19 (2020).
7. M. Heinzmann, A. Weber, and E. I-Tiffée, *Journal of Power Sources*, **402**, p. 24–33 (2018).

Chapter 10

Bipolar Plates

ECS Transactions, 104 (8) 257-267 (2021)
10.1149/10408.0257ecst ©The Electrochemical Society

The Effects of Testing Conditions on Corrosion Behaviours of SS316L for Bipolar Plate of Proton Exchange Membrane Fuel Cell

Yu Leng[a,b], Daijun Yang[a,b], Pingwen Ming[a,b], Bing Li[a,b], Cunman Zhang[a,b]

[a] New Energy Automotive Engineering Center, Tongji University, 4800 Caoangong Road, Shanghai 200029, China
[b] School of Automotive Studies, Tongji University, 4800 Caoangong Road, Shanghai 200092, China

The corrosion of stainless steel bipolar plate (BPP) remains a big challenge while it has been considered to be one of the most appropriate candidates for proton exchange membrane fuel cell (PEMFC) in automotive application. This work aims to study comprehensively the effects of temperature, pH, bubbled gas and potential on corrosion behaviours of SS316L. Moreover, SEM and EDX are performed to reveal the evolutions of surface morphology, microstructure and chemical composition of SS316L under different testing conditions. The results indicate that temperature, pH and potential have significant influences on corrosion potential ($E_{corr.}$), corrosion current density ($I_{corr.}$) and passive current density (I_p) of SS316L. The interactions between different testing conditions on corrosion resistance are strong. The main corrosion mechanism of SS316L would be shifted from pitting to intergranular or uniform corrosion as pH decreases from 3 ~ 5 to 0.3 ~ 1.

Introduction

PEMFC has been regarded as the ultimate energy solution for solving problems caused by fossil fuels, such as global warming, environmental pollution and energy shortage due to its high efficiency, low operating temperature, near zero emission and unlimited sources of hydrogen [1-3]. However, large-scale commercial application of PEMFC is still hindered by high cost, limited performance and durability. As one of the key components, BPP has a great impact on performance, durability and cost of PEMFC. Stainless steel 316L (SS316L) has been considered to be one of the most appropriate candidates for automotive application because of its high thermal and electrical conductivity, superior mechanical properties, ease of manufacture and relatively low cost [4]. However, corrosion as well as the corresponding problems, such as improvement of interfacial contact resistance (ICR) and release of metal ions of stainless steel BPP in typical PEMFC working environment remains big challenges [5].

The corrosion of BPP may lead to deteriorate of performance and durability, or even the damage of PEMFC. Therefore, it is important to improve the corrosion resistance of stainless steel BPP. Although problems, such as low corrosion resistance and interfacial conductivity of BPP can be solved by adding coatings currently, a higher corrosion resistance of the base stainless steel is still of great significance when concerning the durability of BPP or PEMFC [6]. In addition, it is critical to evaluate comprehensively the

corrosion resistance of materials for BPP under the complicated working conditions of PEMFC. However, most of the tests performed for corrosion resistance evaluation of BPP materials in previous studies are conducted under the conditions with specific temperature, pH and potential. The typical working environment of PEMFC is generally considered to be weak acidic with pH in the range of 3 ~ 6 containing different anions, such as F^{-1} and Cl^{-1} while the temperature is in the range of 60 ~ 80 ℃ [7]. However, a much harsher condition of 0.5 M H_2SO_4 with 2 ppm HF has been utilized in most of the former studies [8].

A few studies have been carried out to study the effects of different testing conditions, such as temperature, pH and anions on corrosion behaviours of BPP materials. Li et al. [9], studied the influences of temperature and pH on corrosion resistance of SS316L. Their research was focused on variation of the passive films under different pH and temperatures. In the work by Yang et al. [10, 11], the effects of temperature and sulphuric acid concentration with pH ranging from about 0.05 ~ 7 on corrosion current density and passive film of SS316L in cathodic environment were studied respectively. Lædre et al. [12] also analyzed the effects of pH (within the range of 0.5 ~ 3) on corrosion resistance and conductivity of SS316L with nitrogen bubbled into the solution. In the work by Li et al. [9] and Yang et al. [13, 14], the influences of anions, such as chloride and sulfide ions on corrosion resistance of SS316L are also studied. In addition, the potential of 0.6 V is generally used to simulate the cathode working environment of PEMFC while higher potential of 1.4 ~ 1.75 V (vs. SHE) may occur due to hydrogen local starvation during the processes of start-stop. Based on the study by Orsi et al [15], the corrosion resistance of BPP materials under higher potentials may need to be considered to better mimic the extreme working conditions.

Although the researches mentioned above have been carried out to study individually the effects of pH, temperature or potential on corrosion resistance of stainless steel for BPP, the combined effects of pH, temperature, bubbled gas and potential on corrosion resistance of stainless steel have not been investigated. In this work, the effects of temperature, pH, bubbled gas and potential on corrosion behaviours of stainless steel are studied comprehensively with the most commonly used SS316L by potentiodynamic and potentiostatic tests. In the meanwhile, SEM and EDX are performed to investigate the evolution of microstructure, surface morphology and chemical composition of SS316L under different testing conditions.

Experimental

Material Preparation

The SS316L utilized in the present paper was cold rolled and bright annealing treated with a thickness of 0.1 mm that produced under the guidance of Japanese Industrial Standards (JIS). Specimens with a size of about 25 mm × 25 mm were cut from the original SS316L foil. Before all electrochemical tests, the specimens were first cleaned ultrasonically in a 0.5 M H_2SO_4 and then in distilled water, both for 5 minutes. Analytical reagent sulfuric acid (Sinopharm Chemical Reagent Co., Ltd) and hydrofluoric acid (Aladdin Reagent (Shanghai) Co., Ltd) with weight percent of 98% and 40%, respectively, were used for preparing the testing solutions with different pH and 2 ppm HF.

Electrochemical Test

All electrochemical tests were conducted on a three electrode electrochemical workstation (CHI660E) with a saturated Ag/AgCl and platinum mesh used as the reference and counter electrodes, respectively. The specimens with an exposure area of 1.25 cm^2 were served as the working electrode, as shown schematically in Figure 1. Temperature of the corrosion solutions were kept constant through a circulating water bath system during the period of testing. In the meanwhile, oxygen and pure argon were bubbled to create different corrosion atmospheres with the bubbling system. Prior to each potentiodynamic and potentiostatic test, the specimen was stabilized at the open circuit potential (OCP) for 1 h. Potentiodynamic tests were carried out from -0.6 to 1.3 V (vs. Ag/AgCl) with a scanning rate of 1 $mV \cdot s^{-1}$. For potentiostatic tests, the constant potential of -0.1 V (vs. Ag/AgCl) and argon gas bubble were utilized to simulate the anode working environment of PEMFC. In addition, the potentials of 0.6 V , 1.0 V and 1.4 V (vs. Ag/AgCl) as well as oxygen bubbling was used to simulate the cathode environment of PEMFC under different working conditions.

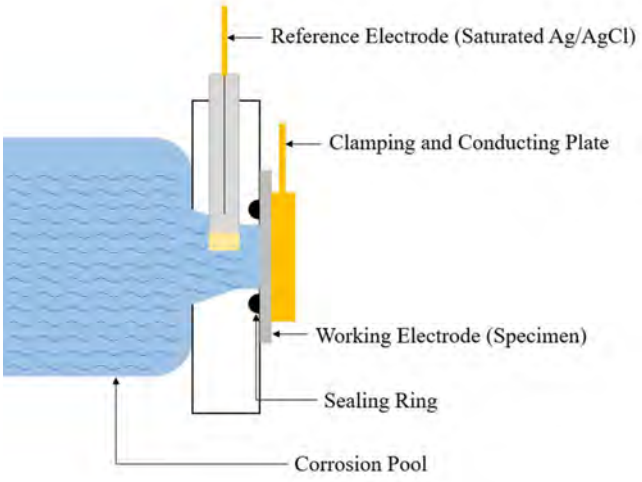

Figure 1. Schematic view of the structure of working electrode for electrochemical test.

Microstructure Characterization

The specimens were taken from the corrosion cell immediately after electrochemical tests and washed with distilled water. Afterwards, they were dried in the air for microstructure characterization. SEM observations were conducted to reveal the morphology and microstructure of the specimens under different testing conditions by using a Quanta FEG 250 environment scanning electron microscope. Besides, the variation of chemical compositions in the surface of the specimens after electrochemical tests are investigated with an energy dispersive X-ray spectrometry attached to the scanning electron microscope.

Results and discussions

Effects of Temperature

Temperature is an important factor which may have significant influence on corrosion resistance of SS316L because both thermodynamics and kinetics in the corrosion processes are affected by temperature. The temperature of 25, 60, 70 and 80 ℃ are adopted in the present paper as simulated conditions for shutdown and operating, respectively, to study the influence of temperature on corrosion resistance of SS316L by potentiodynamic tests. The effects of temperature on $E_{corr.}$, $I_{corr.}$ and I_p of SS316L of SS316L under different pH and bubbled gases are shown in Figure 2.

As can be drawn from Figure 2 (a) - (d), the Tafel curve of SS316L can be divided into three typical regions, namely active region, passive region and transpassive region in accelerated testing conditions. $E_{corr.}$ of SS316L becomes more positive at higher temperature when pH is in the range of 0.3 ~ 1 with argon bubbled in the solution. However, the effect of temperature on $E_{corr.}$ of SS316L is contrary when the pH of the solution is larger than 3, as shown in Figure. 2 (e) - (h). For the tests conducted in the solutions with pH in the range of 3 ~ 5, $E_{corr.}$ of SS316L becomes more negative as temperature increases from 25 ℃ to 80 ℃, for both argon and oxygen bubbled conditions. The results in Figure 2 also show that $I_{corr.}$ of SS316L generally increases with higher temperature. However, the effect of temperature on $I_{corr.}$ of SS316L tends to be small when temperature is in the range of 60 ~ 80 ℃. The potentials of SS316L in the passive region are normally in the range of -0.1 ~ 0.9 V (vs. Ag/AgCl). The effect of temperature on I_p of SS316L is relatively small when pH is in the range of 0.3 ~ 1 for both argon and oxygen bubbled solutions (Figure 2 (a) - (d)). However, I_p of SS316L will increase significantly as temperature becomes higher when pH of the solutions are in the range of 3 ~ 5 (Figure. 2 (e) - (h)).

Based on the results of potentiodynamic tests for SS316L under different temperatures with varying pH and bubbling conditions, it can be concluded that $E_{corr.}$, $I_{corr.}$ and I_p of SS316L are determined together by temperature, pH and gas bubbled in the solution. In addition, the evaluation of corrosion resistance of materials for BPP through corrosion potential as in some literatures may be improper, which is consistent with the theoretical analysis provided by Cao [16].

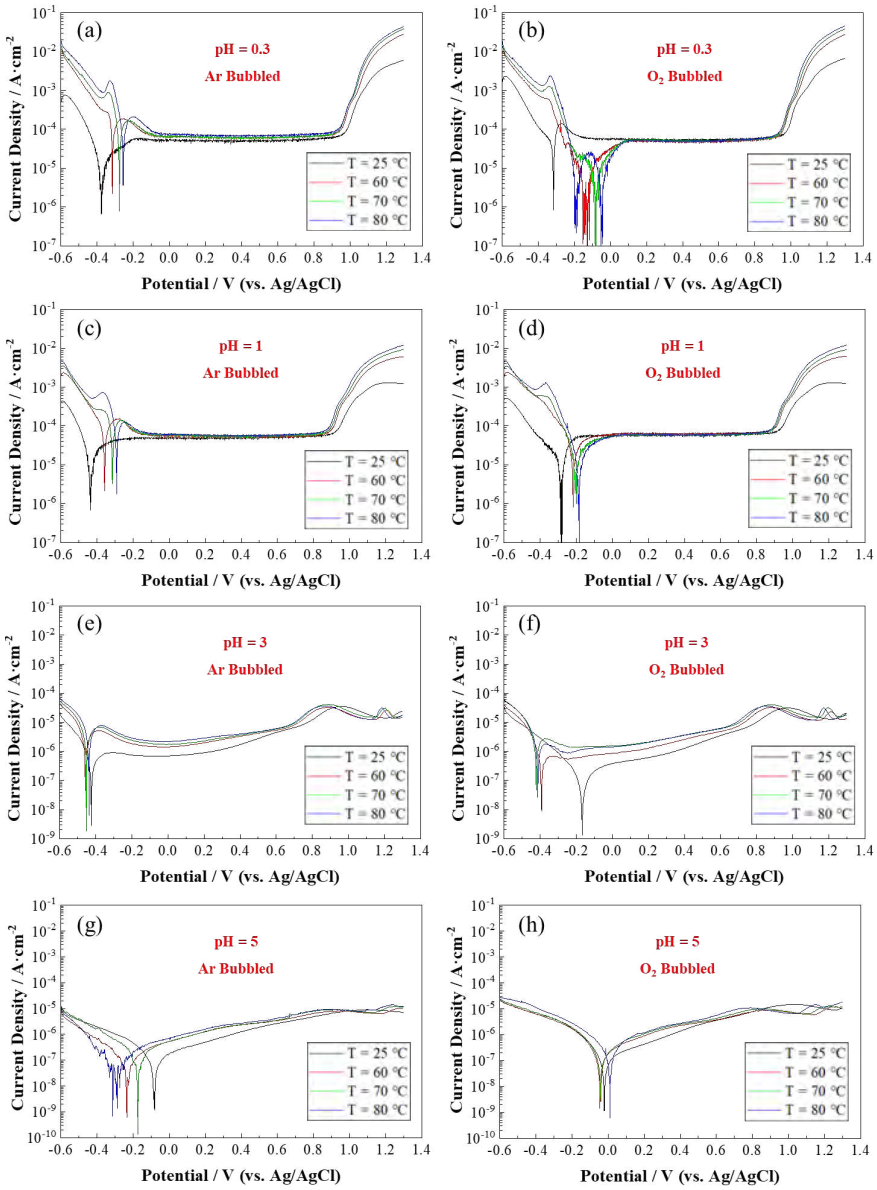

Figure 2. The effect of temperature on Tafel curve of SS316L under different pH and gases bubbled by potentiodynamic tests. (a), (c), (e), and (g) Ar bubble with pH = 0.3 ~ 5; (b), (d), (f), and (h) O_2 bubble with pH = 0.3 ~ 5

Effects of pH

The pH of working environment of PEMFC is normally in the range of about 3 ~ 6 while 0.5 M H_2SO_4 with pH about 0.3 has been utilized by many researches. Therefore, the effects of pH on $E_{corr.}$, $I_{corr.}$ and I_p of SS316L under different temperatures and bubbled gases are also examined through potentiodynamic tests. The results are shown in Figure 3. It can be seen that $E_{corr.}$ of SS316L would become more negative as pH increases from 0.3 to 3, and then it becomes much more positive as pH further increases from 3 to 5 for tests in solutions bubbled with argon and under the temperature range of 25 ~ 80°C. The effect of pH on $E_{corr.}$ of SS316L in solutions bubbled with oxygen is basically the same as those in solutions bubbled with argon at higher testing temperatures of 60 ~ 80°C. However, $E_{corr.}$

of SS316L in solutions bubbled with oxygen would continuously become more positive as pH increases from 0.3 to 5. It can also be drawn that $I_{corr.}$ and I_p of SS316L decreases for tests conducted at all temperatures in both argon and oxygen bubbled solutions when pH increases from 0.3 to 5. The results indicate that the variation of $I_{corr.}$ and I_p of SS316L in PEMFC mainly depends on pH rather than temperature and bubbled gas. In addition, both pH and temperature have significant influences on change of $E_{corr.}$ of SS316L while the effects of bubbled gas tends to be small. However, there is a big difference between the values of $E_{corr.}$ of SS316L tested in solutions bubbled with different gases. $E_{corr.}$ of SS316L would be more positive in oxygen bubbled solutions at the same pH and temperature.

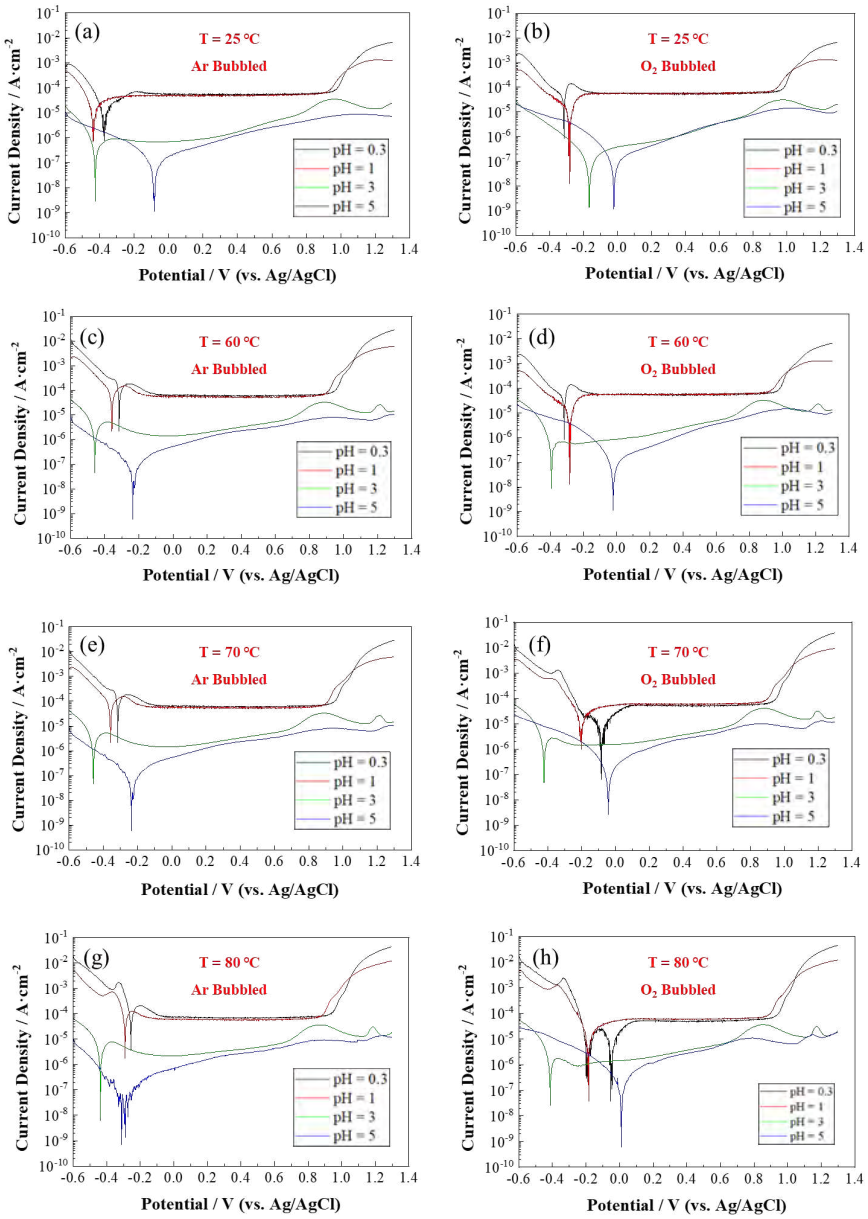

Figure 3. The effect of pH on Tafel curve of SS316L under different temperatures and bubbled gases by potentiodynamic tests. (a), (c), (e), and (g) Ar bubble with temperature in the range of 25 ~ 80℃; (b), (d), (f), and (h) O_2 bubble with temperature in the range of 25 ~ 80℃

Effects of Bubbled Gas

In typical working environment of a PEMFC, hydrogen and oxygen are the gases in anode and cathode, respectively. Potentiodynamic tests are also conducted to investigate the influences of bubbled gas on corrosion resistance of SS316L in solutions with pH = 0.3 at different temperatures. The reductive atmosphere created by hydrogen in anode of PEMFC is replaced by using the gas of argon in the present paper. $E_{corr.}$, $I_{corr.}$ and I_p of SS316L under conditions of argon, oxygen and no bubbling are derived from the Tafel plots of potentiodynamic tests, as shown in Figure 4. The results show that $E_{corr.}$ of SS316L would get more positive as the atmosphere of testing solution changes from reductive to oxidizing environment. This phenomenon is more obvious at higher temperatures. In the meanwhile, it can also be seen that the variation of $I_{corr.}$ and I_p of SS316L under different atmospheres is relatively small, which means that bubbled gas may have a small impact on corrosion resistance of SS316L as compared to temperature and pH in typical working environment of PEMFC.

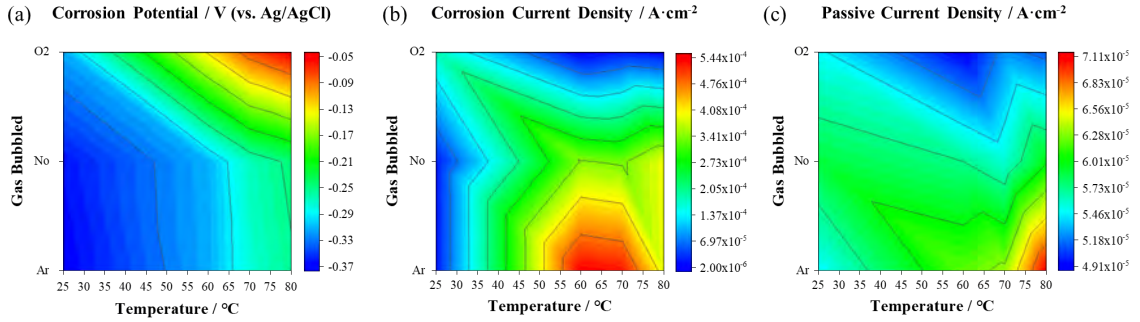

Figure 4. The effects of bubbled gas on $E_{corr.}$, $I_{corr.}$ and I_p of SS316L. (a), (b) and (c), $E_{corr.}$, $I_{corr.}$ and I_p of SS316L, respectively.

Effects of Potential

Besides temperature, pH and bubbled gas, potential is another important factor having great influence on corrosion resistance of bipolar plate during working conditions of PEMFC. Therefore, potentiostatic tests are performed to investigate corrosion current densities of SS316L at specific potentials in solutions with different pH, as shown in Figure 5. The corrosion current densities of SS316L in solutions with pH = 3 and pH = 0.3 are about 0.01 μA cm^{-2} and 0.1 μA cm^{-2}. For cathode side of PEMFC, corrosion current density of SS316L increases significantly as the applied potential is raised from 0.6 to 1.4 V (vs. Ag/AgCl). The results show that SS316L at the anode side of PEMFC with an applied potential of -0.1 V tends to have a smaller corrosion current density as compared to the ones at cathode side with applied potentials in the range of 0.6 ~ 1.4 V (vs. Ag/AgCl). In addition, when potentiostatic tests are conducted at the applied potential of 0.6 V, the corrosion current densities of SS316L in solutions with pH = 3 and pH = 0.3 are about 0.14 μA cm^{-2} and 0.23 μA cm^{-2}, respectively, which are close to each other. However, the corrosion current densities of SS316L in solutions with pH = 3 would increase to about 3 μA cm^{-2} and 50 μA cm^{-2}, respectively, while the ones in solutions with pH = 0.3 would increase to 500 μA cm^{-2} and 50000 μA cm^{-2}, respectively, when the applied potential is

improved to 1.0 V and 1.4 V (vs. Ag/AgCl). The results also show that a larger impact of potential would have on corrosion current density of SS316L in solutions with lower pH.

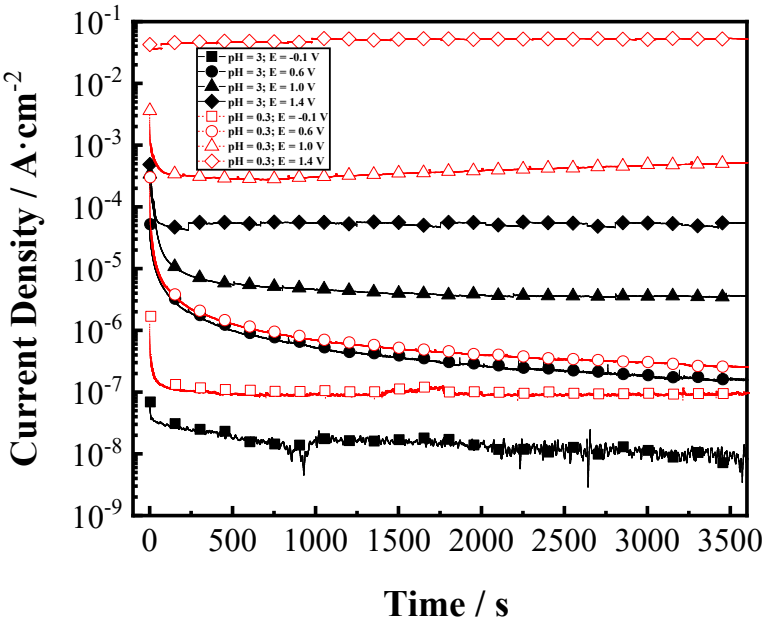

Figure 5. The effect of potential on corrosion current density of SS316L in solutions with different pH by potentiostatic tests.

Microstructure characterization

SEM are utilized to reveal the effects of potential and pH on evolution of surface morphology and microstructure of SS316L during potentiostatic tests, as shown in Figure 6. The results indicate that pitting is the main corrosion mechanism for SS316L in solutions with pH = 3, even at higher applied potentials of 1.0 ~ 1.4 V (vs. Ag/AgCl) (Figure 6 (b) - (d)). Moreover, the surface morphology of SS316L tested in solutions with pH = 0.3 show that pitting is also the main corrosion mechanism for SS316L when the applied potential is -0.1 V (Figure 6 (e)) and 0.6V (Figure 6 (f)). However, the main corrosion mechanism would be changed to intergranular and uniform corrosion, respectively, as the applied potential further increases to 1.0 V (Figure 6 (g)) and 1.4 V (Figure 6 (g)). In addition, the main chemical compositions in the surface of SS316L are determined by EDX, as shown in Figure 7 and TABLE I. It can be seen that the content of nickel would be lowered after potentiostatic tests in both solutions with pH = 3 and 0.3. Besides, the weight reduction of nickel element in the surface of SS316L increases as pH of the test solution is lowered from 3 to 0.3. The results show that nickel may be a more soluble element in PEMFC environment when compared to chromium although it has been added as an alloying element for improvement of corrosion resistance.

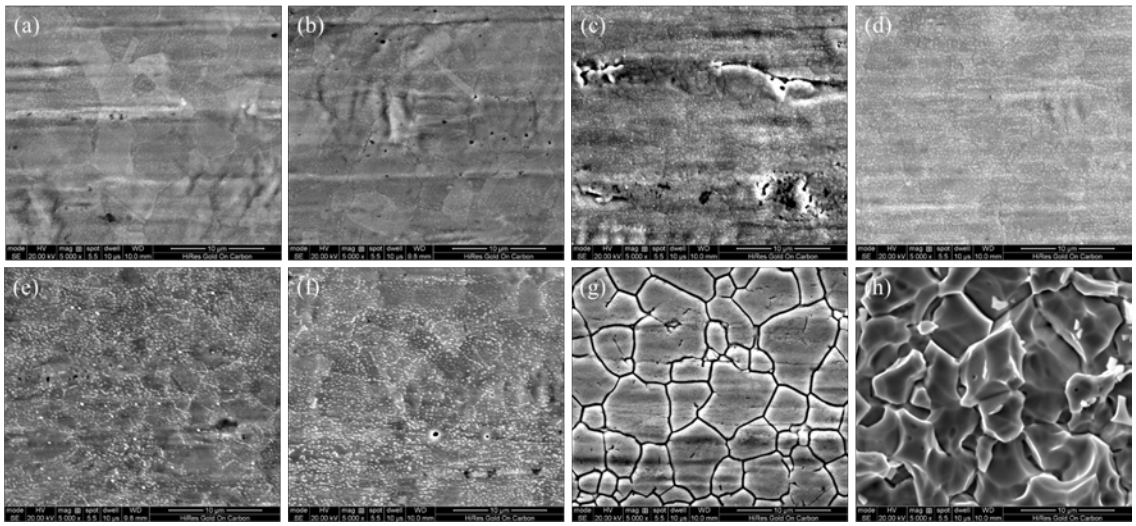

Figure 6. The surface morphology and microstructure of SS316L before and after potentiostatic tests by SEM. (a) Original specimen; (b) - (d) Specimens after potentiostatic tests in solutions with pH = 3 at the applied potential of 0.6 V, 0.8 V and 1.4 V (vs. Ag/AgCl), respectively; (e) - (f) Specimens after potentiostatic tests in solutions with pH = 0.3 at the applied potential of -0.1 V, 0.6 V, 0.8 V and 1.4 V (vs. Ag/AgCl), respectively

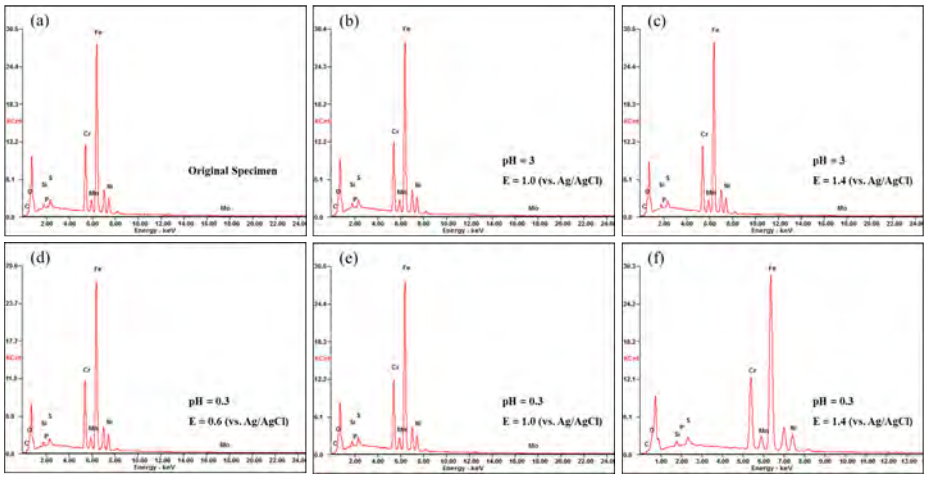

Figure 7. Element contents in the surface of SS316L under different potentiostatic tests by EDX. (a) Original specimen; (b) T = 70 ℃; pH = 3, E = 1.0 V (vs. Ag/AgCl), O2 Bubble ; (c) T = 70 ℃; pH = 3, E = 1.4 V (vs. Ag/AgCl), O2 Bubble ; (d) T = 70 ℃; pH = 0.3, E = 0.6 V (vs. Ag/AgCl), O2 Bubble; (e) T = 70 ℃; pH = 0.3, E = 1.0 V (vs. Ag/AgCl), O2 Bubble; (f) T = 70 ℃; pH = 0.3, E = 1.4 V (vs. Ag/AgCl), O2 Bubble

TABLE I. The contents (wt. %) of chemical compositions in the surface of SS316L.

Element	C	O	Si	P	S	Cr	Mn	Fe	Ni
(a) Original specimen	0.55	3.66	1.17	0.46	1.43	16.24	1.46	65.70	9.33
(b) pH = 3, E = 1.0 V	0.57	3.72	1.20	0.49	1.40	16.30	1.44	65.65	9.21
(c) pH = 3, E = 1.4 V	0.51	3.55	1.10	0.45	1.35	16.18	1.40	66.38	9.08
(d) pH = 0.3, E = 0.6 V	0.48	3.07	0.91	0.33	1.20	16.44	1.56	66.81	9.19
(e) pH = 0.3, E = 1.0 V	1.02	3.59	1.20	0.42	1.35	16.59	1.46	65.38	9.01
(f) pH = 0.3, E = 1.4 V	0.71	3.53	1.14	0.47	1.37	16.41	1.28	66.28	8.80

Conclusions

In this study, the effects of temperature, potential, pH and bubbled gas on corrosion behaviours of SS316L for BPP of PEMFC are investigated comprehensively by electrochemical tests. In addition, SEM and EDX are conducted to reveal the evolutions of surface morphology, microstructure and chemical composition of SS316L under different testing conditions. Based on the results, main conclusions are made as follows.

Temperature, pH and bubbled gas all have significant influences on $E_{corr.}$ of SS316L. When temperature increases from 25 ℃ to 80 ℃, $E_{corr.}$ of SS316L would become more positive in solutions with pH is in the range of 0.3 ~ 1 and argon bubble, while it would become more negative for both argon and oxygen bubbled conditions. $E_{corr.}$ of SS316L would become more negative as pH increases from 0.3 to 3, and then it becomes much more positive as pH further increases from 3 to 5 for tests in solutions bubbled with argon at the temperature range of 25 ~ 80℃. This is the same for solutions bubbled with argon at higher testing temperatures of 60 ~ 80℃. However, $E_{corr.}$ of SS316L in solutions bubbled with oxygen would continuously become more positive as pH increases from 0.3 to 5 at the temperature of 25℃. Therefore, $E_{corr.}$ may be inappropriate to evaluate materials for BPP of PEMFC.

Bubbled gas tends to have a small effect on $I_{corr.}$ and I_p of SS316L while temperature and pH have a large impact on them. $I_{corr.}$ of SS316L generally increases with higher temperature or pH value. The effect of temperature on I_p of SS316L is relatively small when pH is in the range of 0.3 ~ 1. However, I_p of SS316L will increase significantly as temperature becomes higher when pH of the solutions are in the range of 3 ~ 5.

The corrosion current density of SS316L increases significantly as the applied potential is raised from 0.6 to 1.4 V (vs. Ag/AgCl). In addition, potential would have a larger impact on corrosion current density of SS316L in solutions with lower pH. Pitting is the main corrosion mechanism for SS316L in solutions with pH = 3, even at higher applied potentials of 1.0 ~ 1.4 V (vs. Ag/AgCl). However, the main corrosion mechanism would be changed to intergranular and uniform corrosion, respectively, as the applied potential further increases to 1.0 V and 1.4 V.

Acknowledgments

The authors would like to acknowledge the support of National Natural Science Foundation of China (Grant No. 2018YFB1502500).

References

1. I. S. Sorlei, N. Bizon, P. Thounthong, M. Varlam, E. Carcadea, M. Culcer, M. Iliescu, and M. Raceanu, *Energies* , **14** (1), 252 (2021).
2. K. Bhaskar, J. M. Solomon, R. Sathyamurthy, S. Anaimuthu, and N. K. Vinayagam, *SAE Tech. Paper*, (2020).

3. A. G. Olabi, T. Wilberforce, and M. A. Abdelkareem, *Energy*, **214**, 118955 (2021).
4. Z. Xu, D. Qiu, P. Yi, L. Peng, and X. Lai, *Prog. Nat. Sci - Mater.*, (2020).
5. D. A. Shores, and G. A. Deluga, *Handbook of Fuel Cells*, p. 1, John Wiley & Sons, John Wiley & Sons, (2009).
6. Y. Song, C. Zhang, C. Y. Ling, M. Han, R. Y. Yong, D. Sun, and J. Chen, *Int. J. Hydrogen Energy*, **45** (54), 29832 (2020).
7. K. Feng, G. Wu, Z. Li, X. Cai, and P. K. Chu, *Int. J. Hydrogen Energy*, **36** (20), 13032 (2011).
8. Y. Leng, P. Ming, D. Yang, and C. Zhang, *J. Power Sources*, **451**, 227783 (2020).
9. D. G. Li, J. D. Wang, D. R. Chen, and P. Liang, *J. Power Sources*, **272**, 448 (2014).
10. Y. Yang, L. Guo, and H. Liu, *J. Power Sources*, **196** (13), 5503 (2011).
11. Y. Yang, L. J. Guo, and H. Liu, *Int. J. Hydrogen Energy*, **36** (2), 1654 (2011).
12. S. Lædre, O. E. Kongstein, A. Oedegaard, F. Seland, and H. Karoliussen, *Int. J. Hydrogen Energy*, **37** (23), 18537 (2012).
13. Y. Yang, L. J. Guo, and H. Liu, *J. Power Sources*, **195** (17), 5651 (2010).
14. Y. Yang, L. Guo, and H. Liu, *Int. J. Hydrogen Energy*, **37** (2), 1875 (2012).
15. A. Orsi, O. E. Kongstein, P. J. Hamilton, I. H. Svenum, and K. Cooke, *Journal of Power Sources*, **285**, 530 (2015).
16. C. N. Cao, *Principles of electrochemistry of corrosion*, p. 75, Chemical Industry Press, Beijing (2008).

ECS Transactions, 104 (8) 269-282 (2021)
10.1149/10408.0269ecst ©The Electrochemical Society

Investigation of Different Electrochemical Corrosion Treatments on Bipolar Plates for High and Low Temperature Polymer Electrolyte Membrane Fuel Cell Application

Lisa M. Uhlig[a], Nadine Pilinski[a], Henrike Schmies[a], Thorsten Hickmann[b] and Peter Wagner[a]

[a] German Aerospace Center (DLR) Institute of Engineering Thermodynamics, Carl-von-Ossietzky-Strasse 15, 26129 Oldenburg, Germany
[b] Eisenhuth GmbH & Co. KG, Friedrich-Ebert-Strasse 203, 37520 Osterode, Germany

This present research focusses on the corrosion behavior of bipolar plate (BPP) materials for high and low temperature (HT and LT) polymer electrolyte membrane fuel cell (PEMFC) applications. BPP materials were investigated by different electrochemical corrosion methods using a three-electrode cell setup. Potentiostatic conditions were recorded in concentrated phosphoric acid (PA) and diluted sulfuric acid, respectively, to investigate the stability of BPP for use in HT- and LT-PEMFC. Cyclic voltammograms (CV) were plotted before and after the potentiostatic treatments to evaluate the oxidation resistance behavior of the BPP. Further investigations with methods like scanning electron microscopy (SEM), confocal microscopy, µ-computed tomography (µ-CT) and titration will be shown to correlate surface area changes with corrosion measurement results.

Introduction

For vehicle, portable and stationary applications PEMFC are most promising and suitable (1). A big advantage among others of PEMFC in automotive vehicles is the zero emission when using hydrogen as fuel and air as oxidant (2). Nevertheless, the high cost, limited durability and missing hydrogen supply infrastructure are hindering commercialization of PEMFC (3).

The PEMFC is classified into low temperature (~70 – 95 °C, LT-PEMFC) and high temperature (~120 – 250 °C, HT-PEMFC) according to its operating temperature (4). Both are promising in use, but HT-PEMFC has advantages in comparison to LT-PEMFC like operation without humidification, tolerances against impurities in the fuel flow and usage of high temperature waste heat for other processes (5).

However, for development of PEMFC the major goals are low-cost, high performance and excellent durability. Hence, among other components like membrane electrode assembly (MEA) BPPs play an important role in a fuel cell system (4, 6). They take on several tasks, such as distributing the reactants homogeneously over the active MEA surface, electrical and thermal conductivity and preventing leakages (6, 7). Challenges are possible corrosion and mechanical failure of BPP (8). The influence on the efficiency and corrosion issues with the material composition is already known (9).

One important focus of durability or corrosion resistance is the control of molecular size pinholes (10-12). Consequently, in order to develop PEMFC materials, reliable analysis of PEMFC materials and components are required (13, 14). In addition to other materials, graphite composites are widely used to produce BPP (15, 16). Graphite-polymer composites with thermoplastic or thermosetting matrices have the advantage over metallic components in terms of corrosion resistance and low weight (16). Different types of commercial BPP material with e.g. polyphenylene sulfide (PPS) and polyvinylidene fluoride (PVDF) are available. One disadvantage of a polymer matrix is the low electrical conductivity which effects the performance of PEMFC (7). In the end, the successful design of composite bipolar plates depends on the compromise between electrical conductivity and corrosion resistance (16, 17).

While the BPP is a necessary component in fuel cell assemblies which undergo degradation or structural changes under the harsh operating condition, performance of PEMFC is reduced (18). In acidic environment, BPP corrosion is one of the failures due to nature of its materials properties. To investigate the influences of test conditions on aging mechanism accelerated stress test (AST) is a useful tool. Additionally, imaging methods like SEM and µ-CT can be used for morphology analysis to study the nano- and microstructures of components in ex-situ tests (9, 19, 20). Here, ante- and post-mortem analysis is helpful to understand the degradation mechanism. Due to reaction with sulfuric acid or PA and thermal degradation in LT- or HT-PEMFC conditions, respectively, BPPs can corrode which has effects on the performance (9). Ex-situ techniques should be implemented to provide insight view into the performance and degradation of key components like BPP under varied operating conditions (21).

Therefore, this study focuses on the electrochemical degradation of commercial BPPs for use in LT- or HT-PEMFC due to different potentiostatic conditions in an electrochemical three-electrode cell setup. Furthermore, imaging methods like SEM, confocal microscopy and µ-CT were used to investigate the surface area changes after the electrochemical treatments.

Experimental

BPP materials

The investigated BPPs contain carbon, PVDF or PPS as polymer for LT- or HT-PEMFC application, respectively and conductive filler (Eisenhuth GmbH & Co. KG, Germany). Three different LT- and HT-materials were provided for analysis and named with LT01, LT02, LT03, HT04, HT05 and HT06. Because the detailed compounding is proprietary data of the manufacturer no more details can be given. For the three-electrode cell setup BPP with a diameter of ~16 mm and thickness of ~3 mm was used. Before experimental measurements BPPs were cleaned in deionized water.

Corrosion methods: chemical and electrochemical aging

The electrochemical measurements were carried out in a three-electrode setup which represents a half-cell setup inside a Faraday cage. A potentiostat/galvanostat (Solartron Analytical Modulab, UK) was used with a BPP as working electrode (WE) with an active

area of 1 cm^2, a reversible hydrogen electrode (RHE) as reference electrode and graphite as counter electrode (CE). Figure 1 shows the used setup. Before each measurement the electrolyte was purged with N_2 for 10 minutes, during the measurement N_2 was placed above the electrolyte. The electrochemical aging was performed by applying potentiostatic conditions such as open circuit (OCP), anodic (AP, 0.1 V) or cathodic potential (CP, 0.8 V) for six hours. Information about electrochemical stability of BPPs will be given by OCP over time (22). The AP and CP are considered as simulation of the PEM fuel cell anode and cathode environments (17).

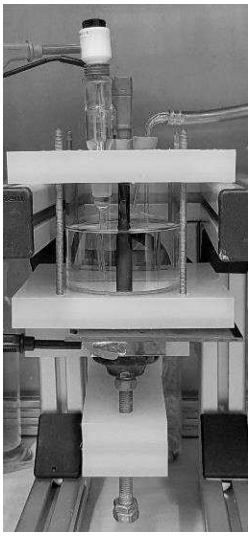

Figure 1. Photo of the used three-electrode set-up.

Procedure for LT-BPP materials. The LT-BPP materials were analyzed by CV in 0.5 M H_2SO_4 (sulfuric acid 96 %, Ultrapur, Merck KGaA). The potential range from 0 to 1.2 V_{RHE} with scan rate of 20 mV s^{-1} at room temperature was used. The second cycle was plotted and compared with the second cycle of the CV after the electrochemical aging of LT-BPP.

Additionally, two measurements with harsher conditions were done to analyze the electrochemical stability of the LT-BPP material LT02. One measurement is applying potentiostatic condition of 1.5 V_{RHE} for 6 h. To investigate the stability with the time, CV with the potential range between 0 and 1.2 V_{RHE} were recorded after defined time of holding. Secondly, an AST was performed based on the cycling of the potential range between 0.6 and 1.5 V_{RHE} with a scan rate of 500 mV s^{-1}. A CV with the potential range between 0 and 1.2 V_{RHE} was recorded every 500 cycles to investigate the stability during the cycling process.

Procedure for HT-BPP materials. The HT-BPP materials were analyzed by CV in concentrated (~14.6 M) phosphoric acid (ortho-phosphoric acid 85 % Suprapur®, VWR International GmbH). The potential range from 0 to 1.2 V_{RHE} with scan rate of 20 mV s^{-1} at room temperature was used. After recording the CV, the HT-BPPs were chemically aged by immersing samples in conc. PA at 160 °C to achieve the operating temperature of HT-PEM fuel cells. After 100 h the aged BPPs were removed from PA solution and electrochemical analysis was continued with recording CV to identify the differences of BPP pristine and after being immersed into 160 °C PA for 100 h. Afterwards the

electrochemical aging was performed. The second cycles of the CV pristine, after 100 h in 160 °C conc. PA and after electrochemical aging were compared.

Imaging methods

For investigation of surface area changes, confocal microscopy (Neox Plμ, Sensofar) was used before and after corrosion tests. The samples were scanned with 20 x magnifications, z-scan of 50 μm and an area of around 600 x 500 μm^2 by using the software SensoScan. 2D images allow comparison of the different materials and investigate the effect of electrolyte and potential conditions on the material. Defects like holes or cracks before and after storage can be determined. To identify the changes on the surface area, scanning electron microscopy (SEM, Neon 40 EsB, Zeiss) measurements were performed with 15-20 kV acceleration voltage.

Additionally, the pristine samples of LT- and HT-materials have been investigated by micro-computed tomography (μ-CT, Skyscan 1172, Bruker). Samples were measured at 80 kV acceleration voltage and 100 μA current of the X-ray source. Reconstruction of all BPP samples was performed using the program NRecon (Bruker) by applying identical parameters for each reconstruction and visualization (CTVox, Bruker) process.

Acid uptake

For investigation of acid uptake of LT-materials under harsher conditions a titrator (TA 20 plus, SI Analytics) was used. Therefore, the samples were stirred for 30 minutes in water to wash out acid. The solutions were titrated with 0.01 mol/l sodium hydroxide and the amount of acid determined by evaluation of the received titration curve.

Results and Discussion

Electrochemical stability of LT-BPP

CV pristine. The CV pristine of the three different LT-BPP materials LT01, LT02 and LT03 are shown in Figure 2. The CVs hardly differ from each other, which suggest that the stability of the materials is similar. The pseudo-capacitance quinone/hydroquinone redox peaks (carbonyl and hydroxyl groups) are detected around 0.6 – 0.7 V_{RHE}, which is in good agreement with literature (23-26).

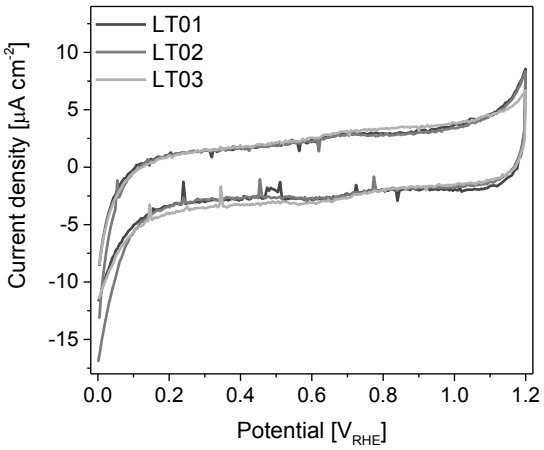

Figure 2. CVs of the three different LT-BPP materials LT01, LT02 and LT03 in 0.5 M H_2SO_4 at room temperature with a scan rate of 20 mV s^{-1}.

CV after potentiostatic treatment. Each potentiostatic treatment was carried out with a pristine sample of LT-BPP material. The corresponding CVs pristine and after the respective potentiostatic treatment (OCP, AP or CP) are shown in Figure 3. The CV pristine of LT-BPP material (LT01, LT02 or LT03) differ only slightly so that the material sample is composed homogeneously, and the different measurements are comparable with each other. After each of the three potentiostatic measurements, the current density increases slightly, mainly in the range of 0.6 and 0.7 V. The amount of the redox couple quinone/hydroquinone is an indication for the degree of surface oxidation of the BPP (27). An increase of the double layer capacitance after potentiostatic treatment might indicate a more wetted surface area due to oxidation and higher hydrophilicity of the BPP (28-30). Also an increasing roughness of the surface area can lead to higher current densities by more pores and penetration of electrolyte into the BPP. Additionally, the CV curves are tilted. This could be attributed to higher resistances due to less oxygen functional groups on the surface (28). Since the influence of the potentiostatic treatment (OCP, AP, CP) on the samples is almost identical, there is no significant influence on the current density and thus the stability of the three different LT-BPP materials.

The OCP measurements over time of the investigated LT-BPP materials are shown in Figure 4a). After one to two hours, all materials reach almost a plateau at different potentials. With LT01 and LT03 a plateau is reached at 719 and 726 mV and with LT02 around 710 mV. While the plateau is almost stable for LT02, the OCP decreases for LT01 or increases for LT03 by 20 mV within the hours two and six. A steady and uniform behavior of OCP over time is an indication of good stability of the material (31). In addition positive and stable values are associated with a high stability and low tendency to corrosion of the material (22). A correlation between content of synthetic graphite and carbon black with the OCP behavior is shown in literature (17). Furthermore, the OCP value can give information about the stability of the BPP. The higher the value, the more stable and corrosion-resistant is the BPP (22).

The current density over time during AP and CP for 6 h of LT01, LT02 and LT03 are shown in Figure 4b) and c), respectively. The noisy behavior could be a result of gas

evolution during the experiment. All LT-BPP materials reach a current density plateau at around -0.25 µA cm^{-2} during AP and at around 0 µA cm^{-2} during CP, respectively.

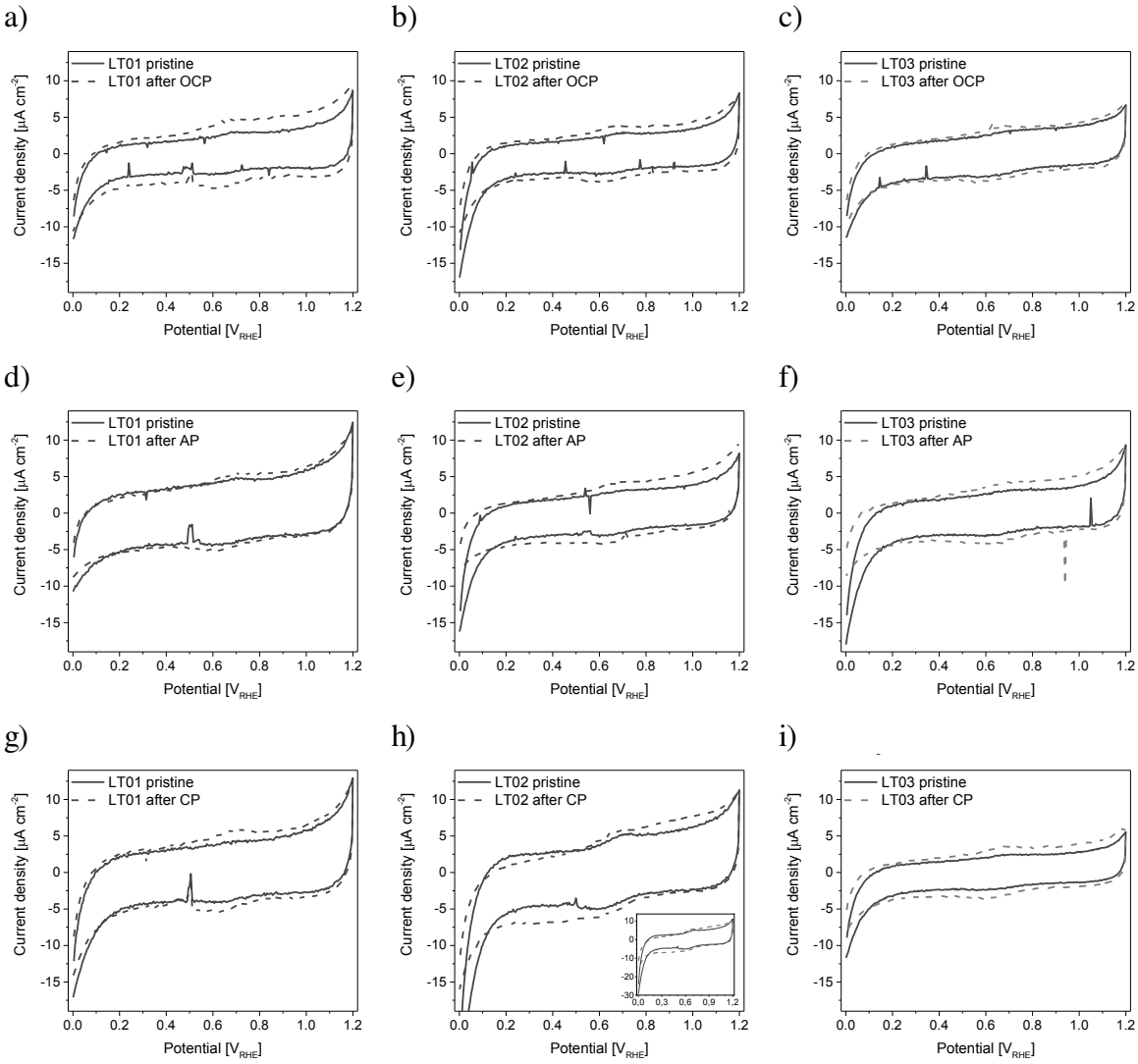

Figure 3. CVs of BPP LT01 (a, d, g), LT02 (b, e, h) and LT03 (c, f, i) in 0.5 M H_2SO_4 at room temperature with a scan rate of 20 mV s^{-1} pristine and after OCP (a, b, c), AP = 0.1 V_{RHE} (d, e, f) and CP = 0.8 V_{RHE} (g, h, i) for 6 h.

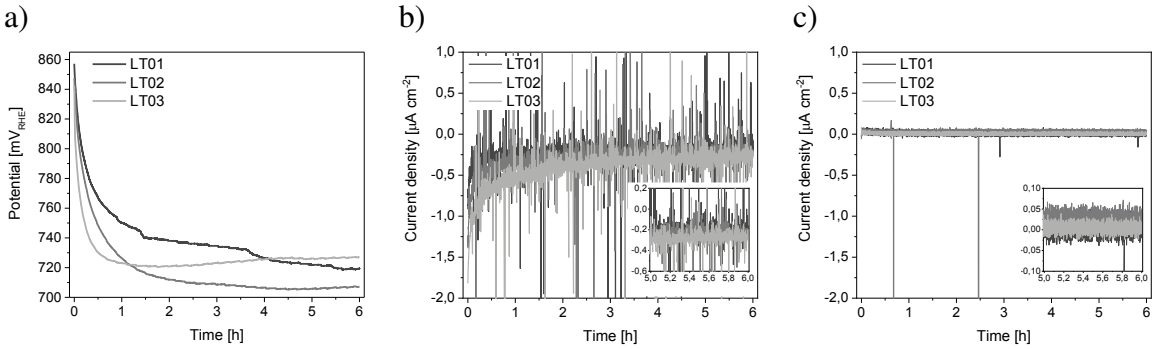

Figure 4: OCP (a), current density over time during AP (b) and CP (c) for 6 h of LT01, LT02 and LT03 in 0.5 M H_2SO_4 at room temperature.

Potentiostatic treatment of 1.5 V for 6 h. To investigate the stability of the LT-BPP material the sample LT02 was exposed to harsher potentiostatic conditions of 1.5 V_{RHE} for six hours. This potential was chosen to potential cause carbon corrosion and to check the stability of the sample under harsher condition. Figure 5a) shows CVs after defined holding times of 1.5 V_{RHE}. After two minutes the double layer capacitance has increased and the quinone/hydroquinone redox peak is much more pronounced. This indicates carbon corrosion. After that, the corrosion takes place to a lesser extent, which is shown by the slighter increase in the double layer capacitance.

The current density of LT02 at a potential of 1.5 V is shown in Figure 5b). The high deviation arises from the respective start of the measurement. However, it can be seen from the graph that the current density approaches the value of 0.5 µA cm^{-2} after 1 h. A constant current density indicates stability of the material. This is confirmed by the slight increase in the double layer in the CV.

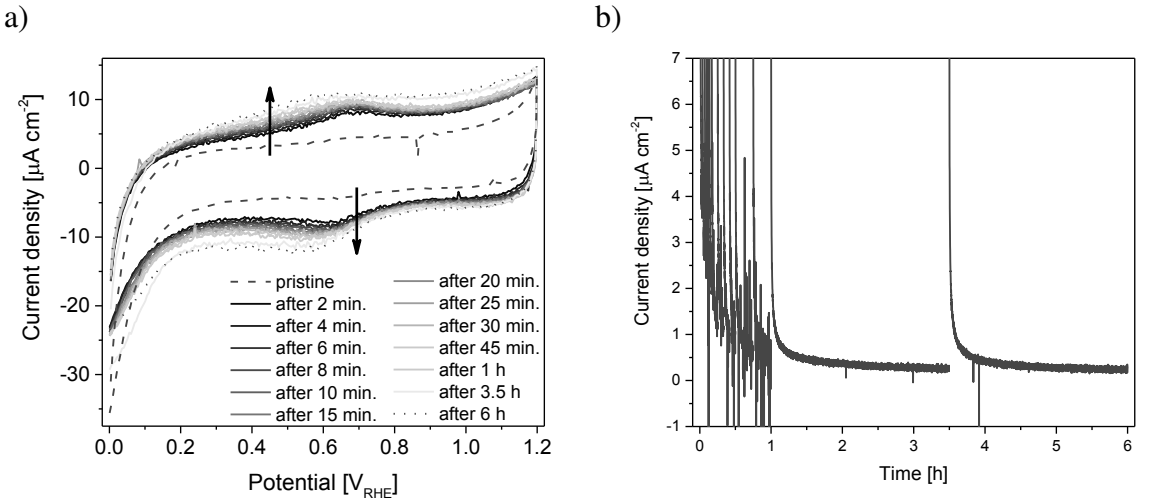

Figure 5: CVs of LT02 in 0.5 M H_2SO_4 at room temperature with a scan rate of 20 mV s^{-1} pristine and after defined time (a) and current density (b) during 1.5 V_{RHE} for 6 h.

Potentiodynamic treatment by AST. Another method to examine the stability of the BPP is the AST. The protocol simulating start-up/shutdown conditions by potential

cycling in the range of 0.6 to 1.5 V_{RHE} for a total of 5000 cycles (32, 33). Figure 6a) shows every 500th cycle with a scan rate of 500 mV s^{-1} of the applied AST to visualize the AST with number of cycles. The corresponding CV with a scan rate of 20 mV s^{-1} after every 500th cycle of AST is shown in Figure 6b) to present the change in the quinone/hydroquinone redox peak with AST cycle. After 500th cycle of AST the current density of the CV has increased sharply and continues to increase slightly with number of cycles. The behavior of cycling procedure observed similar results, but more or less stable values in comparison to the steady state conditions over 6 hours at high potentials of 1.5 V.

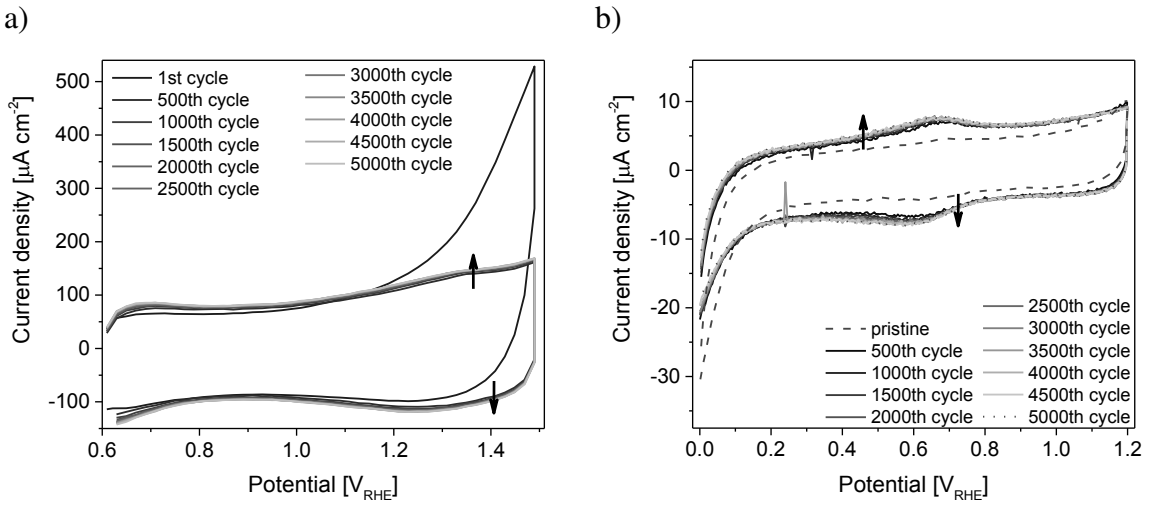

Figure 6: CVs of LT02 in 0.5 M H_2SO_4 at room temperature with a scan rate of 500 mV s^{-1} every 500th cycle of AST (a) and CV pristine and every 500th cycle with a scan rate of 20 mV s^{-1} (b).

Electrochemical stability of HT-BPP

CV pristine. Figure 7 shows the CV pristine of the three different HT-BPP materials HT04, HT05 and HT06. The three HT-BPP pristine materials behave differently. The highest current density is detected with HT06, whereas the lowest current density is detected with HT05. Nevertheless, for all materials the curve shape is typical with quinone/hydroquinone redox peaks detected around 0.6 – 0.7 V_{RHE}, which is in good agreement with literature (23).

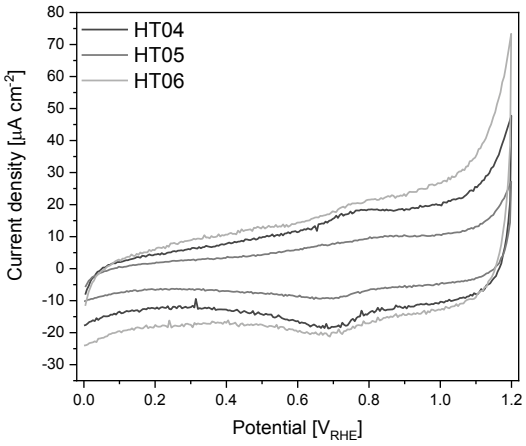

Figure 7. CVs of the three different HT-BPP materials HT04, HT05 and HT06 in conc. PA at room temperature with a scan rate of 20 mV s^{-1}.

CV after chemical aging and potentiostatic treatment. Similar to the LT-BPP materials, each potentiostatic treatment (OCP, AP, CP) was carried out with a pristine sample of HT-BPP material. The CVs pristine and after the applied potentiostatic treatment (OCP, AP or CP) are shown in Figure 8. After each of the three potentiostatic measurements, the current density increases slightly and mainly in the range of 0.6 and 0.7 V, the peak for the redox couple quinone/hydroquinone due to surface oxidation and thus degradation of composite material. This is already discussed above for the LT-BPP material and also affects the HT-BPP material. Since the influence of the potentiostatic treatment on the samples is almost identical, there is no significant influence on the current density and thus the stability of the three different HT-BPP materials.

The OCP over time of all three HT-BPP materials is shown in Figure 9a). The OCP value decreased over the six hours and did not reach a plateau. This means that the material is not stable even after 6 hours. With HT05 and HT06 almost the same value of 709 and 712 mV and with HT04 the value of 767 mV after six hours is reached.

The current density over time during AP and CP for 6 h of HT04, HT05 and HT06 are shown in Figure 9b) and c), respectively. All three HT-BPP materials reach a current density plateau at around -0.3 µA cm^{-2} during AP and at around 0 µA cm^{-2} during CP, respectively. A constant current density indicates stability of the material.

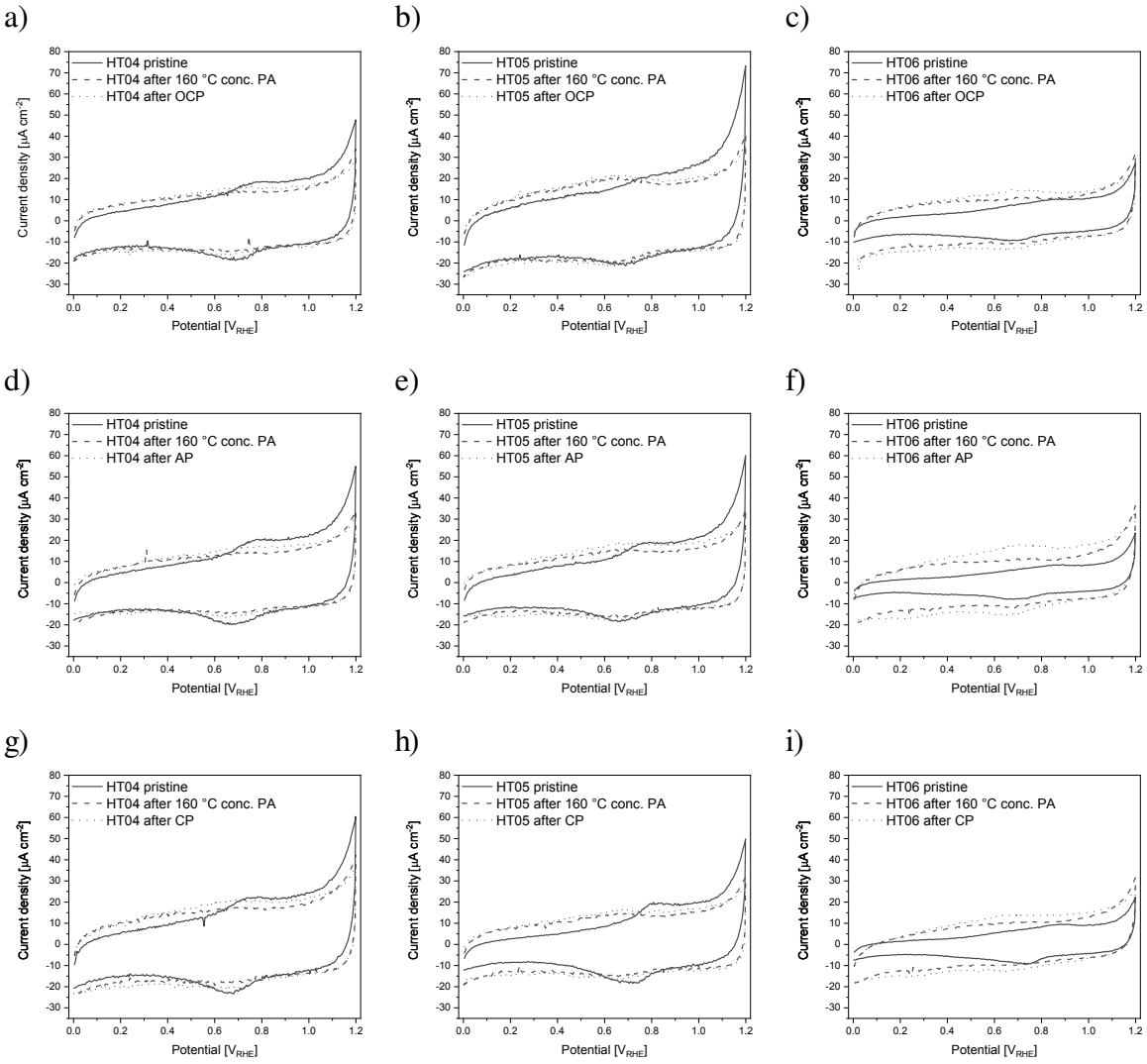

Figure 8. CVs of BPP HT04 (a, d, g), HT05 (b, e, h) and HT06 (c, f, i) in conc. PA at room temperature with a scan rate of 20 mV s^{-1} pristine and after holding OCP (a, b, c), AP = 0.1 V_{RHE} (d, e, f) and CP = 0.8 V_{RHE} (g, h, i) for 6 h.

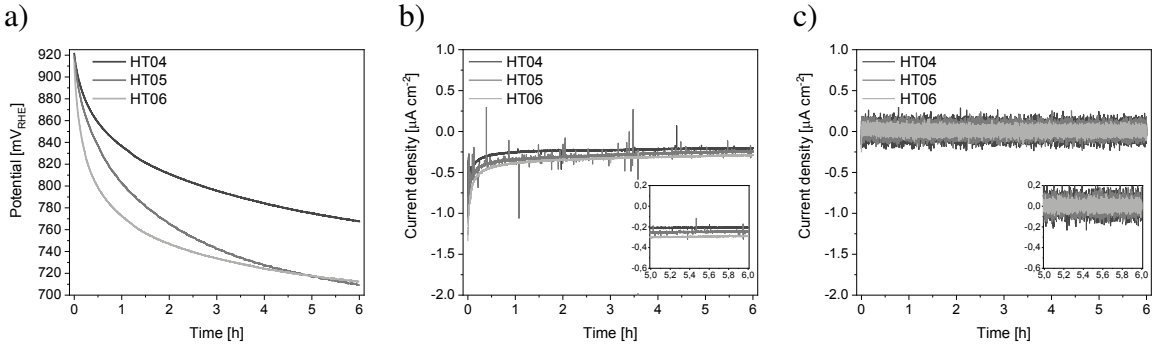

Figure 9: OCP (a), current density over time during AP = 0.1 V_{RHE} (b) and CP = 0.8 V_{RHE} (c) for 6 h of HT04, HT05 and HT06 in conc. PA at room temperature.

Imaging methods

The LT- and HT-BPP samples were analyzed before and after the electrochemical treatment with imaging methods like confocal microscopy, SEM and µ-CT in order to investigate the effect of the electrochemical treatment on the morphology of the BPP. For LT- and HT-BPP the pristine sample shows a homogeneous surface detected by confocal microscopy as well as SEM (Figure 10). There is no huge difference observed between LT- and HT-BPP or between the LT- or HT-BPP themselves. Same behavior is detected for bulk material by µ-CT. Additionally, confocal microscopy measurements were performed after the treatment. No significant differences in morphology were found in any (chemical or) electrochemical method compared to the pristine samples. Results are not shown here. With the used imaging method it was not possible to clearly show a correlation between the morphology and the different potentiostatic methods. One reason could be that the effect of corrosion methods is less aggressive for significant changes in the surface or bulk material. Further explanations could be that the time of experiment is too short to cause changes or possible surface changes are not detectable with the applied methods. Additional methods with a higher sensitivity towards surface changes have to be used in future analysis.

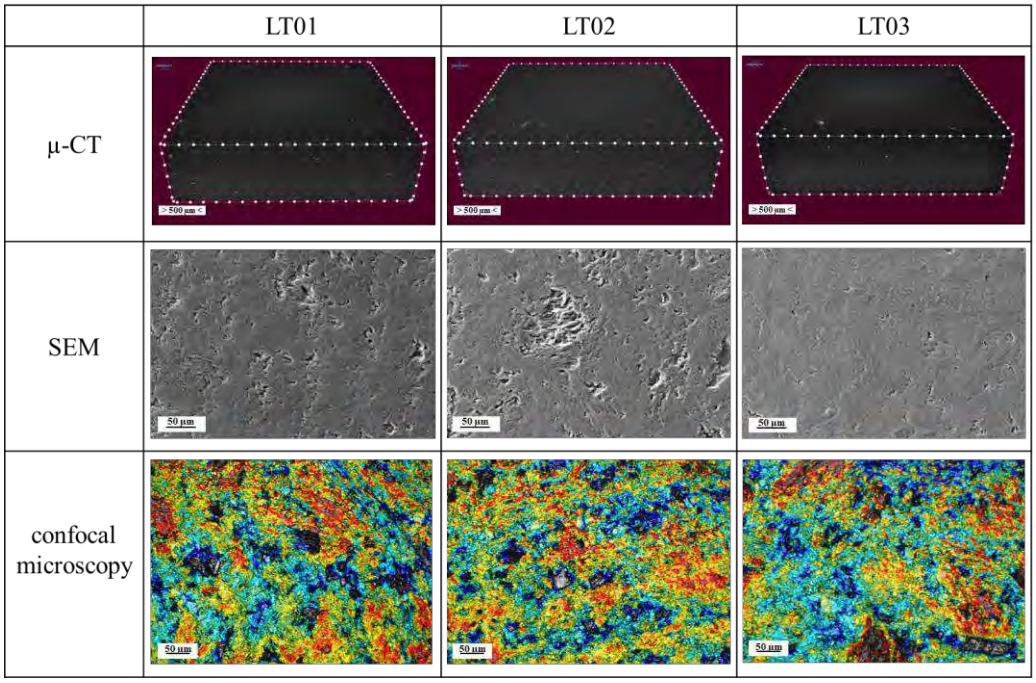

Figure 10: µ-CT, SEM and confocal microscopy images of the three different pristine LT-BPP materials.

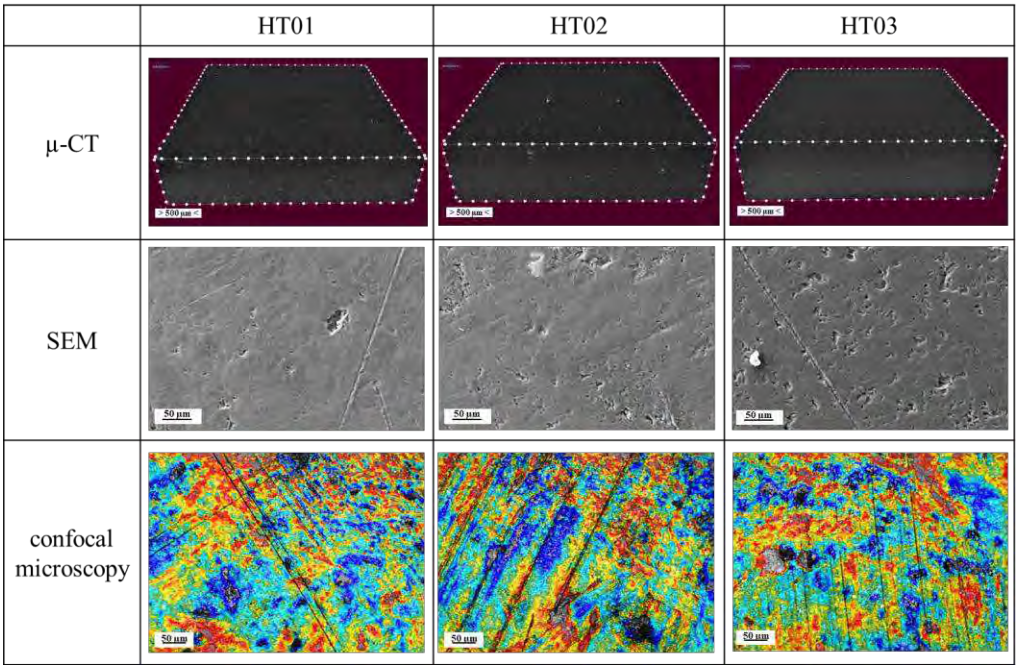

Figure 11: µ-CT, SEM and confocal microscopy images of the three different pristine HT-BPP materials.

Acid uptake

Regarding possible higher acid uptake at harsher conditions, the LT02 material were analyzed by titration after test procedure at 1.5 V and cycling in the range of 0.6 to 1.5 V. The acid uptake for potentiostatic treatment of 1.5 V for 6 hours and potentiodynamic treatment by AST is around 0.02 and 0.03 mg/g, respectively. Slightly higher impact of potential cycling is indicating, but nevertheless, acid update is negligible in this case. Therefore, more results are not shown here.

Conclusion

Different graphite based BPP materials for use in LT- or HT-PEMFC were electrochemical treated to investigate the stability of the BPP. The electrochemical treatment was performed by applying potentiostatic conditions such as open circuit (OCP), anodic (AP, 0.1 V) or cathodic potential (CP, 0.8 V) for six hours. To investigate the stability of BPP for use in HT- and LT-PEMFC the treatments were done in conc. PA or diluted sulfuric acid, respectively. The CV before and after potentiostatic treatment were compared to visualize the effect of treatment on the BPP.

In CVs of all three different pristine LT-BPP no significant differences can be detected, which means the stability is almost the same. After potentiostatic treatment (OCP, AP or CP) the double layer capacitance slightly increased, but with no difference between OCP, AP or CP. The OCP value over time for all three LT-BPP is stable after an initial decrease. Under harsher conditions like potentiostatic treatment of 1.5 V_{RHE} or the potentiodynamic treatment like AST the double layer capacitance increases more sharply

in comparison to CV pristine, which indicates carbon corrosion. After strong initial corrosion the double layer capacitance increased slightly over time.

The double layer capacitance in the CV of the HT-BPP materials is different. The highest double layer capacitance was recorded with HT06 and the lowest with HT05. Therefore, HT05 show the highest stability. The double layer capacitance increases slightly after every potentiostatic treatment (OCP, AP or CP) with no difference between the treatments. The value for OCP over time is the highest for HT04 and the lowest for HT05 but for no HT-BPP material stable after 6 h.

The work showed that there is barely any influence of the three different potentiostatic treatments OCP, AP and CP on the LT- or HT-BPP materials. After harsher conditions such as holding the potential 1.5 V_{RHE} or AST, a difference in the CV compared to the CV pristine is visible on the basis of the double layer capacitance. This could not be proven by the imaging methods, since no difference could be seen here before and after the different treatments. For this reason, further investigations in ex-situ methods with harsher conditions have to be done.

Acknowledgements

The authors would like to thank the Federal Ministry of Transport and Digital Infrastructure for financial support within the project InProPlate (reference number 03B11008B/2). Nina Bengen and Shirin Karaman are acknowledged for help with confocal microscope and titration measurements.

References

1. R. E. Rosli, A. B. Sulong, W. R. W. Daud, M. A. Zulkifley, T. Husaini, M. I. Rosli, E. H. Majlan and M. A. Haque, *Int. J. Hydrogen Energy*, **42**, 9293 (2017).
2. X. Cheng, Z. Shi, N. Glass, L. Zhang, J. Zhang, D. Song, Z.-S. Liu, H. Wang and J. Shen, *J. Power Sources*, **165**, 739 (2007).
3. S. Simon Araya, I. F. Grigoras, F. Zhou, S. J. Andreasen and S. K. Kær, *Int. J. Hydrogen Energy*, **39**, 18343 (2014).
4. R. Haider, Y. Wen, Z.-F. Ma, D. P. Wilkinson, L. Zhang, X. Yuan, S. Song and J. Zhang, *Chem. Soc. Rev.*, **50**, 1138 (2021).
5. A. Chandan, M. Hattenberger, A. El-Kharouf, S. Du, A. Dhir, V. Self, B. G. Pollet, A. Ingram and W. Bujalski, *J. Power Sources*, **231**, 264 (2013).
6. A. Hermann, T. Chaudhuri and P. Spagnol, *Int. J. Hydrogen Energy*, **30**, 1297 (2005).
7. R. A. Antunes, M. C. L. Oliveira, G. Ett and V. Ett, *Int. J. Hydrogen Energy*, **35**, 3632 (2010).
8. E. Quartarone, S. Angioni and P. Mustarelli, *Materials*, **10**, 687 (2017).
9. C. Hartnig and T. J. Schmidt, *Electrochim. Acta*, **56**, 4237 (2011).
10. P. Alnegren, J. G. Grolig, J. Ekberg, G. Göransson and J. E. Svensson, *Fuel Cells*, **16**, 39 (2016).
11. D. Lee, J. W. Lim and D. G. Lee, *Compos. Struct.*, **167**, 144 (2017).
12. A.-R. Kim, H.-M. Jung and S. Um, *Energy*, **66**, 50 (2014).

13. P. Schneider, C. Sadeler, A.-C. Scherzer, N. Zamel and D. Gerteisen, *J. Electrochem. Soc.*, **166**, F322 (2019).
14. D. Froning, J. Yu, U. Reimer and W. Lehnert, *Applied Sciences*, **8**, 2536 (2018).
15. S. R. Dhakate, R. B. Mathur, S. Sharma, M. Borah and T. L. Dhami, *Energy & Fuels*, **23**, 934 (2009).
16. R. A. Antunes, M. C. L. de Oliveira, G. Ett and V. Ett, *J. Power Sources*, **196**, 2945 (2011).
17. M. C. Lopes de Oliveira, I. J. Sayeg, G. Ett and R. A. Antunes, *Int. J. Hydrogen Energy*, **39**, 16405 (2014).
18. FSEC, Procedure for Performing PEM Single Cell Testing, in, US Department of Energy, Arlington, Virginia (2009).
19. V. Weissbecker, U. Reimer, K. Wippermann and W. Lehnert, *ECS Trans.*, **58**, 693 (2013).
20. J. H. Liao, Q. F. Li, H. C. Rudbeck, J. O. Jensen, A. Chromik, N. J. Bjerrum, J. Kerres and W. Xing, *Fuel Cells*, **11**, 745 (2011).
21. X. X. Wang, M. T. Swihart and G. Wu, *Nat. Catal.*, **2**, 578 (2019).
22. G. Bolat, D. Mareci, R. Chelariu, J. Izquierdo, S. González and R. M. Souto, *Electrochim. Acta*, **113**, 470 (2013).
23. K. Kinoshita and J. A. S. Bett, *Carbon*, **11**, 403 (1973).
24. B. Satola, L. Komsiyska and G. Wittstock, *J. Electrochem. Soc.*, **164**, A2566 (2017).
25. H.-S. Choo, T. Kinumoto, S.-K. Jeong, Y. Iriyama, T. Abe and Z. Ogumi, *J. Electrochem. Soc.*, **154**, B1017 (2007).
26. B. Satola, C. N. Kirchner, L. Komsiyska and G. Wittstock, *J. Electrochem. Soc.*, **163**, A2318 (2016).
27. B. Satola, L. Komsiyska and G. Wittstock, *J. Electrochem. Soc.*, **165**, A963 (2018).
28. A. Jaiswal and S. C. Chalasani, *J. Energy Storage*, **1**, 15 (2015).
29. M.-A. Goulet, M. Skyllas-Kazacos and E. Kjeang, *Carbon*, **101**, 390 (2016).
30. J. Chmiola, G. Yushin, R. K. Dash, E. N. Hoffman, J. E. Fischer, M. W. Barsoum and Y. Gogotsi, *Electrochemical and Solid-State Letters*, **8**, A357 (2005).
31. L.-N. Wang and J.-L. Luo, *Appl. Surf. Sci.*, **258**, 4830 (2012).
32. C. A. Reiser, L. Bregoli, T. W. Patterson, J. S. Yi, J. D. Yang, M. L. Perry and T. D. Jarvi, *Electrochemical and Solid-State Letters*, **8**, A273 (2005).
33. S. Alinejad, M. Inaba, J. Schröder, J. Du, J. Quinson, A. Zana and M. Arenz, *Journal of Physics: Energy*, **2**, 024003 (2020).

ECS Transactions, 104 (8) 283-292 (2021)
10.1149/10408.0283ecst ©The Electrochemical Society

In-situ Diagnostics of Composite Filament Material Suitable for Bi-Polar Plate Using Additive Manufacturing

D. Alexander IV[a,b], J. T. Pellicotte[b], A. Mejia[b], C. M. Benway[b], C. M. Stewart[b], E. Cole[c], R. Borup[a], T. Rockward[a]

[a] Los Alamos National Laboratory, Los Alamos, New Mexico 87545, USA
[b] Department of Mechanical Engineering, The University of Texas at El Paso, El Paso, Texas 79968, USA
[c] Kansas City National Security Campus, Kansas City, Missouri 64147, USA

Extrusion-based 3D printing processes have the lowest cost for equipment and materials used in Additive Manufacturing (AM). Recently, AM technology has been extended beyond the typical polymer-based parts to include the capability to print metal parts via Bound Metal Deposition (BMD). This technological advancement has, in turn, increased the potential application range of printed components particularly for Polymer Electrolyte Fuel Cells (PEFCs). Although AM offers some design and cost advantages over traditional manufacturing, the post processing must yield acceptable bi-polar plate mechanical properties such as >40MPa for flexural strength and 40% forming elongation. These targets are outlined by the HFTO. The post-processing techniques employed are de-binding, sintering, and heat treating in controlled inert environments. The objective of this study is to investigate the effects of thermal processing parameters on the AM bi-polar plate using a polylactic-acid (PLA)-based metal composite filament via various characterization methods such as thermogravimetric analysis mass spectroscopy, mechanical testing, electrical characterization, and elemental analysis.

Introduction

Proton exchange fuel cells (PEFCs) have an overall efficiency up to 60% compared to 33-35% for conventional combustion-based power plants with virtually no carbon emissions. PEMFCs can operate at low temperature, start quickly, have a high-power density and energy conversion efficiency; and are easily scaled (1). The working principle of the PEMFC converts the chemical energy in hydrogen to electricity, with the only by-products being water and heat. Continuous research efforts are directed toward material development of the components, including hardware, to reduce costs and extend the lifetime of the fuel cell. While low-cost, high volume manufacturing processes will aid in making the fuel cell cost-competitive with conventional technologies, additive manufacturing can be employed to rapidly iterate designs complementing the new materials to reduce costs and improve durability (2-4). There is an under-explored area of research pertaining to bound metal deposited parts and their applicability in engineering applications. This study will investigate the effects of titanium grade 2-PLA composite material and the necessary post-processing to achieve properties suitable for engineering applications. The objectives of this study are to characterize the feasibility of the composite material. The objectives are achieved by thermally processing the composite material and characterizing before and after post-processing using scanning electron microscopy (SEM), x-ray computed tomography (XCT), optical profilometry (OP), and mechanical testing.

Bipolar Plate

The bipolar plate is an important component in the PEMFC functionally and financially. It has vital roles including electron conduction, fluid management, and heat dissipation (5). Crucial factors that determine bipolar plate viability are electrical conductivity, corrosion resistance, chemical stability, thermal conductivity, gas permeability, mechanical strength, formability, and weight. Bipolar plates account for approximately 80% of the total PEMFC weight and 45% of the total cost (6). Metallic bipolar plates reduce weight costs without sacrificing important properties like electrical and thermal conductivity, mechanical properties, machinability, and gas sealability. However, uncoated bipolar plates are susceptible to corrosion in the PEMFC environment and cause membrane degradation due to leaching of the component constituents. For metallic bipolar plates to be effective, the exposed surface must be treated with a protective passivation layer to decrease the affection of the corrosive environment (7). Surface modification techniques include electrodeposition, chemical vapor deposition, and high energy micro-arc alloying (8-21). Common investigated bipolar plate materials are stainless steel, copper, aluminum alloys, nickel alloys, and titanium. Recent interest has been directed toward titanium because of its high corrosion resistance, insoluble corrosion products, strength-to-weight ratio, electrical properties, and formability. Furthermore, titanium is also manageable regarding surface treatments for corrosion resistance enhancements (22-31).

Bound Metal Deposition

AM has proved its worth regarding the ability to change how energy systems are designed and employed. The ability to manufacture complex 3D structures, with bespoke design freedoms including mass customization, topology optimization, and surface texturing offers drastic potential for fuel cell design innovation. The three main established methods for manufacturing bipolar plates are subtractive machining, molding, and stamping. These traditional methods are expensive in low volumes and have greater design limitations compared to AM techniques. The AM methods used for metal-based prints are electron beam melting (EBM), selective laser melting (SLM), binder jetting, direct metal laser sintering (DMLS), and bound metal deposition (BDM). Costly components such as electron beams, vacuums, and lasers increase the price for the EBM, SLM, and DMLS manufacturing methods. However, BMD is accomplished using the material extrusion process, which does not require a laser or electron beam as shown in figure 2 (32, 33). The feedstock is actuated through a resistance heated nozzle whilst precisely controlled in three axes. The flow through the nozzle in controlled as the part layers are built one at a time. BMD is derived from powder injection molding (PIM), where metal powders are mixed into a polymer binder matrix to form the feedstock before injection into a die cavity.

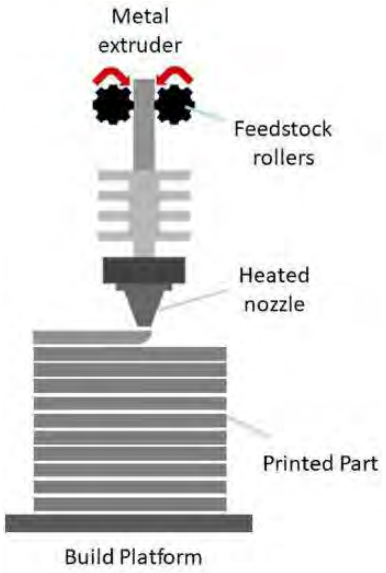

Figure 1. Schematic of the BMD process (32).

The BMD process can use an array of metal powders such as stainless steel, copper, tungsten, chromium, and titanium. The material variety contain wide range of powder size distribution including fine powders.

Post-Processing

Post Processing is defined as any tasks that need to be performed on an as-printed part for enhancement. In this study, post-processing includes support structure removal, debinding, sintering, and heat treatment. The sintering and heat treatment of the bound metal is imperative because this process is the equalizer to obtaining adequate properties of traditionally manufactured components.

Titanium Polylactic Acid

Composite material are combinations of two or more materials with different properties. When combined, they create a specialized material to accomplish advanced tasks. Titanium grade 2 powders are mixed into a polylactic acid (PLA) matrix then extruded and wound on a spool to create the metal-polymer composite feedstock. PLA is a thermoplastic polyester with the backbone formula, $(C_3H_4O_2)_n$, widely used in additive manufacturing. The PLA matrix is leveraged for printability of the titanium powders. The material of interest is commercially pure titanium grade 2, an alpha phase titanium, widely used as an alloy for industrial services because of its moderate strength, excellent corrosion resistance, and formability. Typical applications for titanium grade 2 include, oil and gas components, reaction and pressure vessels, piping systems, heat exchangers, liners, and flue-gas desulphurization systems (28-30).

Materials and Methods

The material used in this study consists of polylactic acid (PLA) and titanium grade 2. The composite feedstock is supplied by The Virtual Foundry where the titanium and PLA

binder content is 76% and 24% respectively. The chemical composition of the titanium grade 2 powder is listed in table 1. The filament was fabricated using an extrusion process and there are no available mechanical properties for the commercial composite.

TABLE I. Chemical Composition of Titanium Grade 2.

Chemical Element	Wt.%
Carbon	0.01%
Hydrogen	0.002%
Iron	0.19%
Nitrogen	0.01%
Oxygen	0.25%
Titanium	Bal.

Equipment

Material characterization was conducted using a ThermoFisher Scientific Quattro Environmental Scanning Electon Microscope (ESEM), EDAX X-ray Fluorescence (XRF), Xradia X-ray Computed Tomography (XCT) system, and Keyence VK-X laser scanning confocal microscope. A NETZSCH thermal analysis system with mass spectrometer (TGA-MS) was used to process the material and analyze the decomposition. Mechanical testing was performed using a Buehler Macromet 3 Hardness tester. The area specific resistance testing was accomplished using an in-house press with gold plates with the voltage drop measured using a Hewlett Packard 34401A multimeter. An Omega DP25-S load cell meter measured the pressure applied by the press. The specimens were additively manufactured using a CreatBot F430 as a 10 mm x 10 mm x 5 mm cube shown in figure 2.

Figure 2. As-printed cubic specimen.

Experimental Method

The composite material filament was characterized using XRF to confirm the metal powders are titanium. SEM, OP, and XTC was utilized to obtain baseline information prior to any thermal processing. SEM illustrated the metal powders in the PLA matrix. OP captured the surface roughness of the metal powder and PLA in addition to the interfaces. XCT showed the cross-sectional uniformity of the metal powder distribution in the PLA matrix.

TGA was employed to characterize the mass loss during debinding and sintering of the metal powders. MS was included to diagnose the decomposition of the evacuating PLA matrix as the metal powders underwent sintering. Post-characterization realized the degree of sintering of the composite material at the surface and through the cross-section in addition to the surface roughness evolution.

Micro-hardness measurements serve as a microprobe of a material's mechanical response. It is known to have good agreement with yield stress and ultimate tensile strength (33). Micro-hardness was used as a measure to qualify the level of sintering. The qualification threshold was based on the Rockwell Hardness-B of ASTM Grade 2 titanium (34).

The area specific resistance determines the through-plane resistance of a material. This is an important parameter because it conveys the ability of the candidate bipolar plate material to conduct electricity with minimal parasitic losses.

Results and Discussion

Pre-Characterization

XRF mapping shown in figure. 3. (a) confirmed the present metal powder as titanium and the distribution across the surface area. The PLA was unable to be directly quantified via XRF because of the energy levels of carbon, hydrogen, and oxygen are below the detectable limits. Lower counts of titanium are associated with the presence of PLA. XCT qualitatively investigated the consistency of the titanium dispersion throughout the PLA from a cross-sectional view. The 50% tomography cross-section represented in figure 3. (b) shows an adequate dispersion of titanium, so the same distribution throughout the composite material can be assumed.

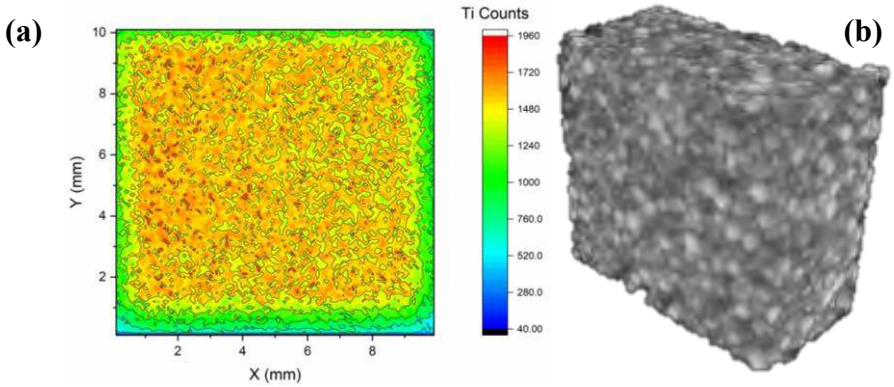

Figure 3. (a) SEM image of composite material with and (b) without the PLA matrix.

The SEM examination illustrated in figure 4. (a) and 4. (b) revealed fine details of the matrix and titanium configuration. Figure 4. (b) displays the metal powders post evacuation of the PLA matrix which ensued between 284°C to 500°C as the thermal profile ramped to 1000°C. This particular thermal profile was used to characterize the thermal degradation of the PLA within the composite and verify the 24% binder content which proved to be true consistently as temperatures went above 1000°C. Results are shown in the next section.

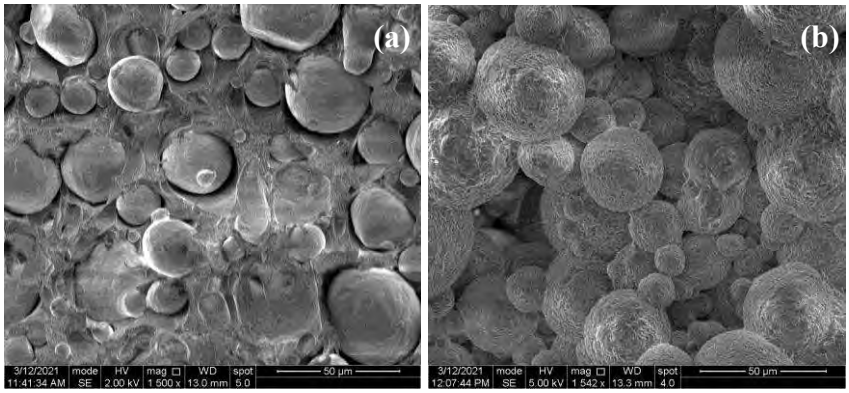

Figure 4. (a) SEM image of composite material with and (b) without the PLA matrix.

Thermal Analysis

Thermal processing at 1400℃ in an argon atmosphere of the specimens showed an average mass reduction of 187.541 mg in addition to the 23.55% mass loss prior to oxidation. It is well established that titanium has a high affinity for oxygen at high temperatures (29) Furthermore, the MS curve in figure 5 showed that PLA decomposed mostly in the form of carbon monoxide represented as the atomic mass of 28.

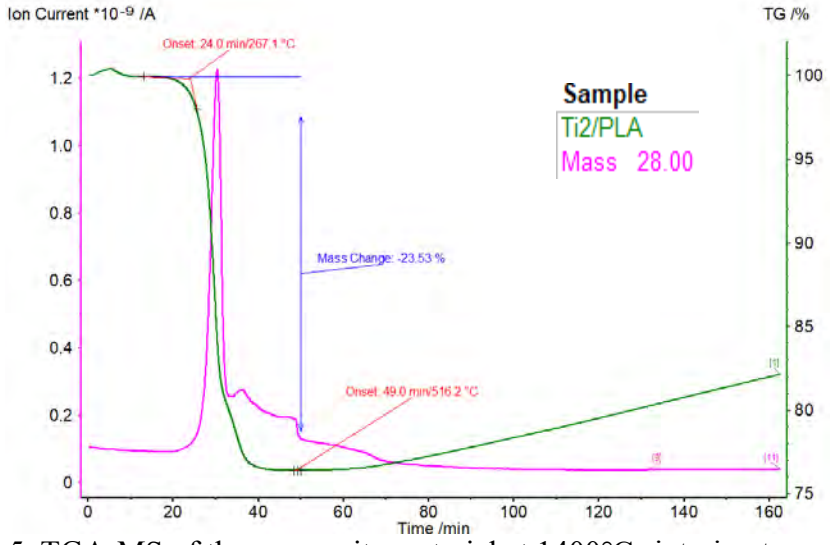

Figure 5. TGA-MS of the composite material at 1400℃ sintering temperature.

XRF mapping showed an increase in titanium spatial proximity and counts meaning there was a reduction in the PLA presence illustrated in figure 6. (a). The mapping information in figure 6. (b) was consistent with the degree of metal powder coalescence shown in the SEM image. The SEM data shows complete metal powder coalescence at the surface in addition to non-uniform porosity.

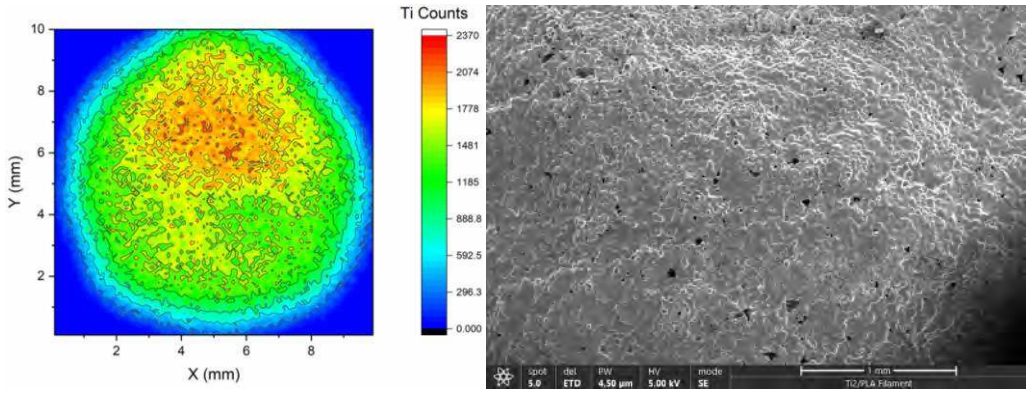

Figure 6. (a) XRF mapping and (b) SEM of the thermally processed cube specimen

Surface roughness of the composite material before and after processing was observed as an effect of the temperature increase. The root-mean-square roughness, R_q, provides 2D deviation height information from the mean surface roughness. R_q decreased from 11.341um to 9.070 um. The root-mean-square height, S_q provides 3D areal surface roughness information. S_q decreased from 14.074 um to 6.284 um. Figure 7 shows the optical and topography comparisons of the specimen before and after processing.

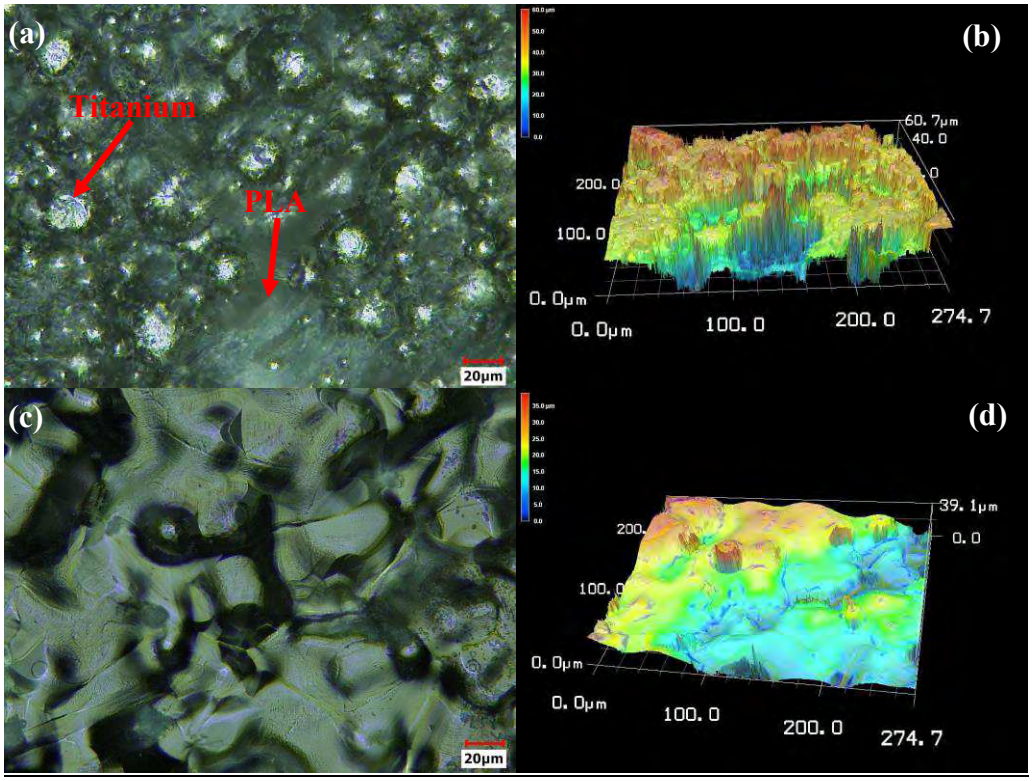

Figure 7. (a) Optical and (b) topography of as-printed cube (c) optical and (d) topography of the thermally processed cube.

Mechanical Testing

Micro-hardness of the processed sample yielded favorable results shown in table 2. The as-printed HRB yielded a minimum 52.9 and a maximum 56.3 value, while the processed HRB yielded a minimum 44.5 and a maximum 77.8. The averages for the as-printed and processed was 55.025 and 61.875 with a standard deviation of 1.5 and 14.62 respectively.

The values for the processed sample were higher because of congregation and proper sintering of the metal powder which increases metal on metal contact. In the as-printed sample there is a 24% presence of PLA that has contact with the metal powders and the hardness value is predicated on metal to PLA contact. The processed values are lower than the wrought hardness because of the at hand porosity which decreases the bulk density. The well-dispersed porosity is also the culprit of the large deviation for the processed sample.

TABLE II. Rockwell Hardness-B of cube specimen before and after thermal processing.

Wrought Ti-Grade 2	As-Printed	Processed
80	52.9	69.1
-	55.8	56.1
-	56.3	44.5
-	55.1	77.8

Material Characterization

The area specific resistance did not achieve a favorable outcome in comparison to the target value of <0.01 ohm cm^2. The value for the processed sample was 0.1 ohm cm^2. This order of magnitude increase in resistance was attributed to the non-uniform contact surface caused by the unbalanced debinding and sintering. The apparent porosity further decreases the amount of contact points with the gold plates which increases the resistance.

Conclusion

Bound metal deposition is an attractive low-cost method to manufacturing parts for engineering applications. Effective post-processing to achieve sufficient properties is the greatest barrier to this AM method being industry certified. Complete sintering features and satisfactory hardness values are encouraging parameters to progress toward tensile and flexural testing in future studies. These tests satisfy the mechanical based properties on the 2030 Department of Energy targets. Future works also include modifying partial pressures of the inert gas to reduce the porosity found in the sintered sample. This will take place prior to the tensile and flexural testing as it will have apparent effects on the mechanical properties.

Acknowledgments

This work was performed under the US Department of Energy's National Nuclear Security Administration (NNSA) Minority Serving Institution Partnership Program, Los Alamos National Laboratory African American Partnership Program, and Partnership for Research Education Consortium in Ceramics and Polymers. The authors wish to acknowledge the NNSA management team David Canty, Jennifer Kline, and Julie Spyres and the Hydrogen Fuel Cell Technology Office

References

1. https://www.energy.gov/sites/prod/files/2015/11/f27/fcto_fuel_cells_fact_sheet.pdf
2. X. Y. Tai, A. Zhakeyev, H. Wang, K. Jiao, H. Zhang and J. Xuan, Fuel Cells, (2019).
3. H. Tsuchiya and O. Kobayashi, International Journal of Hydrogen Energy, **29**, 985-990 (2004).
4. V. Mehta and J. Cooper, Journal of Power Sources, **114**, 32-53 (2003).
5. Y. Wang, D. Diaz, K. S. Chen, Z. Wang and X. C. Adroher, Materials Today, (2020).
6. J. Scholta, B. Rohland, V. Trapp and U. Focken, Journal of Power Sources, **84**, 153-286 (1999).
7. R. Makkus, A. Janssen, F. Bruijin and R. Mallant, Journal of Power Sources, **86**, 274-282, (2000).
8. F. Madadi, A. Rezaeian, H. Edris and M. Zhiani, Materials Chemistry and Physics, (2019).
9. S. Lee, C. Huang and Y. Chen, Journal of Materials Processing, **6**, 688-693 (2003).
10. S. Wang, J. Peng and W. Lui, Journal of Power Sources, **162**, 486-491 (2006).
11. L. Wang, Y. Tao, Z. Zhang, Y. Wang, Q. Feng, H. Wang and H. Li, International Journal of Hydrogen Energy, **44**, 4940-4950 (2019).
12. Z. Sadeghian, M. R. Hadidi, D. Salehzadeh and A. Nemati, International Journal of Hydrogen Energy, **45**, 15380-15389 (2020).
13. J. Shi, P. Zhang, Y. Han, H. Wang, X. Wang, Y. Yu and J. Sun, International Journal of Hydrogen Energy, **45**, 10050-10058 (2020).
14. Ingle, V. S. Raja, J. Rangarajan and P. Mishra, Fuel Cells, (2019).
15. Tudose, C. Florin, P. Dorneanu, B. Stefan, L. Rusen, F. Iacomi, E. Koudoumas and M. Suchea, in Functional Nanostructured Interfaces for Environmental and Biomedical Applications, Elsevier, (2019).
16. J. Wang, L. Min, F. Fang, W. Zhang and Y. Wang, International Journal of Hydrogen Energy, **44**, 16909-16917 (2019).
17. S. Wang, J. Peng, W. Lui and J. Zhang, **162**, 486-491 Journal of Power Sources, (2006).
18. P. Manso, F. F. Marzo, X. Garicano, C. Alegre, A. Lozano and F. Barreras, International Journal of Hydrogen Energy, **45**, 20679-30691 (2020).
19. M. Tahir, M. Rafique, M. Rafique, T. Nawaz, M. Rizwan and M. Tanveer, in Micro and Nano Technologies, Amsterdam, Elsevier, (2020).
20. R. He, J. Jiang, R. F. Wang, Y. Yue, Y. Chen and T. J. Pan, Corrosion Science, (2020).
21. C. Changjun, W. Maocai, L. Yiming, W. Dongsheng and J. Ren, Journal of Material Processing Technology, **198**, 275-280 (2008).
22. H. Tawfik, Y. Hung and D. Mahajan, Journal of Power Sources, **163**, 755-767 (2007).

23. Hermann, T. Chaudhuri and P. Spagnol, International Journal of Hydrogen Energy, **30**, 1297-1302 (2005).
24. P. Zhang, C. Hao, Y. Han, F. Du, H. Wang, X. Wang and J. Sun, Surface and Coatings Technology, (2020).
25. N. Asri, T. Husaini, A. Sulong, E. Maijlan and W. Daud, International Journal of Hydrogen Energy, **42**, 9135-9148 (2017).
26. P. Gao, Z. Xie, X. Wu, C. Ouyang, T. Lei, P. Yang, C. Liu, J. Wang, T. Ouyang and Q. Huang, International Journal of Hydrogen Energy, **43**, 20947-20958 (2018).
27. S. Dubent and A. Mazard, International Journal of Hydrogen Energy, **44**, 15622-15633 (2019).
28. G. Lutjering and J. Williams, in Titanium, Berlin, Springer, (2003).
29. M. Donachie, in Titanium: A Technical Guide 2nd Edition, Materials Park, ASM International, (2000).
30. F. H. Froes, "Applications of Titanium," in Titanium Physical Metallurgy Processing and Applications, Materials Park, ASM International, 2015, pp. 353-379.
31. G. Yoganjaneyulu, C. Narayanan and R. Narayanasamy, Journal of Manufacturing Processes, **35**, 197-204 (2018).
32. Bose, C. Schuh, J. Tobia, N. Tuncer, N. Mykulowycz, A. Preston, A. Barbati, B. Kernan, M. Gibson, D. Krause, T. Brzezinski, J. Schroers, R. Fulop, J. Myerberg, M. Sowerbutts, Y. Chiang, A. Hart, E. Sachs, E. Lomeli and A. Lund, International Journal of Refractory Metals and Hard Materials, **73**, 22-28 (2018).
33. G. E. Lucas, in Encyclopedia of Materials: Science and Technology, 2001.
34. http://www.matweb.com/search/DataSheet.aspx?MatGUID=24293fd5831941ec9fa01dce994973c7&ckck=1

Chapter 11

Poster Session

ECS Transactions, 104 (8) 295-305 (2021)
10.1149/10408.0295ecst ©The Electrochemical Society

The Effects of Anode Serpentine Flow Field Structure and Humidity on Performance of PEMFCs

P. Y. Liao[a,b], S. N. Xu[a,b], P. W. Ming[a,b], B. Li[a,b], C. M. Zhang[a,b], D. J. Yang[a,b*]

[a]School of Automotive Studies, Tongji University, Shanghai 201804, China;
[b]New Energy Automotive Engineering Center, Tongji University, Shanghai 201804, China

The flow field is an important place for gas distribution and liquid water discharge, which plays a vital role in improving the performance of proton exchange membrane fuel cell (PEMFC). Liquid flooding is a thorny problem occurring in the flow field frequently. However, the appropriate flow field structure and operating condition can help solve flooding issue. In this paper, the PEMFC performance and the water discharging ability is obtained by variety of experiments in different serpentine flow field structures and relative humidity (including setting as 10%, 30%, 50% and 70%). This study provides a proposal is that using the anode plate with a double serpentine structure and conducted under the humidity condition as 30% can result in perfect water management and achieve the max power density value to 0.898 W/cm^2.

1 Introduction

Hydrogen is one of the promising energy sources as its clean and effective properties. Proton exchange membrane fuel cell (PEMFC) utilizes hydrogen and oxygen to produce electrical energy through electrochemical reactions (1). PEMFC can be applied in wide fields for its high efficiency (2), no pollution (3), low working temperature (4), and high-power density (5). However, the water accumulation would hinder the electrochemical process in catalyst layer (CL) (6). Water transportation generally includes three forms, namely proton drag, concentration diffusion, permeation by pressure deviation. Thus, the flooding phenomenon can be found both on the cathode side and anode side. In addition, as the gas flow rate at the anode side is lower than that of cathode side, the anode without suitable design and management is more likely to be flooded under higher current densities (7).

Bipolar plate is an essential component of a PEMFC, and responsible for transporting gas and liquid water. In addition, the flow fields of the bipolar plate can greatly affect the distribution of two-phases flow, and it will further change the output

properties of the PEMFC (8). Serpentine flow field is one of the typical flow fields as it can facilitate the reactant convection and the mass transfer within a cell (9). However, the serpentine flow field tends to suffer from the liquid water flooding problem due to its long channel (10). Thus, the optimum of the flow field structure is necessary to address the water accumulation issue. Watkins et al (11) proposed using the single serpentine flow field which contains only one continuous channel connecting the inlet and outlet to force the reactant flow to traverse the entire active area of the corresponding electrode thereby eliminating areas of stagnant flow. However, they found that this structure gained large pressure drop and may promote the flooding procedure. Thus, they further put forward to adopt continuous separate flow channels in order to limit the pressure drop (12). In their report, the output power from the cell could be significantly enhanced by using multiple serpentine flow field in cathode side. However, the water management difference of changing the serpentine flow field have not been illustrated clearly. M. R. Esbo et al. (13) compared the pressure, velocity and temperature toward single serpentine and multiple serpentine flow field to expound the effect of serpentine flow field structure on the performance of PEMFC. But they only use the CFD as the illuminating method, so that it lacks of some experimental evidences. Besides, among the operating conditions, relative humidity (RH) has a significant influence on the water volume fraction within a cell and then partly define the output parameters of fuel cell (14,15). Thus, when RH varied, the capability of water removal toward different serpentine flow fields needs further investigation.

In this paper, in-situ segmented cell measuring technique, Computational Fluid Dynamics (CFD) method, and pressure drop tests were used to evaluate the water accumulation of the anode side. Simultaneously, the effects of the serpentine flow field structure modification and different RHs on the PEMFC water management have been explained through these experimental results.

2 Experiments and Method

2.1 Fabrication of Monopolar Plate

The 316L stainless steel was selected as the anode plate substrate material. The flow channel is obtained by etching process. Besides, the metal plate surface is coated with silver to ensure its anti-corrosion and decrease the interface contact resistance between the polar plate and gas diffusion layer (GDL). Graphite plate (SZ-G03H, Jiangsu Shenzhou Carbon Product Co., Ltd.) is used as the cathode plate. The graphite plate is so-called a “standard flow field” with a dimension of 1 mm × 1 mm ×1 mm (rib width channel depth×channel width). And the active area is 25 cm^2 for both two single cells. The structure and parameters of the two types anode plate were exhibited in Table I.

Table I. The structure and parameter of the two types flow field.

Design	Description	Parameters		Schema
Single serpentine	Fluids flow through a continuous path from start to end	Channel length	47 mm	
		Channel width,	0.8 mm	
		Rib width	1.2 mm	
		Inner diameter of bends	1.2 mm	
		External diameter of bends	1.4 mm	
Double serpentine	Fluids flow through two continuous paths from start to end	Channel length	45 mm	
		Channel width	0.8 mm	
		Rib width	1.2 mm	
		Inner diameter of bends	1.2 mm	
		External diameter of bends	1.4 mm	

2.2 Preparation of Single Cell

Commercial membrane electrode assembly (MEA) employed in experiments was provided by Yuqing Power Co., Ltd. The platinum loading is 0.4 mg/cm^2 and 0.1 mg/cm^2 in cathode and anode, respectively. Gore-select® M732.15 were used in the MEA.

2.3 Fluid Mechanics Simulation

The ANSYS FLUENT CFD platform was employed for the steady simulation of hydrogen transport. The steady governing equation was solved by employing the pressure-based solver. Taking into account the gravity effect. The SIMPLE algorithm is adopted to solve the governing equations. The solution is considered to be convergent once the relative error for each dependent variable between two consecutive iterations is less than 1.0×10^{-3}.

2.4 Experimental

The electrochemical test was conducted with a single-cell test station (G20, Greenlight Innovation Co.). The operating condition is listed in Table II. The RHs of the series experiment was set to 10%, 30%, 50% and 70% respectively (The gas inlet temperature is 70 ºC, and tune the DP temperature to achieve the corresponding RH). Before testing, the MEAs should suffer the activation process as (i) Set the

anode/cathode pressure as 130/120 kPa and increased the load current from 0 to a maximum value I_{max} which makes the voltage as low as 0.3 V. Each adding current step at a magnitude is 2.5 A, (ii) operated at I_{max} for 4 h, (iii) reduced load current to 0 A and each reducing step gap is also 2.5 A.

In-situ segmented cell measuring technique was conducted by adding a partition current density plate (RG200, Dalian Rigor New Energy Co., Ltd.) between the anode plate and the current collector plate, in order to detect the regional current density (Figure 1). By presetting resistance and grid on PCB, the fuel cell interior is divided. A high-speed acquisition system based on FPGA is used to synchronously collect the current flow signal of each segmentation. The region of active area was divided to 64 segments. The uniform level for the current density on the anode side was evaluated and it can provide valuable information for optimization of flow field design and operated condition.

TABLE II. Fuel cells test conditions.

MEA active area(cm^2)	Stoichiometry (A/C)	Cathode gas	Anode gas	Inlet pressure (kPa, A/C)	Cell temperature (°C)
25	1.72/3	air	Hydrogen (Purity: 99.9999%)	100/80	75

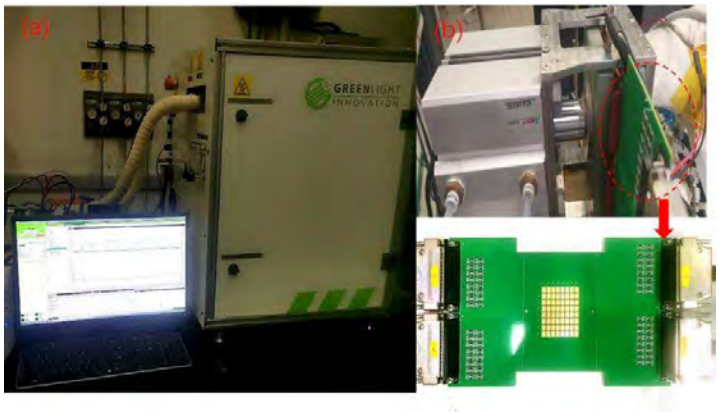

Figure 1. Experimental system: (a) Fuel cell test station; (b) current density distribution tester.

3 Result and Discussion

3.1 Performance Evaluation Result

The performance comparison of two single cells under different RH conditions is exhibited in Figure 2. Figure 2 shows that both two structures present the same trend

which the power density maximum value and limited current value increase when the RH is raised from 10% to 30%. However, along with further increase of the RH, the power generation capacity of the cell declines. Arguably, 30% RH is the most suitable humidification condition for the reaction within the explored range in this paper. Using the anode plate with a double serpentine flow field, and under the RH 30% condition can reach the highest power density of 0.898 W/cm^2.

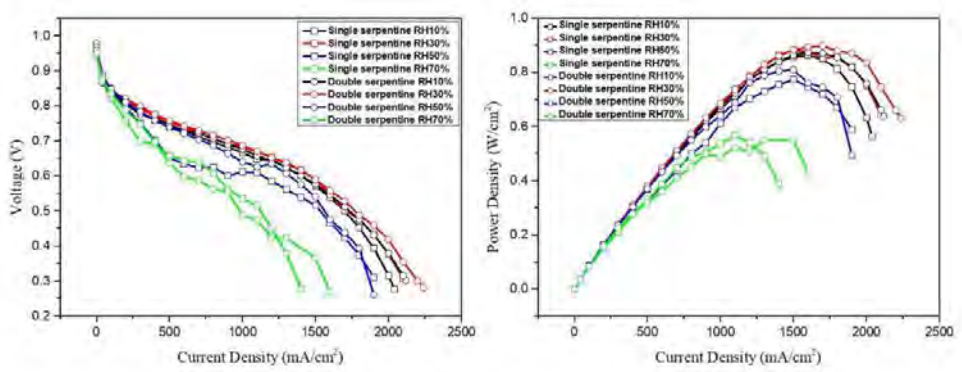

Figure 2 The performance of two single cells under different RHs: (a) polarization curves; (b) power density curves.

3.2 Effect of Flow Field Structure

3.2.1 Current Density Distribution toward Two Structure Anode Plates. The current density distribution results evaluation aiming at different serpentine structure flow fields are demonstrated in Figure 3. Figure 3 illustrated that the double serpentine structure flow field makes the current density distribution more uniform than the single serpentine structure. The well-distributed current density would achieve less electric potential loss as it produces less regional voltage gap and interfaces current while non-uniform current distribution result in poor reactant utilization and reduced energy efficiency in the cell (16).

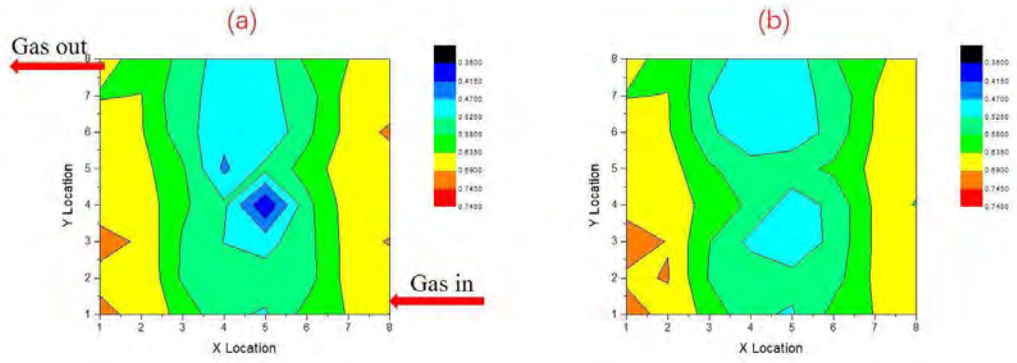

Figure 3 current density distribution test results of two anode plates under 600 mA/cm^2 and 30% RH: (a) The single structure serpentine plate; (b) The double structure serpentine plate.

3.2.2 Flow Resistance Evaluated Simulation Outcomes toward Two Structure Anode Plates. For investigating the unhindered ability of these two structure flow fields, the hydrogen pressure drops which passed the two type flow fields were simulated. In this part, the velocity inlet is calculated according to the current density of 2000 mA/cm^2, which is near to the limited current density of the cell. Then, using the formulation [1] to work out the inlet velocity. In the equation [1], i represents the current, and n is the number of electrons for each reaction produced. Complementally, *dN*/*dt* represents the electrochemical reaction rates, whose unit is mol•s^{-1}. Figure 4 displays the hydrogen pressure drop along with the channels. The pressure loss in the double serpentine flow field （3.7 kPa） is smaller than that of the single serpentine flow field (16.6 kPa). From this information, it can be suggested that the water movement is more easily in the double serpentine flow field under the same condition as the single serpentine structure (17).

$$i = nF \times \frac{dN}{dt} \qquad [1]$$

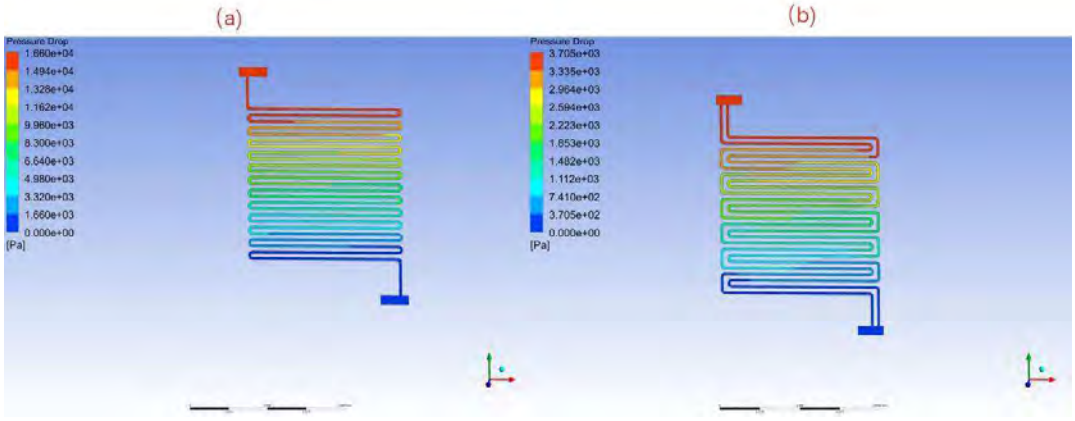

Figure 4 Pressure drops along channel simulation results with two structure flow fields: (a) The single structure serpentine plate; (b) The double structure serpentine plate.

3.3 Effect of Gas Humidity

3.3.1 In-situ Segmented Cell Measuring Technique Test under Different RHs.

The current density distribution results comparison under different RH conditions is displayed in Figure 5 and Figure 6. These results were obtained according to current density of 800 mA/cm^2, and all the diagrams were obtained by using the same anode plate (double structure serpentine plate). Figure 5 reflects the anode plate surface current density distribution at various reactant humidification. Furthermore, based on Figure 5 data, Figure 6 shows the gap between maximum regional current density and the minimum one. The large gap can lead to a performance decline as it causes more electric potential loss. Figure 6 suggested that under the RH 50% condition, the difference of regional current density is the largest. Thus, it can explain the output power maximum drop when the RH is increased to 50% (Figure2).

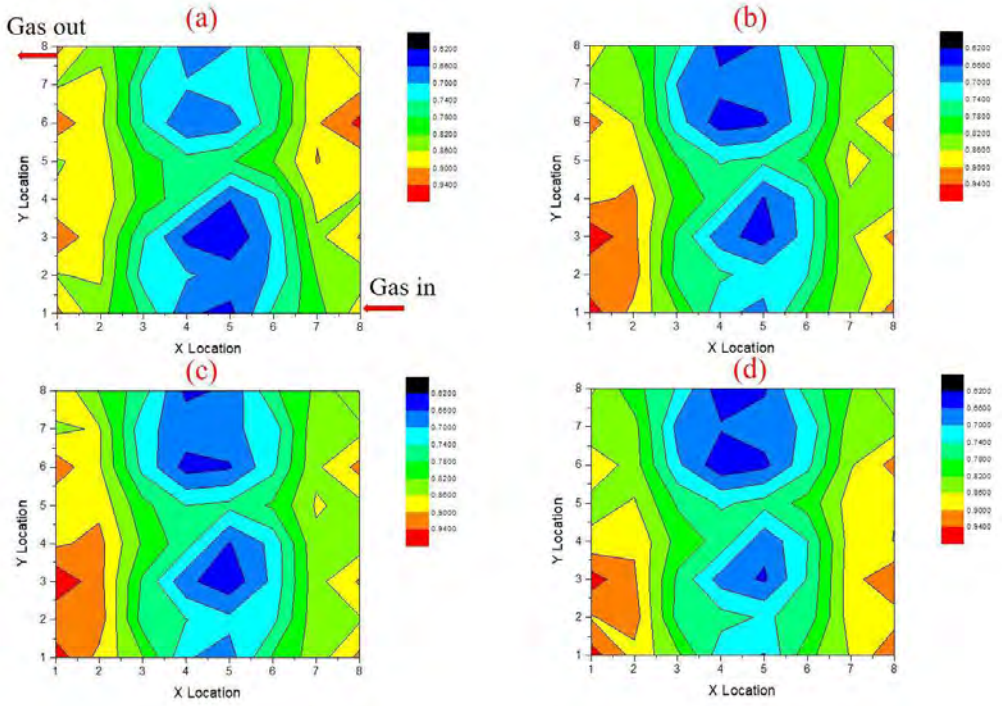

Figure 5 The current density distribution results at 800 mA/cm^2 under different RH conditions: (a)~(d) represent the RH of 10%, 30%, 50% and 70%, respectively.

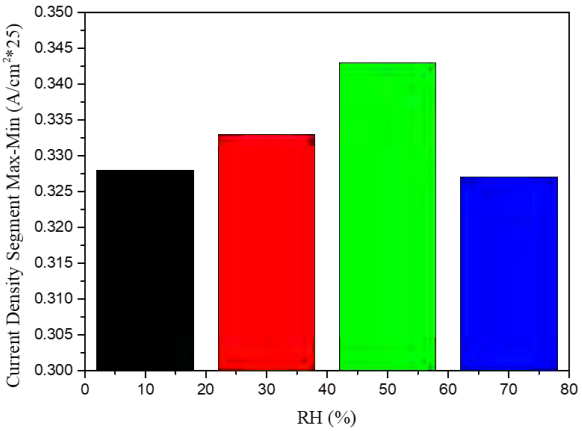

Figure 6 The current density distribution at 800 mA/cm^2 Max-Min results under different RHs.

3.3.2 The analysis of RH effect on the Anode Side and Cathode Side Respectively.

For investigating the RH at both two sides, different RH settings at two sides experiments were conducted by using double structure serpentine anode plate and the results were shown in Figure 7. It can be seen from Figure 7 that the maximum power density was obtained by six different RHs. By comparing column 1st&2rd, 3th&4th and 5th&6th, it can be seen that when humidity is above 50%, the output power can be improved by converting hydrogen into a non-humidifying gas. Furthermore, from the comparative study with case 4 and 6, it can be concluded that even though without humidifying hydrogen, but increased air humidification temperature can also affect the single-cell performance greatly, especially when the cathode RH raised to 70%. To sum up, the results indicates that the flooding phenomenon may occur when anodic humidity conditions are above 50%. When the RH reaches to 70%, both cathode and anode sides may exhibit a large area of flooding in the flow field, which in turn causes the cell's performance appears to be significantly reduced.

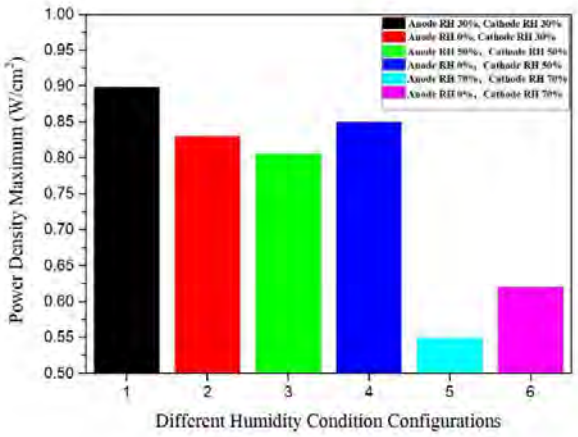

Figure 7 The power density maximum value obtained by different RH solutions.

In order to further prove that when the RH reaches 70%, the cathode is seriously flooded. The pressure drops locate at the cathode side (under the 1600 mA/cm^2 current density) are exhibited in Figure 8. This diagram presents an increasing trend when the RH raises from 10% to 70%. These results show that the higher RH condition causes the larger pressure drop along the channel. As the higher pressure drop brings from more water production (18), the relationship can be realized that the increasing RH leads to more water trapped between the inlet and outlet. It means that the RH increment would cause the flooding phenomenon, resulting in a sharp drop in performance.

Even though CL flooding seldom takes place at low anode humidity, e.g 10% RH, it will reduce the electrochemically active surface area (ESA) significantly because of drying out of the proton exchange membrane (19) and increase the active resistance and ohmic resistance, so that hinder the proton transportation (20). Thus, combing the analysis as above, it can help explain the best performance was achieved under 30% humidity condition.

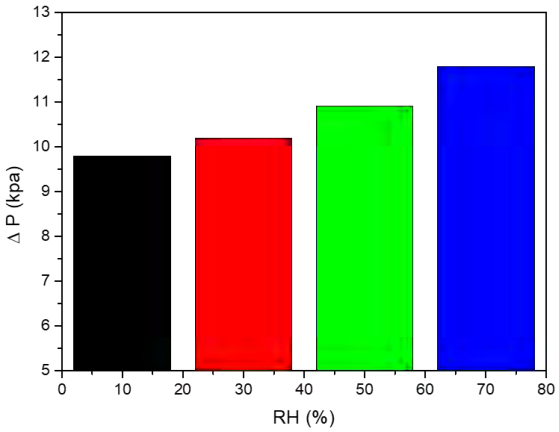

Figure 8 The pressure drops between inlet and outlet of cathode side at 1600 mA/cm^2.

4 Conclusion

According to the current density distribution experimental results and the simulation evaluation, it can draw a conclusion carefully that the double serpentine structure is a benefit to fluid pass the channel, leading to remove water effectively. Furthermore, the potential loss of the double structure serpentine PEMFC is less, comparing with the single structure serpentine PEMFC. These advantages could make the double serpentine structure flow field more conducive to the performance of a single cell.

Toward the same fuel cell composition, the conducted humidity condition can also change the output power of the cell greatly. The 30% RH is the essential factor to improve the maximum power density. Higher humidity levels would cause larger regional potential loss and more serious flooding. However, low humidity will reduce membrane wetting level for the transport the proton. Thus, the 30% RH is a proper humidity condition to obtain a better water management ability, and shows the superiority of the single-cell output power.

In summary, the optimal anode flow field structure and humidification condition can enhance the performance of PEMFC. This paper provided a prospective way to keep water contents within a reasonable range for fuel cell is that employed the anode plate with double serpentine structure flow field and conducted at the humidity condition as the RH 30%.

Acknowledgments

This work was financially supported by the Ministry of Science and Technology

of the People's Republic of China (Grant No: 2018YFB1502505).

References

1. P. Ribeirinha, M. Abdollahzadeh, A. Pereira, F. Relvas, M. Boaventura, and A. Mendes, *Applied Energy*, **215**, 659 (2018).
2. Y. Li, Y. Feng, and X. D. Sun, *ACS Sustain. Chem. Eng*., **6**, 10 (2018).
3. S. Caux, W. Hankache, M. Fadel, and D. Hissel, *Energ Convers Manage*, **51**, 320 (2010).
4. A. Raj, T. Shamim, *Energ Convers Manage*, **86**, 443 (2014).
5. H. Park, *Energ Convers Manage*, **103**, 623 (2015).
6. Z. Shi, W. Xia, *J. Power Sources*, **185**, 985 (2008).
7. M. Kim, N. Jung, K. S. Eom, S. J. Yoo, J. Y. Kim, J. H. Jang, H. J. Kim, B. K. Hong, and E. A. Cho, *J. Power Sources*, **266**, 332 (2014).
8. H. Kahraman, M. F. Orhan, *Energ Convers Manage*, **133**, 363 (2017)
9. F.B. Weng, A. Su, and G. B. Jung, *J. Power Sources*, **145**, 546 (2005).
10. E. Middelman, W. Kout, B.Vogelaar, J. Lenssen, and E. D. Waal, *J. Power Sources*, **118**, 44 (2003)
11. D. S. Watkins, K. W. Dircks, and D. G. Epp, US Patent No. 4, 988,583, 1991.
12. D. S.Watkins, K. W. Dircks, and D. G. Epp, US Patent No. 5, 108, 849, 1992
13. M. R. Esbo, A. A. Ranjbar, E. Alizadeh, and M. Aghaee, *Int. J. Hydrog. Energy*, **41**, 3023 (2016).
14. B. O. Emmanuel, P. Barendse, J. Chamier. *IEEE ECCE*, (2018).
15. Z. Liu, J. Shen, H. Pei, Z. Tu, and L. Wei, *Int. J. Energy Res.*, **39**, 504 (2015).
16. S. J. C. Cleghorn, C. R. Derouin, M. S. Wilson, and S. Gottesfeld, *J Appl Electrochem*, **28**, 663 (1998).
17. J. Wang, H. Wang, *Fuel Cells*, **12**, 989 (2012)
18. V. Coeuriot, J. Dillet, G. Maranzana, O. Lottin, and S. Didierjean, *Int. J. Hydrog. Energy*, **40**, 7192 (2015).
19. D. Malevich, E. Halliop, B. A. Peppley, J. G. Pharoah, and K. Karan, *ECS Trans.*, **16**(2), 1763 (2008).
20. C. W. Roh, J. Choi, and H. Lee, *Electrochem Commun*, **97**, 105 (2018).

Chapter 12

Poster Session

ECS Transactions, 104 (8) 309-316 (2021)
10.1149/10408.0309ecst ©The Electrochemical Society

Molecular Dynamics Study of Proton Conductivity at an Interface between Nafion and Graphene Sheet

R. Tanaka[a,b], T. Mabuchi[b, c], Y. Zang[d], B. Hinds[d], and T. Tokumasu[b]

[a] Graduate School of Engineering, Tohoku University, Sendai, Miyagi 980-8577, Japan
[b] Institute of Fluid Science, Tohoku University, Sendai, Miyagi 980-8577, Japan
[c] Frontier Research Institute for Interdisciplinary Sciences, Tohoku University, Sendai, Miyagi 980-8577, Japan
[d] Department of Materials Science and Engineering, University of Washington, Seattle, WA 98195-2120

In order to clarify the proton transport phenomena in Nafion/carbon nanotubes (CNTs) composite membranes, we focused on the interfacial transport between Nafion and graphene sheets (GSs). We investigated the water content dependence of proton transport and structural properties at the interface between Nafion and GSs using molecular dynamics simulations. The density distribution, water cluster analysis at the interface region, and the self-diffusion coefficient of protons at the interface region were obtained at different water contents. The self-diffusion coefficients of protons at the interface were larger than those of the Nafion bulk for all the water contents because of the formation of water layer near the interface. Our findings provide insight into the relationship between the proton transport and the interfacial structure at molecular level, which suggests a possible improvement on proton transport with addition of CNTs with high specific surface area.

Introduction

Polymer electrolyte fuel cells (PEFCs) have attracted much attention in the fields of stationary power generation and automobiles because of their low environmental damage, high energy conversion efficiency and high power density. Proton transport inside PEFCs has a significant effect on PEFC's performance(1,2). In our previous studies, therefore, we focused on proton transport in membranes(3–5) and thin films(6) as well as the film formation processes(7–10). The proton exchange membrane (PEM) is one of the most important parts in PEFCs, where proton transport occurs between the anode and the cathode. Nafion has long been used as a typical material for PEMs due to its good chemical stability and proton transport properties. In previous studies, Mabuchi and Tokumasu et al used molecular dynamics (MD) simulations to analyze proton transport properties in a Nafion bulk membrane(9,11). They clarified that the relationship between the water cluster and the contributions of the vehicle mechanism and the Grotthuss mechanism in proton transport. However, Nafion has some disadvantages such as poor proton transport under high temperature and low humidity, and increased methanol crossover in direct methanol fuel cells (DMFCs). One way to overcome these disadvantages is the introduction of additives into Nafion. Many studies have been conducted on composite membranes with

various additives to improve the properties of Nafion(1). One of additives is carbon nanotubes (CNTs). CNTs have high aspect ratios, high specific surface areas, and their good mechanical properties. In previous studies, it was reported that the introduction of CNTs improved the mechanical properties and decreased the methanol crossover(12). In Nafion/CNT composite membranes, the proton transport was enhanced by the introduction of CNTs, suggesting that the molecular structure at the interface between CNTs and Nafion contributes to higher proton transport(13–18). However, the relationship between transport and structural properties at the interface have not been clarified yet. In this study, we used graphene sheets (GSs) and Nafion to model the interface between Nafion and CNTs in a composite membrane, and investigated the molecular structure and proton transport at the interface using molecular dynamics simulations.

Simulation Methodology

GSs were placed at the top and bottom of the simulation box, and a Nafion bulk membrane system was constructed between the GSs. The proton transport at the interface between GS and Nafion was analyzed using MD simulation. The Nafion model was used for the polymer, with an equivalent weight of 1146. The molecular structure is shown in Figure 1. An all-atom model was used as the atomic model, and a potential based on the DREIDING force field was adopted for the intermolecular interaction for Nafion and GS. The anharmonic two-state empirical valence bond (*a*TS-EVB) model was adopted for hydronium ion to describe the Grotthuss hopping mechanism(19). The particle mesh Ewald method was used to calculate the Coulomb force. In this system, the number of hydronium ions was set at the same as that of sulfonic acid groups. The number of water molecules used in the system was based on the water content of the membrane.

$$\lambda = (N_{H2O} + N_{H3O+})/N_{SO3-} \quad [1]$$

where N_{H2O}, N_{H3O^+} and $N_{SO^{3-}}$represent the numbers of each molecule. The water content was set at λ= 5, 10, and 14. These water contents correspond to the relative humidity of the Nafion bulk membrane of about 40%, 80%, and 90%, respectively. Periodic boundary was applied on *x* and *y* directions. The procedure for constructing the calculation system is as follows. Two GSs were placed at the top and bottom of the initial calculation box, (x,y) = (54.6, 53.284 Å^2) and (x,y,z) = (160,160,220 Å^3), respectively, and Nafion, water molecules, and hydronium ions were randomly placed between the GSs. The number of molecules in the system is shown in Table 1. Annealing was performed to equilibrate the computational system in the following manner, where *N* is the number of molecules, *V* is the volume, and *P* is the pressure. i) *NPT* ensemble is run for 100 ps at *T*=350 K, P_x=P_y=0.1 MPa. By this calculation, the size of the calculation box is fitted to the GS size. ii) The calculation system was compressed in the z direction until the density of Nafion matched the experimental density of the bulk Nafion membrane(19). iii) *NPT* ensemble is run for 100 ps at *T*=350K, P_z=0.1MPa, then *NVT* ensemble for 50 ps at *T*=350 K, *NVT* ensemble for 50 ps at *T*=1000K, *NVT* ensemble for 50 ps at *T*=350K. Step iii) is repeated four times.

In the fourth and fifth steps, the density of the system was almost the same, and we judged that the system had reached a stable state. iv) *NPT* ensemble is run for 600 ps at *T*=350 K, *Pz*=0.1 MPa to complete the annealing. v) *NVT* ensemble is run for 6 ns at *T*=350 K. This is the sampling time. The time step was set at 1 fs and the sampling interval was set at 1,000 steps. The simulation system is shown in Figure 2. It is important to note that the motion of the carbon atoms constituting the GS was fixed in all calculations.

TABLE 1. Number of Molecules in the Calculation System

Water content	Nafion	H_3O^+	H_2O
5	18	180	720
10	18	180	1620
14	18	180	2340

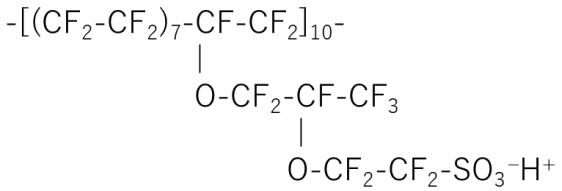

Figure 1. Molecular structure of the Nafion polymer.

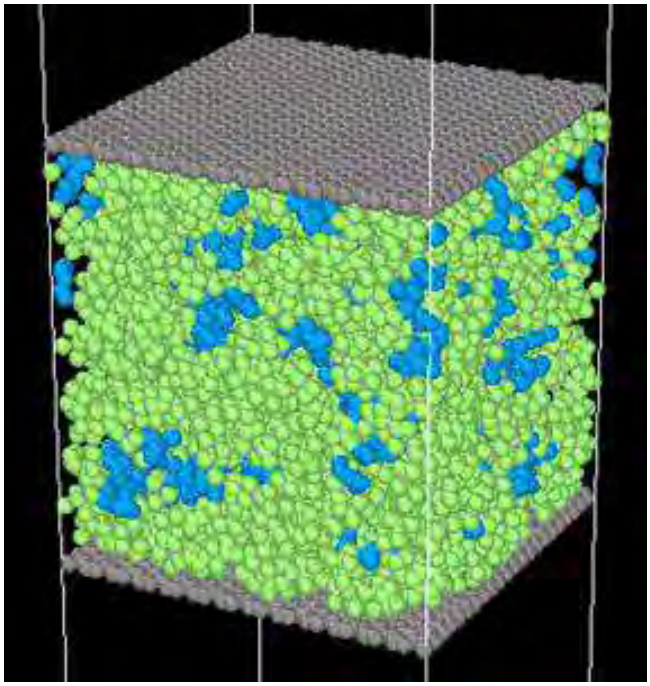

Figure 2. Snapshot of Nafion polymers between carbon walls. The system is composed of polymer, water, hydronium ion, and carbon walls.

Result and Discussion

Nafion Structure at the Interface

The effect of the water content on molecular structure of the system was analyzed using the density distribution in the vertical direction of GS. The system was divided into single cells whose width, *dz* as shown by Fig 3, is set at 1.0 Å and the density distribution function was obtained by calculating the density of each cell. The result is shown in Fig.4. From this result, the hydrophobic main chain of Nafion was attracted to the GS, and the sulfur of Nafion were aligned in the opposite direction to GS. The water adsorption layer attracted by sulfur was formed near the GS. In addition, the density distribution at the center of the system was almost unchanged, indicating a bulk-like structure at the center. A black dot line shown in the Fig4 is a boundary separating the interface region from the intermediate region. This line is defined as the end of the peak near the GS in the density distribution of water. Table 2 shows the interfacial distance according to the water content. As the water content increased, the interface distance gradually increased. The interfacial distance is about 2.5-3 nm.

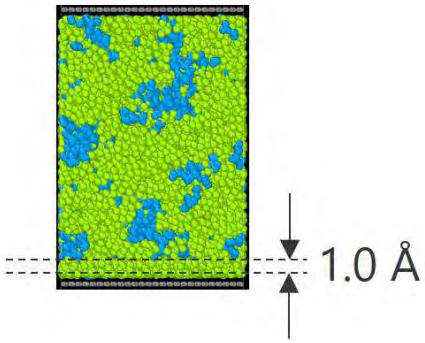

Figure 3. The *dz* of the density distribution in the calculation system.

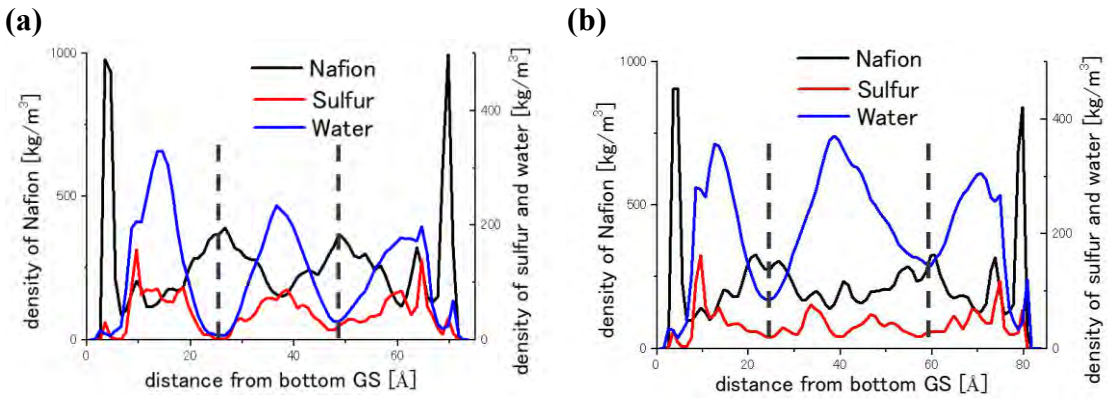

(c)

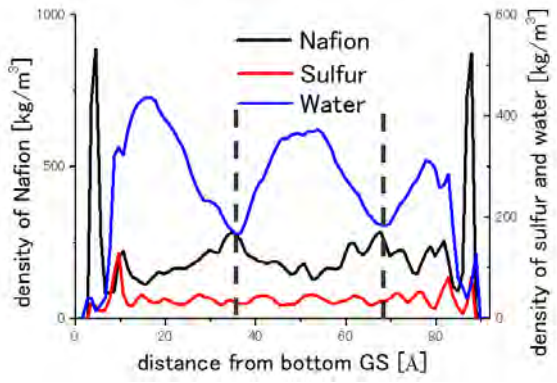

Figure 4. Density distribution .(a), (b), (c) shows the result when $\lambda = 5, 10, 14$. A black dot line shows a boundary separating the interface region from the intermediate region.

TABLE2. distance from bottom GS to upper GS and interface distance.

Water content	Interface distance [Å]
5	25.1
10	29.3
14	31.1

Cluster Analysis in Interface

To analyze the structure of water molecules at the interface as water content changes, water cluster analysis was performed. In this study, water clusters were defined as a group of water molecules and hydronium ions whose distance between oxygen atoms of each molecules is within 3.3 Å. This distance is based on the first peak distance of the RDF of oxygen atoms of water molecules in bulk water(20). The interface distance is taken from the value determined in the previous section. The mean cluster size is defined as the following equation,

$$S_{mean} = \sum n_s S^2 \Big/ \sum n_s S \qquad [2]$$

where n_s is the cluster size distribution and S is the number of water molecules and hydronium ions in a cluster. The largest cluster is excluded from the summation. This result is shown in Fig5. The number of clusters at the interface decreased with increasing water content, but the largest cluster size increased. Therefore, with increasing water content, water clusters connect with each other and then larger clusters are formed. The S_{mean} has a peak at λ =10. Note that the largest cluster is excluded from the summation in Eq. [2]. This result indicates that the water clusters percolates between λ =10 and 14 of water content as shown in Fig6, and form a proton path at the interface, which leads to higher proton transport.

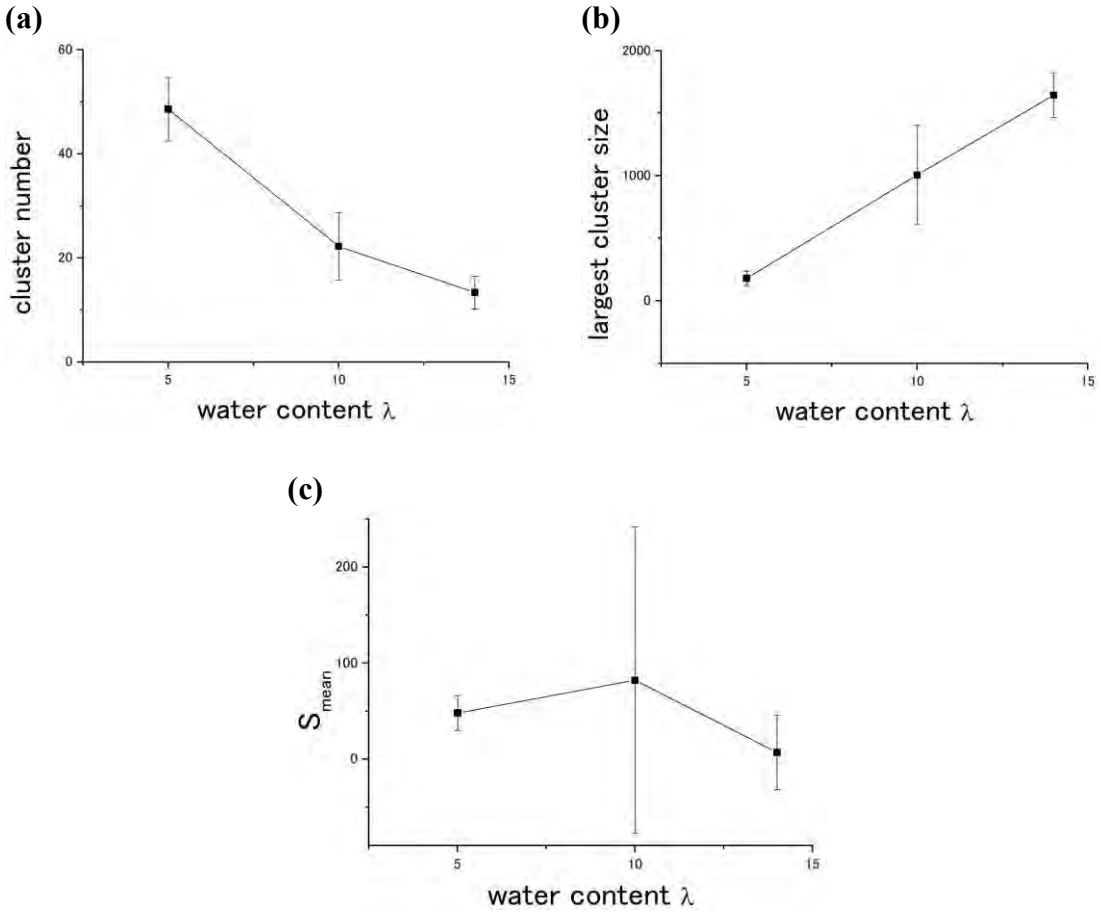

Figure 5. (a) Number of cluster (b) largest cluster size (c) averaged cluster size.

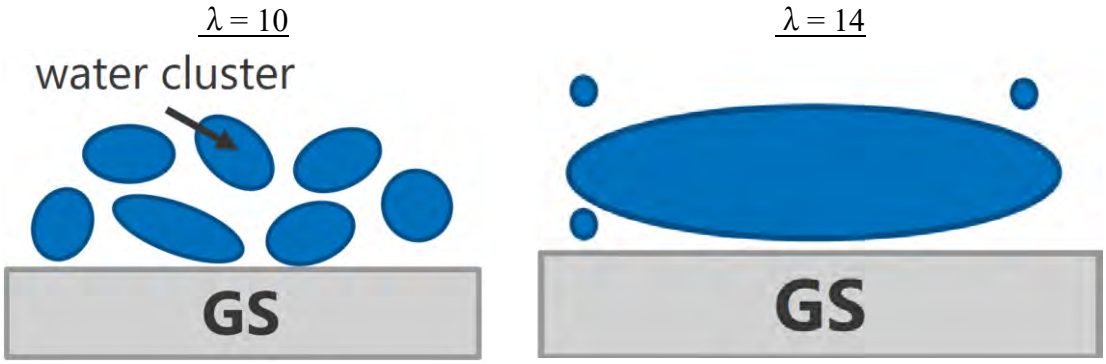

Figure 6. Schematic diagrams of water clusters at the interface.

Proton Transport in Interface

In order to analyze the proton transport at the interface, the self-diffusion coefficients of protons in the GS parallel to the surface were calculated. The self-diffusion coefficients were calculated from Einstein's equation.

$$D = \lim_{t\to\infty} \frac{1}{4Ndt} \sum_{i=1}^{N} \left| \boldsymbol{r}_i(t) - \boldsymbol{r}_i(0) \right|^2 \quad [3]$$

where $\boldsymbol{r}_i(t)$ and $\boldsymbol{r}_i(0)$ are the position of atom at time t and 0 respectively, and N is the number of hydronium ions. It is important to note that only the mean square displacement molecules which stay in the interface region during the time interval are calculated. Figure 7 shows the proton self-diffusion coefficients in the interfacial region as a function of water content, and it can be seen that the self-diffusion coefficients in the interfacial region are higher than those in the bulk Nafion at all water contents. This may be attributed to the formation of a water adsorption layer and water clusters at the interface shown in Fig. 8. In the future, it is necessary to analyze the network structure of water clusters at the interface and clarify the difference from the Nafion bulk.

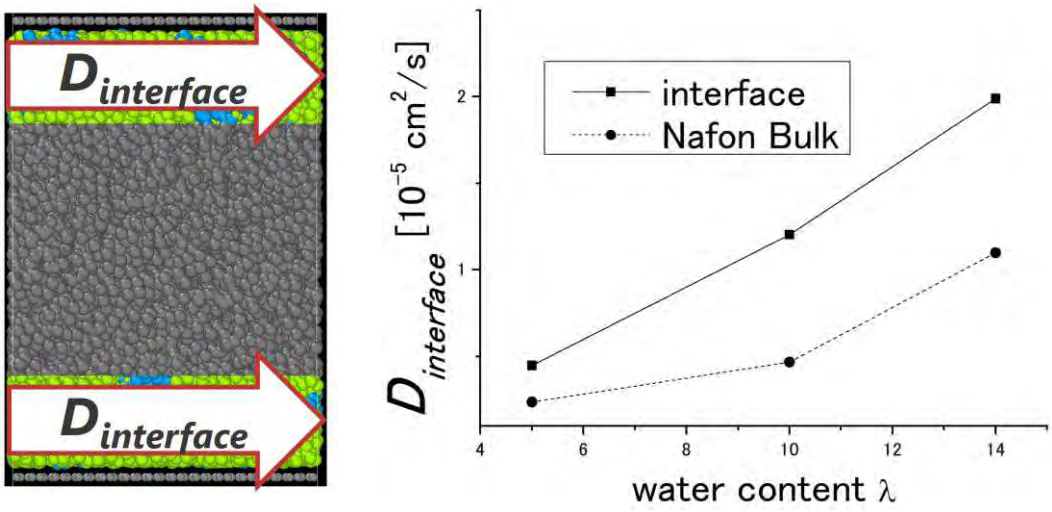

Figure 7. Self-diffusion coefficient of protons at the interface (solid line) and in the bulk (dotted line).

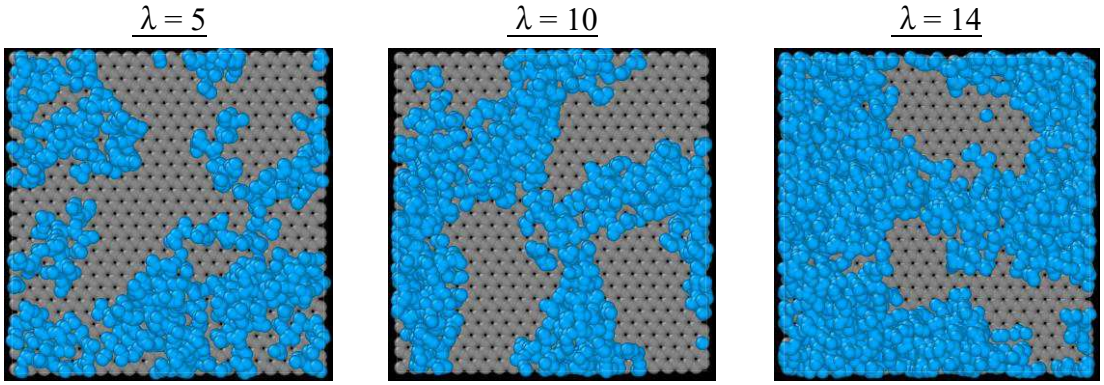

Figure 8. Snapshots of water molecules and hydronium ions (blue atoms) within the interfacial distance from the GS when $\lambda = 5, 10, 14$

Conclusions

The water content dependence of proton transport and structural properties at the interface between Nafion and the GS was studied using MD simulations. The proton hopping phenomenon was calculated using the *a*TS-EVB method. The density distribution and cluster analysis at the interface region were carried out to investigate the structural properties. From the density distribution results, it was found that the hydrophobic main chain of Nafion is attracted to the GS, resulting in the formation of a water adsorption layer

near the GS. The results of water cluster analysis at the interface show that the water clusters become percolated and the cluster size increases as the water content increases. To gain the transport properties of protons, the self-diffusion coefficient of protons at the interface region was calculated from the gradient of MSD at the interface region parallel to the GS. The diffusion coefficients of protons at the interface were found to be larger than those of the Nafion bulk for all the water contents. This is caused by the proton paths of the connected water clusters are formed at the interface. The effect of wettability on the interfacial structure and transport properties by modifying GSs with sulfonic acid groups will be a next focus in the future.

Acknowledgments

It was performed, in part, using the supercomputer at the Institute of Fluid Science, Tohoku University.

References

1. Wang, Y., Ruiz Diaz, D. F., Chen, K. S., Wang, Z. & Adroher, X. C. *Mater. Today* **32**, 178–203 (2020).
2. Kreuer, K. D., Paddison, S. J., Spohr, E. & Schuster, M. *Chem. Rev.* **104**, 4637–4678 (2004).
3. Mabuchi, T. & Tokumasu, T. *J. Phys. Chem. B* **122**, 5922–5932 (2018).
4. Mabuchi, T. & Tokumasu, T. *J. Nanosci. Nanotechnol.* **15**, 2958–2963 (2015).
5. Mabuchi, T. & Tokumasu, T. *J. Polym. Sci. Part B Polym. Phys.* **57**, 867–878 (2019).
6. Matsuda, T., Kobayashi, K., Mabuchi, T., Inoue, G. & Tokumasu, T. *ECS Trans.* **98**, 187–196 (2020).
7. Mabuchi, T., Huang, S.-F. & Tokumasu, T. *J. Polym. Sci.* **58**, 487–499 (2020).
8. Mabuchi, T., Huang, S. F. & Tokumasu, T. *Macromolecules* **53**, 3273–3283 (2020).
9. Mabuchi, T. & Tokumasu, T. *AIP Conf. Proc.* **2255**, (2020).
10. Mabuchi, T., Huang, S. F. & Tokumasu, T. *Macromolecules* **54**, 115–125 (2021).
11. MABUCHI, T. & TOKUMASU, T. *Mech. Eng. J.* **4**, 17-00054-17–00054 (2017).
12. Choi, B. G., Park, H. S., Im, H. S., Kim, Y. J. & Hong, W. H. *J. Memb. Sci.* **324**, 102–110 (2008).
13. Yin, C. *et al. ACS Appl. Mater. Interfaces* **10**, 14026–14035 (2018).
14. Zhao, B., Hu, H. & Haddon, R. C. *Adv. Funct. Mater.* **14**, 71–76 (2004).
15. Yun, S., Im, H., Heo, Y. & Kim, J. *J. Memb. Sci.* **380**, 208–215 (2011).
16. Kannan, R., Kakade, B. A. & Pillai, V. K. *Angew. Chemie - Int. Ed.* **47**, 2653–2656 (2008).
17. Liu, X. *et al. J. Memb. Sci.* **504**, 206–219 (2016).
18. Asgari, M. S., Nikazar, M., Molla-Abbasi, P. & Hasani-Sadrabadi, M. M. *Int. J. Hydrogen Energy* **38**, 5894–5902 (2013).
19. Mabuchi, T., Fukushima, A. & Tokumasu, T. *J. Chem. Phys.* **143**, (2015).
20. Cui, S. *et al. J. Phys. Chem. B* **111**, 2208–2218 (2007).

Chapter 13

Membrane Durability

ECS Transactions, 104 (8) 319-324 (2021)
10.1149/10408.0319ecst ©The Electrochemical Society

Development of the Soaking Method for Manufacturing Polymer Electrolyte Fuel Cells with a High-Aspect-Ratio Microstructure

Akihisa Tanaka, Keisuke Nagato, Morio Tomizawa, Kohei Nagai, and Masayuki Nakao

Department of Mechanical Engineering, The University of Tokyo, 7-3-1 Hongo, Bunkyo-ku, Tokyo 113-8656, Japan

To improve power generation performance of polymer electrolyte fuel cells (PEFCs), it is necessary to decrease the activation overpotential of the oxygen reduction reaction (ORR). We propose a method for manufacturing PEFCs with a high-aspect-ratio microstructure to further increase the triple-phase boundary, where ORR occurs. The cathode surface of a Nafion membrane with a high-aspect-ratio microstructure was soaked in catalyst ink using spraying equipment. After drying, the cross-section observations revealed that the catalyst layer went deep into the microstructure without forming a bridge structure. This was probably because the catalyst ink was impregnated into the microstructure before the solvent evaporated. The impregnation process must be the Cassie-Wenzel transition, and the driving force might be the gravity force of the ink or spray pressure. Power generation tests were conducted on PEFCs with microstructures fabricated using the soaking method, and the cells exhibited better power generation performance than conventional cells.

Introduction

Polymer electrolyte fuel cells (PEFCs) are one of the major devices that utilize hydrogen. Owing to their small size and capacity for low-temperature operation, PEFCs are used in practical applications such as fuel cell vehicles.

The power generation efficiency of PEFCs is relatively low. Heinzmann et al. suggested that the main cause of the decrease in efficiency is the activation overpotential of the oxygen reduction reaction (ORR) at the cathode (1). Therefore, having a large triple-phase boundary (TPB), where an ORR occurs, is crucial. Bea et al. reported that the performance of a PEFC was improved by introducing micro-patterns on the surface of a Nafion membrane (2). Organizing a high-aspect-ratio microstructure on the surface of the Nafion membrane is very effective for increasing the size of the TPB. However, in previous studies, the fabricated microstructures had an aspect ratio of approximately 1 at most, which resulted in numerous challenges.

Because Nafion is a water-repellent material, it is necessary to apply force to impregnate the water-based catalyst ink deep into the microstructure. Moreover, carbon particles in the ink tend to agglomerate and subsequently form bridge structures on the microstructure because van der Waals forces are dominant at the submicron scale (3).

Therefore, fabricating a high-aspect-ratio microstructure on the surface of a Nafion membrane is challenging.

Experimental

Line-and-space patterns with three different dimensions—width/spacing/height of 1/1/2 μm, respectively—were introduced on the cathode surface of a Nafion membrane (NRE-212) via thermal nanoimprint lithography (120 °C, 5 MPa) (4). The composition of the cathode catalyst ink is listed in TABLE I. It was prepared by ultrasonication at 20 kHz for more than 1 h. As shown in Figure 1, two samples (A and B) were fabricated by spraying the catalyst ink on the micro-patterned surface with a 1-cm^2 mask attached at 80 °C and 30 °C, respectively. For sample A, the time interval between one push and another was controlled at 5 s to maintain the membrane surface dry. In contrast, for sample B, the time interval was controlled at 0.5 s to soak the surface in the catalyst ink. The same amount of catalyst ink was sprayed on both samples under the same relative pressure (0.1 MPa) using a self-made automatic spraying equipment.

After drying, the cross-sections of both samples were investigated using scanning electron microscopy (SEM).

TABLE I. Compositions of cathode and anode catalyst inks.

	Pt/C [g] (TEC10V50E)	10 wt.% ionomer solution [g]	Deionized water [g]	Isopropyl alcohol [g]
Cathode	0.144	0.69	20.44	0
Anode	0.237	1.14	4.69	11.44

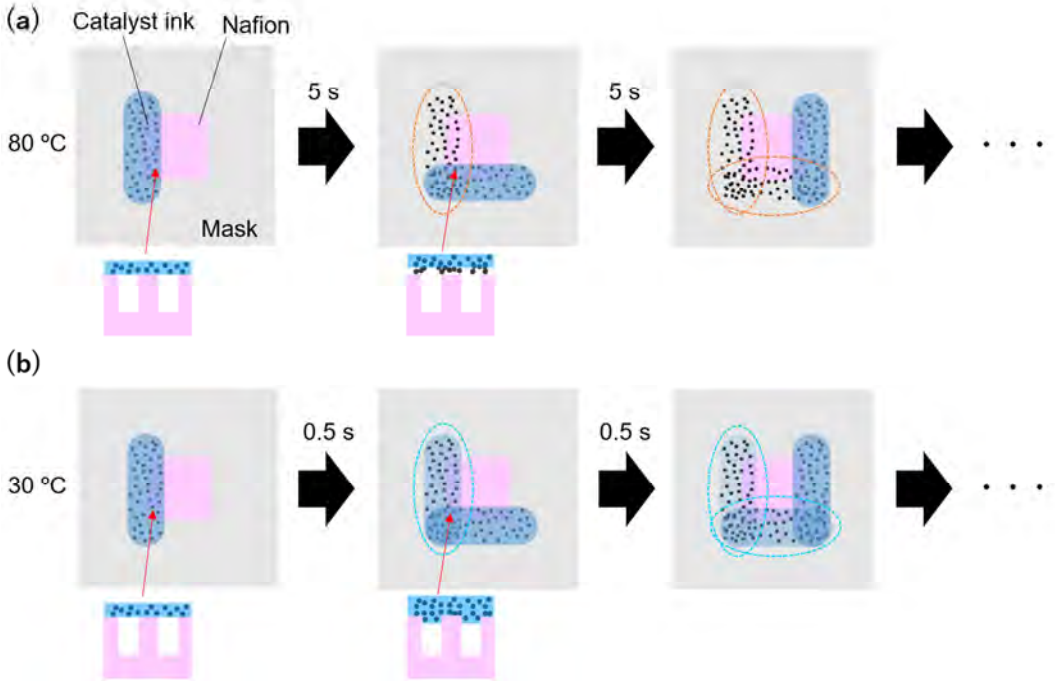

Figure 1. Schematics of catalyst-ink spraying on (a) sample A and (b) sample B.

The performance of a membrane electrode assembly (MEA) with a microstructure fabricated using the soaking method was investigated. The fabrication process of the MEA is shown in Figure 2. Line-and-space patterns were introduced on the cathode surface via thermal nanoimprint lithography. The compositions of the cathode and anode catalyst inks are listed in TABLE I. The cathode surface with micro patterns was first soaked and dried as the process of making sample B, as shown in Figure 1 (b). Subsequently, the catalyst inks were normally sprayed on both the cathode and anode surfaces. The loaded Pt content was 0.19 mg/cm^2 and 0.18 mg/cm^2 in the cathode and anode of each MEA, respectively. Three MEAs with different heights of the ditches of line-and-space patterns were fabricated. Power generation tests were conducted on these MEAs under the operating conditions listed in TABLE II.

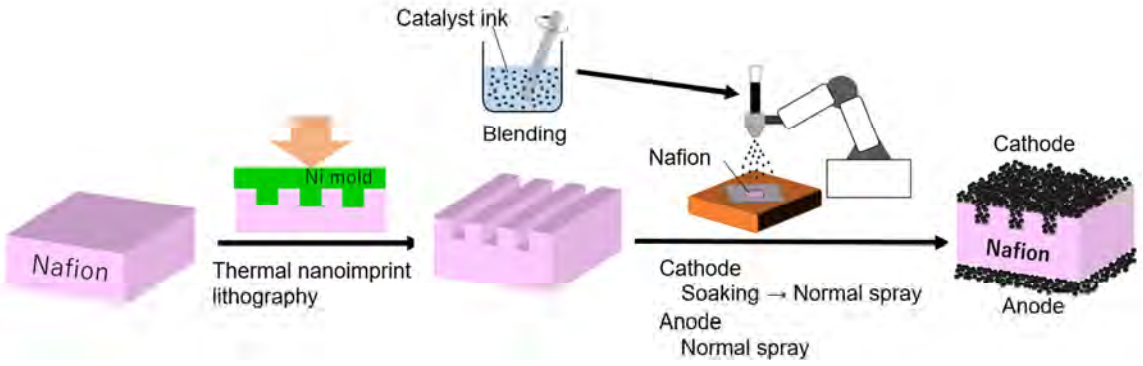

Figure 2. Fabrication process of the MEAs.

TABLE II. Operating conditions.

	O_2 [sccm]	H_2 [sccm]	N_2 [sccm]	Total flow rate [sccm]	Cell temp. [°C]	Bubbler temp. [°C]
Cathode	40.0	0	92.8	200.0	80	72
Anode	0	80.0	52.8	200.0	80	72

Results and discussion

Figure 3 shows the appearance of each sample immediately after spraying. As shown in Figure 3 (a), the ink on sample A had already dried, whereas, as shown in Figure 3 (b), the Nafion membrane of sample B was soaked in ink. Figure 4 shows the SEM images of the cross-sections of both samples. As shown in Figure 4 (a), the catalyst layer formed a bridge structure in sample A. By contrast, as shown in Figure 4 (b), the catalyst layer went deep into the spaces of line-and-space patterns without forming a bridge structure in sample B.

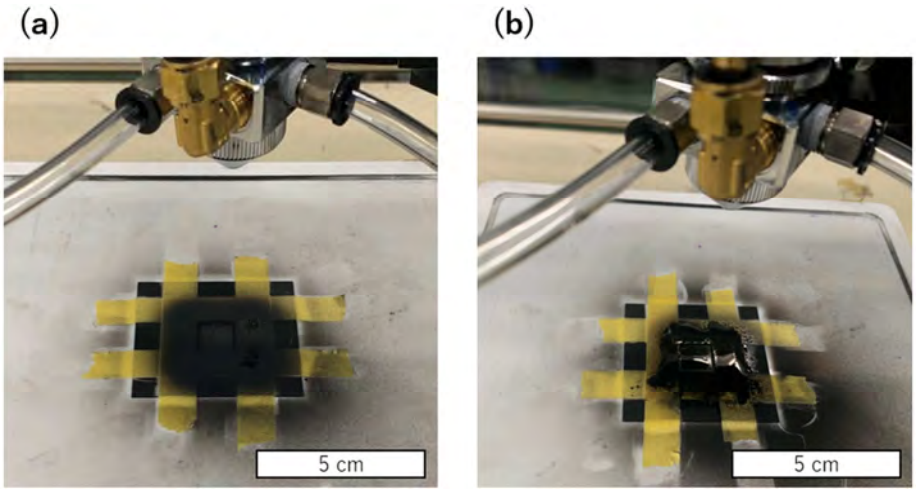

Figure 3. (a) Sample A and (b) sample B after spraying.

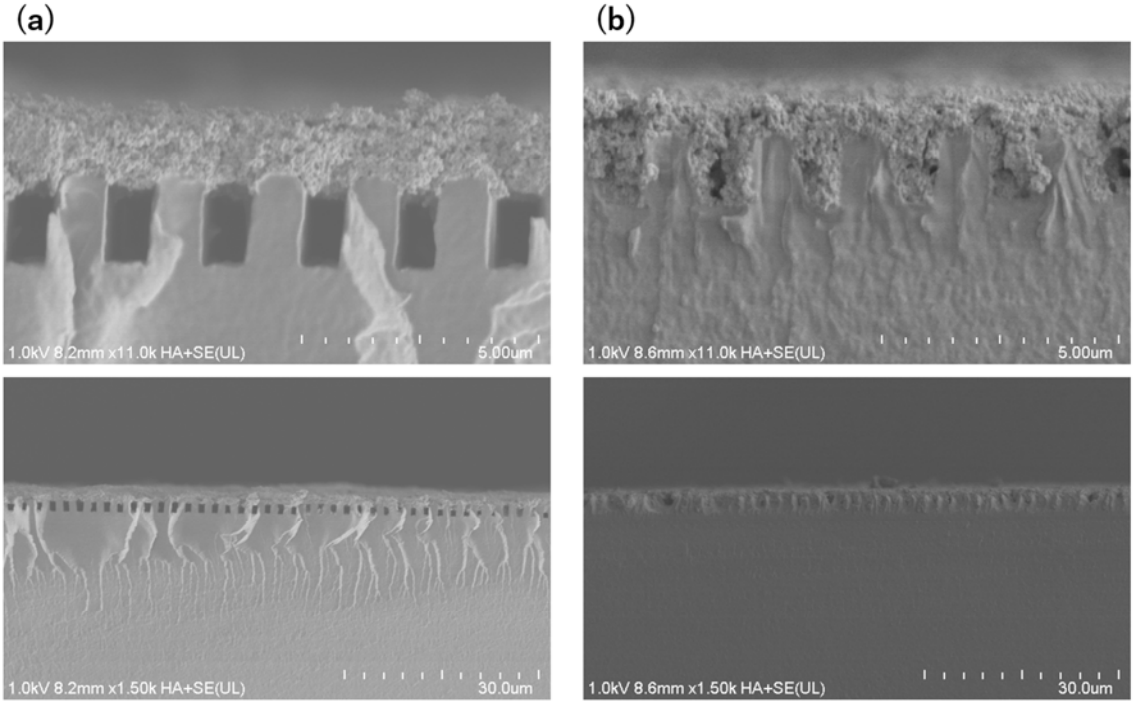

Figure 4. SEM images of (a) sample A and (b) sample B cross-sections.

Figure 5 shows the polarization and power density curves of the MEAs. The SEM images of the cross-sections shown in the right column are the MEAs fabricated under the same conditions. The MEA with 2 μm ditches (D2) exhibited the highest power generation performance, whereas the MEA without microstructure (Flat) exhibited the lowest power generation performance. This could be explained as follows: the TPB increased by the microstructure improved the ORR in the cathode and reduced the polarization resistance.

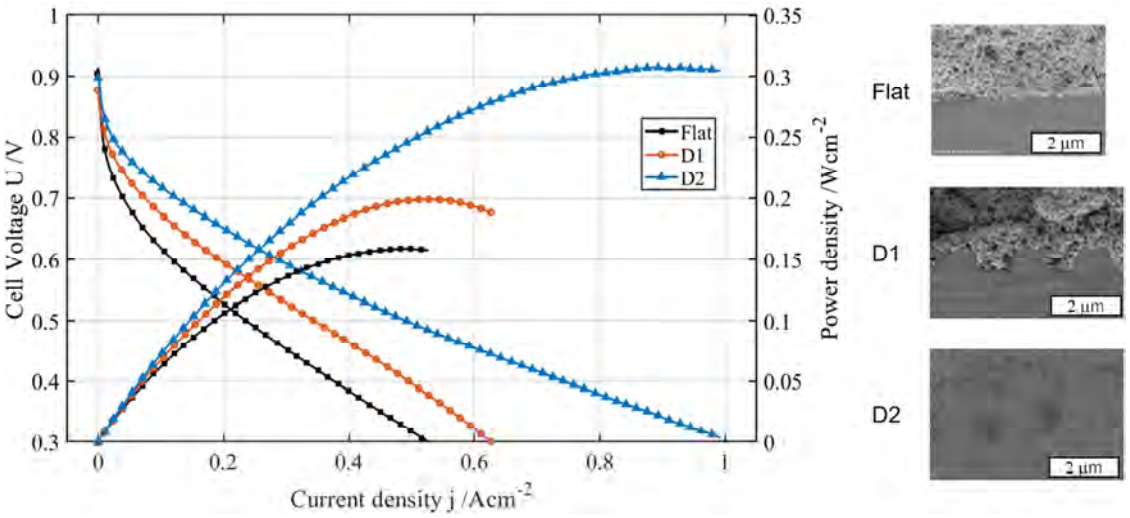

Figure 5. Polarization and power density curves of the MEAs.

Figure 6 shows the estimated mechanism of the bridge structure formation. The reason for the formation of a bridge structure when normally sprayed as sample A could be that water, which is a solvent, rapidly evaporates before the catalyst ink enters the spaces of line-and-space patterns. On the contrary, the reason for preventing the bridge structure from forming when the sample is soaked in ink could be that water evaporates after the catalyst ink goes deep into the spaces.

The contact angle of water on hydrophobic surfaces increases if they are microtextured (5). Nafion, which was used in this study, is also a hydrophobic material, and it was observed that the contact angle of water increased after fabricating the microstructure. The first phase shown in Figure 6 is referred to as Cassie state, where air is trapped in the ditches of the microstructure, and the state is metastable. The transition from Cassie state to Wenzel state, shown in Figure 6, can be induced by imposing a force (5). The driving force for this transition in the soaking method could be the gravity of the ink or the spray pressure.

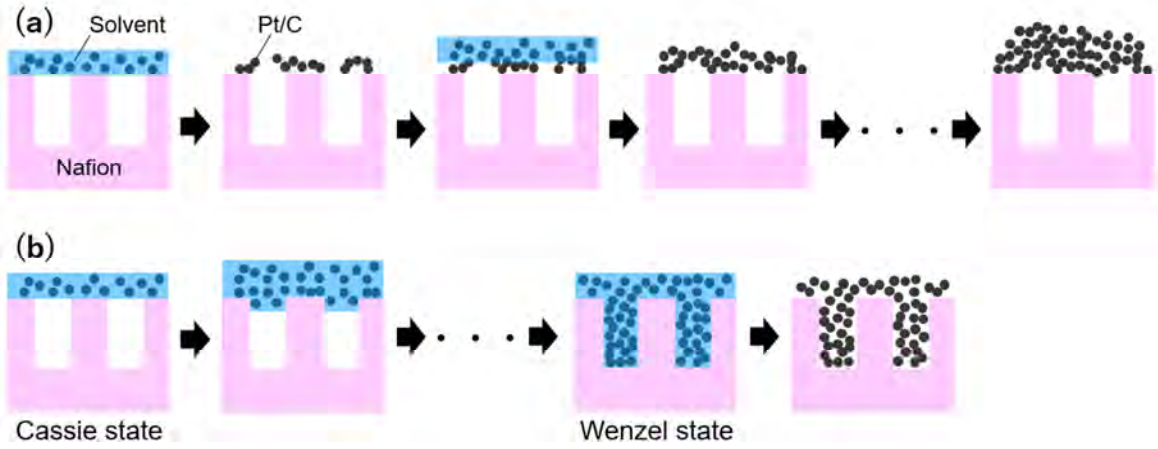

Figure 6. Mechanism of formation of the bridge structure.

Conclusions

By employing the original soaking method, a high-aspect-ratio microstructure was successfully arranged in the cathode without the formation of a bridge structure. As expected, an MEA with a microstructure fabricated using the soaking method exhibited better power generation performance than a conventional MEA. The mechanism of catalyst-ink impregnation into the microstructure using the soaking method could be explained by the Cassie-Wenzel transition. However, the driving force remains unclear and needs to be clarified in future studies. Moreover, optimization of the soaking process parameters is required to manufacture a microstructure with a higher aspect ratio and to increase the size of the TPB.

Acknowledgements

The authors gratefully acknowledge Mr. S. Amaya (UTokyo) for his useful advice on microstructure preparation. We are grateful to Editage (www.editage.com) for the English language editing.

References

1. M. Heinzmann, A. Weber, and E. Ivers-Tiffée, *J. Power Sources*, **402**, p. 24–33 (2018).
2. J. W. Bae, Y.-H. Cho, Y.-E. Sung, K. Shin, and J. Y. Jho, *J. Ind. Eng. Chem.*, **18**, p. 876–879 (2012).
3. P. A. Hartley and G. D. Parfitt, *Langmuir*, **1**, p. 651–657 (1985).
4. S. Y. Chou, P. R. Krauss, and P. J. Renstrom, *Appl. Phys. Lett.*, **67**, p. 3114–3116 (1995).
5. A. Lafuma and D. Quéré, *Nat. Mater.*, **2**, p. 457–460 (2003).

Chapter 14

Non-PGM Catalysts 2

ECS Transactions, 104 (8) 327-333 (2021)
10.1149/10408.0327ecst ©The Electrochemical Society

Effects of Ink Formulation on the Structure and Performance of PGM-Free Catalyst Layer in PEMFCs

Chenzhao Li[a, b], Shengwen Liu[c], Yachao Zeng[c], Yadong Liu[b], Gang Wu[c], David A. Cullen[d], and Jian Xie[b]*

[a] Department of Mechanical and Energy Engineering, Purdue School of Engineering and Technology, Indiana University - Purdue University Indianapolis, Indianapolis, Indiana 46202, USA
[b] School of Mechanical Engineering, Purdue University, West Lafayette, IN 47907, USA
[c] Department of Chemical and Biological Engineering, University at Buffalo, The State University of New York, Buffalo, New York 14260, USA.
[d] Materials Science and Technology Division, Oak Ridge National Laboratory, Oak Ridge, TN 37831, USA

We proposed a novel method of fabricating PGM-Free catalyst MEAs so that the intrinsic catalyst activity from RDE can be translated into MEA performance. The method is based on the catalyst coated membrane (CCM) method using optimized ionomer to carbon (I/C) ratio and solvent mixture of catalyst ink. Using this method, the PGM-free catalyst MEA achieved the current density 44.9 mA cm^{-2} at 0.9 V $_{iR\text{-}free}$ in H_2/O_2 and 150 mA cm^{-2} at 0.8 V in H_2/air, which exceeds the performance targets of US Department of Energy (DOE) for PGM-Free catalyst MEA. The property (solvent composition, dispersion of catalyst and ionomer in an ink), structure (pore structure) and the MEA performance have been characterized using, mercury intrusion porosimetry (MIP) and MEA testing. A property-structure-performance relationship has been established.

Introduction

Polymer electrolyte membrane fuel cells (PEMFCs) is a promising energy conversion technology, which provides the clean and efficient power sources for vehicles propulsion. One of the major factors affecting the performance of the PEMFCs is the slow oxygen reduction reaction, which needs to use the precious group metal (PGM) catalysts. However, PGM is very expensive and the PGM reserve is very limited in the earth which makes PGM unsustainable for large scale application. To solve this critical issue, the PGM-free catalyst is the solution. There are several types of PGM-Free catalysts emerged from numerous research groups.(1, 2) Among these catalysts, Fe-N-C based catalyst: iron atoms coordinated with nitrogen and anchored on porous carbon, shows very promising ORR performance using rotating disk electrode (RDE) while it has the potential to compete with PGM catalyst. Recently, the great effort has been devoted to the development of PGM-Free catalyst with great RDE performance to close the performance gap between PGM and PGM-Free catalysts. But to the best of our knowledge, differing from the PGM catalysts, the progress on the fabrication of membrane electrode assembly (MEA) for PGM-free catalyst has made little progress. The fabrication of PGM-free

MEA is very important for PGM-free catalyst development: the optimal MEA fabrication method would sacrifice much less performance in MEA from its theoretical ORR activity (i.e., RDE performance). Previously, the majority of reported PGM-Free MEA performance was obtained from the MEA fabricated using the gas diffusion electrodes (GDE) method, on which the PGM-free catalyst ink was painted over the gas diffusion layer. However, the electrode made using this method is too thick to efficiently transport the O_2 gas molecules. Besides, there is a serious reproducibility issue with the GDE method. MEA performance, made by GDE method, highly depends on the person who fabricated it, because catalyst ink was manually coated on gas diffusion layer (GDL) using a blade. For a reliable fabrication method, the quality of the fabricated MEAs should be highly consistent, namely, with good reproducibility so that the performance difference between MEAs made with the same conditions using the same method is negligible. In this regard, a new fabrication method has the paramount significance in making high performance PGM-free MEAs with great reproducibility.

The catalyst coated membrane (CCM) technique is a commonly used in making PGM catalyst MEAs because the catalyst and ionomer particles of a catalyst ink can be directly sprayed over the membrane surface with good dispersion and forming an ideal interface between the catalyst layer and membrane. The porosimetry and morphology of the catalyst layers of the MEA can be easily controlled using the spraying method. The ionomer/catalyst interface formed in the catalyst ink can also be preserved in the solid catalyst layer using the spraying method. In addition, CCMs made by using a commercial spray machine have very high reproducibility, which makes the optimization of MEA fabrication possible. Based on this high reproducibility, using a machine spraying technique, the MEA fabrication method was optimized on catalyst ink composition and ionomer/catalyst ratio (I/C ratio). After fabrication method optimized, the PGM-free catalyst MEAs shown the very excited results, met or exceed the DOE 2025 PGM-Free catalyst targets.

Experimental

For the anode electrode, 20 wt. % Pt/XC-72 catalyst and ionomer ink were prepared by mixing the catalyst powder and ionomer dispersion (25 wt. %, Aquivion D-79-25BS). The ionomer to carbon ratio was controlled to be 0.45 as well as the mixture of 1-propanol and deionized-water (DI-water). The prepared ink was firstly sonicated for 30 minutes in a water bath with a temperature under 30°C. The prepared ink was then sprayed onto a Nafion 212 membrane (5 cm^2) by Exacta Coat spray machine (Sono-Tek, NY), and the Pt loading at the anode was controlled as 0.2 mg_{Pt} cm^{-2}. For the cathode, the prepared ink was sprayed on the opposite side of the anode, and the loading was controlled around 4.0 $mg_{catalyst}$ cm^{-2}. Two pieces of SGL-22BB served as the gas diffusion layer sandwiched an MEA. MEAs were measured using a fuel cell test station (Fuel Cell technology, Inc., Albuquerque, NM, USA). First, the cell was heated to 80 °C without flow, then 200 sccm of N_2 in the anode and cathode for 2 hours to hydrate the membrane and ionomer. Air/oxygen flowing at 500 mL sccm and H_2 (purity 99.999%) flowing at 300 sccm was supplied to the cathode and anode, respectively. The pressures during the fuel cell tests are 150 kPa_{abs} on both sides for reactant gases. The Dew point of anodic flow and cathodic flow is 80, and 80 □ cell temperature was maintained during the recording of VIR polarization curves. Flow rates of air 500 sccm and H_2 300 sccm were

controlled as 300 sccm and 500 sccm (H_2/O_2(air)) for anode and cathode, respectively. The MEAs were tested using scan current method: 0 to 1.0 A, 0.1 A per step; after 1.0 A. 1.0 A per step; 30 sec holding time for each step.

Results and Discussion

Fabrication Method Comparison

First, the performance of MEAs made from GDE method and CCM method were compared. The MEA made by spraying method shows similar performance with that of GDE (Fig.1). Under H_2/O_2 condition, above 0.65V, the polarization curve of CCM MEA overlaps with that of GDE MEA, and the current density at 0.9 V $_{iR\text{-}Free}$ is 31 mA cm^{-2} for GDE and 35 mA cm^{-2} or CCM MEA, respectively, which is slightly higher than that of GDE MEA. However, for air performance, CCM MEA and GDE MEA perform almost the same above 0.60 V, but at high current density region, beyond 750 mA cm^{-2}, CCM MEA performs much better than GDE MEA. From these results, it is clear that spraying method can fabricate a better quality MEAs. The performance of this kind of MEA is better than most reported PGM-Free MEAs tested under similar condition.

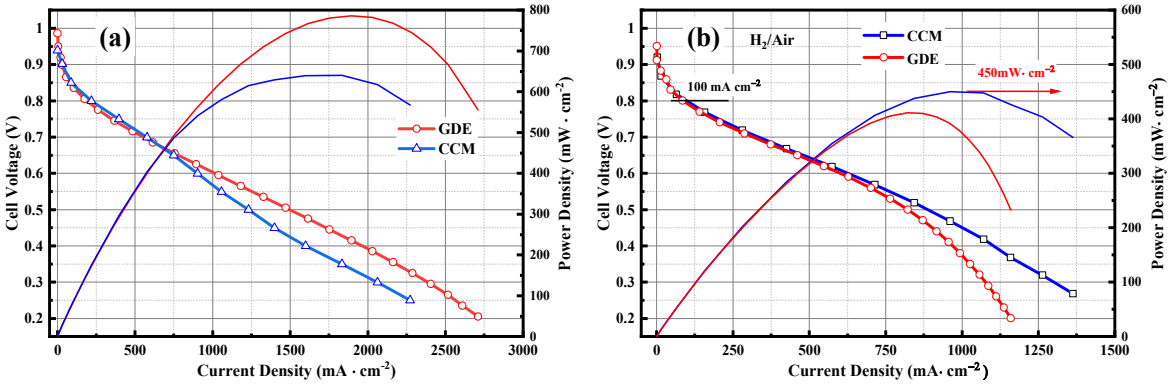

Figure 1. Polarization curves of MEAs made with GDE method versus CCM MEA, H_2-O_2, reactant flow rate:300/500 sccm H_2/O_2, (a) H_2-Air, reactant flow rate:500/1000 sccm H_2/Air. (b) MEA geometric active area: 5.0 cm^2; catalyst loading: 0.1 mg_{Pt} cm^2: 4 mg cm^2 (Anode: cathode=20% Pt/C (E-TEK): Fe-N-C- catalysts); membrane: NF212(H^+); temperature: 80/80/80 °C (Anode/Cell/Cathode); RH:100%, backpressure: 1.5 atm_{abs}; ionomer/carbon ratio: 0.8.

Ink Formulation

Three IPA/H_2O ratio were chosen, 1:1, 4:1 and 1:4 for the ink formulation for high water and low water and equal water content of three sets of conditions. MEAs made with three ratios were designated as 1:1-MEA,4:1-MEA and 1:4-MEA. For pure oxygen performance (i.e., H_2-O_2), 1:1-MEA and 1:4-MEA have the exact same performance until 0.55 V and slightly better performance for 1:1-MEA below 0.55 V while 4:1-MEA has much less performance than those two. For air performance, the order of performance is

1:1-MEA > 4:1-MEA > 1:4-MEA (Figure 2b). The mercury porosimetry data of these three MEAs explain well about the performance of these MEAs (Figure 2c). For all MEAs, the mesopore specific pore volume (mL/g) (table I) is in the order of 1:1-MEA (0.391) > 4:1-MEA (0.199) > 1:4-MEA (0.147), which perfectly demonstrate that the meso-pore is dominant for MEA performance in the high current density region. The micro-pore specific pore volume does not match the MEA performance trend, suggesting that the micro-pore has much less effect on the MEA performance. This also indicates that the mass transport of air mainly occurs within the meso-pore, not in micro-pores. Specifically, the optimization of ink formulation leads to a significant performance enhancement, for air, 1:1-MEA reaches 65.9 mA cm^{-2} at 0.8 V with the peak power density of 400 mW cm^{-2}. For the current density at 0.9 V $_{iR\text{-}Free}$, all three MEAs reach 32 mA cm^{-2} (close to DOE 2025 target, 44 mA · cm^{-2}). In addition to the polarization curves, high frequency impedance was measured for these three MEAs (Figure 2d). Interestingly, 1:1-MEA has the smallest semi-circles, indicating the lowest cathodic resistance (table II) which matches the pore structure as well as MEA performance. The mercury porosimetry and AC impedance data all suggest that the ink formulation indeed affects the structure of the catalyst layer, consequently, the performance. Specifically, in table III, the best performance was from the MEA that made by water- IPA (1-1) solvent. Here, we have high frequency resistance data and polarization data as well as mesopore percentage data all consistent to each other, demonstrated that our optimization work is solid and effective.

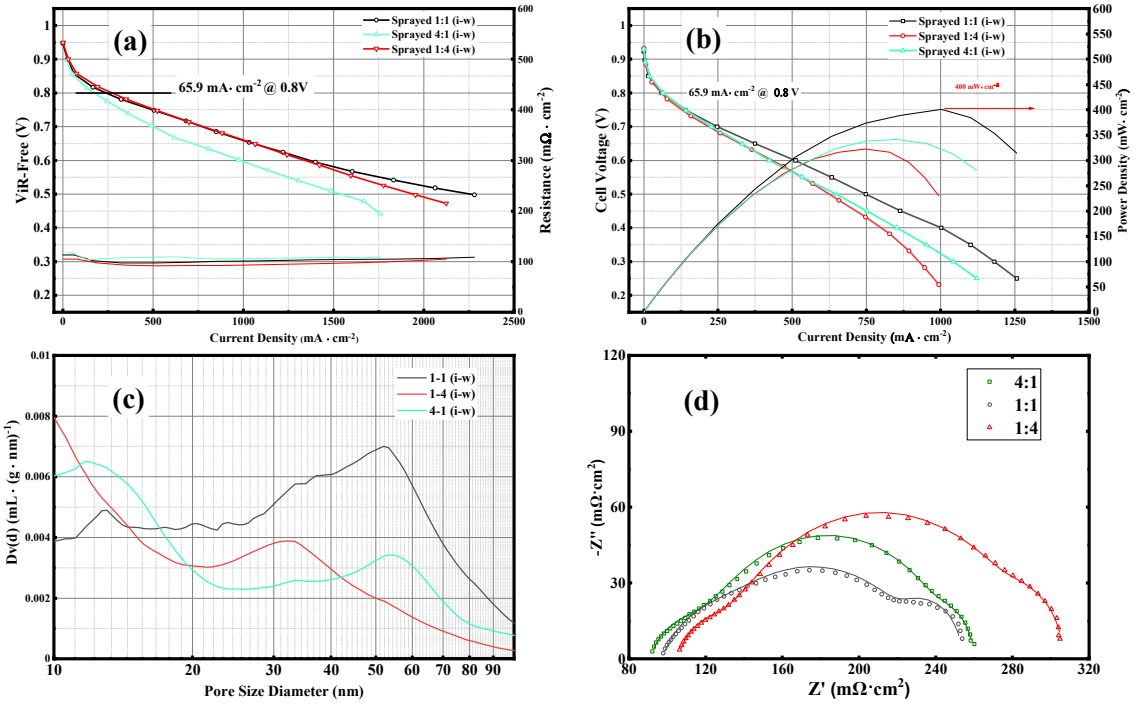

Figure 2. Polarization curves of MEAs made with Fe-N-C- catalysts using different IPA/H_2O, H_2/O_2, with IPA/ water ratio =1:1, 4:1, and 1:4, reactant flow rate:300/500 sccm H_2/O_2, (a) H_2/Air, reactant flow rate:500/100 sccm H_2/Air; (b) Mercury porosimetry results; (c) high frequency impedance (HFR) measurement results; (d) impedance measured at constant current, 1.0 A cm^{-2}, from 10000HZ to 10 HZ, after MEA polarization measurement. MEA geometric active area: 5.0 cm^2; catalyst loading: 0.1 mg_{Pt} cm^{-2}: 4 mg cm^{-2} (Anode: cathode=20% Pt/C (E-TEK): Fe-N-C- catalysts); membrane: NF212 (H^+); temperature: 80/80/80 °C (Anode/Cell/Cathode); RH:100%, backpressure: 1.5 atm_{abs}; ionomer/carbon ratio: 0.8.

TABLE I. Summary of the MIP test results for catalyst layer.

	IPA-water (1-1)	IPA-water (1-4)	IPA-water (4-1)
Pore volume 0-20nm (mL/g)	0.104	0.128	0.107
Pore volume 20-200nm (mL/g)	0.391	0.147	0.199
Mesopore percentage (%)	79.1	53.3	65.0

TABLE II. Summary of the HFR test results for catalyst layer.

water/i-Pa	R_{Ω}	R_{anode}	$R_{cathode}$	R_{mt}
4:1	91.0	30.4	127.3	11.7
1:1	97.3	37.6	90.9	28.6
1:4	105.5	24.5	159.7	18.1

After ink formulation, we focused on the I/C ratio of the catalyst layer of MEA. Excessively high I/C ratio could cause a series mass transfer issue while too low I/C ratio could undermine the utilization of catalyst because the ionomer coverage over catalyst surface could be insufficient, particular, when I/C ratio drop to a certain level. In this case, the most optimized I/C ratio should be applied on MEA to utilize active sites as much as possible while keeping enough proton conductivity and maintaining a good mass transfer rate. To find the best I/C ratio, 4 MEAs made by Fe-C-N PGM-Free catalyst in different I/C ratio, 0.8, 0.7, 0.6 and 0.5 using 1:1 (IPA: water) as solvents for the catalyst ink were tested. The MEAs behave similar in low current density (LCD) region while quite difference appears when current density is beyond 1000 mA cm^{-2}, in the high current density region (HCD). In this region, the MEA performance increased with decreased I/C ratio (Fig. 3a) and reached maximum at I/C=0.6, further drop of I/C ratio to 0.5 did not result in any improvement. The lower I/C ratio may benefit the mass transport on both O_2 diffusion through the ionomer film and pore structure (i.e., more pore volume) while it may lead to lower catalyst utilization, lower mass activity due to less coverage of ionomer over the catalyst particle (table III). Further decrease of I/C ratio did not improve HCD MEA performance too much (Fig. 3a) which may be limited by the proton conduction (further improve O_2 diffusion through ionomer film but may suffer the reduction on proton conduction due to less ionomer film). The Tafel analysis (Figure 3b and Table III) shows that too much ionomer causes lower Tafel slope, the lowest Tafel slope is 41.7 mV/dec for the highest I/C ratio, 0.8, which may be caused by too thick ionomer film, increasing the O_2 diffusion barrier at LCD region, causing the mass transport at LCD region. The lower Tafel slops of PGM-Free catalyst MEA, 40s mV/dec, indicates that their serious mass transport issue for PGM-Free catalyst MEAs while PGM catalyst MEA usually have Tafel slope around 68 or 72 mV/dec.

TABLE III. Summary of Figure.2.

I/C ratio	Current density @ 0.9 $V_{iR\text{-}Free}$ in O_2 ($mA \cdot cm^{-2}$)	Current density @ 0.8 V in air ($mA \cdot cm^{-2}$)	Peak power density in air ($mW \cdot cm^{-2}$)	Tafel slope (mV/dec.)
0.5	35	120	548	-50.4
0.6	44.9	116	525	-46.2
0.7	37	103	490	-48.7
0.8	44.6	84	480	-41.7

For the air performance, the MEA performance increased with the decreased I/C ratio, in both LCD and HCD regions, consequently, peak power density (Figure 4 and Table III). This is easy to understand because the mass transport of oxygen in nitrogen blanket is the major issue for PGM-Free catalyst MEAs, the lower I/C ratio led to the catalyst layer with thinner ionomer film, which facilitates the O_2 diffusion through the ionomer film, leading to better performance. It is worthwhile to point out that 120 mA cm^{-2} at 0.80 V has been reached which is close to the DOE target of 150 mA cm^{-2}. It seems that there is still room to increase the current density at 0.80 V and we may try to further optimize the I/C ratio. Additionally, peak power density of 0.6 and 0.5 I-C ratio MEA exceed 500 mW cm^{-2}.

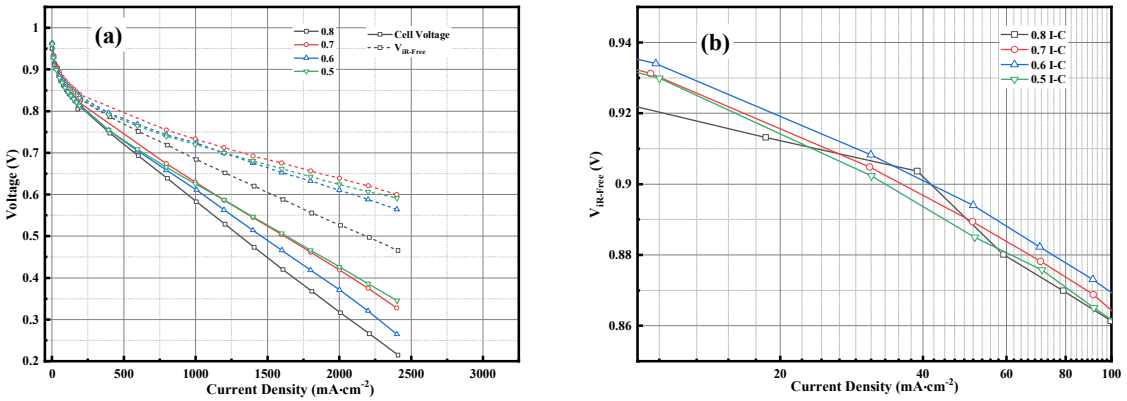

Figure 3. Polarization curves of MEAs made with different I/C ratio using Fe-N-C-catalysts, H_2-O_2, reactant flow rate: 300/500 sccm H_2/O_2; (a) Tafel Plot of (b) from 0.90 V-0.94 V VIR curve in (a). MEA geometric active area: 5.0 cm^2; catalyst loading: Cathode: PGM-Free 4 mg cm^{-2}, and anode: 0.1 mg_{Pt} cm^{-2} (Anode: cathode = 20% Pt/C (E-TEK): Fe-N-C-catalysts); membrane: NF212(H^+); temperature: 80/80/80 °C (Anode/Cell/Cathode); RH:100%, backpressure: 1.5 atm_{abs}; ionomer/carbon ratio: 0.8, 0.7, 0.6, 0.5.

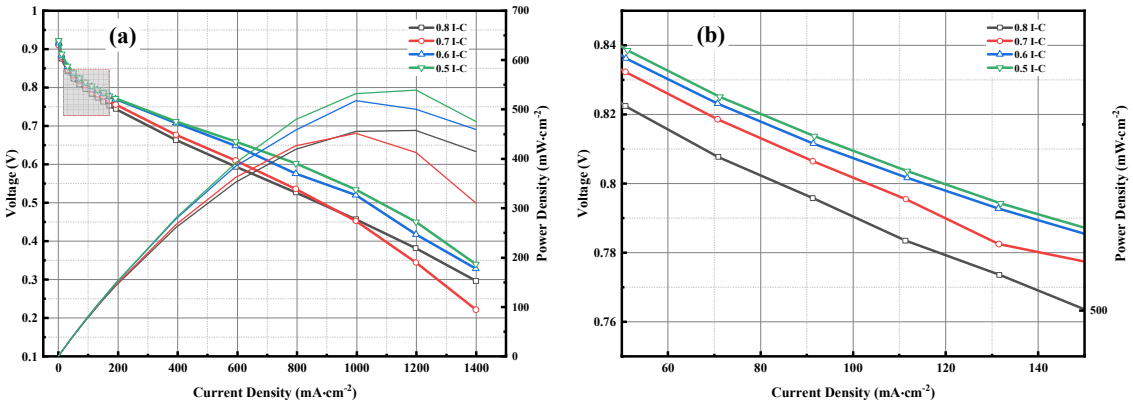

Figure 4. Polarization curves of MEAs made with Fe-N-C- catalysts using different I/C ratio, reactant flow rate: 300/500 sccm H_2/Air, (a); zoom in of polarization curves in (a) for 0.8V(b). MEA geometric active area: 5.0 cm^2; catalyst loading: 0.1 mg_{Pt} cm^{-2}: 4 mg cm^{-2} (Anode: cathode=20% Pt/C (E-TEK): Fe-N-C-catalysts); membrane: NF212(H^+); temperature: 80/80/80 °C (Anode/Cell/Cathode); RH:100%, backpressure: 1.5 atm_{abs}; Ionomer/carbon ratio: 0.8, 0.7, 0.6, 0.5.

Conclusion

The optimized MEA fabrication method based on spraying is successfully developed. The ink formulation reveals the property-structure-performance relationship and the optimization of I/C ratio leads to the much improved MEA performance. The mass activity of MEAs reaches 44.9 mA cm^{-2} at 0.9 $V_{IR\text{-}Free}$ (H_2/O_2) exceeds the 2025 DOE target, 44 mA cm^{-2}.

Leave two lines of space between sections.

References

1. X. X. Wang, M. T. Swihart, and G. Wu, *Nat. Catal.*, **2**, 578 (2019).
2. R. Devanathan, *Energy Environ. Sci.*, **1**, 101 (2008).

Chapter 15

Non-PGM Catalysts - Digital Session

ECS Transactions, 104 (8) 337-344 (2021)
10.1149/10408.0337ecst ©The Electrochemical Society

Noble Metal-Added Titanate Nanosheets for PEFC Cathode

Y. Takeuchi[a], K. Matsuzawa[b], T. Nagai[c], K. Ikegami[c],
Y. Kuroda[b, c], R. Monden[c], and A. Ishihara[c]

[a] Graduate School of Engineering Science, Yokohama National University, Yokohama, Kanagawa, 240-8501, Japan
[b] Graduate School of Engineering, Yokohama National University, Yokohama, Kanagawa, 240-8501, Japan
[c] Institute of Advanced Sciences, Yokohama National University, Yokohama, Kanagawa, 240-8501, Japan

Improvement of the activity of the oxygen reduction reaction (ORR) at a polymer electrolyte fuel cell (PEFC) cathode is one of the serious problems to widespread PEFCs. We focused on Rh- or Pd-doped titanate nanosheets (TiNSs) to form the appropriate electron conduction path using tunneling effect of electrons and high quality active sites with Rh or Pd doping. To apply the tunneling effect of electrons to TiNSs, TiNSs were attempted to be supported on vapor growth carbon fiber (VGCF) with a large diameter. The surface of the VGCF was modified by poly (diallyl dimethylammonium) chloride (PDDA) as polycation because the TiNSs were anionic. The electrostatic interaction improved slightly the contact between the PDDA modified VGCF and the TiNSs to increase the ORR activity of the TiNSs. Rh- or Pd-added TiNSs were successfully synthesized via the solid phase method and ionic exchange reaction processes.1 atomic % addition of Rh and Pd was found to be effective to enhance the ORR activity of the TiNSs.

Introduction

A large overpotential of oxygen reduction reaction (ORR) at a cathode in polymer electrolyte fuel cells (PEFCs) is one of the serious problems to decrease the energy conversion efficiency. Nørskov's group reported that even Pt which is currently used as an ORR catalyst cannot reach the theoretical oxygen electrode potential of 1.23 V at room temperature (1). The adsorption energies of the intermediate oxygenated species in the ORR cannot take the appropriate values on the noble metal surfaces. On the other hand, Yamamoto et al. recently suggested that noble metal added titanium dioxides (TiO_2) can reach the theoretical potential by changing the absorption energies of the ORR intermediates according to the first-principle calculation (2). This was due to the high degree of freedom of titanium oxides, including their various crystalline structures and electronic states. However, the continuous electron supply to the active sites was not considered in the first-principle calculation. It is difficult to form the sufficient electron conduction path from supports to active sites on the TiO_2 because TiO_2 has low conductivity due to a large band gap.

Then, we think that there are two important points to reach the theoretical potential using titanium oxide-based catalysts. One is to form the electron conduction path between

the electro-conductive supports and the active sites on the catalyst surface. Another is to form the active sites which can optimize the adsorption energies of the intermediates on the catalyst surface. Needless to say, these two formations such as the appropriate electron conduction path and the high quality active sites are simultaneously required to obtain high ORR activity. Then, we attempted to apply "tunneling effect of electrons" to form the electron conduction path between the supports and the active sites on the catalyst surface. The tunnelling effect of electrons occurs when the thickness of the films of insulators such as TiO_2 is less than several nanometers. In case of titanium compounds, we focused on titanate nanosheets which are generally composed of very thin titanate layer with the thickness of less than several nanometers. In addition, nanosheets have a high surface area originated from their 2D structure (3). The high surface area is essential to obtain a large ORR current. In this study, we chose $[Ti_3O_7]^{2-}$ nanosheets because the preparation method of the nanosheets was well known and nanosheets with a huge size were easily obtained. The $[Ti_3O_7]^{2-}$ nanosheets (designated as TiNSs) were prepared by an exfoliation of $Na_2Ti_3O_7$ with layered titanate structure, which synthesized by solid state reaction (4).

Because the TiNSs were essentially insulators, the formation of electron supply path to the active sites was required. Therefore, we attempted to form the electron supply path using non-doping TiNSs. First, the direct dispersion of the TiNSs on the top of the GC-rod was examined. Then, the highly dispersion on the electric conductive supports was examined using thick carbon nanofiber such as vapor growth carbon fiber (VGCF) with a large diameter of ca. 150 nm as a support. Because TiNSs are anionic, the modification of polycation of the surface of the VGCF is expected to improve the adhesion through positive and negative electrostatic interactions. In this study, poly (diallyl dimethylammonium) chloride (PDDA) was selected as the polycationic agent according to the previous study (5). No surface treated VGCF (As received) and mixed acid treated VGCF were also prepared to compare the effect of the modification of PDDA.

On the other hand, we need to attempt to form the active sites by the doping of noble metals such as Rh or Pd. Rh-added TiNSs were prepared by solid phase method according to the previous paper (6). Because there is almost no research about the Pd-added TiNSs, the similar preparation method was applied to the preparation of the Pd-added TiNSs. Pd can be reduced easier than Rh, so that the heat-treatment condition was changed to prevent the deposition of metallic Pd particles. In addition, because noble metals such as Pd and Rh have relatively high ORR activities, the effect of deposition of Rh or Pd on TiNSs should be investigated. From this point of view, the solid-solubility limits of Rh or Pd into TiNSs were required to evaluate. In this study, we attempted to synthesize Rh- or Pd-added TiNSs and evaluated the solid-solubility limits of Rh or Pd and the ORR activities to obtain the principle of the formation of the active sites by noble metals.

Experimental

Rh or Pd-added $Na_2Ti_3O_7$ was synthesized by the solid-state reaction according to previous paper (6). Noble-metal added $Na_2Ti_3O_7$ was designated as $Na_2Ti_3O_7$:Mx where M was Rh or Pd and x was atomic % of M against Ti. Na_2CO_3 (Fujifilm Wako Pure. Inc., 99.8 %), TiO_2 (US Nano Research, 99.0 %, Anatase), and Rh_2O_3 (Fujifilm Wako Pure. Inc., 98.0%) or PdO (Sigma Aldrich, 99.97%) were mixed and grinded in a mortar. The mixture with Rh_2O_3 addition was calcined at 900 °C in air for 24 h (6). Whereas the mixture with

PdO addition was calcined at 800 °C in O_2 for 48 h to prevent the decomposition of metal Pd. In both cases, these processes were repeated two times. The amount of Rh or Pd was adjusted with the atomic ratio against Ti of 0, 1, 5, and 10. To evaluate the effect of addition of Rh or Pd, TiNSs without Rh or Pd were calcined at 900 °C in air for 24 h or at 800 °C in O_2 for 48 h two times, respectively.

To obtain titanate nanosheets (designated as TiNSs), ionic exchange reactions were proceeded to obtain negatively charged titanate nanosheets as colloidal suspension (3). The synthesized Rh or Pd-added $Na_2Ti_3O_7$ powder was immersed in 1.0 mol dm^{-3} hydrochloric acid for exchanging the counter cation Na^+ to H^+ and shaken for three days continuously at room temperature. The Rh or Pd-added $H_2Ti_3O_7$ powder was filtered and washed by ultrapure water and dried at 60 °C under the vacuum condition for a day. The Rh or Pd-added $H_2Ti_3O_7$ powder was immersed by methylamine aqueous solution and shaken for a week to obtain the Rh or Pd-added $(CH_3NH_2)_2$-Ti_3O_7 powder. This powder was dispersed in a tetramethylammonium aqueous solution (TMAOH) by shaken for a week to exfoliate sufficiently the Rh or Pd-added $[Ti_3O_7]^{2-}$ nanosheets (This nanosheets was designated as TiNS:Mx where M was Rh or Pd and x was atomic % of M against Ti). Non-exfoliated TiNS:Mx was removed by the centrifugation at 3000rpm for 15 min. Finally, TiNS:Mx was obtained as colloidal suspension dispersed in TMAOH solution.

Vapor Growth Carbon Fiber (VGCF; Average diameter: 150 nm, Average length: 8 μm, BET surface area: 13 m^2 g^{-1}, Specific resistance: 1×10^{-4} Ω cm, SHOWA DENKO K.K.) was used as a support to form an electric conduction path from support to active site on the surface of the TiNS:Mx. Three types of VGCF were prepared; non-treated (designated as VGCF), immersed in mixed acid solution (sulfuric acid of 75 cm^3 was mixed with nitric acid of 25 cm^3) at 70 °C for 24 h (designated as VGCF-MA), and mixed acid with Poly (diallyl dimethylammonium) chloride (PDDA) solution (designated as VGCF-MA-PDDA).

The catalyst powder was dispersed into 1-propanol (150 cm^3) and 5wt% Nafion® solution (0.005 cm^3) to prepare a catalyst ink. The ink was dropped on a glassy carbon rod (GC-rod; φ = 5.2 mm, TOKAI CARBON CO., LTD.) and dried at 60 °C for an hour.

Electrochemical measurements were performed in 0.5 mol dm^{-3} H_2SO_4 at 30 °C with a conventional 3-electrode cell. A reversible hydrogen electrode (RHE) and a glassy carbon plate was used as used as a reference and counter electrode, respectively. Cyclic voltammetry for 300 cycles was performed at a scan rate of 150 mV s^{-1} from 0.05 V to 1.2 V vs. RHE under N_2 as pretreatment. Slow scan voltammetry (SSV) was performed at a scan rate of 5 mV s^{-1} from 0.2 V to 1.2 V vs. RHE under O_2 and N_2. The ORR current (i_{ORR}) was determined by calculating the difference between the current under O_2 and N_2. The current density was based on the total mass of catalyst such as TiNS:Mx with carbon materials.

The crystalline structures of the Rh or Pd-added $Na_2Ti_3O_7$ were investigated by X-ray diffraction (XRD, Rigaku, UltimaIV) for phase identification. The morphology was investigated by Transmission Electron Microscope (TEM, JEOL, JEM-2100F) and Scan Electron Microscope and Energy Dispersion X-ray spectrum analysis (SEM-EDX, JEOL, JCM-7000).

Results and Discussion

Figure 1 shows the bright-field TEM image of TiNSs calcined at 900 °C in air for 24 h two times. The TiNSs were successfully synthesized with a large horizontal size of an order of several micrometers. Although the TiNS has large surface area, several sheets seemed to be stacked. Because the TiNSs were essentially insulators, the formation of electron supply path to the active sites was required. Therefore, we attempted to form the electron supply path using non-doping TiNSs calcined at 900 °C in air for 24 h two times. First, the direct dispersion of the TiNSs on the top of the GC-rod was examined.

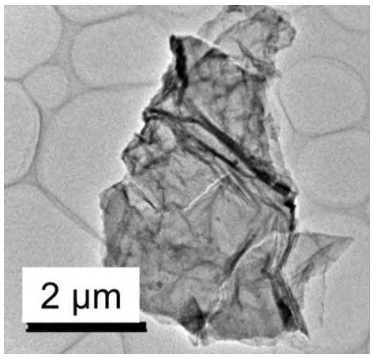

Figure 1 TEM image of TiNSs calcined at 900 °C in air for 24 h two times.

Figure 2 shows the ORR polarization curve of TiNSs supported on GC-rod in 0.5 mol dm^{-3} H_2SO_4 at 30 °C with a scan rate of 5 mV s^{-1}. For comparison, the i_{ORR}-E curve of GC-rod was also plotted. Surprisingly, the ORR activity of TiNSs supported on GC-rod was lower than that of the GC-rod only. This might be responsible for the agglomeration the TiNSs not to highly disperse on the GC-rod. Because the electron conductivity of TiNSs was very low, the agglomerated TiNSs covered on the GC-rod to decrease the electrochemical efficient surface area of the GC-rod. Therefore, the TiNSs were attempted to highly disperse on the electron conductive support. In this study, we chose the thick carbon nanofiber such as VGCF with a large diameter of ca. 150 nm as a support. Although it might be insufficient to highly disperse TiNSs on the VGCF because of a large horizontal size of the TiNSs of an order of several micrometers, the electron conduction of catalysts was expected to improve as much as possible. As described in introduction, the effect of surface treatment of the VGCF was investigated.

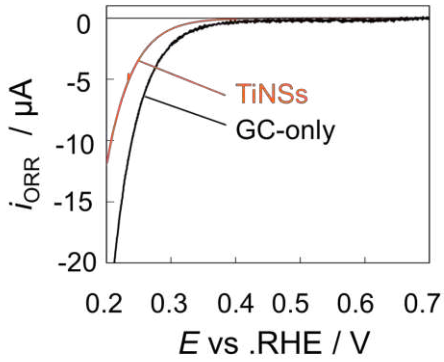

Figure 2. ORR polarization curves of GC-rod with and without TiNSs in 0.5 mol dm^{-3} H_2SO_4 at 30 °C with a scan rate of 5 mV s^{-1}.

Figure 3(a) shows the ORR polarization curves of the TiNSs supported on VGCF with various surface treatment in 0.5 mol dm^{-3} H_2SO_4 at 30 °C with a scan rate of 5 mV s^{-1}. The TiNSs supported on VGCF with no surface treatment (TiNSs/VGCF) showed the lowest ORR activity. Although the onset potential of the TiNSs supported on VGCF with MA treatment (TiNS/VGCF-MA) for the ORR was almost the same as that of the TiNS/VGCF, the ORR current density slightly increased. The mixed acid treatment of VGCF had a small effect on the ORR activity. On the other hand, the onset potential of the TiNSs supported on VGCF with MA and PDDA treatment (TiNS/VGCF-MA-PDDA) increased approximately 0.2 V and the ORR current density at 0.5 V increased by ten times over compared to that of the TiNS/VGCF and the TiNS/VGCF-MA. Saito et al. reported the ORR activity of TiNSs supported on Vulcan XC-72 (7), and its ORR activity was almost the same as the TiNS/VGCF as shown in Fig. 3. Because the surface of the TiNSs is negatively charged, the electrostatic interaction between the positive charge by PDDA and TiNSs may improve the electrical contact and contribute to form the electron conduction path. These results revealed that the surface treatment of carbon supports strongly affected the onset potentials and the ORR current densities. In addition, the ORR polarization curve of the TiNS/VGCF-MA-PDDA revealed that the TiNSs without no addition had some ORR activity.

Figure 3(b) shows the TEM image of the TiNS/VGCF-MA-PDDA to observe the contact between the TiNSs and the VGCF-MA-PDDA. The cylindrical rod form corresponded to the VGCF-MA-PDDA. The shape of the VGCF-MA-PDDA was almost straight. The VGCF-MA-PDDA and the TiNSs were contact partially, and some TiNSs were stacked on each other, indicating that the contact interface between the TiNSs and the VGCF-MA-PDDA was not well controlled. It will be necessary to control the interface by improving the adhesion between the TiNSs and the conductive support such as VGCF, or by making the small size of TiNSs. Although the contact between the TiNSs and the VGCF-MA-PDDA was insufficient, we attempted to evaluate relatively the effect of Rh or Pd addition into the TiNSs using the VGCF-MA-PDDA as a support.

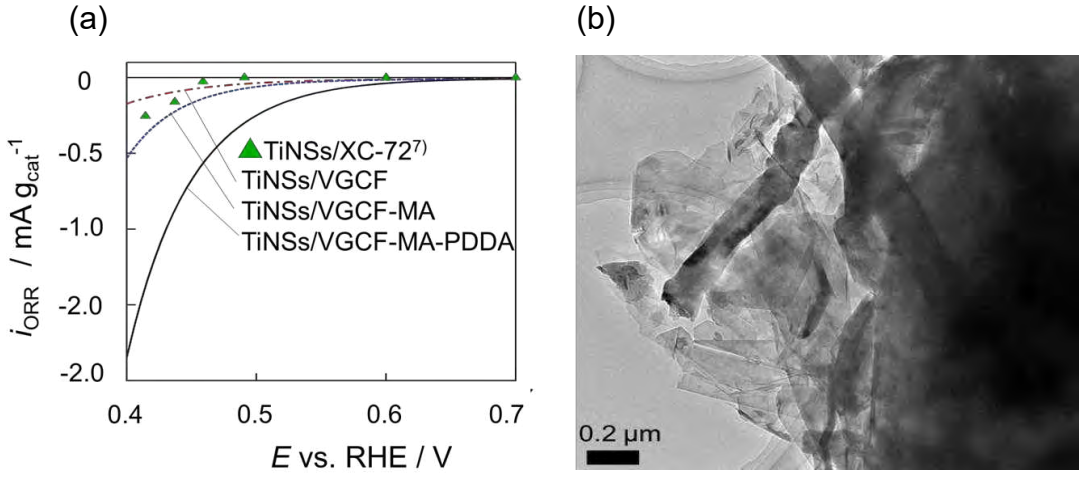

Figure 3. (a) ORR polarization curves of the TiNS supported on VGCF with various surface treatment in 0.5 mol dm^{-3} H_2SO_4 at 30 °C with a scan rate of 5 mV s^{-1}. (b) TEM image of the TiNS/VGCF-MA-PDDA.

We attempted to synthesize the Rh- or Pd-added TiNSs and evaluate the solid-solubility limits of the Rh or Pd into TiNSs. The XRD patterns of the $Na_2Ti_3O_7$ with 0, 1, 5, and 10 atomic% of Rh or Pd addition are shown in Fig. 4 (a) and (b), respectively. The main phase was confirmed to be $Na_2Ti_3O_7$ in both the Rh- and Pd-added $Na_2Ti_3O_7$ diffraction patterns. The reduced metallic phases of both Rh and Pd were not observed in the XRD patterns, suggesting that the calcination conditions for the formation of the layered titanate structure were appropriate to prevent the reduction of the noble metals. The ionic radii of Rh^{3+} (0.665 nm) and Pd^{2+} (0.86 nm) are larger than that of the Ti^{4+} (0.605 nm) (8). The larger ionic radii make it difficult to substitute the Ti^{4+} in the titanate layered structure. Therefore, noble metal oxides such as Rh_2O_3 or PdO were possible to deposit in the large content of Rh and Pd.

As shown in Fig. 4(b), in the case of Pd, the XRD peaks identified as PdO were clearly observed in the $Na_2Ti_3O_7$:Pd5 and $Na_2Ti_3O_7$:Pd10. In the case of Rh, Fig. 4(c) shows the magnified patterns of Fig. 4(a). Small peaks identified as Rh_2O_3 were observed in the XRD pattern of the $Na_2Ti_3O_7$:Rh10. These XRD patterns indicate that the appropriate doping amounts of Rh and Pd by the solid phase method are at least less than 10 at% and 5 at%, respectively. A larger amount of Rh can be doped than Pd. This tendency corresponds to the difference of the ionic radii of Rh^{3+} (0.665 nm) and Pd^{2+} (0.86 nm). The ionic radius of Pd^{2+} is much larger than that of Ti^{4+} (0.605 nm).

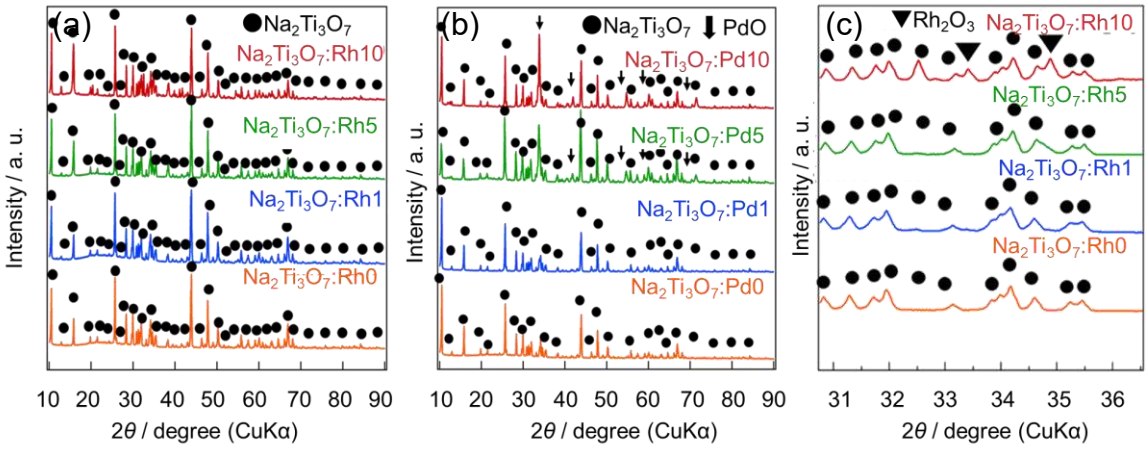

Figure 4. XRD Patterns of the $Na_2Ti_3O_7$: (a) Rh and (b) Pd. (c) the magnified patterns of (a).

Figure 5 shows that SEM images (Back Scattered Electron compositional images; BSE images) of (a) $Na_2Ti_3O_7$:Rh10 and $Na_2Ti_3O_7$:Pd10. The atomic number increases, the greater generation of the back scattered electrons. Thus, Rh_2O_3 and PdO particles were brighter than $Na_2Ti_3O_7$. In the BSE images, Rh_2O_3 and PdO were observed as white particles as shown in Fig. 5(a) and (b). $Na_2Ti_3O_7$ crystals were observed prismatic shape as reported (9), and Rh_2O_3 and PdO particles were observed on the surface of the $Na_2Ti_3O_7$. The particle sizes of Rh_2O_3 and PdO were a micrometer order, suggesting that Rh_2O_3 and PdO were agglomerated during the high temperature and long-time treatments. This BSE observation corresponded to the existence of Rh_2O_3 and PdO indicated by the XRD patterns.

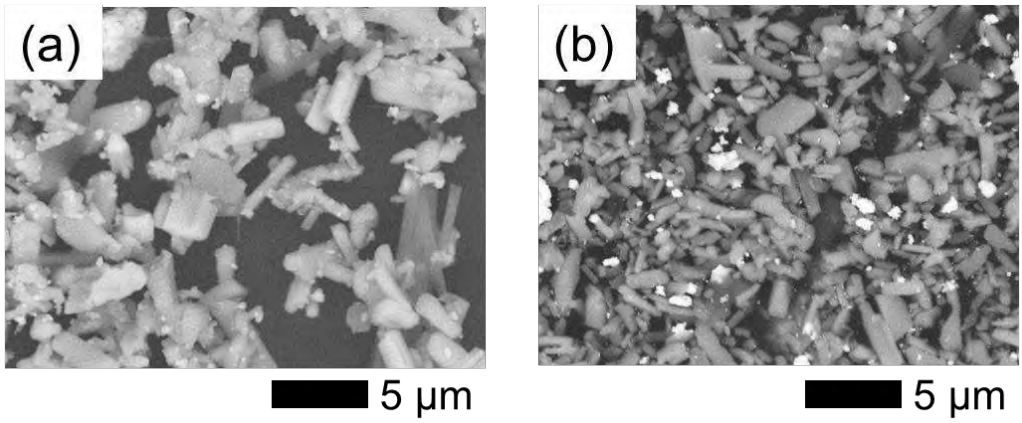

Figure 5. BSE images of (a) $Na_2Ti_3O_7$:Rh10 and $Na_2Ti_3O_7$:Pd10.

Figure 6 (a) and (b) show that the ORR polarization curves of the Rh- and Pd-added TiNSs catalysts supported on the VGCF-MA-PDDA. In Fig. 6(a) and (b), although the expression of "VGCF-MA-PDDA" was omitted, the catalysts were supported on the VGCF-MA-PDDA. TiNS:Rh0 and TiNS:Pd0 were calcined at 900 °C in air for 24 h and at 800 °C in O_2 for 48 h two times, respectively. For comparison, the results for the VGCF-MA-PDDA without nanosheet are also shown. In the case of Rh, the ORR activities of the TiNS:Rh0 and the TiNS:Rh5 are low comparable to that of VGCF-MA-PDDA as shown in Fig. 6(a). The TiNS:Rh10 showed a dramatic improvement in the onset potential and the ORR current density. The onset potential increased to almost 0.8 V. According to the XRD pattern and the BSE image, the TiNS:Rh10 shows the deposition of Rh_2O_3. Saida et al. reported that the onset potential for the ORR of Rh_2O_3 supported on Ketjenblack (10) was almost the same as our result, so that the dramatical improvement of the ORR activity of the TiNS:Rh10 may be responsible for the Rh_2O_3. However, the ORR activity of the TiNS:Rh1 slightly increased even the amount of added Rh was less than TiNS:Rh5. The enhancement may be due to the doping of Rh into titanate nanosheets.

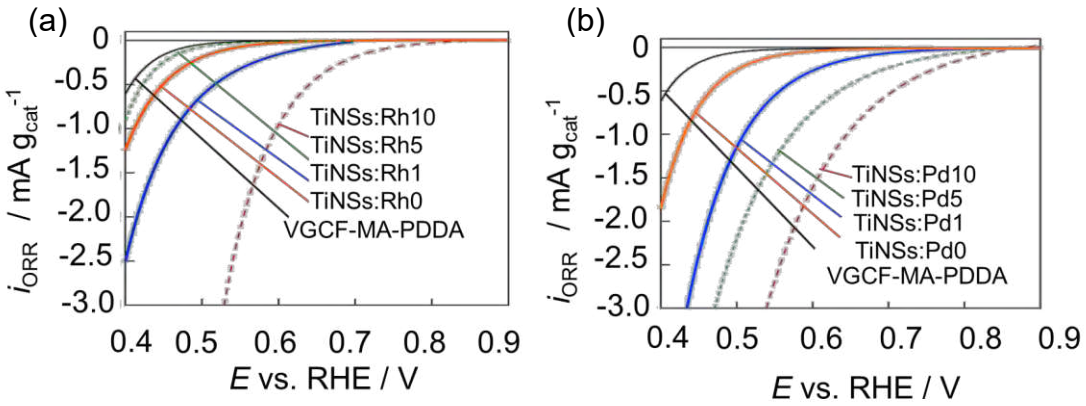

Figure 6. ORR polarization curves of (a) Rh-added and (b) Pd-added TiNSs supported on the VGCF-MA-PDDA in 0.5 mol dm^{-3} H_2SO_4 at 30 °C with a scan rate of 5 mV s^{-1}.

In the case of Pd addition, as shown in Fig. 6(b), the onset potential for the ORR and the ORR current density increased in the amount of Pd addition. The onset potential of the TiNS:Pd10 increased to 0.85 V. However, according to the XRD patterns and BSE image, because the TiNS:Pd5 and TiNS:Pd10 showed the deposition of PdO, their ORR activities might be due to the PdO. An et al., reported that the onset potential for the ORR of Pd/C

was almost 0.9 V (11), suggesting that our results were almost corresponded to Pd/C. On the other hand, the TiNS:Pd1 shows a drastic increase in the ORR activity compared to TiNs:Pd0. In both cases of Rh and Pd, 1 atomic % additions were effective to enhance the ORR activity. Thus, we need to investigate the Rh and Pd addition of 1 atom% and around into the TiNSs.

Conclusion

The applicability of $[Ti_3O_7]^{2-}$ nanosheets to ORR catalysts were investigated. The following points are found to apply the TiNSs to PEFC cathode.

(1) TiNSs with horizontal size of more than 10 μm were successfully synthesized.
(2) Because TiNSs are negatively charged, the modification of polycation of the surface of the VGCF was found to be effective to improve the adhesion through positive and negative electrostatic interactions to increase in the ORR activity.
(3) The solid-solubility limits of Rh or Pd into TiNSs by the solid phase method are at least less than 10 at% and 5 at%, respectively.
(4) Rh- or Pd-added TiNSs were successfully synthesized via the solid phase method and ionic exchange reaction processes.
(5) 1 atomic % addition of Rh or Pd was effective to enhance the ORR activity of the TiNSs.

Acknowledgments

The authors thank the New Energy and Industrial Technology Development Organization (NEDO) for their financial support. This work was partly supported by TOKYO CITY UNIVERSITY Interdisciplinary Research Center for Nano Science and Technology for instrumental analysis.

References

1. A. Kulkarni, S. Siahrostami, A. Patel, and J. K. Nørskov, *Chem. Rev.*, **118**, 2302 (2018).
2. Y. Yamamoto, S. Kasamatsu, and O.Sugino, *J. Phys. Chem. C*, **123**, 19486 (2019).
3. R. Ma and T. Sasaki, *Adv. Mater.*, **22**, 5082 (2010).
4. H. Izawa, S. Kikkawa, and M. Koizumi, *J. Phys. Chem.*, **86**, 5023 (1986).
5. T. Sasaki, Y. Ebina, M. Watanabe, and G. Decher, *Chem. Commun.*, **21**, 2163 (2000).
6. W. Soontornchaiyakul, T. Fujimura, and R. Sasai, *RSC Adv.*, **7**, 21790 (2017).
7. M. Saito, Y. Akeboshi, N. Ohno, J. Kuwano, H. Shiroishi, and Y. Uchimoto, *ECS Trans.*, **16**(25), 97 (2009).
8. R. D. Shannon., *Acta. Cryst.*, **A32**, 751 (1976).
9. A-L. Sauvet, S. Baliteau, C. Lopez, and P. Fabry, *J. Solid State Chem.*, **177**, 4508 (2004).
10. T. Saida, S. Hirano, E. Niwa, F. Sato, and M. Maruyama, *ECS Trans.*, **85**(13), 865 (2018).
11. L. An, Y. Chen, J. Shi, J. Cao, B. Liu, and J. Yang, *Front. Chem.*, **6**, 596 (2018).

Chapter 16

Poster Session

ECS Transactions, 104 (8) 347-357 (2021)
10.1149/10408.0347ecst ©The Electrochemical Society

Preparation of PEFC Electrocatalysts Using SnO_2 Thin Layer Support

Y. Inoue[a], Z. Noda[b], J. Matsuda[b,c], M. Nishihara[c,d], A. Hayashi[a-d], and K. Sasaki[a-f]

Kyushu University
[a] Faculty of Engineering, Department of Hydrogen Energy Systems,
[b] International Research Center for Hydrogen Energy,
[c] Next-Generation Fuel Cell Research Center (NEXT-FC),
[d] Platform of Inter / Transdisciplinary Energy Research (Q-PIT),
[e] International Institute for Carbon-Neutral Energy Research (WPI-I2CNER),
[f] Center of Coevolutionary Research for Sustainable Communities,
Motooka 744, Nishi-ku Fukuoka 819-0395, Japan

Pt/C is widely used as a PEFC electrocatalyst. However, Pt detachment and aggregation due to carbon support corrosion can occur. Therefore, the conventional Pt/C electrocatalyst has a difficulty in durability. We have developed Pt-based electrocatalysts dispersed on graphitized carbon black (GCB) coated with SnO_2 thin layer support, achieving both high activity and high durability. Here in this study, Pt-Co alloy based electrocatalysts, $Pt_3Co/Sn_{0.98}Nb_{0.02}O_2$/GCB, are prepared. XRD measurement confirmed that the catalyst was supported on the oxide. STEM analysis confirmed the alloying of Pt with Co. The catalytic activity was characterized by half-cell electrochemical measurements. The electrochemical activity and pore structure were examined by preparing membrane electrode assemblies (MEA) using $Pt_3Co/Sn_{0.98}Nb_{0.02}O_2$/GCB as the cathode catalyst.

Introduction

Pt/C is widely used as an electrocatalyst in polymer electrolyte fuel cells (PEFC), where Pt is highly dispersed on carbon black or mesoporous carbon. However, carbon-based materials are likely to be electrochemically oxidized under high potential conditions at the cathode, which leads to degradation of the electrocatalysts. Therefore, the conventional Pt/C electrocatalyst has a difficulty in durability (1-3). The use of conductive oxides such as SnO_2 and TiO_2 as electrocatalyst supports has been proposed (4-7). To mention a few, Matsumoto et al (7) developed electrocatalysts with tin oxide (SnO_2) supports where vapor-grown carbon fibers act as conducting backbones, achieving both high ORR activity and high durability. However, their electrocatalytic activity has to be further improved. Here, we are focusing on the use of highly conductive GCB as the support framework and Pt-Co alloy catalysts to further increase the catalytic activity. Co is one of the relatively stable metals in the PEFC environment, and Pt-Co alloy catalysts are known to be capable of exhibiting higher activity over pure Pt catalysts (8, 9). The aim of this study is to develop active electrocatalysts with higher durability by depositing Pt_3Co alloy catalyst particles on Nb-doped SnO_2 thin layer support, $Sn_{0.98}Nb_{0.02}O_2$/GCB.

Experimental

Support Materials Preparation

GCB (GCB200, Cabot) with high graphitization, spherical shape, and high electrical conductivity was used as the conductive backbone. First, Nb-doped SnO_2 was prepared on the GCB by the ammonia co-precipitation method. Nb doping concentration was fixed to be 2% due to the highest electronic conductivity ($Sn_{0.98}Nb_{0.02}O_2$/GCB) reported (10). $SnCl_2{\cdot}2H_2O$, $NbCl_5$ ethanol solution, and then diluted NH_3 solution (in 5 mL/min) were added to the ethanol dispersion of GCB ball-milled for 1 h. The precipitates were then dispersed in pure water and filtered three times, dispersed in ethanol and filtered once, and dried at 100 °C for 10 h. After dry milling, these powder samples were then heat-treated in N_2 at 600 °C for 2 h after dry milling. Agglomeration was suppressed by additional ball milling for 30 min after the heat treatment. The amount of SnO_2 deposited on the GCB was controlled to set the SnO_2 loading to be 70 wt.% to maintain a large specific surface area of SnO_2 without SnO_2 aggregation and to secure a conductive pass among GCB.

Electrocatalysts Preparation

Co-impregnation of Pt-Co nano-particles was made using their acetylacetonate (acac) complexes (11) to prepare Pt_3Co. In this procedure, rotary evaporator was used with depressurization and rotation function. After mixing the $Sn_{0.98}Nb_{0.02}O_2$/GCB powder and the acac reagents, the mixture was stirred in the organic solvent, acetylacetone. After all the solvents were evaporated upon ultrasonical stirring, the powder samples were heat-treated in N_2 at 210 ºC for 3 h, 240 ºC for 3 h, and then 270 ºC for 1 h (here after, denoted as 210ºC→240°C→270ºC).

Characterization of Catalysts

The nanostructure of the electrocatalysts was observed by using a field-emission scanning electron microscope (FESEM, SU-9000, Hitachi High-Technologies Co., Japan) and a high-resolution scanning transmission electron microscope (STEM, JEM-ARM200F, JEOL, Japan). The loading of $Sn_{0.98}Nb_{0.02}O_2$ to the GCB was determined by thermo-gravimetry (TG) measurements, which can remove carbon materials by the oxidation in air at high temperatures. Pt and Co loading on the $Sn_{0.98}Nb_{0.02}O_2$/GCB was measured using inductively-coupled plasma atomic emission spectrometry (ICP-AES), to check the Pt/Co atomic ratio. The crystallization of $Sn_{0.98}Nb_{0.02}O_2$ was verified by XRD measurements.

Electrochemical Measurements (Half-Cell)

Half-cell measurements were made to evaluate electrochemical activities of the electrocatalysts prepared. Each electrocatalyst was deposited on the Au disk electrode (0.196 cm^2) with a loading of 17.3 $\mu g_{\text{-Pt}}\, cm^{-2}$, used as the working electrode (12). Pt wire electrode and Ag|AgCl electrode saturated in KCl were used as a counter electrode and a reference electrode, respectively. Cyclic voltammogram (CV) measurement was made at a scanning rate of 50 mV s^{-1} in the N_2-saturated 0.1M $HClO_4$ solution at 25 ºC. The potential range was set between 0.05 and 1.2 V_{RHE}. From the hydrogen desorption region (between

0.05 and 0.4 V_{RHE}) obtained from the CV measurements, electrochemical surface area (ECSA) of Pt catalysts was determined after 50 potential cycles. Oxygen reduction reaction (ORR) activity was characterized by measuring the kinetic current determined from rotating disk electrode (RDE) measurements. Rotating speed of the electrode was set at various rates ranging from 2500 to 400 rpm, and the potential was swept from 1.2 to 0.2 V_{RHE} at a scanning rate of 10 mV s^{-1} at 25 ºC. Mass activity (j_m) per Pt unit mass at 0.9 V_{RHE} was derived to evaluate ORR activities of the electrocatalysts.

Preparation of MEAs

Electrocatalyst paste, consisting of $Pt_3Co/Sn_{0.98}Nb_{0.02}O_2$/GCB or the standard 46.4 wt.% Pt/C (TEC10E50E, Tanaka Kikinzoku Kogyo (TKK), Japan), 99.5% ethanol, ultra-pure water, and 5% Nafion solution, was dispersed using ultrasonic homogenizer. The paste was then printed on electrolyte membranes (Nafion 212) using a spray printing system (Nordson). The electrode area was 1.0 cm^2. For the cathode, the $Pt_3Co/Sn_{0.98}Nb_{0.02}O_2$/GCB electrocatalyst was used, and Pt loading was 0.3 $mg_{\text{-Pt}}/cm^2$. For the anode, the standard 46.4 wt.% Pt/C electrocatalyst was used, and Pt loading was also 0.3 $mg_{\text{-Pt}}/cm^2$. After the spray printing, electrode-printed membrane was hot-pressed with GDLs at 132 ºC, 0.3 kN for 180 s. For the MEA, the electrode was contacted with gas diffusion layers (GDL). As the GDL, Teflon-coated carbon paper with micro-porous layer (MPL, 22BB, SGL Carbon) was used for the cathode, and Teflon-coated carbon paper without MPL (Electrochem, EC-TP1-060T) was used for the anode.

Cell Performance

I-V characteristics of MEAs were measured at the relative humidity (RH) of 100%, by setting both cell temperature and gas humidification temperature at 80 ºC. Gas flow rate of H_2 (695 mL min^{-1}) and air (1660 mL min^{-1}) was set, corresponding to the gas utilization to be 2 % for 2 A cm^{-2} for both the anode and the cathode. Cell holder developed in a New Energy and Industrial Technology Development Organization (NEDO) project (13) was used, MEAs were pre-treated at 0.6 V for 4 h before the I-V measurements. For evaluating various overvoltage contributions, ohmic resistance was measured by an AC impedance analyzer (SP-240, Bio-Logic Science Instruments), and activation overvoltage and concentration overvoltage were then separated by using the Tafel plot. A regression line was derived from 3 or 4 data points in low current density region on the Tafel plot. The potential difference between the voltage on the Tafel plot and the voltage on the regression line was derived as concentration overvoltage; and the potential difference between the voltage on the Tafel plot and the theoretical electromotive cell voltage was derived as activation overvoltage (14).

Results and Discussion

Characterization of Electrocatalysts

Figure 1 shows FESEM images of $Sn_{0.98}Nb_{0.02}O_2$/GCB. SnO_2 particles are uniformly dispersed on the surface of GCB particles. $Sn_{0.98}Nb_{0.02}O_2$ mass % was 71 wt.% measured by the TG measurements, confirming that $Sn_{0.98}Nb_{0.02}O_2$/GCB close to the designated ratio was prepared.

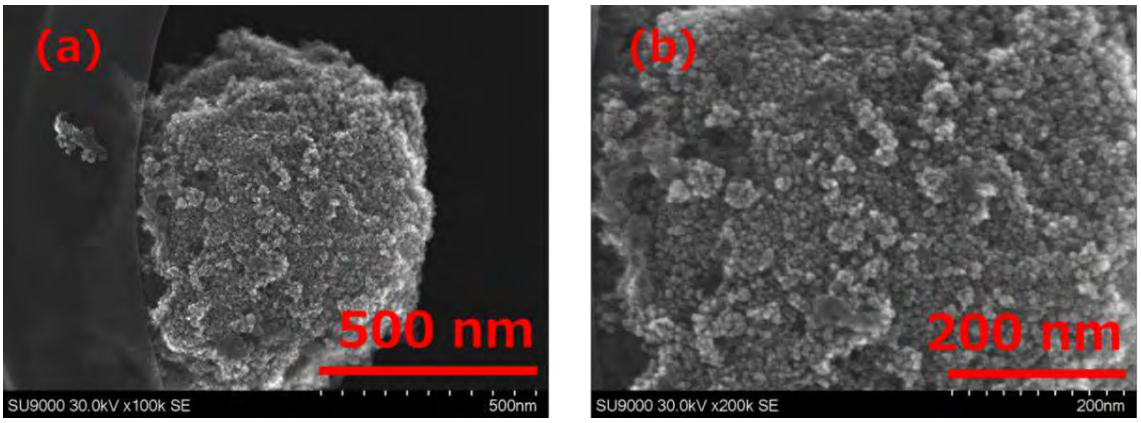

Figure 1. FESEM images of $Sn_{0.98}Nb_{0.02}O_2$/GCB: (a) low-magnification, and (b) high-magnification.

Figure 2 shows FESEM images of the $Pt_3Co/Sn_{0.98}Nb_{0.02}O_2$/GCB electrocatalyst. Catalyst particles were selectively supported on $Sn_{0.98}Nb_{0.02}O_2$ with a diameter of 2 to 3 nm. ICP measurement revealed that the actual loading of Pt and Co was 18.3 and 2.05 wt. %, respectively. This means that the atomic Pt/Co ratio was 72.94/27.06, confirming that Pt_3Co alloy electrocatalyst was successfully prepared.

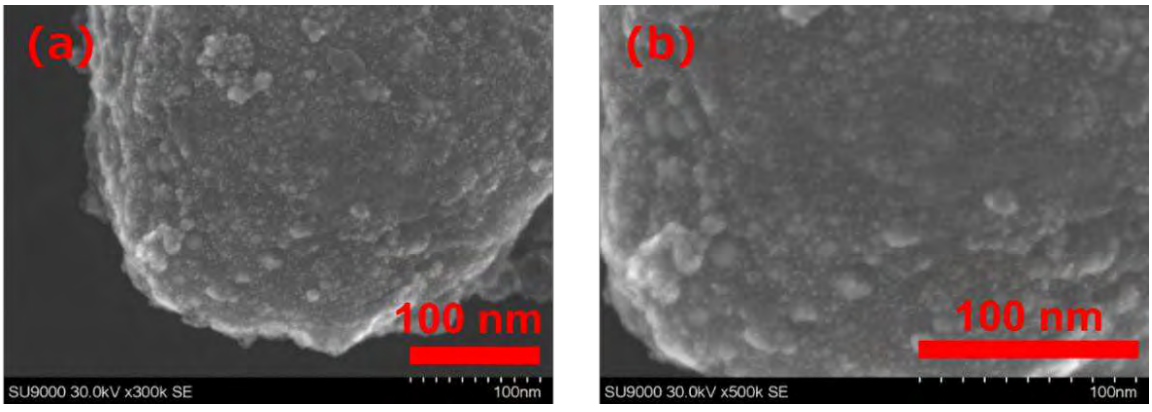

Figure 2. FESEM images of $Pt_3Co/Sn_{0.98}Nb_{0.02}O_2$/GCB electrocatalyst prepared: (a) low-magnification, and (b) high-magnification.

Figure 3 shows (a) high-resolution STEM image and (b)-(f) STEM-EDS elemental mappings of the $Pt_3Co/Sn_{0.98}Nb_{0.02}O_2$/GCB electrocatalyst. It was confirmed that SnO_2 thin layer was deposited to cover the GCB surface, and Pt-based catalysts were dispersed on the SnO_2 thin layer.

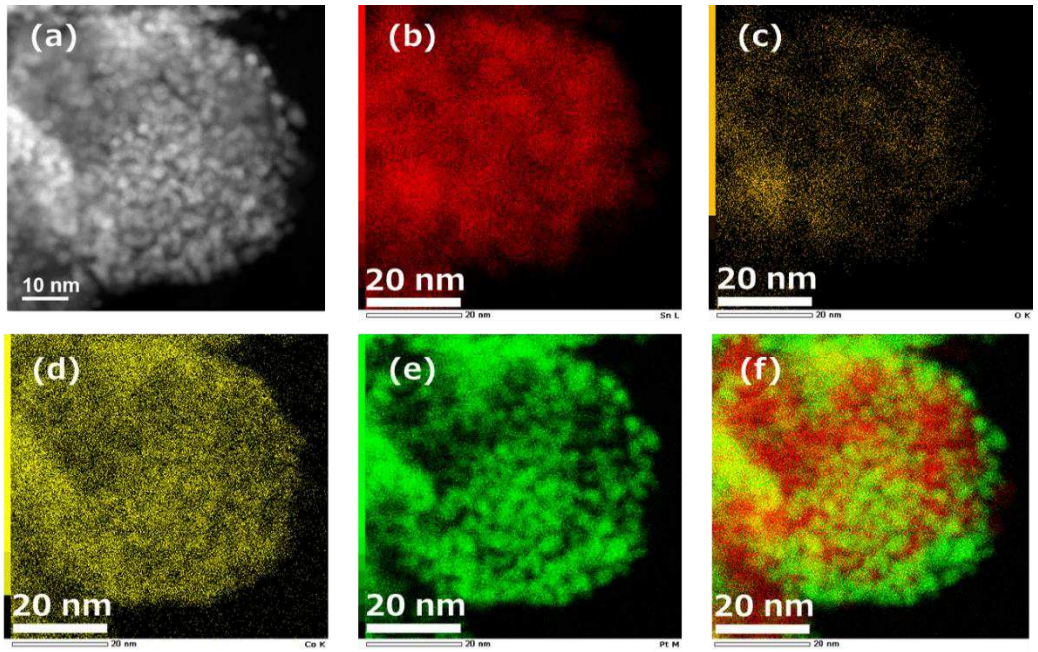

Figure 3. (a) STEM image and EDS elemental mappings of (b) Sn, (c) O, (d) Co, (e) Pt, and (f) Sn and Pt of the $Pt_3Co/Sn_{0.98}Nb_{0.02}O_2$/GCB electrocatalyst.

Figure 4 shows STEM high-angle annular dark field (HAADF) images and EDS line profiles for Pt and Co distributions. The concentration of Co was generally low, and background signals from SnO_2 were also present. Therefore, line analysis was made to clarify the distribution of Pt and Co. The EDS signals from Pt and Co come from the same place, indicating a homogeneous alloying of Pt with Co.

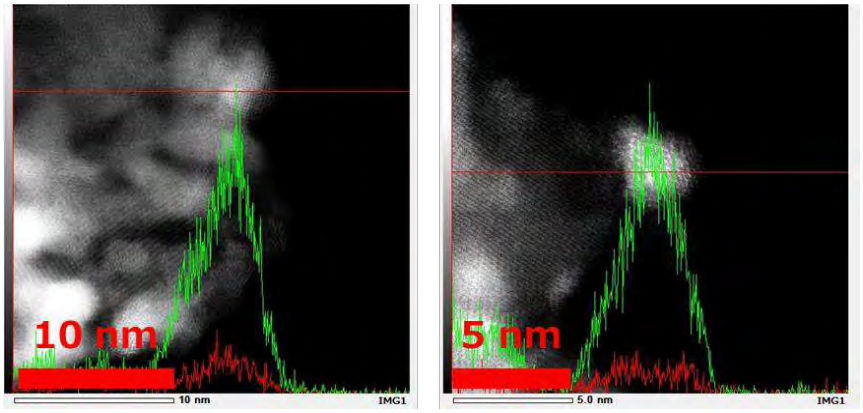

Figure 4. STEM-EDS HAADF images with Pt (green) and Co (red) line profiles (along the red lines in the STEM images) for the $Pt_3Co/Sn_{0.98}Nb_{0.02}O_2$/GCB electrocatalyst.

Figure 5 shows the spacing of the crystal lattice planes of the catalyst particles described in the STEM image. The spacing of the lattice planes was identical to that of pure Pt, 0.23 nm in the (111) plane, 0.26 nm in the (011) and (101) planes; and 0.24 nm in the (200) plane of SnO_2. From the XRD database, possible compositions of the Pt-Sn alloys could be $PtSn_2$, PtSn, and Pt_3Sn, and their crystal structures are face-centered cubic (fcc), hexagonal close-packed (hcp), and primitive cubic, respectively. $PtSn_2$ has a fluorite-type crystal structure with a lattice constant of 0.642 nm, which is different from that of Pt. Therefore, if $PtSn_2$ would be formed, the lattice planes are different from those of Pt. The catalyst particles have a face-centered cubic structure and the lattice constant close to that of Pt, indicating that no Pt-Sn alloy was formed.

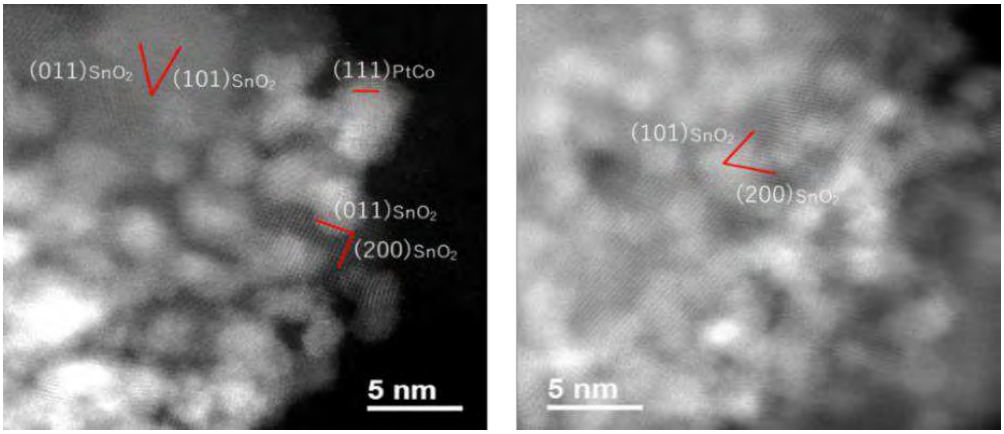

Figure 5. HAADF-STEM images and the Miller indices of Pt-Co and SnO_2 for the $Pt_3Co/Sn_{0.98}Nb_{0.02}O_2$/GCB electrocatalyst.

XRD Measurements

Figure 6 shows XRD pattern of the $Pt_3Co/Sn_{0.98}Nb_{0.02}O_2$/GCB electrocatalyst. The SnO_2 peaks were observed, suggesting that the crystallization of SnO_2 was promoted by the heat treatment after the ammonia coprecipitation method. TABLE I shows the crystallite diameter derived from the width at half maximum of the obtained XRD peaks. SnO_2 crystallite diameters were less than 10 nm. Since SEM images showed that some particles were larger than 10 nm in diameter, SnO_2 particles exist as secondary particles composed of a few SnO_2 crystallites of several nm in diameter, deposited as the thin surface layer of the catalyst supports.

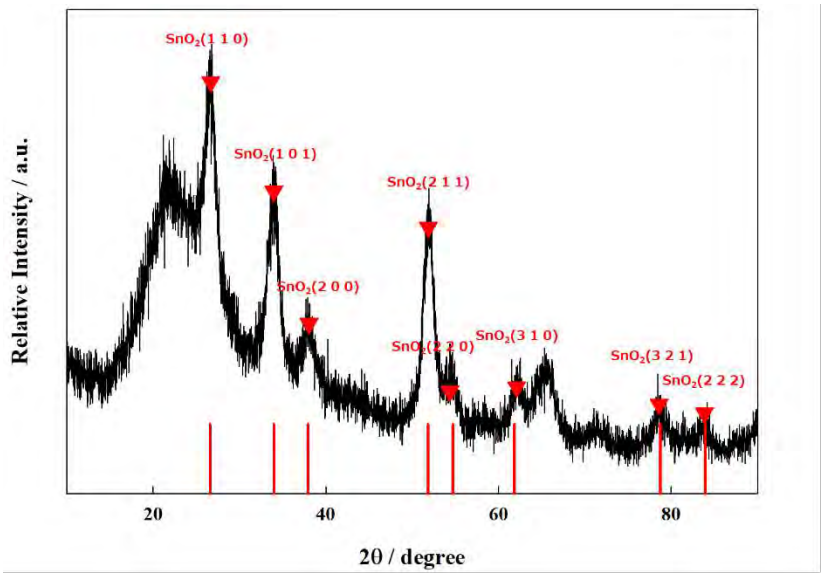

Figure 6. XRD pattern of the $Pt_3Co/Sn_{0.98}Nb_{0.02}O_2$/GCB electrocatalyst.

TABLE I. Crystallite size of SnO_2 derived from its full width at half maximum (FWHM)

Lattice planes	Crystallite diameter (nm)
SnO_2(110)	6.50
SnO_2(101)	5.41
SnO_2(200)	6.70
SnO_2(211)	6.20
SnO_2(220)	5.90
SnO_2(310)	6.20
SnO_2(321)	7.80
SnO_2(222)	8.80
Average	6.69

Electrochemical Activities (Half-Cell)

Figure 7 shows (a) cyclic voltammograms and (b) linear sweep voltammograms at 1600 rpm of the $Pt_3Co/Sn_{0.98}Nb_{0.02}O_2$/GCB and Pt/C (TEC10E50E, TKK) electrocatalysts. For the $Pt_3Co/Sn_{0.98}Nb_{0.02}O_2$/GCB electrocatalysts, ECSA was 62.42 $m^2\ g^{-1}$ and mass activity was derived to be 93.17 A g^{-1}.

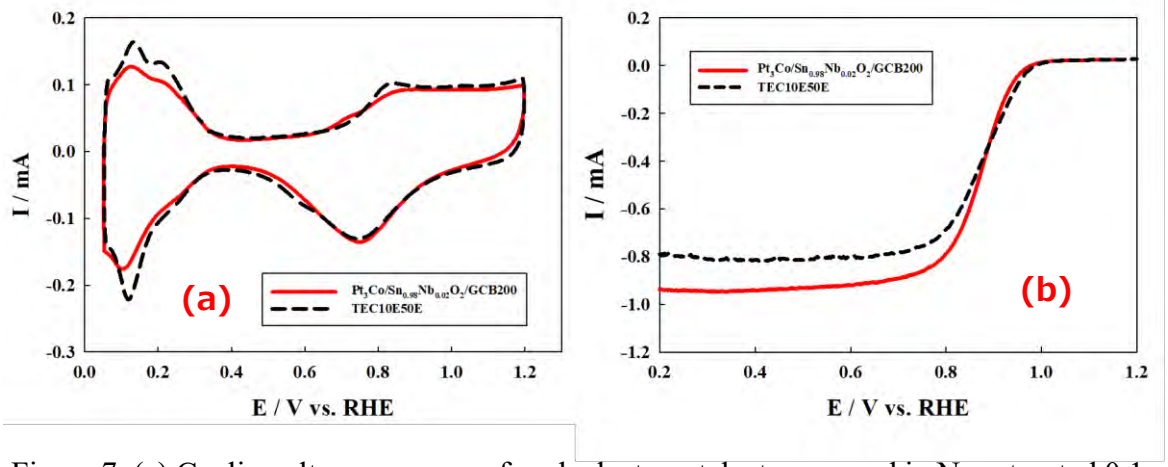

Figure 7. (a) Cyclic voltammograms of each electrocatalyst measured in N_2-saturated 0.1 M $HClO_4$ at 25 °C and 50 mV s^{-1}; and (b) linear sweep voltammograms of each electrocatalyst measured in O_2-saturated 0.1 M $HClO_4$ at 25 °C and 10 mV s^{-1} at 1600 rpm.

Cell Performance (MEA)

TABLE II shows the MEA preparation conditions. Figure 8 shows the single-cell electrochemical characteristics. The cell voltage was 0.759 V at 0.2 A cm^{-2} and 0.528 V at 0.8 A cm^{-2}. The Nafion ratio of the cathode catalyst layer is the same as that by Nakazato et al (15).

TABLE II. MEA preparation conditions.

	Anode	Cathode
Electrocatalyst	Pt/C (TEC10E50E)	$Pt_3Co/Sn(Nb)O_2/GCB$
Electrolyte membrane	Nafion 212	
Gas diffusion layer	carbon paper	MPL carbon paper (22BB)
Electrode area / cm^2	1.0	
Pt loading / mg cm^{-2}	0.3±0.01	
Nafion ratio / wt.%	28	13

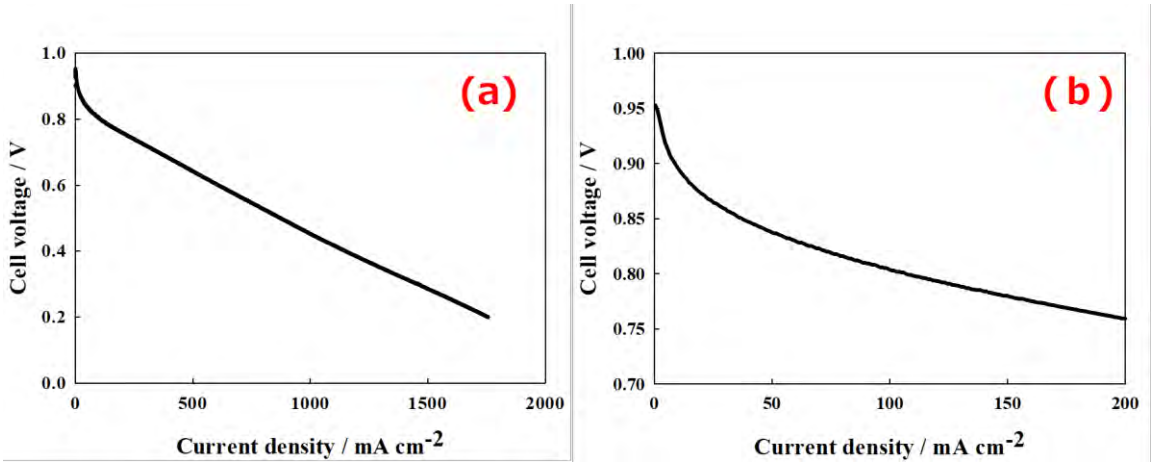

Figure 8. I-V characteristics of the MEA with the Pt/C (TEC10E50E) electrocatalyst for the anode, and with the Pt_3Co /$Sn_{0.98}Nb_{0.02}O_2$/GCB for the cathode: (a) current density range from 0 to ca. 2 A cm^{-2}, and (b) current density range from 0 to 200 mA cm^{-2}.

In order to examine the factors causing the change in cell voltage in more detail, we separated the overall overvoltage into three components: activation overvoltage, ohmic overvoltage, and concentration overvoltage. The results are shown in Figure 9. Figure 10 shows the SEM images of the cross-section of the MEA after the I-V measurement, showing the anode (a, b) and cathode (c, d) catalyst layers. It can be seen that the cathode catalyst layer has a lower porosity than the anode catalyst layer, and the electrocatalyst particle size tends to increase. The pore size of the cathode catalyst layer was smaller than that of the anode catalyst layer. In order to obtain higher I-V characteristics, it is necessary to optimize such porous microstructure of the catalyst layers.

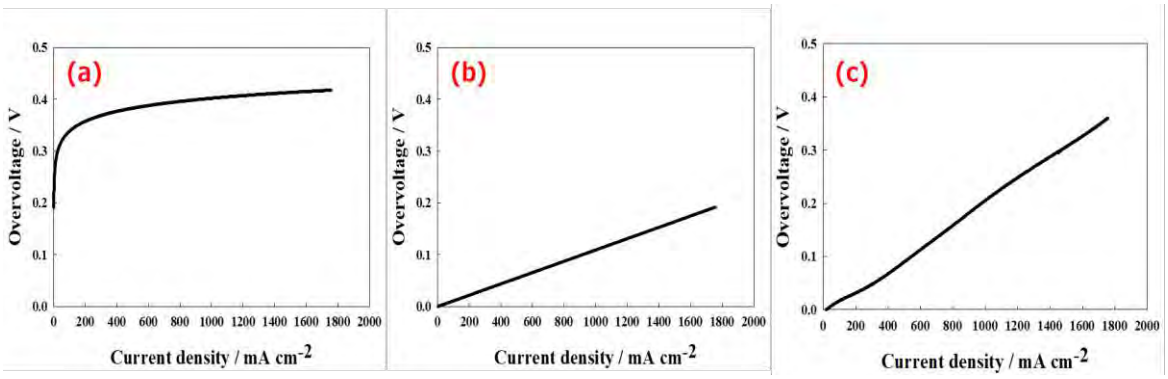

Figure 9. Overvoltage contributions of the MEA separated: (a) activation overvoltage, (b) ohmic overvoltage, and (c) concentration overvoltage.

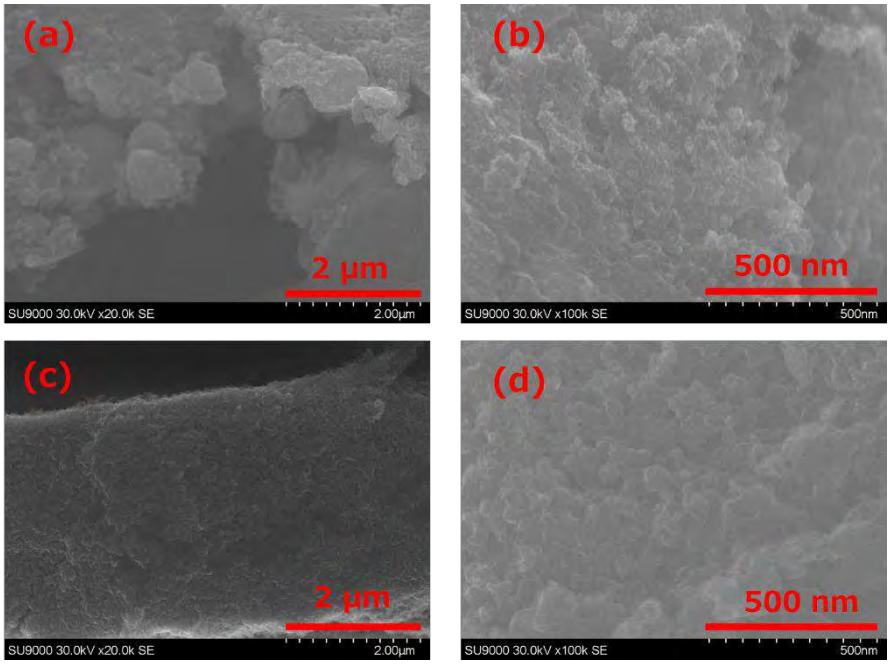

Figure 10. SEM images of the cross-section of the MEA after the I-V measurement: (a) the cathode catalyst layer (low-magnification), (b) the cathode catalyst layer (high-magnification), (c) the anode catalyst layer (low-magnification), and (d) the anode catalyst layer (high-magnification).

Conclusions

Pt-Co alloy catalysts on SnO_2-based thin layer support could be prepared, using GCB as conductive backbone in the eletrocatalyst layers. From the results of single-cell electrochemical measurements, it was found that the microstructure of the Pt_3Co /$Sn_{0.98}Nb_{0.02}O_2$/GCB electrocatalyst layer has to be optimized. In addition to the optimization of the porous microstructure, the $Pt_3Co/Sn_{0.98}Nb_{0.02}O_2$/GCB electrocatalyst should be subjected to various durability tests to confirm the role of SnO_2 thin layer support on durability, as a future study.

Acknowledgment

Financial support from New Energy and Industrial Technology Development Organization (NEDO) is gratefully acknowledged (Contract No. 20001214-0).

References

1. L. M. Roen, C. H. Paik, and T. D. Jarvi, *Electrochem. Solid-State Lett.*, **7** , A19 (2004).
2. A. Taniguchi, T. Akita, K. Yasuda, and Y. Miyazaki, *J. Power Sources*, **130**, 42 (2004).
3. S. Maass, F. Finsterwalder, G. Frank, R. Hartmann, and C. Merten, *J. Power Sources*,

176, 444 (2008).
4. W. S. Baker, J. J. Pietron, M. E. Teliska, P. J. Bouwman, D. E. Ramaker, and K. E. Swider-Lyons, *J. Electrochem. Soc.*, **153**, A1702 (2006).
5. K. Sasaki, F. Takasaki, Z. Noda, S. Hayashi, Y. Shiratori, and K. Ito, *ECS Trans.*, **33**(1), 473 (2010).
6. K. Kakinuma, M. Uchida, T. Kamino, H. Uchida, and M. Watanabe, *Electrochim. Acta*, **56**, 2881 (2011).
7. S. Matsumoto, M. Nagamine, Z. Noda, J. Matsuda, S. M. Lyth, A. Hayashi, and K. Sasaki, *J. Electrochem. Soc.*, **165**, F1164 (2018).
8. T. Tada, Y. Yamamoto, K. Matsutani, K. Hayakawa, and T. Namai, *ECS Trans.*, **16**(2), 215 (2008).
9. M. Watanabe, D. A. Tryk, M. Wakisaka, H. Yano, and H. Uchida, *Electrochim. Acta*, **84**, 187 (2012).
10. F. Takasaki, S. Matsuie, Y. Takabatake, Z. Noda, A. Hayashi, Y. Shiratori, K. Ito, and K. Sasaki, *J. Electrochem. Soc*., **158**, B1270 (2011).
11. A. Hayashi, H. Notsu, K. Kimijima, J. Miyamoto, and I. Yagi, *Electrochim Acta*. **53**, 6117 (2008).
12. M. Inaba, H. Ito, H. Tuji, T. Wada, M. Banno, H. Yamada, M. Saito, and A. Tasaka, *ECS Trans*., **33**(1), 231 (2010).
13. M. Hori, K. Kobayashi, Y. Oono, and A. Daimaru, *222nd ECS meeting abstract*, **MA2012-02**, #1497 (2012).
14. *Protocols for Evaluation of Cell Performances*, New Energy and Industrial Technology Development Organization (NEDO), http://www.nedo.go.jp/content/100537904.pdf.
15. Y. Nakazato, D. Kawachino, Z. Noda, J. Matsuda, S. M. Lyth, A. Hayashi, and K. Sasaki, *J. Electrochem. Soc.*, **165**, F1154 (2018).

ECS Transactions, 104 (8) 359-369 (2021)
10.1149/10408.0359ecst ©The Electrochemical Society

PEFCs Using Metallic Ti and Sn Gas Diffusion Layers

Kotaro Yamamoto[a], Masahiro Yasutake[b], Zhiyun Noda[c], Junko Matsuda[c, d], Masamichi Nishihara[d], Akari Hayashi[a, c-f], and Kazunari Sasaki[a-f]

Kyushu University
[a] Faculty of Engineering, Department of Hydrogen Energy Systems,
[b] Center of Coevolutionary Research for Sustainable Communities,
[c] International Research Center for Hydrogen Energy,
[d] Next-Generation Fuel Cell Research Center (NEXT-FC),
[e] Platform of Inter / Transdisciplinary Energy Research (Q-PIT),
[f] International Institute for Carbon-Neutral Energy Research (WPI-I2CNER),
Motooka 744, Nishi-ku, Fukuoka 819-0395, Japan

Porous carbon materials, which are widely used as gas diffusion layer (GDL) in PEFCs, have several issues including high cost and mechanical strength. In order to reduce the cost and thickness of GDLs, we focus on the possible use of metallic Ti and Sn as alternative GDL materials. In this study, Sn/Ti and Sn/Sn GDLs are prepared, which are based on porous Ti or Sn plates coated with Sn layer. Microstructural observations using scanning electron microscope (SEM) confirmed that porous Sn dendrite layer could be formed on the metallic GDLs. Current-voltage measurements of the cells using these materials revealed that the porous structure of the GDLs, on which Sn dendrites were formed, is advantageous to improve electrical contact.

Introduction

Various carbon materials are currently used in PEFCs. In particular, relatively expensive porous carbon materials such as carbon fiber cloth and carbon paper with a thickness of around 0.2 mm are commonly used as the GDL, which ensures gas flow, electron transport, and water management in fuel cells (1). However, electrical conductivity of these carbon materials is generally not as high as that of metallic materials. Another technical issue is the reduction of GDL thickness to achieve higher power density per cell stack volume, which could however lead to a decrease in mechanical strength of GDLs.

Whilst polymer electrolyte fuel cells are polymer-based energy devices, the use of inorganic materials such as metals and oxides may be of technological interest as such materials are thermochemically stable and widely used in industrial sectors. In particular, tin and titanium are stable in strongly-acidic environment of PEFCs containing proton-conducting membranes. In order to improve their durability against start-stop potential cycling causing corrosion of carbon-based catalyst support (2), conductive oxides such as Nb-doped SnO_2 are considered as alternative catalyst support materials (3-16). Titanium is also known as a stable material under such acidic conditions (3, 12). As metallic Sn and Ti have high electronic conductivity, beside their electrochemical stability, it may be of technological interest to apply such materials to GDLs. On one hand, metallic GDLs could

be much thinner than the current carbon-based GDLs. Comparable or even higher electronic conductivity could be obtained. On the other hand, the use of metallic GDLs is challenging because almost no studies have been reported so far on electrochemical performance of MEAs using metallic GDLs. There are many issues unknown, including selection of suitable materials and their compositions, overvoltages in such MEAs using metallic GDLs, as well as ideal structure to ensure electronic transport, gas transport, and water management. Fabrication procedures may be reconsidered in applying such metallic GDLs instead of carbon-based GDLs. To mention a few, Ti fiber sheets have already been considered as possible metallic GDL materials (9, 10).

Here in this study, various metallic GDLs are prepared, the current-voltage characteristics of fuel cells using metallic GDLs are examined, and their overvoltage components are separated and analyzed. Possible candidate materials with different types, thickness, and porosity are compared. Cell fabrication conditions are varied to reveal their influence on cell performance. The aim of this study is to develop porous metallic GDL materials with sufficient electrical conductivity, durability, and gas permeability.

Experimental

Preparation of Gas Diffusion Layers

In this study, several commercial materials were used as base sheets, using which metallic GDLs were prepared. Photographs of these metallic sheets used are shown in Figure 1. As starting materials to prepare metallic GDLs, (i) Ti fiber sheet with a porosity of 70% and thickness of 200 μm, (ii) Ti fiber sheet with a porosity of 70% and a thickness of 100 μm, (iii) Ti sheet (perforated metal) with a thickness of 12 μm and a hole diameter of 300 μm, and (iv) Sn sheet (perforated metal) with a thickness of 100 μm and a hole diameter of 300 μm were used. Sn layers were deposited on such metallic sheets by using conductive Sn paste or by Sn plating, described in the following sections.

Preparation of 95%Sn - 5%Sb Porous Layer

The commercially available 95%Sn - 5%Sb conductive paste (Senju Metal Industry Co., Ltd, Japan) used in the study is shown in Figure 2. The procedure to prepare Sn/Ti sheets by using the 95%Sn - 5%Sb conductive paste is described in Figure 3. First, the 95% Sn - 5% Sb conductive paste was screen-printed on the Ti fiber sheet (i). Reduction treatment was then performed at 200 °C for 2 h in 5% H_2-N_2 atmosphere. The Sn-based conductive layer was uniformly deposited on one side of the metallic sheets.

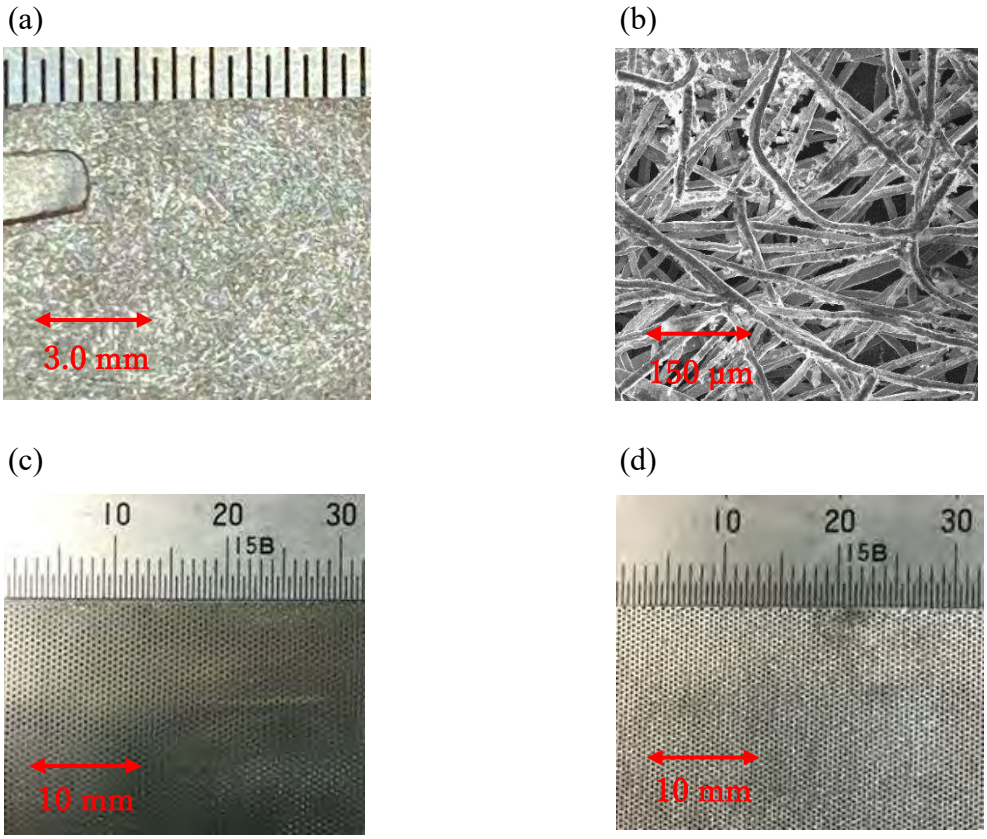

Figure 1. Metallic sheets used to prepare GDLs: (a) optical photograph of Ti fiber sheet, (b) scanning electron microscope (SEM) image of Ti fiber sheet, and optical photograph of (c) Ti porous sheet and (d) Sn porous sheet.

Figure 2. 95%Sn - 5%Sb paste to prepare Sn-based porous layers.

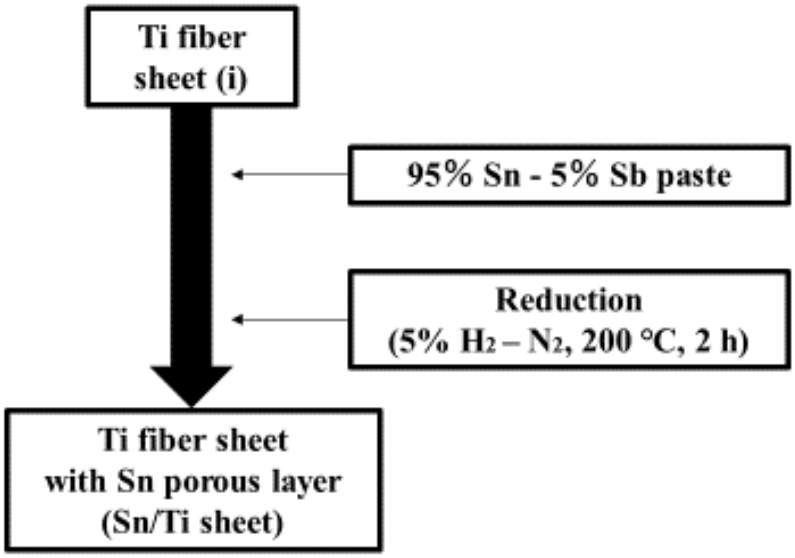

Figure 3. Preparation procedure of Ti fiber sheets with porous Sn-based layers.

Preparation of Sn Plating Layer

For Sn plating, a Sn metal plate (10 cm × 1 cm × 0.5 cm thick) was connected to the positive electrode of a power supply, and a porous metal sheet to be plated was connected to the negative electrode. Both electrodes were immersed in the electrolytic solution (HCl, 0.1 mol/L) and current was applied for 20 min under a constant voltage of 1.5 V for the Sn plating. The liquid electrolyte was stirred during the plating for homogeneous deposition. After plating, the sheets were washed with pure water and were subjected to a reduction treatment at 180 °C for 2 h in 5% H_2 - N_2 atmosphere. The procedure for preparing the Sn/Sn sheets by the Sn plating is described in Figure 4. The setup for the Sn plating is schematically illustrated in Figure 5.

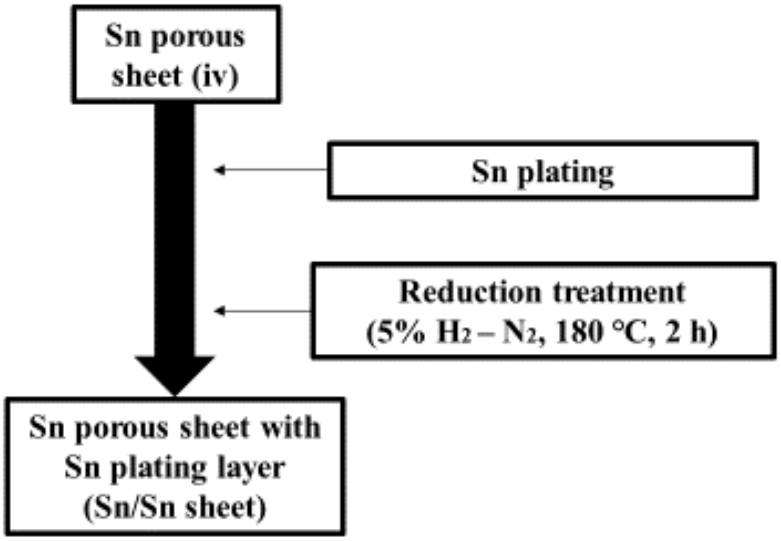

Figure 4. Preparation procedure of Sn porous sheets with Sn plating layers.

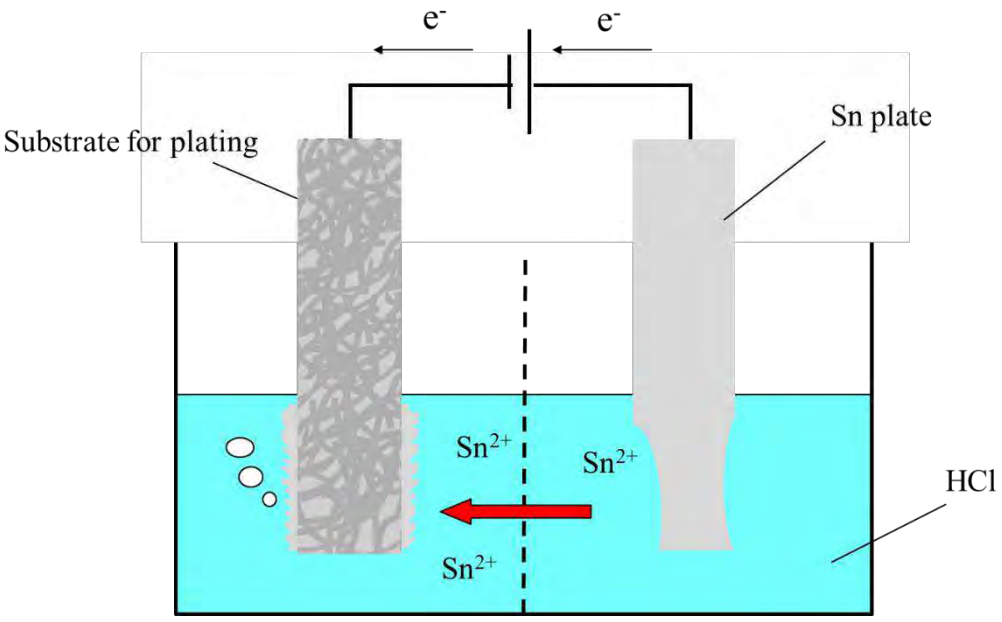

Figure 5. Principle of Sn plating.

Characterization of Gas Diffusion Layers

SEM was used to observe the microstructure of various GDLs prepared. The microstructures of metallic sheet substrates, and Sn layers deposited on the sheets were observed.

Electrochemical Measurements (Full-Cell)

Electrochemical properties of the prepared metallic GDLs were evaluated using a full cell. The conditions for the preparation of membrane electrode assemblies (MEA) are compiled in TABLE I. For all evaluations, the electrocatalyst layers were prepared by dispersing Pt/C (Pt 46.5%, TEC10E50E, Tanaka Kikinzoku Kogyo Corp., Japan), 99.5% ethanol, pure water, and 5% Nafion solution using an ultrasonic homogenizer. The dispersions were printed on the electrolyte membrane (Nafion 212) using a spray printer (C-3 J, Nordson). The electrode area was 1.0 cm^2 (1.0 cm × 1.0 cm), and the Pt loading on both electrodes was 0.3 mg-Pt cm^{-2}. The metallic GDL was used for the cathode, and a carbon paper (EC-TPI-060T) was used as the standard GDL for the anode.

In the electrochemical characterization of this study, the electrochemical impedance spectroscopy (EIS, 1255WB, Solatron) was applied to measure the current-voltage characteristics and to separate overvoltages.

TABLE I. Specifications of MEAs prepared in this study.

	Anode	**Cathode**
Gas diffusion layer	Carbon paper	Metallic GDL
Electrode area / cm^2	1.0	
Electrocatalyst	46.5 wt.% Pt/C	46.5 wt.% Pt/C
Catalyst loading / mg cm^{-2}	Pt 0.3	Pt 0.3
Cell temperature / °C	80	
Electrolyte membrane	Nafion®212 (50 μm thick)	

Results and Discussion

Preparation

95%Sn - 5%Sb Porous Layer. Before the reduction treatment, the 95%Sn - 5%Sb conductive paste screen-printed on the surface of the Ti fiber sheet was gray in color. However, after the reduction treatment, the 95%Sn - 5%Sb layer became silver white.

Sn Plating Layer. After the Sn plating process, a plating layer was formed inside the holes of the porous Sn sheet, while only a thin plating layer was formed on the surface of the Sn sheet. The distribution of the plated Sn layer was common, independent of e.g. the stirring speed of the electrolytic solution.

Microstructures

95%Sn - 5%Sb Porous Layer. SEM images of the Ti fiber and the Sn porous layer in the Sn/Ti GDL are shown in Figure 6. The cross-sectional structure of the Sn/Ti GDL is illustrated in Figure 7.

As shown in Figure 6 (a), Sn particles with diameters ranging from 20 to 30 μm were deposited on the Ti fiber sheet. The Sn conductive paste before the reduction treatment consisted of isolated particles with diameters of several tens of micrometers, but after the reduction, the particles became interconnected forming a porous structure. Sn particles were partially sintered in the reducing heat treatment at 200°C, which is slightly lower than the melting point of Sn (231.9°C). Sn particles formed one monolayer or multi-layer on the porous Ti fiber sheets, forming porous metallic layers. In addition, as shown in Figure 6 (b), some Sn particles with diameters ranging from tens to hundreds nanometers were observed on the Ti fibers. This may be caused by the diffusion of Sn on the Ti fibers.

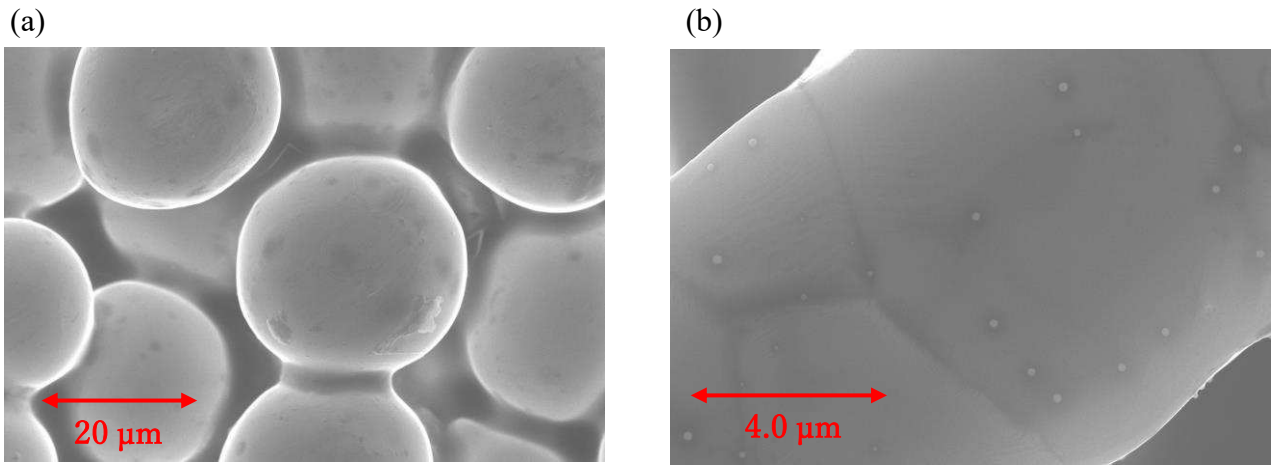

Figure 6. SEM image of (a) the Sn porous layer on the Sn/Ti GDL and (b) the Ti fiber within the Sn/Ti GDL.

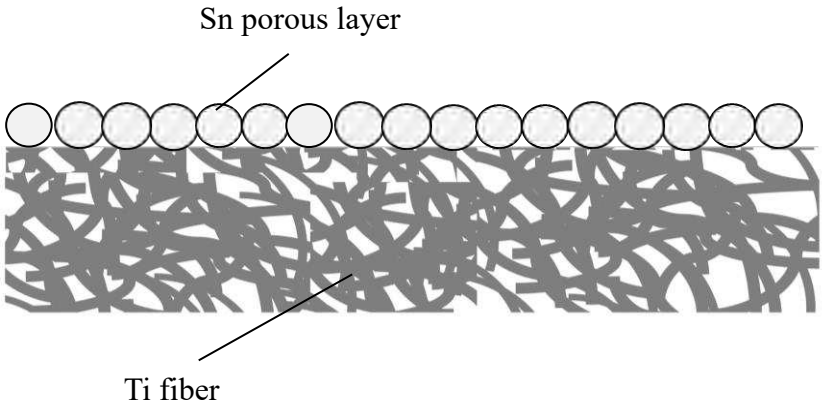

Figure 7. Cross section of the Sn/Ti sheet, schematically illustrated.

Sn Plating Layer. SEM images of the Sn/Sn GDL prepared are shown in a lower magnification in Figure 8 (a) and in a higher magnification in Figure 8 (b). Metallic Sn dendrites were observed within the hole of the Sn plate. The dendrite-like crystals were clearly grown, where tree-like micro-rods were overlapped each other to form porous network. The micro-rods have a diameter of 2 to 3 µm. On the surface of the sheet, no dendritic crystals were formed, but metallic Sn particles with diameters of 0.5 to 5 µm were formed instead.

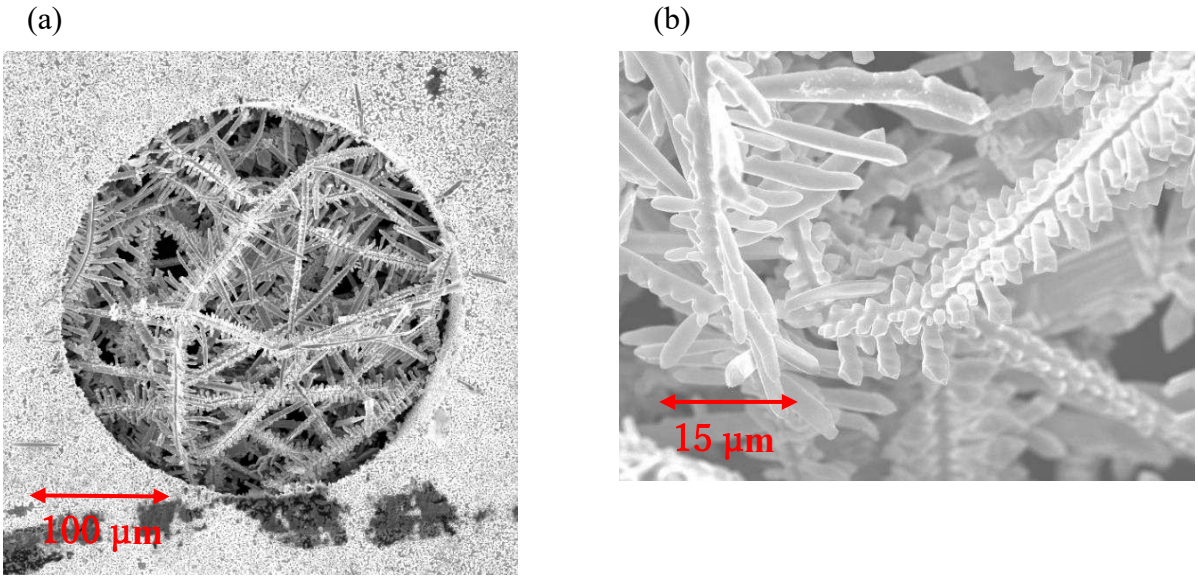

Figure 8. SEM images of (a) the Sn-plated porous Sn sheet near a hole, and (b) the Sn-dendrite grown within the hole observed at a higher magnification.

Electrochemical Properties (Full-Cell)

The current-voltage (I-V) characteristics of the MEAs using various metallic GDLs on the cathode side are shown in Figure 9. Each overvoltage separated are shown in Figure 10.

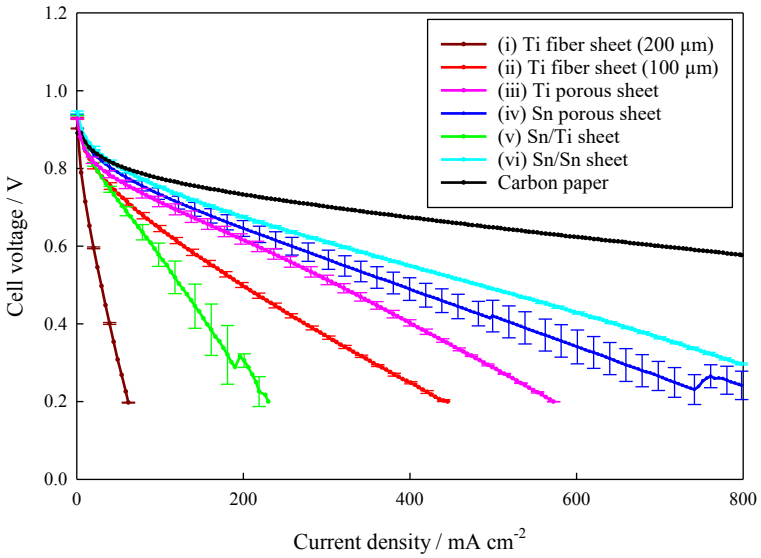

Figure 9. Current - voltage characteristics of the MEAs with various metallic GDLs, measured at 80 ℃ and 100 % relative humidity. The flow rates of H_2 gas and air were 0.139 L min^{-1} and 0.332 L min^{-1}, respectively, corresponding to a stoichiometric ratio of 2:5.

(a) Activation overvoltage

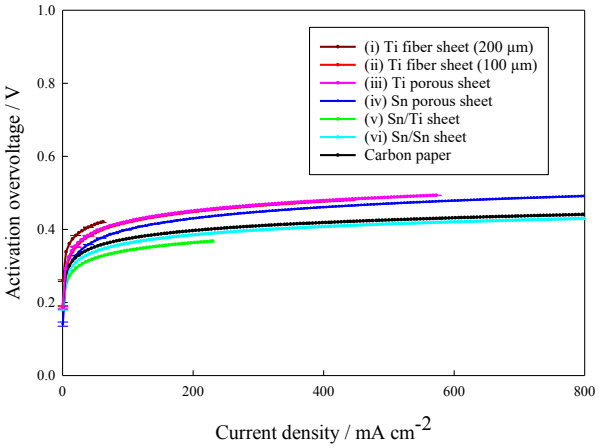

(b) IR loss

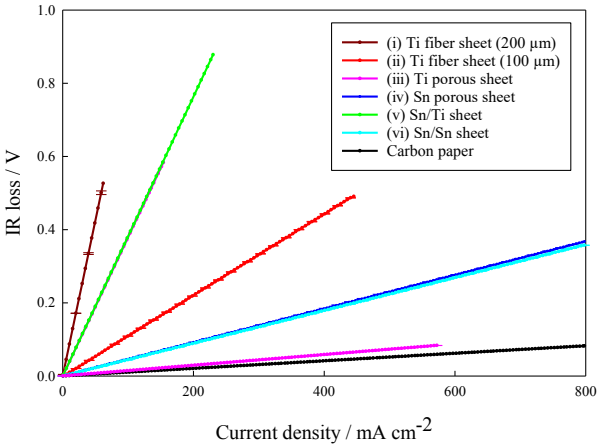

(c) Concentration overvoltage

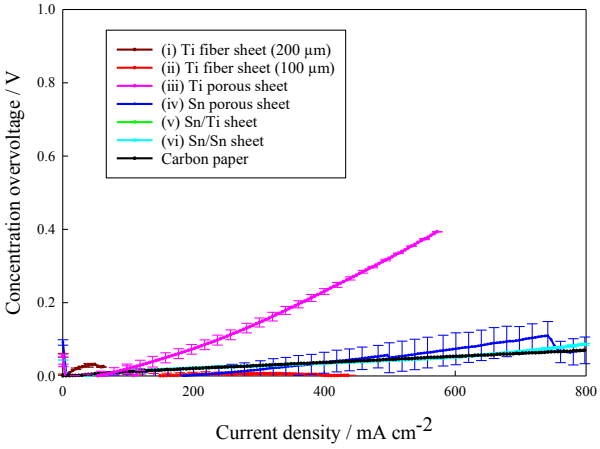

Figure 10. Overvoltages of the cells with 6 types of metallic GDLs and a standard carbon-based GDL, measured at 80 °C and the identical conditions in Figure 9: (a) activation overvoltage, (b) IR loss, and (c) concentration overvoltage.

For all the I-V curves in Figure 9, the decrease in cell performance was mainly caused by the IR loss, shown in Figure 10 (b). In contrast, the contributions from the activation overvoltage in Figure 10 (a) and the concentration overvoltage in Figure 10 (c) are relatively small. Comparing the MEA (i) to the MEA (vi) in Figure 10 (b), the GDLs using metallic Sn tend to exhibit lower IR loss, suggesting higher conductivity than that using metallic Ti.

The porous Ti sheet in (iii) showed better performance compared to the Ti fiber sheets (200 μm thick and 100 μm thick) used in (i) and (ii). In addition to the thinness of the Ti sheet (iii) (12 μm thick), good contact with the MEA could contribute to this improvement.

The Sn/Ti sheet in the MEA (v) showed improved cell performance compared to the Ti fiber sheet in the MEA (i), but the IR loss was still large. Further study is needed e.g. to improve the electrical contact between the porous Sn layer and the Ti sheet.

When the porous Sn sheet in the MEA (iv) was used, the concentration overvoltage tended to fluctuate in each measurement. This may be because the water generated by the electrode reaction was retained in the GDL due to a hydrophilic nature of metallic Sn, which may impede gas flow. In contrast, the GDL of the MEA (vi), in which Sn dendrites were formed in the holes of the porous Sn sheet, exhibited improved cell performance with negligible fluctuation of the concentration overvoltage in each measurement. This suggests that the Sn dendrite in the holes may improve electronic contact between the electrocatalyst layer and the porous Sn sheet, and local water management.

All of the metallic GDLs used in this study still showed higher IR loss than the conventional carbon paper (EC-TPI-060T). This could be due to a decrease in electronic conductivity caused e.g. by the formation of oxide film on the metal surface (TiO_2, SnO_2), increasing contact resistance. Further study is in progress to improve cell performance using such metallic GDLs.

Conclusions

A variety of metallic GDLs were prepared and their current-voltage characteristics were evaluated in real cells. In particular, the formation of Sn dendrite in the metallic GDLs by the Sn plating can increase the surface area of the GDLs and improved cell performance. Microstructural observations reveal that the Sn dendrite is durable in heat treatment up to about 180°C. On the other hand, the electrical conductivity, which is essential for GDLs, has to be further improved. Optimization of fabrication conditions, microstructure, electrical contact, and water management is a matter of important future studies.

Acknowledgements

Financial support from New Energy and Industrial Technology Development Organization (NEDO) is gratefully acknowledged (Contract No. 20001214-0).

References

1. J. Larminie and A. Dicks, *Fuel Cell Systems Explained*, 2nd Edition, Wiley (2003)
2. C. A. Reiser, L. Bregoli, T. W. Patterson, J. S. Yi, D. Yang, M. L. Perry, and T. D. Jarvi, *Electrochem. Solid-State Lett.*, **8**, A273 (2005).
3. K. Sasaki, F. Takasaki, Z. Noda, S. Hayashi, Y. Shiratori, and K. Ito, *ECS Tran.*, **33**(1), 473 (2010).
4. A. Masao, S. Noda, F. Takasaki, K. Ito, and K. Sasaki, *Electrochem. Solid-State Lett.*, **12**, B119 (2009).
5. F. Takasaki, S.Matsuie, Y. Takabatake, Z. Noda, A. Hayashi, Y. Shiratori, K. Ito, and K. Sasaki, *J. Electrochem. Soc.*, **158**, B1270 (2011).
6. K. Kakinuma, M. Uchida, T. Kamino, H. Uchida, and M. Watanabe, *Electrochim. Acta*, **56**, 2881 (2011).
7. Y. Nakazato, D. Kawachino, Z. Noda, J. Matsuda, S. M. Lyth, A. Hayashi, and K. Sasaki, *J. Electrochem. Soc.*, **165**, F1154 (2018).
8. S. Matsumoto, M. Nagamine, Z. Noda, J. Matsuda, S. M. Lyth, A. Hayashi, and K. Sasaki, *J. Electrochem. Soc.*, **165**, F1164 (2018).
9. D. Kawachino, M. Yasutake, H. Odoi, Z. Noda, J. Matsuda, A. Hayashi, and K. Sasaki, *ECS Trans.*, **86** (13), 541 (2018).
10. D. Kawachino, M. Yasutake, Z. Noda, J. Matsuda, S. M. Lyth, A. Hayashi, and K. Sasaki, *J. Electrochem. Soc.*, **167**, 104513 (2020).
11. T. Kitahara, T. Konomi, and H. Nakajima, *J. Power Souces,* **195**, 2202 (2010).
12. T. Kuroki, K. Sasaki, H. Kusaba, and Y. Teraoka, "PEFC Electrode Catalysts Supported on Nanocrystalline Semiconducting Oxides", Abstract #1527, 2004 Joint International Meeting, Electrochemical Society (2004).
13. L. M. Roen, C. H. Paik, and T. D. Jarvi, *Electrochem. Solid-State Lett.*, **7**, A19 (2004).
14. A. Taniguchi, T. Akita, K. Yasuda, and Y. Miyazaki, *J. Power Sources*, **130**, 42 (2004).
15. S. Maass, F. Finsterwalder, G. Frank, R. Hartmann, and C. Merten, *J. Power Sources*, **176**, 444 (2008).
16. D. Horiguchi, T. Tsukatsune, Z. Noda, A. Hayashi, and K. Sasaki, *ECS Trans,* **64** (3), 215 (2014).

ECS Transactions, 104 (8) 371-376 (2021)
10.1149/10408.0371ecst ©The Electrochemical Society

Analysis of the Effect of Surface Diffusion on Effective Diffusivity of Oxygen in Catalyst Layer by Direct Simulation Monte Carlo

T. Hori[a,b], T. Mabuchi[b,c], I. Kinefuchi[d], and T. Tokumasu[b]

[a]Graduate School of Engineering, Tohoku University, Sendai, Miyagi 980-8577, Japan
[b]Institute of Fluid Science, Tohoku University, Sendai, Miyagi 980-8577, Japan
[c]Frontier Research Institute for Interdisciplinary Sciences, Tohoku University, Sendai, Miyagi 980-8577, Japan
[d]Department of Mechanical Engineering, The University of Tokyo, 7-3-1 Hongo, Bunkyo-ku, Tokyo 113-8656, Japan

We analyzed the transport properties of oxygen molecules using the Monte Carlo method. We obtained the effective diffusion coefficient of oxygen molecules in a catalyst layer of polymer electrolyte fuel cells. In this calculation system, when oxygen molecules hit a wall, it diffuses on the ionomer surface for a period of time and then diffusely reflected. The simulation was performed using various conditions of the surface diffusion. The conditions are defined by the surface diffusion coefficient and the time constant that controls the residence time of oxygen molecules. When the surface diffusion coefficient is small, the increase in the time constant results in the decrease in the effective diffusion coefficient of oxygen. However, when the surface diffusion coefficient is large, as the time constant increases, the effective diffusion coefficient of oxygen has a peak value and then decreases. This phenomenon occurs due to the three-dimensional bending structure of the catalyst layer. When an oxygen molecule moves along the bending three-dimensional structure, the distance along the ionomer surface becomes larger than the straight line segment between the start and end points.

Introduction

Because in the catalyst layers (CLs) of polymer electrolyte fuel cells (PEFCs) platinum (Pt) is used as catalyst, we need to reduce the amount of Pt for cost reduction. In order to maintain the same output even when the amount of Pt is reduced, it is necessary to increase the current density per unit area of Pt surface. At high current density, mass transport is a major factor in voltage drop. Therefore, improving the oxygen transport property in CLs will lead to cost reduction of PEFCs. The CLs of PEFCs are configured such that a thin film of ionomer covers platinum-supported carbon. Y. Yakovlev et al. studied proton, electron and oxygen transport in catalyst layers with different ionomer content (1). They found that the aged CL tends to retain more liquid water, causing a significant decrease in actual porosity (1). T. Mabuchi et al. analyzed the evolution of ionomer morphologies in solutions during solvent evaporation by using molecular dynamics (MD) simulations (2-4). The Knudsen number is important for the diffusion phenomenon of gas in a porous structure. The Knudsen number is defined by

$$Kn = \frac{\lambda}{L}, \qquad [1]$$

where λ is the mean free path of gas molecules, and L is the representative length of the system. When the Knudsen number is large enough ($Kn \geq 10$), gas transport is in the Knudsen diffusion regime, where the diffusion process is determined by the collisions between gas molecules and wall surfaces rather than by the collisions between gas molecules (5). In such a case, the behavior of gas molecules on solid surfaces is important. The transport of oxygen in the CLs is dominated by the Knudsen diffusion because the mean free path of oxygen is sufficiently large with respect to the pore size. Kinefuchi et al. performed a numerical analysis of gas transport in a microporous layer using the direct simulation Monte Carlo (DSMC) method (6). They analyzed the oxygen diffusion resistance in a structure reproduced from X-ray CT imaging. However, in the analysis, the adsorption of gas molecules and subsequent surface diffusion on ionomer thin films were not introduced. Nakauchi et al. analyzed the scattering mechanism of oxygen molecules impinging on ionomer thin films using MD simulations (7-9). They classified the behavior of oxygen molecules impinging on the ionomer into "diffuse reflection" and "surface diffusion", in the latter of which oxygen molecules are diffusing on the surface while colliding with the surface multiple times. W. Wang et al. analyzed the interfacial interactions in the three-phase interface, i.e., carbon, Pt, and ionomer using MD simulations (10). They indicated that increasing water content improves water aggregation and cluster interconnection, both of which benefit the transport of oxygen and proton in the CL. Kurihara et al. analyzed the permeability of oxygen in ionomers using the MD method (11-12). They indicated that the oxygen permeability of ionomers is governed by the oxygen solubility at the interface. Although the transport properties of oxygen in the porous structure of CLs have been studied, the effect of surface diffusion, which is the motion of oxygen molecules on ionomer thin films, on the transport properties has not yet been clarified. In this study, we analyzed the transport properties of oxygen molecules in the CLs of PEFCs using the Monte Carlo method. We focused on the effect of surface diffusion on the overall transport characteristics of oxygen in the CLs.

Simulation Methodology

We used the three-dimensional structure data of a CL constructed by T. Kaneko et al. (13). Briefly, a computational system was constructed by the following procedure for a catalyst layer sample made of platinum-supported carbon (Tanaka Kikinzoku Kogyo TEC10V30E) and Nafion with the ionomer to carbon (I/C) weight ratio of 1.0. The three-dimensional structure of the sample was obtained as sequential slice images using a focused ion beam-scanning electron microscope (FIB-SEM). Figure 1 shows the three-dimensional structure of the sample. The threshold value for extracting the isosurface was chosen so that the porosity was equal to that of the sample ($\varepsilon = 0.387$). Molecules were assumed to reflect specularly on the boundaries of the computational domain. Oxygen molecules were randomly placed in the calculation system ($x \times y \times z = 5.4 \times 5.4 \times 4.728$ μm). The time step was set at 5 ps and the calculation time was set at 4 μs. When an oxygen molecule hits a wall, it diffuses on the ionomer surface for a period of time and then diffusely reflected (14). In order to examine the effect of surface diffusion on the transport properties of oxygen molecules, the simulation was performed using various conditions of the surface diffusion. The conditions are defined by the surface diffusion coefficient that controls the diffusion velocity of the surface diffusion as $D_s = 1\times10^{-m}$ m^2/s (m = 4, 5, 6, 7, 8) and the time constant, which controls the residence time of oxygen molecules as $\tau = 1\times10^{-n}$ s (n = 8, 9, 10, 11, 12, 13). The residence time of oxygen molecules follows a probability density function,

$$P(t) = \frac{1}{\tau}\exp\left(-\frac{t}{\tau}\right). \quad [2]$$

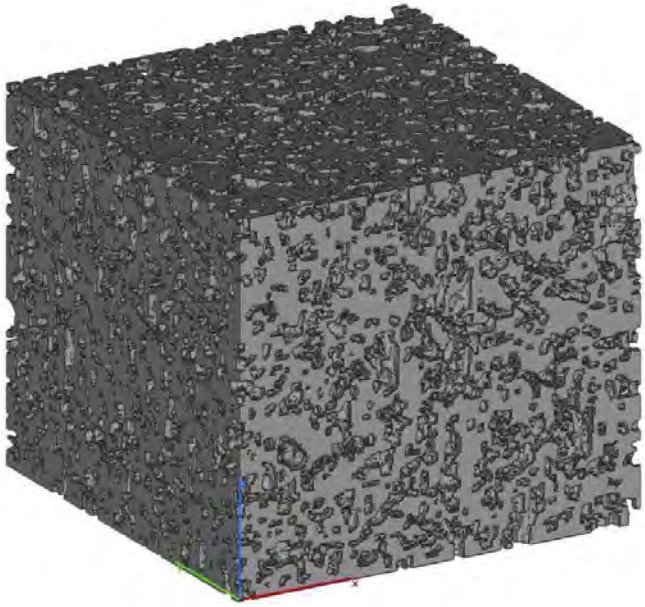

Figure 1. 3D structure of a catalyst layer sample. The dimensions of the structure in the *x*-, *y*-, and *z*-directions are 5.4, 5.4, and 4.728 μm.

Results and Discussion

The dependence of the oxygen mobility in the CLs on the surface diffusion was analyzed by evaluating the effective diffusion coefficient

$$D_{\mathrm{e}} = \varepsilon \lim_{t\to\infty} \frac{1}{6(t-t_0)} \langle |\mathbf{r}(t) - \mathbf{r}(t_0)|^2 \rangle, \quad [3]$$

where $\mathbf{r}(t)$ is a position vector and t_0 is a start time. Figure 2 shows the effective diffusion coefficient of oxygen in the CL for various surface diffusion coefficients D_s. The red horizontal line shows the effective diffusion coefficient of oxygen without the surface diffusion, which is 2.75×10^{-6} m^2/s. As the surface diffusion coefficient increases, the effective diffusion coefficient of oxygen increases. When the surface diffusion coefficient is small, the increase in the time constant results in the decrease in the effective diffusion coefficient of oxygen. This result can be considered that D_s is smaller than diffusion coefficient in the porous (D_g = 2.75×10^{-6} m^2/s). However, when the surface diffusion coefficient is large, as the time constant increases, the effective diffusion coefficient of oxygen has a peak value and then decreases. Thinking in the same way, if time constant increases, so should the effective diffusion coefficient, because the surface diffusion coefficient, D_s, is larger than diffusion coefficient in the porous (D_g = 2.75×10^{-6} m^2/s).

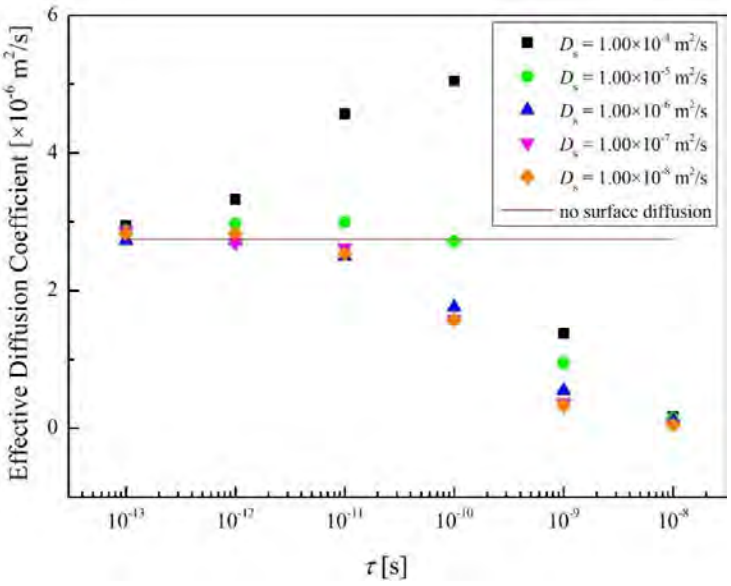

Figure 2. Effective diffusion coefficient of oxygen in the CL as a function of the time constant of surface residence time. The results for various surface diffusion coefficients are plotted with different markers. The red horizontal line shows the effective diffusion coefficient of oxygen in the calculation without surface diffusion.

In order to analyze the reason why the effective diffusion coefficient of oxygen does not continue to increase when the residence time of surface diffusion increases on condition that the surface diffusion coefficient is large, the trajectories of oxygen molecules were analyzed. The result of $D_s = 1\times10^{-4}$ m^2/s was used. Figure 3 shows the effective diffusion coefficient, D_e, and the average moving distance (See the inset for the definition) of oxygen during surface diffusion, L_m, as a function of the time constant of the surface residence time. Rectangular markers show the effective diffusion coefficient and circular markers show the average moving distance during surface diffusion. A larger time constant results in an increase in the distance traveled during surface diffusion and the effective diffusion coefficient before the time constant exceeds 1×10^{-10} m^2/s. The further increase in the time constant reduces both of them in spite of the longer surface residence time.

When the surface diffusion coefficient is large and the surface residence time increases, the moving distance of oxygen molecules on the surface per surface resistance time decreases due to the tortuosity in the three-dimensional structure of the CL. Oxygen molecules move on a bending surface as shown in Fig. 4. When the product of the surface residence time and the time constant ($D_s\tau$) is small, the effect of tortuosity on the surface is small as illustrated in Fig. 4(a). When $D_s\tau$ is large, the tortuosity effect becomes significant as shown in Fig. 4(b). When the residence time of surface diffusion is small, the difference between the moving path and the moving distance in surface diffusion is not so large. However, the difference becomes significant when the residence time is large. As a result, the moving distance per residence time is smaller than that when the oxygen molecule moves linearly.

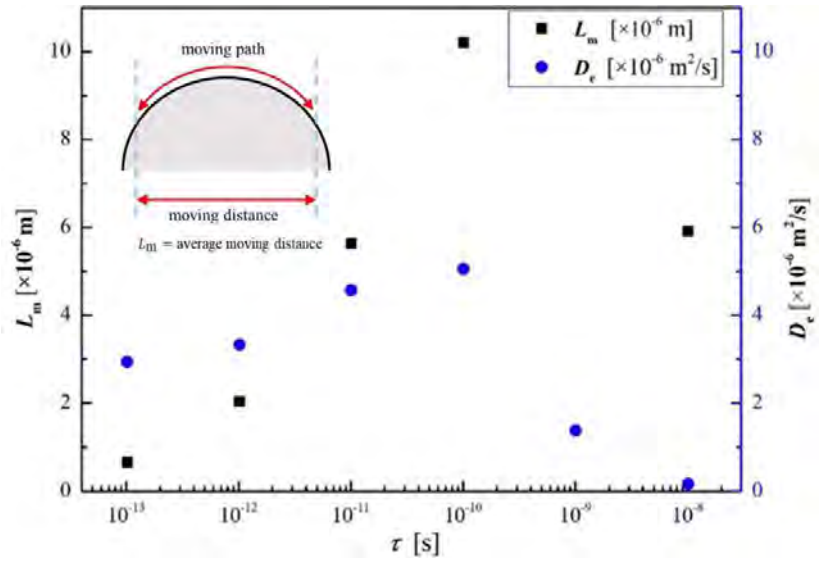

Figure 3. Effective diffusion coefficient and average moving distance during surface diffusion of oxygen in the CL as a function of the time constant of the surface residence time. The surface diffusion content is $D_s = 1.00\times10^{-4}$ m^2/s. Circular markers show the effective diffusion coefficient and rectangular makers show the average moving distance during surface diffusion.

Therefore, when oxygen molecules diffuse on a surface as shown in Fig. 4(b), the effective surface diffusion does not become large, although the product of the surface diffusion coefficient and the time constant is large. The behavior of surface diffusion is influenced by the surface diffusion coefficient, time constant and the tortuosity of the three-dimensional structure of the CLs. Therefore, in order to understand the oxygen transport in the CLs, it is necessary to understand elements of the three-dimensional structure that affect the oxygen transport, such as the porosity of bending structure.

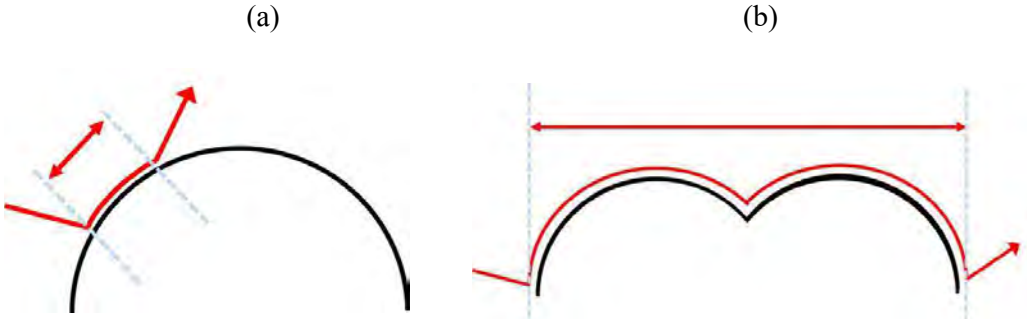

Figure 4. Behavior of oxygen molecule moving on the bending surface. (a) shows the behavior when the product of D_s and τ is small and (b) shows the behavior when the product of D_s and τ is large.

Conclusions

In this study, we calculated the oxygen transport characteristics in a CL of PEFCs considering the behavior of surface diffusion of oxygen on ionomer thin films using the Monte Carlo method. The effective diffusion coefficient of oxygen was evaluated by

changing the surface diffusion coefficient and the time constant of surface residence time. When the surface diffusion coefficient is small and the time constant increases, the effective diffusion coefficient of oxygen decreases. When the surface diffusion coefficient is large, the effective diffusion coefficient of oxygen has a peak value as the time constant increases. This phenomenon occurs due to the three-dimensional bending structure of the pore surface.

Acknowledgments

This research was supported by the New Energy and Industrial Technology Development Organization (NEDO) of Japan. We used the integrated super computation system at the Institute of Fluid Science of Tohoku University.

References

1. Y. V. Yakovlev, Y. V. Lobko, M. Vorokhta, J. Nováková, M. Mazur, I. Matolínová, and V. Matolín, *J. Power Sources*, **490**, 229531 (2021).
2. T. Mabuchi, S. F. Huang, and T. Tokumasu, *Macromolecules*, **54**(1), 115 (2021).
3. T. Mabuchi, S. F. Huang, and T. Tokumasu, *J. Polym. Sci.*, **58**(3), 487 (2020).
4. T. Mabuchi, S. F. Huang, and T. Tokumasu, *Macromolecules*, **53**(9), 3273 (2020).
5. O. Pinazza and M. Spiga, *Int. J. Heat Fluid Flow*, **24**(2), 236 (2003).
6. I. Kinefuchi, J. Oyama, K. Yokoyama, N. Kubo, T. Tokumasu, and Y. Matsumoto, *ECS Trans.*, **58**(1), 71 (2013).
7. M. Nakauchi, T. Mabuchi, I. Kinefuchi, H. Takeuchi, and T. Tokumasu, *Renewable Energy & Power Quality Journal*, **1**(14) 349 (2016).
8. M. Nakauchi, T. Mabuchi, T. Hori, Y. Yoshimoto, I. Kinefuchi, H. Takeuchi, and T. Tokumasu, *AIP Conf. Proc*., **2132**, 170001 (2019).
9. M. Nakauchi, T. Mabuchi, Y. Yoshimoto, T. Kaneko, I. Kinefuchi, H. Takeuchi, and T. Tokumasu , *ECS Trans*., **92**(8), 23 (2019).
10. Y. Kurihara, T. Mabuchi, and T. Tokumasu, *J. Electrochem. Soc.*, **164**(6), F628 (2017).
11. Y. Kurihara, T. Mabuchi, and T. Tokumasu, *J. Power Sources*, **414**, 263 (2019).
12. W. Wang, Z. Qu, X. Wang, and J. Zhang, *Membranes*, **11**(2), 148 (2021).
13. T. Kaneko, Y. Yoshimoto, T, Hori, S. Takagi, J. Ooyama, T. Terao, and I. Kinefuchi, *Int. J. Heat Mass Transf.*, **150**, 119277 (2020).
14. T. Hori, T. Kamino, Y. Yoshimoto, S. Takagi, and I. Kinefuchi, *Phys. Rev. E*, **97**(1), 013101 (2018).

Chapter 17

Non-PGM Catalysts & Pt-Based Catalysts

ECS Transactions, 104 (8) 379-386 (2021)
10.1149/10408.0379ecst ©The Electrochemical Society

Durability of Platinum Overlayers formed by Self-Terminating Electrodeposition

Khantesh Agrawal[a], Saroj Chaudhary[b], Damaraju Parvatalu[b], and Venugopal Santhanam[a]

[a] Department of Chemical Engineering, Indian Institute of Science, Bangalore, Karnataka 560012, India
[b] ONGC Energy Centre, Phase-II IEOT Complex, ONGC Panvel, Maharashtra 410221, India

The self-terminating electrodeposition (STED) method was used to synthesize platinum (Pt) atomic overlayers comprising 20 layers of Pt on gold substrates. The deposition of Pt on evaporated gold (Au) films was studied through linear sweep voltammetry (LSV) and potentiostatic deposition. The thickness of the synthesized Pt thin films after 20 cycles of STED was estimated from Energy Dispersive Spectroscopy (EDS) and X-ray Photoelectron Spectroscopy (XPS) measurements. The Pt loading was measured using Inductively coupled plasma-optical emission spectrometry (ICP-OES) and corroborated with chronoamperometry (CA). We further demonstrate the ability of these thin films to withstand the stringent targets of <40% loss in ECSA after 30,000 cycles of ex-situ durability analysis for Fuel Cell Vehicle (FCV) application. The ability to synthesize durable Pt films in the atomic layer regime by electrodeposition is a promising step towards a cost-effective route for PEMFC manufacturing.

Introduction

Proton exchange membrane fuel cells (PEMFC) are promising energy-efficient alternatives to combustion engines for automotive applications (1). Research efforts over the last two decades helped move towards a practical technology that can be mass adopted. Nonetheless, there is still significant scope for innovation to lower costs while meeting the stringent durability targets for FCV applications. The Pt electrocatalyst architecture in the existing FCVs uses Pt alloy nanoparticles coated on carbon black microspheres with ~0.375 mg_{Pt}/cm^2 Pt loading (2). A drawback of this architecture is that the potential transients experienced during vehicle startup and shutdown cycles lead to carbon support corrosion, loss of active surface area, and reduced electrochemical activity. Therefore, carbonless Nanostructured thin film (NSTF) electrode designs are presently being explored. One such embodiment utilizes evaporated Pt thin films with sufficient thickness to ensure macroscopic uniformity of coating for electrical connectivity and prevent corrosion of the underlying substrate (3). However, there is ample scope for developing simpler, cost-effective, additive fabrication processes to further reduce Pt/PGM loading of thin-film nanostructured electrode designs.

Electrodeposition is conventionally used for preparing a thin film of functional material on conducting substrates (4, 5). It is also a scalable technique as it is currently used for coating vessels or ornaments. An effective way to reduce Pt loading is to coat the Pt as

ultrathin skin, having only a few atomic layers. Thereby, the fraction of total Pt atoms participating in the electrochemical reaction is maximized. STED method was recently (6) demonstrated for depositing ultrathin Pt layers as a sequence of atomic layers. This article reports the results of ex-situ durability tests of such ultrathin Pt layers deposited on Au substrates. We present the material and the electrochemical characterization for Pt films synthesized using 20 cycles of STED, which can meet the guidelines in terms of Pt loading and durability for FCV applications. Overall, this work aims to evaluate STED as an additive process for synthesizing electrocatalyst with ultralow platinum loading for PEMFCs.

Experimental Methodology

Thin-film Au Substrates

Au (nominally 150 nm thick) films were deposited on a silicon wafer with an underlying adhesive layer of titanium (nominally 20 nm) using an e-beam evaporation facility at the National nanofabrication centre (NNFC), CeNSE, IISc Bangalore (India). These were then diced into samples of the desired size.

Synthesis of Pt Overlayers on Au:

The Pt overlayer on Au was synthesized using the STED method, as reported (6). The working electrode was an e-beam evaporated Au film having an exposed area of 90 mm^2. $Ag_{(s)}/AgCl_{(s)}/KCl_{(aq)}$(1M) from CH Instruments, Inc. was used as a reference electrode. For convenience, the potential values are reported with respect to the reversible hydrogen electrode (RHE). Pt foil having a surface area of 4 cm^2 was used as a counter electrode. The experiments were carried out in a standard three-electrode cell configuration used in cyclic voltammetry (CV). CH Instruments 608D potentiostat was used to carry out electrochemical characterization. The thin film of Pt overlayers was synthesized from a nitrogen purged electrolyte having 3.0 mM K_2PtCl_4, with 0.5 M KCl as a supporting electrolyte and pH adjusted to 4 (using $HClO_4$), using periodic pulsing of potential between -0.328 V and 0.872 V for 30 s each.

EDS:

A FESEM (ULTRA55, ZEISS) equipped with X-Max EDS system (Oxford Instruments, Oxford, UK) was used for EDS analysis. The accelerating voltage was set to 15 kV, with a working distance of ~9 mm and a sample tilt of 2° clockwise to maximize the SE2 electron signal and characteristic X-rays collection at the detector.

Ex-situ Durability Analysis:

The ex-situ durability analysis involved estimating ECSA values using H_{upd} measurements after subjecting the sample to the desired number of fast voltage cycles between 0.659 V and 1.009 V at a scan rate of 700 mV/s. The CV measurements were carried out in a 0.1 M $HClO_4$ electrolyte at a 50 mV/s scan rate over a voltage range of 0.059 V and 1.259 V. The electrolyte was purged using N_2 for 30 minutes prior and during the durability analysis. The samples were electrochemically activated before durability

analysis by scanning between 0.059 to 1.409V at 100 mV/s for 20 cycles to obtain a stable response in CV measurements.

ICP OES Analysis

The amount of Pt electrodeposited was calculated using Inductively Coupled Plasma Optical Emission Spectroscopy (Perkin Elmer Avio 200 ICP Optical Emission Spectrometer). The samples were leached in aquaregia for 30 s, and each sample was diluted to three concentration levels (100x, 200x, 500x). The calibration curves were obtained using a blank and three known solutions of K_2PtCl_4.

XPS:

XPS analysis was performed using a Kratos Axis Ultra, having monochromatic Al-Kα excitation (1486.6 eV). The analyzed samples were in the form of thin-film mounted on carbon tape.

Results and Discussion

Potential-dependent Pt Deposition

The underlying Au substrates were characterized by CV before Pt deposition to ensure repeatability. The charge corresponding to the gold oxide reduction peak had < 5% relative variation (303.9 ± 15.1 $\mu C/cm^2$) across three different samples. The Pt deposition profile was analyzed by linear sweep voltammetry from 0.956 V to -0.454 V at 2 mV/s (Figure 1). Appreciable currents for Pt reduction onto Au surface start to appear below 0.5 V. As the potential scan is continued, there is a substantial increase in the current, to a maximum around 0.1 V, which is related to diffusion-limited $PtCl_4^{2-}$ reduction (6). Further, the current diminishes because of increased mass transfer layer thickness. This sharp drop culminates in a minimum near -0.25 V, indicating quenching of bulk Pt deposition. The current rise beyond -0.25 V is attributed to the hydrogen evolution reaction (HER). The deposition profile at different potentials was analyzed by potentiostatic experiments for 500 s each at -0.328 V, 0.072 V and 0.872 V, which correspond to faintly visible Pt thin film (corresponding to atomically thin layered Pt), bulk deposit of Pt film, and no Pt film respectively (see insets of Figure 1). Despite having an overpotential of more than 1V, where bulk deposition would have been expected ordinarily, a very thin film corresponding to a Pt monolayer could be synthesized at -0.328 V because of the remarkable alteration of double-layer arising out of H adsorption, as described earlier (6).

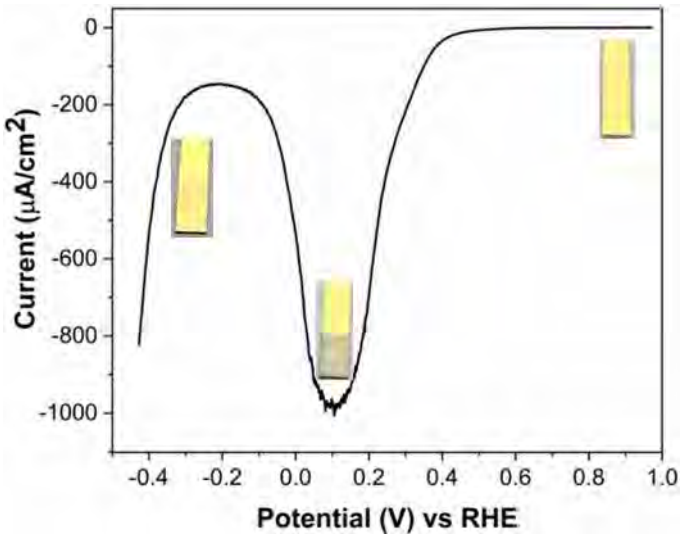

Figure 1. LSV profile for Pt deposition on Au substrate from 3.0 mM K_2PtCl_4 solution maintained at pH 4. The insets are digital images of potentiostatic deposition of Pt on Au for 500 s at -0.328 V, 0.072 V and 0.872 V respectively.

Pt Overlayers Formation with 20 Cycles of STED

The potential scheme, as shown in Figure 2(a), was applied to synthesize Pt overlayers on Au. The current corresponding to Pt reduction attenuates to ~0 A within a few seconds, denoting how fast deposition quenching happens. The current spikes for electrodeposition with and without K_2PtCl_4 were compared to confirm the Pt deposition. As shown in Figure 2(b), the current profile in the case of K_2PtCl_4 is higher with more time to attenuate to 0 A due to the Pt reduction process. The I-t response for the chronoamperometric deposition for 20 cycles of Pt deposition is shown in Figure 2(c), where the negative current spikes correspond to Pt deposition, while positive spikes correspond to H_{upd} desorption (IUPAC convention). The increase in the current maximum with the number of cycles indicates increasing surface coverage with the number of Pt cycles and suggests that the deposition is not strictly happening in a layer-by-layer fashion. The area under the I-t curve corresponds to the total charge required for Pt deposition. Using Faraday's law of electrolysis, the mass of Pt and was found to be 39.99 ± 0.84 μg/cm^2; which is in close agreement with the value of 41.94 ± 8.18 μg/cm^2 measured using ICP-OES.

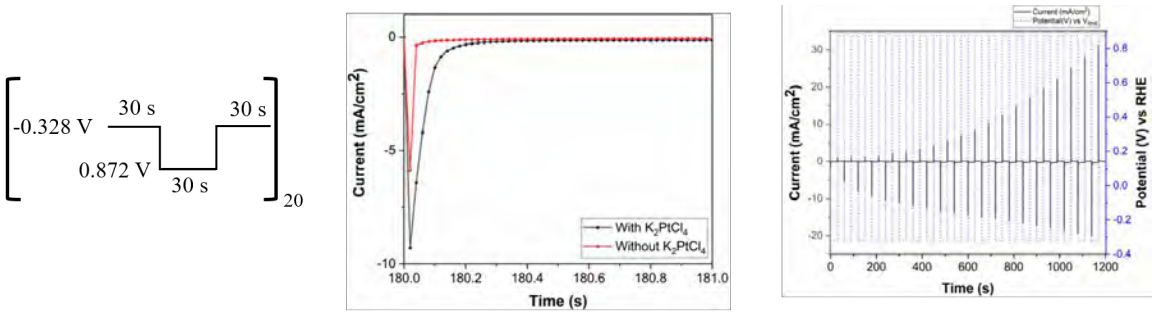

(a) (b) (c)

Figure 2. (a) Potential scheme applied for STED, (b) Difference in the CA profiles with and without K_2PtCl_4 in the electrolyte, (c) CA profiles for 20 cycles of Pt deposition. The applied potential profile is also shown as dotted lines.

Ex-situ Durability Analysis

The Pt samples after activation underwent ex-situ durability protocol that simulate the effects of varying power demand, which a typical drive cycle in a fuel cell vehicle would enforce on the electrocatalyst (7). The total charge density ($\mu C/cm^2$) corresponding to desorption of H_{upd} between 0.06 to 0.4 V is used as a measure of electrochemical activity. The corresponding CVs after the desired numbers of load cycles are shown in Figure 3(a). The initial H_{upd} charge, averaged over three different samples, was 395.3 ± 23.9 $\mu C/cm^2$ (corresponding to ECSA of 4.71 ± 0.34 m^2/g_{Pt}). The < 7% variation in measured H_{upd} activity attests to the excellent repeatability of the deposition protocol followed. The variation of electrochemical activity (averaged over three different samples) with the number of load cycles is shown in Figure 3(b). This corresponds to ECSA retention of 62.9 ± 4.9% after 30,000 durability cycles which meets the DOE criterion of < 40% loss in ECSA for FCV applications. The complete coverage of Au substrate by the Pt layer was confirmed by the absence of a cathodic peak around 1.1 V, corresponding to the reduction of gold oxide. The characteristic peaks around 0.12 V and 0.22 V in the H_{des} region correspond to the desorption of H atoms from polycrystalline Pt samples (8).

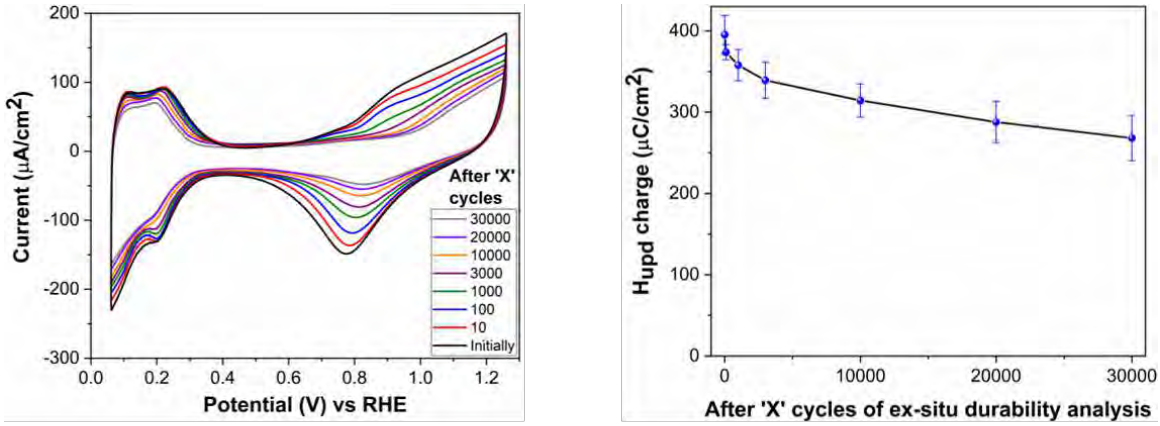

(a) (b)

Figure 3. (a) Representative CV curves in 0.1M $HClO_4$ obtained intermittently during ex-situ durability test for 30,000 cycles (b) H_{upd} variation with number of load cycles during ex-situ durability analysis.

Material Characterizations

EDS characterization of the as-synthesized samples confirms the presence of Pt. Table I presents the elemental analysis from five different randomly chosen spots. The average volumetric ratio of Au/Pt is determined to be 31.47 ± 4.76 (atomic ratio normalized with atomic density). Since the Au layers nominal thickness is 150 nm, the average Pt overlayer thickness is estimated to be 4.86 ± 0.78 nm. This value corresponds well with the thickness expected (~4.6 nm) for 20 atomic layers with Pt(111) d-spacing.

TABLE I. Elemental analysis (atom %) based on EDS spectra from five different spots

Elements	Spot 1	Spot 2	Spot 3	Spot 4	Spot 5	Average
Si K	38.92	38.74	38.89	39.43	39.81	39.16
Ti K	1.40	1.75	1.48	2.17	1.31	1.62
Pt M	1.76	1.92	2.27	2.44	1.79	2.04
Au M	57.93	57.59	57.35	55.95	57.09	57.18
Volumetric ratio of Au/Pt (atomic ratio scaled with atomic density)	36.21	33.01	27.80	25.23	35.10	31.47

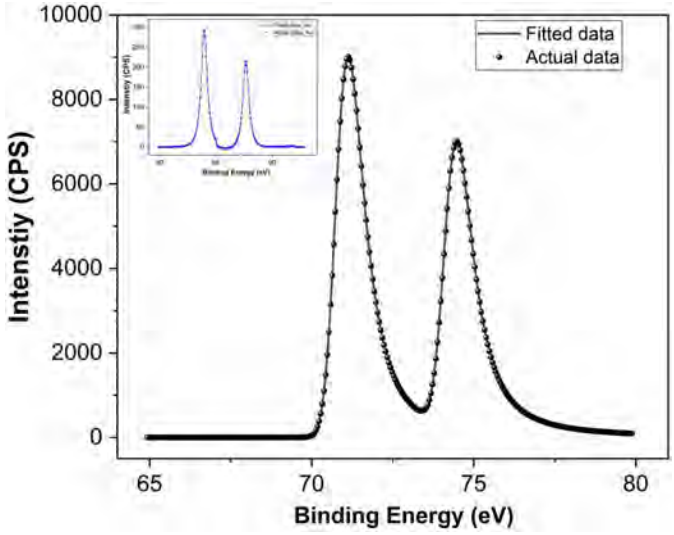

Figure 4. XPS spectra of Pt4f region for samples synthesized using 20 cycles of STED. The inset shows signal from Au4f region

XPS characterization confirms the presence of Pt on the surface, as the Pt signal is much higher in magnitude than the Au signal (Figure 4). Such Pt surface enrichment is expected for overlayer deposition. The presence of Pt $4f_{7/2}$ peak and Pt $4f_{5/2}$ peaks at 70.84 eV and 74.19 eV, respectively, confirm that Pt is present mainly in the Pt(0) state. The thickness of the Pt overlayers was approximated from the XPS signal using a simple homogeneous overlayer model derived from Beer-Lambert law applied to the straight-line attenuation as described earlier (9, 10). The computed value of the thickness is 5.08 ± 0.25 nm (from three different samples), lies within 5% of the value estimated by EDS (five different spots within a sample).

Conclusions

Twenty atomic layers of Pt were electrodeposited using the STED technique on e-beam evaporated Au substrate. The chronoamperometric currents corresponding to Pt reduction show an increase with the number of cycles, indicating increasing coverage with the number of cycles. The measured Pt loading using ICP OES (41.94 ± 8.18 μg/cm^2) matches closely with that calculated from the area under the Pt reduction peaks in the chronoamperometry curve (39.99 ± 0.84 μg/cm^2). The estimated thickness of Pt overlayer using EDS (4.86 ± 0.78 nm) and XPS (5.08 ± 0.25 nm) closely match with the expected thickness equivalent to 20 atomic layers of Pt with Pt(111) d spacing. These results *in toto* suggest that the initial cycles have less than complete monolayer coverage, and the deposition in subsequent cycles fills these voids. A systematic study to unravel this issue is currently underway. The samples show excellent repeatability in terms of electrochemical performance for H_{upd} activity. The samples retain 62.9 ± 4.9% of their initial ECSA after 30,000 ex-situ durability cycles, fulfilling the US DOE criterion for <40% loss in ECSA.

Acknowledgements

This work was supported by the ONGC Energy Centre Trust (OECT) under project agreement IN-DL22367285507560R, 18/07/2019. The authors are thankful for the technical support provided by Mr Adarsh Ajith Naik and Mr M. Disesh. The use of e-beam evaporation facility for gold deposition at the NNFC and material characterization facilities at MNCF, CeNSE, IISc are acknowledged. K.A gratefully acknowledges support from the Prime Minister's Research Fellowship (PMRF).

References

1. P. Joghee, J. N. Malik, S. Pylypenko, and R. O'Hayre, MRS Energy & Sustainability, **2**, E3 (2015).
2. H. Lohse-Busch, K. Stutenberg, M. Duoba, and S. Iliev, *Technology Assessment of a Fuel Cell Vehicle; 2017 Toyota Mirai,* ANL/ESD-18/12, Argonne National Lab.(ANL), Argonne, IL, United States (2018).
3. M. K. Debe, *Nature*, **486**, 43 (2012).
4. X. Lu and C. Zhao, *Nat. Commun.*, **6**, 6616 (2015).
5. J. Hassoun, S. Panero, P. Simon, P. L. Taberna, and B. Scrosati, *Adv. Mater.*, **19**, 1632 (2007).
6. Y. Liu, D. Gokcen, U. Bertocci, and T. P. Moffat, *Science*, **338**, 1327 (2012).
7. J. Parrondo, T. Han, E. Niangar, C. Wang, N. Dale, K. Adjemian and V. Ramani, *Proc. Natl. Acad. Sci.*, **111**, 45 (2014).
8. L. García-Cruz, V. Montiel, and J. Solla-Gullón, *Physical Sciences Reviews*, **4**(1), 20170124 (2019).
9. Y. Liu, C. M. Hangarter, D. Garcia, and T. P. Moffat, *Surf. Sci.*, **631**, 141 (2015).
10. S. H. Ahn, Y. Liu, and T. P. Moffat, *ACS Catal.*, **5**, 2124 (2015).

Chapter 18

Pt-Based Catalysts and New Supports -Digital Session

ECS Transactions, 104 (8) 389-399 (2021)
10.1149/10408.0389ecst ©The Electrochemical Society

PEFCs Using Metallic Ti and Sn Electrocatalyst Supports

T. Ikehara[a], Z. Noda[b], J. Matsuda[b,c], M. Nishihara[c], A. Hayashi[a-d], and K. Sasaki[a-f]

Kyushu University
[a] Faculty of Engineering, Department of Hydrogen Energy Systems,
[b] International Research Center for Hydrogen Energy,
[c] Next-Generation Fuel Cell Research Center (NEXT-FC),
[d] Platform of Inter / Transdisciplinary Energy Research (Q-PIT),
[e] International Institute for Carbon-Neutral Energy Research (WPI-I2CNER),
[f] Center of Coevolutionary Research for Sustainable Communities,
Motooka 744, Nishi-ku Fukuoka 819-0395, Japan

Carbon supports, which are widely used for electrocatalysts of polymer electrolyte fuel cells (PEFCs), can be electrochemically oxidized and corroded under high potential conditions of PEFCs. Therefore, metal oxides, which are stable under PEFC conditions, have been proposed as alternative support materials. In this study, metals with porous structure, forming stable metal oxides on the outermost surface, are applied to electrocatalyst supports. Metallic titanium and metallic tin are examined, as their oxides (TiO_2 and SnO_2) are highly durable even under strongly-acidic PEFC conditions. In addition, by tailoring porous structures, their metallic supports can potentially act as both the electrocatalyst layer and the gas diffusion layer (GDL), simplifying the MEA structure and possibly fabrication processes. Such catalyst-integrated electrodes are prepared, and their electrochemical properties are evaluated.

Introduction

Currently, Pt-based catalyst on carbon-based support such as carbon black (Pt/C) is widely used as the electrocatalyst for polymer electrolyte fuel cells (PEFCs). Carbon black support has high electronic conductivity and large specific surface area for supporting highly-dispersed Pt catalyst nanoparticles. However, under cathode conditions of PEFCs, especially during start-stop cycles, the cathode potential can reach up to 1.5 V, and carbon black support can be electrochemically oxidized, causing detachment and aggregation of Pt catalyst nanoparticles (1-4). In order to solve this issue, as alternative materials of electrocatalyst support, we are developing SnO_2 and TiO_2 supports, which are relatively stable even under cathode conditions, coated on carbon-based materials acting as the conductive backbone, exhibiting high durability (5-11). However, as far as carbon materials are used, carbon corrosion problem may still be remained (6).

Here in this study, we focus on metallic materials with high electronic conductivity as electrocatalyst supports. Among them, metallic titanium and metallic tin with porous structure are applied as catalyst supports. Regarding metallic Ti, stable TiO_2 layer is formed on the outermost surface. As shown in Figure 1 (a), the Pourbaix diagram thermochemically calculated indicates that TiO_2 is stable under the PEFC cathode

condition, so that high durability is expected (5, 12, 13). Regarding metallic Sn, stable SnO_2 layer is formed on the outermost surface. As shown in Figure 1 (b), the Pourbaix diagram thermochemically calculated indicates that SnO_2 is stable under the cathode condition. SnO_2 is known to have relatively high electronic conductivity among metal oxides, so that high electrochemical activity could be expected. In addition, the electrocatalyst supports of metallic Ti and metallic Sn could have porous structure with high gas diffusivity, which may also act as gas diffusion layer (GDL). Such electrode concept can be expected to simplify the whole MEA structure, and fabrication processes. In this study, carbon-free catalyst/GDL integrated electrodes using metallic Ti and metallic Sn are prepared and characterized.

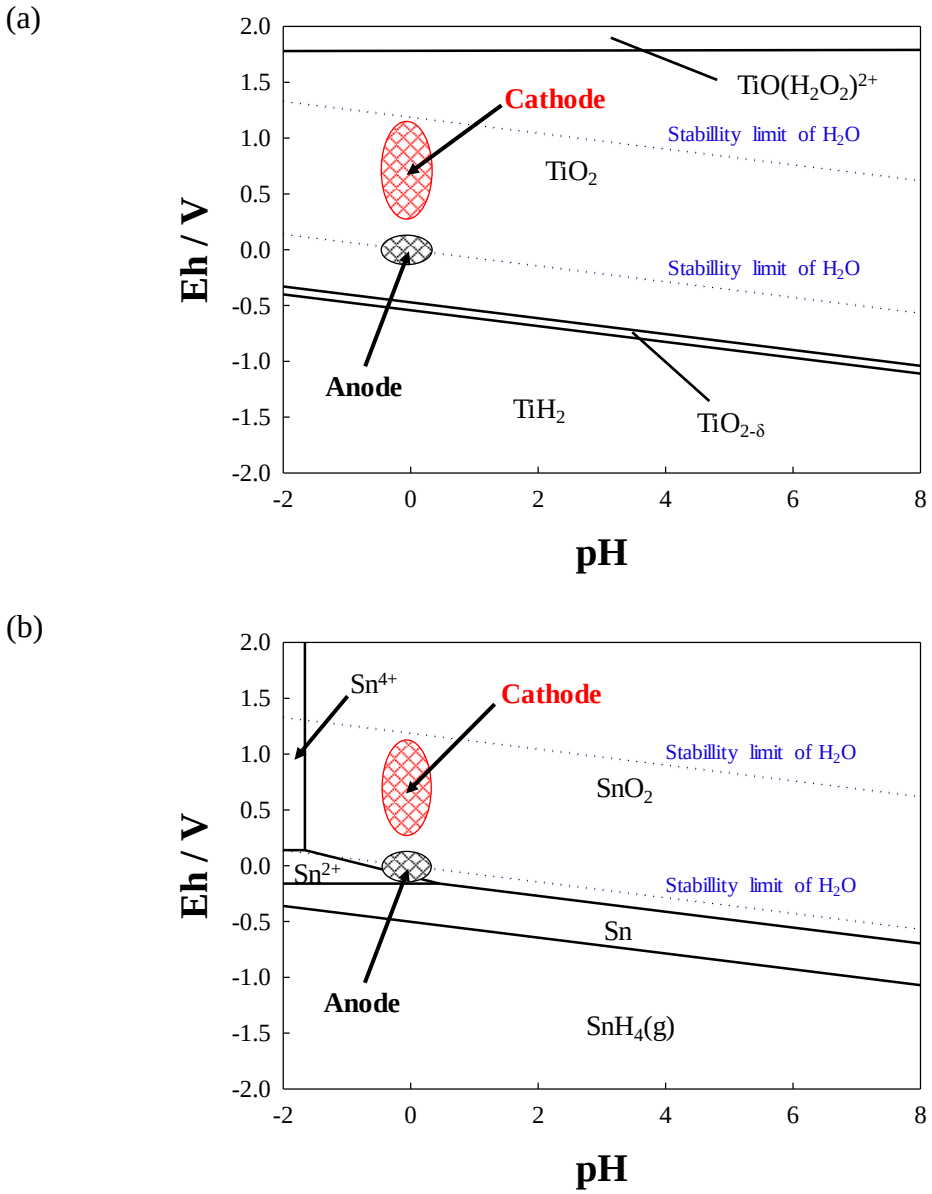

Figure 1. Pourbaix (E-pH) diagram of (a) the Ti-H_2O system and (b) the Sn-H_2O system at 353.15 K (80 °C), thermochemically calculated (HSC Chemistry, Metso Outotec, Finland).

Experimental

Preparation of Porous Pt/Ti Sheets: Surface Treatment for Larger Surface Area

Figure 2 shows the preparation procedure of the porous Pt/Ti sheets. In this study, porous Ti sintered sheet was used to prepare the Pt/Ti sheet (WEBTi-K, Toho Titanium, Ltd., Japan). Since the surface area of the initial Ti sintered sheet was too small as a catalyst support, surface treatment was made with NaOHaq to increase the specific surface area. First, Ti sheet was etched in 1 M NaOHaq at 60 °C for 1 h (13-15). After the etching, the Ti sheet was immersed in 0.01 M HNO_3aq for 30 min for neutralization to remove NaOH. Furthermore, in order to improve the crystallinity of the Ti sheet surface, heat treatment was made at 500 °C for 30 min in reducing atmosphere (5%H_2-N_2). In addition, Nb-doped Ti sheets were also prepared by impregnating in $NbCl_5$ to improve the electronic conductivity of the Ti sheet surface (Figure 2 (iii)).

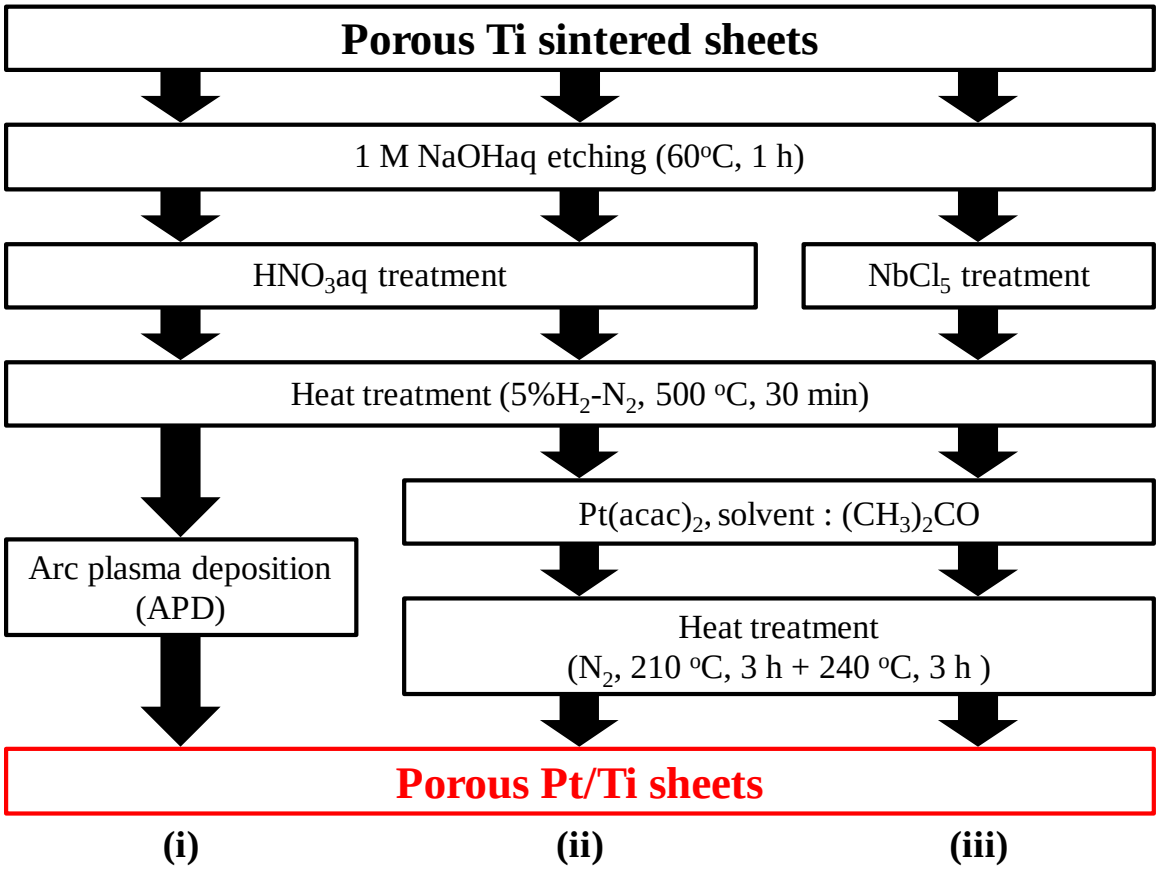

Figure 2. Preparation procedure of the porous Pt/Ti sheets.

Preparation of Porous Pt/Ti Sheets: Pt Catalyst Decoration

Arc Plasma Deposition (APD) Method. Pt nanoparticles were deposited on the etched Ti sheets by applying arc plasma deposition (APD) system (Advanced RIKO, Inc., Japan). APD is a method using which Pt can be made into plasma and vapor-deposited on a substrate by discharging the electric charge filled in the capacitor at once (16). Pt loading

on the Ti sheet can be digitally controlled by varying the number of APD pulses. Pt loading was e.g. 0.063 mgPt cm^{-2} at 1000 pulses (14).

Platinum(II) Acetylacetonate (acac) Method. Pt nanoparticles were deposited on the etched Ti sheets by applying platinum(II) acetylacetonate (acac) method. This is a method in which platinum(II) acetylacetonate is used as a precursor, followed by thermal reduction of Pt(II) to Pt(0) to prepare Pt nanoparticles (17). In this study, acetone was selected as the solvent, and the prepared solution was immersed. Thermal reduction treatment was made at 210 °C for 3 h and then at 240 °C for 3 h in N_2 atmosphere.

Preparation of Porous Pt/Sn Sheets

Figure 3 shows the preparation procedure of the porous Pt/Sn sheets. In this study, cellulose-based filter paper (MF-Millipore, Merck Millipore Ltd.) was used as a template for the preparation of porous Pt/Sn sheets. First, SnO_2 sol (Taki Chemical, Ltd., Japan) was impregnated into the filter paper in vacuum. The cellulose-based template was then removed by oxidizing heat-treatment at 300 °C in air for 1 h. After that, porous Sn sheets were prepared by reducing heat-treatment at a given temperature for 1 h in 5%H_2-N_2 atmosphere in order to reduce SnO_2 to metallic Sn. Pt nanoparticles was then deposited on the porous Sn sheets by the platinum(II) acetylacetonate (acac) method.

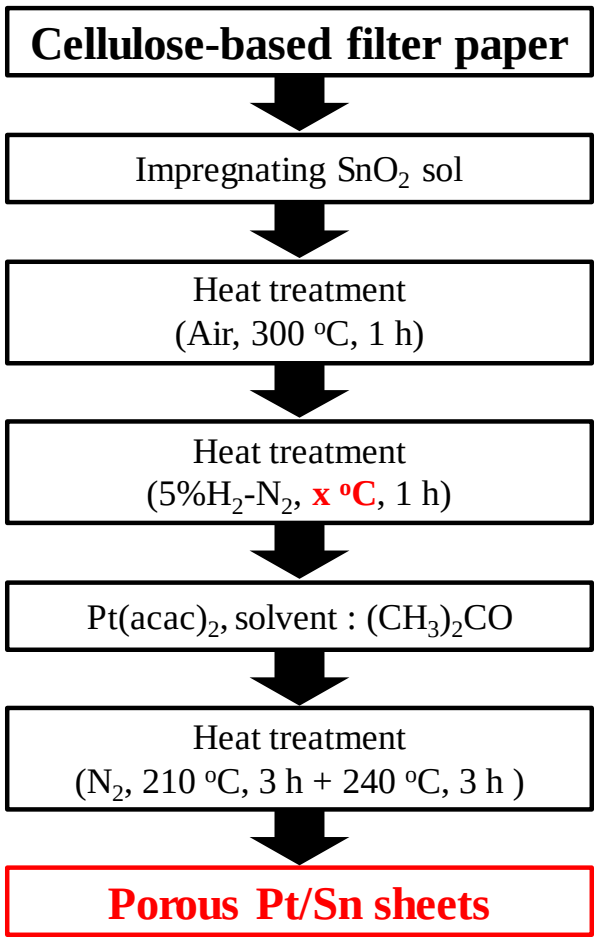

Figure 3. Preparation procedure of the porous Pt/Sn sheets.

Characterization of Electrocatalysts

Microstructural observation of the two kinds of porous metallic sheets prepared, Pt/Ti sheets and Pt/Sn sheets, was made by a field-emission scanning electron microscopy (FE-SEM, SU-9000, Hitachi High-Technologies, Japan). Thermogravimetry / differential thermal analysis (TG-DTA, Thermo plus EVO2, Rigaku, Japan) was applied to examine changes at high temperatures. Pt loading on the sheets was measured by using inductively coupled plasma atomic emission spectroscopy (ICP-AES, ICPE-9000, Shimazu, Japan), after dissolving samples into aqua regia.

Electrochemical Measurements (Half-Cell)

Electrochemical half-cell measurements of the Pt/Ti sheets and the Pt/Sn sheets were performed using an automatic polarization system (HZ-5000, Hokuto Denko Co., Japan). The working electrode was 0.196 cm^{-2} disk-shaped electrode based on Au. Pt wire was used as the counter electrode. Ag/AgCl electrode in saturated KCl was used as the reference electrode. The electrolyte solution was 0.1 M HCl_4. Cyclic voltammogram (CV) measurements were performed at a scanning speed of 50 mV s^{-1} and in a scanning potential range of 0.05-1.2 V_{RHE} with N_2 bubbling. Linear sweep voltammogram (LSV) measurements were performed at a scanning speed of 10 mV s^{-1} and in a scanning potential range of 0.2-1.2 V_{RHE} with O_2 bubbling.

Results and Discussion

Microstructure of Porous Pt/Ti Sheets

Figure 4 shows an FE-SEM micrograph of the porous Pt/Ti sheet prepared. After the NaOH etching, the surface on the Ti porous structure was covered with needle-like TiO_2 structures with a diameter of several nm, indicating a large surface area (13-15, 18). By the ICP-AES measurement, the Pt/Ti sheets prepared by the acac method (Figure 2 (ii) and (iii)) were deposited at a Pt loading of 25.3 μgPt cm^{-2}. Pt loading of the Pt/Ti sheets prepared by the APD method (Figure 2 (i)) could be digitally controlled by changing the number of APD pulses.

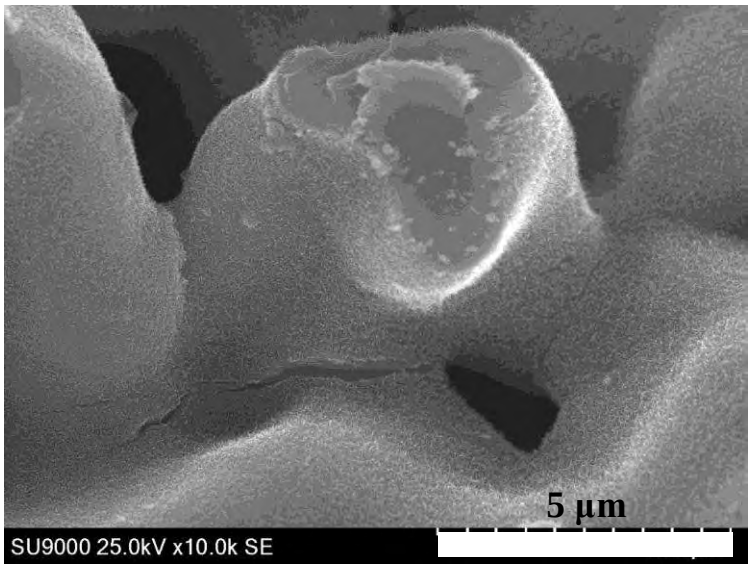

Figure 4. FE-SEM micrograph of the porous Pt/Ti sheet.

Electrochemical Measurements of Porous Pt/Ti Sheets

Figure 5 shows the results of the half-cell measurements ((a) CV, and (b) LSV) of the Pt/Ti sheets prepared by the different processes (Figure 2 (i) to (iii)). From the CV results, the Pt/Ti sheet prepared by the acac method (ii) exhibited twice larger electrochemically active surface area (ECSA) than that prepared by the APD method (i), but almost no ORR activity was found. From these results, it was considered that the electronic conductivity at the surface of the Ti support may be relatively low due to the formation of insulating TiO_2, so that the Pt catalyst particles remained electronically isolated. In order to obtain better electrochemical activity, Pt/Ti sheet prepared by the acac method was Nb-doped in order to improve electronic contact between the Pt catalysts and the metallic Ti support (Figure 2 (iii)). The Nb-doped Pt/Ti sheet (iii) exhibited improved ORR activity in Figure 5 (b), while maintaining ECSA in Figure 5 (a). These results suggest that the electronic conductivity of the outermost surface of the Ti support may be improved due to the Nb-doping of the Ti sheets.

(a)

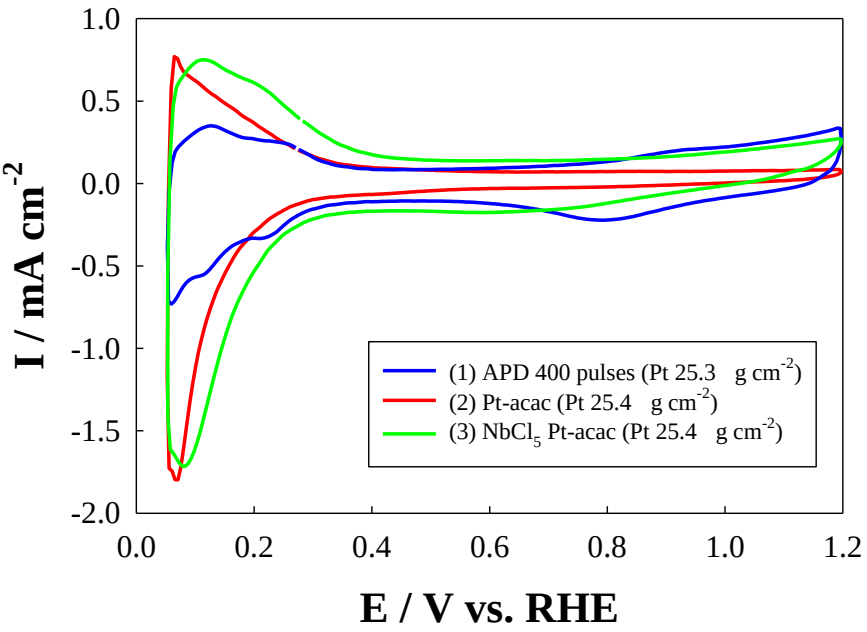

(b)

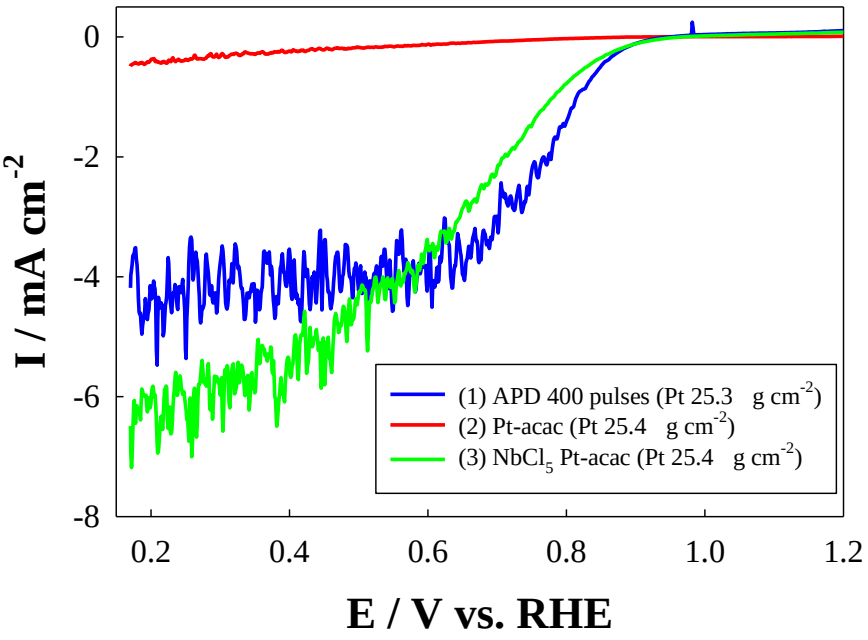

Figure 5. Electrochemical activity of the Pt/Ti sheet electrodes measured using the half-cell setup: (a) cyclic voltammograms (CV), and (b) linear sweep voltammograms (LSV).

Microstructure of Porous Pt/Sn Sheets

Figure 6 shows the FE-SEM images of the porous Pn/Sn sheets prepared. It was confirmed that porous microstructure originated from the filter paper template is formed. It was also confirmed that Pt nanoparticles of several nm in diameter were highly decorated on the porous microstructure.

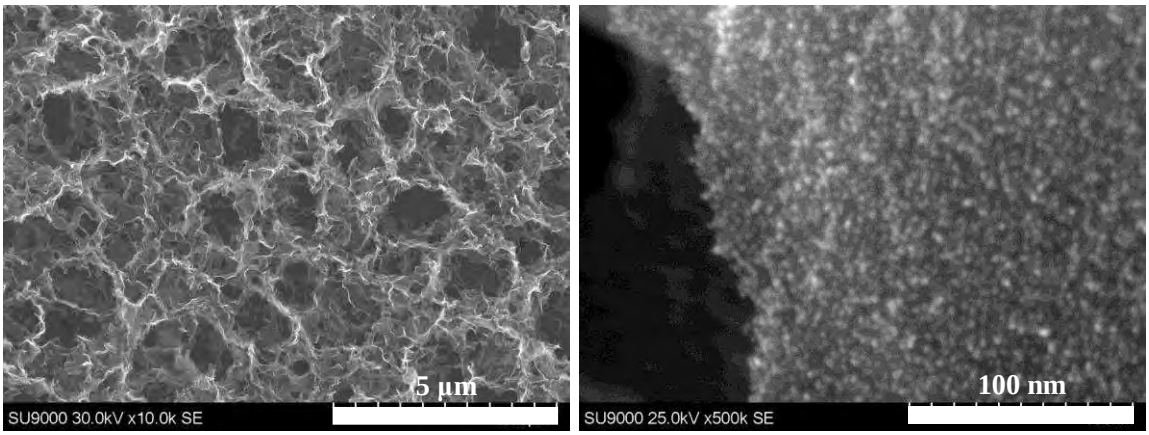

Figure 6. FE-SEM micrographs of the porous Pt/Sn sheets in a lower magnification (left) and in a higher magnification (right).

Optimization of Heat Treatment Conditions for Reducing SnO_2 to Sn

Optimizing reducing heat-treatment condition is necessary for the preparation of metallic Sn with porous microstructure. If heat treatment temperature is too low, the reduction of SnO_2 to metallic Sn is kinetically difficult and high electronic conductivity needed as a catalyst support cannot be achieved. In contrast, if heat treatment temperature is too high, the reduced metallic Sn will be melted because the melting point of metallic Sn is 231.9 °C. Therefore, porous Sn sheets reduced at 230 °C (below the melting point of metallic Sn), 300 °C, 400 °C, and 500 °C were prepared. Figure 7 shows FE-SEM mkicrographs of the porous Sn reduced at each heat treatment temperairture. The Pt/Sn sheets after reducing heat-treatment at and below 400 °C were able to maintain the porous microstructure originated from the filter paper templates. It may be possible that the surface of SnO_2 was reduced and melted, but a part of SnO_2 was remained to retain such porous microstructure.

In contrast, in the Pt/Sn sheets after reducing heat-treatment at 500 °C, porous microstructure was destroyed. TG-DTA measurements were also performed for SnO_2 in the same 5%H_2-N_2 atmosphere. Figure 8 shows the TG-DTA results for SnO_2. From these results, the weight of the sample started to decrease rapidly around 500 °C, suggesting that the SnO_2-containing sample was reduced to metallic Sn, losing oxygen, which was in the liquid state above the melting temperature. The initial porous structure is therefore collapsed, losing the surface area, which makes it difficult to decorate Pt catalysts to obtain high electrochemical activity. These results indicate that the reducing heat-treatment should be made below 400 °C.

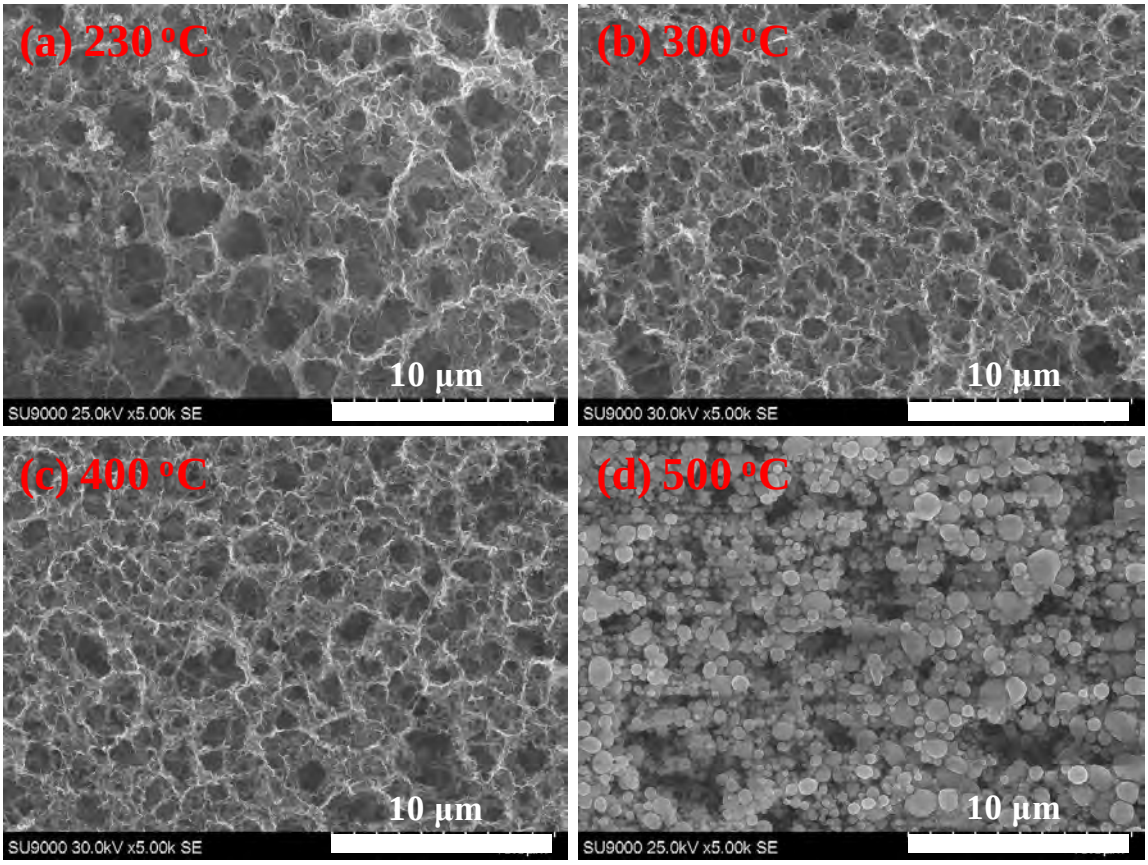

Figure 7. FE-SEM micrographs of the porous Pt/Sn sheets with different reducing heat-treatment temperatures: (a) 230 °C, (b) 300 °C, (c) 400 °C, and (d) 500 °C.

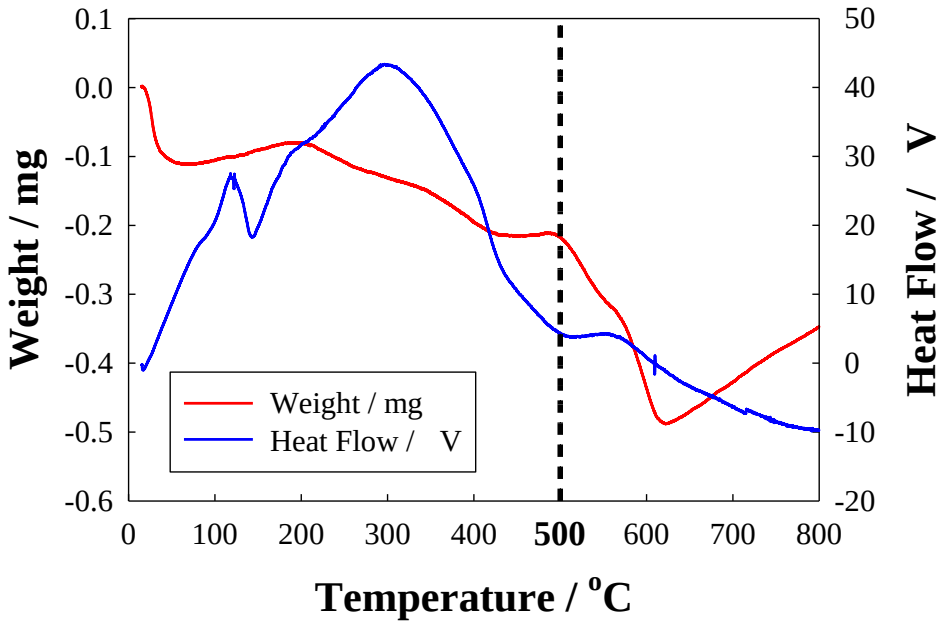

Figure 8. TG-DTA results of porous SnO_2 in 5%H_2-N_2 atmosphere.

Pt Catalyst Decoration on Porous Sn sheets

Pt nanoparticles were decorated by the acac method on the porous Sn sheets after reducing heat-treatment at 230 °C, 300 °C, 400 °C, and 500 °C. Pt loading on the prepared porous Sn sheets was determined by ICP-AES measurements. TABLE I shows the ICP-AES results of the Pt catalyst loading on each Sn sheet. Whilist the designated Pt loading on the Sn sheets was 30 wt.%, the Pt loading after the heat-treatment of the Sn sheets at 500 °C was much lower, 3.41 wt.%. From the FE-SEM micrographs and the TG-DTA results, it is considered that the metallic Sn was partially melted, leading to a decrease in surface area of the catalyst support. As shown in TABLE I, larger amount of Pt could be impregnated on the porous Sn sheets with larger surface area. Optimization of porous microstructures is needed by further controlling preparation conditions of such catalyst-impregnated metallic electrodes for PEFCs.

TABLE I. Pt catalyst loading on the porous Sn sheets after different reducing heat-treatments, defined as the weight ratio of Pt in the Pt/Sn sheets.

Reducing Heat-treatment Temperature	Pt loading
230 °C	13.4 wt.%
300 °C	12.6 wt.%
400 °C	9.84 wt.%
500 °C	3.41 wt.%

Conclusions

Catalyst-impregnated porous metallic electrodes such as Pt/Ti and Pt/Sn have been prepared. For the porous Pt/Ti sheet electrodes, additional Nb-doping on the porous Ti surfaces was effective to improve electrochemical properties. For the porous Pt/Sn sheet electrodes, further improvement of e.g. reducing heat-treatments is needed to optimize their porous microstructure and Pt loading. Further studies are needed and are in progress.

Acknowledgment

Financial support from New Energy and Industrial Technology Development Organization (NEDO) is gratefully acknowledged (Contract No. 20001214-0).

References

1. L. M. Roen, C. H. Pail, and T. D. Jarvi, *Electrochem. Solid-State Letters*, **7**, A19 (2004).
2. A. Ohma, K. Shinohara, A. liyama, T. Yoshida, and A. Daimaru, *ECS Trans.*, **41** (1), 775 (2011).
3. C. A. Resiser, L. Bregoli, T. W. Patterson, J. S. Yi, J. D. Yang, N. L. Perry, and T. D. Jarvi, *Electrochem. Solid-State Letters*, **8**, A273 (2005).
4. A. Taniguchi, T. Akita, K. Yasuda, and Y. Miyazaki, *J. Power Sources*, **130**, 42 (2004).

5. K. Sasaki, F. Takasaki, Z. Noda, S. Hayashi, Y. Shiratori, and K. Ito, *ECS Tran.*, **33** (1), 473 (2010).
6. Y. Takabatake, Z. Noda, S. M. Lyth, A. Hayashi, and K. Sasaki, *Intl. J. Hydrogen Energy*, **39**, 5074 (2014).
7. T. Tonosako, Z. Noda, J. Matsuda, M. Nishihara, A. Hayashi, and K. Sasaki, *ECS Trans.*, **98** (9), 523 (2020).
8. S. Matsumoto, M. Nagamine, Z. Noda, J. Matsuda, S. M. Lyth, A. Hayashi, and K. Sasaki, *J. Electrochem. Soc.*, **165**, 1165 (2018).
9. Y. Nakazato, D. Kawachino, Z. Noda, J. Matsuda, S. M. Lyth, A. Hayashi, and K. Sasaki, *J. Electrochem. Soc.*, **165**, F1154 (2018).
10. T. Yoshizumi, M. Nagamine, Z. Noda, J. Matsuda, A. Hayashi, and K. Sasaki, *ECS Trans.*, **92** (8), 479 (2019).
11. A. Masao, S. Noda, F. Takasaki, K. Ito, and K. Sasaki, *Electrochem. Solid-State Lett*, **12**, B119 (2009).
12. W. Q. Han, and A. Zettl, *Nano Lett.*, **3**, 681 (2003).
13. D. Kawachino, M. Yasutake, H. Odoi, Z. Noda, J. Matsuda, A. Hayashi, and K. Sasaki, *ECS Trans.*, **86** (13), 541 (2018).
14. T. Ikehara, Z. Noda, J. Matsuda, M. Nishihara, A. Hayashi, and K. Sasaki, *ECS Trans.*, **98** (9), 573 (2020).
15. Y. F. Chen, C. Y. Lee, M. Y. Yeng, and H. T. Chiu, *Mater. Chem. Phys.*, **80**, 39 (2003).
16. Y. Agawa, M. Kunimatsu, T. Ito, Y. Kuwahara, and H. Yamashita, *ECS Electrochem. Lett.*, **4**, F57 (2015).
17. A. Hayashi, H. Notsu, K. Kijima, J. Miyamoto, and I. Yagi, *Electrochim. Acta*, **53**, 6117 (2008).
18. D. Kawachino, M. Yasutake, Z. Noda, J. Matsuda, S. M. Lyth, A. Hayashi, and K. Sasaki, *J. Electrochem. Soc.*, **167**, 104513 (2020).

Chapter 19

Pt-Based Catalyst Layers 2

ECS Transactions, 104 (8) 403-413 (2021)
10.1149/10408.0403ecst ©The Electrochemical Society

Durability Studies on PBI Based High Temperature PEMFC

H. A. Hjuler[a], K. Azizi[a], N. Seselj[a], S. M. Alfaro[a], H. R. Garcia[a], D. Gromadskyi[a], L. Hromadska[a], S. Primdahl[a], J. O. Jensen[b], Q. Li[b], S. Celenk[b], and L. N. Cleemann[b]

[a] Blue World Technologies, Egeskovvej 6C, 3490 Kvistgaard, Denmark
[b] Department of Energy Conversion and Storage, Technical University of Denmark, Fysikvej B310, 2800 Lyngby, Denmark

HT-PEMFC based on phosphoric acid-doped polybenzimidazole membranes are a technology characterized by simplified construction and operation along with methanol reformers. Durability issues including acid loss, platinum sintering and carbon corrosion are recognized for both steady state and start-stop cycling operations. This work reports experimental studies on the degradation of PBI-based fuel cells operating with synthetic reformate fuel and air. Degradation stressors include elevated temperatures, pressures, current densities, and start-stop cycles. An average degradation rate of 9.3 μV/h is observed for continuous operation at 0.4 A/cm^2 and 160 ˚C for 12,000 h. High pressure (1.5 bar$_{abs}$) operation at 170 ^{o}C and 0.8 A/cm^2 shows an average degradation rate of 12.6 μV/h during a period of 2,000 h. A start-stop test from 50 ^{o}C consisting of 240 cycles between temperatures of 165 and 175 ^{o}C and current density of 0.31 and 0.55 A/cm^2 reveals a performance decay by 0.48-0.58 mV/cycle.

Introduction

Fuel cells are an environmentally friendly and efficient energy technology to provide power and heat for industrial, transport and energy storage sectors (1). Among the fuel cell types, polymer electrolyte membrane fuel cells (PEMFCs) are of special interest for automobile applications and have achieved considerable progress in the last decade (2, 3). High-temperature (HT-) PEMFCs operating at above 100 °C have attracted significant attention in recent years. Polybenzimidazoles (PBI), a relatively large class of polymers containing benzimidazole repeat units (1), are the most successful electrolyte materials for high-temperature operation. Phosphoric acid is used as the exclusive dopant due to its thermal stability, low volatility and high intrinsic proton conductivity (4). The operation of PBI based HT-PEMFCs is simplified by elimination of humidification and efficient cooling. More importantly the HT-PEM cells can tolerate fuel impurities e.g. up to 3 vol% CO and 20 ppm H_2S without significant performance losses, which makes it possible to operating using reformate hydrogen as fuel from e.g. a methanol reformer.

Higher operational temperatures impose more challenges for the material durability. The carbon corrosion, platinum dissolution and polymer oxidation are aggravated at elevated temperatures. In addition the presence of phosphoric acid and its maintenance add also critical issues to the HT-PEMFC durability. Lifetimes of up to 18,000 h at 150-160 °C have been demonstrated for PBI cells (5). The early studies by Schmidt et al. (6)

and Oono et al. (2) showed a degradation rate of 5–10 μV/h. Søndergaard et al. (7) reported a voltage degradation rate of 0.5 μV/h for a period of 9,200 h followed by 5.0 μV/h for the following 3,800 h. Pingitore et al. (3) reported a durability test for 17,500 h and observed a voltage decay of 0.69 μV/h for the period from 5,500 to 17,500 h. These studies were conducted under continuous steady-state operations with a constant current density of 0.1 A/cm^2. These studies have shown the great potential of PBI membranes in meeting the lifetime requirements of many devices. Any increase in the current density, temperature and reactant stoichiometry accelerates the degradation rate of PBI cells (8). Thermal and load cycling as well as shutdown-startup will cause further performance losses (9,10). In addition operation with synthetic reformate fuel containing hydrogen, carbon dioxide, carbon monoxide and moisture has been tested for 1,000 h (11).

In this work the durability of PBI-based MEAs is tested at high current density of 0.4 A/cm^2 at 160 ˚C for more than 12,000 h with reformate fuel and air feed. During the testing period, additional interruptions including open circuit voltage, fuel and air starvation are assessed. Another test is performed at high (1.5 bar_{abs}) pressure and 170 ˚C. Effect of start-stop cycling has also been evaluated. The study is furnished with post mortem TEM analysis of the catalyst morphologies.

Materials and Methods

Preparation of the m-PBI

The *m*-polybenzimidazole (*m*-PBI) was synthesized by Blue World Technologies (BWT) from DAB and IPA at a molar ratio (1:1) in PPA at 160-280 °C under N_2 for 2-3 h. The obtained polymer solution was poured into a water bath to obtain *m*-PBI fibres. The polymer was then washed with distilled water and dried in an oven at 120 °C. The obtained PBI was dissolved in N,N-dimethylacetamide (DMAc) (6-12% PBI in DMAc) at 100 °C under continuous stirring for 12 h. The membrane was prepared by casting the PBI solution onto a glass plate and allowing the solvent to evaporate slowly in a temperature range of 40-120 °C. The membranes were then washed and further dried at 130 °C. The cast membranes were finally doped with acids to become proton conductive. In 85% wt% H_3PO_4, corresponding to molarity of 14.8 mol/L, the acid doping level can reach about 10-11 H_3PO_4 per polymer repeating unit (PRU).

MEA Fabrication

Gas diffusion electrodes were prepared from Pt/Co on one side and pure Pt on the other side, with a catalyst loading of 0.9 mg Pt/cm^2. The MEAs of active electrode area 5×5 cm^2 were prepared by sandwiching the doped membranes between two pieces of gas diffusion electrodes and hot-pressed at 100 °C.

Fuel Cell Assembling and Testing

Cell Assembly. The MEA was sandwiched between current collector and bi-polar plates made of carbon with a serpentine flow pattern (reaction area: 5×5 cm^2). This assembly

was further clamped with two pieces of end plates with Viton insulation attached to the outermost surfaces. The cell was tightened using eight bolts at a torque 2.5 Nm.

Durability Test Control. After assembly, the cell was connected to the fuel cell test house with tubes and wires. The cell was first heated to 120°C, then both fuel and air flows were started with flow rates corresponding to λ_{Ref} /λ_{Air} = 1.3/2.5 for a current density of 0.4 A/cm^2. After checking the OCV (above 900 mV) the cell was further heated to 160 °C. A a constant current e.g. 8.4 A was then applied and the V-t data was recorded with sampling frequency of every 60 sec. The polarization (i-V) curve measurements were carried out at 160 ˚C with a constant stoichiometry of 1.3 for reformate and 2.5 for air, which means for each current step the gas flow rates were accordingly adjusted. The voltage data were recorded by varying current from low to high values.

High Pressure Test Control. The break-in was performed at 0.4 A/cm^2 at 160°C and at no back-pressure for 172 h. Then, gas flows were stoichiometrically increased and the current density was set to 0.8 A/cm^2. Temperature was increased to 170°C and back-pressure was set to 0.5 bar at both anode and cathode. The exhaust lines were connected to a back-pressure system which consisted in two tanks and two regulating valves where the water produced in the cell was accumulated. In order to empty the tanks periodically, the current was decreased to 0.1 A/cm^2 and the gas flow was stoichiometrically adjusted.

Start-Stop Cycling Protocol. For the start-stop cycling study, the MEA was tested according to the following protocol (Table I). In brief, each cycle consists of a startup at 120 °C, a constant current (0.10 A/cm^2) only Reformate flow on the anode side and then increasing the current to 0.050 A/cm^2 (flow on both sides), heating up to 165 °C in 30 min, operation at 165 °C for 4 h at current density of 0.310 A/cm^2, a temperature stressing period at 175 °C for 2 h and current density of 0.55 A/cm^2, back to 165 °C for 4.5 h and cooling down to 120 °C in 30 min, 10 s flushing with H_2 and then stop at 50 °C. Each cycle takes ca. 13.3 h (starting from 50 and ending at 50 °C).

Table I. Protocol for a start-stop cycle

Step	Anode Reformate (mL/min)	Cathode Air (mL/min)	T (° C)	Current (A) // Current density (mA/ cm^2)	Comments
1	0	0	120	0.2 // 10	Avoiding OCV. Start-up (15 min)
2	46	0	120	0.2 // 10	Flushing.30 s
3	15	48	120	1.05 // 50	Gas flows Setting
4	15	48	165	1.05 // 50	Heating up to 165 °C (30 min)
5	89	295	165	6.510 // 310	4 h
6	158	523	175	11.55 // 550	Up to 175°C.2 h
7	89	295	165	6.510 // 310	Down to 165°C. 4.5 h
8	15	48	120	1.05 // 50	Cooling down to 120 °C, (30 min)
9	15	0	120	1.05 // 50	10 s. Consuming H_2
10	0	0	120	1.05 // 50	Avoiding OCV
11	0	0	To 50	0.2 // 10	Avoiding OCV. Stop (90 min)

Results and Discussion

Polarization Curve Studies

The polarization (I-V) curve measurements are carried out to evaluate the cell performance at 160 °C with a constant stoichiometry of 1.3 for reformate fuel and 2.5 for air, which means that for each current step the gas flow rates are accordingly adjusted. Figure 1 shows I-V curves recorded from 5 to 1,251 h. The cell activation can be observed from the positive onset shift, which continues throughout the entire range of tested current densities. The cell voltage rise is prominent in the first 120 h when the MEA activation takes place. During this period, the interfacial state equilibrium is established between acid and catalyst active sites, resulting in approximate 50 mV voltage increase. The highest performance recorded at 459 h is about 565 mV at 0.7 A/cm^2, which is only slightly improved after the 120 h I-V curve. The consistency of I-V plot slopes suggests that no significant change in the MEA resistance occurs within the timeframe of the measurement. Generally, the main contributors to the cell performance loss are the membrane acid loss, catalyst particle aggregation and component oxidation. Considering the experimental timeframe of 1,200 h and testing conditions the MEA has been subjected to, significant particle aggregation of catalysts and harsh oxidative processes can be excluded. The slope stability is, therefore, attributed to the effective acid retention in the *m*-PBI chain network of the membrane electrolyte.

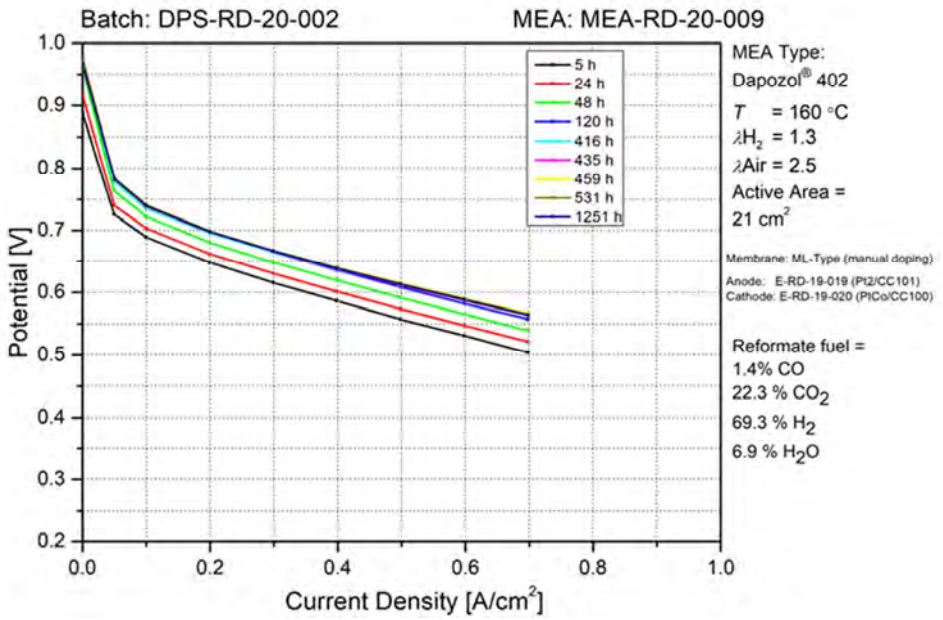

Figure 1. Polarization curves of PBI cells during the first 1,200 h. The active surface area of the electrodes was 21 cm^2. The fuel was synthetic reformate containing 69.3% H_2, 22.3% CO_2, 6.9% H_2O and 1.4% CO. The stoichiometries of hydrogen and air were $\lambda_{H_2}/\lambda_{air}$ =1.3/2.5. The cell was operated under ambient pressure at 160 °C.

It should be emphasized that the fuel cell test was carried out using synthetic reformate fuel consisting of 69.3% H_2, 22.3% CO_2, 6.9% H_2O and 1.4% CO. First of all the CO content is within the tolerance range of the PBI cell, which means that at the

operating temperature (160 °C) the presence of 1.4% CO may result in a small voltage loss of 20-30 mV at current density of 0.7 A/cm^2 (12). The presence of CO_2 and water vapor in the reformate fuel, in addition to the dilution effect on hydrogen, may influence the equilibrium of the water-gas shift reaction and hence the CO poisoning.

Long-term Durability Test

Figure 2 shows the recorded cell voltage at 0.4 A/cm^2 during the durability test period of 10,000 h. A decay rate of only 9.3 µV /h at 0.4 A/cm^2 over extended period of time (10,000 h) was observed. The long-term stability performance can be split and analyzed in three segments: (1) from 0 to 4,800 h, (2) from 4,800 to 9,000 h, and (3) from 9,000 to 10,000 h.

The first segment is characterized by the cell activation and high performance. The cell peak of life (PoL) is achieved within the first 500 h. Although technical failures such as evaporator clogging or fuel starvation are present in the entire measurement, the first segment attests to the cell robustness and its ability to regain the high-performing voltages even after experiencing damaging testing conditions. The cell degradation is the lowest during this segment, with only 4.8 µV/h.

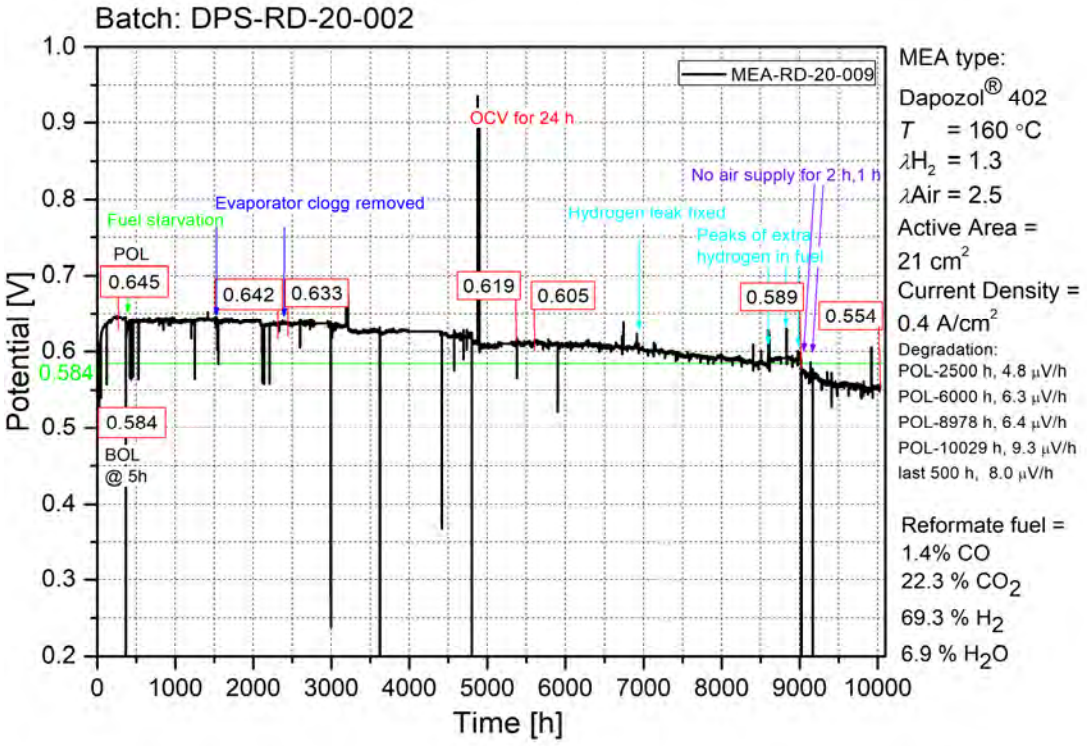

Figure 2. Cell voltage versus time during the long-term test. The active surface area of the electrodes was 21 cm^2.The fuel was synthetic reformate containing 69.3% H_2, 22.3% CO_2, 6.9% H_2O and 1.4% CO. The stoichiometries of hydrogen and air were $\lambda_{H_2}/\lambda_{air}$ =1.3/2.5. The cell was operated at 0.4 A/cm^2 and 160 °C.

The second segment is marked by the initial incident at 4,800 h, when the cell was exposed to the open circuit voltage (OCV) for 24 h. Under this condition, the oxidation of the cathode catalyst easily takes place and the formed surface platinum oxide (PtO_x)

dissolves in the phosphoric acid. The carbon support of the cathode is corroded. Both processes trigger the platinum particle growth. Another change is the water vapor in two electrode chambers. Under normal operation with λ_{air} = 2.5 the water formation in the cathode stream corresponds to a water content of ca. 15% at the cathode exit, which is in good balance with the water content in the anode exit. Under OCV, there was no current drawn and hence no water formation on the cathode while the water content on the anode side is also low (6.9%) as no hydrogen is consumed. As a result, the condensation of phosphoric acid may occur during the OCV period, leading to decrease in the membrane conductivity. This can be recovered when the cell operation is re-started. Moreover the MEA has already been performing for almost 5,000 h and was more sensitive to mistreatment than at the beginning of life (BoL). The performance dip is, therefore, immediately apparent after the prolonged time at OCV, with a subsequent negative voltage drift occurring at a rate of 6.4 µV/h.

The last segment is characterized by a detrimental testing condition as well. The cell was under air starvation at two intervals of 2 and 1 h, respectively. Considering the harsh fuel-starved environment and the performance longevity, the damage is observed instantly as a voltage drop and a continuous performance decay with the highest degradation rate of 9.3 µV/h.

Durability Test and Polarization Curve at Higher Pressure

Further, we have illustrated that an increase in the pressure of the in-going gases to 1.5 bar_{abs} (absolute pressure) – as expected – increases the performance. The preliminary results affirmed a power density of 0.48 W/cm^2 at 0.8 A/cm^2. The cell voltage increases by further ca. 60 mV via the modest pressurization. Figure 3a shows the polarization and power density curves at 170 ˚C and pressure of 1.5 bar_{abs}.

It has been well recognized that the phosphoric acid loss is a major cause of the PBI cell degradation. At 150-160 °C and 0.2 A/cm^2, the acid loss rate is reported to be in a range of 0.5 - 1.0 µg m^{-2} s^{-1}, corresponding to 2 - 4 mg/cm^2 H_3PO_4 over the duration of 10,000 h (7,13). The primary mechanism of the acid loss seems via the acid evaporation, as the reported acid loss follows the trend estimated from the acid vapor pressure (1). Operation at elevated pressures is expected to be beneficial for the cell durability, considering the inhibition of the phosphoric acid loss by lowering its vapor pressure at these conditions. This test was however made with other stressors. First of all high temperatures dictate the acid vapor pressure, which is documented by a 5 time increase from 0.8 to 4 ppm when the temperature is elevated from 160 to 190 ^{o}C. In addition, the high current density under the same air stoichiometry means a higher total gas flow, which increases the rate of acid loss, as rationalized by Søndergaard et al. (8). The issue of the phosphoric acid mobility is recently raised by Becker et al. (14), who measured the anion ($H_2PO_4^-$) transference numbers of 0.04 and the diffusion coefficient of 10^{-10} m^2/s through acid doped PBI membranes in HT-PEM cells. The authors have estimated that the acid concentration difference across a PBI membrane may increase by 10 times when the current density is increased from 0.2 to 0.8 A/cm^2. This will ultimately lead to severe acid imbalance and additional acid loss, as reported by Wannek et al.(15).

Figure 3b shows the test result at an elevated pressure of 1.5 bar_{abs}, a higher temperature of 170 °C and an increased current density of 0.8 A/cm^2. A slight change of

the test condition for this pressure test as well as the next start-stop cycling test was that no water vapor was added in the synthetic reformat fuel. The activation of the cell in the first 200 h was performed at the atmospheric pressure at 160 ^{o}C to ensure the cell reliability. The cell performance reached a voltage of above 0. 6 V at 0.4 A/cm^2. Pressurization was undertaken after the activation period when the cell temperature and current density were also increased. It should be noted that a power failure happened at the time interval from 236 to 268 h during which the cell was exposed to OCV. The cell performance was then slowly improved, reaching the peak voltage of 0.584 V @ 0.8 A/cm^2 after a total operation time of 434 h. At the point of 1,533 h, a short fuel starvation occurred. Otherwise a steady test was carried out, showing an overall degradation of 12.6 µV/h for the 2,000 h of operation at 0.8 A/cm^2.

a)

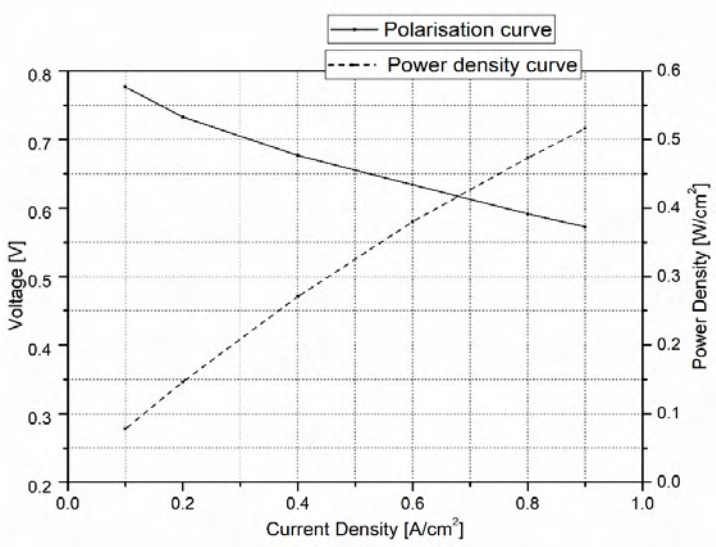

b)

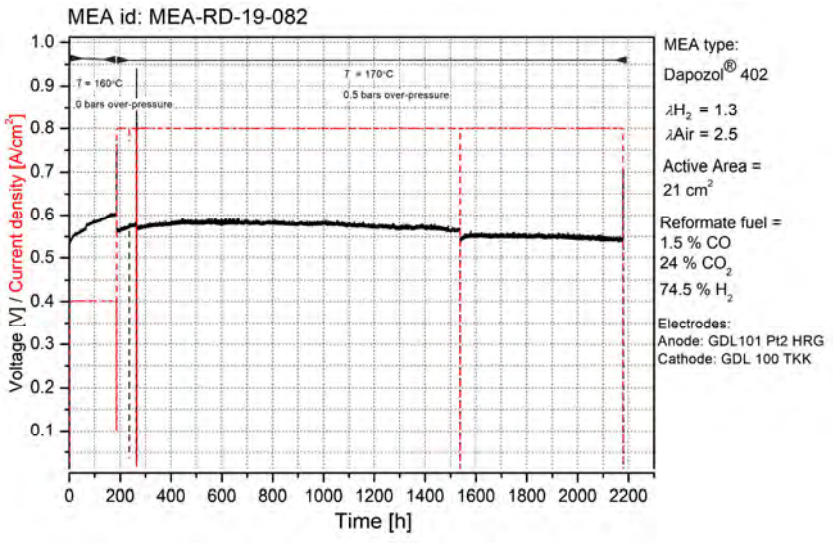

Figure 3. a) Polarization and power density curves at 170 ^{o}C and pressure of 1.5 bar$_{abs}$. b) Cell voltage and current density versus time curves of the long-term test at 170 ^{o}C and pressure of 1.5 bar$_{abs}$. Other operation conditions are specified in the Figure.

Start Stop Cycling Test

Fuel cells will experience significantly more stressing when operating under dynamic modes involving thermal, load and start-stop cycling, which are mandatory for practical applications particularly in automobiles. The start-stop or/and temperature cycling can expose the cells to the severe corrosion of carbon supports and the sintering of noble metal catalysts.

First of all, platinum catalysts, more precisely, the formation and dissolution of the metal surface oxide, will be intensified during the load cycling. Variation of the cathode potential from an operating point of 0.7 V to OCV may result in an increase of the metal solubility by several orders of magnitude in phosphoric acid at 160-180 ^{o}C, while the dissolution and precipitation of the metal are the major mechanism of the particle growth. Under fuel cell operation conditions the carbon support is known to be susceptible to corrosion, which is a function of temperature, electrode potential, water partial pressure and corrosive electrolyte. Significant thinning of the catalyst layers has been observed due to the carbon corrosion (2), which triggers further growth of the catalyst particles. In addition the carbon corrosion may lead to formation of surface oxides that in turn may deteriorate the hydrophobicity of catalyst layers and hence the acid retention.

A start-stop protocol was used in the present study is according to table 1. The start and stop temperature was at 50 ^{o}C with cycling of temperatures and loads from 165 ^{o}C at 0.31 A/cm^2 to 175 ^{o}C at 0.55 A/cm^2. Each cycle took ca. 13.3 h and totally 240 cycles correspond to a period of more than 4,000 h.

The performance degradation in term of cell voltage is shown in Figure 4. Continuous operation and more than 240 start stop cycles have been performed in order to study the degradation effects of both continuous operation and of repeated start stop processes, emulating automotive applications, Fig. 4. The empty data slots at hour 1440, and 3840 are results of technical nature during testing. These are, as in Fig. 2, the main culprits to abrupt voltage drops. However, start stop cycles led to a degradation of 0.48 mV/cycle at a current density of 0.310 A/cm^2 and 0.58 mV/cycle at 0.550 A/cm^2.

Conclusions

The first long-term durability tests of HT-PEMFCs using PA doped PBI membranes are conducted at a temperature of 160 ^{o}C and a current density of 0.4 A/cm^2 for periods of more than 12,000 h. A decay rate of 9.3 µV/h at 0.4 A/cm^2 over this extended period of time is observed, which is comparable with the 5-10 µV/h at 0.2 A/cm^2 reported in literature.

The second durability tests are performed at a pressure of 1.5 bar$_{abs}$ with a stressing temperature of 170 ^{o}C and even a higher current density of 0.8 A/cm^2. Within a timeframe of 2,000 h, a steady performance degradation in a rate of 12.6 µV/h is observed.

A start-stop test at 50 °C is conducted including 240 cycles with cycling between temperatures of 165 and 175 °C and current density of 0.31 and 0.55 A/cm^2. The observed performance decay is 0.48-0.58 mV/cycle.

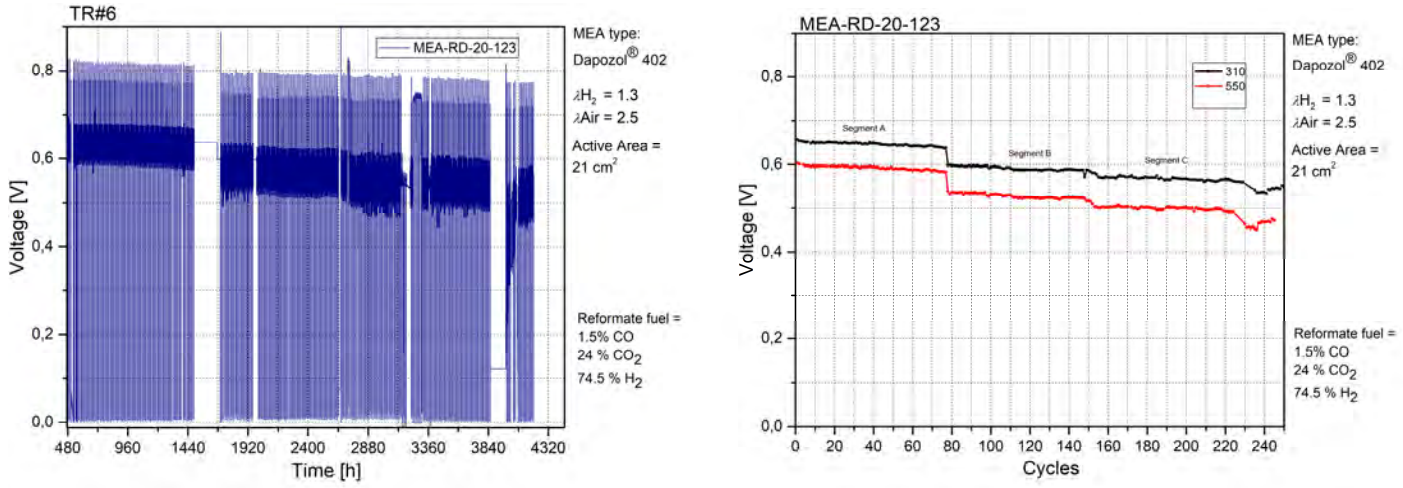

Figure 4. Start-stop cycles of single MEA. The test protocol is given in Table I.

Acknowledgments

Financial support from EUDP (Danish Energy Agency) for COBRA Drive project is gratefully acknowledged.

References

1. D. Aili, D. Henkensmeier, S. Martin, B. Singh, Y. Hu, J. O. Jensen, L. N. Cleemann, and Q. Li, *Electrochem. Energ. Rev*., **3**, 793 (2020).
2. Y. Oono, A. Sounai, and M. Hori, *J. Power Sources*, **241**,87(2013).
3. A. T. Pingitore, F. Huang, G. Qian, and B.C. Benicewicz. *ACS Appl. Energy Mater*., **2**, 1720 (2019).
4. H. Steininger, M. Schuster, K. D. Kreuer, A. Kaltbeitzel, B. Bingöl, W. H. Meyer, S. Schauff, G. Brunklaus, J. Maier, and H. W. Spiess, *Phys. Chem. Chem. Phys*., **9**, 1764 (2007).
5. M.T.D. Jakobsen, J. O. Jensen, L. N. Cleemann, and Q. Li, In: High Temperature Polymer Electrolyte Membrane Fuel Cells, Q. Li, D. Aili, H. A. Hjuler, and J. O. Jensen, Editors, pp. 478-509, Springer, New York (2016).
6. T. J. Schmidt, J. Baurmeister, *ECS Trans*., **3**(1), 861 (2006).
7. T. Søndergaard, L. N. Cleemann, H. Becker, D. Aili, T. Steenberg, H. A. Hjuler, L. Seerup, Q. Li, and J. O. Jensen, *J. Power Sources*, **342**, 570 (2017).
8. T. Søndergaard, L. N. Cleemann, H. Becker, D. Aili, T. Steenberg, H. A. Hjuler, L. Seerup, Q. Li, and J. O. Jensen, *J. Electrochem. Soc*., **165**, F3053 (2018).
9. D. Schonvogel, M. Rastedt, P. Wagner, M. Wark, and A. Dycket, *Fuel Cells,* **16**, 480 (2016).

10. F. J. Pinar, M. Rastedt, N. Pilinski, and P. Wagner, *Int. J. Hydrogen. Energy,* **41**, 19463 (2016).
11. F. J. Pinar, M. Rastedt, N. Pilinski, P. Wagner, and A. Dyck, *Int. J. Hydrogen. Energy*, **42**, 13860 (2017).
12. Q. Li, R. He and J.-A. Gao, J. O. Jensen, and N. J. Bjerrum, *J. Electrochem. Soc*., **150**, A1599 (2003).
13. S. H. Eberhardt, T. Lochner, F. N. Büchi, and T. J. Schmidt, *J. Electrochem. Soc*., **162**, F1367 (2015).
14. H. Becker, U. Reimer, D. Aili, L. N. Cleemann, J. O. Jensen, W. Lehnert, and Q. Li, *J. Electrochem. Soc*., **165**, F863 (2018).
15. C. Wannek, I. Konradi, J. Mergel, and W. Lehnert, *Int. J. Hydrogen. Energy,* **34**, 9479 (2009).

Chapter 20

12 Electrolysis Modeling and Transport

ECS Transactions, 104 (8) 417-427 (2021)
10.1149/10408.0417ecst ©The Electrochemical Society

Sensitivity and Effective Parameterization of a Multi-Scale Model of Proton-Exchange-Membrane Water Electrolysis

Julie C. Fornaciari [a,b], Arthur Dizon [a], Maria Rochow [a,c], Adam Z. Weber [a]

[a] Energy Conversion Group, Lawrence Berkeley National Laboratory, Berkeley, CA 94720, USA
[b] Department of Chemical and Biomolecular Engineering, University of California, Berkeley, Berkeley, CA 94720, USA
[c] Department of Material Science and Engineering, The Pennsylvania State University, State College, PA 16802, USA

The development of proton-exchange-membrane water electrolysis (PEMWE) is crucial to establishing a green-hydrogen infrastructure. Active research in hydrogen technologies is focused on minimizing costs, improving efficiency, and mitigating safety risks. In this study, sensitivity analyses were performed using a physics-based model and used to identify critical parameters capable of reducing overpotentials and safety risks. These parameters include operational (i.e. temperature), structural (i.e. thickness of the components), and material properties (i.e. exchange current density). Simulated results suggest that better engineering of the membrane electrode assemblies (MEA) can offset intrinsic limitations. Membrane thickness and conductivity yielded the largest percent change on performance. Gas crossover was observed to be sensitive to diffusion, solubility, and bubble formation. Current density regimes were identified, where each crossover parameter was most influential. MEA parameterization serves as a framework for theoretical PEMWE optimization simulations and input for design criteria for future research targets.

Introduction

As renewable-energy generation grows, an increase of inexpensive surplus electricity is predicted. A goal of carbon-free technologies and products is the storage of this excess electrical energy. Amongst these technologies, hydrogen has been shown to be a promising medium for storage applications (1-7). The development of proton-exchange-membrane water electrolysis (PEMWE) is a crucial part of establishing a viable hydrogen infrastructure and the current research is working to minimize capital and operational costs, improving efficiency, and mitigating safety risks (7). Empirical optimization of PEMWE is challenging due to the complex, nonlinear phenomena that occur within the membrane-electrode assembly (MEA), the safety risks associated with the generation and handling flammable and oxidizing gases, and the time and inability to explore the large parameter space.

The purpose of this paper is to introduce and exercise a physics-based, cell model for PEMWE. Here, we demonstrate the agreement between simulation and experimental data, and identify the most sensitive parameters and how they can impact the performance, through the polarization curve, or the safety of the cell, such as the crossover of hydrogen to the anode. In general, the polarization curve is composed of

kinetic, ohmic, and mass-transport losses (8). While coupled effects are prevalent, systematically looking at the impact on the polarization behavior due to single parameters can provide a guide for future PEMWE research. The parameters can be those that are chosen and fabricated, such as component thickness, or intrinsic material properties, such as ionic conductivity or exchange current density. The sensitivity analysis can provide a guide as to where to focus PEMWE research efforts.

Theoretical

Electrolysis Model

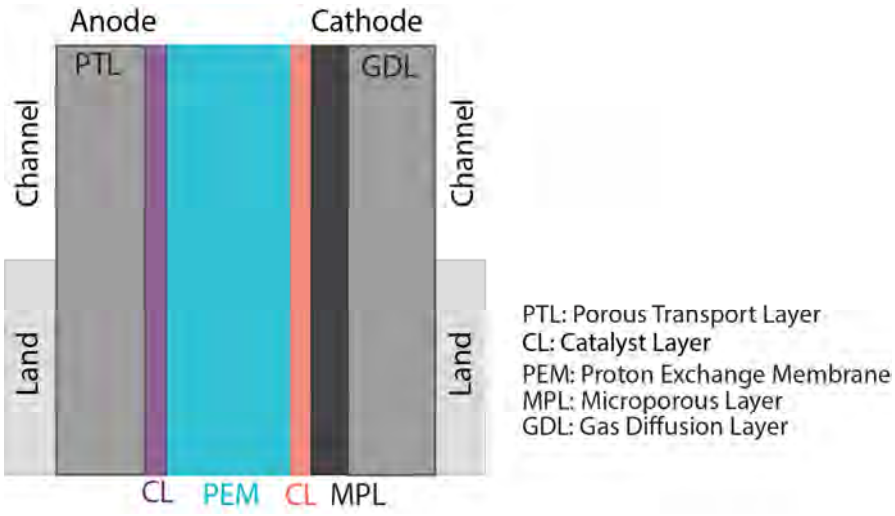

Figure 1. 2D cell model with the various domains shown.

In Figure 1, a schematic diagram of the simulation domain is shown. The mathematical model used was adapted from 2D fuel-cell models developed by Balliet *et al*. (9) and Zenyuk *et al*. (10) and a vapor-fed electrolysis model developed by Fornaciari *et al*. (11). Mass transfer within the porous layers, including the PTL, GDL, MPL, and CL, is comprised of diffusion and convection, which are modeled using multicomponent Stefan-Maxwell diffusion and Darcy's Law, respectively. Concentrated-solution theory is used to model mass and charge transport within the membrane and ionomer. The oxygen-evolution reaction (OER) is governed by Tafel kinetics and the hydrogen-evolution reaction (HER) is governed by Butler-Volmer kinetics. The proposed model accounts for reactant water in the liquid phase for the cell and two-phase flow within the PTL and anode CL, under the assumption of a relative humidity equal to unity.

This model was validated using cell data from the National Renewable Energy Laboratory for MEAs that had iridium-catalyst loadings of 0.1, 0.2, and 0.4 mg/cm^2 (12). Rotating-disk-electrode experiments measured the exchange current density, which was used as an input to the model itself (12).

Once validated, the model was conducted to determine the impact and initial performance at the operating parameters, such as water content, temperature distribution, and the applied-voltage breakdown using the post-processing method proposed by Gerhardt *et al*. (8,13),

$$V = U^{ref} + \eta_{cathode} + \eta_{anode} + \eta_{cathode,ionomer} + \eta_{anode,ionomer} + \eta_{membrane} + \eta_{MT} \quad (1)$$

where U^{ref} is the Nernstian thermodynamic potential (referenced to the conditions in the gas channel), $\eta_{cathode}$ and η_{anode} are the kinetic overpotentials for the cathode and anode reaction, respectively, $\eta_{i,ionomer}$ is the ohmic loss from the ionomer within the CL, and $\eta_{membrane}$ is the ohmic loss across the membrane, η_{MT} is the loss from mass transport.

A simultaneous concern of PEMWE technology development is the mitigation of safety-risks associated with the production of combustible mixtures of hydrogen and oxygen product gases. A crossover model, which was adapted from model developed by Balliet *et al*. (9) and Zenyuk *et al*. (10), was developed to inform safety-risks mitigation strategies during PEMWE operation by accounting for gas crossover influenced by supersaturation of dissolved gas species in the membrane and catalyst layers. The model was inspired by Trinke *et al.* who accounted for dissolved gas diffusion, solubility, and dissolved-gas bubble nucleation controlled by a general mass-transfer coefficient and reaction (14). Diffusion and gas solubility were governed by Fick's Law and Henry's Law, respectively.

Sensitivity Analysis

The sensitivity of the parameters in Table I were assessed systematically by changing the parameter value one at a time. Each parameter value was increased and decreased by an order of magnitude while all the other parameters and properties of the model remained unchanged, which entailed two simulations per parameter. The polarization curve was evaluated to determine the percent change in performance, with a positive change in performance resulting in lower overpotential and, conversely, a negative change in performance resulting in higher overpotentials.

Table I. Key parameters and their baseline values within the model.

Parameters	Baseline Values
Interfacial specific surface area	$a_{o,a} = 1.96 \times 10^7$ 1/m $a_{o,c} = 3.0 \times 10^6$ 1/m
Component thickness	t_{PTL} = 254 µm t_{GDL} = 190 µm t_{aCL} = 4.0 µm t_{cCL} = 4.1 µm t_{mem}= 150 µm
Exchange Current Density	$i_{0,a} = 1.9 \times 10^{-2}$ A/m^2 $i_{0,c}$=215 A/m^2
Ionic Conductivity	κ = 20.8 S/m
Thermal Conductivity	kT_{GDL}=1.4 W/m/K kT_{PTL} =6 W/m/K kT_{CL} =0.27 W/m/K kT_{mem}= 0.2 W/m/K
Transport Coefficient	$\alpha = 3 \times 10^{-2}$ s mol^2/(kg m^3)

The sensitivity of the crossover model to the product-gas concentrations was evaluated for the gas-crossover parameters gas-nucleation mass-transfer, diffusion, and solubility

coefficients. Varying the principal values by an order of magnitude was not informative. Thus, the crossover parameters were varied by ±30% of the principal value to demonstrate the sensitivity of the concentrations of the product gas streams.

Results and Discussion

Model Validation

The baseline performance of the MEA electrolyzer was simulated using the parameter values in Table I and at iridium-catalyst loadings of 0.2 and 0.4 mg/cm^2. The baseline parameter values, such as the PTL or membrane thicknesses were obtained from the experimental setup. The values of the intrinsic parameters, such as the conductivity of the materials, were obtained from literature (9-11). The simulated results exhibited good agreement with the experimental data throughout the entire current density range.

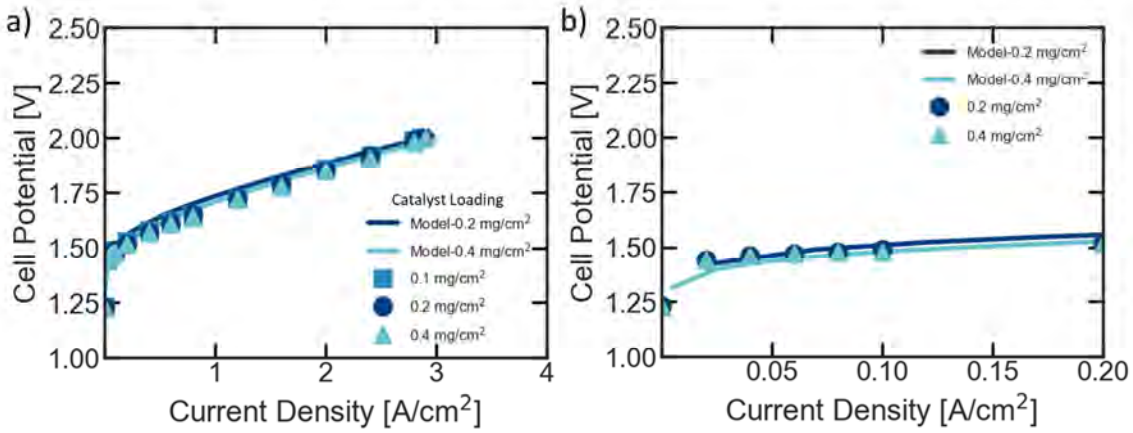

Figure 2. Simulated (solid line) and experimental (square, circle, and triangle data points) polarization curves are shown with iridium loadings as a parameter. The entire polarization curve is shown in (a) and the kinetic regime is showed in (b).

The model provides increased granularity into the variables inside the cell, which is often challenging to measure experimentally, as well as enables detailed breakdowns of the various phenomena. As shown in Figure 3, the main losses that are observed are from the OER kinetics and the ohmic losses in the membrane. For this specific MEA simulation, mass-transport losses were not observed, which may be due to the higher loadings of the catalyst layer and the abundance of water.

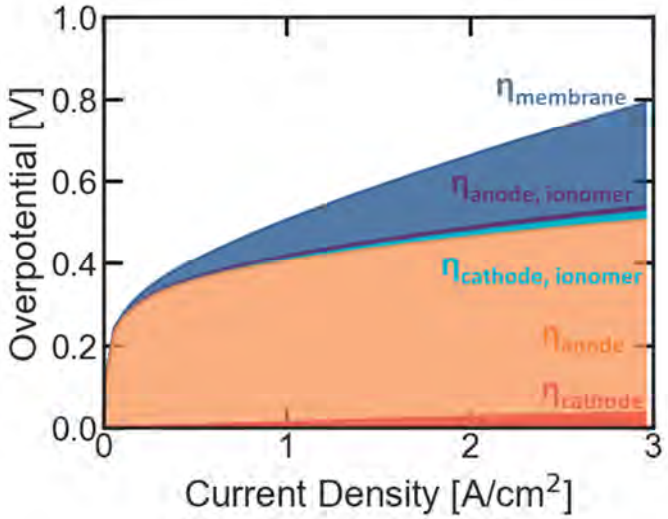

Figure 3. Applied-voltage breakdown showing the overpotentials for the kinetics ($\eta_{cathode}$, η_{anode}) and ohmic contributions from the catalyst layers ($\eta_{cathode,ionomer}$, $\eta_{anode,ionomer}$) and the membrane ($\eta_{membrane}$). The mass transport contributions (η_{MT}) were negligible.

Performance Sensitivity

Exploring the sensitivity of the PEMWE is crucial to identify which components hinder or help efficiency, durability, and/or performance. There are a wide variety of operating parameters that can be explored and not all of them are detailed in this transaction. One operating parameter to manipulate is the cell temperature. Cell temperature varies quite significantly in the literature (3, 7, 15) and influences various components of the MEA. While higher temperatures improve kinetics and conductivity, dehydration of the membrane could be detrimental to the proton-exchange membrane. Fortunately, the liquid water feed to the anode helps maintain conductivity and reduce dehydration while still benefiting from enhanced kinetics.

In Figure 4, the benefit from increasing the cell from 50 to 80°C is significant, decreasing the cell's overpotential by 150 mV at 3 A/cm^2. The additional heat needed within the system will reduce the overall energy efficiency, but the cell potential remains under 2 V at 3 A/cm^2. Maintaining the cell below 2 V helps reduce degradation of the cell components over its lifetime. Interestingly, if the cell temperature is further increased to 90°C, the benefit is minimal. Comparing the rate of cell potential change per degree at 3 A/cm^2 from 50 to 80°C, the change is 5 mV/°C, unlike the change from 80 to 90°C where the change is a maximum of 3 mV/°C, showing that the conductivity losses are greater than the kinetic gains at elevated temperature.

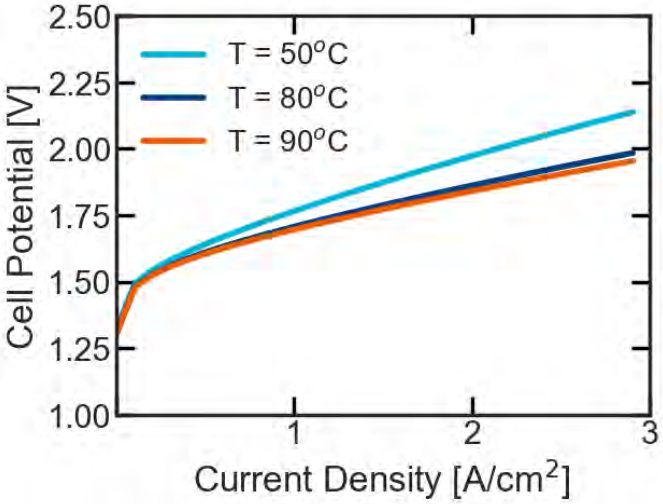

Figure 4. Simulated polarization curves at 50, 80, and 90°C with the rest of the parameters at the baseline values in Table I.

Shown in Figure 1 and Figure 3, the PEMWE is comprised of many parts and many losses. The decision on the thickness of the PTL, GDL, CLs, and membrane all contribute to the cell's overall performance. There are consequences and tradeoffs to each decision, knowing the specific contribution and effect from each individual part is nontrivial. For example, a thin membrane can decrease the cell's ohmic losses, but induces higher hydrogen gas crossover that may limit the cell potential, efficiency, and introduce safety concerns. Additionally, there are intrinsic properties that are much harder to change, such as the conductivity of the membrane or the exchange current of the catalyst that is used. A larger exchange current density is ideal for the HER and OER, but finding such a viable catalyst is challenging.

In Figure 5, the percent change on performance is shown for fifteen different parameters at three different current densities. The three different current densities represent the different regimes in a typical polarization curve. The regimes are kinetic, ohmic, mass transport, which are shown in Figures 5a, 5b, and 5c, respectively. Investigating these three different regimes helps to identify the benefit of different parameters within the different regimes. For example, the exchange-current density impacts the lower current densities (< 50 mA/cm^2) most, since, at lower current densities, the cell's overpotential is limited by the OER kinetics. This result is shown in Figure 5a, where increasing the exchange-current density ($i_{0,a}$) yields a positive change (a lower overpotential) for the cell. Additionally, if the interfacial surface area ($a_{o,a}$) is increased, there is a similar improvement in performance. Improving the interfacial surface area could be done through better electrode-fabrication techniques, which is an active area of research.

In the ohmic regime at 1.5 A/cm^2 in Figure 5b, while a few parameters can be detrimental to the performance, the largest contributor is unsurprisingly the membrane. The membrane's thickness and conductivity can improve performance by ~5% if they are decreased and increased, respectively. Interestingly, when those parameters are subjected to the opposite change in magnitude, the negative percent change in performance is greater than 50%. This result shows that while the MEA performance can be improved, the MEA is more sensitive to negative changes.

Similar to the ohmic regime, the expected mass-transport regime at 3 A/cm^2 in Figure 5c shows a similar sensitivity to the membrane properties. In Figure 3, there are negligible amounts of mass-transport losses in the AVB, yet at these high current densities, the sensitivity of the parameters changes from the purely ohmic regime at 1.5 A/cm^2. Curiously, the baseline parameters appear to be at an optimized value for high current densities for the interfacial surface area ($a_{o,a}$), thickness of the PTL (t_{PTL}), and the thickness of the anode catalyst layer ($t_{a,\ CL}$). If those three parameters are increased or decreased, they result in a negative change in the performance of the cell.

While fifteen different parameters were assessed, ten appear to influence the performance of the cell and only the membrane properties impacted the performance more than 15%. This result suggests improved membrane properties can assist in the performance of the cell. Since the membrane is crucial, this result reveals the importance of future research in more conductive and thinner proton exchange membranes.

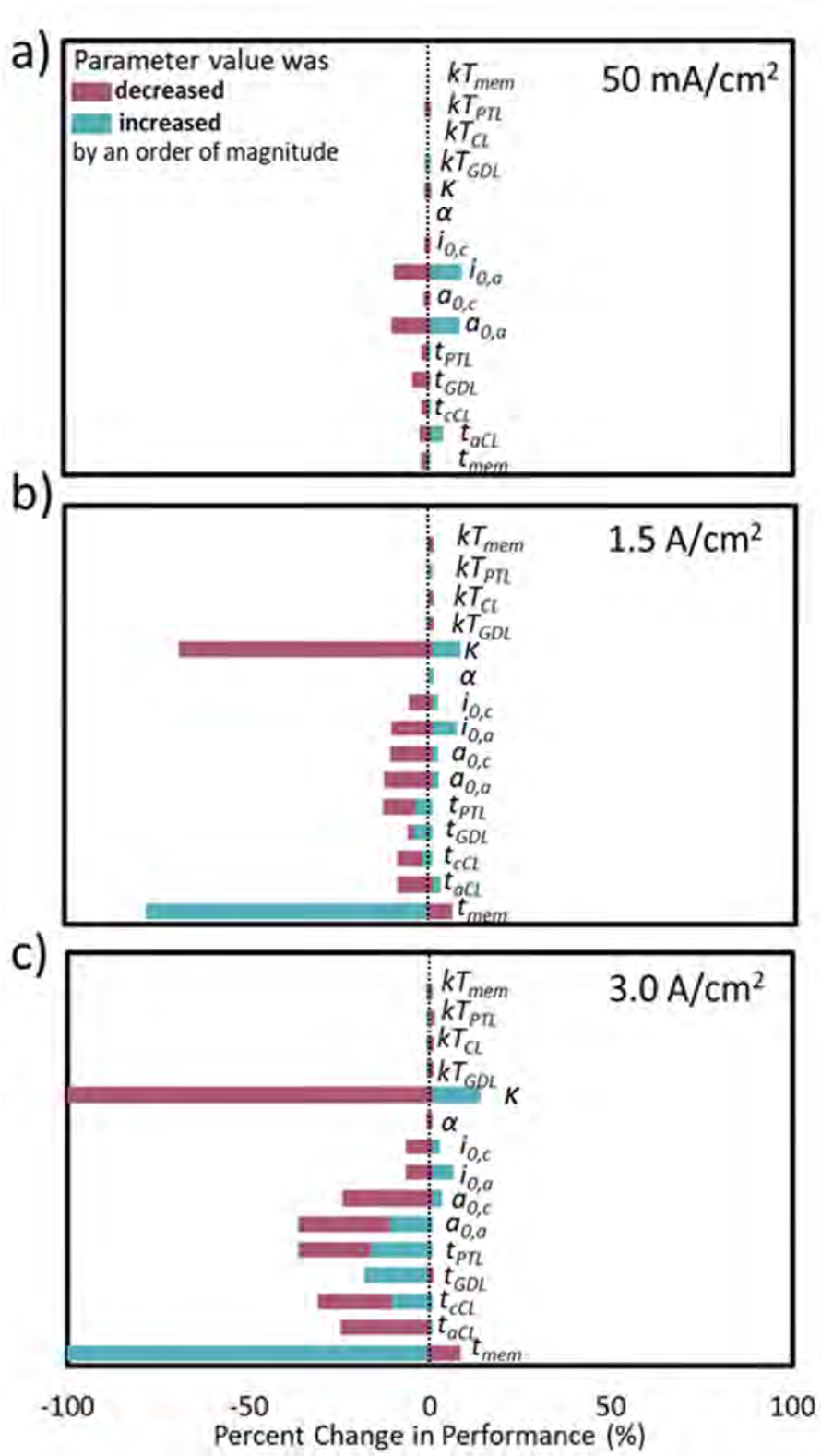

Figure 5. Percent change in performance due to an increase or decrease in the parameters. All parameters are from Table I. The plots are for the three different regimes in the polarization curve, (a) kinetic regime at 50 mA cm^{-2}, (b) ohmic regime at 1.5 A/cm^{-2}, and (c) mass-transport regime at 3.0 A cm^{-2}.

Hydrogen- Crossover Sensitivity

The mole fraction of H_2 in O_2 on the anode side was found to be highly sensitive to the crossover parameters. In Figure 6, the sensitivity of the diffusion coefficient, D_i (a), solubility, H_i (b), and mass-transfer coefficient, k_i (c), is demonstrated in plots of the mole percent of H_2 in O_2 on the anode side as a function of cell current.

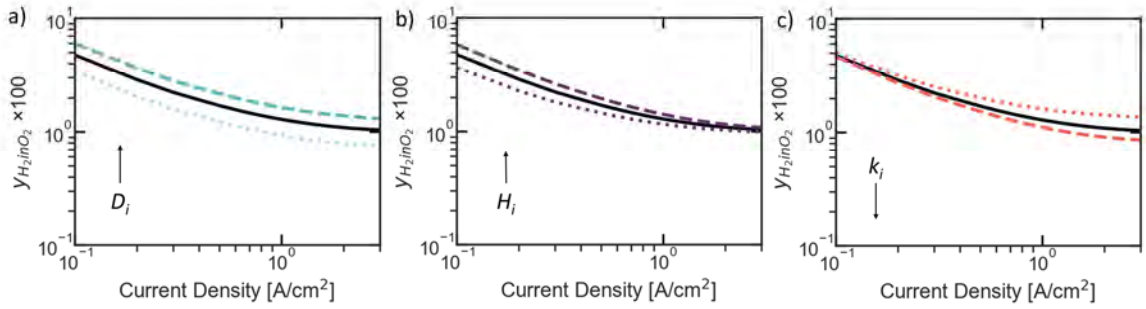

Figure 6. Mole percent of H_2 in O_2 on the anode side at a differential pressure of 10 bar as a function of cell current with ±30% variation in the crossover parameter. The crossover parameters are (a) diffusion coefficient, (b) solubility, and (c) mass-transfer coefficient. The solid, dashed, and dotted lines represent the crossover parameter values at nominal, +30%, and -30%, respectively.

The sensitivity analysis of the crossover parameters was used to identify current density regimes where each parameter influenced on gas crossover. In Figure 6a, the diffusion coefficient was observed to uniformly influence crossover over the entire simulated current density range by shifting the crossover profile proportionally to the diffusion coefficient magnitude. This finding suggests that crossover is diffusion limited throughout the current density range. In Figure 6b, gas crossover was sensitive to solubility at low current densities, whereas; gas crossover was sensitive to the nucleation mass-transfer coefficient at high current densities. This trade-off between parameters suggests at low current densities, gas-nucleation is not limited by catalyst active sites, therefore crossover is driven by gas solubility. At high current densities, the production of gas is large and the rate of gas production is limited by nucleation sites on the catalyst particles. Thus, a decrease in the nucleation mass-transfer coefficient yields an increase in gas crossover. The tunability of these parameters is dependent on the layer materials and structure. For example, the diffusion coefficient is a function of the membrane and ionomer material properties; whereas, the solubility and mass-transfer coefficient are dependent on the properties and materials of the catalyst layers.

Conclusions

In this study, a working PEMWE model was developed and validated with experimental data. The model was used to quantify the main contributions to the polarization curve, mainly the OER kinetics and ohmic losses. A sensitivity analysis was conducted with the model to elucidate the impact of increasing temperature and component properties on PEMWE performance. Additionally, key parameters were identified that impact the performance the most including the OER exchange current density, anode catalyst interfacial surface area, and membrane thickness and conductivity. The study results

suggest that the most influential parameters are structural and material properties. Thus, efforts should be put into how to manufacture thinner membranes with low hydrogen crossover and/or more conductive membranes. The influence of gas crossover mechanisms of diffusion, solubility, and gas nucleation influence was shown to be a function current density. Directions for future work include investigating additional operating parameters, including pressure at the cathode and at both electrodes, as well as developing more complex models for gas crossover that account for material properties such as the active sites and surface area coverage of the catalyst. Additionally, the sensitivity analysis has only focused on the influence of a single parameter within the MEA model, which does not account for the influence of coupled parameters. Understanding how these coupled effects can be compounded is crucial for further guidance in PEMWE design.

Acknowledgements

The authors would like to acknowledge Dr. Jie Zhou for help discussions and pivotal work in the model development. The authors would also like to thank the Department of Energy (DOE) Student Undergraduate Laboratory Internship program at Lawrence Berkeley National Laboratory. This research is supported by DOE Hydrogen and Fuel Cell Technologies Office, through the H2NEW Consortium. JCF acknowledges support from the National Science Foundation (grant DGE 1106400).

References

1. K. Mazloomi and C. Gomes, Hydrogen as an energy carrier: Prospects and challenges, *Renewable and Sustainable Energy Reviews*, p. 3024 (2012).
2. F. Barbir, *Solar Energy*, p. 661 (2005).
3. K. Ayers, N. Danilovic, R. Ouimet, M. Carmo, B. Pivovar, M. Bornstein, *Annual Review of Chemical and Biomolecular Engineering* **10**, 219-239 (2019).
4. A. Buttler and H. Spliethoff, *Renewable and Sustainable Energy Reviews*, p. 2440, (2018).
5. J. D. Holladay, J. Hu, D. L. King and Y. Wang, *Catalysis Today*, p. 244 (2009).
6. S. Shiva Kumar and V. Himabindu, *Materials Science for Energy Technologies*, p. 442, (2019).
7. M. Carmo, D. L. Fritz, J. Mergel and D. Stolten, *International Journal of Hydrogen Energy*, **38**, 4901 (2013).
8. M. R. Gerhardt, L. M. Pant, J. Bui, A. R. Crothers, V. M. Ehlinger, J. C. Fornaciari, J. Liu and A. Z. Weber. *Journal of the Electrochemistry Society.* Accepted manuscript (2021).
9. R. J. Balliet and J. Newman, *Journal of The Electrochemical Society,* **158,** B927 (2011).
10. I. V. Zenyuk, P. K. Das and A. Z. Weber, *Journal of The Electrochemical Society*, **163,** 691 (2016).
11. J. C. Fornaciari, M.R. Gerhardt, J. Zhou, Y.N. Regmi, N. Danilovic, A.T. Bell, and A. Z. Weber. *Journal of the Electrochemistry Society.* **167** 104508 (2020).

12. H.N. Dinh, G. Groenewold, E. Fox, A. McDaniel, T. Ogitsu, and A. Weber. HydroGEN Overview:A Consortium on Advanced Water Splitting Materials, in *Department of Energy's Annual Merit Review* (2020).
13. M. R. Gerhardt, L. M. Pant and A. Z. Weber, *Journal of The Electrochemical Society*, **166,** 3180 (2019).
14. P. Trinke, P. Haug, J. Brauns, B. Bensmann, R. Hanke-Rauschenbach, and T. Turek, *Journal of the Electrochemistry Society* **165** F502 (2018)
15. G. Bender, M. Carmo, T. Smolinka, A. Gago, N. Danilovic, M. Mueller, F. Ganci, A. Fallisch, P. Lettenmeier, K.A. Friedrich, K. Ayers, B. Pivovar, J. Mergel, D. Stolten, *International Journal of Hydrogen Energy,* **44**, 18 (2019)

Chapter 21

32 Electrolysis Electrocatalysis

ECS Transactions, 104 (8) 431-436 (2021)
10.1149/10408.0431ecst ©The Electrochemical Society

The Impact of Mn addition on Ta Oxide-Based Electrocatalysts for Oxygen Evolution Reaction in Acid

K. Matsuzawa[a], S. Hirayama[b], Y. Kohara[b], and A. Ishihara[c]

[a] Graduate School of Engineering, Yokohama National University, Yokohama, Kanagawa 240-8501, Japan
[b] Graduate School of Engineering Science, Yokohama National University, Yokohama, Kanagawa 240-8501, Japan
[c] Institute of Advanced Science, Yokohama National University, Yokohama, Kanagawa 240-8501, Japan

In order to develop non-platinum group metals anode electrocatalyst for the proton exchange membrane water electrolysis, the catalytic activity of Ta oxide-based electrocatalyst with and without Mn addition for the oxygen evolution reaction (OER) have been investigated. The Ta oxide-based electrocatalyst with Mn addition (Mn-TaO_x) has greatly increased current density than that without any addition. From XPS spectra, the Mn-TaO_x after electrochemical measurement did not detect the peak identified Mn oxides while the sample before electrochemical measurement showed clearly the peak that identified Mn oxides. From the slow scan voltammogram of Mn-TaO_x, the redox peak of Mn species was detected. Since the electric charge of redox peak and the OER current density has linear relation in Mn-TaO_x, the Mn content which is below the detection limit of XPS is affected on the enhancement of OER activity at Ta oxide-based electrocatalyst.

Introduction

On October 2019, Intergovernmental Panel on Climate Chang (IPCC) released special report named "Global Warming of 1.5 ºC", and the report alarmed that if the average temperature of earth at 2030 reaches 1.5 ºC higher than that at era of industrial revolution, the global warming cannot stop itself and its speed will also be accelerated. To overcome this crisis, carbon dioxide emission gas must be reduced, and it must be widely installed of hydrogen all over the world. Moreover, it is not enough to install hydrogen but should be change to establish CO_2-free–hydrogen society, especially "Green Hydrogen[1]" society. As is well known, water electrolysis is essential technology to produce "Green Hydrogen" from renewable energies such as wind and solar power. Proton exchange membrane water electrolysis (PEMWE) is one of promising water electrolysis to expand production and installation. In Japan, hydrogen-based autonomous energy supply system have released from Toshiba Corp., Japan as nick name of "H_2One^{TM}" and uses for Power-to-Gas as distributed power supply in demonstration project[2]. The PEMWE is one of device installed in H_2One, so that its system reaches demonstration stage and will be ready to commercialize in near future. However, the conventional electrocatalysts for PEMWE are precious metal materials, and especially, the iridium oxide (IrO_2) uses as anode. As the iridium is by-product of platinum, its resources is very poor, and it is afraid that the cost

will be higher with installation PEMWE system. Moreover, it is reported that the IrO_2 is easy to cause the degradation under dynamic operation condition which is simulated variable renewable energy (VRE) and the catalytic activity of oxygen evolution reaction (OER) became lower by dynamic operation[3-4]. Therefore, the non-platinum group metals (PGM) oxide anode should be required for Green Hydrogen production. We focused on group 4 and 5 metal oxide, such as titanium (Ti) and tantalum (Ta) oxide. It is already reported that Ti oxide has potential for OER activity from density functional theory (DFT) calculation[5]. In our previous results, Ti oxide-based electrocatlyst has OER activity in sulfuric acid. However, it does not have significant activity for the OER[6]. In the term of Ta oxide, it has enough stability in the acidic media[7] but it had also poor activity for the OER[8-10]. In this study, we have prepared not Ta oxide but Ta oxide-based electrocatalyst with and without addition and investigated its catalytic activity for the OER in acidic solution.

Experimental

Synthesis of Ta compounds film with and without addition

Ta compound films were formed on Ti rods (ϕ = 5.0 mm, The Nilaco corp., Japan) as a base material, using the R.F. magnetron sputtering (MUE-ECO-EV, Ulvac). Target was Mn or Ta disks (ϕ = 50.8 mm, t = 5 mm, 99.9%, E-Metals; Mn, Furuuchi Chemical Corp.;Ta, Japan). Gas atmosphere in the chamber was a mixture of Ar and O_2 gas. After polishing and washing by acetone and pure water, the Ti rods were heated from 300 °C during the film formation by use of an infrared lamp heater. The flow rates of Ar and O_2 during the sputtering were kept at constant for 10 cm^3min^{-1}. Ta-based thin film catalysts prepared by Ta target, and Mn target with Ta piece of plate are expressed as TaO_x or Mn-TaO_x, respectively. In the case of formation of binary electrode such as Mn-TaO_x, it is considered the difference of sputtering rate between Mn and Ta. Mn addition was varied from 0 to 80 at%. Partial pressures of Ar (p_{Ar}) and O_2 (p_{O_2}) were calculated by multiplying the ratio of the flow rate of each gas by the total pressure in the chamber. Sputtering power and sputtering time were fixed at 150 W and 20 min, respectively. To compare with another oxide-based electrocatalyst, we also prepared Ti compound films with Mo addition of 10 at% formed on Ti rods (Mo-TiO_x) by the sputtering under at 0.23 Pa of p_{Ar} and p_{O_2} at 100 °C of substrate heating temperature for 20 min of formation time.

Electrochemical measurements

All electrochemical measurements were carried out using a three-electrode cell at 30 °C in 1 M H_2SO_4. A reversible hydrogen electrode (RHE) and a carbon plate were used as a reference and a counter electrode, respectively. Ta compound films with and without addition formed on Ti rod used as working electrode. In order to evaluate the catalytic activity for the OER, slow scan voltammetry (SSV) using potentiostat (Model PS-08, Toho Technical Research, Japan) and function generator (FG-02, Toho Technical Research, Japan) was performed under N_2 atmosphere. Current density was based on the geometric surface area of the working electrode. The resistance of the film (R_{film}) and charge transfer (R_{ct}) was evaluated by AC impedance spectroscopic measurements in the frequency range from 10^5 to 10^{-1} Hz using frequency response analyzer (FRA5022, NF Corporation, Japan). In the case of demonstration for Mott-Schottky plots, the potential was varied from 0 to 2.5

V while the frequency range was constant at 1 kHz.

Results and discussion

Figure 1 shows XPS spectra of Ta oxide-based electrocatalyst with Mn addition of 50% (Mn50-TaO_x) before and after electrochemical measurement. The color of sample has not changed before and after electrochemical measurement. According to Fig. 1(a) of XPS spectra of Mn2p, the peak identified Mn oxides such as MnO, Mn_2O_3, and MnO_2 was clearly detected around 641 eV in the spectra of sample before electrochemical measurement[11]. It means that surface of Mn50-TaOx was contained Mn oxides. After electrochemical measurement, the peak which was identified Mn oxides was completely disappeared, and it is suggested that most amount of Mn oxides contained in the sample before electrochemical measurement was disappeared during electrochemical measurement, and very few amount of Mn species below detection limit of XPS (< 1 at%) was possibly remained in the surface of electrode.

In Fig. 1(b) of XPS spectra of Ta4f, the peak was observed slightly lower region which is corresponded to Ta_2O_5 at 26.5 eV[12] in the spectra of sample before electrochemical measurement. After the electrochemical measurement, the peak was shifted in higher binding energy and that is corresponded to Ta_2O_5 at 26.5 eV. According to result of spectra, the initial oxidation state of tantalum was slightly lower than Ta_2O_5, and the state after electrochemical measurement was shifted to higher state which was identified Ta_2O_5. From Fig. 1(a) and (b), the surface of sample after electrochemical measurement was mainly consisted of Ta_2O_5 with very few amount of Mn species.

Figure 2 shows Tafel plots of TaO_x and Mn-TaO_x in 1 M H_2SO_4 at 30°C. The horizontal axis is based on the geometric current density (i_{geo}). The samples of Mn-TaO_x have obviously higher i_{geo} than that of TaO_x, and Mn addition is effective for enhancement of i_{geo} of TaO_x. Moreover, the redox peak of Mn(III)/Mn(IV)[13-15] around 1.5 V was also detected in Tafel plots of Mn2-, Mn40-, and Mn50-TaO_x. Considering this phenomenon and XPS results, it implies that these samples of Mn-TaO_x has contained a very little amount of Mn species after electrochemical measurement and these Mn species lead to

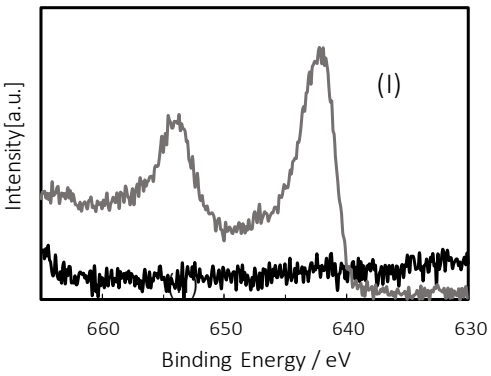

Figure 1(a). XPS spectra of Mn2p at Mn50-TaO_x before (I) and after (II) electrochemical measurement.

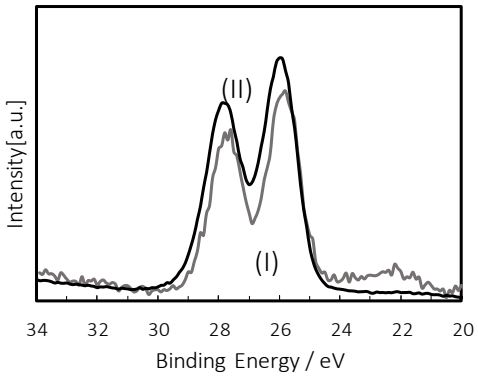

Figure 1(b). XPS spectra of Ta4f at Mn50-TaO_x before (I) and after (II) electrochemical measurement.

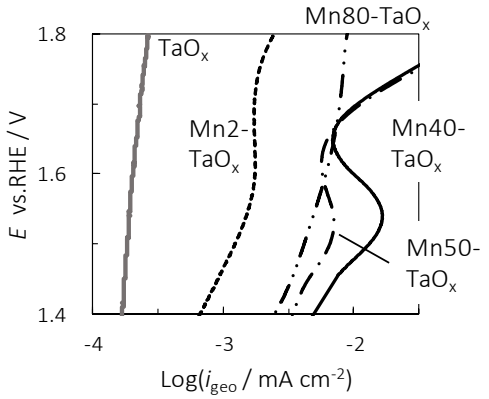

Figure 2. Tafel plots of Mn-TaO_x and TaO_x in 1 M H_2SO_4 at 30 °C.

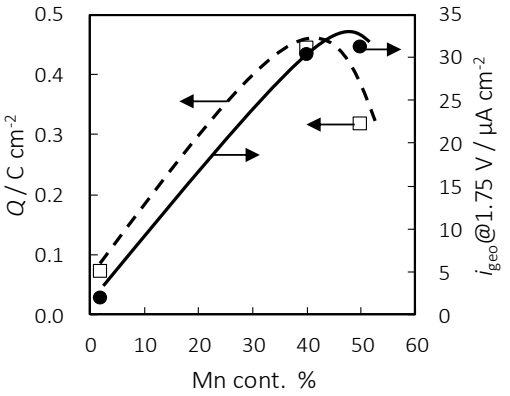

Figure 3. Relationship Q and i_{geo} at 1.75 V as a function of Mn content.

enhance the i_{geo} of TaO_x for the OER. To discuss the relationship between Mn species in Mn-TaO_x and the i_{geo} for the OER quantitatively, we calculated the electric charge of redox peak as shown in following equation:

$$Q = \int_{t_1}^{t_2} \left(i_{\text{geo\_SSV}} - i_{\text{geo\_explt}}\right) dt \quad [1]$$

where Q, i_{geo_SSV}, and i_{geo_explt} means the electric charge of redox peak, the geometric current density from SSV, and the geometric current density extrapolating from Tafel plots, respectively.

Figure 3 shows the Q and the i_{geo} at 1.75 V as a function of Mn addition. From this figure, there is linear relation between the i_{geo} and the Q. This means that Mn species including in Mn-TaO_x whose containing amount was below detection limit of XPS measurement enhances the catalytic activity for the OER.

To compare with our past results[16-17], Fig. 4 shows polarization curve of Mn40-TaO_x. This figure also shows polarization curves of Mo-TiO_x. Tafel slope of Mn40-TaO_x and Mo-TiO_x were 105, and 91 mV·dec^{-1} while that of TaO_x was 280 mV·dec^{-1}. According to Fig. 4, the i_{geo} at 2.0 V of Mn40-TaO_x was 350 times larger than that of Mo-TiO_x.

To analyze the factors for OER current, we have also evaluated results from EIS measurement. Figure 5 shows the charge transfer resistance (R_{ct}) at 2.0 V of Mn40-TaO_x and Mo-TiO_x. The R_{ct} of Mn40-TaO_x was one-fiftieth smaller than that of Mo-TiO_x. As a

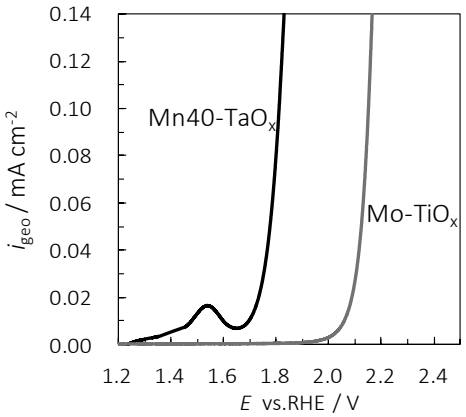

Figure 4. Polarization curves of Mn40-TaO_x and Mo-TiO_x in 1 M H_2SO_4 at 30 °C.

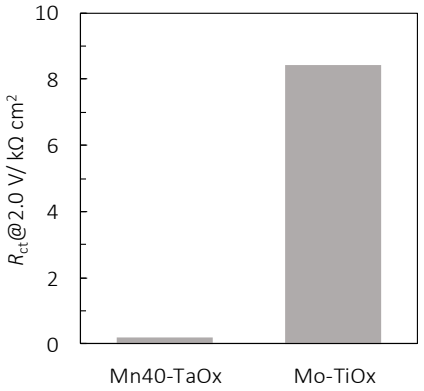

Figure 5. Charge transfer resistance (R_{ct}) at 2.0 V of Mn40-TaO_x and Mo-TiO_x.

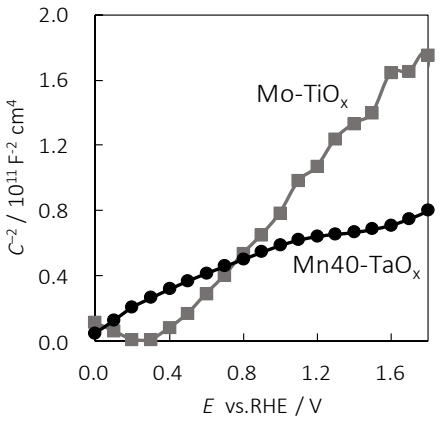

Figure 6. Mott-Schottky plots of Mn40-TaO_x and Mo-TiO_x.

result, the catalytic activity of Mn40-TaOx for the OER was clearly higher than that of Mo-TiO_x.

Figure 6 shows the Mott-Schottky plots of Mn40-TaO_x and Mo-TiO_x to evaluate the properties of semiconductor. Both samples showed n-type semiconductor because of positive slope in Fig. 6. The slope of Mn40-TaO_x and Mo-TiO_x were 1.2×10^{-11} and 6.2×10^{-10}, and the slope of Mn40-TaO_x was smaller than that of Mo-TiO_x. It is suggested that the carrier concentration of Mn40-TaO_x was larger than that of Mo-TiO_x, so that the electric conductivity of Mn40-TaO_x was higher than that of Mo-TiO_x. Above all, the OER current at Mn40-TaO_x has enhanced by both effects on the catalytic activity and the electric conductivity compared to that at Mo-TiO_x.

Conclusion

In order to develop non-PGM anode electrocatalyst for proton exchange membrane water electrolysis, the catalytic activity of Ta oxide-based electrocatalyst with and without Mn addition for the oxygen evolution reaction (OER) have been investigated. Analyzing XPS spectra of Ta oxide-based electrocatalyst film with Mn addition of 50 at% (Mn50-TaO_x), Mn oxide was contained before electrochemical measurement, but it was almost disappeared after electrochemical measurement. Mn50-TaO_x after electrochemical measurement was mainly consisted of Ta_2O_5. According to results from electrochemical measurement, Ta oxide-based electrocatalyst film with Mn addition (Mn-TaO_x) has higher geometric current density (i_{geo}) than that without any addition (TaO_x). Especially, some polarization curves of Mn-TaO_x have redox peak of Mn(III)/Mn(IV). There is linear relation between the i_{geo} for the OER and the electric charge (Q) of redox peak of Mn species. It is suggested that Mn species including in Mn-TaO_x whose containing amount was below detection limit of XPS measurement enhances the catalytic activity of TaO_x for the OER. In addition, Ta oxide-based electrocatalyst film with Mn addition of 40 at% (Mn40-TaO_x) has also much higher i_{geo} than Ti oxide based electrocatalyst with Mo addition of 10 at% (Mo-TiO_x) as our past results. Since the charge transfer resistance (R_{ct}) and slope of Mott-shottky plots of Mn40-TaO_x were smaller than that of Mo-TiO_x, the

reason why the Mn40-TaO_x has much higher i_{geo} than Mo-TiO_x is that Mn40-TaO_x was improved by both effects on the catalytic activity and the electric conductivity compared with that at Mo-TiO_x.

Acknowledgments

This work is partially supported by the Toyota Mobility Foundation (TMF), Tonen General Sekiyu Research / Development Encouragement & Scholarship Foundation, and Iketani Science and Technology Foundation.

References

1. K. Ota, A. Ishihara, K. Matsuzawa, and S. Mitsushima, *Electrochemistry*, **78**, 970 (2010).
2. https://www.toshiba-energy.com/hydrogen/file/H2One_Leaflet_EN.pdf
3. S. M. Alia, and G. C. Anderson, *J. Electrochem. Soc.*, **166**, F282 (2019).
4. G. Papakonstantinou, G. Algara-Siller, D. Teschner, T. Vidaković-Koch, R. Schlőgl, and K. Sundmacher, *Appl. Ener.*, **280**, 115911 (2020).
5. M. García-Mota, A. Vojvodic, H. Metiu, I. C. Man, H-Y Su, J. Rossmeisl, and J. K. Nørskov, *ChemCatChem*, **3**, 1607 (2011).
6. K. Matsuzawa, K. Sumi, R. Suzuki, Y. Kuroda, S. Mitsushima, A. Ishihara, and K. Ota, *Abst. 235th ECS Meeting*, I01-1423, Dallas, USA (2019).
7. A. Ishihara, Y. Ohgi, K. Matsuzawa, S. Mitsushima, and K. Ota, *Electrochim. Acta*, **55**, 8005 (2010).
8. K. Matsuzawa, K. Yamauchi, C. Igarashi, M. Aihara, S. Mitsushima, and K. Ota, *ECS Trans.*, **33**(39), 247 (2011).
9. K. Yamauchi, K. Matsuzawa, K. Ota, and S. Mitsushima, *ECS Trans.*, **41**(17), 21 (2012).
10. K. Matsuzawa, K. Goto, K. Takahashi, Y. Kohno, K. Ota, and S. Mitsushima, *ECS Trans.*, **53**(9), 3 (2013).
11. M. C. Biesinger, B. P. Payne, A. P. Grosvenor, L. W.M. Lau, A. R. Gerson, and R. St.C. Smart, *Appl. Surf. Sci.*, **257**, 2717 (2011).
12. Y. Kuo, *J. Electrochem. Soc.*, **139**, 579 (1992).
13. M. Moria, C. Iwakura, and H. Tamura, *Electrochim. Acta*, **24**, 357 (1979).
14. A.M. Moussard, J. Brenet, F. Jolas, M. Pourbaix, and J. van Mylder, *Atlas d'e´quilibres Electrochimiques*, p. 286, Gauthier-Vil-lars, Paris (1963).
15. B. Messaoudi, S. Joiret, M. Keddam, and H. Takenout, *Electrochim. Acta*, **46**, 2487 (2001).
16. K. Sumi, A. Ishihara, Y. Kuroda, S. Mitsushima, K. Ota, and K. Matsuzawa, *Abst. IUMRS-ICA 2019*, #179, Perth, Australia (2019).
17. K. Matsuzawa, S. Hirayama, K. Sumi, and A. Ishihara, *Abst. PRiME2020*, I01-1423, Online (2020).

Author Index